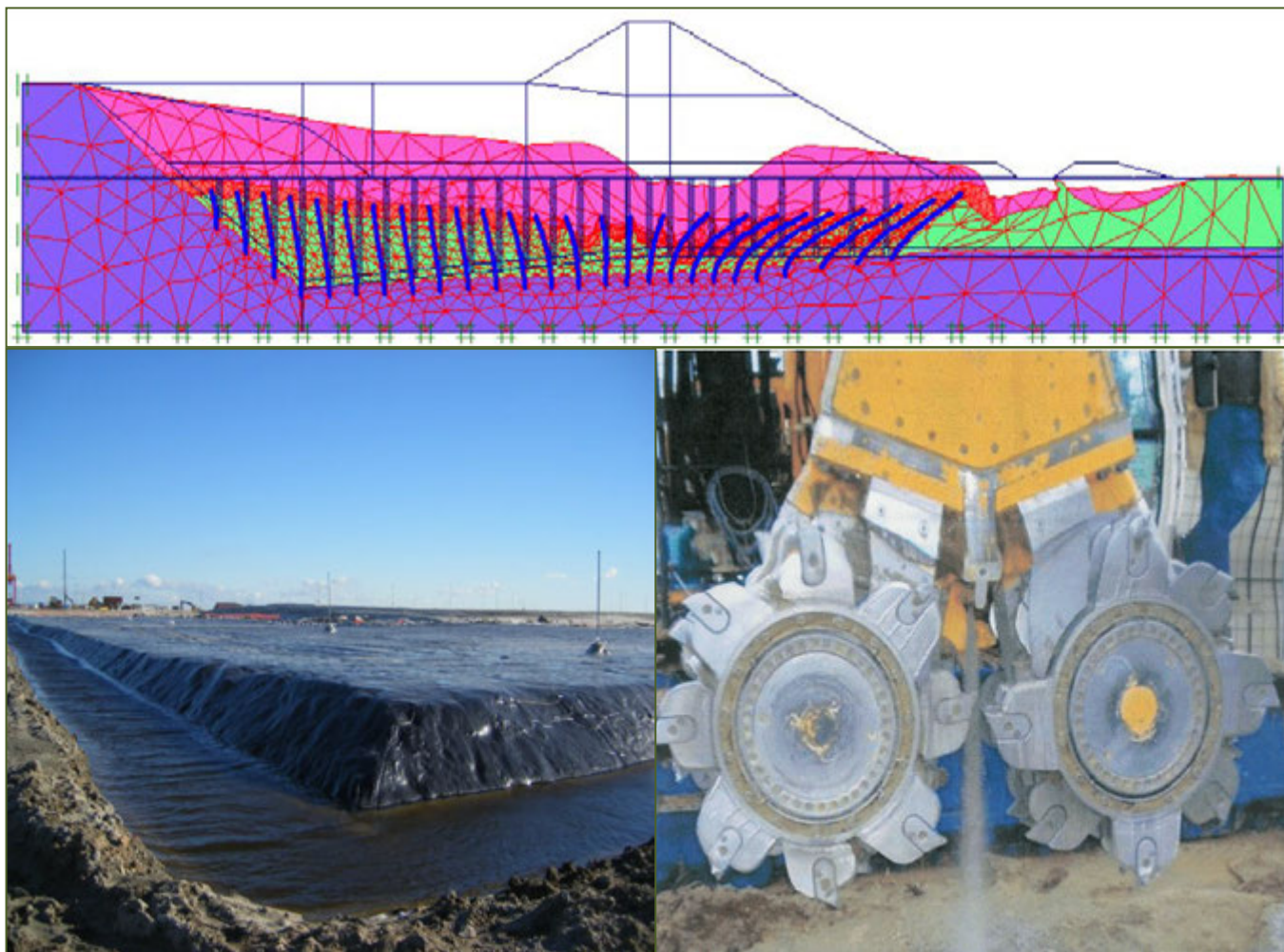


PROCEEDINGS OF THE INTERNATIONAL SYMPOSIUM

TC 211

IS-GI Brussels 2012



Recent Research, Advances & Execution Aspects of **GROUND IMPROVEMENT WORKS**

31 May – 1 June 2012, Brussels, BELGIUM

VOLUME IV

Organised by:

ISSMGE Technical Committee TC 211 Ground Improvement

Edited by:

Nicolas Denies & Noël Huybrechts

Belgische Groepering voor Grondmechanica en Geotechniek
Groupement Belge de Mécanique des Sols et de la Géotechnique

Comité Français de Mécanique des Sols



Recent Research, Advances & Execution Aspects of Ground Improvement Works

Edited by

Dr. Ir. Nicolas Denies

Belgian Building Research Institute (BBRI-CSTC-WTCB), Belgium

Ir. Noël Huybrechts

Belgian Building Research Institute (BBRI-CSTC-WTCB), Belgium

Editorial address

Ground Improvement is a large and important domain in soil mechanics and geotechnical engineering and consists in a wide variety of techniques and methods adapted to a broad range of problems. The amount of contributions to the proceedings of this symposium is certainly a proof of that.

It cannot be denied that during the last decades the importance of the ground improvement market has enormously increased. New methods, tools and procedures have been developed and applied in practice. In order to support this evolution in a scientific way, research programs have been and are being carried out worldwide, leading to more and better insights and delivering the basis for the establishment of design methods, quality control procedures and standards.

Due to the increasing interest of the construction sector for Ground Improvement techniques, the Belgian Building Research Institute (BBRI) has got more and more involved in projects addressing ground improvement during the last decade, most of them in a fruitful partnership with the Belgian Association of Foundation Contractors (ABEF).

In line with this evolution, the Geotechnical Division of the BBRI supports since 2005 the activities of the ISSMGE TC 211 Ground Improvement, which results today in the organization of an international symposium with more than 1600 pages of publications spread out over 4 Volumes:

- *Volume 1* of the proceedings contains the contributions of the 7 General Reporters, the Louis Ménard lecture held by *Patrick Mengé*, and the specialty lecture of the ISSMGE president *Jean-Louis Briaud*.
- *Volumes 2 to 4* contain more than 140 papers, subdivided in 7 Sessions, each of them dealing with a particular domain of Ground Improvement.

It can be noted that 40% of the papers deal with soil stabilisation and deep mixing, proving the huge interest in these techniques. This is not surprising, as they are outstanding and competitive sustainable construction methods.

We believe that the content of the present proceedings gives a very good overview of recent and on-going research actions and practices with regard to Ground Improvement. Moreover, we are convinced that they will contribute significantly to the further development of quality control procedures and standards.

Finally we would like to thank the Belgian Federal Public Service Economy, the NBN (Belgian standardization organization) and the Flemish Governmental Agency for Innovation by Science and Technology (IWT) for their financial support of the BBRI research programs addressing Ground Improvement techniques.

The Editors,

*Nicolas Denies & Noël Huybrechts
Geotechnical Division, Belgian Building Research Institute, Brussels, Belgium*

Table of contents of VOLUME IV

Session 6 – SOIL REINFORCEMENT IN FILL AND IN CUT

15 years of experience with geotextile encased granular columns as foundation system <i>D. Alexiew, M. Raithel, V. Küster and O. Detert</i>	IV-3
Modelling and analysis of the pullout behaviour of Granular Pile Anchor in expansive soils <i>A. N. Aljorany</i>	IV-21
Bearing Capacity of Foundations Reinforced with Micropiles <i>J. Bolouri Bazaz and H. Jalilan</i>	IV-29
Numerical Analysis of walls constituted by fine soil reinforced with Geosynthetics <i>D.M. Carlos, M. Pinho-Lopes and M.L. Lopes</i>	IV-41
The undrained mechanical behaviour of a fibre-reinforced heavily over-consolidated clay <i>A. Ekinici and P.M.V. Ferreira</i>	IV-53
A simple expression of the shear strength of anisotropic fibre-reinforced soils <i>A. Flora and S. Lirer</i>	IV-63
Comparison of the performance of rectangular footings on cohesionless soils reinforced with geogrid and geotextile <i>C. Gel, S. Oguzhan Akbas and O. Anil</i>	IV-75
Drilled shafts for slope stabilization in expansive soils <i>Ramanuja Chari Kannan</i>	IV-85
Soil Reinforcement Vegetation Effect An analysis applied to the Earth moving volume of California High Speed Railway System <i>L. Fort López-Tello and C. Fort Santa-María</i>	IV-95
Realization of a railway enlargement in unstable excavations alongside the existing line at Dilbeek (Belgium) <i>W. Maekelberg, J. Verstraelen and E. De Clercq</i>	IV-107
Performance of multi-anchor walls under cyclic transient flooding <i>Y. Miyata, R. J. Bathurst, T. Konami and K. Dobashi</i>	IV-123
Laboratory study of displacements in a geogrid reinforced soil model under lateral earth pressures <i>L. Ruiz-Tagle and F. Villalobos</i>	IV-133
Case studies on application of sandwich connection design for shored reinforced earth walls <i>J. E. Sankey and S. Rafalko</i>	IV-141
Study of shored mse walls (smse) in high earthquake <i>K Truong, J. Sankey and J. Sullivan</i>	IV-151
Ice-Soil Composites Created by Method of Cryotropic Gel Formation: A preliminary report of direct shear and permeability tests <i>N. Vasiliev, A. Ivanov, V. Sokurov, I. Shatalina and K. Vasilyev</i>	IV-161
Realisation of integrated steep landscape slopes within existing railway embankments <i>J. Verstraelen, C. Lejeune and E. De Clercq</i>	IV-169

Session 7 – BIOGROUT and other GROUTING METHODS

Numerical Studies on the Design of Compaction Grouting <i>A. Anthogalidis, U. Arslan and O. Reul</i>	IV-183
Grand Carré de Jaude: an exceptional building site of soil treatment by jet-grouting in the middle of a volcano <i>P. Berthelot, Fr. Durand, O. Madec and A. Reynaud</i>	IV-193
A large diameter jet grouting method for arrival of shield tunnelling machine <i>S. H. Cheng, R. K. N. Wong and H. J. Liao</i>	IV-205
Prediction of jet grouting efficiency and columns average diameter <i>P. Croce, A. Flora, S. Lirer and G. Modoni</i>	IV-215
Offshore Jet Grouting - A Case Study <i>T. Durgunoglu, F. Kulac, S. Ikiz, O. Sevim and O. Akcakal</i>	IV-225
Construction of the Bellinzona Portal Ceneri Base Tunnel, AlpTransit Gottard Tunnel <i>R. D. Essler and Fr. M. Rossi</i>	IV-235
Modelling of Jet Grouting and its interactions with surrounding soils <i>J. M. Gesto, A. Gens and M. Arroyo</i>	IV-247
Laboratory investigations on groutability of the alluvial used in ground improvement for construction metro tunnels <i>M. Gharouni Nik, M. Esmaeili, and H. Hosseinpour</i>	IV-257
The design and execution of Settlement Mitigation Measures for Bridge 404, North South Metro Project, Amsterdam <i>F.J. Kaalberg, R.D.Essler and R. Kleinlugtenbelt</i>	IV-267
Jet grouting foundation under the overpass of the A27 in the polder construction sealed with a foil at Amelisweerd <i>O.S. Langhorst</i>	IV-281
Injections of microfine cement grouts into sand columns for penetrability and effectiveness evaluation <i>I.N. Markou, D.N. Christodoulou and A.I. Droudakis</i>	IV-291
Ground Improvement Solutions for the new Cruise Terminal in Lisbon <i>A. Pinto, R. Tomásio and J. Ravasco</i>	IV-303
Analysis of soil solidification with the help of “jet grouting” method when constructing a municipal collector <i>A.B. Ponomaryov, A.L. Novodzinsky and A.V. Zakharov</i>	IV-311
Application of a sensitivity analysis procedure to interpret uniaxial compressive strength prediction of jet grouting laboratory formulations performed by SVM model <i>J. Tinoco, A. Gomes Correia and P. Cortez</i>	IV-317
Innovative monitoring tools for on line monitoring of excavations. A monitoring test site <i>G. Van Alboom, L. De Vos, K. Haelterman and W. Maekelberg</i>	IV-327
Preservation of Panorama Mesdag, The Hague <i>A.E.C. van der Stoel and M. de Koning</i>	IV-339
Groutability of clean sand using sodium pyrophosphate modified bentonite suspensions <i>J. Yoon, C. El Mohtar</i>	IV-349

OTHER

Ground freezing of diaphragm wall joints in Amsterdam <i>J.K. Haasnoot and D.G. Goeman</i>	361
SHRP 2 R02: Geotechnical Solutions for Transportation Infrastructure: A Web-Based Toolkit <i>V. R. Schaefer, R. R. Berg and S. Caleb Douglas</i>	367

CONTRIBUTIONS

SESSION 6
SOIL REINFORCEMENT IN FILL AND IN CUT

15 years of experience with geotextile encased granular columns as foundation system

Dimiter Alexiew, HUESKER Synthetic GmbH, Gescher, Germany, dalexiew@huesker.de
Marc Raithel, Kempfert + Partner Geotechnik, Würzburg, Germany, m.raithel@kup-geotechnik.de
Volker Küster, Josef Möbius Bau-Aktiengesellschaft, Hamburg, Germany,
volker.kuester@moebiusbau.com
Oliver Detert, HUESKER Synthetic GmbH, Gescher, Germany, detert@huesker.de

ABSTRACT

The Geotextile Encased Column (GEC) foundation system for earthwork structures built on soils of low bearing capacity was launched onto geotechnical engineering some 15 years ago and is now considered state-of-the-art in Germany. The GEC system provides a geotechnical foundation solution for weak and very weak soils where more traditional ground improvement techniques are unlikely to be viable. This paper provides a system description, the required design procedure and details of ongoing long-term monitoring. Information is also included on the continuous improvements which have been made to the GEC system in response to the technical and financial requirements of large civil engineering projects as well as current potential and research directions and the current regulations and guidelines governing use of the system in Germany. In the future, GECs are likely to be used world-wide for water and land engineering projects in very soft soils.

1. INTRODUCTION

Beginning in 1994, the German contractor Möbius, with the assistance of Huesker Synthetic and Kempfert & Partners, developed a system for the foundation of embankments in soft and very soft soil areas. The general idea was to create an alternative to conventional piles or columns of any kind, and at the same time allow the possibility of constructing compacted gravel (and in reality, sand) columns in very soft soils (Figure 1), which previously would have had insufficient lateral support. Compacted gravel column techniques are usually limited to soft soils with undrained cohesion (undrained, unconsolidated shear strength) $s_u \geq 15 \text{ kN/m}^2$. The problem was solved by confining the compacted sand or gravel column in a high-modulus geosynthetic encasement (Huesker's Ringtrac[®] GEC). The general idea of Geosynthetic Encased Columns (GEC) is shown in Figure 2. Development of the technology, design procedures [1] and appropriate geosynthetics went hand-in-hand throughout the 1990's. The first projects started successfully in Germany around 1995. Since the inception of GEC's, more than 30 successful projects have been completed in countries including Germany, Sweden, Holland, Poland and Brazil. The GEC system is now accepted as a proven foundation solution and is now included within German design recommendations [2].



Figure 1: Installation of GEC from pontoons in extremely soft mud

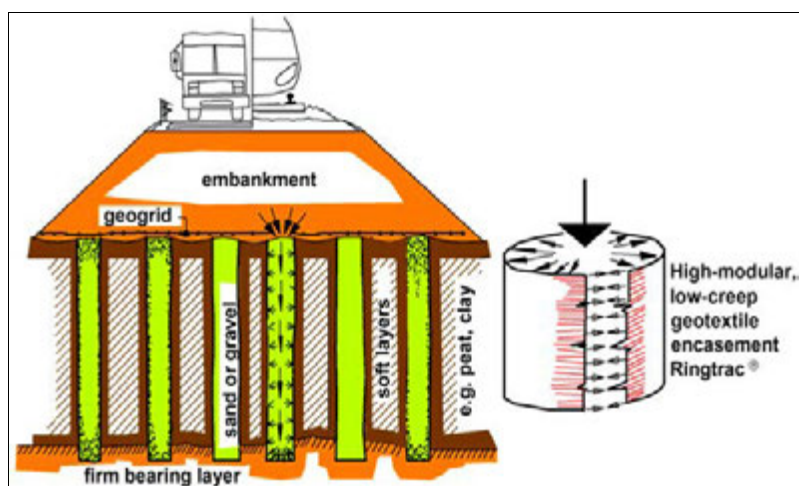


Figure 2: General idea of embankment on soft soil set on Geosynthetic Encased Columns (GEC)

2. GEC - SYSTEM DESCRIPTION

By the GEC-columns the main part of the load from the embankment will be transferred directly through the soft soil down to a firm stratum. Embankments on concrete, steel, and wooden piles are nearly settlement-free. The compression stiffness of the piles is so high, that practically no settlement occurs at the level of pile tops or caps. High strength horizontal geosynthetic reinforcement is typically installed above the piles to bridge over the soft soil between piles and equalize the embankment's deformations.

The vertical compressive behavior of the GECs is less rigid. The compacted vertical sand or gravel column starts to settle under load mainly due to radial outward deformation. The geosynthetic encasement, and to some extent the surrounding soft soil, provides a confining radial inward resistance acting similar to the confining ring in an oedometer, but being more extensible. The mobilization of ring-forces requires some radial extension of the encasement (usually in the range of 1 to 4 % strain in the ring direction) leading to some radial "spreading" deformation in the sand (gravel) columns and resulting consequently in vertical settlement of their top.

The GEC system therefore cannot be completely settlement-free. Fortunately, most of the settlement occurs during the construction stage and is compensated by some increase of embankment height. Finally, ensured by the strength and stiffness of sand or gravel, confining ring-force in the encasement and soft soil radial counter-pressure, a state of equilibrium is reached.

The specific characteristics of the GEC system are:

1. The primary function of the high-modular high-strength geotextile encasement is the radial confining reinforcement of the bearing (sand or gravel) column.
2. The secondary functions of the encasement are separation, filtration and drainage.
3. The system is not completely settlement-free.
4. The GEC is typically an end-bearing element transferring the loads to a firm underlying stratum.
5. The GECs are water-permeable; they practically do not influence the flow of groundwater streams, which has potential ecological advantages.
6. The GECs may also perform as high-capacity vertical drains.
7. The geotextile encasement is a key bearing / reinforcing element, capable of meeting high quality engineered design standards and specifications.
8. It is strongly recommended to install horizontal geosynthetic reinforcement on top of the GECs (at the base of the embankment). The horizontal reinforcement is used for the global stability, for transferring spreading forces or to facilitate load transfer into the columns.

The GEC foundation system was specially developed for earthwork structures built on weak and very weak subsoil. It comprises uniformly arranged columns, filled with non-cohesive material and enclosed in a geosynthetic sleeve, which transmit the structural loads to the bearing stratum (Figure 2).

The overall loads and stress concentrations above the column heads induce outwardly directed radial horizontal stresses in the columns. The particularity of the GEC system is that these stresses are counteracted not only by the inwardly acting pressure of the soft soil, but also – most importantly – by the radial resistance of the geotextile casing of high tensile stiffness (low radial extension).

The substantial circumferential tensile forces generated in the casing provide radial support to the columns and ultimately safeguard the equilibrium of the system, thereby allowing its use even in very soft

soils (and strictly speaking even in air with zero lateral soil support, Figure 3). The arrangement of geotextile-encased columns produces a ductile bearing system that is immune to buckling under the incident column loads. The use of GEC considerably reduces both absolute and differential settlement, while enhancing structural stability both during construction and after completion.



Figure 3: Demonstration of the confining capability of high strength geotextile encasement for GEC “in air”

As the columns also act as filtration-stable (thanks to the sleeve) mega-drains, they speed up the settlement and consolidation process. Later settlement, e.g. caused by traffic loads, is low and can, if necessary, be largely offset by means of temporary cover fill/surcharge. The GEC are arranged in a regular column grid. Based on the unit cell concept (Figure 4), a single column in a virtual infinite column grid can be considered. The influence area A_E of a single column A_C in triangular grid is a hexagonal element, which can be transformed into a circular element with an equivalent diameter D_E (“single cell design concept”).

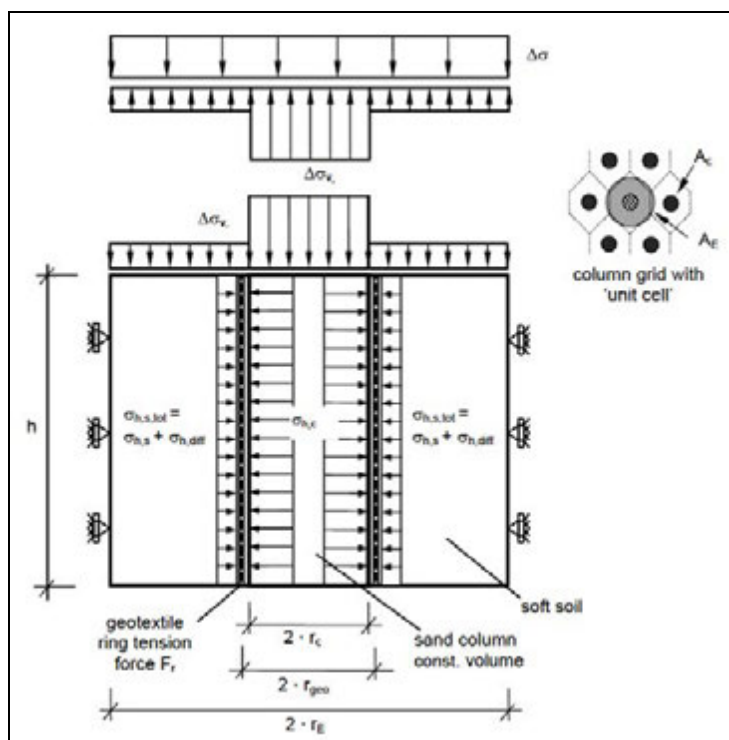


Figure 4: Geosynthetic Encased Column load-bearing system and “single cell” analysis model

Generally the German State-of-the-Art design procedure regarding the vertical and radial GEC-behaviour in the “single cell” is based on a second order theory, say deformations and strains are taken into account

while analysing the systems equilibrium. It reflects the real behaviour of the system including the stress-strain interaction of column fill, surrounding soft soil and the geotextile encasement. Consequently, the results of the procedure described shortly below include not only e.g. the required radial “ring” strength and (important) tensile stiffness of the encasement, but also e.g. the settlement of the top of the columns which controls finally the settlement of the embankment on top of them.

3. GEC: ANALYSIS AND DESIGN

The analysis and design of an embankment GEC foundation consist generally of two steps: First, what is sometimes called “vertical” design, concentrates on the vertical bearing and deformation behavior of the system neglecting overall stability etc. issues.

Second, the global stability (and sometimes the load transfer to the GECs) has to be guaranteed by means of appropriate horizontal geosynthetic reinforcement on top of the columns.

Analysis and design of a GEC foundation is undertaken either using an analytical method [1], [2], [3] or by numerical methods [1]. However, the most commonly adopted method is the analytical method, which is herein described in greater detail and included in the newly published German design guidance [2].

3.1. Column design

The procedure includes a confining force in the ring direction of the encasement based not only on tensile force at failure (“strength”) but on the complete stress-strain behavior of the geosynthetic. This behavior is defined by the tensile stiffness modulus in “ring” direction J , kN/m. Consequently, it is possible to calculate from the ring strain the radial widening of the GEC and the resulting vertical settlement on top of the GEC that will be equal to the average settlement of the embankment.

The bearing elements (GECs) are significantly stiffer than the surrounding soil and therefore attract a higher load concentration from the overlying embankment. Conversely, the pressure acting on the adjacent soil is lowered resulting in an overall reduction of the total settlements.

Generally, an analytical, axial symmetric model [1], [2], [3] is used for calculating and designing a geotextile encased column foundation (Figures 2 & 4) from the point of view of vertical bearing capacity and settlements. The model was developed on the basis of the conventional calculation models used for granular columns [4], [5] and updated to include the effect of the geotextile casing. There is an additional horizontal stress in the column $\Delta\sigma_{h,c}$ due to the additional vertical stress $\Delta\sigma_{v,c}$ over the column head. In view of the equilibrium between the additional surface loading $\Delta\sigma$ and the corresponding vertical stresses on the column $\Delta\sigma_{v,c}$ and the soft soil $\Delta\sigma_{v,s}$, it can be stated:

$$\Delta\sigma \cdot A_E = \Delta\sigma_{v,c} \cdot A_c + \Delta\sigma_{v,s} \cdot (A_E - A_c) \quad (1)$$

The vertical stresses due to the loading and the different soil weights produce horizontal stresses, where $\sigma_{h,c}$ and $\sigma_{h,s}$ are the surcharge stresses in the column and in the soft stratum:

$$\sigma_{h,c} = \Delta\sigma_{v,c} \cdot K_{a,c} + \sigma_{v,0,c} \cdot K_{a,c} \quad (2)$$

$$\sigma_{h,s} = \Delta\sigma_{v,s} \cdot K_{0,s} + \sigma_{v,0,s} \cdot K_{0,s}^* \quad (3)$$

(Note: $K_{0,s}^*$ replaced with $K_{0,s}$ if using the excavation method of installation rather than the displacement method, see Chapter 5)

The geotextile casing (installation radius r_{geo}) has a linear elastic behaviour (tensile stiffness J), whereby the ring tensile force F_R can be transformed into a horizontal stress $\sigma_{h,geo}$, which is assigned to the Ringtrac® geotextile:

$$F_R = J \cdot \Delta r_{geo} / r_{geo} \quad \text{and} \quad \sigma_{h,geo} = F_R / r_{geo} \quad (4)$$

By the use of the separate horizontal stresses, a differential horizontal stress can be defined, which represents the partial mobilisation of the passive earth pressure in the surrounding soft soil:

$$\sigma_{h,diff} = \sigma_{h,c} - (\sigma_{h,s} + \sigma_{h,geo}) \quad (5)$$

The stress difference results in an expansion of the column. The horizontal deformation Δr_s and the settlement of the soft soil s_s are calculated according to *Ghionna & Jamiolkowski* [4]. Assuming equal settlements of column s_c and soft soil s_s , the following calculation equation can be derived (oedometric modulus $E_{S,B}$, poisson ratio ν_B):

$$\Delta r_c = \frac{\Delta \sigma_{h,diff}}{E^*} \cdot \left(\frac{1}{a_E} - 1 \right) \cdot r_c \quad (6)$$

$$s_s = \left(\frac{\Delta \sigma_{v,s}}{E_{oed,s}} - 2 \cdot \frac{1}{E^*} \cdot \frac{\nu_s}{1-\nu_s} \cdot \Delta \sigma_{h,diff} \right) \cdot h \quad (7)$$

with:

$$E^* = \left(\frac{1}{1-\nu_s} + \frac{1}{1+\nu_s} \cdot \frac{1}{a_E} \right) \cdot \frac{(1+\nu_s) \cdot (1-2\nu_s)}{(1-\nu_s)} \cdot E_{oed,s}$$

and

$$a_E = A_c/A_E \quad (8)$$

The relationship between the settlement of the column s_c and the radial deformation at the column edge Δr_c for a constant volume of column material as a function of the original/installed radius r_0 or the original/installed height h_0 is:

$$s_c = \left(1 - \frac{r_0^2}{(r_0 + \Delta r_c)^2} \right) \cdot h_0 \quad (9)$$

A comparability of the horizontal deformations must be given,

$$\Delta r_c = \Delta r_{geo} + (r_{geo} - r_c) \quad (10)$$

There are equal settlements between the column and the soft soil:

$$s_c = s_s \quad (11)$$

At last the following calculation equation can be derived:

$$\left\{ \frac{\Delta \sigma_{v,s}}{E_{oed,s}} - \frac{2}{E^*} \cdot \frac{\nu_s}{1-\nu_s} \left[K_{a,c} \cdot \left(\frac{1}{a_E} \cdot \Delta \sigma_0 - \frac{1-a_E}{a_E} \cdot \Delta \sigma_{v,s} + \sigma_{v,0,c} \right) - K_{0,s} \cdot \Delta \sigma_{v,s} - K_{0,s} \cdot \sigma_{v,0,s} + \frac{(r_{geo} - r_c) \cdot J}{r_{geo}^2} - \frac{\Delta r_c \cdot J}{r_{geo}^2} \right] \right\} \cdot h = \left[1 - \frac{r_c^2}{(r_c + \Delta r_c)^2} \right] \cdot h \quad (12)$$

$$\text{and } \Delta r_c = \frac{K_{a,c} \cdot \left(\frac{1}{a_E} \cdot \Delta \sigma_0 - \frac{1-a_E}{a_E} \cdot \Delta \sigma_{v,s} + \sigma_{v,0,c} \right) - K_{0,s} \cdot \Delta \sigma_{v,s} - K_{0,s} \cdot \sigma_{v,0,s} + \frac{(r_{geo} - r_c) \cdot J}{r_{geo}^2}}{\frac{E^*}{(1/a_E - 1) \cdot r_c} + \frac{J}{r_{geo}^2}} \quad (13)$$

By adopting this deformation, the only unknown variable is $\Delta \sigma_{v,s}$. The equation can be solved iteratively by estimating this variable (although use of suitable software is recommended due to the potentially time consuming process of undertaking this by hand). More details are shown in Raithel [1] and also in Raithel & Kempfert [3]. It is important to note that the stress-strain behavior of the encasement is the key element for the performance of the system. Note also that the tensile stiffness modulus J is a time dependent parameter due to the creep strain of the encasement. Also from this point of view (say deformation long-term control) low-creep encasements have to be preferred.

3.2. Horizontal reinforcement design

The horizontal reinforcement (Figures 2 & 6) is used to ensure global stability, to taking over spreading forces as well as to facilitate if necessary (see below) load transfer into the columns and to equalize settlements.

Load transfer into the GEC is achieved primarily by the formation of stress arches in the embankment over them. Some additional support may be necessary similar to the situation with reinforced embankments on rigid piles (“membrane” or “bridging” function of the horizontal reinforcement). Generally, designing the horizontal reinforcement layers above the column heads for membrane forces can be dispensed with. However, the application of horizontal reinforcement for “membrane” bridging action is dependent upon the stiffness ratio between the column (stiffness $k_{s,T}$) and the soft soil (stiffness k_s) [2], see herein Table 1 corresponding to Table 10.2 in [2].

Table 1: Requirement for designing horizontal reinforcement for membrane forces as a function of stiffness ratios

Zone	Stiffness ratio	Design of horizontal geosynthetic reinforcement
I	$k_{s,T}/k_s \leq 50$	Design unnecessary
II	$50 < k_{s,T}/k_s \leq 75$	Design recommended
III	$k_{s,T}/k_s > 75$	Design necessary

For Zone 1 the horizontal reinforcement is installed as a structural element to satisfy global stability and/or to transfer spreading forces. For Zone 2, although significant changes in load behavior or larger settlements are not anticipated, in certain cases it may be necessary to design the reinforcement to act as a load transfer “membrane” component. For Zone 3, where the stiffness ratios are higher, the effectiveness of the foundation system is no longer guaranteed without designing the horizontal reinforcement for membrane forces. A minimum reinforcement is required using design resistance R_{Bd} no matter which zone is relevant. If it is necessary to design the horizontal reinforcement for membrane forces, then the appropriate methodology should be adopted [2].

For the GEC-System the second main function of horizontal reinforcement (to ensure global stability and to take over spreading forces) controls its design. Common geotechnical design procedures (as Bishop or Janbu) can be used modified by the presence of the horizontal reinforcement and additionally be the higher “mixed” strength of soft subsoil due the GECs [2].

The final result of the design of GEC-Foundation is a flexible, ductile, to a significant extent self-regulating and thus robust system, what can be in many cases a key advantage. Self-regulating load bearing behavior means that if the columns yield, the load is redistributed to the soft stratum, thereby increasing the ground resistance supporting the columns, which in turn leads to load redistribution back into the columns.

4. DESIGN POSSIBILITIES TO INFLUENCE THE SYSTEMS BEHAVIOR

Following are several options to control settlement and the vertical bearing capacity of the system:

1. Increase the percentage of column area to the total area (usually 10% to 20%) by increasing the diameter of GEC (usually 0.6 to 0.8 m) and/or decreasing their spacing (usually 1.5 to 2.5 m).
2. Use a better quality fill for the columns (e.g. gravel instead of sand).
3. Increase the tensile stiffness and strength of the ring direction of the geosynthetic encasement thus reducing settlement and increasing single column bearing capacity. The higher the tensile stiffness, the less the radial strain and consequently the compressibility of the column; this results in less settlement.

Additional information on the influence especially of the ring tensile stiffness and area ratio can be found e.g. in [6, 7]. Usually the increase of the ring tensile stiffness is the most flexible and powerful tool to reducing settlement and increasing bearing capacity.

And last but not least: the encasement has to be seamless - this results in significantly higher guaranteed strength and in a homogeneous stress-strain behavior in the most important bearing ring direction (Figure 5).

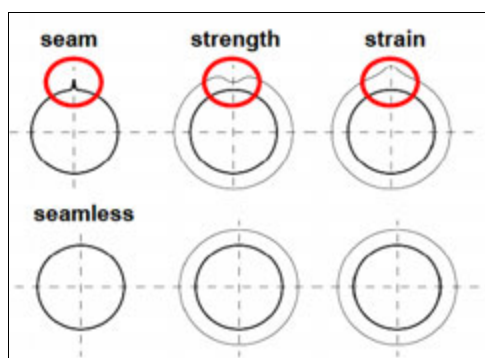


Figure 5: Difference between seamed and seamless encasements in terms of stress-strain behaviour



Figure 6: Example of horizontal geosynthetic reinforcement on top of already covered GECs for heavy loaded sensitive runways (left) and under a land reclamation embankment (GECs still visible) (right)

5. INSTALLATION METHODS

Two different options are generally available with regards to the GEC construction technology. The first option is the displacement method (Figure 7) where a closed-tip steel pipe is driven down into the soft soil followed by the insertion of the circular weave geotextile (Figure 8) and sand or gravel backfill. The tip opens, the pipe is pulled upwards under optimized vibration designed to compact the column. The displacement method is commonly used for extremely soft soils (e.g. $s_u < 5 \text{ kN/m}^2$) and/or where vibrations are not important.

The second construction option is the replacement method (Figure 9) with excavation of the soft soil inside the pipe. This method uses an open pipe where special tools remove the soil during or after driving the pipe down into the ground. The rest of the operation is identical to the displacement method. The excavation method is likely to be preferred with soils with high penetration resistance or when vibration effects on nearby buildings and road installations have to be minimised.

The advantage of the displacement method compared to the excavation method is based on the faster and more economical column installation and the effects of pre-stressing the soft soil. Furthermore it is not necessary to excavate and dispose soil. The excess pore water pressure, the vibrations and deformations have to be considered.

There are two options available when selecting the diameter of the circular weave geotextile (Ringtrac[®]). In the first option the diameter of the circular geotextile is slightly larger than the diameter of the steel pipe, thus allowing for a better mobilization of soft soil radial counter-pressure after extracting the pipe. The disadvantage is a larger column settlement based on the larger radial deformation due to an “unfolding” phase prior to mobilization of the geotextiles tensile modulus. In the second option, the diameter of the geotextile and the pipe are the same. This provides for a quick strain–tensile ring force mobilization, which results in less soft soil mobilization and higher ring-tensile forces, but in reduced settlement. The equal diameter option is preferred at present.

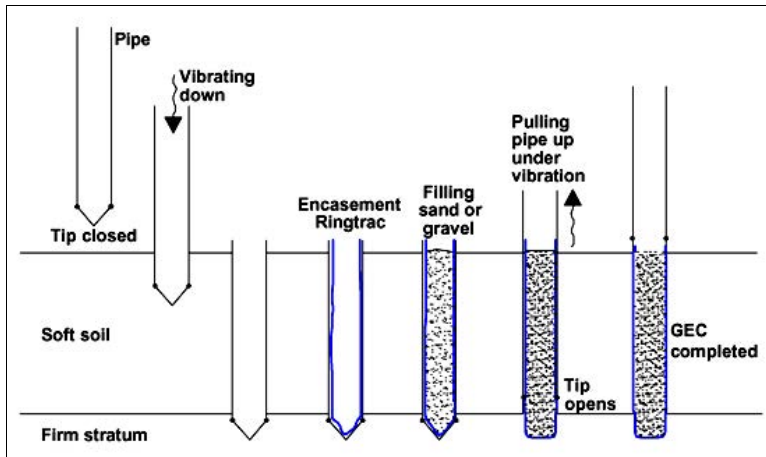


Figure 7: Displacement method of construction



Figure 8: Installation of geotextile encasement (displacement method)

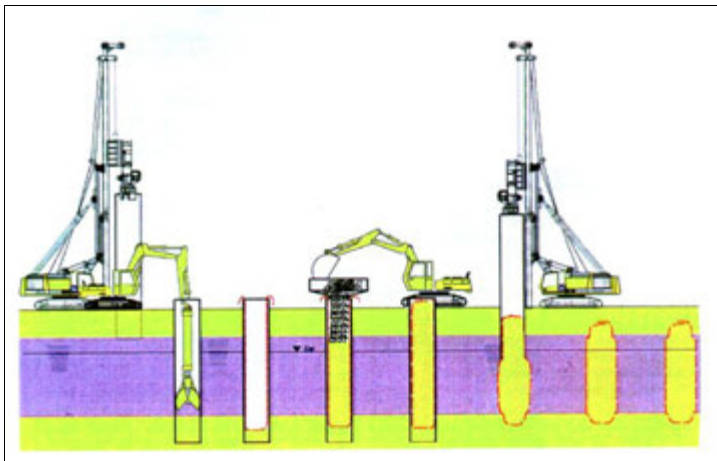


Figure 9: Replacement method of construction



Figure 10 : Completed columns

6. GEOTEXTILE ENCASUREMENT SELECTION

As previously explained the ring tensile stiffness and strength can influence the behaviour of the system significantly. The geotextile is required to support the horizontal radial stress variance for the design life of the structure.

In order to maintain the equilibrium state, designers need to have confidence in the long-term behaviour of the geotextile which provides radial support to the columns over their service life. In this regard, not only is the design strength of the encasing geosynthetic important, but so is the short- and long-term stress/strain behaviour. Insufficient radial support due to low ring-tensile modulus (in the short- or long-term) would result in bulging of the columns and redistribution of the horizontal and vertical stresses, resulting in potential large settlement of top of the GEC (i.e. and the embankment), and in a proportional increase in the vertical stresses acting on the adjacent soft soil thereby leading to further settlement. Partial or total loss of radial support would exacerbate this settlement, which could lead to settlements exceeding serviceability limits or even result in ultimate limit state conditions for the system.

The long-term behavior of geotextiles has long been an issue with designers, however extensive research on their durability and long-term behavior, including creep, mechanical damage and environmental degradation, have helped to allay most of these concerns. The polymer employed largely determines the properties of the encasement. The design engineer's ideal geosynthetic reinforcement would possess the following characteristics [8]:

- high tensile modulus (low strain values compatible to the common strains in soils, rapid mobilisation of tensile force)
- low propensity for creep (high long-term tensile strength and tensile modulus, minimum creep extension, lasting guarantee of tensile force)
- high permeability (lowest possible hydraulic resistance and as a result, no increasing pressure problems)
- little damage during installation and compaction of contacting fills
- high chemical and biological resistance

In the specific case of GEC the geotextile reinforcing encasement may not include joints or seams. This guarantees no weak zones without any reduction factors for joints and a constant tensile stiffness around the entire bearing ring direction. Up until now, the project designs required short- and long-term tensile stiffness from $J = 1.500$ to 6.000 kN/m and ultimate tensile ring strengths from 100 to 400 kN/m. Higher moduli and/or strengths have been also used for particular projects.

7. LONG TERM MEASUREMENTS OF THE GEC SYSTEM

7.1. General

The determination of residual settlement requires consideration of both primary settlement and secondary or creep settlement. The latter invariably determines the settlement behaviour of GEC foundations in service, given that primary settlement is accelerated through the action of the encased columns as large vertical drains and has usually abated by the end of the construction period.

The background literature [9], [10], describes how creep settlement is proportional to those changes in load that bring about deformation. As the stress concentration over the column heads entails a reduction

in the loads acting on the soft stratum, creep settlement is likely to be lower where encased columns are used than in unimproved subsoils. Moreover, where creep settlement is allowed for, the soft stratum undergoes a greater degree of settlement than the column.

Consequently, the interactive bearing system will normally bring about a redistribution of loads, with a higher proportion borne by the encased columns, and ultimately a new equilibrium state with even lower levels of stress in the soft soil. This, in turn, will further lower the degree of creep settlement in comparison to the unimproved scenario.

The achievement of reductions in creep settlement has been confirmed by long-term measurements.

7.2. Extension of AIRBUS Hamburg-Finkenwerder site at "Mühlenberger Loch"

This project, which was presented among others at the Austrian Geotechnical Conference in 2001, was successfully implemented between 2001 and 2004. Completed in September 2002, the 2,500 m long dike enclosing the extension area was founded on a total of approximately 60,000 GECs. As part of the structural checks on the ground engineering concept, the stability and deformation predictions were verified by on-site measurements during construction. The comprehensive measurement instrumentation included horizontal and vertical inclinometers, settlement indicators and measurement marks, as well as water pressure and pore-water pressure transducers. Most of the measurement instrumentation was designed for continued monitoring after completion of the dike. Typical results are shown in Figures 11 & 12.

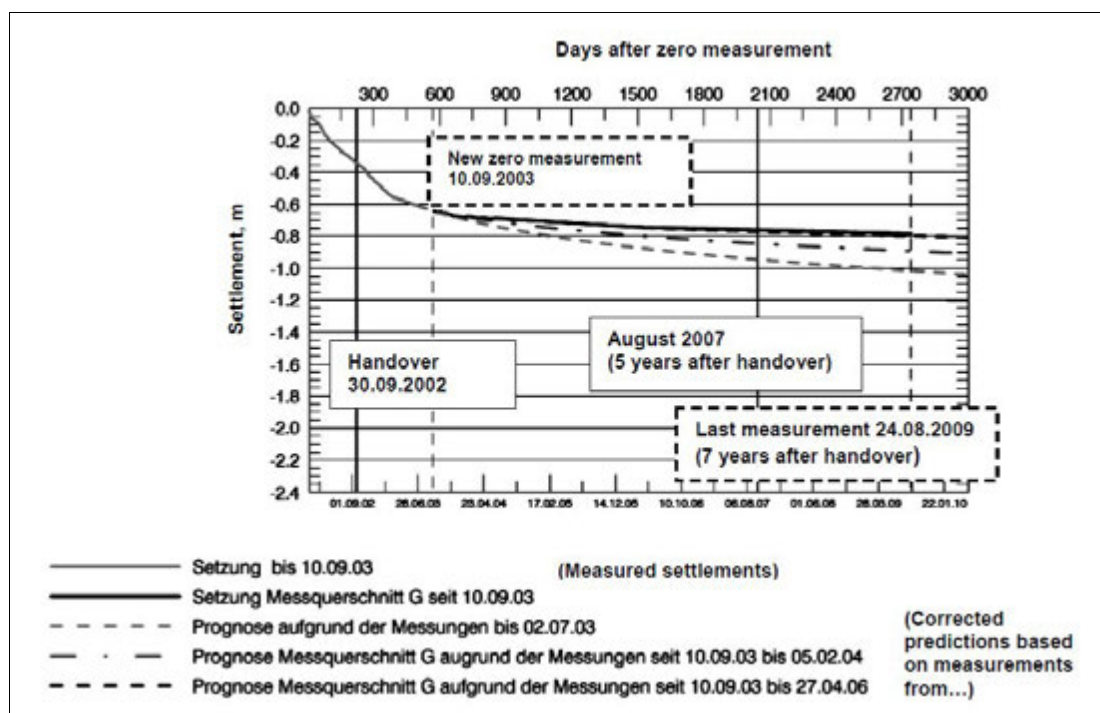


Figure 11: Results of long-term measurements and comparison with creep settlement predictions for foundation to dike enclosing extension to aircraft production site at Hamburg-Finkenwerder

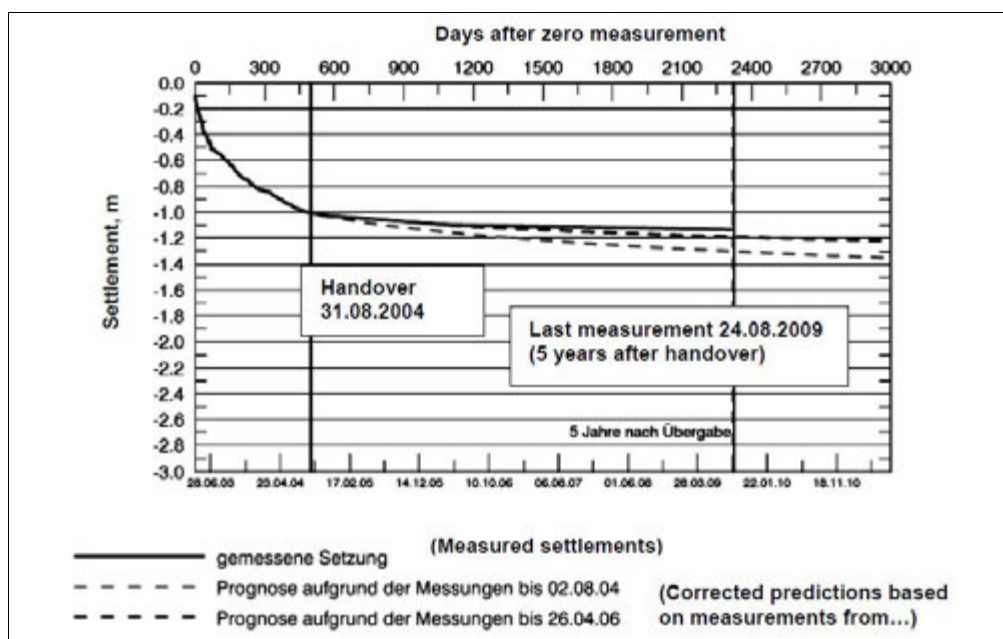


Figure 12: Results of long-term measurements and comparison with creep settlement predictions for GEC foundation to front Finkenwerder dike

The dike camber provided to offset long-term settlement was first checked when primary settlement was practically complete after roughly one year. A computational prediction was then made of further creep settlement. A further check in 2004 already revealed significantly lower creep settlement than initially forecast. A new prediction was then made using creep factors derived from the measurements by means of logarithmic regression functions. The predictions were revised again in 2006 on the basis of further settlement measurements and these have since proved to reliably model the pattern of creep settlement measured over the last eight years or so. The GEC foundation of the front Finkenwerder dike, which is a continuation of the dike enclosing the AIRBUS site extension, has exhibited similar behaviour. As Figures 11 and 12 indicate, a significant downward adjustment of creep settlement predictions proved necessary for both dike structures.

7.3. Widening of A115 motorway embankment near Saarmund, Germany

A project to widen the A115 motorway south of Potsdam to six lanes started in the summer of 1998. At one point, the motorway embankment crosses an approx. 300 m wide strip of low-lying land comprising organic soils. The existing embankment was built using the bog blasting method. To widen the embankment in the low-lying area, 80 cm diameter GEC were installed on a 10% grid.

Horizontal and vertical inclinometers were incorporated during construction to monitor the deformation behaviour of the embankment. Readings from two of the horizontal inclinometers have been taken up to the present. Figure 13 shows a typical time-settlement curve. Creep settlement in the order of max. 1-2 cm has been measured over the past seven years.

7.4. Creep settlement for GEC foundations

The above and other settlement measurements suggest that the application to GEC foundations of creep factors specified for or derived from unimproved subsoils (i.e. without column foundations) leads to a significant overestimation of creep settlement compared to actual effective behaviour. Suitable laboratory tests (creep tests) would appear to be a prerequisite for the accurate prediction of long-term deformation and creep settlement. These would allow derivation of the creep behaviour of soft strata under various loading conditions and levels, and thereby permit quantification of the creep-settlement-reducing impact of GEC foundations.

Given the lack of suitable test results, however, a reduction factor derived from measurement results is frequently applied, by way of approximation, to the creep settlement determined for the unimproved subsoil.

On the basis of comparisons between computational predictions and measurements, the reduction factor to be applied to the creep settlement for the unimproved subsoil is estimated at between 0.25 and 0.50, depending on the project parameters. In other words, GEC foundations achieve an approx. 50-75% reduction in creep settlement.

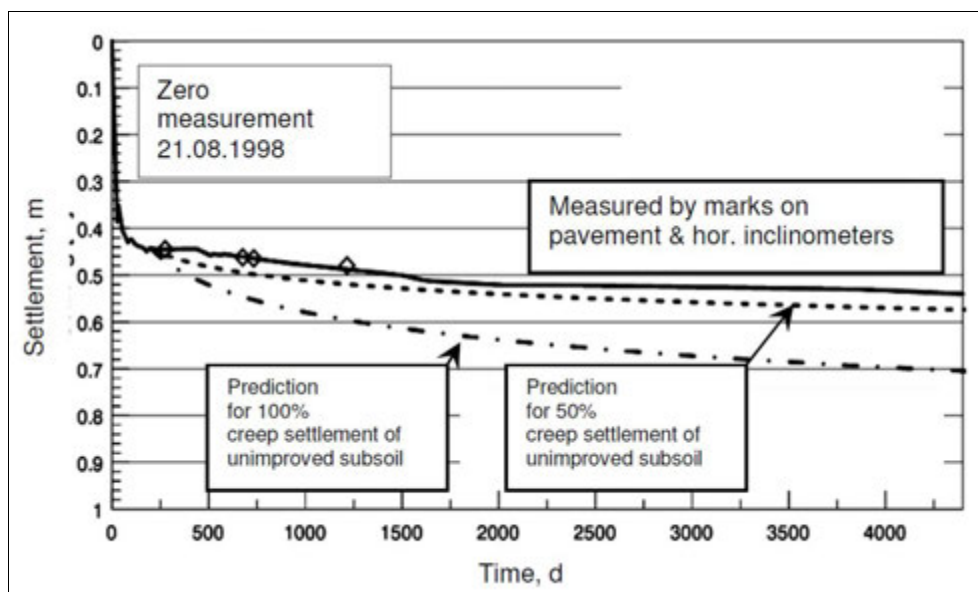


Figure 13: Time-settlement curves of representative cross-section of A115 motorway near Saarmund

8. FURTHER SYSTEM REFINEMENTS

8.1. Waterproofing against rising groundwater

Where the GEC foundation is sunk into a water-bearing sand/gravel horizon, the columns create a hydraulic connection between the ground surface and the aquifer. Apart from the risk of groundwater-polluting substances infiltrating into the subsoil, any existing artesian pressure may result in a constant upward flow of groundwater and a discharge at ground level that limits the water pressure in the column. The water permeability of the GEC can be minimized by installing a sand/bentonite mix in the body of the column. Here, the stiff geotextile sleeve plays an important, if not decisive, role. This solution has undergone a series of comprehensive in-situ tests by J. Möbius Bau GmbH and has already been successfully deployed in several road construction projects in Northern Germany.

Figure 14 shows part of a production drawing for a GEC foundation for a road embankment. In this case, the 1 m high waterproof barrier is located at the foot of the columns. The level of the barrier can, however, be adapted to the particular subsoil stratification (e.g. location at column head in case of intermediate sand aquifers).

8.2. Geotextile casing

The process of refining and optimizing the GEC system has also resulted in developments to the Ringtrac[®] geotextile casing. As a key reinforcing structural element, the casing significantly influences the load bearing and deformation behaviour of the column and overall system. The requirements placed on integrity, durability, robustness, mechanical behaviour etc. are accordingly high. Of particular importance is the decisive role by the circumferential stiffness (tensile modulus) in addition to the tensile strength [9]. To create ample scope for system optimization, the provision of a wide range of Ringtrac[®] diameters, tensile strengths and circumferential tensile moduli is essential, though time (permanent loading, creep, creep strain) is also a significant factor. To meet these demands, three seamless Ringtrac[®] lines made from different polymers are now available with diameters between 50 cm and 100 cm, short-term circumferential strengths of 400 kN/m or more, and circumferential stiffnesses (circumferential tensile moduli) ranging from 1000 kN/m to 8000 kN/m. The choice of polymers also guarantees high resistance, e.g. in alkaline environments. The wide variety of casing products thus offers considerable potential for system optimization.

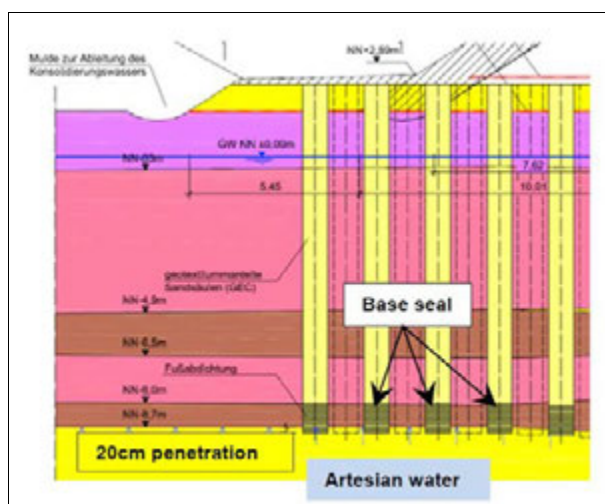


Figure 14: GEC with base seal – excerpt from highway production drawing

8.3. Column length

A construction project in Poland necessitated the installation of GEC with a maximum length of nearly 30 m. Refinements to the driving equipment allowed the installation of columns to a depth never previously achieved. The A2 motorway, handed over to traffic in December 2011 and linking the city of Poznań with the German-Polish border, crosses an approx. 300 m long channel with organic sediment. Ground conditions comprise peat and gyttja mud, with undrained shear strengths well below 10 kPa in some cases, are present in thicknesses up to 28 m below ground level. Installation of the longest columns – 800 mm in diameter, with an open pipe and lost base plate – using the displacement method was achieved with the help of a high-performance belt vibrator (Figure 15). For the longest columns, the inner surface of the displacement pipe was lubricated by means of an extra-lean bentonite suspension as a means of reducing the friction forces between pipe and column.



Figure 15: LRB 255 rig with 30 m long displacement pipe on construction site in Poland

8.4. Trial loading of a column group

A trial loading of a group of GEC, which will provide a better understanding of system behaviour, was carried out in February and March 2011. The loads applied to the 10-column group were gradually stepped up until one of the limit states was reached. Standard computational methods have been used to calculate the magnitudes of the action needed to achieve the "base failure" and "geotextile casing failure" limit states. The tests were adopted the same parameters as the calculations. The system behaviour was

closely monitored during the tests by means of detailed measurements and subsequently compared with the computational results. The aim of this procedure was to identify and quantify the structural reserves offered by the system. First results and analyses were published separately [15].

8.5. Acoustic ground investigation methods

Additional ground investigations are performed at the design stage to determine the required sinking depths for the columns. During installation of the columns, the equipment parameters are used to check for compliance with the specified sinking depth. As a rule, these clearly indicate the point at which adequately strong soil has been reached. In exceptional cases, e.g. with closely graded, loosely packed fine sands, the horizon to which the columns are to be sunk cannot be identified precisely enough. This leads to extended columns and increased effort for structural checks, e.g. due to further ground explorations.

An additional ground investigation method that uses acoustic techniques for the identification of adequately strong subsoils is currently under development by J. Möbius Bau-AG in collaboration with Clausthal University of Technology. This involves the transmission of signals, via a protected cable, from an accelerometer fitted at the tip of the pipe to a receiver at the pipe head, and from there by radio to the operating cabin. Here, a special software application filters the data and provides the operator with a simple visual indication of the soil type in which the pipe tip is currently located (Figure 16). The procedure results in a both safe and economical solution.



Figure 16: Displacement pipe equipped with measurement instrumentation to record acoustic signals

9. NEW POTENTIAL APPLICATIONS

9.1. Incorporation behind quay walls

Harbour construction projects frequently involve the placing of backfill behind newly built walls. Here, the fill is often placed on top of highly compressible soft strata with low shear resistance. The high earth and pore water pressures typically encountered in such cases necessitate an extremely compact wall construction.

In the initial state, i.e. prior to the onset of settlement and action of the geotextile casing in load transmission, the GEC already serve as a simple ground improvement measure due to the sand component incorporated in the soft stratum. The resulting increase in shear resistance is factored into the structural calculations for the subsequent states. In addition to this, some of the backfill loads are transmitted to the bearing subsoil via the GEC without imposing any horizontal earth pressure on the wall. Close control of the backfilling process is, however, necessary to exploit this effect. The backfill has to be placed in layers, with adequate time allowed for consolidation. The reduced earth pressure thus achieved automatically paves the way for an optimized and economical quay wall solution. Figure 17 shows a production drawing (cross-section) for a new quay wall at the Europakai docks in Hamburg.

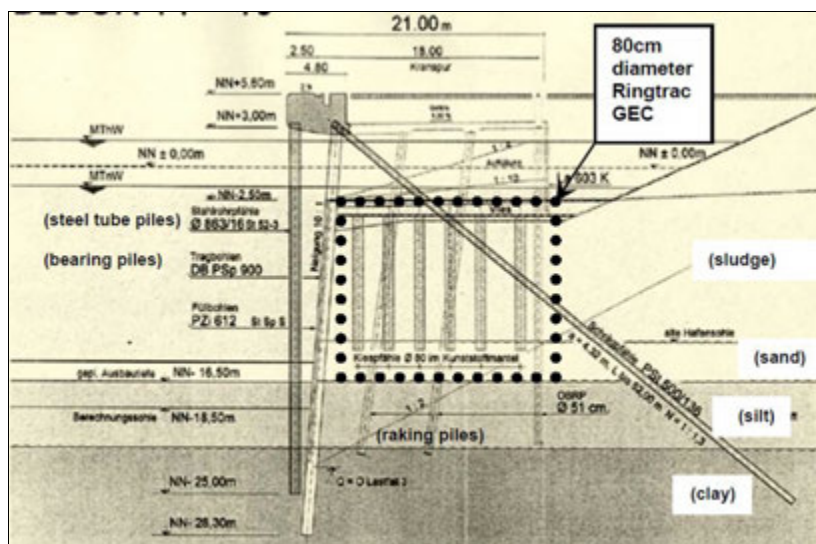


Figure 17: GEC behind new quay wall at Hamburg docks

9.2. Earthquake regions

In examining the action of GEC in earthquake regions, a distinction must be drawn between the applications and mechanisms relevant to different subsoil conditions.

In the case of primarily coarse granular soils, such as silty or poorly graded sands, that are prone to liquefaction under earthquake loads on account of their grading and low packing density, the use of ground improvement measures such as vibrated stone columns (to improve strength and density) is now state of the art.

The mechanisms that operate with GEC are essentially the same as those for stone columns, albeit with the added bonus of the reinforcement provided by the casing:

- a) Increased resistance to slope or soil shear failure in the event of an earthquake
- b) Ultimate confinement and strengthening of the non-cohesive columns
- b) Reduction of pore water overpressures through subsoil drainage accompanied by the additional separating and filtering functions of the geotextile encasement, thereby preventing liquefaction effects where liquefaction-prone soils (e.g. loosely packed fine sands) are present, as well as
- c) Reduction of seismic shear stresses in subsoil through columns and improvement of damping properties of subsoil

Irrespective of these mechanisms, it should be remembered that greater quake intensity, a longer quake duration, a higher water table and a lower packing density all serve to increase the liquefaction risks. Hence, an improvement already results from compaction of the surrounding soils achieved by sinking the pipe. The displacement method is, of course, more effective than the excavation method in this regard. The more compact soil conditions resulting from the column installation process are thus one of various factors that combine to enhance earthquake resistance.

A further application in the field of earthquake protection involves the use of GEC in soft, cohesive or organic soils that essentially provide little lateral support to the columns.

In the event of an earthquake, the seismic loads in such soils are likely to bring about widespread and virtually complete structural failure, which, in the absence of an additional foundation system, would inevitably lead to the failure of any existing superstructure. No increase in structural stability can be achieved in such cases through the use of vibrated stone columns or other non-encased systems as these will likewise suffer a more or less complete loss of their bearing capacity in the event of an earthquake, due to the lack of adequate lateral support. Similarly, piles, despite their inherent load bearing strength, would be highly susceptible to buckling.

With GEC, on the other hand, the supporting effect of the casing will ensure adequate short-term bearing capacity, even in the absence of any lateral support to the columns from the surrounding soil during the earthquake. Hence, in addition to their familiar advantages in terms of structural behaviour, GEC foundation systems can also be used to provide enhanced earthquake resistance.

9.3. Increase in dynamic performance of railway lines

The term "dynamic stability" is frequently used in the assessment of earthworks where particular allowance is needed for cyclic and dynamic action from rail traffic. This concept has, however, also been used in relation to the increasing settlement of the track over time that results from the soil behaviour under the dynamic loads imposed by rail traffic - even though this merely constitutes a gradual loss of serviceability, rather than a failure of structural stability.

As practical experience and the relevant literature [11] suggests, soft cohesive soils along with organic and organogenic soils, in particular peat, must be deemed critical in terms of their dynamic stability and performance. Particularly in the frequent case of rail sections that require enhanced maintenance due to their non-standards-compliant substructure or vibration-sensitive subsoils, or due to a planned increase in train speeds or frequency along the relevant rail section, the assessment of the subsoil's dynamic stability generally dictates the choice of rehabilitation method.

The shear strain γ occurring in soils under dynamic action [12] is regarded as the key parameter in the assessment of long-term dynamic stability and dynamic performance. Any such assessment needs to determine whether, under the dynamic action of rail traffic, that volumetric cyclic threshold shear strain $\gamma_{v,U}$ is reached whose exceedance is likely to bring about, within a short period, a level of deformation that could no longer be offset, for example, by packing. The computational model for this situation turns out to be relatively complex due to the interaction between track-dynamic [13] and soil-dynamic FEM computations [14].

The use of GEC in existing soft strata entails a reduction in dynamic action in these vibration-sensitive soils. This, in turn, significantly increases dynamic stability and performance, and allows higher train speeds.

One key advantage of GEC in such applications results from the use of geosynthetic materials and their linear-elastic behaviour. This guarantees the integrity and flexible, self-regulating structural performance of the columns over their entire lifespan.

Due to their greater flexibility and the adaptable reaction of the subsoil to the track superstructure and dynamic loads imposed by rail vehicles, GEC foundations offer distinct advantages over rigid systems such as piles or concrete columns. Moreover, GEC help to minimize problems at the junctions between rehabilitated and non-rehabilitated sections.

It should also be noted that, unlike non-encased granular (e.g. vibrated stone) columns, GEC are protected over their entire lifespan, thanks to the filtration stability of the geotextile casing, from the inward migration of surrounding soil, even under the dynamic loads imposed by rail traffic. The use of GEC thus ensures dynamic stability and performance during the entire lifespan or service life (i.e. 50-100 years) of the structure.

10. SUMMARY

Some 15 years after their market launch, geotextile-encased columns (GEC) have evolved into a sophisticated and absolutely reliable earthwork foundation system, underpinned by both theory and practice. Due to the confining encasement of the columns in the GEC-system it can be applied even in extremely soft soils with e.g. $s_u < 2$ kPa, which is in fact more a suspension than a soil. In particular, the system's long-term behaviour can now be accurately predicted, subject to the usual tolerances applicable to creep settlement calculations for foundations on organic soils.

In Germany, GEC foundation systems are governed by Section 10 of the current edition of the EBGEO (Recommendations for Design and Analysis of Earth Structures using Geosynthetic Reinforcements) issued by the German Geotechnical Society (DGGT). This describes the associated terminology, mechanisms, applications, production methods, design recommendations, materials, computational procedures and test criteria. In Germany, then, GECs have been definitively acknowledged as state-of-the-art technology.

The advantages of the GEC system, particularly for soft strata with extremely low shear resistances, are not only demonstrable by computational methods, but have also been substantiated by measurement results.

Ongoing refinements to the system are based on the standard EBGEO guidelines effective in Germany. Various research and development projects are currently in progress with the aim of improving the reliability of on-site installation and widening the scope of application of the GEC foundation system.

REFERENCES

- Raithel, M. (1999): *Zum Trag- und Verformungsverhalten von geokunststoffummantelten Sandsäulen*. Schriftenreihe Geotechnik, Universität Gesamthochschule Kassel, Heft 6, Kassel, Germany.
- EBGEO 2011: *Recommendations for Design and Analysis of Earth Structures using Geosynthetic Reinforcements – German Geotechnical Society (DGGT)*.
- Raithel, M., Kempfert, H.G. (1999): *Bemessung von geokunststoffummantelten Sandsäulen*. Die Bautechnik, 76, Heft 12, Germany.
- Ghionna, V. and Jamiolkowski, M. (1981). "Colonne di ghiaia." *X Ciclo di conferenze dedicate ai problemi di meccanica dei terreni e ingegneria delle fondazioni metodi di miglioramento dei terreni*. Politecnico di Torino Ingegneria, atti dell'istituto di scienza delle costruzioni, n°507.
- Priebe, H. (1995): *Die Bemessung von Rüttelstopfverdichtungen (The design of vibro displacement compaction) (in German)*. Bautechnik 72, pp. 183 – 191.
- Alexiew D., Brokemper D., Lothspeich S. (2005): *Geotextile Encased Columns (GEC): Load Capacity, Geotextile Selection and Pre-Design Graphs*. Proc. Geofrontiers 2005, Austin.
- Alexiew, D.; Brokemper, D.; Sobolewski, J. (2007): *Geokunststoffummantelte Säulen: Einflussfaktoren, Nomogramme für den Vorentwurf und Vorstellung eines aktuellen Bauwerks (Geotextile-Encased Columns: Parameters, Nomograms for Outline Design and Presentation of Current Construction Project)*. Proc. 7th Austrian Geotechnical Conference. Vienna.
- Alexiew, D., Sobolewski, J., Pohlmann, H. (2000): *Projects and optimized engineering with geogrids from "non-usual" polymers*. Proc. 2nd European Geosynthetics Conference, Bologna, pp. 239-244.
- Edil T. B., Fox, P. J., Lan, L.-T. (1994): *Stress-Induced One-Dimensional Creep of Peat. Advances in Understanding and Modelling the Mechanical Behaviour of Peat*, Balkema, Rotterdam.
- Krieg, S. (2000): *Viskoses Bodenverhalten von Mudden, Seeton und Klei (Viscous Behaviour of Marine Muds, Marine and Marsh Clays)*. Publication of Institute of Soil Mechanics and Rock Mechanics at Karlsruhe University of Technology, Volume 150.
- DB Netz AG: *Ril 836 – Erdbauwerke planen, bauen und instand halten (Design, Construction and Maintenance of Earthwork Structures)*. Edition of 20.12.1999.
- Vucetic, M. (1994): *Cyclic threshold shear strain soils*. Journal of Geotechnical Engineering, ASCE, 120, 12.
- Knothe, K. (2001): *Gleisdynamik (Track Dynamics)*. Ernst & Sohn Verlag, 1st edition.

Kempfert, H.-G.; Raithel, M.; Krist, O. (2010): Fahrweggründungen – Nachweise und Untersuchungen zur dynamischen Stabilität (Foundations for Permanent Railways – Investigation and Verification of Dynamic Stability). ETR – Eisenbahntechnische Rundschau (Railway Technical Review) Vol. 07+08/2010.

Raithel, M., Werner, S., Küster, V., Alexiew, D. (2011) : Analyse des Trag- und Verformungsverhaltens einer Gruppe geokunststoffummantelter Säulen im Großversuch. Bautechnik, Heft 9/2011

Modelling and analysis of the pullout behaviour of Granular Pile Anchor in expansive soils

Ala N Aljorany, Baghdad University, Iraq, alaljorany@msn.com

ABSTRACT

Expansive soils are characterized by their swelling potential upon wetting due to the presence of some hydrophilic clay minerals like Sodium Montmorillonite. Such soils may cause severe damages to the structures that are founded on. Granular pile anchor (GPA) is one of the recent innovative techniques devised for mitigating the problems posed by soil swelling. In a GPA system, the footing is tied to an anchor plate fixed at the bottom of granular pile. This makes the granular pile tension resistant and enables it to absorb the tensile force caused by footing upon soil swelling.

In this study, the pullout resistance of GPA is analyzed by using the well-known finite elements package ABAQUS. The expansive clayey soil is modelled as Von-Mises material while the pile granular material is modelled as Drucker-Prager plasticity model. The soil swelling is simulated as thermal expansion making use of the analogy between coupled temperature-displacement problems and that of coupled pore water pressure-displacement.

Different values of GPA length/diameter (L/D) ratio have been examined for both with or without swelling condition prior to pullout loading step. The results indicate that the soil swelling has a significant effect in applying additional confinement that increases the pull-out resistance of the GPA, especially for L/D ratios less than 10. The value of L/D at which the mode of GPA failure changes from short pile to bulging action is about 7.5.

1. INTRODUCTION

Expansive soils cover vast areas in many countries around the world. Due to the presence of some hydrophilic clay minerals, these soils exhibit significant volume changes upon wetting or drying. Foundations of light weight structures, floors, pipelines and roads that built on such soils are often subjected to severe structural damages. The cost associated with damage due to swelling soils is more than twice as much as the cost associated with damage from floods, hurricanes, tornadoes, and earthquakes (Jones and Holtz 1973).

There are many measures to mitigate swelling soil troubles. Some of these measures deal with altering the chemical or mineralogical structure of swelling clay skeleton by blending lime, cement, or fly ash (Hunter, 1988, Phanikumar, and Sharma, 2004 and Stavridakis, I.E, 2006). Others are by installing tension resistant members to absorb the swelling pressure, such as piers or under-reamed piles.

Falling under the second category, an innovation technique of Granular Pile Anchor (GPA) recently becomes the topic of many geotechnical researches (Rao, et al, 2007, Phanikumar, et al, 2004 and Madhav et al 2007). The GPA is an adjusted version of the widely used (conventional granular pile or stone column) technique. Stone columns usually act as compression members to resist downward loads applied on their tops. For an individual stone column or GP, the most probable failure mechanisms are pile or bulging failure (Hughes, et al, 1975 and Barksdale and Bachus, 1983) . Pile mechanism controls the ultimate load for short GP resting on soft to medium stiff bearing layer (the tip of the pile is floating in the soft soil) while bulging failure is most likely for long GP bearing on stiff stratum. In general, there will be a stress concentration at the pile top where the confinement radial pressure is low.

In GPA assembly, an anchor (relatively rigid plate) is fixed at the pile tip. This plate is connected to a steel rod or cable passing along the pile centerline. Through this rod and the anchor plate, the upward pull out load is transmitted to the pile tip where the confining pressure is relatively high. The GPA behavior under pullout loads depends on its geometry and the mechanical properties of pile and surrounding soil. It may behave as a short pile and the ultimate pullout capacity will therefore be controlled by the failure of the bond between the pile and the surrounding soil in addition to its self-weight. Considering figure 1, the ultimate pullout capacity (P_{ult}) of the GPA, in this situation will be:

$$P_{ult} = \gamma_G \cdot \pi \cdot \frac{D^2}{4} \cdot L + C_u \cdot \pi \cdot D \cdot L \quad (1)$$

where: γ_G is the unit weight of granular material, C_u is the undrained shear strength of soil, and D and L are the diameter and length of GPA, respectively.

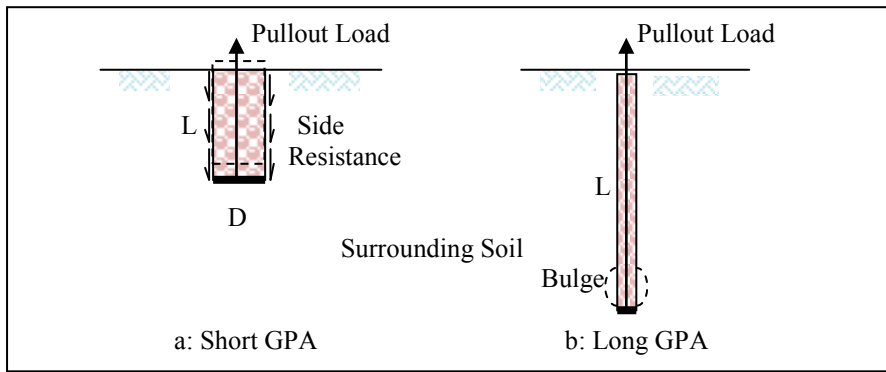


Figure 1: Failure mode of short and long GPA.

For relatively long GPA, the equation proposed by Hughes and Withers (1974) for stone column under bulging effect, can be used to evaluate the ultimate pullout capacity:

$$q_{ult} = \frac{1 + \sin \phi}{1 - \sin \phi} \cdot \left[\sigma_r + C_u \left(1 + \ln \frac{G}{C_u} \right) \right] \quad (2)$$

in which: q_{ult} is the ultimate pullout pressure, σ_r is the lateral soil pressure, ϕ is the angle of internal friction of the granular pile material and G is the shear modulus of the surrounding soil.

Madhav, M. R. et.al (2007) stated that for short GP (i.e. L/D value less than 5 to 6) the ultimate capacity under compression is greater than that under pullout, since the (pile) mechanism that depends on the L/D ratio controls the failure. For long GP, the ultimate pullout capacity is significantly greater than the corresponding values for compression, thereby establishing that GPA is much more effective and preferable to withstand pullout loads.

In this research, the finite element method is used to analyze the behavior of GPA under pullout loading. The effect of swelling of the surrounding soil on the pullout resistance of GPA is investigated as well. The finite element package ABAQUS is utilized in the analysis.

2. PROBLEM STATEMENT AND SIMULATION

Figure 2 illustrates the problem in hand, where the granular pile extends to mid-depth of the surrounding soil. The upper half of this soil is subjected to swelling. The pullout load is applied to the tip of granular pile through the axial rod and the connected base plate. The geometric parameters and material properties shown in the figure are used in the analysis.

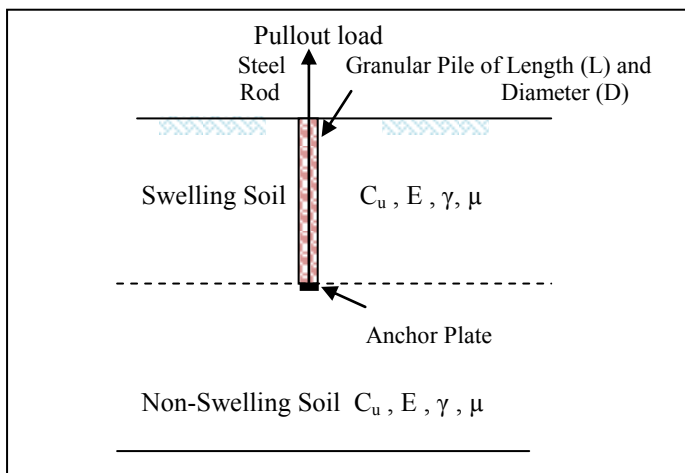


Figure 2: Definition of the problem parameters used in the analysis.

Due to the nature of problem loading and geometry, it is analysed as an axisymmetric problem. The axial rod and anchor plate are simulated as rigid members while the granular pile is modelled as an elasto-plastic material basing on Drucker-Prager Model. The surrounding clay is modelled as Von-Mises material which is quite suitable for the undrained behavior of such soil.

The pullout loading is applied as prescribed displacement at the top end of the axial rod and transmitted to the pile tip through the anchor plate.

Different L/D ratios of the GPA are examined for no swelling condition first then the same values of this ratio are considered with swelling condition of the upper half of the surrounding soil. In all cases, the analysis starts with an initial step, at which the boundary conditions and geostatic stresses are applied. For no swelling condition, the anchor displacement is then applied until failure condition.

By ABAQUS the soil swelling can be simulated by using coupled pore pressure- displacement analysis step. Such analysis is somewhat cumbersome and needs a lot of parameters regarding the soil-water characteristic curve of the soil, the “moisture swelling” and the “sorption adsorption” behavior (ABAQUS Analysis user’s manual, 2009).

In the present analysis, the soil swelling is simulated as thermal expansion making use of the analogy of the coupled temperature-displacement problems and the coupled pore pressure-displacement one. This is mainly because the problem in hand is devoted to investigate the effects of volume changes resulting due to swelling on the pullout resistance of GPA only and not swelling process itself.

The analogy of coupled temperature- displacement analysis and pore pressure- displacement problems was first stated by Terzaghi in 1943. The following table is proposed by Long, X. (2006) to illustrate the similarity of the two analyses

Table 1: Analysis Similarity of Sequentially Coupled Flow/Displacement Analysis with Sequentially Coupled Thermal Stress/Displacement Analysis. (After Long, X 2006.)

Phase	Sequentially coupled flow/displacement analysis		Sequentially coupled thermal Phase stress/displacement analysis	
	Physical Meaning	Symbol	Physical Meaning	Symbol
Mechanical	Stress	$\sigma -u$	Stress	σ
	Strain	ϵ	Strain	ϵ
	Displacement	u, v, w	Displacement	u, v, w
	Young’s Modulus	E	Young’s Modulus	E
	Poisson’s Ratio	μ	Poisson’s Ratio	μ
	Suction Compression index	γ_h	Coefficient of Expansion	α
Flow	Coefficient of Permeability	k	Coefficient of conductivity	k
	Dry Unit Weight	γ_d	Density	γ
	Diffusion Coefficient	α	Specific Heat Capacity	C_T
Flow/mechanical	Time	t	Time	t

By normalizing γ_w to be a unity, the differential equation for one dimensional flow of heat through isotropic body becomes identical with the differential equation of Terzaghi’s consolidation theory. The relationship between suction compression index γ_h in flow- displacement analysis and the coefficient of expansion α for axisymmetric problems is $\alpha = \gamma_h (1 + 2 \mu) / 3$.

The swelling step in present problem which starts after the geostatic step is therefore simulated by posing a certain temperature boundry condition at the upper boundary of the soil. Meanwhile, the temperature at the lower half of the soil layer is kept at the reference temperature. This step is transient and sufficient time interval is given to complete the swelling process. After that the pullout displacement is imposed untill the failure of the GPA.

Figure 3 exposes the finite element mesh of the problem regarding L/D ratio=6. As shown, a quaderlateral quadratic element is adopted with reduced integration scheme. Except the swelling part where the elements are coupled temerature displacement, all other elements are axisymmetric stress elements.

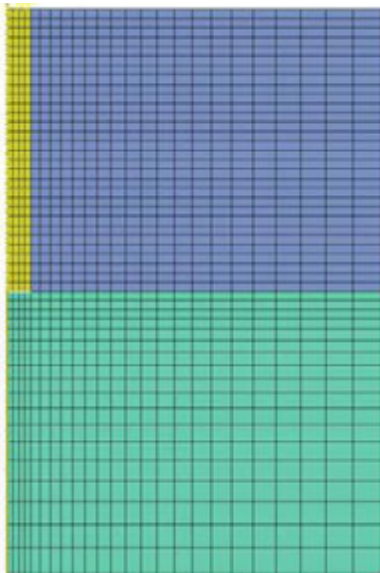


Figure 3: A typical finite element mesh of the problem.

3. ANALYSIS RESULTS AND DISCUSSION

Seven values of L/D ratio are considered by changing the GPA diameter of length 3 m, namely; L/D= 3, 4.5, 6, 7.5, 10, 12 and 15. The load- displacement curves for no swelling condition are shown in figure 4.

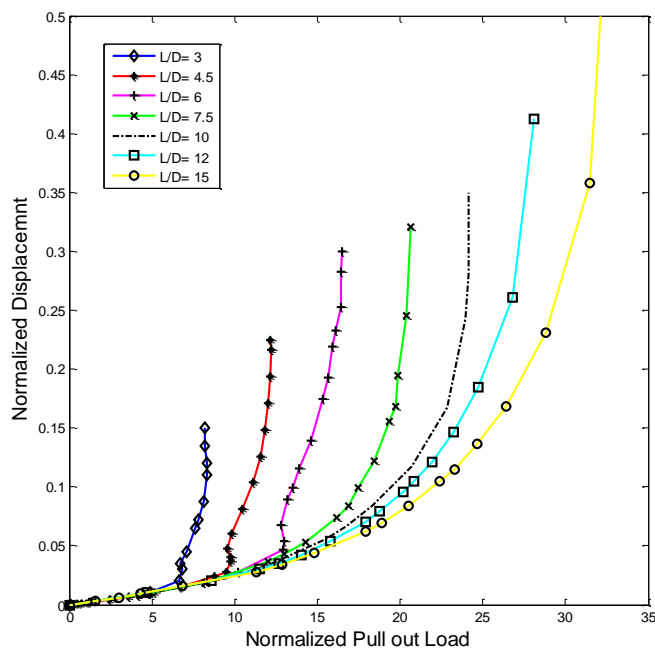


Figure 4: Load- displacement curves for different ratios of L/D under no swelling condition.

The pullout load in this and the following figures is normalized by the vertical effective stress (σ_{v0}) at the tip of granular pile ($P_u/A*\sigma_{v0}$) where A is the GPA cross sectional area and the displacement is normalized by the GPA diameter (δ/D). It is noticed that the ultimate pullout resistance increases from about 8 for L/D=3 to 32 for L/D= 15 but the rate of increase indicates a descending trend. This finding can be clearly observed in figure 5 (the dashed blue line).

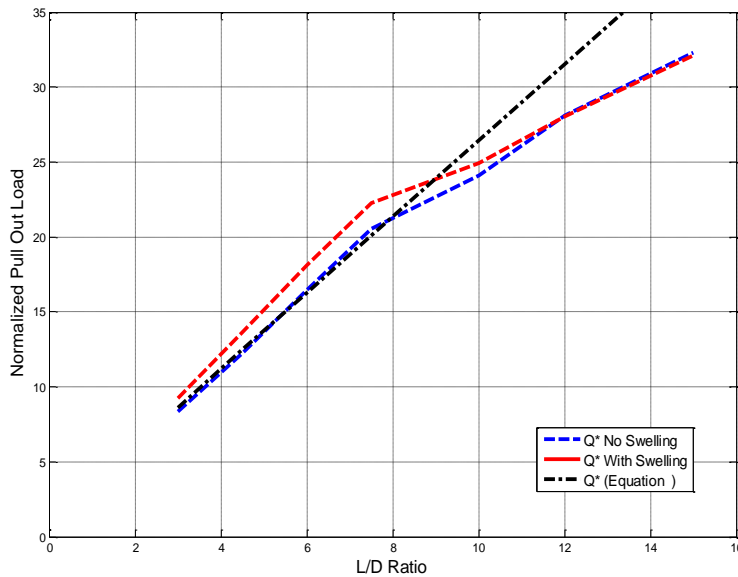


Figure 5: The ultimate pullout resistance variation with L/D ratio under no swelling and swelling condition.

The black line in this figure represents equation (1) in its normalized form:

$$Q_{ult}^* = P_{ult} / A \cdot \sigma_{vo} = 1 + 4 \cdot (C_u / \sigma_{vo}) \cdot L / D \quad (1^*)$$

which is a linear relation with respect to the L/D ratio. It is also indicating the short pile failure mechanism of the GPA. This line almost coincides with the obtained results of the current analysis for no swelling condition up to L/D ratio of 7.5. The point of deviation of the obtained results from this line indicates the change in GPA failure mechanism from short pile action to the bulging failure mode of long GPA. The critical GPA length at which this change takes place is around 7.5D.

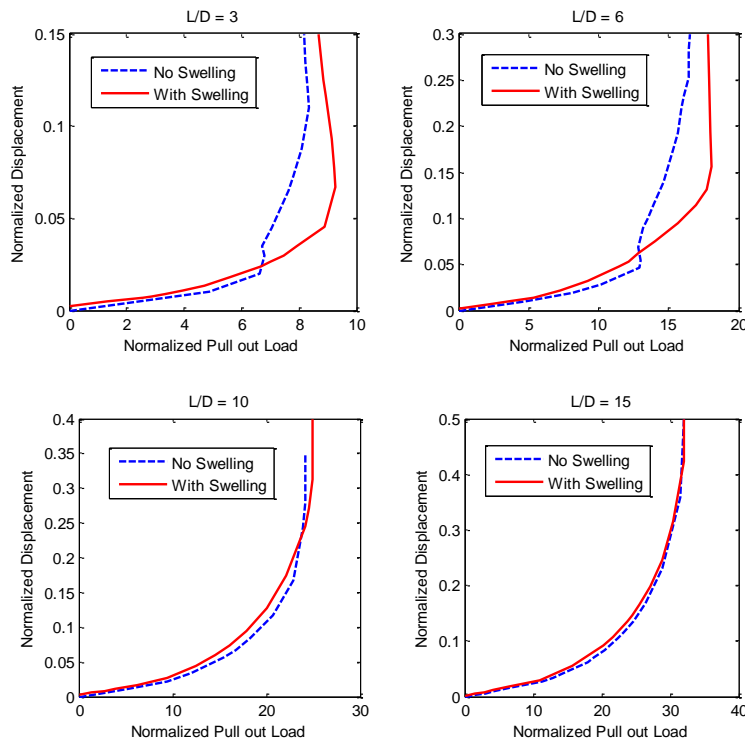


Figure 6: Effect of swelling on the load-displacement curves of GPA.

Figure 5 illustrates also the effect of soil swelling on the ultimate pullout capacity of GPA. It is worthy to mention that the obtained value of volumetric strain resulting due swelling is about 2.5% and varies from zero at clay layer mid-depth to its maximum value at the upper boundary.

It is seen that this amount of swelling causes significant increase in the ultimate pullout resistance for moderate values of L/D (from 4.5 to 10) and diminishes for L/D more than 10. The effect of swelling can be noticed in Figure 6 as well. It is quite obvious that the soil swelling imposes an additional confinement on the GP. For relatively long GP, the bulging takes place at a distance of about (D) above the pile tip. At that level there is no significant volume change due to swelling because it is close to the reference temperature boundary. This may explain vanishing of swelling effects for long pile mode of failure.

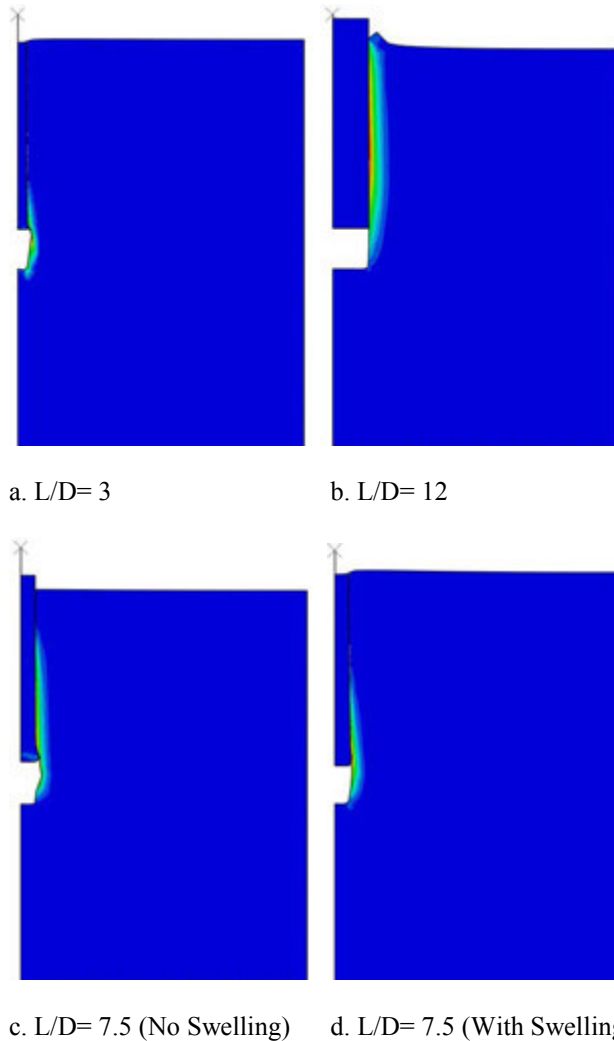


Figure 7: The extension of equivalent plastic strain around GPA for different modes of failure.

In figure 7, the equivalent plastic strain (PEEQ) around the GPA for different modes of failure is displayed. This identifier indicates the extent of material yielding and calculated as:

$$\bar{\epsilon}^{pl} |_0 + \int_0^t \dot{\bar{\epsilon}}^{pl} dt \tag{2}$$

where $\bar{\epsilon}^{pl} |_0$ is the initial equivalent plastic strain.

It can be noticed that for L/D=3, the yield zone extends along the interface between GP and the surrounding soil indicating a short pile failure mode. For L/D= 12, the bulging failure mode is quite clear and the yield zone is limited near the pile tip only.

The value of L/D = 7 can be considered as the critical ratio, at which the mode of failure changes from short pile to long (bulging) action. At this ratio, the GPA behavior is sensitive to the swelling volume changes as can be noticed in figure 7 c and d.

4. CONCLUSIONS

In this study, the pullout resistance of GPA is analyzed by using ABAQUS. The effect of surrounding soil swelling on this resistance is investigated as well and the following points can be deduced as concluding remarks:

- For no swelling condition, the GPA behaves as short pile for L/D ratios up to about 7.5. After that critical ratio, the bulging mode of failure becomes dominant.
- The swelling of the surrounding soil poses some confinement on the GP and increasing its pullout resistance. This finding is more pronounced for moderate L/D ratios and diminishes for L/D ratios > 10.
- In terms of ABAQUS terminology, the coupled temperature-displacement analysis can be efficiently used to analyze the coupled pore pressure-displacement problems by making use of the mathematical analogy between the two problems provided that the corresponding parameters are carefully selected.

REFERENCES

ABAQUS Analysis user's manual, 2009, Dassault Systèmes Simulia Corp., Providence, RI, USA.

Barksdale, D. R. and Bachus, C. R., 1983, "Design and Construction of Stone Columns, Vol 1", Technical Report, Federal Highway Administration, Office of Engineering and Highway Operations, Research and Development, Washington, D.C.

Evangelos I. Stavridakis, 2006, "Stabilization of problematic soils using cement and lime", in "Expansive Soils, Recent advances in characterization and treatment" edited by Amer Ali Al-Rawas and Mattheus F.A. Goosen, Taylor & Francis Group, London, UK.

Hughes, J. M. O, and Withers, N. J, 1974, "Reinforcing of soft cohesive soils with stone columns." Ground Eng., Vol. 17, No 3, pp 42-49.

Hughes, J.M.O., Withers, N.J. and Greenwood, D.A 1975. "A Field Trial of the Reinforced Effect of Stone Column in Soil" Geotechnique, Vol. 25, No.1, pp. 31-44.

Hunter, D. (1988), "Lime-induced heave in sulfate-bearing clay soils." Journal of Geotechnical Engineering, Vol.114, No. 2, pp 150-167.

Jones, D. E. and Holtz, W. G. ,1973, "Expansive soils—the hidden disaster." Civil Engineering, ASCE, Vol. 43, No. CE8, pp 49-51.

Madhav,R. M., Vidyaranya, B., Suresh, K. and Sivakumar, V., 2007, "An Overview of Compression and Uplift Behavior of Granular Piles", International conference on soil and rock engineering, Colombo, Sri Lanka.

Phanikumar, B. R., and Sharma, R. S., 2004, "Effect of fly ash on engineering properties of expansive soils." Journal of Geotechnical and Geoenvironmental Engineering, Vol.130, No.7, pp 764-767.

Phanikumar, B.R., Sharma, R.S., Srirama Rao, A.and Madhav, M.R., 2004, "Granular Pile Anchor Foundation (GPAF) System for Improving the Engineering Behavior of Expansive Clay Beds" Geotechnical Testing Journal, American Standard Testing Machines, Vol.27, No.3, pp 1-9.

Xiaoyan Long, 2006, "Prediction of shear strength and vertical movement due to moisture diffusion through expansive soil", PhD Thesis, Texas A&M University.

Bearing Capacity of Foundations Reinforced with Micropiles

Jafar Bolouri Bazaz, Ferdowsi University of Mashhad, Mashhad, Iran, bolouri@um.ac.ir
Hadis Jalilian,, Ferdowsi University of Mashhad, Mashhad, Iran, jalilian.hadis@gmail.com

ABSTRACT

The development of the effective method for the reinforcement of existing foundations is an urgent problem to improve the stability of urban buildings. Micropile, which is a cast in place mortar pile of small diameter, is one of the most promising methods for reinforcing foundations and improving their bearing capacity. The mechanism which enhances the bearing capacity of foundations reinforced with micropiles under the static loading condition was the subject of this study. A series of loading tests were carried out on the model micropile-foundations located on loose sand. Micropiles of 6mm and 200mm in diameter and length, respectively, were prepared. Rigid circular foundation with a diameter of 100mm was reinforced with micropiles. Various arrangements of micropiles were tested; the number and inclination angle of micropiles were parametrically changed. The micropile foundations placed on sand grounds with low relative density were loaded. From the comparative examination of the observed behavior of micropile foundations, the influence of micropiles' arrangement on the mechanism and improvement of bearing capacity of foundation was discussed. To assess quantitatively the degree of improvement in the bearing capacity of surface foundations reinforced with micropiles, an index R called "Network Effect Index" was introduced in this study. The index R of unity means that the bearing capacity of foundations reinforced with micropiles is simply equal to the summation of the individual value of the surface foundation and that of the micropile group. There is an upward trend in the rate of index R when the number of micropiles is increased. On the other hand, in high numbers of micropiles used to reinforce the foundation, index R declines with increasing the inclination angle. In the case of micropiles with low-inclination-angle being implemented, bearing capacity is improved remarkably; An index R of 1.997 is achieved in this study where 8 micropiles inclined at an angle of 15° were used to reinforce the foundation.

1. INTRODUCTION

Micropile is a small-diameter, cast-in-place replacement pile, which is built in a drilled borehole with reinforcement and grout. Micropiles are generally used both for structural support and for in-situ earth reinforcement. Micropiles are installed with the technique which causes minimal disturbance to structure, subsoil and the environment. The principle was conceived in Italy [FHWA, 2000], and micropiles are now widely used in the world for various purposes [Bruce, et al., 1995; FHWA, 1997]. The improvement of bearing capacity of existing foundations is one of the main problems in Geotechnical Engineering. Micropile is expected as a promising solution for this problem. Micropile method has been practically used for reinforcement of existing foundations in sites. With practical experiences in the sites, the mechanism of bearing capacity and network effect concerning micropiles has been discussed continuously [Aschenbroich, 2001; Ball, 2002; Morsy, 2002; Han, 2006; Dietz, 2006; Wolosick, 2007; Tsukada et al., 2006].

Micropiles can withstand axial and/or lateral loads, and may be considered as either one component in a composite soil/pile mass or a small-diameter substitute for a conventional pile, depending on the design concept. They can sustain sufficient skin friction due to being grouted under controlled pressures. Owing to their flexibility and installation in small diameters, they can be used conventionally as a group in reinforcing foundations and so it is important to understand the mechanism of bearing capacity and to propose a rational design method. In the case of foundation reinforced with a group of micropiles, the interaction between micropile group and foundation plays an important role, especially when the foundation is subjected to critically large loads with perceptible displacement. The micropile design must be considered in the concept of piled raft foundation especially for reinforcing existing foundations.

Although the applications of micropiles are increasing in various situations, the mechanism of developing the bearing capacity of foundations is not yet understood sufficiently. Thus the aim of this study is to examine some important aspects which classify and quantify the improvement of the bearing capacity in micropile foundations based on the comparative

examination of the observed behaviors in the loading tests. In order to clarify the mechanism of bearing load with micropiles, loading tests on the model foundations reinforced with a micropile group were carried out by some researchers: e.g., Lizzi [1978] and Francis et al. [1996]. They showed the importance of the group effect in micropiles, and discussed on the influence of arrangement of micropiles on the bearing capacity. In this study a series of model loading tests was carried out on the foundations reinforced with micropiles on loose sand ground, regarding the interaction among micropiles, foundation and ground material. Various types of micropile arrangements were prepared; the number and inclination angle of micropiles were varied parametrically. Observed behavior of the micropile foundations under vertical loads are examined comparatively, and the influence factors on the bearing capacity are discussed. The Present research focuses on the influence of inclination angle of micropiles on the behavior of foundation reinforced with these elements.

2. METHOD FOR MODEL LOADING TESTS

2.1. Model Tests

Ideally speaking, centrifugal model tests have superior characteristics under many conditions; nevertheless, ordinary model tests under gravitational force can also contribute to a better understanding of the salient features which enhance the bearing capacity of foundations reinforced with micropiles. Model tests are easy to perform and thus a large number of tests can be carried out to ensure the repeatability of the data. Additionally, these tests are easy to perform and the fabrication of the equipment and its function are easily verifiable [Tsukada et al., 2006].

2.2. Model Micropile Foundation

A typical model micropile foundation employed in this study is shown in Fig. 1. The model consists of a rigid circular foundation made of polyamide with a diameter of 100mm, which is reinforced with a group of thread-bar steel micropiles; the diameter and length of micropiles are 6 and 200 millimeters, respectively. The number and inclination angle from vertical direction are designated as N and θ .

The stiffness of steel micropiles was measured through tensile strength tests according to ASTM E8M. Table 1 contains the properties of model micropiles. The surface of micropiles is made rough by means of covering it with a thin sand layer in order to mobilize sufficient skin friction; sand grains were glued to the surfaces of micropiles.

In the model tests with small scale, relative particle size of soil sometimes effects on the tests results. As the ratio of micropile diameter to the largest sand particle size is about 7.5 in this investigation, the unfavorable scale effect can be considered to be minor in this model test condition.

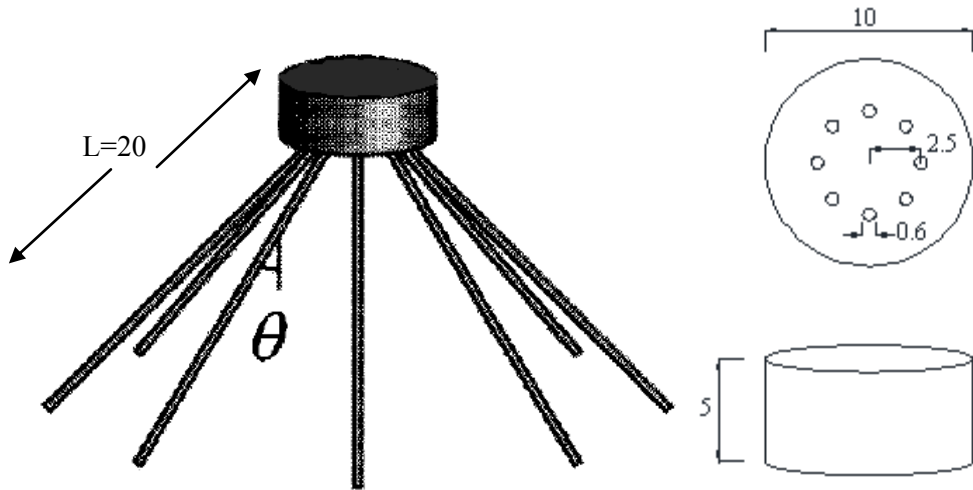


Figure 1: Model Micropile Foundation, units in cm

Figure 2 shows this sand container which is made of a GRP pipe, 700 mm in diameter, 500 mm in depth and 8 mm in wall thickness. The model micropile foundation was suspended in the container during the deposition of sand (see Fig. 2). In order to minimize the disturbance of the sand around the micropiles and also avoid the unnecessary prestress both in the micropiles and in the sand, a procedure was thought to deposit the sand in the container freely. The container is rigid enough not to be deformed while loading the model located in it.

Table 1: Mechanical Properties of the Micropiles

Material	Stainless Steel
Diameter without Sands Glued on It(mm)	5.5
Diameter with Sands Glued on It(mm)	6.8
Young's Modulus, E(GPa)	230
Bending Stiffness, EI(N×m ²)	24.1

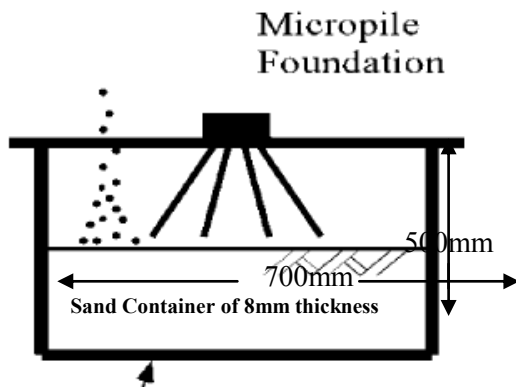


Figure 2: Sand Container, units in mm

2.3. Soil Material

A special type of sand, called Firouzkooh, was deposited in the mold through the air so as to obtain low relative density and form a loose ground under the foundation. Figure 3 shows the soil distribution of this sand for which ($G_s=2.71$).

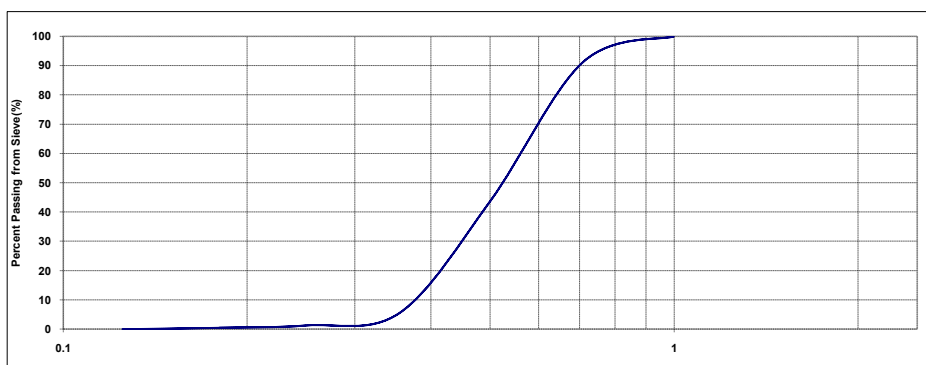


Figure 3: Grain Size Distribution Using the USCS Definitions of Particle Size

2.4. Loading Apparatus

The loading apparatus, and controlling system used in this study are shown in Photo. 1. A vertical loading ram equipped with direct-drive motor and a load ring are mounted on a rigid frame. With this operatable ram, the vertical component of the motion of micropile foundation can be controlled, where displacement in vertical direction is concerned. The accuracies are 1.0×10^{-2} mm and 320×10^{-3} kgF for displacement and applied load, respectively. A constant rate of penetration of 13 mm/min was maintained in the vertical direction.



Photo 1: Loading Apparatus Implemented in the Study

3. TEST RESULTS AND DISCUSSION

The loading tests conducted in this study consist of three test series, as illustrated in Fig. 4. First, the behavior of surface foundation without reinforcement is observed in F-Test series (Fig. 4(a)). The second series of tests designated as M-Tests series contains observations on the tests conducted on foundations reinforced with micropiles, where the foundation was standing free from the ground surface (Fig. 4(b)). In this series, several types of groups of micropiles with different numbers of micropiles inclined at various angles were employed. Finally, the bearing capacity of foundations reinforced with micropile groups of different number and inclination angle was investigated in the M-F-Test series (Fig. 4(c)). In addition to the vertical direction of loading, the application point of it is maintained at the center of foundation on ground surface, throughout all the test series.

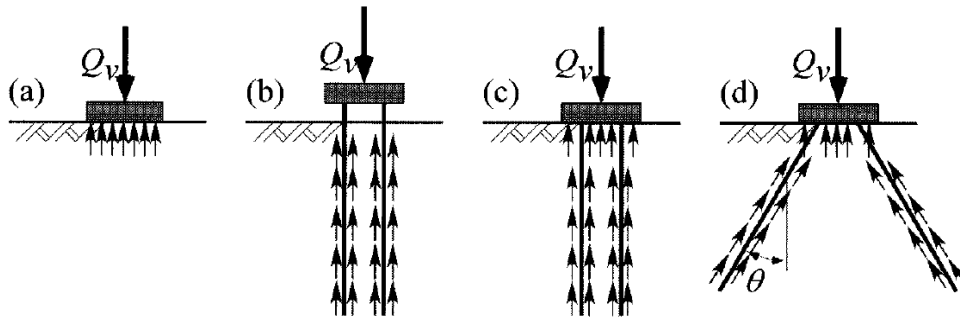


Figure 4: Series of Loading Tests: (a)F-Test, (b)M-Tests, (c)M-F-Tests with Vertical Micropiles and (d) M-F-Tests with Inclined Micropiles

3.1. Bearing Capacity Characteristics of Surface Foundation on Sand(F-Test)

The behavior of spread foundation observed under vertical load in F-Test is shown in Fig. 5 in the form of load supported Q_v vs. vertical displacement S_v relationship.

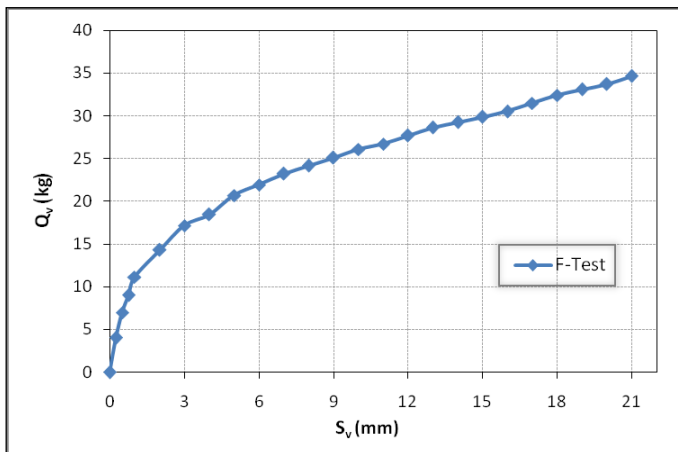


Figure 5: Vertical Load Supported versus Displacement of the Foundation(F-Test)

In this test series, Q_v tends to rise steadily with increasing S_v , and the load-displacement behavior was of typical local shear failure type; shear failure plane was not recognized on the surface of the ground, as illustrated in Photo 2.



Photo 2: Shear Failure Pattern Appeared at the Surface for Relative Displacement S_v/D of 20%

This load bearing behavior and failure pattern is due to the relative density dependent dilatancy properties of the sand, as illustrated in Fig. 6. Contractive behavior of loose ground material beneath foundation restrains the extension of shear failure plane, while in the case of dense ground material, dilative behavior of sand may extend shear failure plane toward ground surface and lead to a general shear failure.

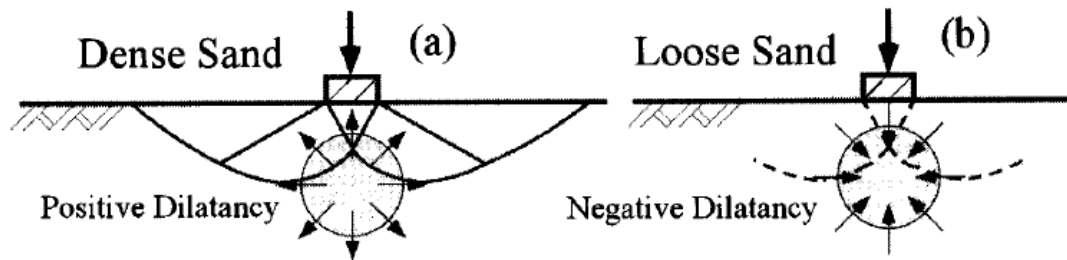
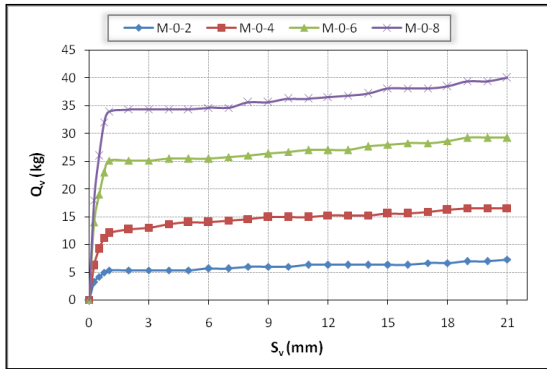


Figure.6: Shear Failure Patterns induced by the movement of the Surface Foundation: (a) general shear failure in a dilative sand and (b) local shear failure in a contractive sand

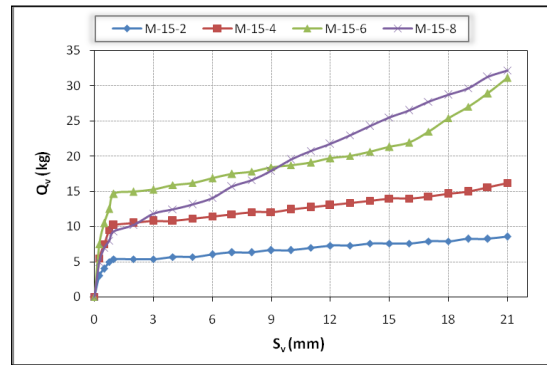
3.2. Bearing Capacity Characteristics of Micropiles in Sand (M-Tests)

Shown in Fig. 7 are the relationships between the vertical load Q_v versus the displacement of group of micropiles with different inclination angles. The number of micropiles installed varies from 2 to 8. According to the results of M-Tests, it can be said that the group effect of the micropile group, which is followed by the reduction in the bearing capacity per pile with increasing number of piles, was not recognized. In addition, the behavior of the micropile groups was not influenced by the limited size of the sand container or its base.

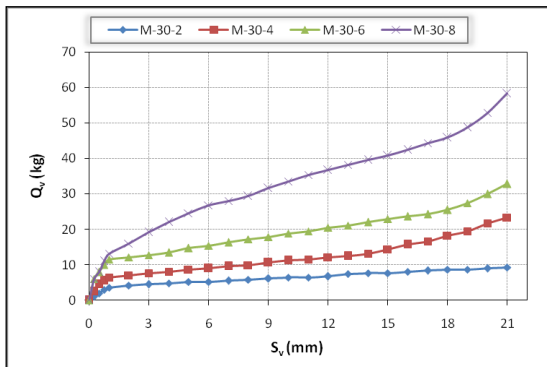
$\theta = 0^\circ$, N=2-8



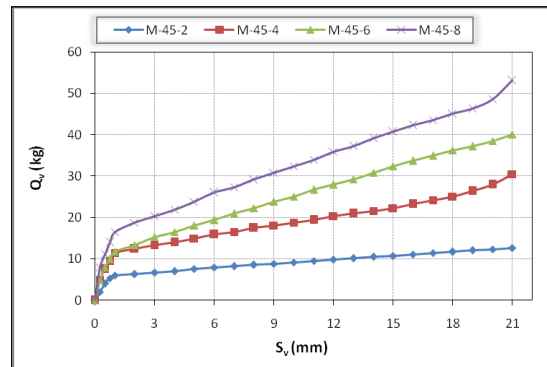
$\theta = 15^\circ$, N=2-8



$\theta = 30^\circ$, N=2-8



$\theta = 45^\circ$, N=2-8



$\theta = 60^\circ$, N=2-8

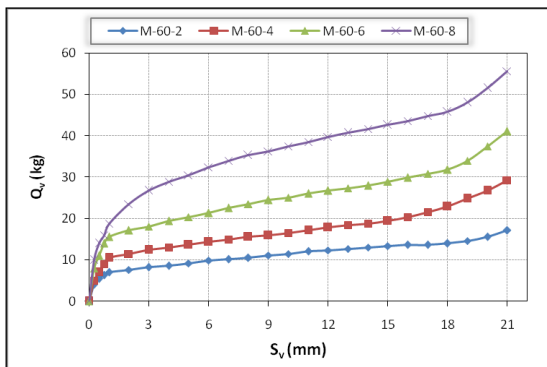


Figure 7: Vertical Load Supported versus Displacement of the Micropile Groups(M-Tests)

In order to assess quantitatively the influence of inclination angle of micropiles on the bearing capacity of micropile group, a dimensionless parameter, designated as K, was introduced. K is calculated by dividing the ultimate load supported by group of micropiles inclined at an angle of θ by the bearing capacity of a group consisting of the same number of micropiles installed vertically. Number of micropiles used varies from 2 to 8. Indicated in Table 3 is the effect of the inclination angle on the bearing capacity of the micropile group with different numbers of micropiles installed. It is apparent from the contents of this table that the bearing capacity of group of micropiles is remarkably dependent on the inclination angle; The ultimate load supported by the group is increased while the inclination angle rises.

Table 3: Parameter K calculated for each number of micropiles used in the group

N \ θ	0	15	30	45	60
2	1.00	1.17	1.28	1.74	2.35
4	1.00	0.98	1.41	1.85	1.77
6	1.00	1.07	1.12	1.37	1.40
8	1.00	0.80	1.45	1.33	1.39

3.3. Bearing Capacity Characteristics of Micropile Foundation on Sand (M-F-Tests)

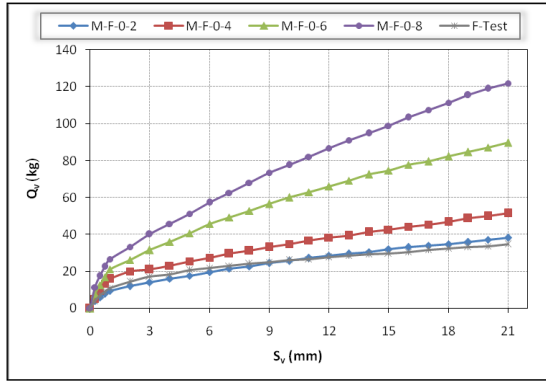
In order to quantify the influence of micropiles' inclination angle on the load bearing behavior of the foundation, a dimensionless parameter designated as P was introduced. Bearing capacity of the foundation reinforced with micropile groups of specific inclination angle divided by that of the foundation without any reinforcement is designated as P . The typical observed behavior of foundations reinforced with groups of different numbers of micropiles installed are depicted in Figure 8.

As illustrated in Table 4, a notable influence of the inclination angle of micropiles is recognized. The bearing capacity tends to become maximum with low inclination angle. In all cases of loading tests conducted, ground beneath the foundations failed in local shear type.

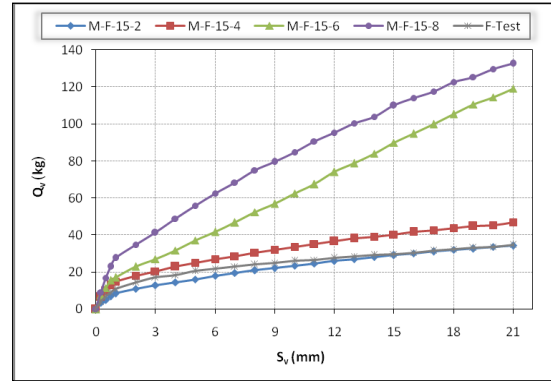
3.4. Improvement of Bearing Capacity of foundation with a Group of Micropiles

To assess the degree of improvement of the bearing capacity with micropiles quantitatively, the improvement ratio R was introduced (Equation 1). The R of unity means that bearing capacity of the foundation reinforced with micropiles is equal to the summation of those of the surface foundation and the group of micropiles.

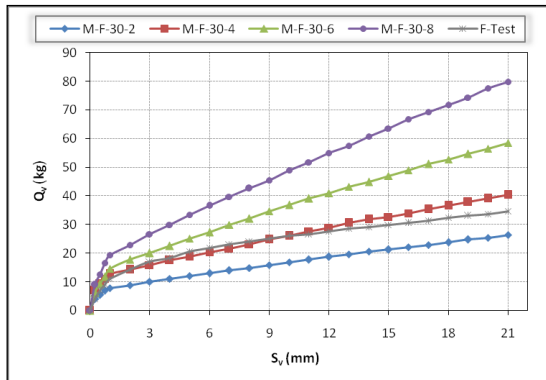
$\theta = 0^\circ, N=2-8$



$\theta = 15^\circ, N=2-8$



$\theta = 30^\circ, N=2-8$



$\theta = 45^\circ, N=2-8$

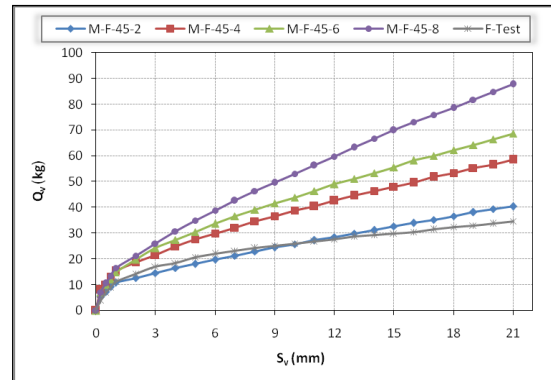


Figure 8: Vertical Load Supported versus Displacement of the Foundation Reinforced with Micropiles (M-F-Tests)

Table 4: Parameter P calculated for each number of micropiles used to reinforce the foundation

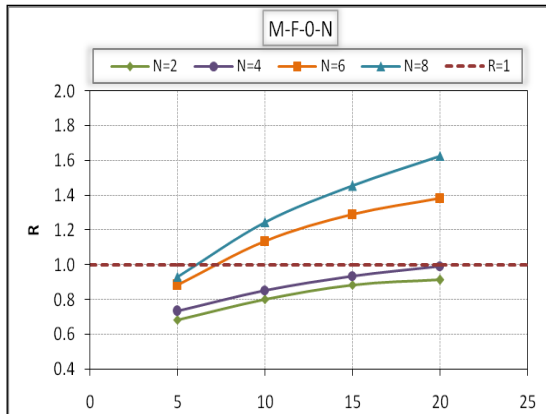
N \ θ	0	15	30	45	60
2	1.10	0.99	0.76	1.16	1.07
4	1.49	1.36	1.17	1.69	1.42
6	2.59	3.44	1.69	1.98	1.67
8	3.51	3.82	2.30	2.53	2.33

$$R = \frac{\left[\frac{Q_v}{A_s} \right]_{M-F-Test}}{\left[\frac{Q_v}{A_s} \right]_{F-Test} + \left[\frac{Q_v}{A_s} \right]_{M-Test}} \quad (1)$$

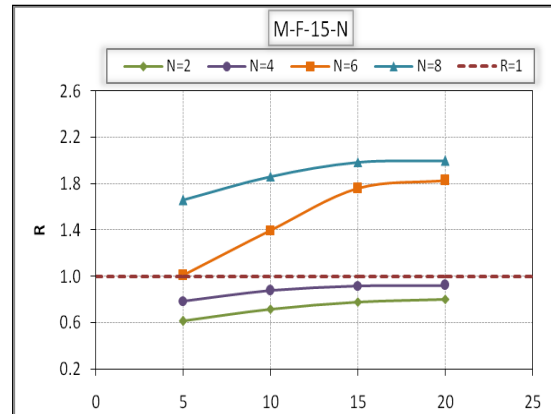
If the network effect is positively mobilized and the confining effect by the interaction between foundation and the group of micropiles is effective, then the bearing capacity is improved and the value of R becomes larger. In Figs. 9-11 the improvement of bearing capacity of foundation via reinforcement with micropiles is presented.

The degree of improvement is remarkably dependent on the rate of the displacement of the micropile foundation as depicted in Fig. 9. This means that a certain amount of displacement is necessary to induce confinement and mobilize the network effect.

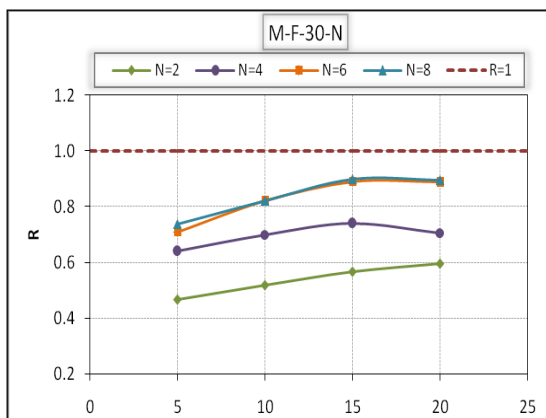
$\theta = 0^\circ$, N=2-8



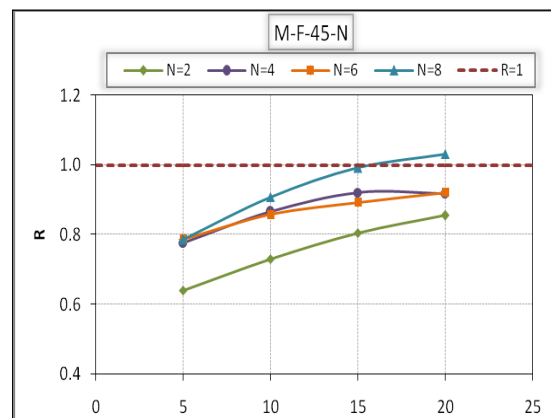
$\theta = 15^\circ$, N=2-8



$\theta = 30^\circ$, N=2-8



$\theta = 45^\circ$, N=2-8



$\theta = 60^\circ$, N=2-8

Figure 9: Influence of degree of displacement on the network index

4. CONCLUDING REMARKS

To clarify the mechanism of improvement of bearing capacity of surface foundation reinforced with a group of micropiles, a series of model loading tests were carried out. The circular foundations were reinforced with a group of micropiles with variety of the arrangement of micropiles, and were subjected to vertical loading. Based on the comparative examinations of the observed load-displacement behaviors, the influence factors on the improvement of bearing capacity was discussed. The following concluding remarks were drawn, as results.

- The failure mode appeared on the surface of the ground material in the F-Test and M-F-Tests series is of local shear type. This can be attributed to the contractive behavior of the loose sand beneath the model foundations.
- Bearing capacity of micropile groups in M-Tests was increased with rising the number and inclination angle of micropiles used.
- An interaction was recognized between foundation and the group of micropiles, and this interaction was significantly effective on the confinement of ground material and on the improvement of the bearing capacity of foundation. Due to the confinement, the base pressure on foundation and the confining pressure on the surface of micropiles were increased. Increasing the number of micropiles in the group results in further confinement of the soil material beneath foundation. On the other hand, there was a decline in the rate of bearing capacity when the inclination angle of micropiles installed to reinforce the foundation. As a general conclusion of this study, it is suggested that micropiles must be arranged so as to enclose the sand beneath the foundation and induce confinement. In the case of the foundation reinforced with a group of micropiles inclined at 15 degrees, the

bearing of the foundation was almost twice the summation of bearing capacities of a surface foundation and a group of micropiles.

- According to the test results, regardless of the inclination angle, using 2 micropiles to reinforce the foundation is not effective.

REFERENCES

- [1] FHWA, (2000), *"Micropile Design and Construction Guidelines-Implementation Manual, Publication No.FHWA-SA-97-070"*, Federal Highway Administration, U.S. Department of Transportation, McLean, Virginia.
- [2] Bruce, D. A., DiMillo, A. F. , Juran, I. , (1995), *"Introduction to Micropiles: An International Perspective"*, *Foundation Upgrading and Repair for Infrastructure Improvement*, ASCE, GSP 50, pp.1-26.
- [3] FHWA, (1997), *"Drilled and Grouted Micropiles – State-of-the-Practice Review, Report No. FHWA-RD-96-016/019"*, U.S Department of Transportation.
- [4] Aschenbroich, H., (2001), *"Micropile Reinforcement Systems and Corrosion Protection"*, ADSC Micropile Seminar, Charlotte, NC.
- [5] Ball, R., (2002), *"Partial Retrofit of Bridges Using Micropiles"*, Research, University of Illinois at Urbana-Champaign, USA.
- [6] Morsy , U.A., (2002), *"Repair of Damietta Bridge Foundations Using Micropiles: A Case Study"*, Annual Conference of the Canadian Society for Civil Engineering, Montréal, Québec, Canada.
- [7] Han, J., Ye, S. L., (2006), *"A Field Study on the Behavior of a Foundation Underpinned by Micropiles"*, *Canadian Geotechnical Journal*, Vol. 43, pp. 19-29.
- [8] Dietz, K., Schrumann, A., (2006), *"Foundation Improvement of Historic Buildings by Microiles, Museum Island, Berlin and St. Kolumba, Cologne"*, *The 7th ISM Workshop, Schrobenhausen, Germany*.
- [9] Wolosick, J. R., Bonar, E., Nufer, P. J., (2007), *"Micropile Foundation Repair and Underpinning, Arts and Science Museum, University of Puerto Rico, Mayaguez"*, *The 8th International Workshop on Micropiles, Toronto, Ontario, Canada*.
- [10] Tsukada, Y., Miura, K., Tsubokawa, Y., Otani, Y., You, G. L., (2006), *"Mechanism of Bearing Capacity of Spread Footings Reinforced with Micropiles"*, *Soils and Foundations*, Vol. 46 , No. 3, pp. 367-376.
- [11] Lizzi, F. , (1978), *"Reticulated Root Piles to Correct Land Slides"* , *Proceedings of ASCE Conference, Chicago, Illinois, October 16-20*.
- [12] Francis, R., Canou, J., Dupla, J.-C., Belmont, G., (1996), *"Group effects of model micropiles in sand"*, *Australian-New Zealand Conference on Geomechanics*, Vol.7, No.1, pp.620-625.

Numerical Analysis of walls constituted by fine soil reinforced with geosynthetics

Carlos, D. M., University of Aveiro and Faculty of Engineering of University of Porto, Portugal, dmc@ua.pt

Pinho-Lopes, M., Department of Civil Engineering, University of Aveiro, Portugal, mlopes@ua.pt

Lopes, M. L., Faculty of Engineering of University of Porto, Portugal, lcosta@fe.up.pt

ABSTRACT

Several studies from the bibliography use numerical simulations and indicate that they are a useful tool that can be used to predict the response to reinforced soil structures. This paper presents the numerical simulation of both the constructive and the consolidation process of a wall in fine soil reinforced with geosynthetics. The design of this structure is presented and was made using the methodology of BS 8006-1:2009; the numerical analysis of the constructive sequence was carried out using commercial software Plaxis (version 8.6). To quantify some of the relevant properties of both soil and reinforcement current tests in soils mechanics and for the characterization of geosynthetics, respectively, were used. In general terms this study can show that the numerical analysis are extremely useful because they are fast; economic; allow the realization of large parametric studies; and allow the verification of the stability of the structure for the ultimate limit states and the verification of its stability during all construction phases. It is also possible to note that with the numerical analysis carried out it is possible to compare and to choose the constructive process that best fits to the conditions of construction (time of construction, maximum strain allowed, maximum level of excess of interstitial pressure allowed to ensure the safety of the structure, etc.).

1. INTRODUCTION

The use of geosynthetics for reinforcement of geotechnical works is normally associated with use of granular soils with good physical and mechanical characteristics. However, the availability of such soils at the construction site is low. This provides an unsustainable increase in the execution cost of such structures. Therefore, the use of this type of construction technique (soil reinforced walls with geosynthetics) can lose its competitive advantage over other types of structures (concrete walls, gravity walls, gabions walls, etc.).

For this reason, it is urgent to use another type of soils (fine soils, cheaper but also with worst physical and mechanical characteristics) for the execution of these structures. The use of such soils in structures where deformations should be limited can be difficult. However, these soils can be used to build less important structures that, in case of failure, do not have consequences in terms of human lives and do not cause substantial economic losses. Some studies where the design of walls constituted by this type of soils was done are presented in Carlos *et al.* (2011), Carlos and Pinho-Lopes (2011a) and Carlos and Pinho-Lopes (2011b).

Several authors use numerical simulations and indicate that it is a useful tool that can be used to predict the response of reinforced soil structures. In this study a set of numerical analysis is presented, where the behaviour of walls constituted by fine soils reinforced with geosynthetics is predicted. These analyses were performed using the finite element program Plaxis (version 8.6) and aimed at studying: the state of stress and strain in the soil and in the geosynthetic; the effect of the soil consolidation process in the constructive process and in the stability of the structure; and the safety of the structure during the period when it is constructed.

To feed the numerical model it was necessary to quantify the relevant properties of the soil and the reinforcement considered. For that, a test program was implemented to characterise these materials. For the soil the tests included the characterization of the grain size distribution, the assessment of the soil unit weight, water content, Atterberg limits and consolidation parameters. The properties of the geosynthetic were assessed using wide-width tensile tests. With these tests it is possible to derive the geosynthetics' tensile strength, the elongation at different loads and its stiffness. The effect of the installation procedures on the relevant properties of the geosynthetic was obtained in Lopes (2010). More, the design of the structure was done according with the British standard BS 8006-1: 2009.

2. DESCRIPTION OF THE STRUCTURE

2.1. Geometry

The idealized structure considered in this study is presented in Figure 1. It was assumed that at the construction site there was already a slope with an inclination with the horizontal of 11.2° . This slope was constituted by a fine soil equal to the soil used to build the new structure and is supported by a competent foundation soil. The new structure is a wall constructed with soil reinforced with geosynthetics and has 6.0 m of height and a face inclination with the horizontal of 70° . This structure has two distinct zones, one with reinforced soil and another with unreinforced soil. The first must have the ability to support the natural slope and the soil placed in the unreinforced zone. It is also important to note that the geometry of reinforced zone of the wall is conditioned by the results obtained in the design. Thus, the reinforcement length and the vertical spacing between reinforcements were found through the design presented in section 3 of this paper.

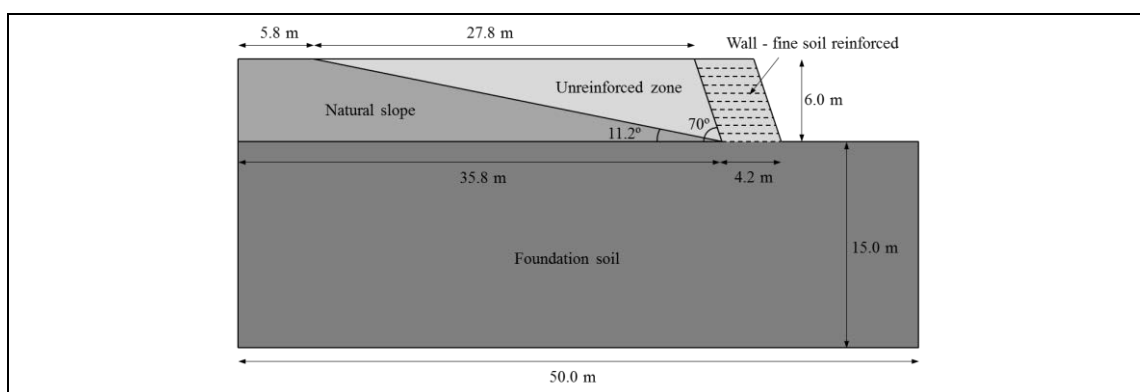


Figure 1: Cross section of the structure considered

2.2. Soils

As mentioned before, in this study two types of soils were assumed. For the natural slope and for the new wall the use of a fine soil with properties similar to soils existing in the region of salt pans of Aveiro Lagoon was considered. The properties that characterize this type of soil were obtained in various laboratory test programs performed by Bonito (2008) and Carlos (2009). Recently a new set of laboratory tests was performed in order to characterize the soil unit weight, the water content, the Atterberg limits and the consolidation parameters of the fine soil. The results of these laboratory tests and some of relevant properties obtained for the authors mentioned above are shown in Table 1. The soil properties presented in this table are: the soil unit weight, γ ; the soil dry unit weight, γ_d ; the natural water content, w ; the liquid limit, w_L ; the plastic limit, w_P ; the plasticity index, I_P ; the compression index, C_c ; the recompression index, C_r ; the soil friction angle and the cohesion in terms of effective stresses, ϕ' and c' , respectively; the undrained shear strength, c_u ; the coefficient of compressibility, a_v ; the coefficient of volume compressibility, m_v ; and the coefficient of vertical consolidation, c_v . In Table 1 the classification of the soil samples tested according with the ASTM D2487-11 and AASHTO M145, is also included.

For the foundation soil an idealised granular soil is considered, with enough resistant capacity to prevent failures in this area. The properties assumed for this soil were taken from Bardet (1997) and Matos Fernandes (2006). In these documents it is possible to find ranges for the different properties that characterize several types of soils. In this study was used the ranges of properties related to sandy soils.

Table 2 includes the properties of the two soils that were used to perform the design and the numerical analysis of the structure. In the case of fine soil, it was considered that the unit weight of soil is equal to the average of the values obtained by Carlos (2009) and by the new test program, the soil consolidation parameters are obtained at the new test program, and because until this moment it was not to obtain values for the mechanical properties from laboratory tests, values obtained by Bonito (2008) for soils with comparable properties were assumed. With regard to the permeability of the fine soil, that was obtained in Matos Fernandes (2006) (in the range suggested for silts). As mentioned, for the foundation granular soil, its properties were chosen in Bardet (1997) and Matos Fernandes (2006) and are: the soil unit weight, γ ; the soil friction angle and the cohesion in terms of effective stresses, ϕ' and c' , respectively; the

Young Modulus, E ; the Poisson's ratio, ν ; and the vertical and horizontal permeability of soil, k_v and k_h , respectively.

Table 1: Properties of the fine soil obtained from several test campaigns

Parameter		Bonito (2008)	Carlos (2009)	New values	
				Sample 1	Sample 2
γ (kN/m ³)		16	17	18.3	17.7
γ_d (kN/m ³)		-	13.8	15	13.8
w (%)		-	23	22	28
w_L (%)		-	35	35	36
w_P (%)		-	22	25	27
I_P (%)		-	13	10.4	9.4
C_c		-	0.17	0.34	0.33
C_r		-	0.02	0.06	0.06
$a_v \times 10^{-4}$ (kPa ⁻¹)		-	0.06 – 14	0.05 – 23	0.07 – 48
$m_v \times 10^{-4}$ (kPa ⁻¹)		4.13	0.5 – 8	0.03 – 13	0.05 – 28
$c_v \times 10^{-8}$ (m ² /s)		5.2	2.6 – 13.2	4.74 – 10.5	5.8 – 17.8
ϕ' (°)		34	-	-	-
c' (kPa)		7 - 27	-	-	-
c_u (kPa)		15 - 25	-	-	-
Soil classification	Unified (ASTM D2487–11)	-	CL – ML – silty clay	ML – sandy silt	ML – sandy silt
	AASHTO M 145	-	A-6	A-4	A-4

Table 2: Soil properties used in the design and in the numerical analysis of the structure

Parameter	Fine soil	Foundation soil
γ (kN/m ³)	17.6	20 [±]
γ_d (kN/m ³)	14.4	-
C_c	0.34	-
C_r	0.06	-
ϕ' (°)	34 [±]	40 [±]
c' (kPa)	7 [±]	5 [±]
c_u (kPa)	15 [±]	-
E (GPa)	-	200 [±]
ν	-	0.35 [±]
$k_v = k_h$ (m/day)	0.0864 [×]	864 [×]

Bonito (2008)[±]; Matos Fernandes (2006)[×]; Bardet (1997)[±]

2.3. Geosynthetics

The geosynthetic used in this study is a reinforcement geocomposite consisting of continuous filament non-woven, reinforced by high tenacity polyester yarns. The relevant properties of these materials used for this study were obtained through laboratory wide-width tensile tests. With this laboratory test it was possible measure the ultimate tensile strength (54.63 kN/m); the strain exhibited by the specimen under maximum load (10.57 %); and the stiffness (600 kN/m). Finally, for the quantification of the effect of damage during the installation the results obtained by Lopes (2011) were used. This author has done wide-width tensile tests after submitting the geosynthetic to damage according with EN ISO 10722: 2007 and obtained a reduction factor for damage during installation of 1.7.

3. DESIGN OF STRUCTURE

The design of this structure has been done using the methodology of BS 8006-1: 2009. This standard is based on the limit states philosophy for the design of reinforced soil walls and slopes, and involves the increasing of soil weight and live loading by applying appropriate partial load factor and reducing of the soil properties and reinforcement base strength by appropriate partial material factors. To analyse the internal stability of these structures, this standard considers that the structure has the potential to fail by the rupture or loss of bond of the reinforcements. Thus, consideration should be given to the local stability of individual layers of elements, sliding on horizontal planes and the stability of wedges. Besides this the following factors which influence stability should be included in the design check: the capacity to transfer

shear between the reinforcing elements; the tensile capacity of the reinforcing elements; and the capacity of the fill to support compression. For the external stability, the safety for bearing and tilt failure, for the failure by sliding along the base, and for the overall stability should be checked for drained (Effective stresses, ES) and undrained (Total stresses, TS) conditions (BS 8006-1: 2009).

For the design of the studied structure the recommendations specified in BS 8006 1: 2009 were used. The parameters used in the design are: the geometry of the structure; the properties of soils and geosynthetics mentioned in section 2; the partial safety factors suggest by the standard; and two types of surcharges, a service surcharge to predict the stability for long-term conditions and a construction surcharge to predict the stability during the construction of the structure (the value used is 10 kPa for the two types of surcharges). Additionally, it was necessary to quantify the parameters that characterize the interaction between soil and reinforcement. In BS 8006-1:2009 this interface is characterized by using two parameters, the coefficient of friction between the soil and the geosynthetic, c_i , and the adhesion coefficient between the soil and the geosynthetic, a' . At the time this paper was written tests to determine such parameters had not yet been carried out. Thus, for the design c_i and a' were considered equal to 0.5.

The parameters resulting from the internal design are the length of the reinforcement, L_R , and the vertical spacing between reinforcements, e_v . The length of the reinforcement is equal to $0.7 \times H$. How it is possible to see, this parameter is only influenced by the height of the wall, H , and for this structure it is equal to 4.2 m. To calculate e_v it is necessary verify the internal mechanism of collapse referred above. In the design it was verified that the factor that influence the dimension of e_v is related with the tensile capacity of the reinforcement. So, the smallest e_v that can be used is 0.6 m and it is not influenced by the interface parameters referred before. Because of that, the value considered for the characterization of interface does not affect the internal design.

For the verification of the external stability the mechanisms of collapse mentioned above were checked. In this study, the safety for bearing and tilt failure and safety for sliding along the base were checked with the equations provided by the standard BS 8006-1:2009 for this purpose. The results obtained for these mechanisms of collapse allowed saying that the structure is stable for the effective stress state (long-term). However, in contrast to what occurs for effective stresses, when the structure is subject to a state of total stress (short term) the safety of the structure to the mechanism of sliding along the base cannot be guaranteed. This occurs because the parameters considered to characterize the soil-reinforcement interface are small (c_i and a' equal to 0.5) and because, for that analysis, the effect of construction process and the effect of the use of a containment structure was not considered.

The overall stability was analysed by using commercial software: Slope/W of GeoSlope (version 2007). To reduce the number of cases to be studied for the overall stability, an overall safety factor was considered, with a minimum admissible value of 1.5. Thus, in this analysis the use of partial safety factors mentioned above was not considered. For this verification, the seepage forces and the effect of geosynthetics used on the face of the slope of the structure were not taken into consideration (the face stability is only assured by the soil strength). The global slip surfaces most critical for the global stability of the structure for both stress states are presented in Figure 4. In the same figure the safety factor obtained for the slip surfaces presented (1.726 for effective stress state and 1.151 for total stress state) are also included.

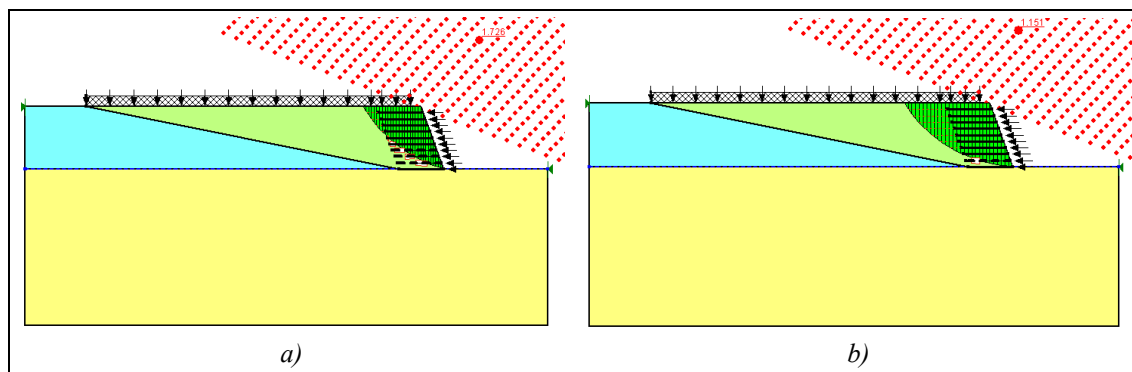


Figure 2: Global slip surface: a) effective stress state; b) total stress state

Thus, it is clear that for this mechanism of failure the stability of the structure can only be ensured for the long term. However, for that analysis the effect of construction process and the effect of the use of a

containment structure were not considered. Thus, the stability of the structure cannot be guaranteed when the soil is subjected to the total stress state. In this way, the construction of the structure should be done in stages, alternating stages of consolidation with the construction of soil and reinforcement layers. To overcome this problem, in the second part of this work is carried out the study of the constructive process and the consolidation of the structure.

4. NUMERICAL SIMULATIONS

4.1. Description of the study

The main objective of this paper is to analyse the behaviour of a wall constructed with fine soil reinforced with geosynthetics during its construction and consolidation processes. To this end several numerical analyses were performed with the finite element commercial software Plaxis (version 8.6). The realization of this type of analysis allows checking the state of stress and strain in soil and reinforcements, allows studying the effect of the consolidation process of soil in the construction process and in the stability of the structure, and allows checking the safety of the structure during the construction period.

First it is important explaining the construction process that can be used for the construction of such structures. The construction of reinforced soil walls usually begins with the regularization of the foundation soil where the first layer of geosynthetic reinforcement is placed. Later the geosynthetic is covered with layers of compacted soil with a thickness ranging from 0.15 and 0.3 m (recommendation of BS 8006-1:2009). Sufficient soil layers are built, in order to achieve the thickness corresponding to the vertical spacing between reinforcement layers. When this first layer of reinforced soil is completed the procedure is repeated for the subsequent layers of reinforced soil until the top of the structure is reached. It is also important to mention that during the construction of the structure it is necessary to perform its containment. In this study it was considered that the face of the structure was constructed with wrap around system.

Usually, for saturated granular soils, where there are no problems with the development of excess interstitial pressure, Δu , the constructive procedure is sufficient to make sure that the construction of the structure is safe. In this case, the behaviour of the soil is drained and the construction of the structure can be performed without breaks for dissipation of Δu . However, for saturated fine soils it is very important the study of impact of the development of Δu on the stability of the structure. Thus, it may be necessary to add periods to the dissipation of Δu , i.e., to allow for the consolidation of the different soil layers.

As the structure considered in this study is to be built with a saturated fine soil, the most determinant parameter for the security of the structure is precisely the increase in interstitial pressure generated during the construction of soil layers. Thus, in this paper an attempt to evaluate the effect of the undrained behaviour of the soil on the safety of structure during the construction period is done. The effect of the consolidation in the construction process is also studied.

One of the essential components to perform a successful numerical analysis of a geotechnical problem is the choice of the soil constitutive model. Currently there are several constitutive models able to reproduce the several aspects of the behaviour of a real soil. Therefore it is necessary to decide which of these soil characteristics regulate the behaviour in a particular geotechnical problem (for example: stiffness, deformation, anisotropy, etc.) and to choose a constitutive model that can reproduce these characteristics in the best way (Potts e Zdravkovic, 2001). The same is true when it comes to evaluating the behaviour of the reinforcing elements.

In this study the soil constitutive model should allow to observe the effect of the consolidation of fine soil. Plaxis has six constitutive models of soil available. From these the most suitable for primary consolidation problems are the soft soil model and the hardening soil model. In Plaxis manual (Plaxis, 2002) is mentioned that the most suitable for primary consolidation problems is the hardening soil model. However, because it is a more advanced model and it needs a greater number of soil parameters, which have not been quantified in this study it was decided to use the soft soil model (this constitutive model is simplest but still widely used by users of this software tool (Plaxis, 2002)). For the characterization of the reinforcements, Plaxis (version 8.6) has two constitutive models available, an elastic model and an elastoplastic model. In this study the elastoplastic model was considered, because the expected strain of reinforcement is high.

In the numerical analyses carried out the effect of several parameters was studied, in order to identify the fastest and the safest way to construct the structure. The cases studies considered are presented in Table 3. They correspond to the study of the effect of: the surcharges caused by equipment used for the construction; consolidating each built soil layer or only when it is necessary to guarantee the security during the construction of the structure; the maximum value of Δu measured after the period of consolidation.

Table 3: Numerical analysis performed in the study

Case of study	Consideration of the surcharge	Maximum value of Δu at the end of the consolidation period (kPa)	Consolidation periods
GC_ss_p1_cc	No	<1	In all layers
GC_ss_p5_cc	No	<5	In all layers
		<1	Additional at the end of construction
GC_cs_p1_cc	Yes	<1	In all layers
GC_cs_p5_cc	Yes	<5	In all layers
		<1	Additional at the end of construction
GC_ss_p1_sc	No	<1	Only those needed
GC_ss_p5_sc	No	<5	Only those needed
		<1	Additional at the end of construction
GC_cs_p1_sc	Yes	<1	Only those needed
GC_cs_p5_sc	Yes	<5	Only those needed
		<1	Additional at the end of construction

ss - without surcharge; cs - with surcharge; p1 - $\Delta u < 1$; p5 - $\Delta u < 5$; cc – with consolidation in all layers; sc - without consolidation in all layers

As mentioned the construction of the structure is done in stages. Plaxis (version 8.6) allows the consideration of the staged construction of the structure. To this end, Plaxis allows creating several stages of computation with the respective output of results. In the numerical analyses carried out it was considered that the construction of each layer of reinforced soil corresponds to a computation stage. In addition, each period of consolidation considered also corresponds to a stage of calculation.

4.2. Presentation and discussion of results

The number of results calculated by Plaxis in each numerical analysis is very high and includes the stresses in the soil (total, effective, interstitial, Δu , etc.), the axial stresses in reinforcement and the displacements in the soil and in the reinforcement (total and incremental displacements in different directions) at all stages considered in the calculation. As an example, Figure 3 shows some results that can be obtained with this numerical tool. However, as this study intends to evaluate the effect of the construction process and the consolidation of the soil, the results compiled here only illustrate the development of Δu , the time required for the dissipation of the Δu , and the total displacements observed in each stage of construction of the structure.

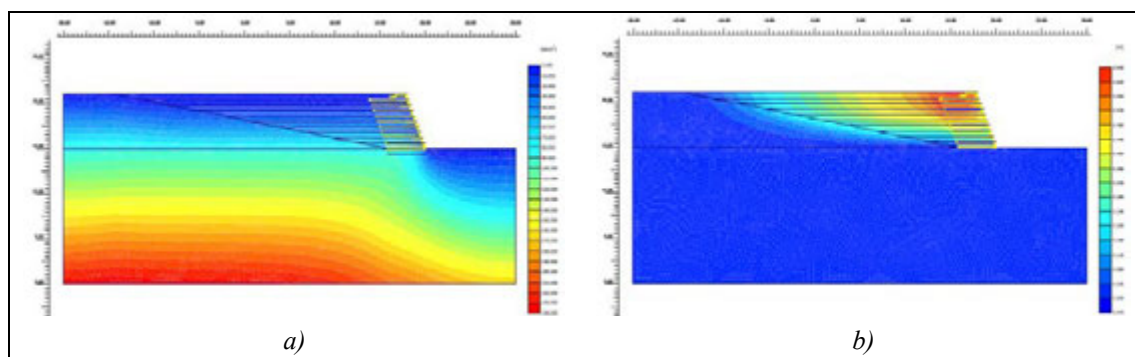


Figure 3: Results obtained in the numerical analysis performed with Plaxis - examples from the last stage of GC_ss_p1_cc: a) vertical effective stress; b) total displacement

First of all, it is important to note that from the results of all numerical analyses carried out it is possible to conclude that it is possible to guarantee the safety of the structure on the short-term. Thus, the stability

issues that were observed in the verification of external stability performed on the design of the structure are not observed. For this reason it is considered that for all cases analysed the stability of the structure is guaranteed.

Regarding to the results obtained in the numerical analyses, the variation of Δu along the construction of the structure is shown in Figure 4. The values of time required for the dissipation of Δu are accumulated, in other words, the value presented in each stage of consolidation is equal to the time required for dissipation of Δu generated in all previously stages of construction. As expected and as it is clear from the figure, in all numerical analyses carried out it is verified that when a layer of soil is built Δu increases, and when the construction of the structure is stopped, in order to consolidate the soil, Δu decreases. Furthermore, when the number of layers built increases, the Δu generated by the construction of another layer of reinforced soil is greater.

Concerning the effect of the surcharges caused by equipment used in the construction it is verified that when this is considered the Δu generated are slightly higher (Figure 4a). In addition, the consideration of the surcharge caused by construction equipment doesn't have great impact on the time required for dissipation of Δu (Figure 4a).

When analyzing the effect of the stage where the consolidation is done it is verified that the Δu generated are much lower when the consolidation is done after the construction of each layer of reinforced soil (Figure 4b). It is also verified the time required for the dissipation of Δu is greater (Figure 4b). In fact, when the consolidation is carried out immediately after the construction of each layer of reinforced soil the Δu generated are smaller, but there are more periods for the consolidation of the soil.

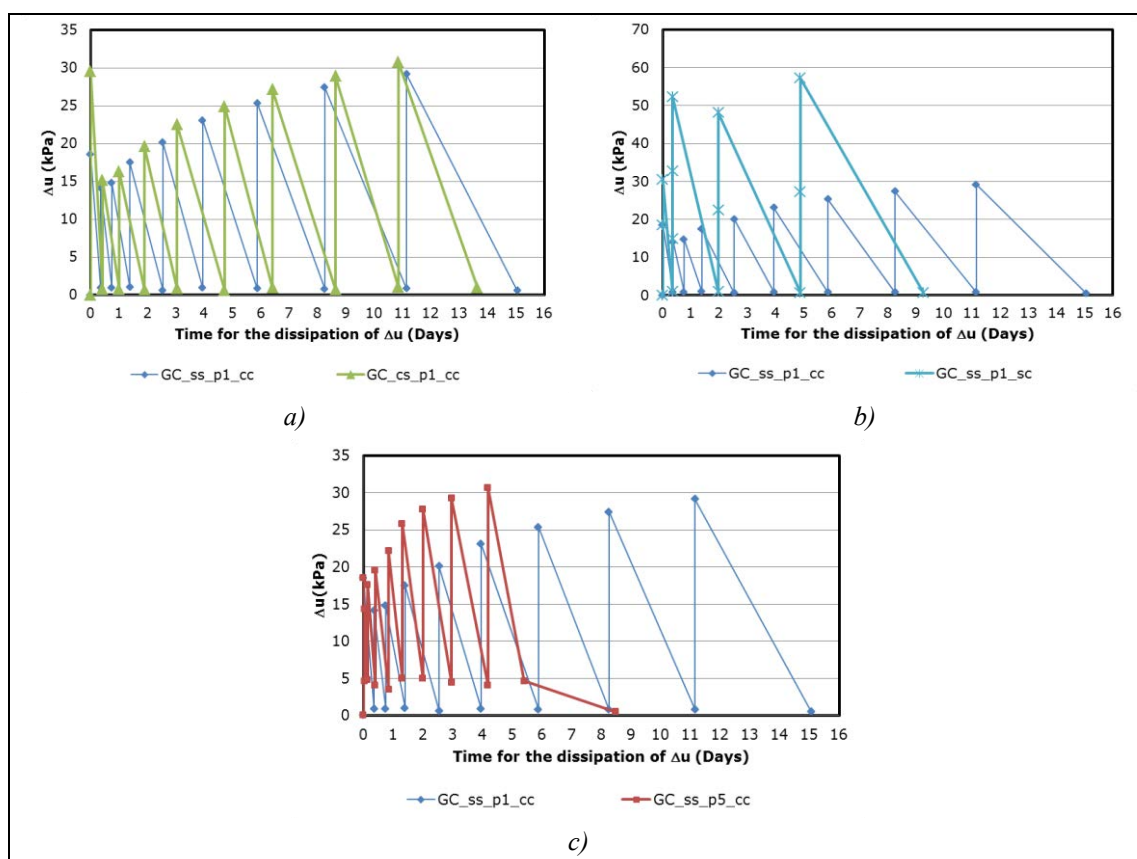


Figure 4: Relation between Δu and the time required for its dissipation: a) effect of surcharge; b) effect of the stage where the consolidation is done, c) effect of the maximum value of Δu after a period of consolidation

Finally, it is verified that when the stages of consolidation end for $\Delta u < 1$ kPa, the Δu generated in the construction of a new reinforced soil layer are lower than when the stages of consolidation end for $\Delta u < 5$ kPa (Figure 4c). As expected, when it is necessary to dissipate more Δu this operation will take more time. It should also be noted that there is an effect of accumulation of Δu when a new layer of

reinforced soil is constructed, in other words, the fraction of Δu that is not dissipated in the earlier stages of consolidation increases the Δu generated by the construction of a new layer.

The variation of total displacement observed during the construction of the structure is shown in Figure 5. In this case, the displacements presented are also accumulated values, in other words, the displacement observed in the stage of construction in study is the sum of the displacement observed in the previous stages with the increment of displacement observed in the stage in study. It is also important to recognize that the displacements may occur at different points of the structure. However, it is only intended to evaluate how the deformation of the structure changes with the different construction processes, so, this doesn't have great significance.

Regarding the results obtained, in this case it is observed that the factors that most significant influence the maximum soil displacement are the surcharge caused by the equipment used in the construction and the stage of construction in which the consolidation is performed. As can be seen in Figure 5a, if the results obtained in the numerical analysis GC_ss_p1_cc and GC_cs_p1_cc are compared, it appears that when the surcharge is considered in the analysis the maximum total displacement observed is considerably higher. This happens because the structure is subjected to an additional load, which naturally causes an increase in the deformation of the structure.

The same effect is observed if the consolidation of the structure is performed only when strictly necessary to ensure the safety in the structure. In this case the maximum total displacements observed are higher when the consolidation was carried out following the construction of each layer of reinforced soil (Figure 5b). Thus, it is natural that the observed deformation is higher. As observed in Figure 5b, the structure is built more rapidly and with higher levels of Δu when the consolidation is performed only when strictly necessary to ensure safety.

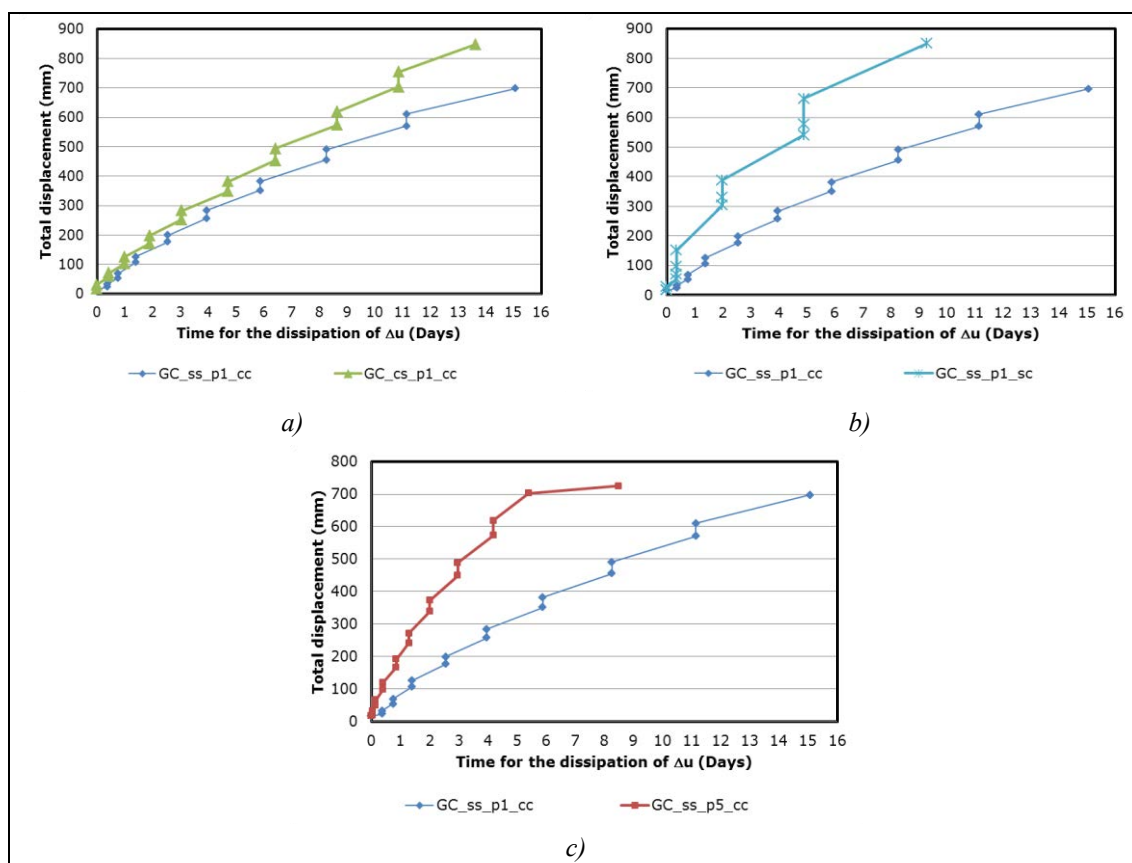


Figure 5: Variation of total displacement observed during the construction of the structure (accumulated values): a) effect of surcharge; b) effect of the stage where the consolidation is done, c) effect of the maximum value of Δu after a period of consolidation

Finally, it is verified that when the stages of consolidation end for $\Delta u < 1$ kPa, the maximum total displacement observed is similar to the one obtained when the stages of consolidation end for $\Delta u < 5$ kPa

(Figure 5c). Thus it is clear that this factor does not influence largely the deformation observed during the construction of the structure.

The results presented so far intended at assessing the effect of the construction process on the behaviour of the structure. However, as shown in Table 3 eight different numerical analyses were performed. In Figure 8 the time required for the dissipation of Δu and the total displacements observed in the performed numerical analysis are compiled. With these results it is possible to choose the constructive procedure that best fits the requirements of the builder and the owner of the structure.

Since is not possible to build the structure without the use of construction equipment, the choice of the construction process used to build this structure must take into account this surcharge. Thus, considering the surcharge caused by the equipment of construction and the results presented in Figure 6 the fastest way to build the structure corresponds to the construction process modelled in the numerical analysis GC_cs_p5_sc (sum of all breaks used to the dissipation of Δu equal to 6.819 days) and the constructive process that causes less deformation in the structure was modelled in the numerical analysis GC_cs_p1_cc (maximum deformation around 848 mm).

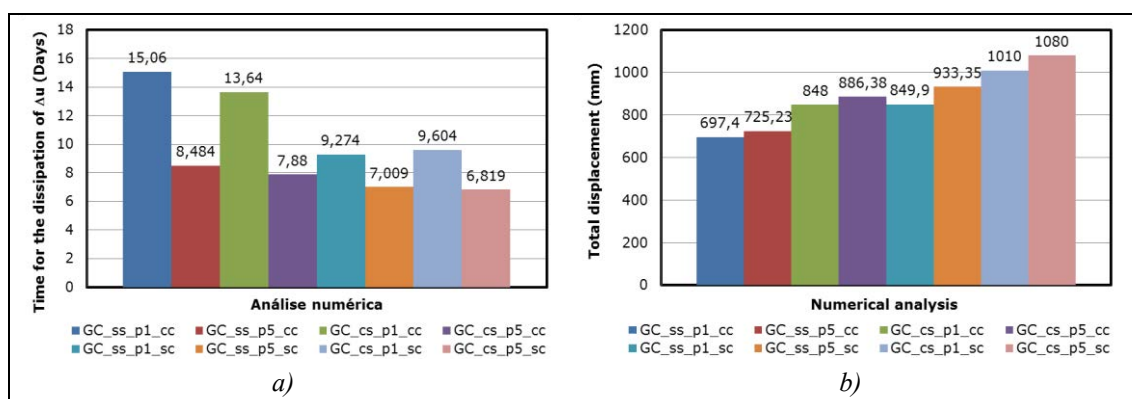


Figure 6: Maximum values obtained in different numerical analysis: a) time required for the dissipation of Δu ; b) total displacement

However, with the results presented in this study it is not possible to choose which constructive process shall be used for the construction of the structure. This choice depends on the time available for the construction of the structure, on the maximum deformation that the structure can suffer and on the level of residual Δu that is considered acceptable during the construction period. However, the results can be used to illustrate that this type of numerical analysis is a fast, reliable and economical way to predict the behaviour of the structure and choose the best procedure to build the structure.

5. CONCLUSIONS

In this paper the design of the walls constituted by fine soils reinforced with geosynthetics performed is presented as well as the results of numerical analysis carried out to simulate the effect of the constructive and consolidation processes of the same structure. The main conclusions that can be observed from the analysis of results of this study can be divided into three groups: those associated with the results achieved, those related to the utility of these results and those allusive to the utility of this kind of numerical analysis.

The conclusions related with the results are:

- as expected, when a layer of soil is constructed Δu increase and when the construction of the structure is stopped in order to consolidate the soil Δu decrease;
- when the number of layers built increases, the Δu generated by the construction of another layer of reinforced soil is greater. This is because the distance that a water particle has to travel also increases;
- the Δu generated in the construction increase when the surcharge related with the construction equipment is considered. The time required for the dissipation of these excess is slightly higher when this surcharge is considered;
- when the consolidation is done after the construction of each layer of reinforced soil the Δu generated are much lower than the ones obtained when the consolidation is done just when is strictly necessary.

However, the time required for the dissipation of Δu is greater in the first case, because more periods for the consolidation of the soil are necessary;

- as expected, when a smaller residual Δu is imposed the consolidation time increases;
- there is an accumulation effect of Δu when a new layer of reinforced soil is built, in other words, the fraction of Δu that is not dissipated in the earlier stages of consolidation increases the Δu generated by the construction the new layer.
- when the surcharge is considered in the numerical analysis the total displacement observed is significantly higher;
- the deformation observed in the structure is higher when the consolidation is done just when is strictly necessary.

Regarding the utility of these results it is possible to note that they allow comparing and choosing the constructive process that best fits to the conditions established by the owner of the structure (time available for the construction of the structure, maximum deformation that the structure can suffer and level of residual Δu what is considered acceptable during the construction period). It also allows checking the safety of the structure during all stages of its construction.

Finally it is important to mention that the numerical analysis are extremely useful because they are fast, economic, allow performing extensive parametric studies, and, besides allowing to check the stability the stability for the ultimate limit states, allow the verification of the stability of the structure during all stages of construction. However, they should always be performed with caution. The results should be validated using results obtained from the instrumentation of real structures and methods validated by well documented cases.

6. ACKNOWLEDGEMENTS

The authors acknowledge the support of FCT (Fundação para a Ciência e a Tecnologia), Research Project PTDC/ECM/099087/2008 and COMPETE, Research Project FCOMP-01-0124-FEDER-009724 and FCT, Research Project PTDC/ECM/100975/2008 and COMPETE, Research Project FCOMP-01-0124-FEDER-009750.

REFERENCES

- ASTM D2487–11. Standard Practice for Classification of Soils for Engineering Purposes.*
- AASHTO M 145. Classification of Soils and Soil-Aggregate Mixtures for Highway Construction Purposes*
- Bardet, J-P. (1997). Experimental Soil Mechanics. Prentice Hall, ISBN: 0133749355, 583p*
- Bonito F. A. B., 2008, Reologia dos lodos e de outros sedimentos recentes da Ria de Aveiro, Ph.D. thesis in Civil Engineering, University of Aveiro, Aveiro, 422p, (In Portuguese)*
- BS8006-1: 2009, Code of Practice for Strengthened/reinforced soils and other fills, BSI London*
- Carlos D. M., 2009, Reforço com geossintéticos de muros das marinhas da Ria de Aveiro, Master's thesis in Civil Engineering, University of Aveiro, Aveiro, 171p, (In Portuguese)*
- Carlos D. M. and Pinho-Lopes M., 2011a, Reinforcement with geosynthetics of walls of the saltpans of the Aveiro Lagoon, Geotechnical and Geological Engineering, Vol. 29, Number 4, 519-536, DOI: 10.1007/s10706-011-9400-6*
- Carlos D. M. and Pinho-Lopes M., 2011b, Reinforcement of non-traditional soil with geosynthetics – application to the walls of the saltpans of the Aveiro lagoon, Proceedings of the 15th European Conference on Soil Mechanics and Geotechnical Engineering, A. Anagnostopoulos et al. (Eds.) IOS Press, Athens, Greece, doi:10.3233/978-1-60750-801-4-1441, pp. 1441-1446*

Carlos D., Pereira M., Costa S., Pinho-Lopes M. and Coelho C., 2011, *Walls of the Saltpans of the Aveiro Lagoon, Portugal – Current Status and Proposed New Solutions Using Geosynthetics*, ICS2011 - 11th International Coastal Symposium, Szczecin, Poland, *Journal of Coastal Research*, SI 64, pp. 1467-1471, ISSN 0749-0208

ISO 10722:2007. *Geosynthetics - Index test procedure for the evaluation of mechanical damage under repeated loading - Damage caused by granular material.*

Lopes P. M. M., 2011, *Efeito do balastro nas propriedades de geossintéticos em vias-férreas*, Master's thesis in Civil Engineering, University of Aveiro, Aveiro, 146p, (In Portuguese)

Matos Fernandes, M. (2006). *Mecânica dos solos. Conceitos e princípios fundamentais. (Vol. 1)*. Porto, Portugal: FEUP Edições.

Plaxis (2002). *Material models manual. Plaxis 2d (version 8)*

Potts, D. M. e Zdravkovic, L. (2001). *Finite element analysis in geotechnical engineering: application (Vol. 2)*. London, UK: Thomas Telford, 427p.

The undrained mechanical behaviour of a fibre-reinforced heavily over-consolidated clay

A. Ekinici, Department of Civil, Environmental & Geomatic Engineering, University College London, United Kingdom
a.ekinci@ucl.ac.uk

P.M.V. Ferreira, Department of Civil, Environmental & Geomatic Engineering, University College London, United Kingdom,
p.ferreira@ucl.ac.uk

ABSTRACT

The benefits of micro-reinforcement in soils have attracted a lot of research in the last couple of decades. However, not enough is known about the effects of the compaction procedure used to prepare samples in the laboratory.

This paper presents data from laboratory undrained triaxial tests on reinforced and unreinforced samples of heavily over-consolidated clay from the Lambeth Group. The samples were prepared by chopping the in-situ natural soil into small peds (typically 10 to 20mm) so that some of the in-situ characteristics of the natural soil would be retained. The soil peds were then dynamically compacted with and without the addition of fibres. Undrained triaxial tests were carried out using 100mm and 38mm diameter triaxial samples. The results presented have shown that the addition of reinforcement appear to cause a shift of the One Dimensional Normal Compression Line (1-D NCL) of the reinforced material.

The undrained shearing behaviour of the reinforced and non-reinforced soil is also analysed and conclusions drawn.

Fibre alignment studies were also conducted, indicating that the majority of the fibres are aligned within $\pm 20^\circ$ with the horizontal plane while more than 50% are oriented within $\pm 10^\circ$. This preferred orientation is believed to be caused by the compaction method used to prepare the samples.

1. INTRODUCTION

The use of tensile elements within the soil mass was introduced more than 3,000 years ago by the Babylonians. They used intertwined palm branches to reinforce the “ziggurat” temple (Jha and Mandal 1988).

A similar procedure was followed by The Romans who built retaining walls by placing timber baulks perpendicular to the face of the walls. More recently, in 1822, Colonel Pasley introduced, in the British Army, a form of reinforced soil where the backfill was reinforced by horizontal layers of brushwood, wooden plants or canvas.

In the 1930s, the modern concept of soil reinforcing was proposed by Casagrande who idealised the problem in the form of a weak soil reinforced by high-strength membranes laid horizontally in layers. However, it was Vidal, in the 1960s, who investigated this field in detail. Vidal’s concept was to lay flat reinforcing strips horizontally in a frictional soil, as this enabled the interaction between the soil and the reinforcement to create a friction force to hold the soil in place (Colin 1996). Reinforcing soils with tensile elements is still a common practice in many developing countries where soil and straw are mixed to be used as a construction material.

This paper presents data from laboratory undrained triaxial tests on laboratory-compacted Lambeth Group clay reinforced with polypropylene fibre. Extensive research has been performed on reinforced sandy soils with numerous types of fibres; however, there is a lack of knowledge in understanding the effects of discrete fibre reinforcement on heavily over-consolidated clays and the effects of in-situ mixing and compaction techniques in the response of the composite soil. This will provide effective guidance in the construction and remediation of slope failures and the widespread use of this type of reinforcement as an effective way to reduce maintenance works and costs on road embankments and cuttings. Improvements in soil characteristics using micro-reinforcement will also lead to a more sustainable way of using unsuitable soils.

The main objectives of this paper are as follows:

- To characterise and understand the undrained behaviour of compacted clay peds with and without reinforcement.
- To map the alignment of fibres generated by the compaction of clay peds in the laboratory and in-situ.

2. BACKGROUND

Consoli et al. (2005) studied the behaviour of polypropylene fibre-reinforced sand under isotropic compression and observed that the inclusion of fibres into sand can change isotropic compression behaviour. They also identified two distinct and parallel compression lines for the fibre-reinforced and non-reinforced sand. Similarly, Santos et al. (2010) assessed the behaviour of the host soil and that of the fibre-reinforced soil and concluded that, in volumetric space, the NCL of the sand-fibre material lies above that of the host sand, and parallel to it.

In a similar study Li (2005) assessed the mechanical response of fibre-reinforced clay by carrying out Consolidated Undrained (CD) tests and concluded that fibre-reinforcement restrains the volume dilation that leads to an increase of the excess pore water pressure in undrained conditions. The author also concluded that an increase in the deviator stress due to fibres is not as obvious as in the case of sand. In addition Ozkul and Baykal (2007) investigated the influence of rubber fibre inclusion on the strength and shear behaviour of clay under different loading conditions; the contribution of fibres to the strength of clay was found to decrease with increasing level of confinement. Maher and Gray (1990) also studied the effect of confining pressure on the response of fibre-reinforced sand samples under static loads. The findings showed that there is a critical confining pressure beyond which the stress-strain behaviour of the sample changes from a curved profile to a linear envelope (or bilinear curve). It was found that the maximum increase in strength for reinforced sand occurred at confining pressures less than this critical value of pressure.

Researchers have presented contradictive results on the compaction parameters of fibre-reinforced soils. Research conducted by Rifai and Miller (2004) and Al-Tabbaa and Aravinthan (1998) on polypropylene-fibre-reinforced soils have shown that the addition of 0% to 1.0% (in weight of dry soil) fibres in soil does not produce significant effects on the magnitude of the dry density or the optimum moisture content of the composite. On the other hand, Cetin et al. (2006) and Prabakar and Sridhar (2002) have reported that the inclusion of any percentage of polypropylene fibres is found to reduce the maximum dry density and increase the optimum moisture content.

Further studies (Ozkul and Baykal 2006) on the effect of compaction on composite materials revealed that the ASTM Standard dynamic compaction process causes a preferential alignment of fibres in a parallel direction to the compaction plane. Similarly, a study by Ozkul and Baykal (2007) confirmed that the compaction process induces preferential alignment of fibres in a horizontal direction. This preferential alignment ($\pm 45^\circ$ of horizontal) was found to be favourable for the improvement of shear strength because it does not coincide with the plane of maximum shear strain expected in a triaxial test. Correspondingly, Diambra et al. (2007) investigated the alignment of polypropylene fibre in sand. The samples were prepared using the moist tamping technique, which produces a soil-fibre fabric that resembles that of compacted reinforced soil in field. The distribution was found to be far from isotropic: typically 97% of fibres have an orientation that lies within $\pm 45^\circ$ of the horizontal plane.

3. EXPERIMENTAL PROCEDURE

3.1. Site and Sampling

For laboratory testing, disturbed samples were collected from an excavation located near junction 23 of the M25, north of London. Mouchel and the Highways Agency, industrial partners on this project, used polypropylene fibres to reinforce a slope in the site. In order to be able to retain natural properties of the collected samples for preliminary testing and to create laboratory compacted samples for triaxial testing the required amount of disturbed samples from the excavated soil were stored in sealed containers to avoid loss of moisture and associated loss of natural properties.

The soil used in this study was Lambeth Group clay, natural over-consolidated fissured clay. The Lambeth Group, which was previously known as the Woolwich and Reading Beds, formed in the London and Hampshire Basins, where it directly overlies the Chalk or Thanet Sand Formation, and is succeeded by the Harwich and London Clay Formations (Skipper 2009). The group features notable lateral and vertical lithological variations, which have contributed to a long history of engineering problems in London (Hight et al. 2004).

3.2. Characterisation Tests

Atterberg limits, specific gravity and particle size distribution were performed on the soil samples. These tests provided standard data for the soil which will be used in subsequent analyses.

The grain size distribution is fairly uniform with 95% passing 0.05mm, 85% passing 0.015, 60% passing 0.004mm and 46% passing 0.001mm (Figure 1). The soil is classified as inorganic clay of high plasticity (CH), according to USCS classification (ASTM D 2487).

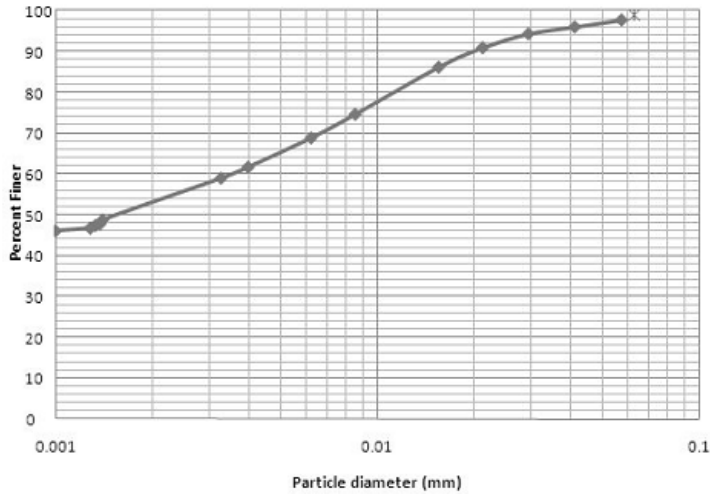


Figure 1: Grain size distribution of Lambeth Group clay tested

Table 1: Index properties of clay soil

Property	Values	Unit
Liquid Limit (wL)	59.5	%
Plastic Limit (wp)	24.1	%
Plasticity Index (Ip)	35.4	NA
Liquidity Index (IL)	0.01	NA
Particle Density (ρ_s)	2.65	g/ml

3.3. Fibre Properties

Most of the research on fibre-reinforced soils has made use of polypropylene fibres. It is the most commonly used synthetic material, mainly because of its low cost and environmental acceptability. The polypropylene fibres used in this investigation have a width of 4mm, length of 63mm and thickness of about 0.021mm. A summary of the properties of the fibres is presented in Table 2.

Table 2: Fibre Properties

Properties	Values
Specific gravity	0.91 g/cm ³
Linear mass density	60 Denier*
Breaking tensile strength	350MPa
Elastic Modulus	3500MPa
Dispersibility	Excellent
Melting point	165 °C
Burning point	590 °C
Acid and alkali resistance	Very good
Moisture absorption	0 %
Breaking elongation	18%

*1Denier=1g/9000m

3.4. Sample Preparation

In order to simulate the in-situ compaction of heavily over-consolidated clays, the retrieved samples were chopped into small pieces of 10 to 15mm diameter (Photo 1). Compaction tests (Figure 2) were carried out to obtain the optimum moisture content (OMC) and the maximum density (MD). The results confirmed that there was no effect of fibres in the OMC and the MD of the soil, with the OMC being equal to 20.5% for the

compacted samples and around 21.5% for the compacted soil with fibres. The maximum dry density of reinforced and non-reinforced compacted samples was found to be 1.70g/cm³ and 1.68 respectively (Figure 2).

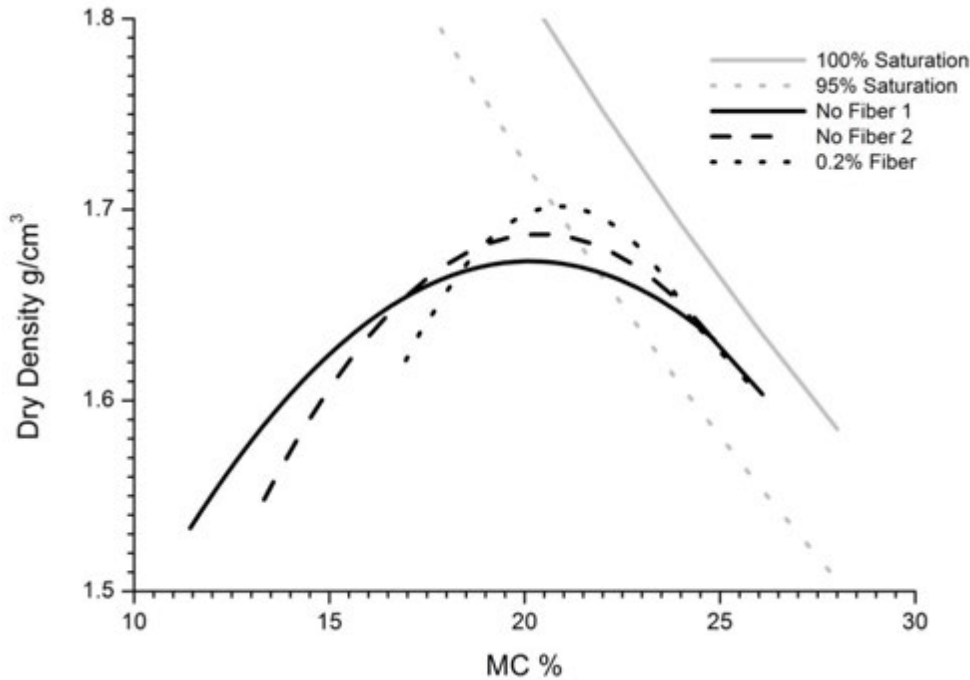


Figure 2: Compaction Curves of reinforced and non-reinforced samples

In order to achieve the desired moisture content, distilled water was sprayed onto the soil at regular intervals, over a period of several hours until reaching moisture contents 4% -5% higher than its respective optimum value. Following this, the clay peds were sealed in plastic containers in a controlled humidity room for several days, in order to achieve a homogeneous moisture content. There are two important reasons to follow such a procedure: a) to be able to retain some characteristics of the in-situ soil that will affect the mechanical response of the compacted soil; b) to create samples that will be representative of the in-situ behaviour of the compacted soil. The size of the peds was chosen to be 1/10 of the sample diameter, while in-situ size was similar to a golf ball.



Photo 1: Chopped clay peds in storage drum

A model proposed by Brackley (1975) considered that unsaturated clay soils exist as packets of soil particles, with each packet being completely saturated and the inter-pocket voids being filled with air (Figure 3). This meant that the soil mass was unsaturated whereas the individual soil packets were saturated. By assuming that the packets were saturated, Brackley developed the idea that the individual packets retain the properties of the natural soil and the total volume change of the soil mass would be due to the summation of the effects of swelling or compression of the packets and their shear behaviour.

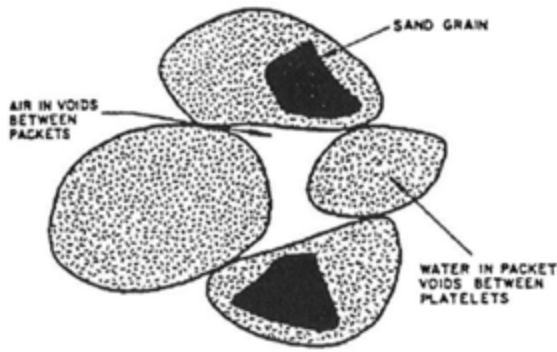


Figure 3: Model of unsaturated soil (Brackley, 1975)

This is one of the assumptions of this work; as you compact peds of heavily over-consolidated clay, the compaction energy is not enough to break shear them and therefore inter-pocket voids filled with air will be present in the compacted soil. The air pockets were assumed to be connected, therefore facilitating saturation; however initial saturation tests on compacted samples indicate that on the wet side of the optimum the saturation of the samples is faster, as would be expected.

All samples were compacted on a cylindrical mould with a diameter of 100mm and 200mm height, with a compaction effort equivalent to the light compaction described in the BS 1377-4:1990. The samples without reinforcement were trimmed down to 38mm diameter and 79mm height. These were tested on different Bishop Wesley triaxial equipment.

A similar methodology was followed in the preparation of reinforced samples. The main difference was the mixing procedure, where the entire mixing process was done manually by hand. The previously calculated weight of clay peds and fibre (0.2% of the dry weight of soil) were hand mixed in bag. As the fibres tended to lump together, considerable care and time was spent to get a homogeneous distribution of the fibres.



Photo 2: Reinforced sample compaction procedure

For the preparation of the oedometer sample a 77 mm diameter by 20 mm height ring was placed in a 100 x100 compaction mould and compacted by following the BS 1377-4:1990 light compaction procedure. In the preparation of the reinforced sample the author used fibre soil composite with 0.2% fibre content and moisture content at 5% wet of optimum.

3.5. Triaxial Testing

Undrained triaxial tests were carried out using two types of Bishop Wesley triaxial equipment, one capable of testing reinforced samples of 100x200mm and the other, more conventional, for samples of unreinforced soil of 38x79mm. Consolidation characteristics, stress-strain and pore pressure response of both reinforced and unreinforced samples were determined. Saturation was monitored in each test, ensuring B values of at least 0.98 for all samples. After saturation, the samples were isotropically consolidated under a back pressure of 320kPa to an effective confining stress between 50 to 500 kPa (table 3), in order to cover the range of stresses of most engineering applications. Local axial strains were measured using LVDT transducers as described by Cuccovillo and Coop (1997). The shearing rates used during the shearing were calculated using the results of the consolidation stage (Table 3). In all tests, the effects of membrane and lateral drains were corrected.

Table 3: Specification of triaxial tests

Drainage Condition	Fibre Content (%)	Size (mm)	Effective Stress (kPa)	Weight (g)	MC (%)	Void Ratio	Shear Rate (%/hr)
CU	0	38	50	138.40	27.49	1.68	0.26
CU	0	38	100	183.08	24.26	1.59	0.08
CU	0	38	150	188.42	23.00	1.53	0.08
CU	0	38	300	185.36	25.30	1.55	0.04
CU	0	38	500	181.92	24.28	1.63	0.08*
CU	0.2	100	100	3456.50	26.47	1.68	0.2
CU	0.2	100	150	3474.50	21.67	1.61	0.15
CU	0.2	100	300	3400.00	25.85	1.70	0.05
CU	0.2	100	500	3500.00	24.40	1.63	0.02

*due to several failures of compressor during compression the stage shear rate has been estimated

3.6. Fibre Alignment

In order to verify the fibre alignment, samples with the same fibre and initial moisture content were dissected. The alignment of the fibres was observed by recording the X, Y and Z coordinates of one of the fibre ends. As the sample was dissected the horizontal and vertical angle of the fibre was determined. This procedure was followed for 100 randomly chosen fibres. A graphical representation of the procedure can be seen in Figure 4 while Photo 3 shows a series of snapshots of the sample being dissected.

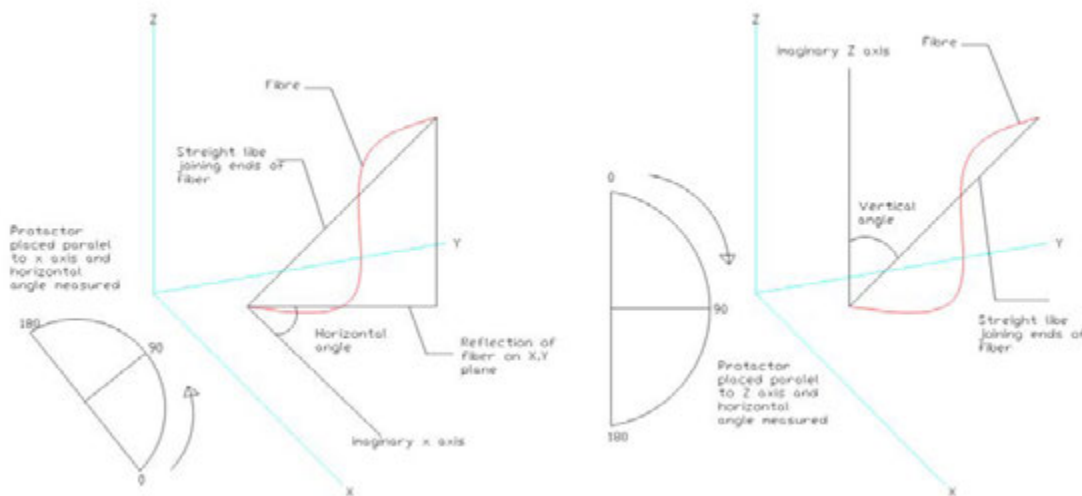


Figure 4: Method used in recording alignment of fibres in sample



Photo3: Extruding fibres from sample

The major challenge during this procedure was estimating the angles of the fibres which were circling peds, bent and overlapping others due to the mixing and compaction procedure.

4. RESULTS

4.1. Consolidation Characteristics

Figure 5 shows the results of the oedometer tests performed on reinforced and unreinforced compacted samples.

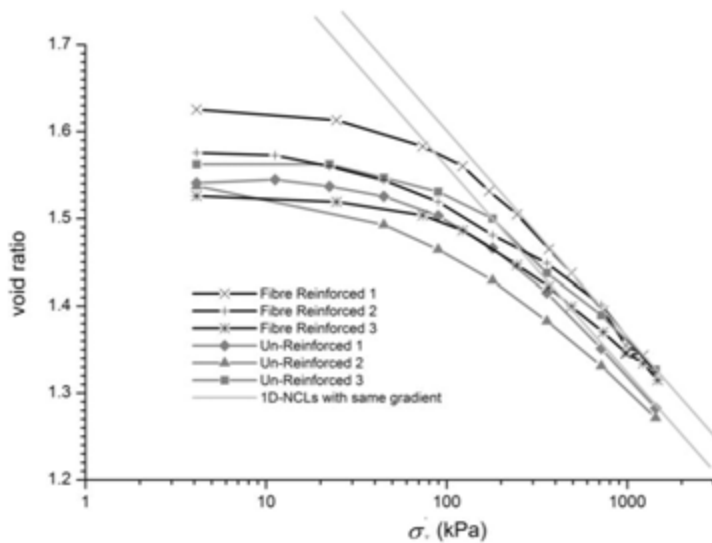


Figure 5: One-dimensional compression of fibre-reinforced and unreinforced clay samples

The oedometer test results appear to define two one-dimensional compression lines (1-D NCL); one for the reinforced soil and another for the un-reinforced soil. The two lines appear to be parallel, with a slope $\lambda=0.114$ and are represented by the two straight lines in Figure 5. Although the results appear to show different 1-D NCL for each type of material tested, the initial void ratio of the reinforced samples was not corrected to remove the effect of fibre inclusion. The authors believe that such correction would be minute but it should lower slightly the consolidation curves of the reinforced samples. It is also important to note that the methodology used to prepare the samples created similar initial void ratios, as described previously in the sample preparation. This fact reduces the confidence in the determination of a unique 1-D NCL for each material.

It is possible that a reinforced soil exists with a larger void ratio, due to the interlocking mechanism, created by the fibres. Dos Santos et al (2010) have seen this phenomenon in the isotropic compression of fibre reinforced sands.

4.2. Shearing behaviour

Figure 6 shows the stress-strain curves together with the changes in pore-pressure during the undrained shearing for all triaxial tests. Due to the long periods of time necessary for consolidation and shearing, the unreinforced samples were tested on 38mm triaxial equipment. Tang et al. (2008) have concluded that stress-strain curves of 38mm and 100mm samples are coincident for clay materials; however, Bishop and Little (1967) have shown that for a natural material, such as London Clay, planes of weakness are more evident in the preferred failure direction. The authors have shown that the strength of 38mm samples can reach values of the order of 1.5 times the strength of 100mm samples.

All tests have shown the same strain softening behaviour regardless of the reinforcement. However, with the unreinforced samples, a shear plane was observed in the samples tested with a confining stress of 150kPa and higher, while barrelling was observed for the lower stresses. All the fibre-reinforced samples have shown barrelling. According to Ozkul and Baykal (2007) this behaviour is linked to the fibres crossing the shear zone and restricting the development of a slip plane by transferring some of the shear stress and strains to zones further away.

Another important difference between the stress strain behaviour of reinforced and non-reinforced samples, is that the latter show no reduction of deviatoric stress for the range of confining stresses used, while the non-reinforced samples have shown a long peak for the higher confining stresses, followed by a continuous reduction of the deviatoric stresses. Even after 20% axial strain, there is no evidence that the samples will reach a constant deviatoric stress.

Although the non-reinforced samples reach higher effective stresses, this is not the case for the test performed with 100kPa of confining stress where the reinforced sample reached a higher strength.

The change in pore-pressure shows a similar behaviour although for smaller stresses it shows a peak, decreasing afterwards.

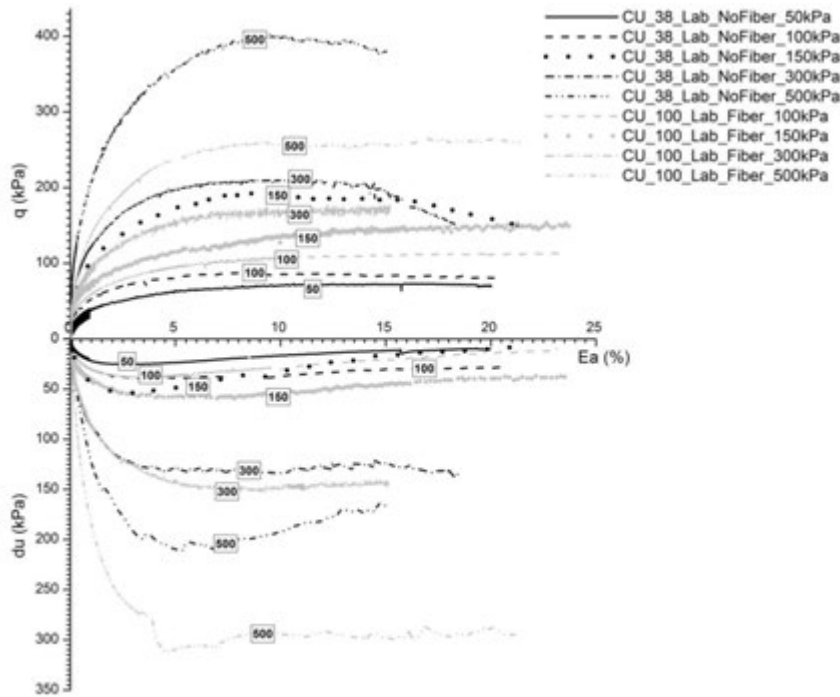


Figure 6: Stress-strain pore-pressure response of Lambeth Group clay and fibre-reinforced clay samples

The pore water pressure generated within the soil sample, which is related to the contractive or dilative tendencies of a soil during shearing, was consistently higher for the reinforced samples. Li (2005) attributed this increase in pore pressures to the fibres distributing stresses within the soil mass and, therefore, increasing the contractive deformations within the fibre-soil matrix. The pore-pressure distribution is also consistent with the study on the pore-pressure distribution at failure, conducted by Sandroni (1977). According to the author, the shear plane is associated with an increment of pore water pressure in the middle of the sample, evidenced only in the unreinforced samples, as the reinforcement provides restraint to the development of shearing surface.

4.3. Fibre alignment

The methodology described previously was used to desiccate 10 samples reinforced with 0.2% of fibres. All samples were prepared with the same initial moisture content. The results showed that nearly 80% of the fibres are located within $\pm 20^\circ$ with the horizontal plane and 51% are aligned within $\pm 10^\circ$. This is a consequence of the sample preparation procedure since the fibre length is longer than the thickness of a compacted layer in the sample (Figure 7).

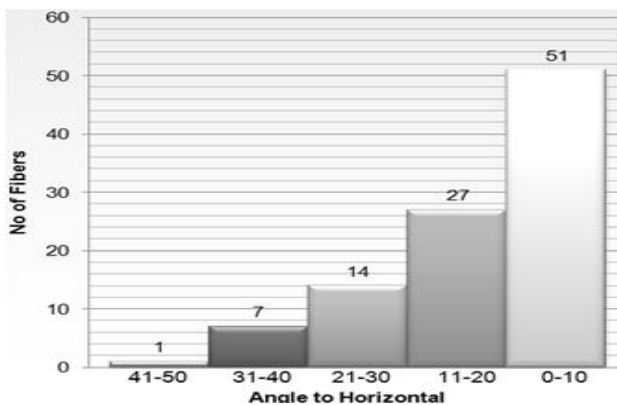


Figure 7: Alignment of fibres

The results are in agreement with Diambra et al. (2007), Ozkul and Baykal (2006) and Ozkul and Baykal (2007). These authors have also concluded that compacting soil-fibre mixtures during sample preparation leads to a preferential alignment of the fibres in a horizontal direction. Figure 8 shows a graphical representation of the fibre distribution on a dissected sample.

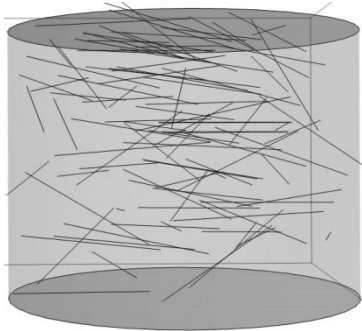


Figure 8: 3D orientation of the fibres on a dissected sample

5. CONCLUSIONS

As can be seen from the 1-D compression tests, the use of reinforcement appears to shift the 1-D NCL of the reinforced soil to the right of the 1-D NCL of the non-reinforced soil. Although this behaviour has been seen before in isotropic tests on sands, more tests on these composite materials are necessary, as these are within the tolerance margins used to determine the void ratios.

During shearing the deviatoric stress of all reinforced samples reaches a constant value while for the non-reinforced samples, tested at 150, 300 and 500kPa, the deviatoric stress decreases with strain. A similar trend was found for the pore-pressure; the reinforced samples reach constant values of pore water pressure while in the non-reinforced samples, pore water pressure reduces after reaching a peak value.

The measurements performed on the fibre alignment have shown that nearly 80% of fibres are aligned within $\pm 20^\circ$ with the horizontal plane. This alignment is caused by the sample preparation procedure as the fibre length is higher than the compaction layer.

6. ACKNOWLEDGEMENTS

The authors would like to thank EPSRC for funding this project, as well as Samuel Parkin and Alan Vooght from Mouchel, who have been very supportive.

REFERENCES

- Al-Tabbaa, A. & Aravinthan, T. 1998. Natural Clay-Shredded Tire Mixtures as Landfill Barrier Materials. *Waste Management*, 18.
- Bishop, A. W. & LITTLE, A. L. The influence of the size and orientation of the sample on the apparent strength of the London Clay at Maldon, Essex, In *Proc. Geot. Conf.*, pp. 89-96.
- Brackley, I. J. A. 1975. A model of unsaturated clay structure and its application to swell behaviour., In *6th Regional Conference for Africa on Soil Mechanics and Foundation Engineering*, Durban, South Africa.
- Cetin, H., Fener, M., & Gunaydin, O. 2006. Geotechnical properties of tire-cohesive clayey soil mixtures as a fill material. *Engineering Geology*, 88.
- Colin, J.F.P. 1996. *Earth reinforcement and soil structures*. London, Thomas Telford Publishing.

- Consoli, N.C., Casagrande, M.D.T., & Coop, M.R. 2005. Effect of Fiber Reinforcement on the Isotropic Compression Behavior of a Sand. *Journal of Geotechnical and Geoenvironmental Engineering*, 131, (11) 1434-1436.
- Cuccovillo, T. & Coop, M.R. 1997. The measurement of local axial strains in triaxial tests using LVDTs. *Geotechnique*, 47, (1) 167-171.
- Diambra, A., Russell, A.R., Ibraim, E., & Wood, D.M. 2007. Determination of fibre orientation distribution in reinforced sands. *Geotechnique*, 57, (7) 623-628.
- Hight, D. W., Ellison, R. A., & Page, D. P. 2004, Engineering in the Lambeth Group, Construction Industry Research and Information Association C583.
- Jha, K. & Mandal, J. N. A review of research and literature on the use of geosynthetics in the modern geotechnical world., pp. 85-93.
- Li, C. 2005. Mechanical Response of Fiber-Reinforced Soil. (Ph.D Thesis). The University of Texas at Austin.
- Maher, M.H. & Gray, D.H. 1990. Static Response of Sands Reinforced with Randomly Distributed Fibers. *Journal of Geotechnical Engineering*, 116.
- Ozkul, Z.H. & Baykal, G. 2006. Shear Strength of Clay with Rubber Fiber Inclusions. *Geosynthetics International*, 13.
- Ozkul, Z.H. & Baykal, G. 2007. Shear Behavior of Compacted Rubber Fiber-Clay Composite in Drained and Undrained Loading. *Journal of Geotechnical and Geoenvironmental Engineering*, 133.
- Prabakar, J. & Sridhar, R.S. 2002. Effect of random inclusion of sisal fibre on strength behaviour of soil. *Construction and Building Materials*, 16.
- Rifai, S. & Miller, C. 2004. Fiber Reinforcement for Waste Containment Soil Liners. *Journal of Environmental Engineering*, 130.
- Sandroni, S. 1977. The Strength of London Clay in total and effective stress terms. (Ph.D Thesis). University of London.
- Santos, A.P.S., Consoli, N.C., & Baudet, B.A. 2010. The mechanics of fiber-reinforced sand. *Geotechnique*, 60, (10) 791-799.
- Skipper, J. Geo-engineering properties and processes of the Lambeth Group. 2009. 10-10-2011.
- Tang, C., Bin, S., Wei, G., Chen, F., & Cai, Y. 2007. Strength and mechanical behavior of short polypropylene fiber reinforced and cement stabilized clayey soil. *Geotextiles and Geomembranes*, 25, 194-202.

A simple expression of the shear strength of anisotropic fibre-reinforced soils

A. Flora, University of Napoli Federico II, Italy, flora@unina.it
S. Lirer, University of Napoli Federico II, Italy, stelirer@unina.it

ABSTRACT

This paper refers on the shear strength of soils reinforced with short randomly distributed fibres, which is a new and effective ground improvement technique. The shear strength of these soils is usually anisotropic because of compaction. In the paper, some of the main characteristics of these reinforced soils, and some considerations on anisotropy in strength are reported. Then, the expression recently introduced by Lirer et al. (2011) to simply model the failure envelope of the reinforced soil is discussed. This expression is based on simple micromechanical considerations and on a number of experimental results, and takes into account the main characteristics of the soil and of the fibres as well as the effect of fibre to grains relative dimensions. However, it only allows to calculate the maximum value of the shear strength of the composite material, being related to the results obtained in triaxial compression tests with fibres mostly oriented in the horizontal direction. In the paper, a possible evolution of the formulation of this shear strength envelope is proposed, to take into account anisotropy. A simple trigonometric reduction function is introduced, which complies with the expected behaviour of reinforced soils under different loading conditions. The proposed approach has the advantage of being a rather general expression that can be used by knowing just some simple and basic information on the host soil and on the fibres.

1. INTRODUCTION

Many experimental researches conducted on fibre-reinforced materials have demonstrated that the addition of discrete fibres improves the mechanical behaviour of granular soils, increasing strength and ductility and reducing the post peak-strength loss. The distributed discrete fibres act as a spatial three-dimensional network to interlock soil grains. Therefore, they can be considered an interesting alternative in the case of superficial layers or embankments to be improved.

Several experimental studies (Gray and Al-Refeai 1986, Gray and Maher 1989, Michalowski and Cermák 2003; Heineck *et al.* 2005, Consoli *et al.* 2007a, 2007b and 2009, Santoni *et al.* 2001, Sadek *et al.*, 2010, Santos *et al.* 2010a, Diambra *et al.* 2010, Tang *et al.* 2010, Lirer *et al.*, 2011) were conducted to explore the effect of various parameters on the shear strength of soils reinforced with randomly distributed fibres. From these studies it is possible to identify the parameters that play a relevant role and therefore must be included in any analytical formulation of the macroscopic behaviour of the reinforced soil, which are: soil state (stress level and soil density), fibre content w_f (defined as the ratio between the weight of fibres W_f and the dry weight of soil W_s , $w_f=W_f/W_s$), fibres aspect ratio ρ (defined as the ratio between the length and diameter of the fibre, $\rho=L_f/d_f$), fibres orientation (connected to the technique adopted for compaction). Even though the fibre to grains relative dimension also plays a relevant role, as clearly stated in some of the previously mentioned works (Michalowski and Cermák, 2003, Sadek *et al.*, 2010, Tang *et al.*, 2010), only recently it was explicitly included in a possible formulation of the shear strength envelope of the composite material (Lirer *et al.*, 2011). As a matter of fact, the reinforcement is more effective when (for a given value of the aspect ratio $\rho=L_f/d_f$, L_f and d_f been respectively fibres length and diameter) the fibre length is large compared to the size of the grains. As the length of fibres reduces, their beneficial effect reduces as well, eventually fading away when it approaches the size of grains.

The design of geotechnical systems involving fibre reinforced soils is typically based on empirical experience or available models developed from experimental data. Traditionally, the approach used in the design of fibre-reinforced soil structures assumes that the addition of fibres leads to an increase in the shear strength of the 'homogenised' composite reinforced mass which should be expressed via a non linear formulation. As a matter of fact, non linearity clearly results from the experimental data, being ruled by the evolution of the fibre to grains interaction mechanism: at small confining stresses, such interaction is mostly mutual sliding, while at higher confining stresses fibres yielding becomes more and more relevant. In the typical engineering applications, however, discrete fibres are used for shallow reinforcements, and so fibres sliding is the most important micromechanical interaction mechanism.

Different formulations are nowadays available to express the non linear shear strength envelope (Zornberg, 2002, Michalowski and Cermak, 2003, Diambra et al. 2010, Lirer et al., 2011).

A further aspect to be considered is the anisotropic behaviour of the reinforced soil. Many experimental results (Fig. 1) have demonstrated that the contribution of fibres to the strength of fibre-reinforced soils is very much dependent on the distribution of orientation of the fibres (Michalowsky and Cermak, 2003, Diambra et al, 2010). The distribution of the fibres determines the anisotropy of the mechanical behaviour of reinforced soil.

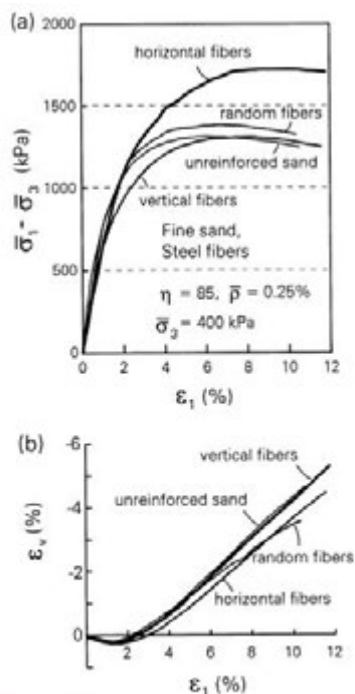


Figure 1: Results of triaxial tests on a fibre reinforced sand (after Micalowski and Cermak, 2003).

The distribution of fibre orientation in practical applications of reinforced soils is usually anisotropic because of the techniques of placement and compaction of the soil with fibres. In typical construction conditions, the horizontal plane is the preferential bedding plane, and the fibre orientation distribution can be described as a function of the inclination angle θ to the horizontal. Obviously, fibres in the direction of largest extension contribute in the most effective way to the strength of the composite material, whereas the fibres under compression have an adverse effect. Therefore, to be effective, the bedding plane of fibres must be inside the tensile strains domain, schematically shown in Fig. 2.

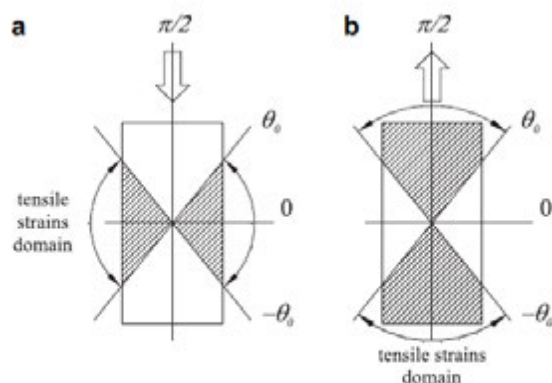


Figure 2: Domains of tensile strain orientation for compression (a) and extension (b), (after Diambra et al. 2010)

An effort to consider the anisotropy in the mechanical behaviour of the fibre/reinforced soils has been done by some authors (e.g. Micalowski and Cermak, 2003). The authors developed a failure criterion for reinforced soils with anisotropically distributed fibres. In this framework, two alternative fibre

distributions can be adopted. In the hypothesis of no fibres in the vertical direction (Fig. 3), a possible fibre distribution can be expressed as:

$$\rho(\theta) = \frac{3}{2} \cdot \bar{\rho} \cdot \cos^2 \theta \quad (1)$$

where $\bar{\rho}$ is the average fibre concentration in an element of volume V.

In the hypothesis of an ellipsoidal distribution (where a and b are respectively the half-axes of the ellipse and ζ is the aspect ratio of the distribution - $\zeta = b / a$), the fibres distribution can be alternatively expressed as:

$$\rho(\theta) = \frac{a \cdot b}{\sqrt{a^2 \cdot \sin^2 \theta + b^2 \cdot \cos^2 \theta}} \quad (2)$$

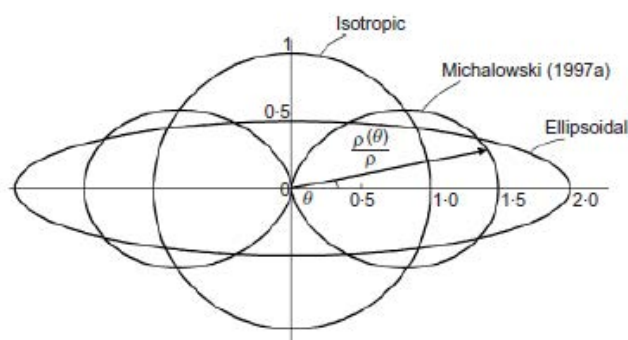


Figure 3: Some hypothetical distribution of fibre orientation (after Michalowski et al. 2008).

Based on such an elliptical distribution (eq. 2), Micalowski and Cermak (2003) developed a failure criterion in which the shear strength under plane-strain conditions is described by a function dependent on the in-plane mean stress and the inclination of the major principal stress to the preferred fibres orientation plane (ψ). Fig. 4 shows that the strength of the reinforced soils significantly changes with the anisotropy of the material (represented by the ratio ζ between the two axes of an elliptical distribution). According to Micalowski and Cermak (2003), for the lower values of ψ the addition of fibres may even reduce the strength of the soil.

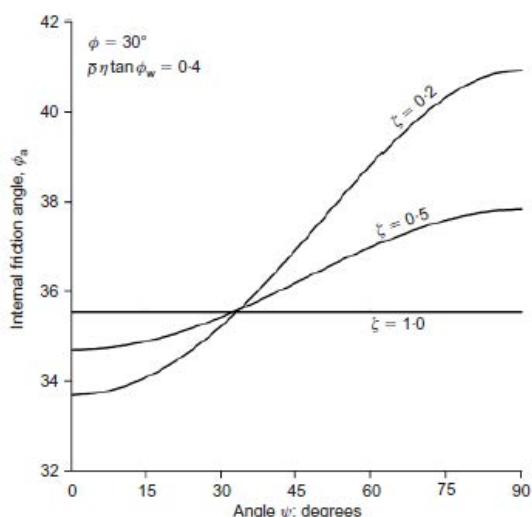


Figure 4: Internal friction angle as a function of the major principal stress inclination to the preferred fibre orientation plane ψ for different aspect ratio of the distribution ζ (after Michalowski 2008).

Diambra et al (2010) have proposed an alternative approach to take into account an anisotropic distribution of fibres, based on reasonable assumptions on the behaviour of the fibres. Their model has the advantage of being independent on the model considered to describe the mechanical behaviour of the

unreinforced soil, and is conceived to simulate the behaviour of the composite material also in stress conditions far from failure.

However, all the approaches available to take anisotropy into account lack of experimental evidences (Diambra et al., for instance, have tested in compression and extension, but not with fibres bedding planes having other inclinations to major principal stress than 0° or 90°).

Anisotropy is rather important in engineering applications: in the case of an embankment obtained by wet compaction of the reinforced soil (therefore with a strongly anisotropic structure), for instance, slope stability analyses (Fig. 5) imply the consideration of shear strength pertaining to different values of the inclination angle ψ along the considered sliding surface.

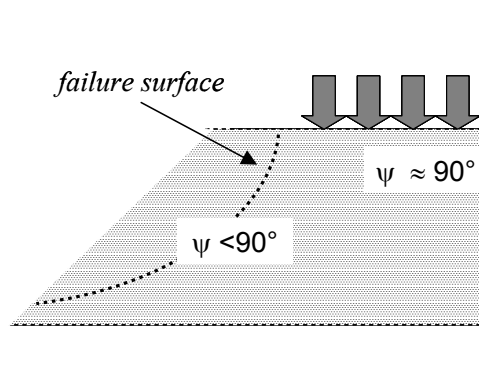


Figure 5: Unknown angle between the preferred plane of fibres (horizontal) and the direction of the major principal stress, in the case of a slope stability analysis.

Considering the reinforced soil as an isotropic material may be largely non conservative in such a case; yet, routine slope stability analyses carried out with refined models may be out of the range for most practitioners. In engineering practice, a reasonable compromise between rigor (and conservativeness) in the solution and simplicity and applicability should be looked for. The simple approach proposed in this work was conceived to this aim, to take into account most of the factors affecting the mechanical behaviour of fibre reinforced soils with an expression which is extremely simple to implement.

2. EXPERIMENTAL EVIDENCES

In order to have an insight in the use of fibre reinforcement, a large experimental programme was recently developed at the University of Napoli. A sandy gravel (Fig. 6) was used to this aim, to consider the case of least effectiveness of the reinforcement (minimum fibre to grain ratio). Triaxial monotonic compression tests were carried out in a large apparatus (specimen diameter $D_s = 200$ mm). All the specimens (non-reinforced and reinforced) were prepared by hand-mixing dry soil, water and polypropylene fibres (properties in Tab. 1), when used. Wet tamping was then carried out to compact the specimens. Fibres with two different diameters ($d_f = 0.076 - 0.1$ mm) and three different lengths ($L_f = 50, 75, 100$ mm) were used.

Some of the triaxial tests (Tab. 2) were carried out on both un-reinforced and reinforced specimens, isotropically consolidated at a cell pressure $\sigma'_c = 50$ kPa. The adopted fibre contents ($w_f = 0.1 - 0.2\%$) are lower than usual, depending on the coarser grading of the soils ($w_f = 0.2\%$ was the largest possible one to avoid extensive fibres tangling).

Table 1: Properties of the adopted fibres

Specific gravity G_f	Length (mm) L_f	Diameter (mm) d_f	L_f/d_{50}	Aspect ratio $\rho = L_f/d_f$	Tensile strength (MPa) σ_y
0.91	$50 < L_f < 100$	$0.076 < d_f < 0.1$	$16.6 < L_f/d_{50} < 3.3$	$658 < \rho < 1316$	100

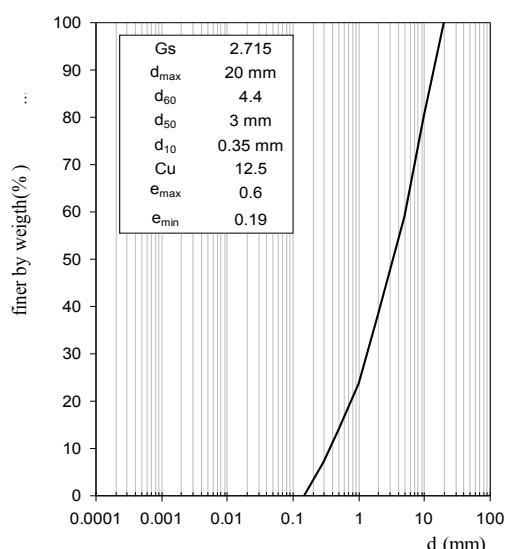


Figure 6: Grain size distribution and physical properties of the sandy gravel.

Table 2: Experimental programme

Soil	Dr_0	L_f (mm)	L_f/d_{50}	w_f (%)	Cell pressure, σ'_c (kPa)
Un-reinforced	0.4	-	-	-	50
Reinforced	0.4	50	16.6	0.1, 0.2	
		75	25.0	0.1, 0.2	
		100	33.3	0.1, 0.2	

As shown in Fig. 7, un-reinforced specimens show the typical behaviour of coarse grained soils, with high shear strength (represented by the stress obliquity ratio $\eta=q/p'$) and a peak reached at medium strain level (deviatoric strain $\varepsilon_q = \varepsilon_a - \varepsilon_v/3 \approx 2.5\%$), followed by a subsequent shear strength reduction. The specimens always show a dilative behaviour. Generally speaking, the triaxial tests results on reinforced specimens (Fig. 7) differ from those on the non reinforced soil: even though peak strength has not increased very much, the increase in shear strength of the reinforced soil at the end of the tests is clear. As expected, the fibre-reinforced specimens show a more ductile behaviour with reduced dilatancy.

As previously mentioned, the increment in soil shear strength is governed by the fibre content w_f and fibre length L_f . For a given fibre content, the longer are the fibres the larger is the macroscopic peak shear strength η_{pk} . At the end of the tests, dilation is never nil.

To have an estimate of a reference critical stress ratio M (even though the concept itself of critical state for fibre reinforced soils may be somehow ambiguous), the experimental results were also plotted (Fig. 8) in the classical η - D plane (where $D=d\varepsilon_v/d\varepsilon_q$). This plot confirms that the tests did not reach a state of no dilatancy ($D=0$). The results also confirm that the addition of small amount of fibres has a small effect on peak strength, but makes the overall mechanical behaviour of the gravel more ductile, with a significant and beneficial increase of final shear strength. From this figure it can be noted that, for a given value of fibre content, both final shear strength and maximum value of dilatancy principally depend on fibre length.

To have an insight of the interaction mechanism between grains and fibres, a sample of fibres was recovered to measure their final length at the end of two tests carried out at different cell pressure (Fig. 9). It can be observed that in the test performed at small confining pressure ($\sigma'_c = 50$ kPa) most of the fibres keep more or less the same initial length, with an asymmetry of the distribution towards the longer lengths. Likely, in this case the main local failure mechanism was fibres slip, as expected, with little or no breakage of the fibres and the elongation for some of them. In the test carried out at higher cell pressure ($\sigma'_c = 400$ kPa), fragments of fibres of small length were found within the specimen. Such result is an evidence of the role of stress level in the interaction between fibres and grains (Michalowski and Cermak 2003, Lirer et al., 2012). As previously stated, in usual engineering applications the stress levels at which fibre reinforced soils work are small or very small, and as a consequence fibre slippage is the ruling mechanism.

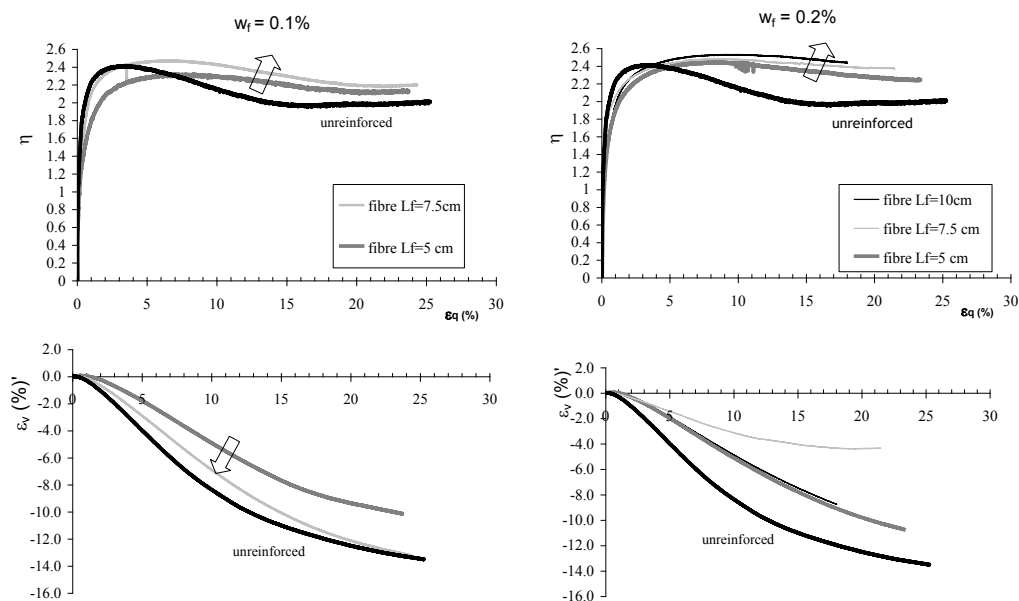


Figure 7: Results of triaxial tests on fibre reinforced sandy gravel: stress obliquity ratio (η) versus deviatoric strains (ϵ_q).

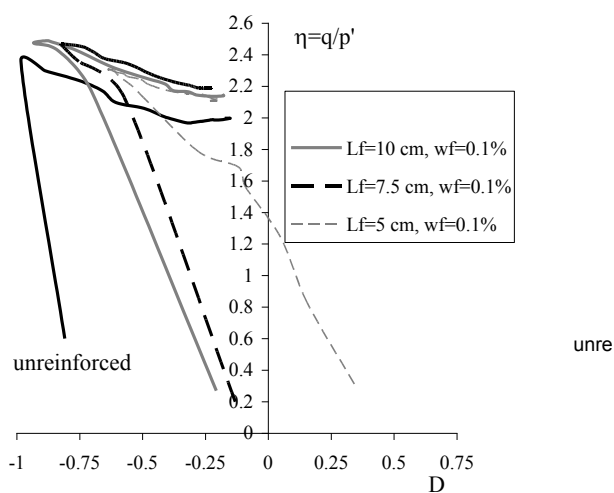


Figure 8: Results of triaxial tests on reinforced and un-reinforced specimens of a sandy gravel: stress obliquity ratio η versus dilatancy D .

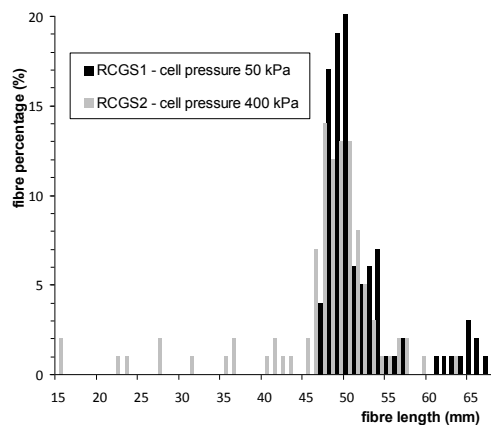


Figure 9: Fibres length measured after triaxial tests on fibre-reinforced sandy gravel (after Lirer et al, 2012).

3. SHEAR STRENGTH ENVELOPE OF FIBRE REINFORCED SOILS

3.1 Maximum shear strength

Since many experimental evidences have highlighted the relevance of the micromechanical interaction among grains and fibres (fibre to grain ‘scale effect’, represented for instance by the ratio L_f/d_{50}) on the shear strength of the composite material, and no model took it explicitly into account, a simple expression of the failure envelope of fibre reinforced soils including the scale effect was recently proposed (Lirer et al., 2011).

Such an envelope is defined as the sum of two terms: one relative to the natural soil (represented by the stress obliquity ratio η), and a non linear one related to the effect of fibres and stress state (represented by the mean confining pressure p'). By means of some micromechanical considerations (explained in detail in Lirer et al., 2011), the effect of fibres is represented by a single parameter β defined as:

$$\beta = \sqrt{w_f \cdot \rho \cdot \frac{L_f}{d_{50}}} \quad (3)$$

Such a parameter takes into account the fibre content, the geometrical properties of fibres and the fibre-grain relative dimension. The expression of the proposed failure envelope is:

$$\eta_r = \eta \left(1 + 0.00004 \cdot \beta \cdot \frac{\sigma_y^{0.85}}{p_a^{0.65} \cdot p'^{0.2}} \right) \quad (4)$$

where p_a is the atmospheric pressure (introduced for dimensional problems). Eq. (4) can be also written in terms of friction angle of the reinforced soil φ_r as:

$$\varphi_r = \sin^{-1} \left(\frac{3 \cdot \sin(\varphi) \cdot \left(1 + 0.00004 \cdot \beta \cdot \frac{\sigma_{y,f}^{0.85}}{p_a^{0.65} \cdot p'^{0.2}} \right)}{3 + \sin(\varphi) \cdot \left(0.00004 \cdot \beta \cdot \frac{\sigma_{y,f}^{0.85}}{p_a^{0.65} \cdot p'^{0.2}} \right)} \right) \quad (5)$$

Even though eq. (5) has been written based on an oversimplified interpretation of the true micromechanical interaction mechanism between grains and fibres, it has proven able to predict the shear strength of a large variety of fibre reinforced soils measured in triaxial tests (Fig. 10).

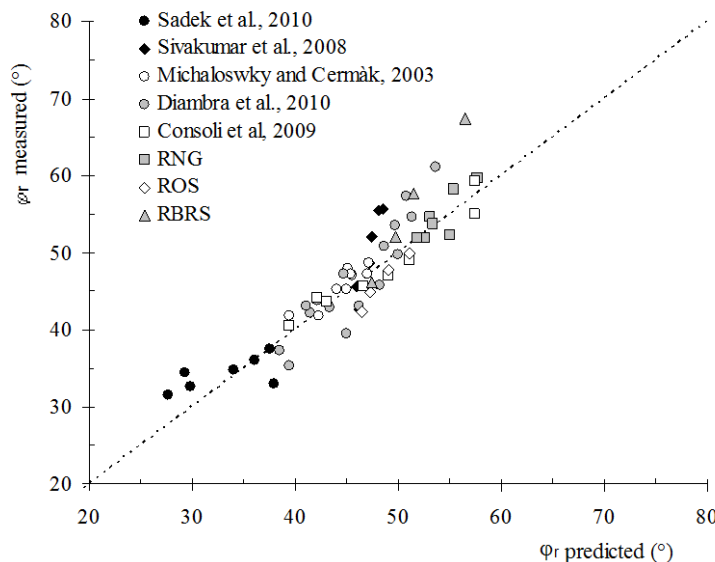


Figure 10: Measured and predicted (eq. 4) friction angles of fibre-reinforced specimens φ_r (Lirer et al., 2011).

For a given confining stress (for instance, the one adopted in the triaxial tests $p'=50$ kPa), eq. (4) can be easily adopted to calculate (Tab. 3) the shear strength increment given by the addition of fibres to three different soils (silt, sand and gravel). It can be observed that, for a given value of fibre content and aspect ratio, the addition of fibres is more effective in fine grained soils (silt) than in coarse soils (gravel). Fig.

11 reports the values of the friction angle ϕ_r predicted by eq. (5) for different gradations and different values of the natural soil friction angles. As expected, for a given soil, ϕ_r increases with the aspect ratio of fibres and with fibre content.

Table 3: Shear strength increment (eq. 4) given by the addition of fibres ($w_f=1\%$).

soil	d_{50} (mm)	ρ_1	ρ_2	$(\eta_r/\eta)1$	$(\eta_r/\eta)2$
silt	0.01	600	800	1.38	1.48
sand	0.4			1.15	1.22
gravel	5			1.04	1.06

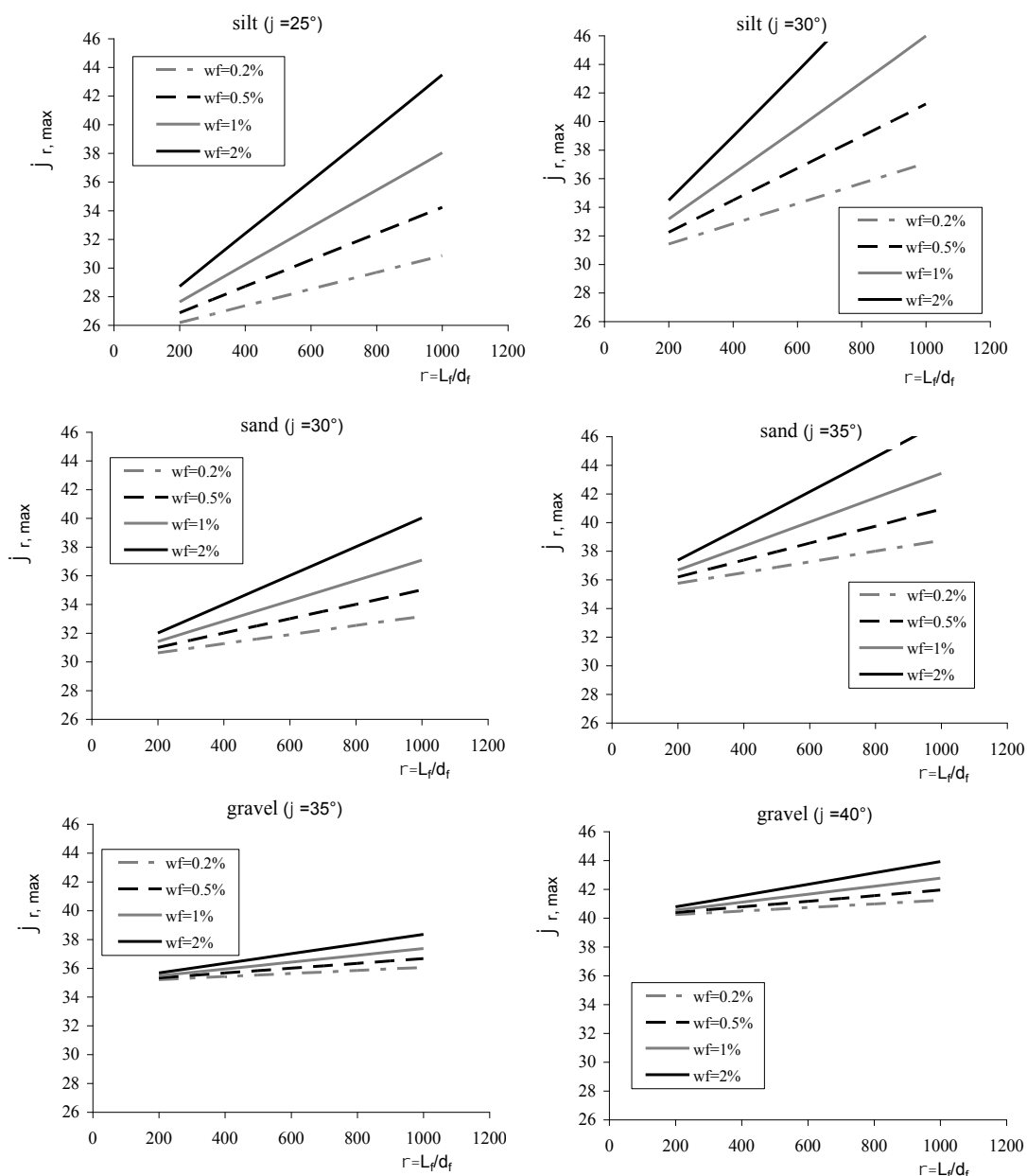


Figure 11: Friction angles of fibre-reinforced soils (ϕ_r) (eq. 5).

What is new is that, for a given friction angle of the natural soil, the shear strength of the reinforced soil is higher for the finer soil, with differences increasing with ρ : comparing for instance the friction angle of reinforced silt and sand (for $\phi=30^\circ$ of the natural soil) or that of reinforced sand and gravel (for $\phi=35^\circ$ of the natural soil), such a result is clearly shown in Fig. 11. This effect is generated by eq. (5) as a consequence of the fibre to grains scale effect, and no other expression of the shear strength envelope

available in literature is able to reproduce it. Even though this result is consistent with the experimental evidence collected by the authors so far, new tests are under course to get a further proof.

Being eqs. 4 and 5 obtained by processing experimental data from triaxial compression tests on compacted specimens in which fibres are mostly laying in the direction of the major tensile strains ($\psi=90^\circ$), the values of φ_r shown in Fig. 11 are the maximum ones. In many practical applications of reinforced soils (Fig. 5), the angle ψ is lower than 90° . For such a reason, the proposed expressions (eqs. 4 and 5) need to be modified to take into account the influence of the angle ψ between the preferred plane of orientation of the fibres and the unknown direction of the major principal stress.

3.2 The effect of anisotropy

It may be worth noting that the authors are seeking for an expression of the shear strength of fibre reinforced soils both able to consider all the relevant parameters and as simple as possible (but, of course, not simpler!). The results reported on the maximum value of the friction angle seem encouraging. At the moment, no results were directly obtained by the authors on specimens having values of ψ different from 90° , so only some preliminary considerations can be drawn on the effect of anisotropy on the reinforced soil friction angle. Certainly, anisotropy will have to reduce it depending on the value of ψ . Considering that the horizontal bedding plane is the preferential one but not the only one, as reported in some detail in the introduction, it is reasonable to assume that the reduction in friction angle should be smooth for bedding angles just a bit smaller than $\psi=90^\circ$, getting sharper and sharper as the angle ψ tends to zero. As a starting hypothesis, it can be considered that for $\psi=0^\circ$, the fibres have no effect on the behaviour of the reinforced soil, even though Michaloswki (2008) suggests that in such a case they could even result into a value of φ_r smaller than that of the natural soil. A simple way to incorporate in eq. (4) the effect of anisotropy in the terms just described is by the adoption of a non linear anisotropy reduction function $f(\psi)$ of the second term of the second member of the equation. Such a function can conveniently be a trigonometric one, like for instance $f(\psi)=\sin(\psi)$, which keeps values close to 1 for values of ψ close to 90° . By doing so, the expression of the anisotropic shear strength becomes :

$$\eta_r = \eta \left(1 + 0.00004 \cdot \sin\psi \cdot \beta \cdot \frac{\sigma_{y,f}^{0.85}}{p_a^{0.65} \cdot p_c^{0.2}} \right) \quad (6)$$

Which has not lost the simplicity of the original expression. In order to illustrate the effect of the anisotropy function $f(\psi)$, the friction angles of a sand and of a gravel reinforced with fibres (for a given value of fibre content $w_f=1\%$) calculated with eq. (6) are plotted in Fig. 12 (for $0<\psi<90^\circ$). The examples reported in the figure show that the nonlinear reduction function $f(\psi)$ has a negligible effect for $\psi>75^\circ$ (for the gravel, no effect at all), and becomes relevant for $\psi<45^\circ$. An experimental research is in progress to check the validity of this simple formulation (eq. 6).

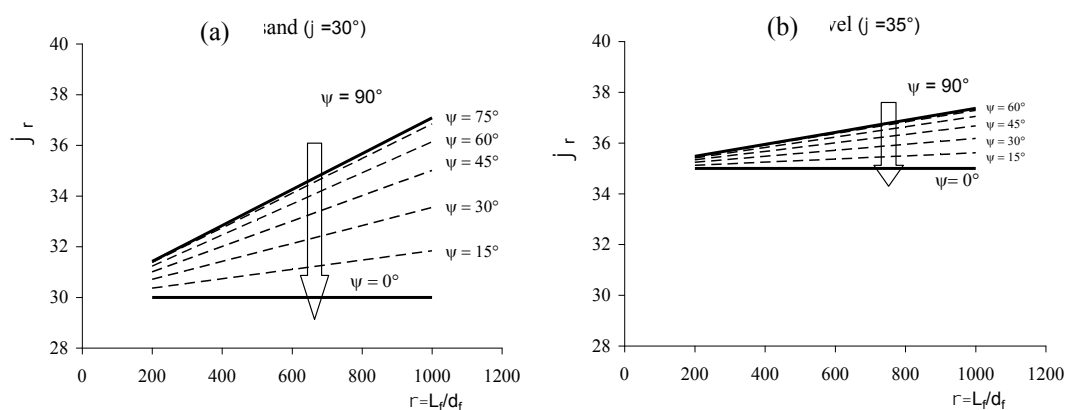


Figure 12: Friction angles of fibre-reinforced soils φ_r ($w_f=1\%$): a) sand, b) gravel.

4. CONCLUDING REMARKS

In the paper, some considerations on the shear strength of fibre reinforced soils are reported, based on the large experimental evidence gained directly by the authors or from literature. The experimental results obtained in triaxial tests have highlighted the relevance of the fibre to grain 'scale effect' on the shear strength of fibre reinforced soils. Since such effect was not considered in the available models, a simple

expression of the failure envelope of fibre reinforced soils has been recently proposed (Lirer et al., 2011). In order to take into account also the effect of anisotropy (due to the technique of placement and compaction of the soil with fibres), such an expression was modified by introducing a simple non linear anisotropy reduction function $f(\psi)$. The expression proposed shows that:

- for a given value of fibre content and aspect ratio, the addition of fibres is more effective in fine grained soils than in coarse soils;
- for a given soil, the shear strength increment given by the addition of fibres increases with their aspect ratio and with fibre content;
- for a given friction angle of the natural soil, the shear strength of the reinforced soil is higher for the finer soil (with differences increasing with ρ); this effect of the proposed expression cannot be obtained with any of the available models, being related to the 'scale effect';
- the shear strength of the reinforced soils decreases as the preferred plane of orientation of the fibres departs from the major tensile strains direction ($\psi < 90^\circ$). Consistently with published experimental evidence, this effect becomes relevant for value of ψ significantly smaller than 90° .

REFERENCES

- Consoli, N.C.; Heineck, K.S. Casagrande, M.D.T., and Coop, M.R. (2007a). *Shear strength behavior of fiber-reinforced sand considering triaxial tests under distinct stress paths. Journal of Geotechnical and Geoenvironmental Engineering*, 133(11), 1466-1469.
- Consoli, N.C., Casagrande, M.D.T. & Coop, M.R. (2007b). *Performance of a fibre-reinforced sand at large shear strains. Géotechnique*, 57(9), 751-756.
- Consoli, N.C., Festugato, L. and Heineck, K.S. (2009). *Strain-hardening behaviour of fibre-reinforced sand in view of filament geometry. Geosynthetics International*, 16(2), 109-115.
- Diambra, A., Ibraim, I., Muir Wood, D. and Russell, A., (2010). *Fibre-reinforced sands: Experiments and modelling. Geotextiles and Geomembranes*, 28(3), 238-250.
- Gray, D.H. & Al-Refaei, T. (1986). *Behaviour of fabric versus fibre-reinforced sand. Journal of Geotechnical Engineering*, 112(8), 804-826.
- Gray, D.H. & Maher, M. H. (1989). *Admixture stabilization of sands with discrete, randomly distributed fibers. Proc., XII Int. Conf. on Soil Mech. and Foundation Engineering.*
- Heineck, K.S.; Coop, M.R.; and Consoli, N.C., (2005). *Effect of micro-reinforcement of soils from very small to large shear strains. Journal of Geotechnical and Geoenvironmental Engineering*, 131(8), 1024-1033.
- Lirer S., Flora A., Consoli N.C. (2011). *On the strength of fibre reinforced soils. Soils and Foundations, Volume 51, n°4, August 2011, Special Issue for IS Seoul 2011.*
- Lirer S., Flora A., Consoli N.C. (2012). *Experimental Evidences of the Mechanical Behaviour of a Fibre-Reinforced Sandy Gravel. Journal of Geotechnical and Geological Engineering. In press.*
- Santoni, R.L., Tingle, J.S. and Webster, S.L., (2001). *Engineering properties of sand-fiber mixtures for road construction. Journal of Geotechnical and Geoenvironmental Engineering*, 127(3), 258-268.
- Santos, A.P.S, Consoli, N.C., Heineck, K.S. and Coop, M.R. (2010a). *High pressure isotropic compression tests on fiber-reinforced cemented sand. Journal of Geotechnical and Geoenvironmental Engineering*, 136(6), 885-890.
- Santos, A.P.S, Consoli, N.C. and Baudet, B.A. (2010b). *The mechanics of fibre-reinforced sand. Géotechnique (10.1680/geot.8.P.159).*
- Michalowski, R.L. and Cermák, J. (2003). *Triaxial compression of sand reinforced with fibres. Journal of Geotechnical and Geoenvironmental Engineering*, 129(2), 125-136.

Michalowski, R.L. (2008). *Limit analysis with anisotropic fibre-reinforced soil*. *Géotechnique* 58 (6), 489-501.

Sadek, S., Najjar, S.S. and Freiha, F. (2010). *Shear Strength of Fiber-Reinforced Sands*. *Journal of Geotechnical and Geoenvironmental Engineering*, 136(3), 490-499.

Zornberg, J.G., (2002). *Discrete framework for limit equilibrium analysis of fibre-reinforced soil*. *Géotechnique*, 52(8), 593-604.

Comparison of the performance of rectangular footings on cohesionless soils reinforced with geogrid and geotextile

Cem Gel, Gazi University, Turkey, cemgel@gmail.com
Sami Oguzhan Akbas, Gazi University, Turkey, soakbas@gazi.edu.tr
Ozgur Anil, Gazi University, Turkey, oanil@gazi.edu.tr

ABSTRACT

Most of the literature on the performance of footings on reinforced soil is devoted to square, circular or strip footings, with little attention to those that are rectangular in shape. In this study, the results from a series of laboratory load tests on 100 mm wide rectangular footings with length (L) to width (B) ratios ranging from 1 to 4, which are supported on sand that are reinforced with a single layer of geogrid or geotextile, are presented. The results indicate that, for ultimate limit state, the efficiency of the reinforcement, as defined by the bearing capacity ratio, increases significantly with larger L/B. This effect is less pronounced for the serviceability limit state. For the generalization of results, a numerical study was also performed using finite element analysis. Based on the agreement between the numerical and the experimental results, critical values of parameters that include the number of layers of reinforcement, and the relative density as a function of footing shape are examined.

1. INTRODUCTION

Parallel to the significant increase in the employment of geotextiles and geogrids for soil improvement during the last few decades, the behavior of reinforced soil foundations have been thoroughly examined considering various construction parameters and performance requirements. These parameters include but are not limited to the number of reinforcing layers, the depth, spacing, length and stiffness of the reinforcement, the soil type as well as the depth and shape of the foundation element. The results of the experimental studies in the literature showed that, in general, the use of reinforcements can significantly increase the bearing capacity and reduce the settlement of foundations. However, it has also been noticed that better improvements in the performance of the foundation systems are obtained when they are designed using certain combinations of the above mentioned parameters.

Although it is a well established fact that the shape of the footing has a profound effect on both the bearing capacity and settlement, the number of published experimental studies that involve loading tests of rectangular shallow foundations on reinforced soil are quite limited. Thus, many questions still remain as to the ultimate and serviceability limit state behavior of footings with different aspect, i.e., width (B) / length (L) ratios, resting on soils improved with geotextiles or geogrids. Therefore, the main aim of this research is to contribute to the understanding of the behavior of such rectangular footings on reinforced cohesionless soils. To achieve this objective, a series of laboratory loading tests on model footings were conducted along with numerical studies using finite element method under a range of sand relative densities and reinforcement parameters.

2. PREVIOUS STUDIES

To the best knowledge of the authors, the only two series of tests conducted for investigating the effect of footing shape on the bearing capacity ratio (BCR) of reinforced sand are those reported by Omar et al. (1993) and Chen (2007). Based on results of laboratory model tests with 76.2 mm surface footings on geogrid-reinforced sand ($D_r = 70\%$, Tensar BX 1000 reinforcement) Omar et al. (1993) reported that the BCRs at ultimate bearing capacity decreased with increasing B/L. Omar et al. (1993) also pointed out that the ratio of BCR at a given settlement level to BCR at ultimate bearing capacity, i.e., BCR_s / BCR_u for a strip foundation is lower than that obtained for a square foundation. On the other hand, Chen (2007)'s results clearly showed that the BCRs for geogrid-reinforced sand at ultimate bearing capacity for a 152 mm-wide square footing are greater than those obtained for 152 mm×254 mm rectangular footing. A similar trend was also identified for the BCRs at settlement ratio less than 12%. This discrepancy can be attributed to the fact that model footings that were constructed at Chen (2007)'s study was embedded at a depth equal to footing width.

In addition to those within the scope of footing shape, disagreements also exist considering the effect of the relative density (D_r) of the cohesionless soil on the BCR. Both the results of Das and Omar (1994) and Shin and Das (2000) suggest that a higher BCR will be obtained for lower D_r , considering that all other variables are kept the same. However, in a recent study conducted by El Sawwaf (2009) on eccentrically loaded footings resting on reinforced sand, for all values of eccentricity including concentric loading, higher BCR values were obtained for geogrid-reinforced soil with higher relative densities. Note that the model foundations in all three studies were strip footings with zero embedment depth. Therefore, there is also no information on whether the shape is also another factor in the $D_r - \text{BCR}$ relationship.

3. LABORATORY MODEL TEST SETUP

The experimental model tests were conducted in steel test box, having inside dimensions of 2.00 m x 2.00 m in plan and 1.00 m in depth, with a concrete base (Figure 1). The loading system was mounted on two horizontal U steel beams supported by two steel columns. It consists of a hand-operated hydraulic jack and pre-calibrated load ring.

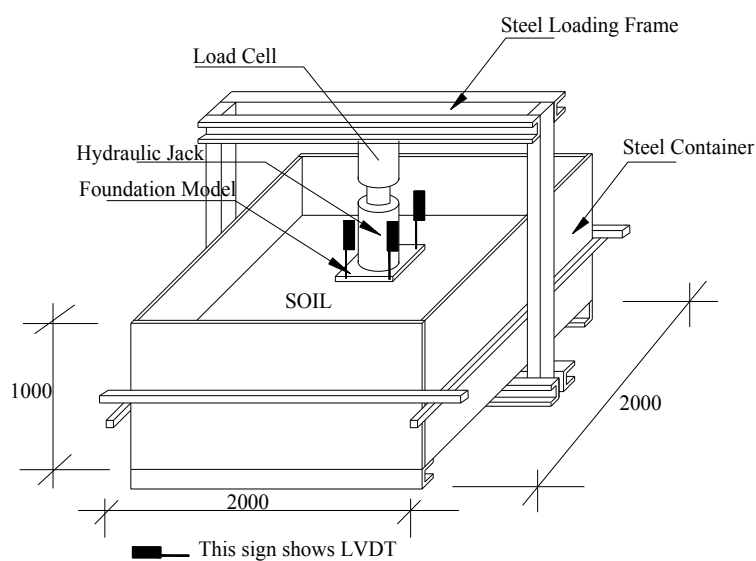


Figure 1: Test setup for model-scale footing tests

The sand with a USCS classification SW that was used in the tests was characterized through its specific gravity, maximum and minimum density, and grain size distribution. The specific density (G_s) of the soil particles as determined by the gas jar method resulted in an average value of 2.71. The maximum and minimum densities of the sand were determined to be 1.88 and 1.49 Mg / m³, with corresponding values of the minimum and maximum void ratios of 0.44 and 0.81. The particle size distribution was determined using the dry sieving method and the results are shown in Figure 2. The effective size (D_{10}), uniformity coefficient (C_u), and coefficient of curvature (C_c) for the sand were 0.12, 7.50 and 1.00, respectively.

Direct shear tests that were performed on sand samples with a relative density (D_r) of 55% resulted in an effective stress friction angle of 35.6°. Note that the normal stresses used to determine this friction angle ranged from 95 to 500 kPa. All loading tests were performed in dry conditions, i.e. using oven-dried sand, with the footing resting on the sand surface (Figure 3). Model-scale square and rectangular steel footings with artificially roughened bases having widths of 0.10 m and lengths ranging from 0.10 m to 0.40 m, with 20 mm thickness were concentrically loaded in this study. The sand was hand compacted in 0.05 m lifts with a steel tamper to 1.68 Mg / m³ ($D_r = 55\%$). For each test, a fresh test bed of sand was prepared.

Dupont Typar® SF 44 type geotextile with a peak tensile strength of 10.3 kN / m and Tensar TriAx™ TX 160 type geogrid with an elastic axial stiffness of 455 kN / m were used as reinforcing materials for the model tests. The intended use of this geotextile is filtration and separation, and its typical physical and technical properties as obtained from manufacturer's data sheet are given in Table 1. Table 2 presents the index, structural integrity and durability properties of the geogrid, which is manufactured from a punched polypropylene sheet, which is then oriented in three substantially equilateral directions so that the resulting ribs will have a high degree of molecular orientation.

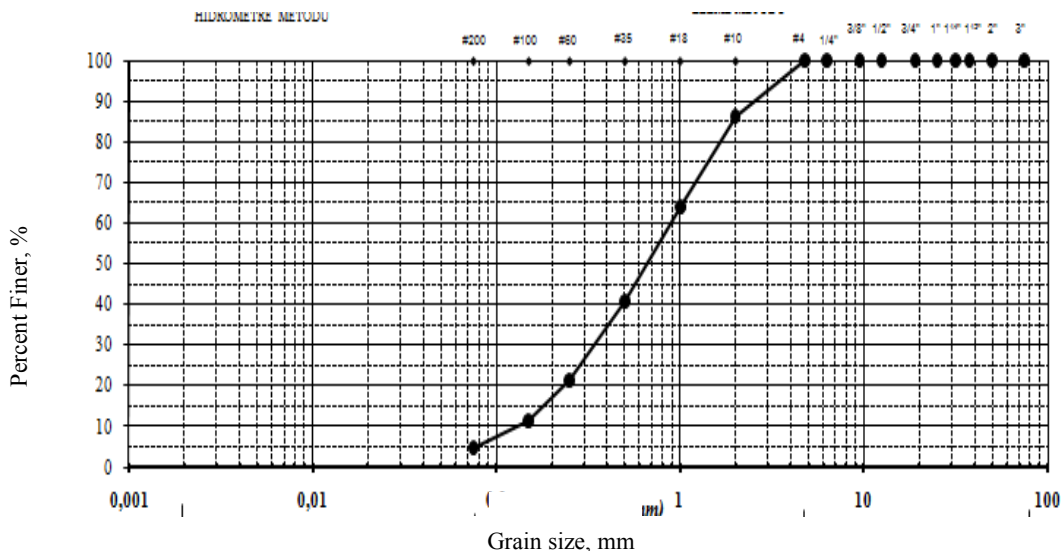


Figure 2: Grain size distribution of the sand

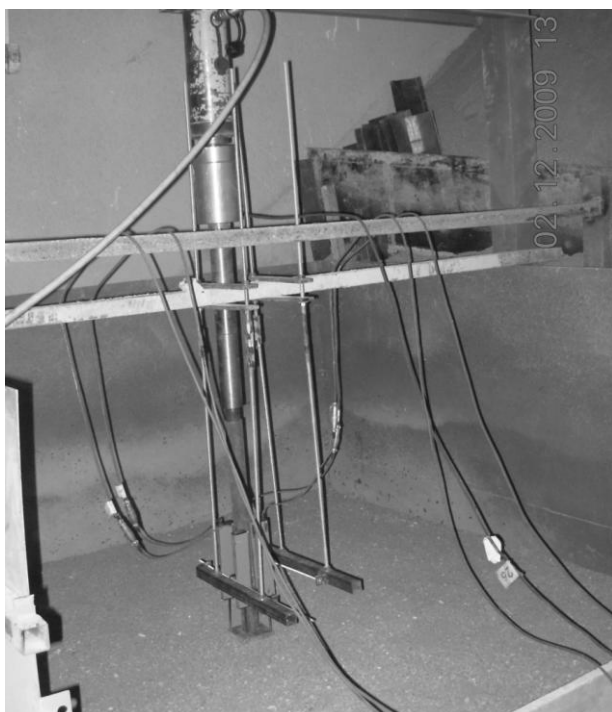


Figure 3: Photo of the test setup

Table 1: Engineering properties of geotextile

Tensile Strength	10.3 kN / m
Dynamic Perforation Resistance	27 mm
Resistance to Static Puncture	1.575 kN
Opening Size	100 μm
Water Permeability	40×10^{-3} m/s
Durability	Minimum 100 years
Strength at 5% Strain	4.5 kN / m
Yield Point Elongation	52 %

Table 2: Engineering properties of geogrid

Property	Longitudinal	Diagonal	Transverse	General
Rib Pitch (mm)	40	40	-	
Mid-rib Depth (mm)	-	1.8	1.5	
Mid-rib Width (mm)		1.1	1.3	
Nodal Thickness (mm)				3.1
Rib Shape				Rectangular
Aperture Shape				Triangular
Junction Efficiency (%)				93
Radial Stiffness at Low Strain (kN/m)				300
Axial Stiffness (kN/m)				455

4. LABORATORY MODEL TEST RESULTS

An experimental program was carried out to study the behavior of model square and rectangular surficial footings resting on sand reinforced with either a single layer of geotextile or geogrid. Model soil samples with a height of 400 mm were prepared at 50-mm layers to achieve a constant and uniform relative density. On reaching the reinforcement level, which is located at a depth of 30 mm, i.e., 0.3 B, from the surface, a geotextile or geogrid layer was placed and the remaining soil thickness was poured and tamped. A new sheet of reinforcement was used for each test. Finally, the footing was placed on position and the load was applied on it through the hydraulic jack in small increments until reaching failure or the limiting displacement. Each load increment was maintained constant until the footing settlement had stabilized. The settlement of the footings was measured using four LVDT (linear variable differential transformer) displacement transducers located at four corners.

Twelve tests on axially loaded footings supported on both unreinforced and geotextile or geogrid-reinforced sand were carried out. In this study, the ultimate capacity (q_{ult}) was interpreted as the bearing stress, which produced a fixed relative settlement: 10%, 15% and 25%B (i.e., for 10%B, the settlements is equal to 10 mm for B = 100 mm). As indicated by Cerato and Lutenegeger (2006), although choosing to define q_{ult} at a relative settlement of s / B is completely arbitrary, it (1) is convenient and easy to remember, (2) is close to the average soil strain at failure, (3) forces a fixed value at q_{ult} , and (4) treats displacement of different footing sizes the same.

Typical results of load – settlement curves for the footing tests performed in this study are presented in Figure 4. The results for the model footing tests in terms of ultimate load and bearing capacity ratio (BCR) are summarized in Table 3 and Table 4, respectively.

Table 3: Summary of model load test results in terms of ultimate load

Footing Dimensions (mm)	B/L	Ultimate Load (kN)								
		Unreinforced			With Geotextile			With Geogrid		
		0.10B	0.15B	0.25B	0.10B	0.15B	0.25B	0.10B	0.15B	0.25B
100x100	1.00	1.08	1.35	1.90	1.76	2.64	3.96	2.43	2.80	4.20
100x200	0.50	1.87	2.50	3.12	4.27	5.96	6.52	4.64	6.40	8.58
100x300	0.33	2.00	2.65	3.92	5.21	6.41	8.58	6.70	7.50	11.44
100x400	0.25	2.92	4.58	6.52	7.67	11.77	14.80	10.82	14.08	19.69

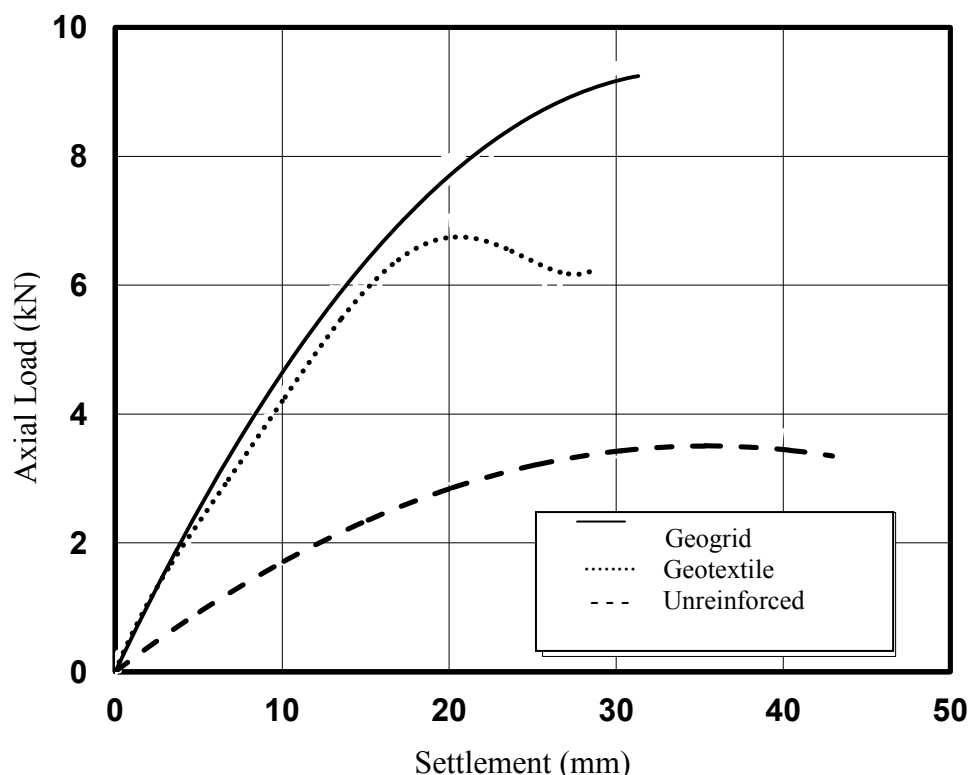


Figure 4: Load-settlement relationships for 100 mm x 200 mm footing

Table 4: Summary of model load test results in terms of BCR

Footing Dimensions (mm)	B/L	Bearing Capacity Ratio					
		With Geotextile			With Geogrid		
		0,10B	0,15B	0,25B	0,10B	0,15B	0,25B
100x100	1.00	1.63	1.96	2.08	2.25	2.07	2.21
100x200	0.50	2.56	2.38	2.09	2.78	2.56	2.75
100x300	0.33	2.60	2.42	2.19	3.35	2.83	2.92
100x400	0.25	2.63	2.57	2.27	3.71	3.07	3.02

The results indicate that, for each footing tested and for every deformation level, a higher BCR is obtained with geogrid than that for geotextile reinforcement. The ratio of BCR values obtained by geogrid and geotextile ranges between about 1.10 and 1.40. This is an expected result because the main intended purpose of the geotextile is filtration and separation. Guido et al. (1986) observed that geotextiles that are used to support loose sand ($D_r = 50\%$) produce beneficial effects in increasing the load bearing capacity of the foundations, but only after a measurable settlement has occurred. Atalar et al. (2009) also indicates that at limited levels of settlement BCR is equal to or less than one when geotextiles are used for reinforcement. The results obtained herein differ from these conclusions because all of the tests resulted in load-settlement relations similar to those given in Figure 4, i.e., BCR is always greater than 1 even for geotextiles.

The variation of BCR as a function of aspect ratio and deformation level is shown in Figure 5. This figure clearly shows that the BCRs at ultimate bearing capacity, without regard to the fixed settlement level for which it is defined for, decreases with increasing B / L. This finding is in agreement with the results presented by Omar et al. (1993). However, no clear correlation could be observed with the deformation level, BCR and B/L.

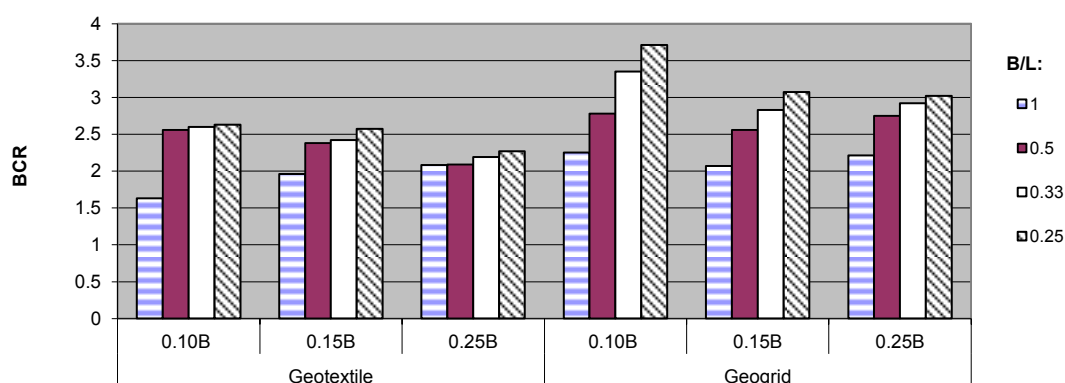


Figure 5: The variation of BCR with B/L and deformation level

5. NUMERICAL MODELING

In order to arrive at a generalization of the findings presented above and in order to investigate the effect of other parameters on the BCR of rectangular footings on reinforced soil, three dimensional finite element analyses were conducted using the finite element program Plaxis. A footing with a 400 mm width and variable length was assumed to rest on a cohesionless soil that extends laterally to a distance of five times the footing width from each side.

The nonlinear behavior of sand was modeled using an elastoplastic hyperbolic stress-strain model named hardening soil model in Plaxis, which is formulated within the framework of friction hardening plasticity. The foundation was modeled using elastic beam elements that are based on Mindlin's beam theory with flexural rigidity and normal stiffness values that approach to a rigid state. Interface elements were used to model the interaction between the geogrid and the soil at both sides. This is necessary to create a reduced wall friction compared to that of the soil. The soil was characterized using secant Young's modulus (E_{50}^{ref}), Poisson's ratio (ν), effective cohesion, effective stress friction angle (ϕ'), and interface reduction factor (R_{int}). In order to investigate the effect of soil relative density on the results, two hypothetical soil models, characterized by the parameters given in Table 5 were employed. A refined fine mesh was used to avoid mesh dependency-related problems in the solution phase. Load control method was selected to be used instead of fixed displacement method during the analyses. A view of the finite element model is shown in Figure 6.

Table 5 : Parameters for the soil models, footing, and the geogrid used in the numerical analyses

Property	Dense Sand	Loose Sand	Footing	Geogrid
Friction Angle	40	31		
Cohesion (kPa)	1	1		
Secant Young Modulus (kPa)	40000	15000		
Soil Unit Weight (kN/m^3)	19	17		
Poisson's Ratio	0.3	0.25		
Interface Reduction Factor	0.80	0.80		
EA (kN/m)			5000000	455
EI (kN m)			9000	

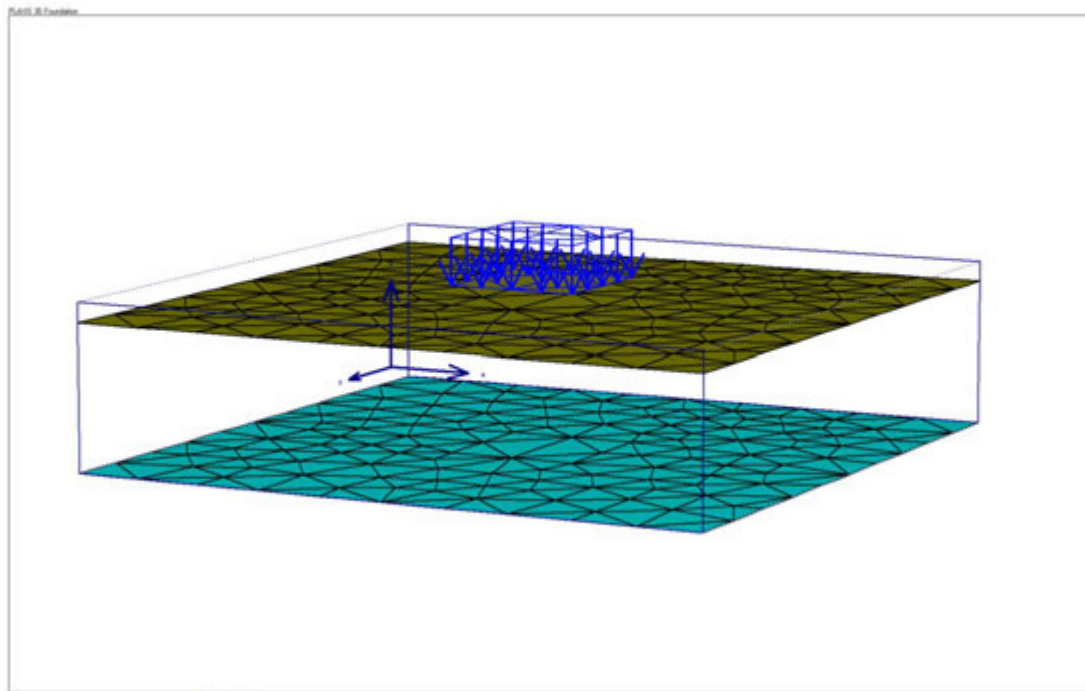


Figure 6: Finite element model

The validity of the finite element model is investigated by comparing the results with those obtained from laboratory model tests. Figure 7 presents the force-displacement behavior of 40 mm x 40 mm model footing on unreinforced soil along with the result obtained from finite element modeling. It can be stated that there is a significant agreement between the two.

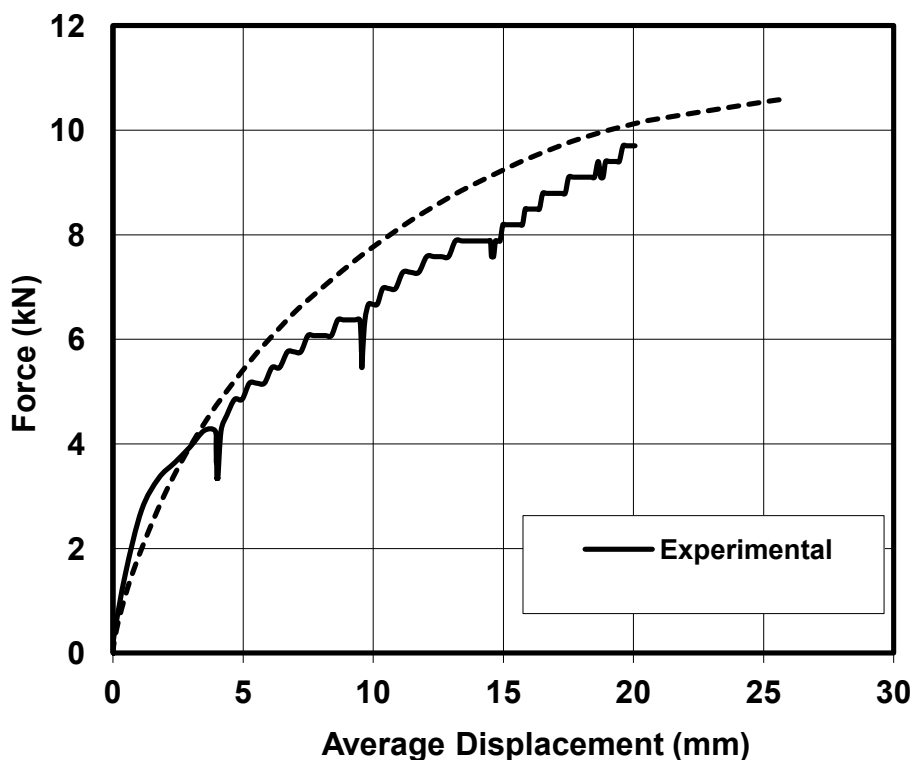


Figure 7: Comparison of numerical modeling and model loading test

Similar to the experimental study, the effect of the geogrid on the bearing capacity is represented by BCR during the numerical analyses. Figure 8 and Figure 9 present the variation of BCR as a function of number of geogrid layers and B / L for loose and dense sand, respectively. For all the models, the first geogrid layer is located at a depth of 12 cm, i.e., 0.3 B from the surface, and the remaining layers are separated at 20 cm distances.

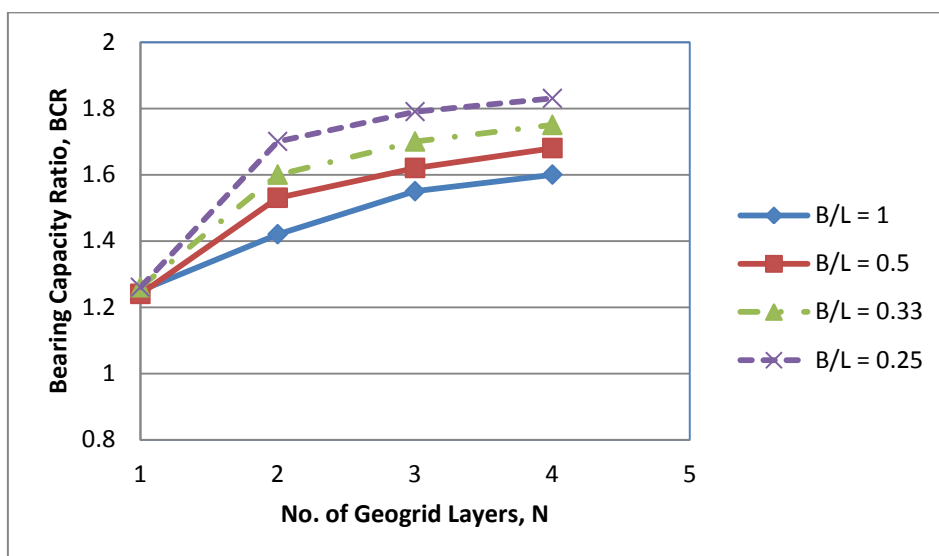


Figure 8: The variation of BCR with N and B/L for loose sand

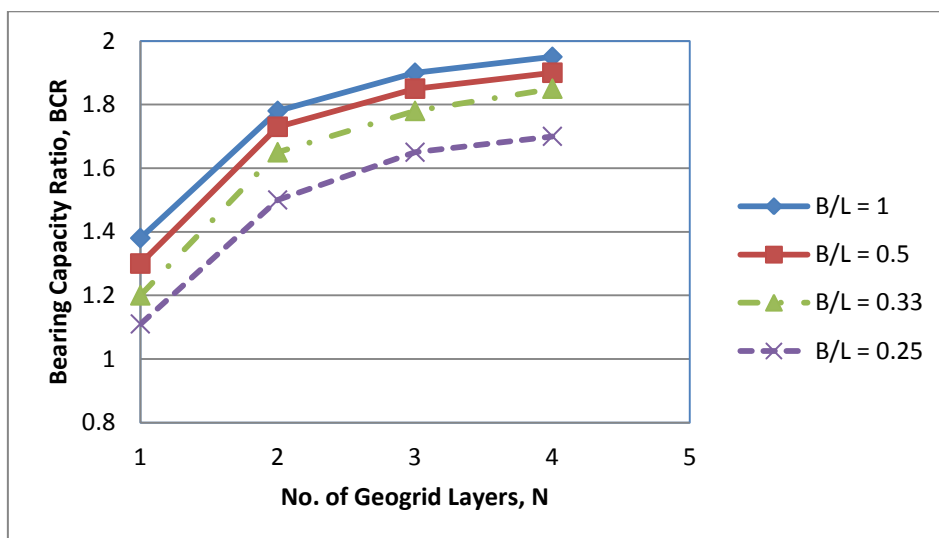


Figure 9: The variation of BCR with N and B/L for dense sand

As expected and similar to the results presented by previous researchers, the efficiency of the number of geogrids as indicated by the BCR, increases with a decreasing slope. The increase in the bearing capacity when two layers of geogrid are used instead of one is quite significant for all cases. However, the bearing capacity increases only marginally when N is increased from three to four. For the cases analyzed herein, without much regard to a detailed economical analysis, it can be stated that the optimum efficiency is obtained when N is equal to three. Similar conclusions stating that N = 3 is the optimum number of layers were stated by Das and Omar (1994) and El Sawwaf (2009) for square and strip footings.

The results of the finite element model calculations indicated some unexpected trends regarding the effect of relative density and the footing shape on the BCR. Except for the footing with the lowest B/L with a value of 0.25, i.e. the footing that is the closest one to a strip footing, the results suggest that a higher BCR can be obtained for higher initial relative density. This result is in agreement with those obtained by a numerical study conducted by El Sawwaf (2009), but is in disagreement with those presented by Das and Omar (1994) and Shin and Das (2000) who suggest that a higher BCR will be obtained for lower D_r ,

as supported by laboratory model loading tests. Note that all of the mentioned studies were conducted on strip footings, and the results obtained herein suggest that with decreasing B/L, a lower D_r means a higher BCR.

The results also indicate that there is not a unique relationship between B/L and BCR. For loose sand modeled in this study, BCR values increased with decreasing B/L without regard to the number of geogrid layers employed. Omar et al. (1993) reached to the same conclusion as a result of load tests on 76.2 mm wide model footings on a dense ($D_r = 70\%$) sand. However, the numerical study presented herein also suggests that for a dense soil, the trend is just the opposite, i.e., BCR increases with higher B/L.

6. DISCUSSION OF RESULTS

The results of a series of laboratory loading tests and a numerical modeling study on model footings supported by geotextile and geogrid reinforced sand are presented. Due to the limited focus on the behavior of rectangular footings in the literature, the main aim was to investigate the variation of BCR as a function of B/L under different conditions. Based on the laboratory tests and the numerical analyses, the following main conclusions are reached:

1. For each model footing load test and for every deformation level, the BCR values obtained on sand reinforced with geogrid is 1.1 to 1.4 times higher than those obtained for geotextile-reinforced sand. At every deformation level the BCR value is greater than 1 for either case.
2. For the cases analyzed herein, the optimum number of geogrid layers was determined to be three, which is a result supported by previous studies. However, it should be noted that optimum number of geogrid layers depends heavily on the vertical spacing between reinforcing layers.
3. No clear relationship could be obtained between the initial D_r and the resulting BCR for a given reinforcing system. The results suggest that for high B/L, BCR increases with D_r .
4. The results of the model load tests indicate that BCR decreases with increasing B/L. Same conclusion was reached from the result of numerical modeling on loose sand, however for the dense sand, the obtained trend is just the opposite. Therefore, no unique relationship between B/L and BCR for a given soil-foundation system can be obtained without considering the D_r . Further model loading tests are required for the clarification of this issue.

REFERENCES

Cerato, A.B. and Lutenecker, A.J., 2006, Bearing Capacity of Square and Circular Footings on a Finite Layer of Granular Soil Underlain by a Rigid Base, Journal of Geotechnical and Geoenvironmental Engineering, 132(11), 1496-1501.

Chen, Q., 2007, An Experimental Study on Characteristics and Behavior of Reinforced Soil Foundation, Dissertation, Louisiana State University.

Atalar, C., Shin, E.C. and Das, B.M., 2009, Elastic Modulus of Granular Soil-Geogrid Composite from Cyclic Plate Load Tests, Proceedings of the XVIIth International Conference on Soil Mechanics and Geotechnical Engineering, Alexandria, Egypt, (3), 2212-2215.

Das, B.M. and Omar, M.T., 1994, The Effects of Foundation Width on Model Tests for the Bearing Capacity of Sand with Geogrid Reinforcement, Geotechnical and Geological Engineering, 12, 133-141.

El Sawwaf, M., 2009, Experimental and Numerical Study of Eccentrically Loaded Strip Footings Resting on Reinforced Sand, Journal of Geotechnical and Geoenvironmental Engineering, 135(10), 1509-1518.

Guido, V.A., Chang, D.K. and Sweeney, M.A., 1986, Comparison of Geogrid and Geotextile Reinforced Earth Slabs, Canadian Geotechnical Journal, 23, 435-440.

Omar, M., Das, B.M., Puri, V., and Yen, S., 1993, Ultimate Bearing Capacity of Shallow Foundations on Sand with Geogrid Reinforcement, Canadian Geotechnical Journal, 30, 545-549.

Shin, E.C. and Das, B.M., 2000, Experimental Study of Bearing Capacity of a Strip Foundation on Geogrid-Reinforced Sand, Geotechnical and Geological Engineering, 20, 169-180.

Drilled shafts for slope stabilization in expansive soils

Ramanuja Chari Kannan, U. S. Army Corps of Engineers, USA, Ramanuja.kannan@usace.army.mil

ABSTRACT

Residual soils derived from the clay shales in Texas and other areas of the United States have been used in the construction of levees and earth dams built 50 to 70 years ago. With the state of the art of technology available at that time, these slopes were designed using shear strength values close to their residual shear strength, derived often from undrained shear strength tests to simulate rapid drawdown conditions, which was assumed to be the worst case scenario. Long-term stability was assumed to be related to the residual shear strength being mobilized. Though this had provided reasonable performance over the years, minor surface failures have occurred frequently and have become a part of the routine maintenance. Such shallow slides have been traditionally repaired with lime stabilization. Larger slides however involve substantial reconstruction of the slope and lime stabilization creates a dissimilar joint between the original and the new construction, resulting in more failures around the stabilized area. In an effort to provide stability against sliding using the original material of the slope, with or without additional stabilization, drilled shafts were recently used in expansive clays. Some preliminary studies have shown that the drilled shafts add to the stability of the repaired slopes. Laboratory tests indicate that first-time slope failures in slopes can occur at stress levels higher than the residual shear strength. Drilled shafts placed either intentionally or by other design constraints on the slope appear to add to the long-term stability and prevent first-time failures occurring long after the slopes are constructed. Further research is needed to establish that installation of drilled shafts can retard or stop further shear once the failure has been mobilized. This paper discusses observations on levees in Texas where drilled shafts have been used or proposed for the purpose of slope stabilization.

1. INTRODUCTION

Residual soils derived from weathered shales of the Eagle Ford Formation in Texas are highly plastic and expansive clays. Because of their easy availability and low permeability they were used extensively since the beginning of 20th century to build levees in Texas. As the cities along the rivers grew and the water demand for agricultural use increased, levees were raised and realigned using the same clay-shale derivatives in the 1950s by the United States Army Corps of Engineers (USACE.) These predominantly montmorillonitic soils are highly expansive, have high liquid limits (70 to 120) and high clay content (65 to 95%). Levee slopes constructed with this material have experienced surface slides ranging from 1 to 2 m deep, 10 to 30 m long (along the axis of the levee) and range in height from 2 m to 10 m, which in some cases represents the full height of the levee. Most of these surface slides occur on the water-side of the levee. Observations indicate that wherever drilled shafts were placed on the slopes either unintentionally to support bridges crossing the levee, or deliberately to stabilize the slope, such failures could be prevented. When a major slide occurred on a newly formed slope in San Antonio, a detailed study of the shear strength characteristics was conducted and drilled shafts were recommended to stabilize the slope. While this represents a rare solution to slope stabilization, using drilled shafts in critical areas might be an effective slope stabilization method.

2. LONG-TERM STABILITY OF CLAY SLOPES

Clayey soils are used in slope construction because of their low permeability and higher shear strength than purely cohesionless soils. Physical properties of clays are influenced by the clay mineral. Though permeability decreases with higher clay content and high liquid limit clays, these clays are subject to high volume changes and the slopes fail often due to two key factors that reduce the strength of clays – high pore pressures and reduction in shear strength. Another factor that influences clay behaviour is over-consolidation. Generally clays used in slopes undergo cycles of shrinkage and expansion, which in effect is the same as loading and unloading cycles. This process tends to eventually reduce the response of the clay to subsequent loading and the clay retains what is termed as the “residual” strength. However slopes have known to fail 20 or more years after construction, even before the strength had dropped to the residual strength value. Research indicates that there might be an interim shear strength value between the peak strength and the residual strength termed the “fully-softened” shear strength that is higher than the residual strength but lower than the peak strength. Recognizing the fact that repeated wetting and drying

cycles could reduce the shear strength to this value, test methods have been developed to simulate this condition. However, introducing methods to avoid failure due to anticipated loss of shear strength over a long time period is not a standard practice. It has been noticed that slope failures at bridge piers on slopes occur more frequently due to erosion than due to loss of shear strength. However, it is rare that drilled shafts are used to improve newly constructed slopes as a means of providing long-term stability. This paper discusses a case of experimental use of drilled shafts for slope stabilization and suggests that this could improve long-term stability of clay slopes.

2.1. Stability of earth slopes

2.1.1. Traditional slope stability analysis

Most methods of slope stability analysis attempt to arrive at a Factor of Safety (FS) defined as

$$FS = \frac{M_R}{M_W} = \frac{\text{Moment of shear along the failure arc}}{\text{Moment of the weight of the failure mass}} \quad (1)$$

Essentially, this is the same principle used in the method of slices recommended by Bishop and Morgenstern (1960) which has been improvised by numerous researchers and has been used as the basis for most commercially used slope stability analysis software. This might be sufficient for the purposes of design where the geometric cross-section of the levee can be designed to provide a stable slope. However, most real-life situations are not two-dimensional, and especially when it concerns back analysis of failures of slopes and landslides, where number of other factors that influence the shear strength need consideration. The analysis of slides for levees for the steady-state condition differs from rapid drawdown condition as the shear strength parameters used in these two cases are different. In the steady-state condition effective shear strength applies and in the rapid drawdown condition total shear stress applies. These shear strength parameters are tested using the drained shear strength test for effective stress and the undrained test for total stress. Typically, a factor of safety is applied to the laboratory-measured shear strength for use in design. But in back analysis of failed slopes it is essential to consider the shear strength at the time of failure and where and how the shear was mobilized. Simons and Menzies (1976) cite the following three factors that affect the measurement of shear strength— strength anisotropy, time to undrained failure and sampling disturbance/test specimen size.

Briefly, shear strength of clayey soils tested in a triaxial cell varies widely with the factors that influence anisotropy—soil structure, mineralogy, depositional history and in-situ conditions. Shear strength decreases with lower rate of shear, especially with over-consolidated clays. Sample disturbance obviously plays a key role in measured shear strength, and it appears that block samples cut out from the field tend to be less disturbed and yield higher shear strength values than samples obtained from sampling tubes pushed in to the ground. It also appears that shear box tests agree closely with in-situ shear tests, such as vane shear.

2.1.2. Slope failure mechanism

Failure in the context of levee slopes could be defined as loss the designed function of the slope. This definition would be adequate for the purposes of this paper, which is applicable to highway embankments, levees (both river and coastal) and natural or man-made hill slopes. Slopes fail due to internal or external factors or a combination of both.

Among the internal factors are:

- Shear strength of the soils used in the levee
- Internal erosion – Seepage through or under the levee, suffusion, piping, increase in internal flow velocity of seepage flow
- Hydraulic loading – overtopping, rapid drawdown, wave action and erosion

Among the external factors are:

- Physical changes in the geometric shape of the levee – settlement, lateral shift due to soft foundation soils, slides caused by bearing capacity loss
- Hydraulic loading – overtopping and submergence, flow velocity
- Seismic loading – directly on the levee or liquefaction of subsurface soils

Most common modes of internal failure are slope instability due to loss of shear strength or piping caused by seepage; and most common external factors are overtopping and slope failure due to erosion or tension cracks caused by drying/shrinkage.

Cohesive soils are typically used for embankment and levee construction because of their high plasticity (high liquid limit) and low permeability. Clays with liquid limit higher than 50 generally tend to be more susceptible to lose shear strength due to cyclic loading caused by changing hot and cold seasonal changes. The effect of such weather variations is to impose over-consolidation. Such repetitive cycles should reduce the clay to its residual shear strength. But Skempton (1964) introduced the concept of “fully softened” shear strength for high plasticity clays, based on his observations on slopes that failed 2 to 4 decades after construction long before the residual strength was reached. First-time failure of slopes that have been through a few years of “steady-state” existence is believed to occur when the fully-softened shear strength is reached. Until recently there was no “standard” method of determining the fully-softened shear strength. Many researchers however (Stark and Eid 1997, Mesri 2003, Wright 2007) have verified Skempton’s (1964) observation that the fully softened shear strength of an over-consolidated clay is numerically equal to the peak strength of remolded normally consolidated clay. This is illustrated in Figure 1.

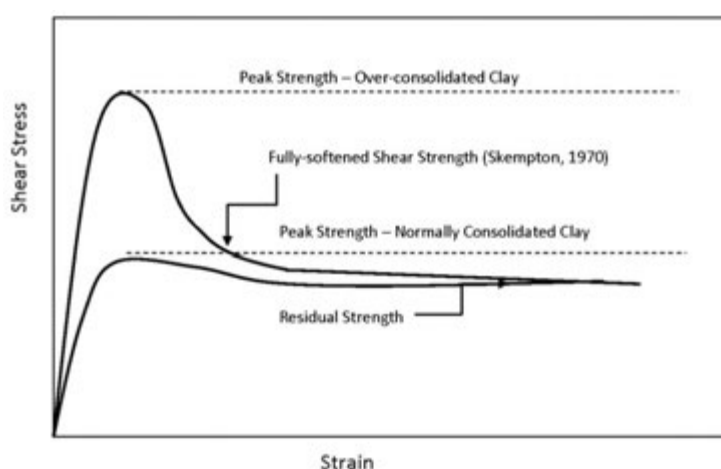


Figure 1: Illustration of peak, residual and fully-softened shear strength values for typical clays

Traditional slope-stability analysis of embankment slopes and levees built in the past 50 to 70 years generally used a fraction of the peak shear strength (with a factor of safety applied) or the residual strength to be on the conservative side. Many of these earth slopes developed failures after forty to fifty years. Likewise, cut slopes in excavations and natural slopes in expansive clays showed similar signs of failure after decades. Skempton (1964) theorized that delayed failures occurred due to strain-softening. However, Vaughan and Walbancke (1973) found that the ratio of pore pressure to the overburden pressure, called the pore water pressure ratio r_u was more critical in the long-term stability of slopes. Further experiments in the London Clay, Paris Clay and Bueaumont (Texas) Clay showed that in compacted soils the r_u had to be very high (0.9 to 1.0) to cause failure. But back-analysis of failed slopes with lower r_u ratio showed that the clays behaved as though the effective cohesion was zero when the fully softened strength condition existed. Research conducted in the next three decades by Skempton (1977), Kayyal and Wright (1991), Mesri and Cepeda-Diaz (1986), Stark and Eid (1997) and Stark et al., (2005) has shown that the shear strength of fully softened clays can be estimated by using consolidated drained tests on normally consolidated remolded samples to analyze first-time failures of clay slopes that fail years after construction. The shear-strength envelope that is obtained in these tests shows a zero cohesion intercept, a curvilinear envelope and failure at relatively small strain levels. The so-called secant angle of the failure envelope is used in the shear strength analysis rather than the traditional $c-\phi$ (cohesion-friction angle) shear strength parameters. This is illustrated in Figure 2.

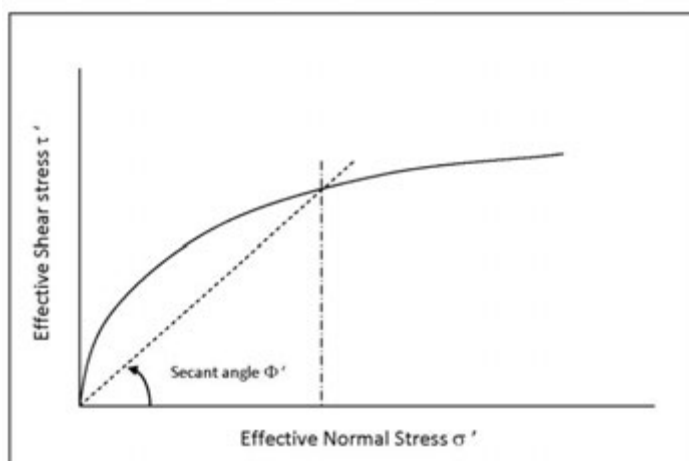


Figure 2: Illustration of Secant friction angle from Mohr envelope curves for remolded, normally consolidated clays

Factors that impact the secant friction angle are the degree of over-consolidation, clay content, liquid limit and clay mineral composition. The following graph proposed by Saleh and Wright (1997) and later revised by Wright (2005) shows the variation of the secant angle with effective stress for various liquid limits. This provides an envelope of values within which most of the stiff, fissured clays fall.

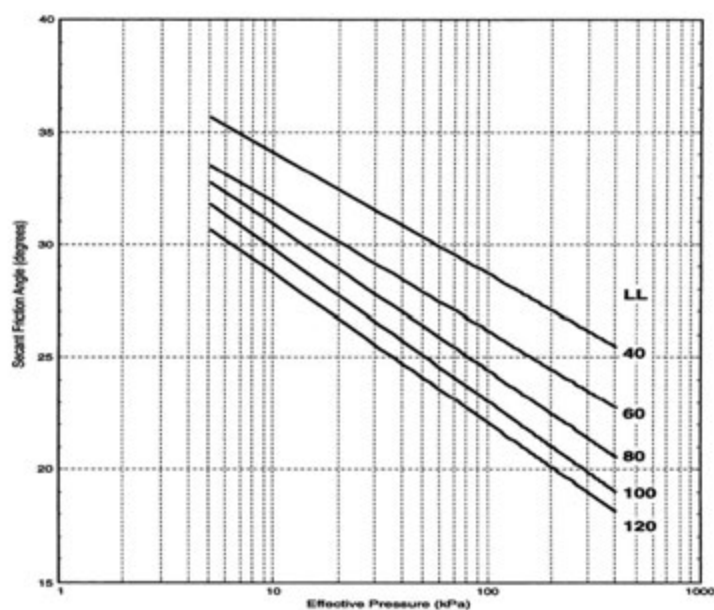


Figure 3: Relationship between Secant Friction angle, Liquid limit and effective stress of clays (Saleh and Wright, 1977)

The foregoing factors appear to be common to slope failures, and treating one or more of the following would add to the stability of the slope:

- First-time failure occurs in slopes that have been in existence for 20 or more years, even at low pore pressure ratios (r_u): Reducing porepressures would therefore add to stability. Seepage control is the frequently applied method to reduce excess pore pressures.
- Long-term stability is related to the development of fully softened condition: The loss of shear strength could be reduced by avoiding repetitive loading and unloading conditions (such as wetting and drying cycles) that result in overconsolidation.
- The analysis of first-time failures in aging slopes should use the effective secant friction angle: There is a developing trend to move away from traditional shear test methods (on “undisturbed samples) to using the fully softened or the residual strength using ring shear tests (on remolded, normally-consolidated samples.) Further, a risk-based method of analysis is preferred over a factor of safety applied to peak the peak strength.

- The factors that influence secant friction angle appear to be the liquid limit, stress level, degree of over-consolidation, clay content and the clay-mineral composition: these factors could be modified by physical or chemical methods.
- Slope geometry- most long-term stability problems arise in slopes steeper than 2.5:1 (Horizontal: Vertical): Where possible slopes should be made flatter (3:1 or better) or benched.

2.1.3. Slope stabilization methods

Following from the foregoing discussion, we could now focus on some of the methods of slope stabilization and remediation methods used. This discussion is not intended to be a complete and comprehensive analysis of all the available methods, but only those commonly used and common sense methods.

Stability could be improved by controlling pore pressures: Slope failures related to pore pressures fall in to two broad categories – gradual increase in the pore pressure ratio due to overconsolidation and sudden increase in pore pressure due to hydraulic loading, known as sudden draw-down condition. The first case occurs in steady seepage and repeated wetting and drying cycles and the latter occurs when flood waters increase pore pressures and there is insufficient time for pore pressures to drop as the water suddenly recedes. Some of the methods of seepage control that increase the stability by controlling pore pressures are chimney and/or toe drains, perhaps coupled with wet wells or sumps and cut-off walls.

Stability could be improved by increasing shear strength: This includes a number of methods; including using soil that is ideally a $c-\phi$ soil that is less susceptible to seasonal high volume change; mechanically stabilizing the material used in the slope by mixing clays with gravel and sand to alter the gradation and hence the physical properties; and chemically stabilize the soil by reducing its plasticity by addition of lime or other chemicals. Lime stabilization has been used especially on high-plasticity clays as a method of slope repair after shallow surface failures have occurred.

Stability could be improved by improving slope geometry: Slopes constructed at 3.5:1 and/or with a stabilizing bench have experienced considerably less failures. Stauffer and Wright (1984) noticed that in Texas Department of Transportation embankments flatter than 2:1 there were no failures and most failures occurred in slopes 2.5:1 to 3.5:1 in the time range of 20 to 25 years. However, it is not always possible to build such shallow slopes, especially in urban areas and in areas where failures have occurred on the protected side. Likewise, introducing benches in urban areas and in slopes that have already failed may not be feasible.

Stability could be improved by externally induced stabilizing forces: Once a potential failure surface has been identified, the probability of failure along that plane could be reduced by applying external stabilizing forces such as soil nails, piles, rip-rap, stabilizing berms (at the toe) and reinforced earth walls (especially in highway embankments.) These methods of slope stabilization are sometimes intentionally used for slope stabilization and often are introduced only after a potential failure has been observed or anticipated. This paper illustrates the use of one such method, the use of drilled shafts for slope stabilization.

3. STABILIZING SLOPES WITH DRILLED SHAFTS

3.1.1. Unintended slope stabilization with drilled shafts

Highway embankments, natural earth slopes, cuts and levees have similar slope failure mechanism when it comes to the long-term stability. As seen in the foregoing discussion, the fully softened shear strength seems to impact the stability of such slopes in the long term. Newly constructed highway embankments and fresh cuts on natural slopes have a different failure mechanism dependent upon the design shear strength parameters, which would apply to $c-\phi$ soils. The focus here would be on long-term stability of slopes with piles or drilled shafts intercepting the slope. Whether these intrusions are placed intentionally or unintentionally, they add to the long-term stability of slopes. While these intrusions may have a beneficial effect on the slope stability in slip failure they could contribute to other adverse effects such as erosion and seepage.

One example of pile intrusion on slopes is shown in Figure 4. In this unusual case in Fort Worth, Texas the levee was constructed in 1910 and repaired in 1920 and upgraded between 1950 and 1957 after a flood in 1949. The bridge in this picture was completed in 1939. There has been no history of slope failure but

there have been periodic erosion problems. In 2009, a 7 m deep excavation was made within 3 m of the toe of the levee in the lean clay and the weathered clay-shale foundation material without any stability problems. This positive influence of the piles on the levee was not intended but was noticed. Piles are socketed in unweathered clay shale encountered at about the same elevation as the bottom of the excavation, or about 7 m below the toe of the levee. The levee at this location is about 5 m high and has a 2.5 to 1 slope.



Figure 4: Lancaster Avenue Bridge in Fort Worth, Texas. The piles were installed in 1938 about 18 years after the levee was upgraded. Second frame shows excavation close to the levee in 2009.

3.1.2. Problems with drilled shafts on slopes

If there were beneficial effects of using drilled shafts for slope stabilization, it has not been an acceptable or desirable practice. In fact, many regulatory authorities either prohibit or actively discourage the intrusion of any structure (undesirable penetrations) on levees, especially in cases where seepage or expansive clays are involved. Apart from these geotechnical concerns, there are also hydraulic concerns. The first and most serious concern is erosion, followed by reduction in channel capacity and then by loss of slope material due to currents. All of these effects are shown in Figure 5 taken from one of the major interstate highways crossing the Dallas Floodway. Though in this case the drilled shafts are at the top of the slope, the problems with erosion and loss of material from the slope can be easily seen, but slope failure has not occurred.



Figure 5: Interstate 35 bridge crossing the Trinity River south of downtown Dallas. The frame on the left is a view looking West. The frame on the right shows erosion under one of the piers of the East-bound lanes on the West bank piers and the Revetmat sloping at the top of the slope.

Figure 6 below shows the effects of erosion at the same bridge on the West bank just beyond the riprap. Erosion is more recent (2009) and is unrelated to slope stability issues.



Figure 6: Left frame shows erosion downstream of the revetmat on the West bank. Right frame shows erosion and riprap placed on the upstream side of the West bank.

Notwithstanding the problems illustrated above, there is a case for using drilled shafts for slope stabilization, which was used in the case study discussed below from San Antonio, Texas, about 450 km southwest of Dallas. The subsurface soil conditions at both these sites are somewhat similar in that the material used in the slope was a highly plastic clay derived from the weathered Eagle Ford Shale. Figure 7 shows why similar soil conditions exist 450 km apart. The clayey soils at the two locations are classified as Texas Blackland Prairie soils and are derived from the Eagle Ford Clay Shale (EFCS) parent material. The “typical” properties of EFCS is shown below, taken from Hsu and Nelson (2002).

Table 1 : Properties of Eagle Ford Clay Shale (from Hsu and Nelson (2002))

Liquid Limit	Plasticity Index	Water content	Clay content	Dominant Clay mineral	Typical Secant friction angle (fully softened)
39 to 140	16 to 113	4 to 25%	38 to 88%	Smectite (Montmorillonite)	19° to 39° (effective)

Quite literally, hundreds of samples have been tested from both the Dallas Floodway and the San Antonio floodway and the test results fall within this range, albeit on the higher end of the liquid limit range (70 to 90). The measured secant friction angle for the Dallas and San Antonio Clays is in the range of 19° to 27° depending upon the applied normal effective stress.

3.1.3. Drilled shafts for slope stability

Since 1957 the San Antonio Channel Improvement Project (SCAIP) has completed over \$230 million of hydraulic, geotechnical and ecosystem improvements on what was originally intended to be a flood control project. The total length of the channel improved is about 50 km, and the southern half of the project called the Mission Reach (named after four Spanish Missions located within this reach) required realignment of the channel from a near-straight run to an ecosystem consisting of artificially introduced curves and re-designed slopes. The new slopes were designed with 3:1 (horizontal:vertical) slope in the clay soils derived from the Eagle Ford Shale.

Following a slope failure at one of the locations within this reach in April 2008, which occurred more or less at the same general location for the fourth time since 1973, a detailed study of the shear strength was undertaken by the US Army Corps of Engineers. Back analysis and tests conducted on bulk samples on the failed slope indicated that the controlling shear strength was the fully softened shear strength value and not the residual shear strength. Though this section of the slope had been in existence for over 5 decades, the failure was analyzed as a first-time failure, as the slope had been recently repaired. Therefore the fully softened shear strength was considered applicable to the analysis. The rationale behind considering this to be a first-time failure was that the slope was rebuilt after the last failure, about 6 years ago.

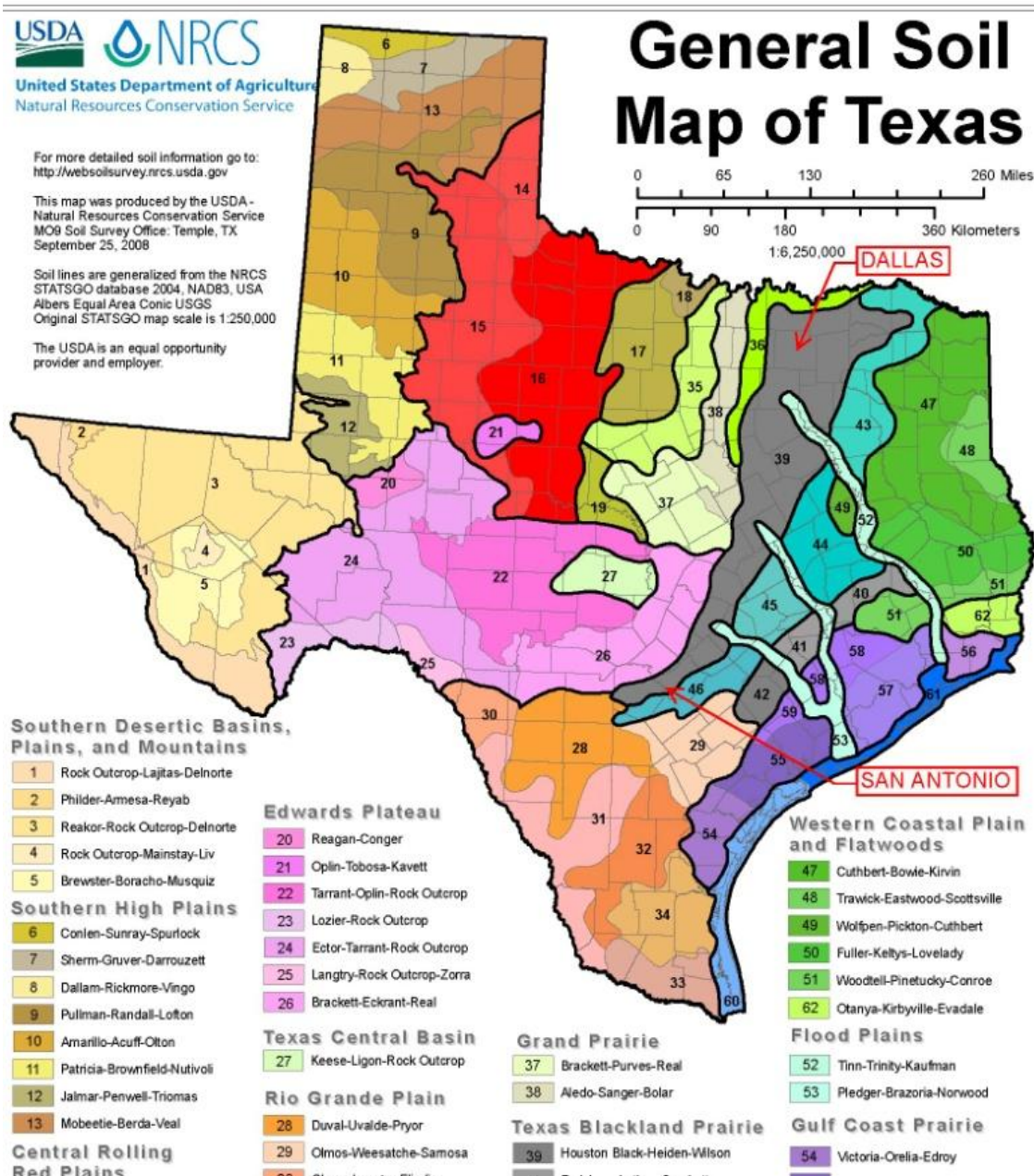


Figure 7: Soil Map of Texas showing similar soil at Dallas and San Antonio, about 450 km apart. Map adapted from US Department of Agriculture, Natural resources Conservation Service (2008).

The failed section was proposed to be repaired with a row of drilled shafts placed on a bench. This proposal was later extended to the long-term stability of the proposed new slopes, which were also analyzed using the fully softened shear strength (secant friction angle of 18° as determined from “slow” drained shear strength tests). This analysis indicated that the probability of slope failure was as high - as high as 96% - even with a computed factor of safety of 1.20. This would be unacceptable as the implication was that a first-time failure could occur within a decade. Hence it was proposed that drilled shafts should be introduced along the mid slope with a bench. When analyzed with the piers, the factor of safety improved to 1.799. The drilled shafts designed were 914 mm diameter (36-inch) and were socketed in to the unweathered shale encountered at a depth of about 7.6 to 8.5 m below the top of the slope. The drilled shaft spacing was determined to be in the range of 3D to 5D or 2.7 to 4.5 m. The final design was provided a 914 mm diameter drilled shaft, reinforced to its full depth of 7.6 to 8.5 m (allowing for local variations) and spaced 2.7 m apart. Approximately 160 drilled shafts were used over a one-kilometer reach and some drilled shafts had to be spaced farther apart to avoid a sewer line crossing the levee. As constructed, these slopes are about a year old and therefore no monitoring records are available at this time. However, the stabilized sections were opened to public use in mid 2011.

4. CONCLUSION

Slope failures on long slopes, such as levees appears to occur when the fully-softened shear strength is reached, rather than at the residual strength, which is much lower. Designing new slopes with drilled shafts to add to the stability - to avoid the first-time failure in highly plastic and expansive clays, seems to be a viable option and an acceptable solution. Unintentionally placed drilled shafts on old slopes seem to substantiate this view. Theoretical analysis of the slope using drilled shafts is not a complicated procedure, but the cost could be justified when the probability of failure or the consequences of failure even with a marginally acceptable factor of safety is high.

Future research in this area should be conducted by using back analysis of first time slope failures in slopes that have existed for four to five decades or more. To ensure the long-term stability of newly constructed slopes, the use of other stabilizing methods, such as soil-lime or soil-cement columns could be considered as an alternative to drilled shafts.

5. ACKNOWLEDGMENTS

The author is grateful to his colleagues at US Army Corps of Engineers at Fort Worth, and the San Antonio Mission Reach Project office for their valuable time in arranging the site visits. The author is also grateful to the engineers at the City of Dallas for organizing the tours of the various locations along their levee system.

REFERENCES

- Bishop A.W. and N. Morgenstern, 1960, *Stability Coefficients for earth slopes*, *Geotechnique*, Vol. 10, pp.129-150, London
- Branch A., 2009, *San Antonio Channel Improvement Project Mission Reach – Slope Stability of Permanent Excavated Slopes in High Plasticity Clay Shale*, US Army Corps of Engineers Infrastructure Conference, Cleveland, OH July 2009 (Unpublished)
- Hsu, S. and Nelson, P.P., 2002, *Characterization of Eagle Ford Shale*, *Engineering Geology* Vol 67, pp. 169 – 183.
- Kayyal, M. K. and Wright S. G., 1991, *Investigation of Long-Term Strength Properties of Paris and Beaumont Clays in Earth Embankments*, Research Report 1195-2F, Center for Transportation Research, The University of Texas at Austin, 125 pgs.
- Mesri, G. and A. F. Cepeda-Diaz, 1986, *Residual Shear Strength of Clays and Shales*, *Géotechnique* Vol.36, No. 2, pp.269-274.
- Mesri G and Shahein M., 2003, *Residual shear strength mobilized in first-time slope failures*, *Journal of Geotechnical and Geoenvironmental Engineering* Jan 2003 pp.12-31, ASCE, Alexandria, VA.
- Simons N.E. and Menzies B.K., 1976, *A short course in foundation engineering*, 2nd Edition, IPS Science and Technology Press, London
- Saleh, A.A. and Wright S.G, 1997, *Shear Strength Correlations and Remedial Measure Guidelines for Long-term Stability of Slopes Constructed of Highly Plastic Clays*, CTR Technical Report 0-1435, Center for Transportation Research, University of Texas, Austin, Texas
- Skempton A.W., 1964, *Long-term stability of clay slopes*, *Géotechnique* Vol. 1. No2, pp.75-102, London
- Skempton A.W., 1970, *First-time Slides in Over-consolidated Clays*, *Géotechnique* Vol. 20. No3, pp.320-324, London
- Stark T.D. and Eid H.T., 1997, *Slope stability analyses in Stiff fissured clays*, *Journal of Geotechnical and Geoenvironmental Engineering* April 1997 pp.335-343, ASCE, Alexandria, VA.

Stark, T. D., H. Choi, and S. McCone, 2005, Drained Shear Strength Parameters for Analysis of Landslides, Journal of Geotechnical and Geoenvironmental Engineering Vol.131, No. 5, pp.575-588.

Stauffer, P. A. and Wright, S. G., 1984, An Examination of Earth Slope Failures in Texas, Research Report 353-3F, Center for Transportation Research, The University of Texas.

USDA Natural Resources Conservation Service, 2008, <http://websoilsurvey.nrcs.usda.gov>

Vaughan, P. R. and Walbancke, H. J., 1973, Pore Pressure Changes and the Delayed Failure of Cutting Slopes in Overconsolidated Clay, Géotechnique Vol.23, No. 4, pp.531-539.

Wright, Stephen G., 2005, Evaluation of Soil Shear Strength for Slope Retaining Wall Stability Analysis with Emphasis on High Plasticity Clays, CTR Technical Report 5-1874-01-1, Center for Transportation Research, University of Texas, Austin, Texas

Wright S.G., Zornberg J.G. and Aguenttant J.E., 2007, The fully-softened shear strength of high plasticity clays, CTR Technical Report 0-5202-3, Center for Transportation Research, University of Texas, Austin, Texas

Soil Reinforcement Vegetation Effect

An analysis applied to the Earth moving volume of California High Speed Railway System

Luis Fort López-Tello, Laboratorio de Geotecnia, Centro de Estudios y Experimentación de Obras Públicas, Spain,
Luis.Fort@cedex.es

Carmen Fort Santa-María, EPTISA, S.I División de Infraestructura del Transporte, Spain, cfort@eptisa.com

ABSTRACT

The revegetation growing on a mass of soil brings about in this, an important increase of its shear strength.

On the one hand, in the superficial zone of itself, in whose inside concentrates the great density of roots, the additional soil shear strength $\Delta\tau_{vr}$, due to themselves, in the depth z_r reached by the main packet of roots, depends on radicular density and is known as "vegetation reinforcing effect". On the other hand, beyond the reinforced zone, as far as z_3 depths at those the moisture of soil belongs to suctions equal or larger than pF_3 , is well-known the increment of soil shear strength $\Delta\tau_{vd}$, "vegetation drying effect".

The soil masses limited for a sloping surface (be sloped land with native vegetation or cutting slope with implanted vegetation), and therefore yielded to shear stresses on the slide surface that they can produce inside them, will be stable with a definite safety coefficient FS, if the soil shear strength along of these slide surfaces surpass in this ratio the shear sliding stresses leaded to by the gravity force.

The expected average growth of vegetation (native or implanted) on a slope, during a period of time (total biomass production UG (underground)+ AG (above ground)), may be estimated beginning with production climatic rates WUE (water use efficiency) and LUE (light use efficiency), depending on the hydric balance of the slope ($BH= P-E$), its orientation (ϵ°) and inclination (θ°) that in turn have influence between them. Depending on the magnitude of vegetation development achieving on a definite slope (height H and inclination θ), function from the climatic characteristics on site and from the solar orientation (obligates by functional layout) the additional soil shear strength that may be mobilized in front of a potential instability, it will depend on its geometry and on the vegetative development of its surface. Learning on the mentioned phytoclimatic characterizations, and in the use, for example, of the Taylor abacus which estimation of the critical sliding circle, it is analysed, for soils from coulombian behaviour, the stage of reinforcement achieved at them, according, the importance of vegetation growth in its surfaces.

As an example, and reducing the accuracy of data by the approximate generalization from global aspects, it is applied this type of analysis to an important and nearly future civil work construction with larger earth-moving volume and cuts length from moderate heights the California High Speed Railway System (CHSR) in U.S.A.

This type of point of view can be of interest for the geoenvironmental design of linear works infrastructures and for the financing of "green works" that carries with themselves.

1. DESCRIPTION OF THE COYOTE PROJECT OF THE CHSRP

The California High-Speed Railway Program (CHSRP) foresees the stage high speed system development, that in its COYOTE alternative, with a 1.288 km length, which will operate in a 15 year term, at 380 km/h top speed and 350 km/h operational speed, connecting the Bay Area, the Central Valley, Sacramento and the Southern of California. The journey time between San Francisco and Los Angeles will be 2h 30 m.

This option assumes that the construction of the system is divided in ten geographic sections, grouped in three phases as shown in Table 1 and Figure 1.

Table 1: Description of CHSRS COYOTE Alternative

Phase	Project	Section	Length (km)	Earth Moving (included tunnelling) (Mm ³)	Estimated Cost (M\$)	Journey time (h.m)
I	Initial Central Valley Connection Bay Area Connection Los Angeles Basin Extension to San Francisco Airport Extension to Anaheim	I Fresno-Bakersfield	157	43,82	1.889	0,29
		II Fresno-Merced	99	7,94	853	0,19
		III Fresno-San José	222	39,46	4.938	0,46
		IV Bakersfield-Los Angeles Airport	166	39,20	6.458	1,00
		V San José- San Francisco Airport	52	6,50	2.027	0,13
		VI Los Angeles Airport-Anaheim	62	8,65	2.177	0,12
	TOTAL PHASE I: San Francisco Airport-Anaheim		758	145,57	18.342	
II	Extension to Sacramento Airport Extension to San Diego Airport & Inland Empire	VII Merced-Sacramento Airport	191	31,66	2.933	0,36
		VIIIa Anaheim-San Diego Airport	117	26,48	4.666	0,30
		VIIIb Branch line to Riverside	55	7,54	1.969	0,14
	TOTAL PHASE II: Ampliation system to Sacramento & San Diego		363	65,68	9.568	
III	Bay Crossing Completion system to Sacramento	IX San Francisco Airport -Vallejo	57	3,67	4.291	0,14
		X Vallejo-Sacramento Airport	110	56,59	2.619	0,22
	TOTAL PHASE III: Closing system through San Fco. Bay		167	60,26	6.910	
TOTAL	SYSTEM		1.288	271,51	34.820	



Figure 1: CHSRS Plan & Thornthwaite Index

2. GEOPHYTOCLIMATIC CHARACTERIZATION OF THE STUDY ZONES

In the Table 2 it carries out to calculate the Thornthwaite index in twelve points of the CHSRS, beginning with the information of the monthly values of basic climatic variables from corresponding meteorological stations of the California network. In the Figures 2a and 2b are included, as an example, the corresponding information to the Fresno Station.

Table 2: Geophytoclimatical Characterization of the zone (CHSRS COYOTE Alternative)

Meteorological Station	CHSR Station	Latitude λ (°N)	T̄ (°C)	P (mm/yr)	H̄ (%)	T̄v (°C)	Pv (mm)	E _v (mm)	(Fe) _v (mmHg)	H̄ _v (%)	δ̄ _v (kPa)	(γ ₀) _v 10 ⁴	Altitude h (m)	ETP (mm)	Thornthwaite Index I	pF	q _u (MPa)
KFAT 723890	FRESNO	36,6	17,7	430	56	21,5	219	323	19,23	51	1,402	101,75	81	894	-29,3	3,4	0,220
KBFL 723840	BAKERSFIELD	35,4	18,4	325	53	22,4	193	232	20,32	52	1,300	101,78	154	902	-39,0	3,7	0,411
KMCE 724815	MERCED	37,3	16,0	435	64	19,9	163	346	17,43	51	1,139	101,68	47	828	-24,3	3,2	0,163
307 749179	GILROY	36,9	13,7	495	74	15,4	238	340	13,12	64	0,630	101,33	72	724	-17,1	3,1	0,124
KLAX 722950	LOS ANGELES Airport	33,9	16,3	587	67	17,2	160	346	14,75	46	1,063	105,53	27	770	-7,1	2,8	0,075
KSFO 724940	SAN FRANCISCO Airport	37,6	14,2	618	72	15,9	159	325	13,55	49	1,103	102,47	3	705	5,0	2,6	0,058
KSMF 724839	SACRAMENTO Airport	38,8	15,5	545	66	19,2	159	332	16,63	48	1,154	101,57	34	802	-8,9	2,8	0,081
KNKX 722930	SAN DIEGO Airport	32,7	16,2	330	71	17,2	193	198	14,71	68	0,628	106,28	3	803	-35,3	3,5	0,299
COPIA NAPA	VALLEJO	38,2	13,9	573	69	16,4	131	291	13,99	46	1,008	101,46	10	726	-2,6	2,7	0,070
KNFG 722926 KOKB 722934	OCEANSIDE	33,2	15,4	700	77	17,0	241	375	14,53	57	0,834	106,03	9	747	8,4	2,5	0,054
TSP 74917	TEHACHAPI/ (Bakersfield-LA)	35,1	11,9	689	56	14,3	465	425	12,22	59	0,668	104,36	1210	715	6,8	2,6	0,058
KBUR 722880	BURBANK / (Bakersfield-LA)	34,2	17,2	576	56	18,8	119	302	16,27	41	1,281	105,28	236	842	-10,2	2,9	0,088
Average	California HSR	Med 35,8 Max 38,8 Min 32,7	15,5 18,4 11,9	525 700 325	65 77 53	17,9 22,4 14,3	203 465 119	320 425 198	15,56 20,32 12,22	53 68 41	1,018 1,402 0,628	103,29 106,28 101,33	157 1210 3	788 902 705	-12,8 8,4 -39,0	3,0 3,7 2,5	0,142 0,411 0

$$I = \frac{100D - 60d}{E}$$

\bar{T} = Yearly average Temperature \bar{P} = Yearly rainfall average \bar{H} = Yearly humidity average \bar{T}_v = zetatik period average Temperature
 P_v = Vegetatif period rainfall average E_v = Vegetatif period actual evapotrans, (Fe)_v = Vegetatif period saturation steam pressure
 H_v = vegetatif period humidity average δ_v = Average vegetatif period saturation deficit
 $(Y_0)_v$ = Vegetatif period solar radiation en horizontal surface ETP = Evapotranspiración potencial anual $D = P - E - C$
 $d = E - P - C$ c = Field capacity (≈100,00 mm, as reference). In the Thornthwaite Index (I) calculation introducing the climatic mensual fluctuations behalif the expresions $\sum_p (E-P)$ y $\sum_e (E-P)$ respectively applied to the months those $P > E$ y $E > P$. Three cases are distinguised:
 1) $\sum_p > 100, \sum_e < 100 \rightarrow D = \sum_p - \sum_e, d = 0$
 2) $\sum_p > 100, \sum_e > 100 \rightarrow D = \sum_p - 100, d = \sum_e - 100$
 3) $\sum_p < 100, \sum_e > 100 \rightarrow D = 0, d = \sum_e - \sum_p$
 pF = Decimal Logarithm of suction expressed in water centimeters
 q_u = Unconfined stress compression

STATION: FRESNO (723890 K FAC)													
n= 55 years Latitude 36,6°N Altitude 81m Longitude 119,8°W													
Months	J	F	M	A	M	J	J	A	S	O	N	D	Year
Climate Characteristics													
T (°C)	8,60	11,00	13,40	15,00	18,40	24,00	28,50	26,20	22,90	18,00	14,30	9,50	17,70
$i = (T/5)^{1,514}$ Monthly Heat index	2,27	3,30	4,45	5,28	7,19	10,75	14,02	12,28	10,01	6,95	4,91	2,64	84,05
Average daily etp adjust less	0,60	0,90	1,30	1,60	2,40	3,80		4,50	3,60	2,30	1,40	0,70	
Monthly (12h w) Illuminatio index	25,90	25,50	30,90	33,00	36,50	36,80	37,40	35,00	30,90	291,00	25,60	25,00	
ETP (mm)	15,00	23,00	40,00	52,00	87,00	139,00	151,00	157,00	111,00	66,00	35,00	18,00	894,00
P (mm)	53,00	35,00	40,00	90,00	6,00	10,00	0,00	9,00	30,00	50,00	35,00	72,00	430,00
P - ETP	38,00	12,00	0,00	38,00	-81,00	-129,00	-151,00	-148,00	-81,00	-16,00	0,00	54,00	-464,00
acc. Potencial losses apl (mm)	-	-	-	-94,00	-175,00	-304,00	-455,00	-603,00	-684,00	-700,00	-	-	
Stored Water ST (mm)	98,00	110,00	110,00	148,00	82,00	43,00	20,00	9,00	6,00	6,00	6,00	60,00	
Variation Storage ΔST (mm)	38,00	12,00	0,00	38,00	-66,00	-39,00	-23,00	-11,00	-3,00	0,00	0,00	54,00	
ETR (mm)	15,00	23,00	40,00	52,00	72,00	49,00	23,00	20,00	33,00	50,00	35,00	18,00	430,00
Y ₀ (cal/cm ² d)	175,00	242,00	362,00	446,00	511,00	532,00	525,00	468,00	380,00	254,00	182,00	150,00	$\frac{101,75}{10^4}$ kcal/m ²
BH (mm)	38,00	12,00	0,00	38,00	-66,00	-39,00	-23,00	-11,00	-3,00	0,00	0,00	54,00	

Figure 2a: Climatologic information Fresno Station. ETP & ETR Calculation (Thornthwaite Method)

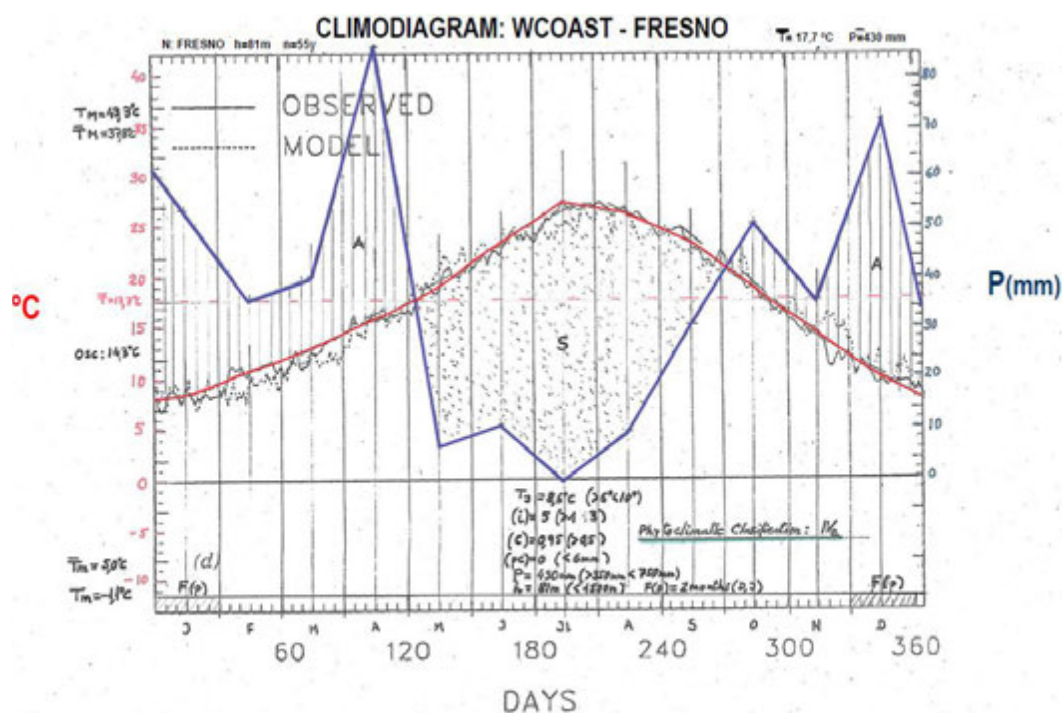


Figure 2b: Climodiagram Fresno Station (WCOAST data from P.E. Waggoner (A.A.A.S.))

The soils of the Central Valley and those coming from the decay of the rocky chain which are crossed by the Projects of the CHSRs (COYOTE Alternative), for connection of the initial Central Valley line with the Bay Area and Los Angeles Basin and by extension to Sacramento and San Diego, might be classified according to the French “Guide Technique 92” as Soils type A2, soils fines, sensitives to the water and from texture intermediate between sands and clays. Therefore for those type of soils the proposal is use a curve as well intermediate to those given by Aitchinson and Richards as a relation between the Thornthwaite index and the matrix suction, with measurements of this one to 3m depth (Figure 3), given the lack of measurements over samples directly extracted in the zones from study.

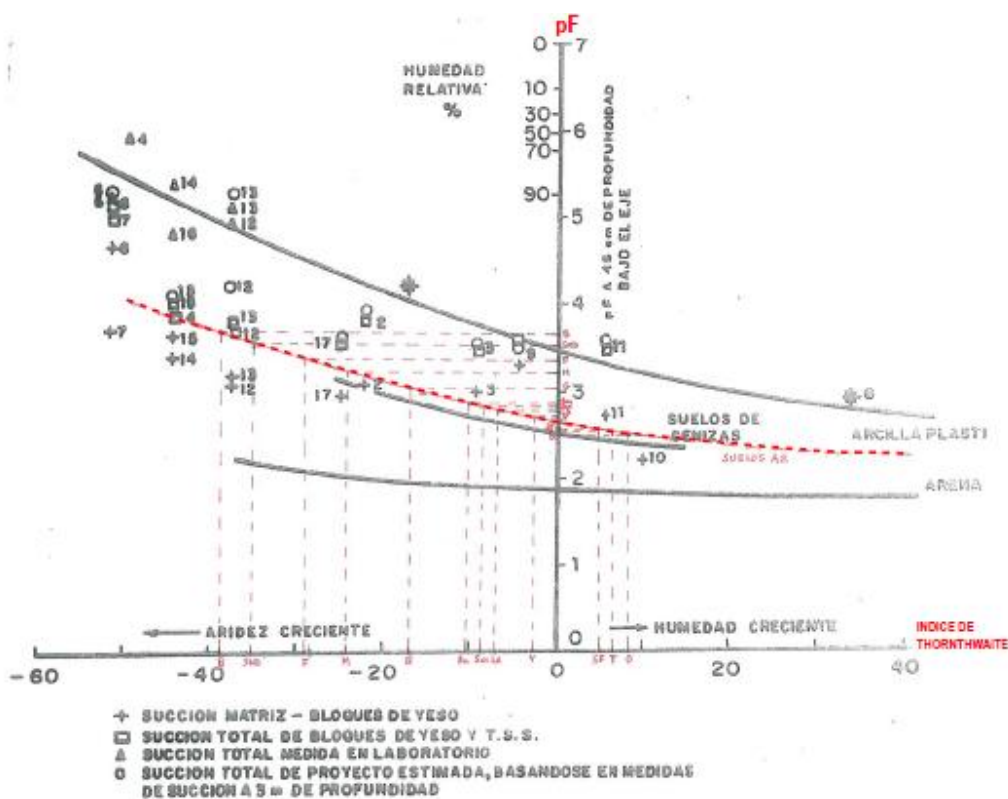


Figure 3: Thornthwaite Index – Suction Relation (I-pF) (Aitchison, Richards, 1965)

Carrying in this way, columns from Table 2 are completed as well as the geotechnic characterization of the strength of the soils representatives of each one of the locations, in conditions of moisture content referred to 3m depth ($\sigma_z \approx 50$ kPa), according with the suction (pF) estimates by correlation with the Thornthwaite index, calculated beginning with the meteorologic information used.

3. ESTIMATION OF THE EXPECTED VEGETATION GROWTH ON SLOPES

The CHSRS in its COYOTE Alternative, projects sections in open air, in addition to a large number of long tunnels and great viaducts, with enormous lengths of embankments, mainly in the Central Valley, and also cutting sections with a total length of 146,25 Km, 7,65 m of average height and 26,374 Mm3 of excavation volume.

In the table 3, with the averages directions ($\bar{\epsilon}$) of the different sections, indicated in the Figure 4, the solar radiation coefficients β are estimated from the graphics in Figure 5, beginning with the corresponding directions, the α values ($\alpha = 90 - \bar{\lambda} + \bar{D}$, where \bar{D} = sun declination, variable long the year between approximately $\pm 23^\circ$, $\bar{\lambda}$ = average latitude of each section) and the slopes grade ($\theta \approx 45^\circ$ for this purpose). The potential biomass productions, total (BM) and airy (AG), on horizontal land and on slopes inclined θ with orientations ϵ , North (N) or South (S), are given in the Table 3, beginning from averages values of climatic variables (obtained for each section from the values in Table 2 for each station).

Table 3. Biomass production on slopes of CHSRS COYOTE Alternative

Sub-Section	Sub-Project	Latitude av. $\bar{\lambda}$ (°N)	Direction av. $\bar{\epsilon}$ (°)	(\bar{T}), (°C)	(\bar{F}_e), (mmHg)	(\bar{H}), (%)	$\bar{\delta}_s$ (kPa)	(\bar{Y}_0), 10^4 Kcal/m ²	(BM) _h , g/m ²	(E) _h , (mm)	(AG) _h , g/m ²	β_{10}	β_{10}^N	(BM) ₁₀ ^N , (g/m ²)	(BM) ₁₀ ^S , (g/m ²)	(AG) ₁₀ ^N , (g/m ²)	(AG) ₁₀ ^S , (g/m ²)
I	FRESNO - BAKERSFIELD	36,0	70 (E-70°S)	21,9	19,71	51,5	1,275	101,77	318	278	184	0,83	1,16	303	327	175	198
II	FRESNO - MERCED	37,0	59 (W-59°N)	20,7	18,31	51,0	1,197	102,31	389	335	236	0,70	1,19	356	408	216	247
III-a	FRESNO - GILROY	37,0	14 (W-14°N)	18,4	15,87	57,5	0,900	101,54	479	332	311	0,42	1,14	285	511	185	322
III-b/V	GILROY - SAN FRANCISCO	37,5	39 (W-39°N)	15,7	13,37	56,5	0,776	101,90	532	333	362	0,54	1,21	367	557	250	379
IV-a	BAKERSFIELD - TEHACHAPI	35,3	58 (E-58°S)	18,3	15,77	55,5	0,936	103,08	466	329	297	0,73	1,18	430	485	274	309
IV-b	TEHACHAPI - BURBANK	34,7	72 (E-72°S)	16,6	14,17	50,0	0,945	104,82	498	364	325	0,87	1,14	480	514	314	336
IV-c	BURBANK - LOS ANGELES	34,0	74 (E-74°S)	18,0	15,48	43,5	1,167	105,41	391	324	234	0,89	1,13	381	402	228	241
VI	LOS ANGELES - ANAHEIM	33,8	3 (E-3°S)	17,2	14,75	46,0	1,063	105,56	443	346	275	0,42	1,02	296	444	184	276
VII	MERCED - SACRAMENTO	38,0	69 (W-69°N)	19,6	17,10	50,0	1,141	102,23	409	339	251	0,79	1,16	385	424	236	260
VIII-a	ANAHEIM - OCEANSIDE	33,5	49 (E-49°S)	17,1	14,62	51,5	0,946	105,78	496	361	322	0,66	1,18	447	516	290	335
VIII-b	OCEANSIDE - SAN DIEGO	33,0	75 (E-75°S)	17,1	14,68	62,5	0,731	106,16	506	287	331	0,90	1,10	494	519	323	339
X	VALLEJO - SACRAMENTO	38,5	28 (E-28°S)	17,8	15,28	47,0	1,080	101,52	400	312	244	0,46	1,20	312	418	190	255
Average	California HSR	Med 35,7 Max 38,5 Min 33,0	51 (E-51°S) 75 3	18,2 21,9 15,7	15,76 19,71 13,37	51,9 62,5 43,5	1,013 1,275 0,731	103,51 106,16 101,52	444 532 318	328 364 278	281 362 184	0,68 0,90 0,42	1,15 1,21 1,02	378 494 285	460 557 327	239 323 175	291 379 198

- (BM)₀ = Biomass total productivity horizontal surface = (UG)₀ + (AG)₀
- (BM)₁₀^N = Biomass total productivity North Orientation, direction ϵ , surface inclination θ (BM)₁₀^N = (UG)₁₀^N + (AG)₁₀^N
- (BM)₁₀^S = Biomass total productivity South Orientation, direction ϵ , surface inclination θ (BM)₁₀^S = (UG)₁₀^S + (AG)₁₀^S
- UG = Underground biomass allocation = $\Sigma W_e - \Sigma F_e$ $\Sigma W_e = \eta Y_0$
- AG = Aboveground actual yearly production = ΣF_e
- $\Sigma F_e = K \Sigma (Fw / \delta) - \Sigma (Fw / \delta) = g(\Sigma (Tr / \delta) - E / \delta)$ $\Delta Tr_{1,2,7}^3 =$ Transpiration rise by moisture content reduction
- (K, η) = Specific rate portencial production of slope vegetation

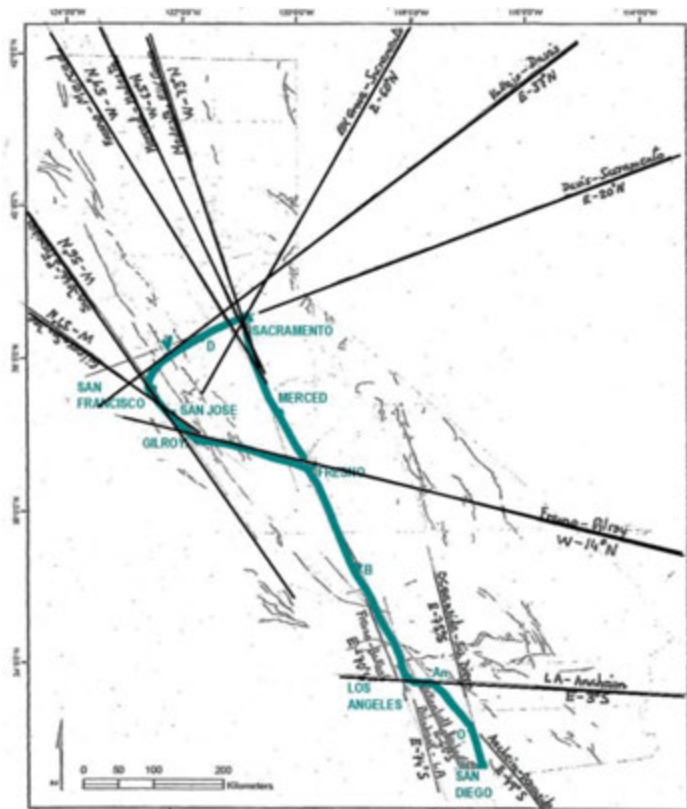


Figure 4: Orientation (Direction) of the Sections in CHRS (Coyote Alternative)

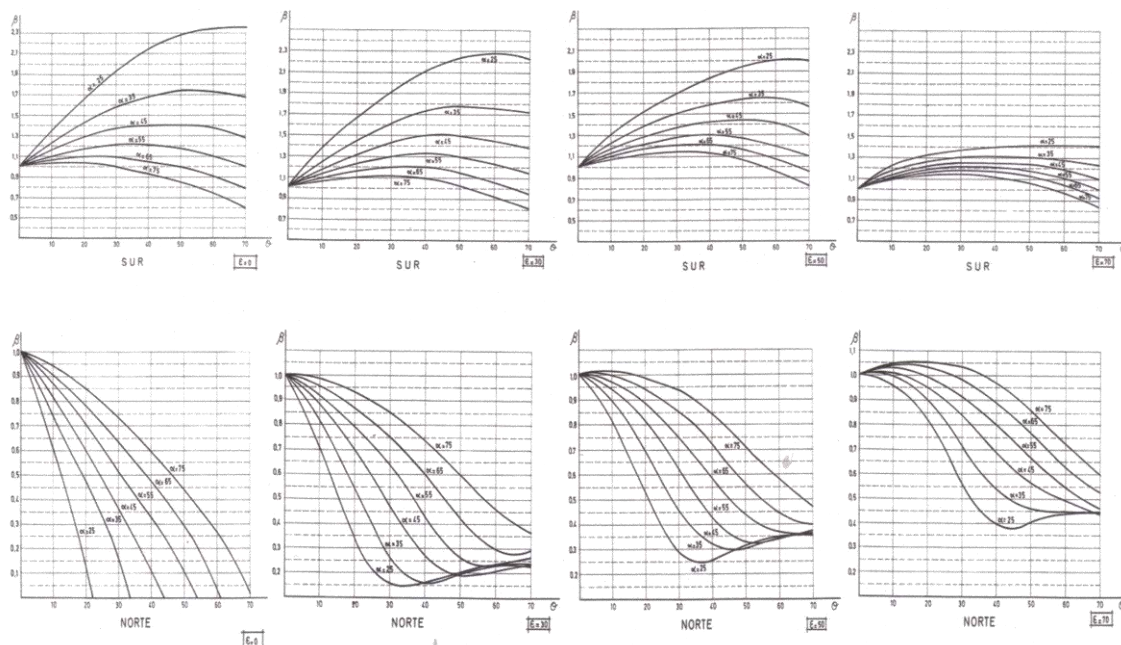


Figure 5: Solar radiation β factor values (Fort, 1.975)

4. SHEAR STRENGTH OF THE SOIL REINFORCED IN VEGETATED SLOPES

The Table 4, goes on the development of the initiated calculation in the Table 3, to be able to estimate, as is indicated, the increments of shear strength of the soil $\Delta\tau_{vr}$, due to the reinforced effect of the roots into the depth z_r (zone with the major radicular profusion) on slopes with vegetation, and $\Delta\tau_{vd}$ till depth z_3 , reached by its dryer effect, that in addition to the shear strength of the soil τ_n , allows to assign a shear strength of the reinforced soil on vegetated slopes τ_v , according depths, with that it can be study the possible landslide instabilities.

Table 4: Vegetation reinforcement effect on slopes of the CHSRs COYOTE Alternative

Sub-Section	Sub-Project	Strength of the soil Coulombian parameters			Shear Strength of the Soil t_u (Kpa)	LUE (ΣW_e) g/m ²	WUE (ΣF_e) g/m ²	Seasonal roots growth rate srg_r (%)	Underground biomass product $(UG)_{10}^h$ g/m ²	Depth with $pF \geq 3$ $Z_{pF \geq 3}^h$ (m)	Underground biomass product $(UG)_{10}^n$ g/m ²	Depth with $pF \geq 3$ $Z_{pF \geq 3}^n$ (m)	Underground biomass product $(UG)_{10}^s$ g/m ²	Depth with $pF \geq 3$ $Z_{pF \geq 3}^s$ (m)	Additional Shear Strength of the Soil			Reinforcement Drying effect $t_{d,d}$ (Kpa)	Soil Shear Strength in vegetated slopes			
		q_u (Kpa)	Φ (°)	C (Kpa)											$\Delta \tau_{v,r}^h$ (Kpa)	$\Delta \tau_{v,r}^n$ (Kpa)	$\Delta \tau_{v,r}^s$ (Kpa)		t_v Kpa		t_v Kpa	
																			$Z < Z_r$	$Z_r < Z_3$	$Z < Z_r$	$Z_r < Z_3$
I	FRESNO - BAKERSFIELD	315	43	68	115	679	184	73	134	6,3	128	6,0	138	6,5	28,4	27,8	28,8	45,8	143,4	142,8	143,8	160,8
II	FRESNO - MERCED	191	28	57	83	683	236	65	153	7,7	140	7,0	161	8,1	30,3	29,0	31,1	33,4	113,3	112,0	114,1	116,4
III-a	FRESNO - GILROY	172	25	55	78	678	311	54	168	9,5	100	5,6	209	10,1	31,8	25,0	35,9	31,2	109,8	103,0	113,9	109,2
III-b-V	GILROY - SAN FRANCISCO	91	0	45	45	680	362	47	170	10,5	117	7,2	178	11,0	32,0	26,7	32,8	18,0	77,0	71,7	77,8	63,0
IV-a	BAKERSFIELD - TEHACHAPI	234	35	61	96	688	297	57	169	9,2	156	8,5	176	9,6	31,9	30,6	32,6	38,4	127,9	126,6	128,6	134,4
IV-b	TEHACHAPI - BURBANK	73	0	37	37	700	325	53	173	9,8	166	9,5	178	10,1	32,3	31,6	32,8	14,8	69,3	68,6	69,8	51,8
IV-c	BURBANK - LOS ANGELES	81	0	40	40	704	234	67	157	7,7	153	7,5	161	7,9	30,7	30,3	31,1	16,0	70,7	70,3	71,1	56,0
VI	LOS ANGELES - ANAHEIM	75	0	38	38	705	275	61	168	8,7	112	5,8	168	8,8	31,8	26,2	31,8	15,2	69,8	64,2	69,8	53,2
VII	MERCED - SACRAMENTO	122	10	51	61	682	251	63	158	8,1	149	7,6	164	8,4	30,8	29,9	31,4	16,3	71,8	70,9	72,4	57,3
VIII-a	ANAHEIM - OCEANSIDE	65	0	32	32	706	322	54	174	9,8	157	8,8	181	10,2	32,4	30,7	33,1	12,8	64,4	62,7	65,1	44,8
VIII-b	OCEANSIDE - SAN DIEGO	176	25	55	87	708	331	53	175	10,0	171	9,8	180	10,3	32,5	32,1	33,0	35,0	119,5	119,1	120,0	122,0
X	VALLEJO - SACRAMENTO	75	0	38	38	678	244	64	156	7,9	122	6,2	163	8,3	30,6	27,2	31,3	15,2	68,6	65,2	69,3	53,2
Average	California HSRS	Med 315	Med 43	Med 68	Med 115,0	Med 708	Med 362	Med 73	Med 175	Med 10,5	Med 171	Med 9,8	Med 209	Med 11,0	Med 32,5	Med 32,1	Med 35,9	Med 45,8	Med 143,4	Med 142,8	Med 143,8	Med 160,8
		Max 65	Max 0	Max 32	Max 32,0	Max 678	Max 184	Max 47	Max 134,0	Max 6,3	Max 100,0	Max 5,6	Max 138,0	Max 6,5	Max 28,4	Max 25,0	Max 28,8	Max 12,8	Max 64,4	Max 62,7	Max 65,1	Max 44,8

$$srg_r = \frac{\sum W_e - \sum F_e}{\sum W_e} \quad \begin{matrix} WUE & = & \text{Water Use efficiency (production rate } Fe) \\ LUE & = & \text{Sun Ligh efficiency (production rate } We) \end{matrix}$$

$$\Delta t_{v,r} = \text{Shear strength rise for vegetation reinforcement root effect}$$

$$\Delta t_{v,d} = \text{Shear strength rise for vegetation drying effect}$$

$$q_u = \text{Unconfined stress compression}$$

$$\Phi = \text{Friction angle}$$

$$c = \text{cohesion}$$

$$z_r = \text{rooting depth}$$

$$z_3 = \text{Soil depth reducing the moisture of the soil to } pF \geq 3 \quad z_3 = \frac{BM}{K_g \Delta T_r /}$$

5. LANDSLIDE STABILITY IN SLOPES WITH VEGETATION

This increment of soil shear strength by the double effect of the vegetation, can be taken into account by an average global shape in the slope stability calculations, assigning an equivalent unitary shear strength uniform along of the sliding line and using, for example, the friction circle method.

As an application of what has been said before, you can find in the Table 5 the analysis of a slope type (Figure 6) representative of each of the nine subsections of the CHSRs. There are cuts with variables accumulated lengths from 1,67 Km to 34,00 Km and 146,25 Km of lump sum; average subsections heights from 3,59 m to 18,25 m, and 7,65 m global average height.

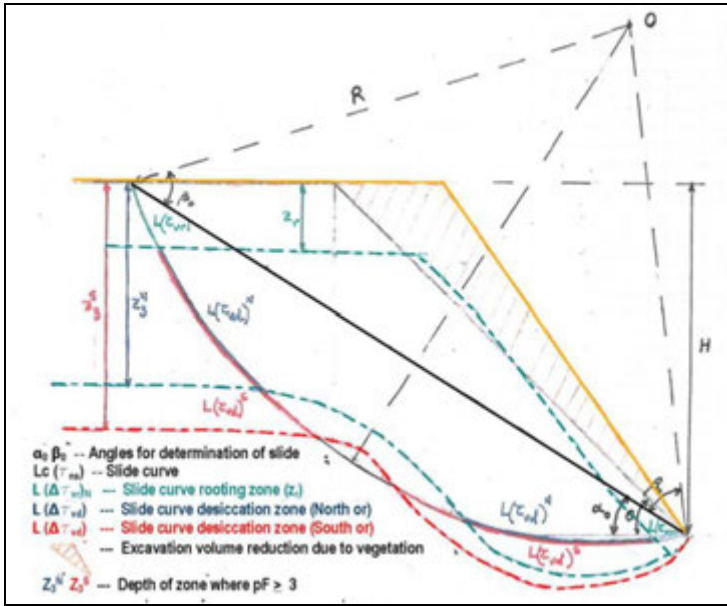


Figure 6: Slope Type Scheme, indicating the meaning of every one calculation magnitudes

The graphic (figure 7a) defines the angles α_0 and β_0 , taking up with the value:

$$\Phi_a = \arctg\left(\frac{tg\phi}{FS}\right) \tag{1}$$

(FS \approx 1,5, trial effect),

that determines the center O, the R radius and the length Lc of the sliding curve. Beginning with z_r (depending of the vegetation type, $z_r\approx$ 1,5 m) it deduces $L(\Delta\tau_{vt})$ and $\Delta\tau_{vt}$ by expression:

$$\Delta\tau_{vt}\approx 0,1z+1,5 \text{ (UG/z) (z(m), UG (Kg/m}^2\text{) } \Delta\tau_{vt} \text{ (Kp/cm}^2\text{))} \tag{2}$$

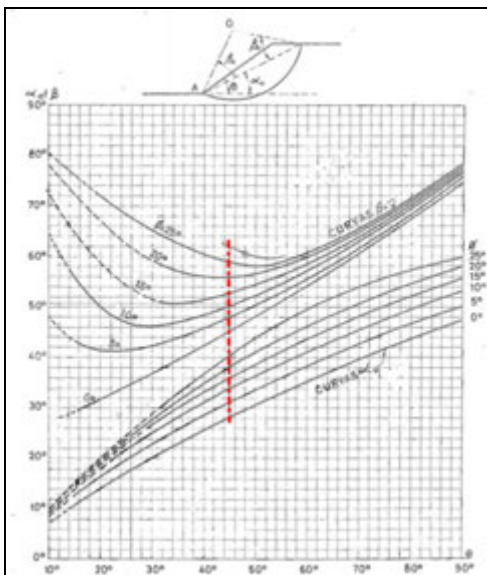


Figure 7a

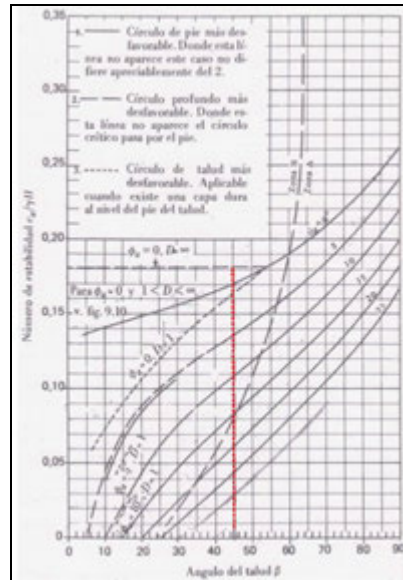


Figure 7b

Figure 7a: Curves of auxiliary angles α_0 & β_0 for determination of the most probably slip circle.

Figure 7b: Taylor abacus (G y C III. Jiménez Salas)

The z_3 depths are estimated beginning with the corresponding characteristic curves soil-water (SWCC), making equal the yearly evapotranspirated water to the necessary water volume to reduce the soil moisture from suction $pF \approx 2,7$ (natural average moisture) to $pF = 3$ (retention moisture), as minimum, saying $\Delta T_{r^{2,7}}$, what in this type of soils can be consider $\Delta \bar{W} \approx 6\%$, $\approx 60\text{mm/year}$.

Function of the estimated values for z_3 in plain and in slopes with North and South orientations, can be obtained the corresponding supposed slide circle L ($\Delta\tau_{vd}$) (Figures 6 and 8d), lengthwise can be consider an shear strength increment $\Delta\tau_{vd}$ by vegetation drying effect, and therefore, together with those estimated in the rooting zone ($L(\Delta\tau_{vr}) \times \tau_{vr}$), they imply a supplementary strength force ΔT_v , that theoretically it is uniformly distributed lengthwise of the slide circle is equivalent to an increment $\Delta\tau_{vr}$.

These equivalents soil shear strength increments, added to the owned by the soil (τ_{ns}) with natural moisture ($pF \approx 2,7$), giving the equivalent vegetated soil shear strength τ_{vseq} .

In the case of this example (CHSRS slopes), τ_{vseq} oscillate between 49,12 Kpa (North)/53,99 Kpa (South) in the Section Richmond-Sacramento, to 114,46 Kpa (North)/115,30 Kpa (Souh) in the Section Fresno-Merced, with respectives (North/South) averages values $\bar{\tau}_{vs}$, for the system 82,61 Kpa and 84,38 Kpa.

Regarding the average shear strength of the soil without vegetation reinforcement $\overline{\Delta\tau_{ns}} = 59,67$ Kpa, the averages values $\overline{\Delta\tau_{ns}}$, imply increments of 38,44% (North) and 41,41% (South).

It will be concluded that the influence of vegetation in the soil shear strength may be based on an approximately law (Figure 8a):

$$\Delta\tau_{vseq}/\tau_{ns} \approx 0,55-0,020(H-2) \quad (3)$$

therefore for the CHSRS an average increase of 40%.

On regards to the value of the average equivalent cohesion \bar{c}_s of the soil without reinforcement (51,63Kpa system average, 68,50Kpa the highest average value of the system, corresponding to the average value of section Fresno-Los Angeles, and the smallest 32,00Kpa in the section San Francisco-Richmond) may it be seen in the Table 6 that due to the vegetation effect the values of the soil reinforced cohesion \bar{c}_{sv} , raise $\approx 39\%$ average, to come in the average to 71,81 Kpa and to values of 87,59 Kpa (+27,87%) on the slopes oriented to the South in the section Fresno-Los Angeles, and 45,60 Kpa (+42,50%) in those oriented to the North in the section San Francisco- Richmond.

The larger relative increment (58,19%) takes place im the section Fresno-Gilroy, which has the direction nearest to the W-E ($\bar{\varepsilon} \approx 14^\circ$), overlooking the average soil cohesion value from 55,00 Kpa to 86,97Kpa.

The increment $\Delta\tau_{vd}$ is evaluated starting with the expression, that for soils type A2 it could be established from results of test carried out on samples from spanish soils, (tertiary and holocen sediments).

$$\log \frac{q_u}{q_{u1}} = (a \approx 0,5)(pF - pF_1) \quad (4)$$

For $\Delta pF = 0,3(2,7 \text{ to } 3) \rightarrow q_u = 10^{0,15} q_{u1} \approx 1,41 q_{u1}$

As for coulombian soils: $\tau = f(\phi), q_u$. Agreeing that ϕ remains almost invariable in the intervale $pF=0,5/4,5$.

$$f(\phi) = \frac{1}{2 \operatorname{tg}\left(45 + \frac{\phi}{2}\right)} + \cos^2\left(45 + \frac{\phi}{2}\right) \operatorname{tg} \phi \quad (5)$$

$$\Delta\tau_{vd} = \tau(pF3) - \tau(pF2,7) \cong 0,41 f(\phi) \tau_{ns} \quad (Eq. 6) \quad (6)$$

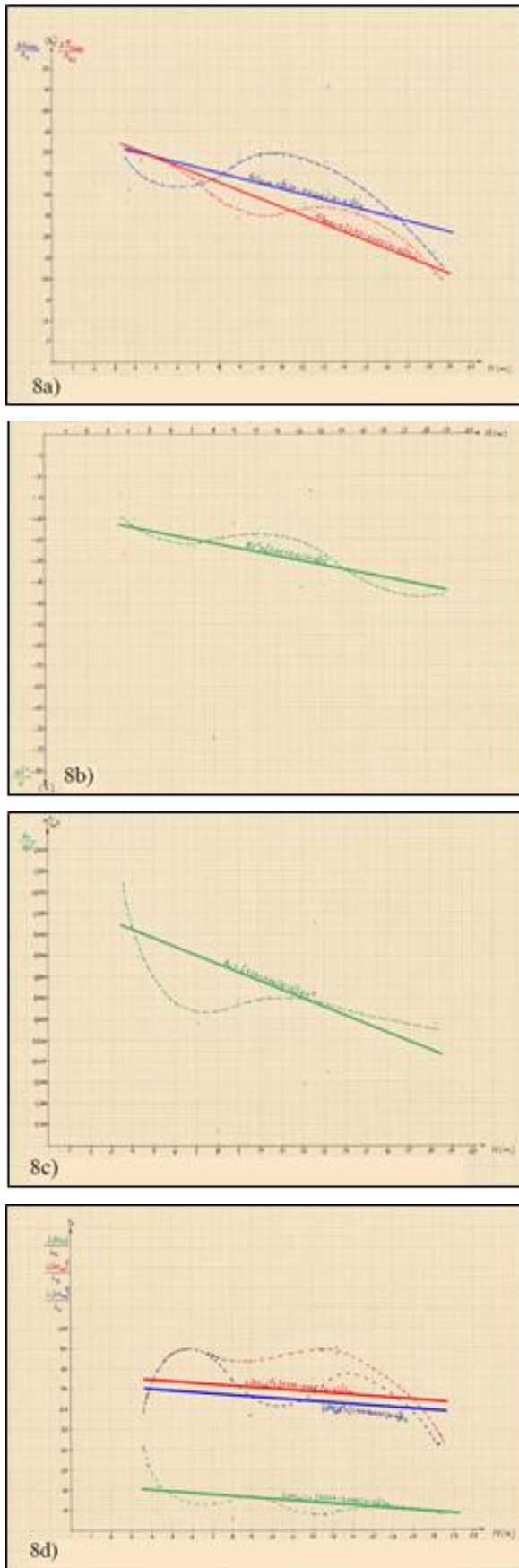


Figure 8: a) Influence of vegetation in the soil shear strength / cohesion
b) Excavation volume reduction
c) Vegetated area S_v versus excavation volume reduction
d) Fractions of sliding curve with rooting/drying effect

In the Table 6, using the Taylor abacus (Figure 7b), and agreeing, as is true, the rare variation of friction angle in soils with moistures characterized by suctions between pF values 0,5 and 4,5, is made the calculation of slope angles that offer, taking in account the effect of vegetation, the same sliding safety than those foreseen without have it taken into consideration. The calculus is made assuming cut sections with slopes of equal height, one of them oriented to the North, and the other, to the South. According to it, is estimated the consistent excavation volume reduction $\Delta V^v (= \Delta V^{vn} + \Delta V^{vs})$, with 28,20% (7,438Mm³) average reduction for the total CHSR system. It can be estimated through an expression depending on height (Figure 8b):

$$\Delta \frac{V^v}{V} = 0,20 + 0,01(H - 2). \tag{7}$$

Table 6: Geoenvironmental impact and cost reduction by slope vegetation (CHSRs COYOTE Alternative)

Sub-Section	Sub-Project	Cuts H (m)	FS Φ _a (°)	Stable Slopes Angles (β) with FS				Reference Volume Excavation V (Mm ³)	Excavation volume reduction due to vegetation of slopes				C _v (KPa)	C _{sv} ^N (KPa)	C _{sv} ^S (KPa)	S _v (Has)	Vegetation effect ratio ($\frac{m^2 v}{m^3}$)	
				N _e	Φ _e ^{vn} C _e ^{vn} (KPa)	N _e ^{vn}	Φ _e ^{vs} C _e ^{vs} (KPa)		N _e ^{vs}	ΔV ^{vn} (Mm ³)	ΔV ^{vs} (Mm ³)	ΔV ^v (Mm ³)						ΔV ^v V (%)
I IV-a IV-b IV-c	FRESNO - LOS ANGELES (323 km)	18,25 9,60	2,90 17,8 23,60	0,077 45	17,8 29,52	0,097 57	17,8 30,20	0,099 58	3,197	0,560	0,599	1,159	-36,25	68,50	85,63 86,61 87,59	25,00 26,44 27,87	66,99 (41,55) (25,44)	0,578
II	FRESNO - MERCED (99 km)	3,59 34,00	7,00 4,4 8,12	0,138 45	4,4 12,62	0,210 77	4,4 12,74	0,213 79	2,391	0,169	0,176	0,345	-14,43	56,90	88,36 88,78 89,20	55,29 56,03 56,77	42,60 (24,96) (17,64)	1,235
III-a	FRESNO - GILROY (172 km)	8,91 12,45	3,40 7,7 16,18	0,115 45	7,7 22,62	0,152 60	7,7 25,58	0,172 70	2,763	0,209	0,314	0,583	-21,10	55,00	76,92 81,95 86,97	39,85 49,00 58,19	40,16 (24,48) (15,68)	0,689
III-b/V	GILROY - SAN FRANCISCO (102 km)	7,10 26,90	2,30 0,0 19,78	0,123 45	0,0 28,10	0,237 82	0,0 28,45	0,240 84	4,412	0,583	0,607	1,190	-26,97	45,50	64,64 65,04 65,44	42,07 42,95 43,82	69,30 (38,48) (30,82)	0,582
IX	SAN FRANCISCO - RICHMOND (51 km)	12,10 1,67	1,10 0,0 29,09	0,144 36	0,0 41,45	0,205 67	0,0 45,17	0,224 77	0,709	0,117	0,140	0,257	-36,25	32,00	45,60 47,65 49,69	42,50 48,89 55,28	7,51 (4,25) (3,26)	0,292
X	RICHMOND-SACRAMENTO (116 km)	12,53 2,33	1,35 0,0 28,15	0,163 45	0,0 36,39	0,174 51	0,0 39,99	0,191 60	0,833	0,035	0,077	0,112	-13,45	38,00	49,12 51,55 53,99	29,26 35,67 42,08	11,81 (7,09) (4,72)	1,054
VI	LOS ANGELES - ANAHEIM (62 km)	4,27 7,40	31,00 5,50 12,10	0,163 45	0,0 17,82	0,250 86	0,0 18,24	0,256 88	0,640	0,063	0,065	0,128	-20,00	37,50	55,09 56,31 56,31	46,91 50,16 50,16	11,43 (5,10)	0,893
VII	MERCED - SACRAMENTO (191 km)	3,71 25,90	2,0 9,24 1,75	0,149 42	2,0 13,02	0,210 74	2,0 13,11	0,212 75	1,894	0,147	0,150	0,297	-28,43	50,82	71,59 71,83 72,08	40,87 41,35 41,83	33,76 (19,94) (13,82)	0,345
VIII	ANAHEIM - SAN DIEGO & Branch to RIVERSIDE (172 km)	13,17 26,00	5,7 4,3 16,62	0,132 45	5,7 42,42	0,193 76	5,7 42,99	0,196 77	9,535	1,693	1,734	3,427	-35,94	50,56	74,24 74,73 75,23	46,84 47,81 48,79	118,17 (70,43) (47,74)	0,345
Average	California HSRS (1.288 km)	7,65 146,62	4,00 16,62	0,14 44,4	4,3 23,77	0,20 74,4	4,3 24,39	0,21 76,8	26,374	3,576	3,862	7,438	-28,20	51,63	71,81	39,09	401,73 (237,51) (164,22)	0,540

The needed area to vegetate S_v to obtain this volume reduction ΔV^v is 0,54m²/m³, that applicated to the total CHSR system achieves at 401,73 Has in 146,25 Km cuts (2,75Has/Km). Function of slopes height (H in m), the Figure 8c give the approximate law for this ratio:

$$S_v / \Delta V^v \left(\frac{m^2}{m^3} \right) = 1,1 - 0,04(H - 2). \tag{8}$$

REFERENCES

Fort, L (1977) "Plantaciones en taludes. Efecto estabilizador"/ Revista de Obras Públicas Agosto 1977, pags. 659 a 668 /Madrid, Spain

Fort, L (1987) "Plantations des Talus: un instrument de planification des réseaux routiers" /Prix Mexique XVIII Congrès Mondial de la Route AIPCR /Brussels, Belgium.

Fort, L (2000) "Consideraciones para el diseño bioestructural de taludes"/ (Geotecnia en el año 2000. Libro homenaje a José Antonio Jiménez Salas. ISBN 84-7790-350-6 pgs. 247 a 255)/ Madrid, Spain

Fort, L (2001) "Análisis Bioestructural de taludes" /ISBN 84-607-3766-7/ Madrid, Spain

Fort, C (2011) "Caracterización de los parámetros de resistencia al corte y erosionabilidad del suelo para su aplicación en los problemas de estabilidad de taludes en obras lineales" / (Doctoral Thesis in the process of public defence in the E.T.S.I.C.C.P.)/ Madrid, Spain

Fort, L and Fort, C (2011) "Earth moving geoenvironmental workability in California". / Paper presented to the " Geocongress 2012 : State of the art and practice in Geotechnical Engineering" /Oakland California, USA.

Realization of a railway enlargement in unstable excavations alongside the existing line at Dilbeek (Belgium)

W. Maekelberg, TUC RAIL n.v., Belgium, Wim.Maekelberg@tucrail.be

J. Verstraelen TUC RAIL n.v., Belgium, Jan.verstraelen@tucrail.be

E. De Clercq, TUC RAIL n.v., Belgium, Eric.declerq@tucrail.be

ABSTRACT

Within the framework of the regional express network around Brussels, two new railway tracks will be added besides two existing tracks linking Brussels to Ghent. The existing railway link crosses a valley with a geotechnical complex lithography. This complexity and the existing slopes beside the railway link up to 20m deep, had an in important influence on the design of the railway enlargement.

Based on historical information and the detailed soil investigation the design is done with respect for the existing soil improvement measures taken in the past and the scope of the project. The design includes slope stability measures such as soil nailing, tieback anchors, construction elements with a secant pile wall and hydraulic measures to avoid water overpressure on the construction.

The design of the construction will be discussed in detail as well as the first monitoring results of the movements and the anchor forces of the construction during execution.

1. INTRODUCTION

The regional express network around Brussels, currently under construction, provides a greater accessibility of Brussels in the future with public transports and improves the mobility in and around Brussels. The main objective is to enlarge the capacity of the existing railway links, linking Brussels to other cities around Brussels such as Ghent, Ottignies, Nivelles and Antwerp. One of these links is the line 50A linking Brussels to Ghent and passing by Dilbeek (Flemish Brabant). This link is one of the most important railway links in Belgium.

Within the framework of the regional express network this link is being enlarged from 2 to 4 lines as shown in figure 1.

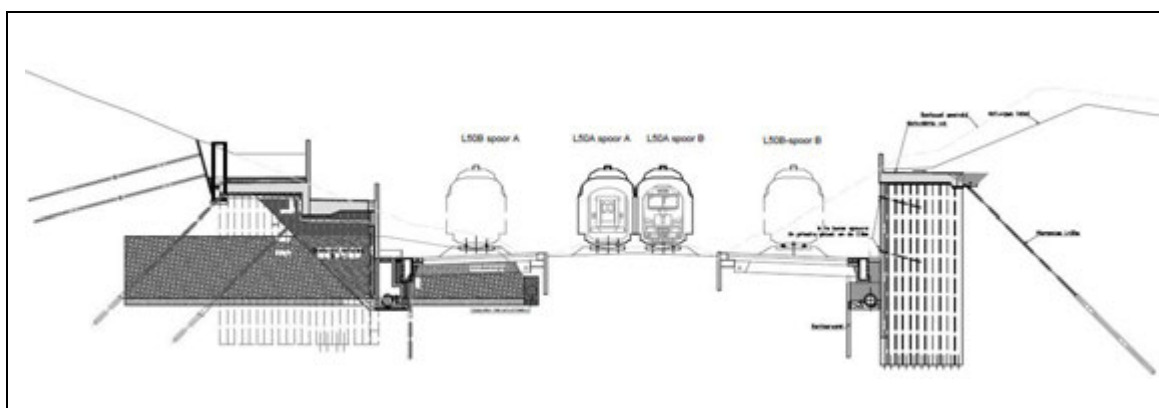


Figure 1: the enlargement of the existing railway track

The project at Dilbeek aimed to enlarge the existing railway link within the existing property limits of the railway company by working on the foot of the embankment. Also other constrains had to be taken into account such as:

- During works the existing railway tracks has to be in service at all times;
- Existing drainage system (see paragraph 2) has to be maintained and embedded in the new construction;
- A bike path along the railway track has to be provided to enlarge the bicycle network in the region.

The existing railway link crosses a valley with a geotechnical complex lithography. This complexity had a mayor influence on the construction of the link in the past and some stability measures had to be taken. Knowing the complexity of the lithography and this historical data, a detailed soil investigation program was elaborated leading to a complex design of the railway enlargement, combining different soil reinforcement techniques.

2. HISTORICAL DATA

The railway link has been constructed over a long period of time, from 1923 to 1937, due to several landslides along the railway track under construction. One of the mayor landslides occurred at Dilbeek, where the railway track is excavated and the slopes have a depth up to 20m.

At first, it was thought the landslide was caused by infiltration of rain water and his effect on the stability of the granular structure of the soil. In the aim of solving this phenomenon the first superficial draining system on the different slopes of important height was installed in 1927 such as shown in figure 2.

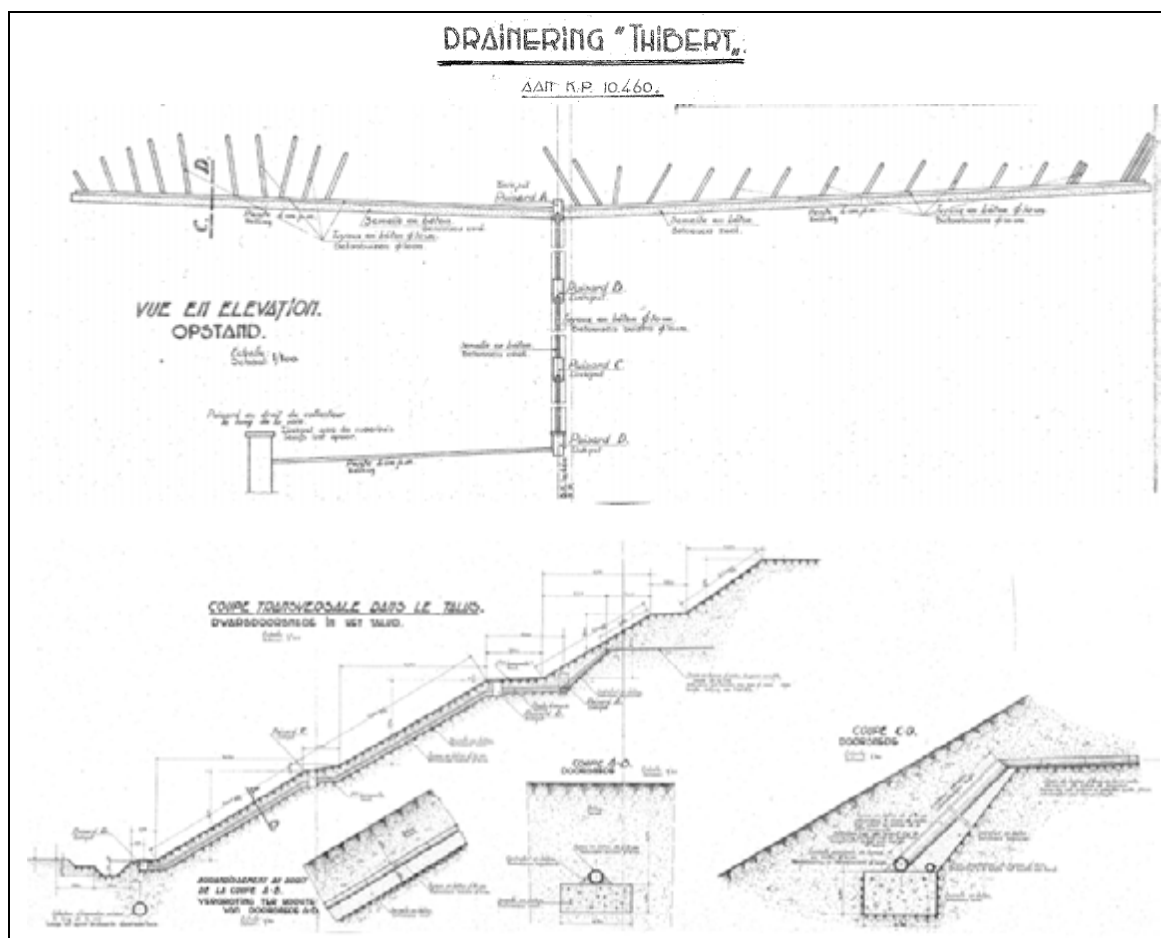


Figure 2: The superficial draining system (1927)

But still landslides occurred and other solutions, solving the phenomenon, had to be investigated. The final solution, a deep drainage system, is given in figure 3.

The latter consisted of installing vertical trenches every 35 to 50m along the slopes and the railway track. These trenches were filled up with granular material with different gradations forming a filter element around the vertical trench. The bottom of the trenches consists of concrete material and was formed to collect the infiltrating water leading it to a longitudinal collector as showed in figure 3. Details of the drainage system are given in figure 4.

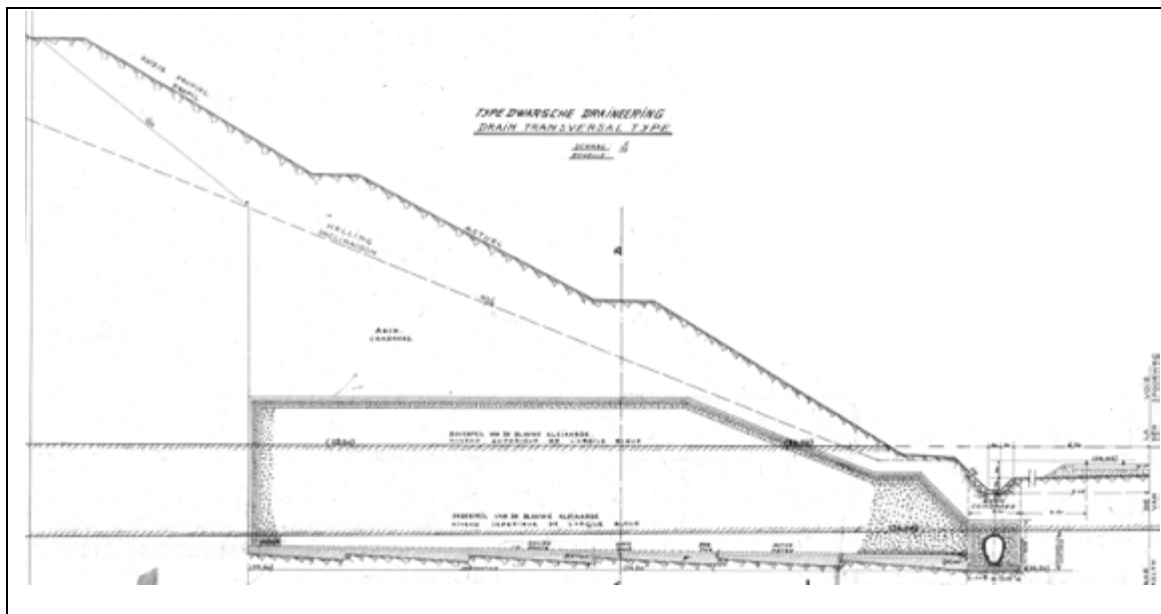


Figure 3: The drainage system before start of exploitation of the railway track (1932)

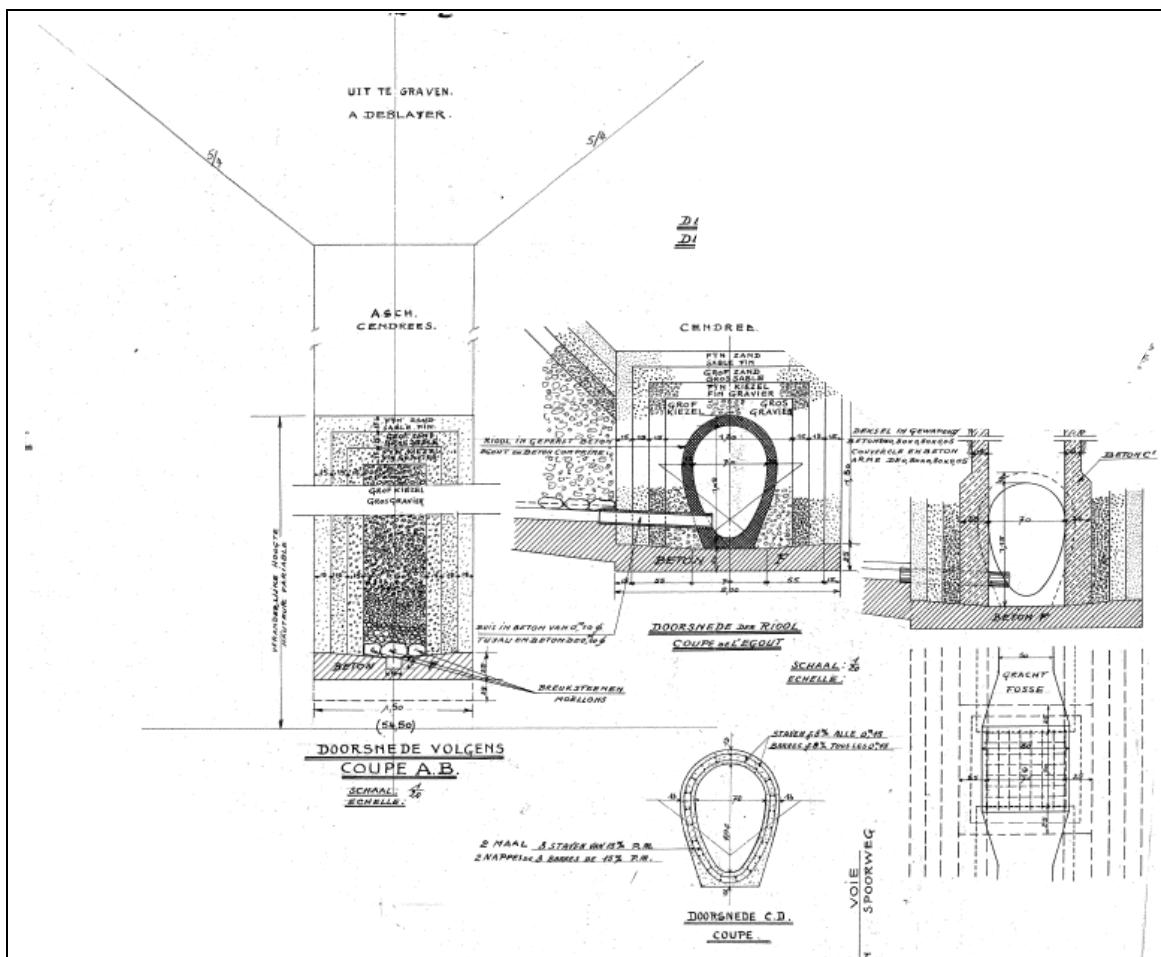


Figure 4: Details of the draining system (1932)

This system was realised between 1932 and 1937 and was still in function at the start of the extension project (2009). As more details on the geological lithography of the subsoil are found on these old execution plans, it can be assumed that the final solution, the drainage system, was based on more detailed soil investigations. Nevertheless the results of this soil investigation could not be found the archives.

However this system allows us to remember that the subsoil at the site in Dilbeek is very sensitive for water fluctuations and a far reaching soil investigation focussing on these fluctuation and the characteristics of the soil layers would be necessary.

Photo 1 shows a view on the existing situation before the works (anno 2009). The photo on the left shows the steepest part of the excavation zone.



Photo 1: View on the existing situation – anno 2009

Photo 2 gives a view on the original vertical trenches. One can notice the small depression in the slope, indicating the position of the draining trench (see also figure 3b).



Photo 2: View on the vertical trenches – anno 2009

3. SOIL INVESTIGATION

The geological investigation focussed on the ground and ground-water conditions by undertaking both field tests and laboratory tests.

Therefore several CPT tests, drill holes with logging of undisturbed and disturbed soil samples and water level measurements at different depths were carried out. Also inclinometers were installed at the top of the excavations and measurements were done to monitor the movement of the slopes before and during the project. The position of the different tests is given in figure 5. One can notice the different drillings defining a profile along the slope to investigate water fluctuations within the slope.

In figure 6, the result of a characteristic CPT is given together with the geological description of the layers.

From the results of the different piezometers, 3 water tables could be distinguished at different levels along the slopes. In figure 6, these water tables are indicated.

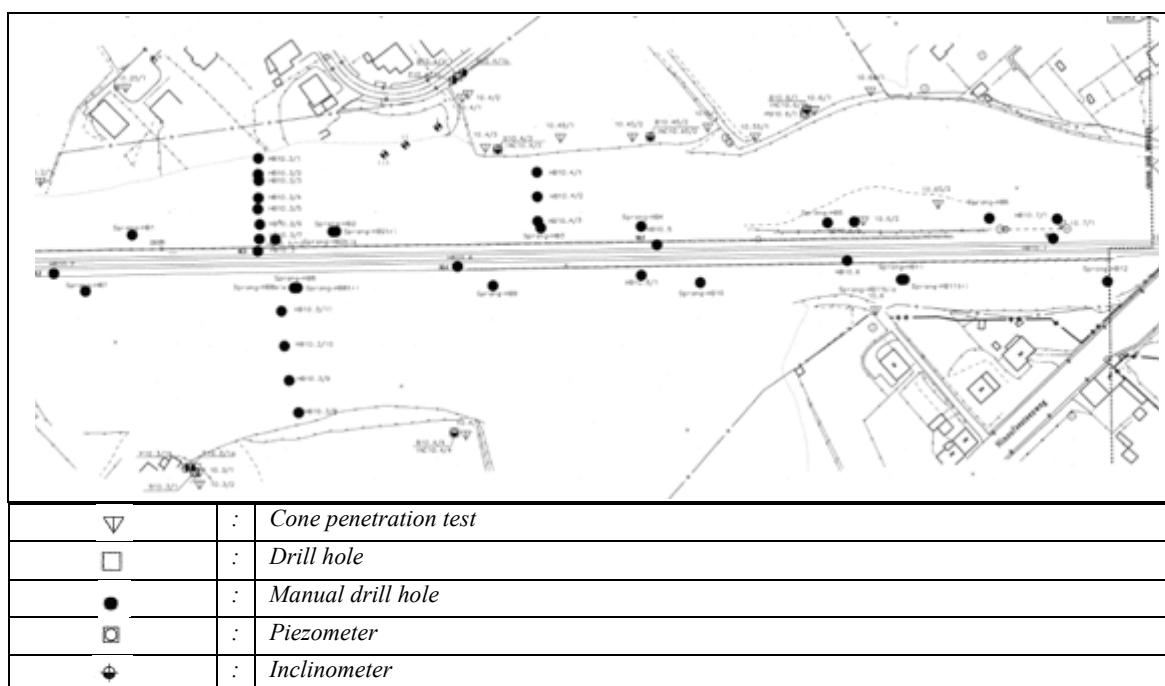


Figure 5: Position of the different field tests

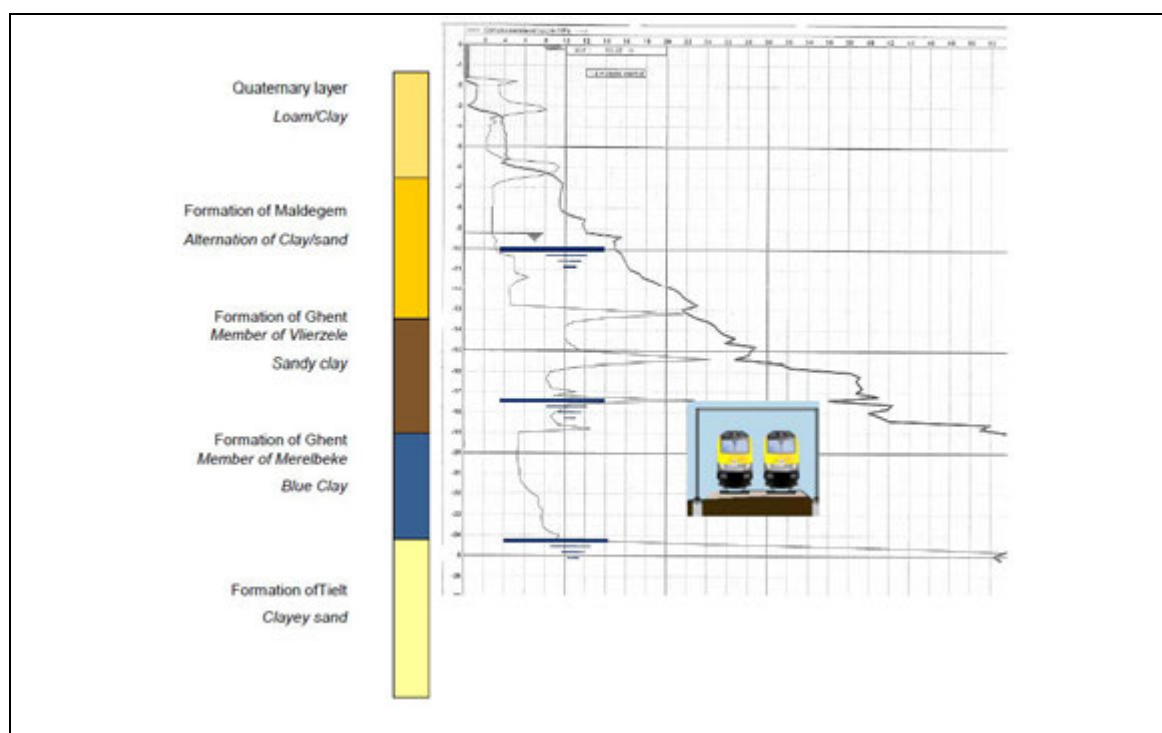


Figure 6: Lithography of the subsoil according to geological description and CPT

On the other hand triaxial tests on the undisturbed samples, compressibility tests and granulometry curves were elaborated in the laboratory. In particular, the ‘blue clay’ (formation of Ghent, member of Merelbeke) was investigated because this layer had an important influence on the stability of the existing slopes. This layer consists of very plastic soft clay material. In figure 7 the PQ-interpretation of the triaxial test on the blue clay is given.

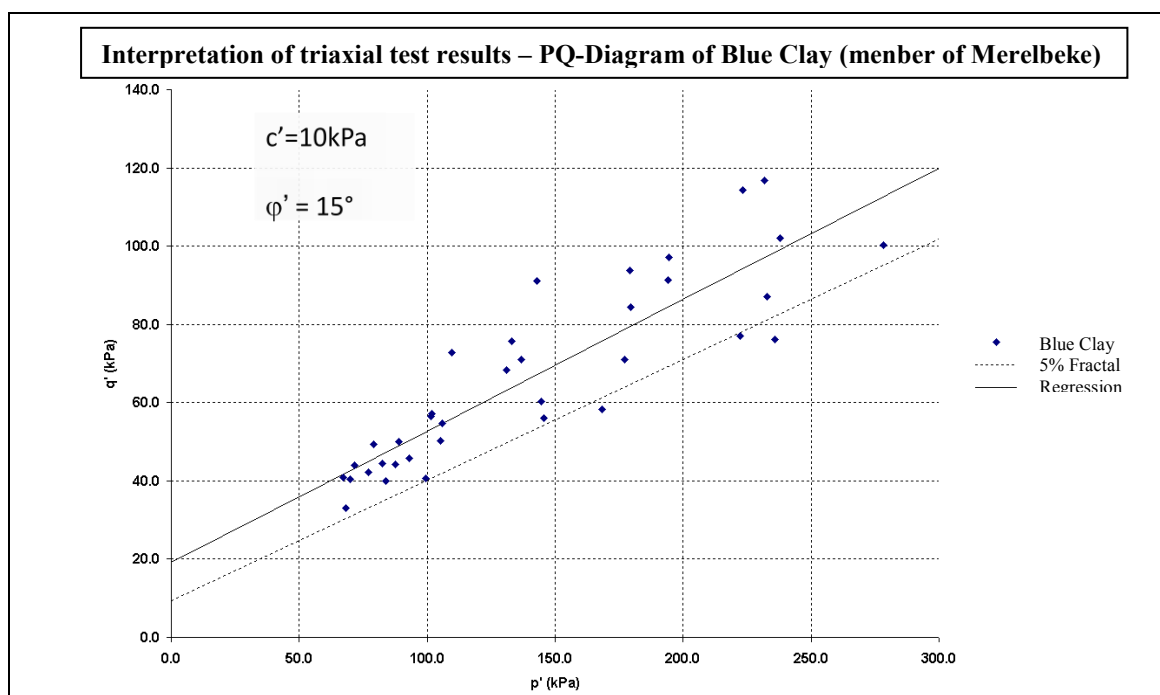


Figure 7: PQ-interpretation of the triaxial test on the blue clay

4. DESIGN OF THE CONSTRUCTION

4.1. Description of the construction

To meet the constraints of the project, mentioned in paragraph 1, the design had to focus on removing the foot of the embankment to create place for the new railway track and to keep any new construction within the property limits. The slope stability became a real challenge.

Considering the important retaining height of the construction and the consequences of possible corrosion, no permanent anchors were used. Nevertheless, soil nailing and temporary anchors are used to stabilise the different construction phases. In figure 8, the planned construction is shown.

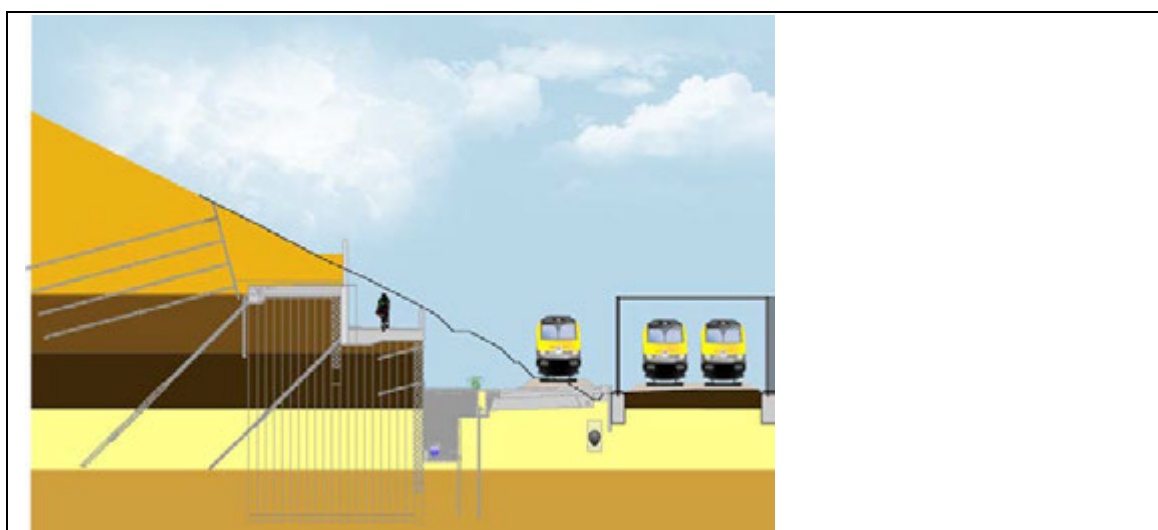


Figure 8: The construction to be build

The construction consists of a gravity wall where the soil within the contours of the wall is used to help stabilising the wall by interaction between the secant pile wall and the soil. The longitudinal secant pile wall is reinforced with transversal walls placed in regular intervals (ca. 8.6m) as shown in photo 3. Figure 9 gives a 3D simulation of one such section.



Photo 3: the longitudinal and transversal pile walls put in place

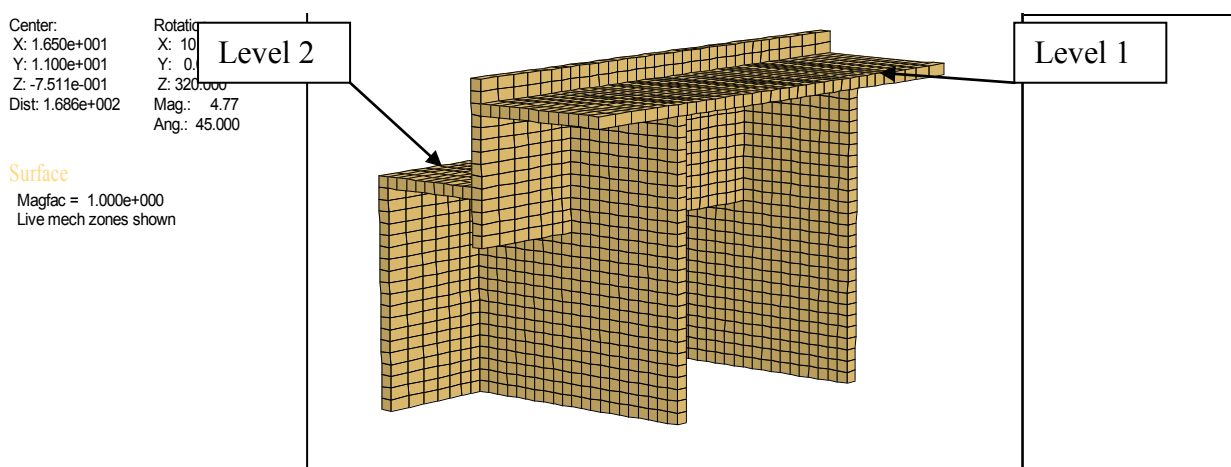


Figure 9: 3D-simulation of one section of the pile wall

The longitudinal pile wall and transversal pile walls are linked together by a concrete slab at the pile heads. Pile reinforcements, steel profiles, are anchored in the concrete slab. The construction wall is realised in two stages, as shown in photo 3b, to create a bike path next to the railway line.

The construction had to be realised with train traffic in service on the existing railway tracks, so a large platform, reinforced with geotextiles has been put into place, creating space to make traffic at working level possible and to supply the different work stations, working at the same time longitudinal to the railway track. In this way the planning of the works could be shortened. Photo 4 gives some details of this reinforced platform.

As the original hydraulic collector is located under the future railway tracks and cannot be maintained in service, the new hydraulic collector at the foot of the construction is installed using temporary anchors. This hydraulic collector is collecting the water of the different vertical trenches. In this way, the existing drainage system, installed to stabilise the slope, is embedded in the construction. The monitoring of the water level in the formation of Tielit made it clear that the water table could become slightly under pressure. For this reason a drain of small diameter was put in place next to the hydraulic collector to collect the water and to avoid this phenomenon. The drain is connected to the hydraulic collector at each vertical trench in an inspection hole.

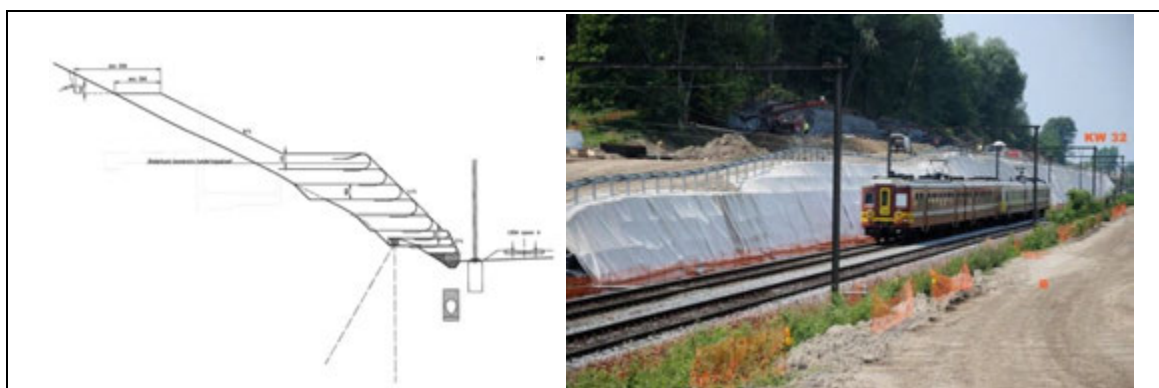


Photo 4: Reinforced embankment

To prevent the good functioning of the vertical trenches in the future to be lost, a transversal pile wall is executed at both sides of the trenches at a limited distance (ca. 1m) as shown in figure 10. This way the pollution of the draining trenches with concrete was avoided and only limited degrounding behind the secant pile wall could occur during construction. The pile wall was closed by a concrete wall filled in place and anchored at both sides in the secant pile wall.

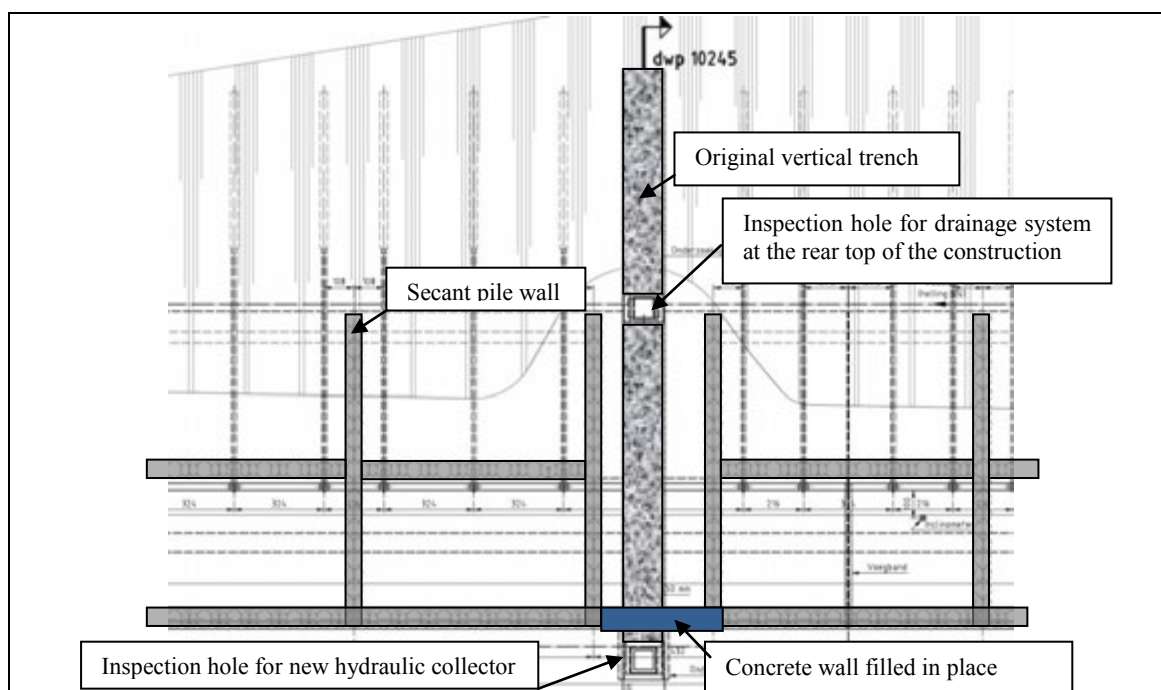




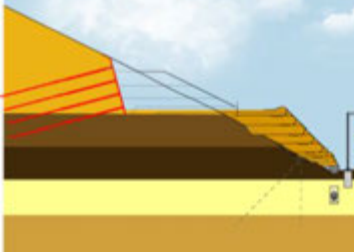

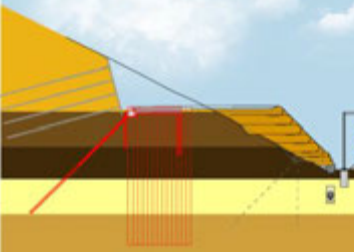

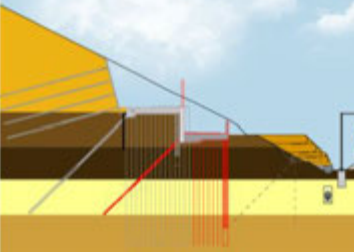

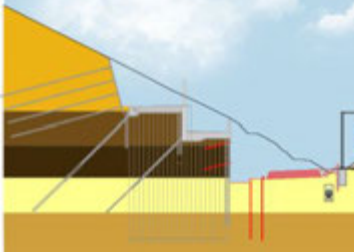
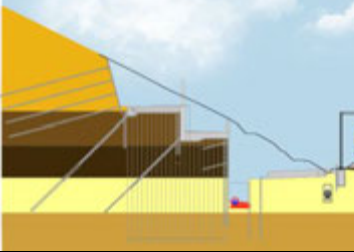
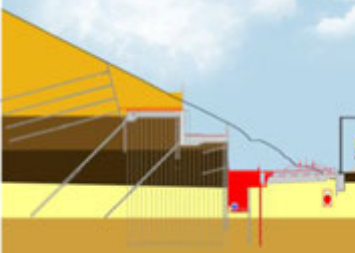
Figure 10: Transversal pile wall next to the vertical trenches.

4.2. Construction phases

In table 1 the different phases of construction are given and illustrated with a photo of the works.

In phase 2, a dense drainage system is put in place behind the shotcrete of the nailed wall. The system consists of draining strips at regular spaces and connected to a collecting tube through the shotcrete. The tubes are spread over the whole shotcrete wall with a density of 1 each 4m². In phase 3 to 7 the water tables are lowered behind the construction to enhance stability during works. In phase 6 the water table in the formation of Tiel is also lowered.

Table 1: Phases of construction

<p>Phase 1 :</p> <ul style="list-style-type: none"> • Realising a reinforced embankment • Creating a work platform for the execution of the soil reinforcement by nailing 		
<p>Phase 2 :</p> <ul style="list-style-type: none"> • Realising nailed wall • A large work platform is created to make passing of traffic possible at the same time of the execution of the works 		
<p>Phase 3 :</p> <ul style="list-style-type: none"> • Realising of the first stage of the secant pile wall (longitudinal and transversal pile walls) • Executing of the tieback anchors and concrete slab 		
<p>Phase 4 :</p> <ul style="list-style-type: none"> • Realising of the second stage of the secant pile wall (longitudinal and transversal pile walls) • Executing of the tieback anchors and concrete slab 		
<p>Phase 5 :</p> <ul style="list-style-type: none"> • Installing permanent drainage tubes to evacuate water on top of the member of Merelbeke • Inserting Berlinerwall profiles to install hydraulic collector 		<ul style="list-style-type: none"> • Creating site road the enable site traffic <p>To be constructed</p>
<p>Phase 6 :</p> <ul style="list-style-type: none"> • Placing hydraulic collector and drainage in the strutted trenches 		<p>To be constructed</p>
<p>Phase 7 :</p> <ul style="list-style-type: none"> • Filling up the strutted trench • Finishing the construction • Installing railway platform and railway infrastructure 		<p>To be constructed</p>

4.3. Finite elements calculation

In a preliminary phase of the design some calculations were done to estimate the feasibility of some ideas and to estimate the order of magnitude of the construction elements. Considering the importance of the construction, the effect on the stability of the slope and the interaction between the different elements a finite element analyses has been done with PLAXIS and controlled with FLAC.

In a first stage, the existing situation has been verified and the soil parameters, used for the different layers have been determined considering the history and overall stability of the slope, the water level measurements in the different water tables and the results of triaxial tests. In table 2 the soil characteristics are resumed. With this set of parameters the slope stability of the existing slopes has a safety factor of 1.03.

Table 2: Soil characteristics

	Model	γ_{unsat} kN/m ³	γ_{sat} kN/m ³	ϕ °	c kPa	E kPa	E ₀ kPa	E _{ur} kPa	m -
Quaternary layer	MC	18	20	30	2	3000			-
Formation of Maldegem	SH	18	20	30	5	4000	4000	13000	0.70
Formation of Ghent									
Member of Vlierzele	SH	18	20	27	5	7000	5465	27080	0.50
Member of Merelbeke	SH	18	20	15	10	10000	17530	32500	1.00
Formation of Tielt	SH	18	20	33	1	15000	10700	48750	0.50

MC = Mohr-Coulomb model

SH = Soil Hardening model

In the model, only external stability of the construction is verified taking into account all construction phases. The internal stability, the interactions within the construction between the different construction elements have been simulated in a FLAC 3D model.

The results of the 2D-modeling are given in figure 11, showing the deformations in the final stage. The maximum deformation at the upper side of the slope is 0.24m, where the maximum displacement of the wall is about 0.05 to 0.06m. The overall safety factor of the construction is greater than 1.25 and is determined by the slope stability of the upper part of the slope, as given in figure 12.

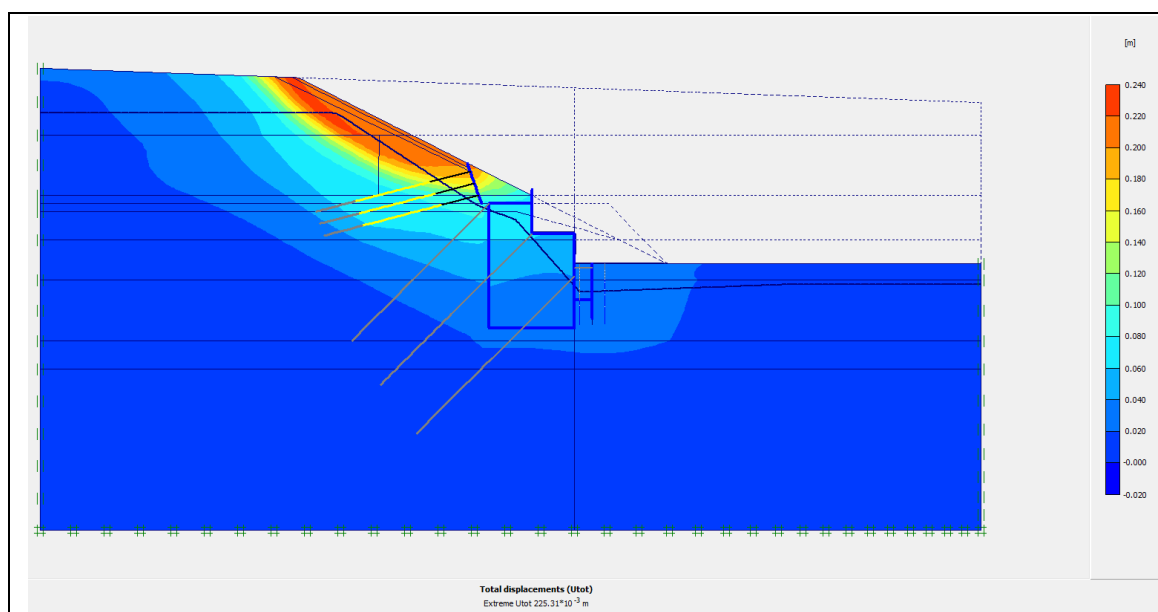


Figure 11: Deformations in the final stage

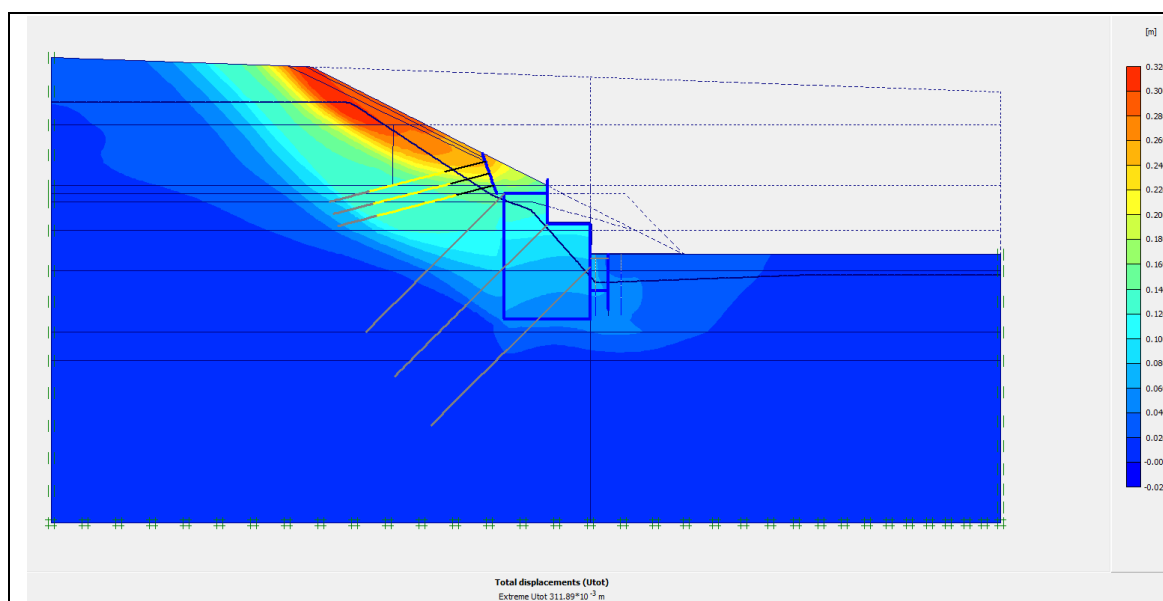


Figure 12: Deformations in the final stage at safety factor 1.27

The internal stability of the construction has been simulated in a FLAC 3D model, modelling only 1 segment of the construction, as shown in figure 9. The cross sections in figure 13 are taken in the middle between (figure 13a) and next to (figure 13b) the transversal screen and show the principal ground pressures in the horizontal X-direction. The cross sections shows larger traction zones (white) zones next to the transversal screens than in the middle.

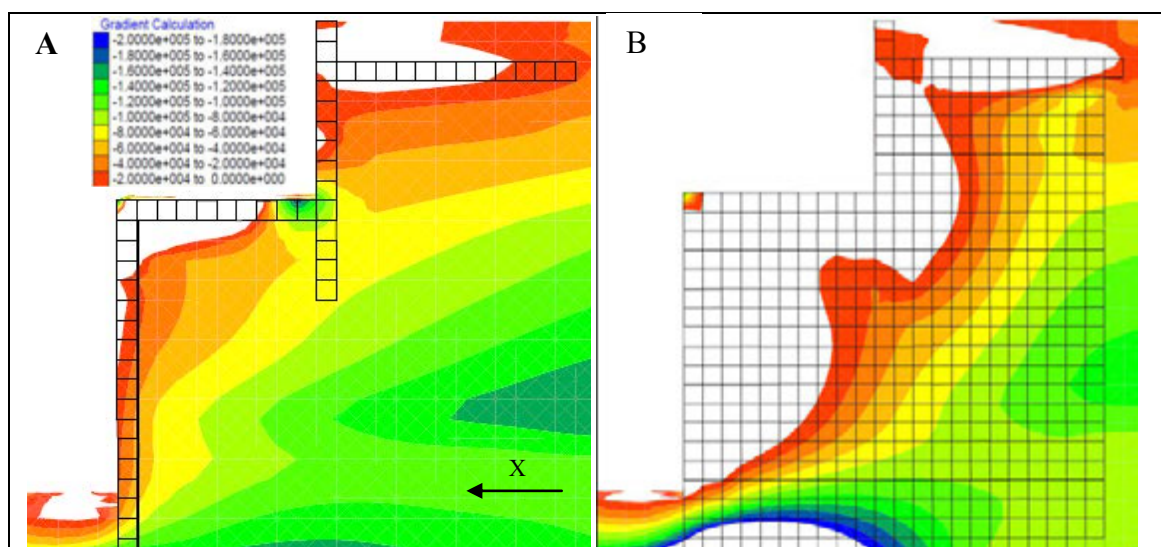


Figure 13: Cross section in middle between and next to transversal screens

The traction is taken by the concrete slab on top of the transversal screens, as given in figure 14a. The zone of maximum traction forms a arch like curve between the 2 transversal screens. In figure 14b, tension in the transversal screen can be noticed in the upper left part of the construction. On the low and right end compression is always present.

In figure 15a, the ground pressures in the horizontal X-direction are given in a horizontal section beneath the upper front screen. One can notice the ground pressure coming into the construction, decreasing nearer to the front side of the construction, due to friction at the rear end of the transversal screens. Just before the upper front screen, a turning point can be noticed. Near to the lower front screen arching can be noticed. In figure 15b ground pressures in the horizontal Y direction are given. At the rear end of the transversal secant walls a higher pressure can be noticed indicating higher friction in this zone.

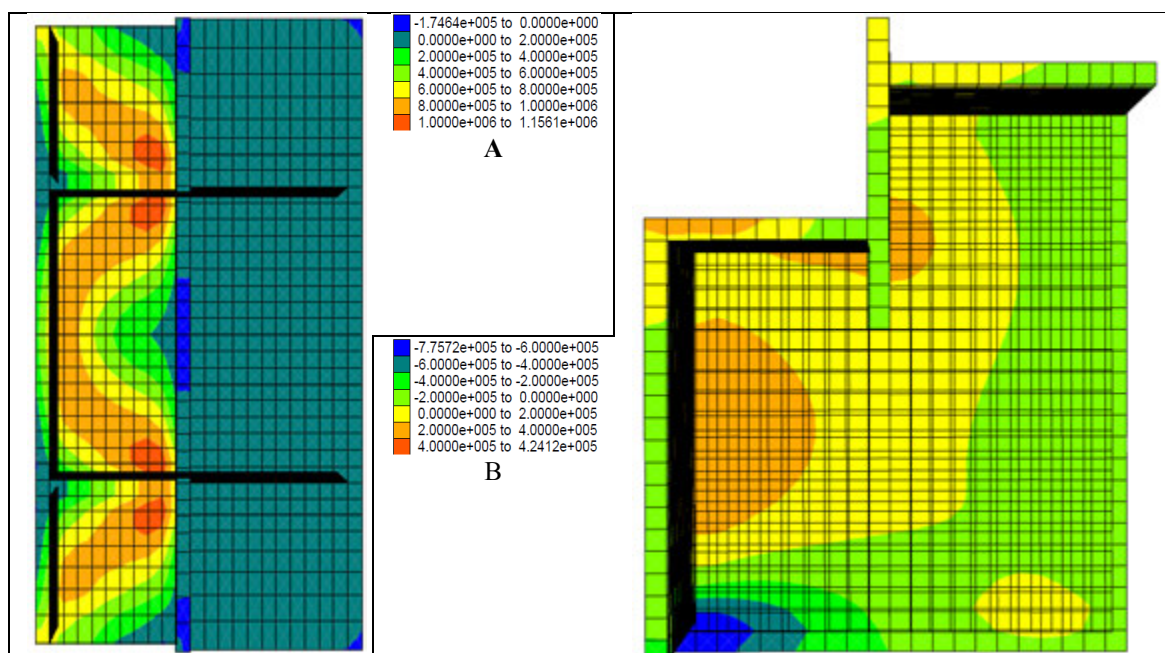


Figure 14: Tensions in concrete slab and transversal screen

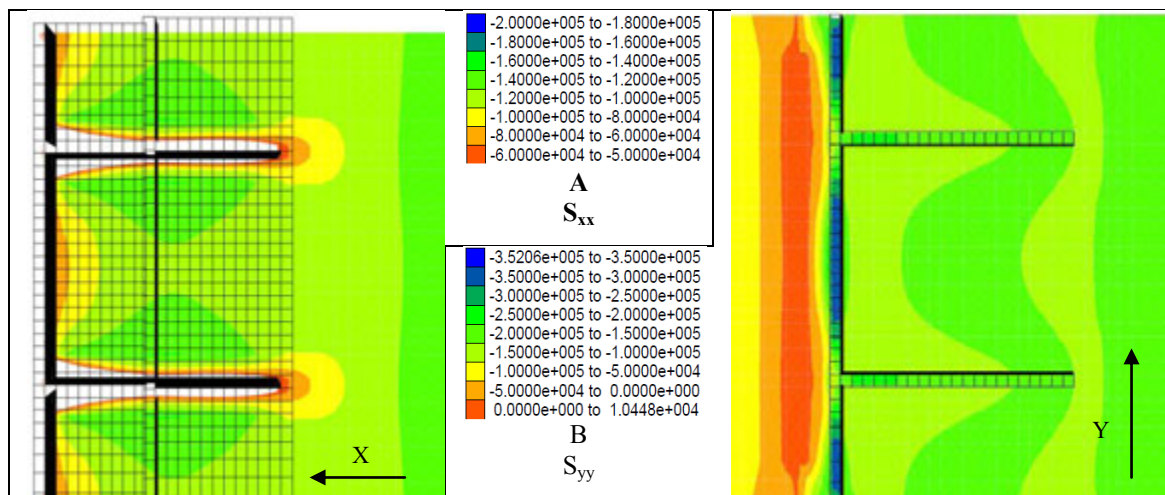


Figure 15: Entrance of soil pressures

4.4. Validation of the analytic model

In the previous paragraph, the design of the most defining cross section is discussed. Considering the whole length of the wall (ca 800m) and the gradual changing height along the railway link, the design had to be optimised and other cross section had to be calculated. As the finite element design is a time consuming process, a validation of an analytic model has been done based on the results of the finite element design in the latest section. In figure 16, the analytic model with all forces is given.

The surcharge represents the effect of the slope above the construction. As the soil reinforcement (soil nailing) has a similar effect on the horizontal pressures as given by Terzaghi [1] for strutted walls, the surcharge has been considered as being uniformly distributed. The height to be considered in the surcharge has been determined by comparison between the horizontal ground pressure calculated in the finite element modelling the slope and the model modelling a surcharge. It was found that the height to be taken into account corresponds to the height between the upper side of the construction and the intersection between the slope inclination and the straight line through the lower point of the construction at ground side with an inclination of the active angle, $45^\circ + \phi/2$. The results of this comparison are given in figure 17.

The slip surface under the construction is given in figure 16B. The average angle of the slip surface is considered to be at $\alpha=\varphi/2$. Only soil within the construction and above the fictive slip surface is taken into account in external equilibrium of the massif wall.

The external equilibrium is calculated with the normal safety factors as mentioned in Eurocode 7, factor 1.5 for slip equilibrium and factor 2.0 for overturning equilibrium. In temporary phases lower safety factors are allowed, respectively 1.20 and 1.75. In these phases the strut forces of the Berliner wall (see phase 6, table 1) are not taken into account.

To control the internal stability of the construction the horizontal earth pressure on the longitudinal pile wall is calculated taking in consideration the reduced earth pressure coefficient mentioned in DIN 4085 [2]. The horizontal force produced by the earth pressure on the longitudinal pile wall of one section has to be subtracted by the friction on the sides and bottom of the transversal pile wall taken into account a safety factor of 1.5 for calculation using neutral earth pressure for the subtraction of the friction and 1.1 when active earth pressure is taken into account. The friction is calculated by friction law given as follows: $\sigma_f = \sigma_v \cdot \tan(\varphi)$. As little movement is expected within the wall, the check based on the neutral earth pressure shall be defining the internal stability.

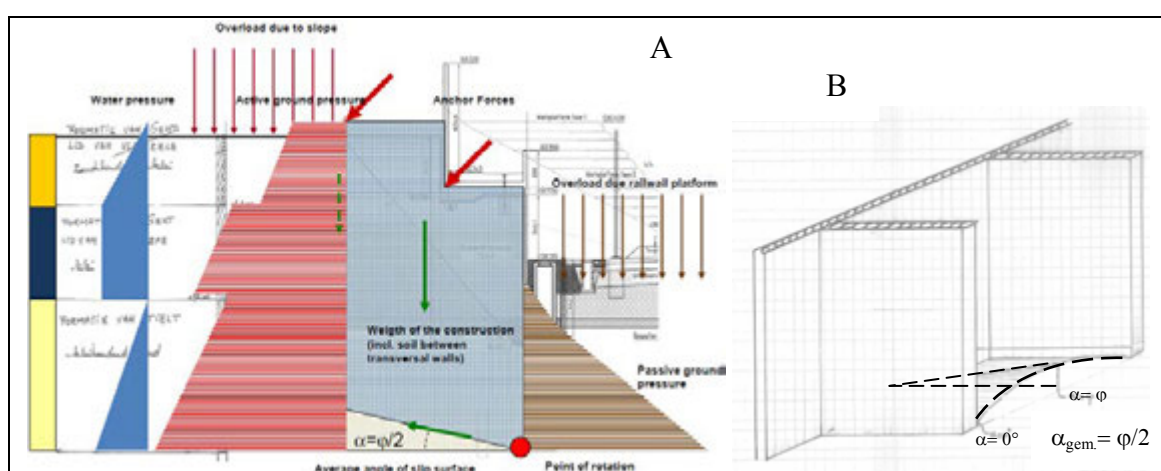


Figure 16: Analytic model

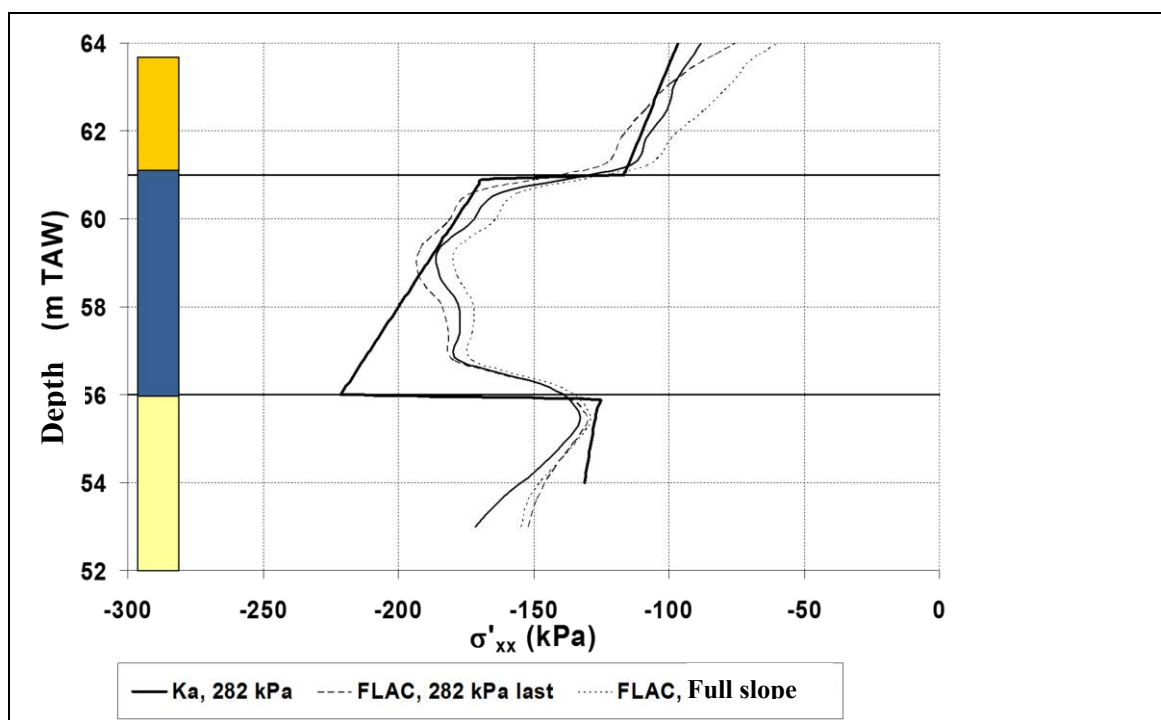


Figure 17: Analytic model

5. MONITORING RESULTS

During execution phases anchor forces and displacement are monitored.

In figure 18 anchor forces in the different execution phase are given as well as the measured anchor forces. The maximum calculated anchor force is 520kN/anchor. The length of the anchors has been calculated according to recommendation TA 95 [3]. For the moment only the first stage of excavation is done and it is too early to draw any conclusions out of these measurements.

The displacement of the wall over the different execution phases is given in figure 19. The maximum displacement in the end phase of construction is 56mm. In this phase no anchor force is taken into account. Until calculation step 25 anchors and anchor forces are taken into account and maximum displacement is limited to 29mm.

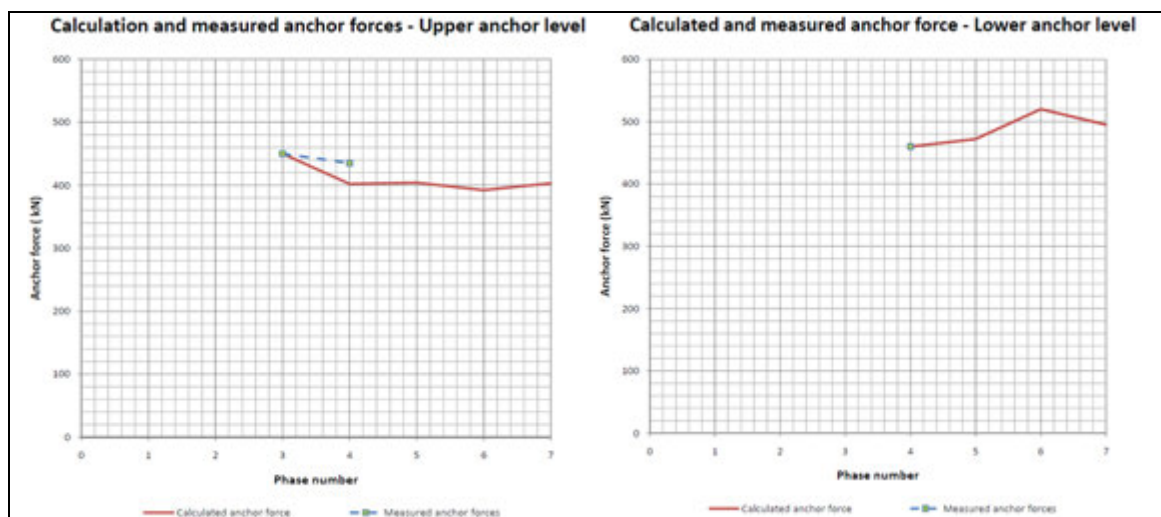


Figure 18: Calculated and measured anchor forces

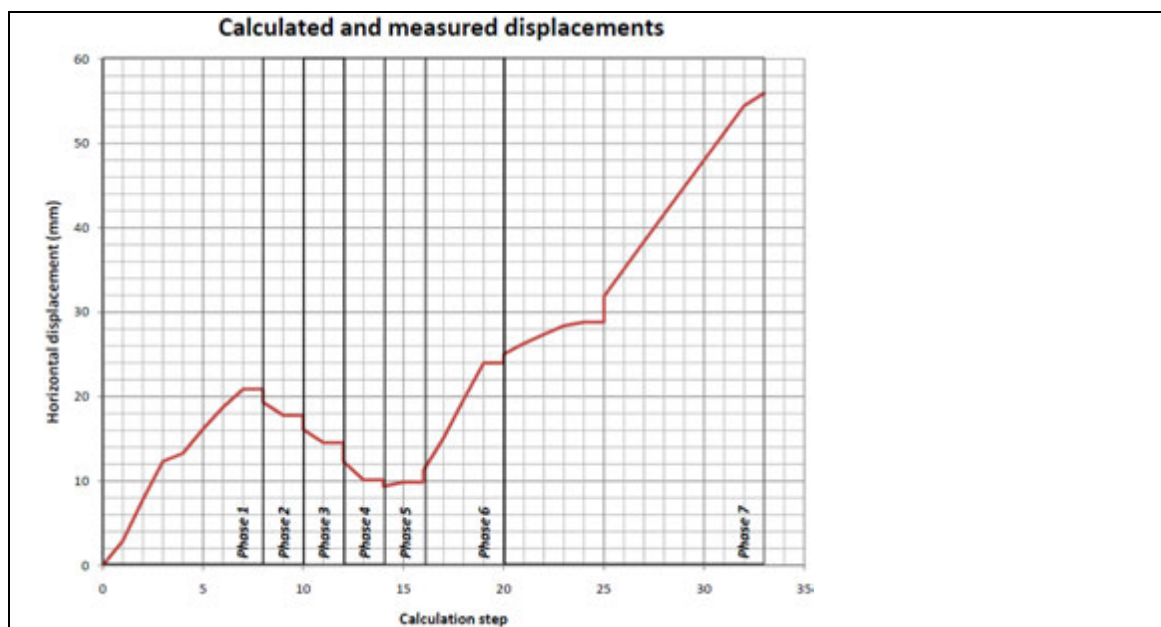


Figure 19: Calculated displacement over the different phases

For the monitoring of displacements inclinometers have been installed as well on top of the slope as in the middle of the bicycle path. The displacements measured in both of the inclinometers are given in the orthogonal direction on the rail tracks (see figure20).

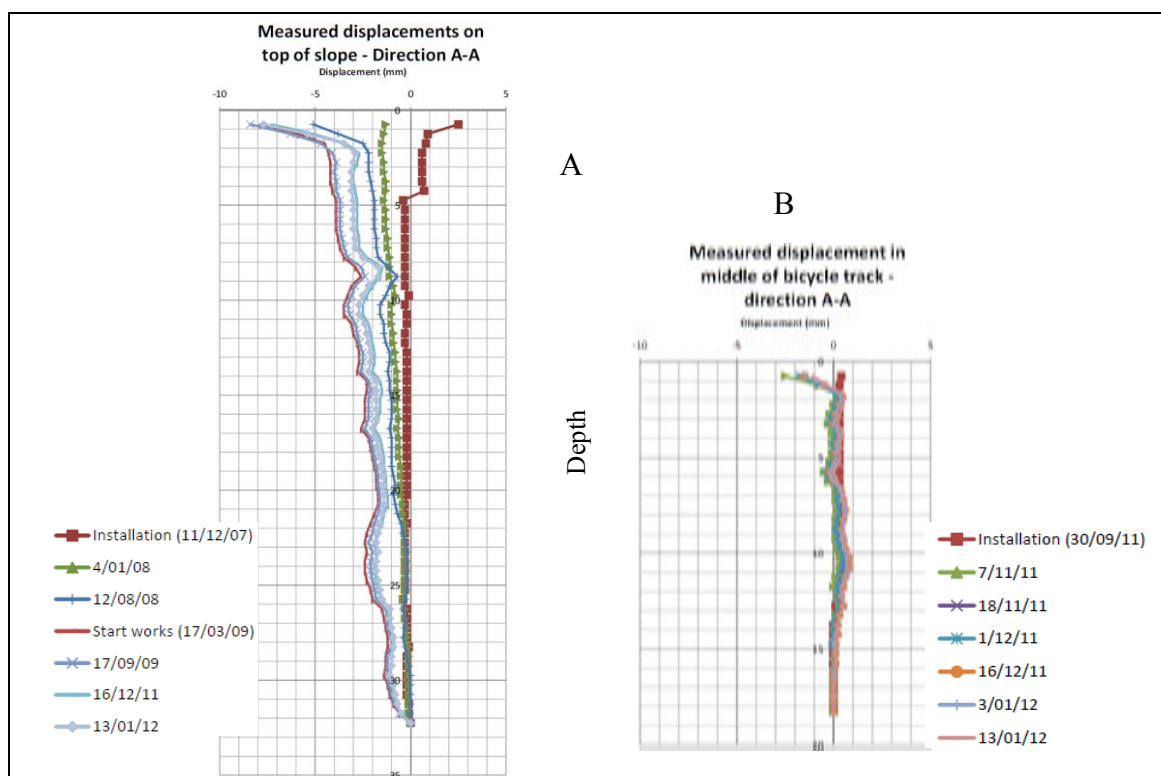


Figure 20: Measured displacements

From these measurements (phase 4) one can determine that no significant movement ($< 5\text{mm}$) on top of the slope is measured. The measured displacement in the middle of the bicycle track is very low ($< 2\text{mm}$). At the moment of the last measurement no excavation for phase 5 was done. The little variation measured can be due to imprecision's.

6. CONCLUSIONS

For the enlargement of the railway track between Brussels and Ghent important slope reinforcements in excavation zones have been necessary as the railway line is passing through a valley with poor and complex ground conditions. As special measures to stabilise the existing configuration have been taken in the past, the designers were aware of the complex underground and detailed soil investigation was done.

Finite element calculations have been elaborated to design the reinforcement measures that had to be taken. Also 3D-simulations of the reinforcement measures have been done for a better understanding of the construction and his interaction with the ground. Out of these understandings an analytical model has been validated for a faster design of this kind of construction, which has been useful as these constructions have been largely used along the railway track. To calibrate the calculations with reality monitoring of displacements and anchor forces are being done and will be reported in the future.

REFERENCES

- [1] Karl Terzaghi, Ralph B. Peck, Gholamreza Mesri, 1996 *Soil mechanics in engineering practice - Third Edition*, pg. 350-359.
- [2] DIN 4085, 1987, *Baugrund, Berechnung des erddrucks, berechnungsgrundlagen*, seite 9 tabelle 2.
- [3] Comité Français de la Mécanique des Sols et des Travaux de Fondations, 1995, *Tirants d'ancrage, Recommandations concernant la conception, le calcul, l'exécution et le contrôle*, Editions Eyrolles

Performance of multi-anchor walls under cyclic transient flooding

Yoshihisa Miyata, National Defense Academy, Japan, miyamiya@nda.ac.jp

Richard J. Bathurst, GeoEngineering Centre at Queen's-RMC, Canada

Takeharu Konami, Okasan Livic, Japan

Kiyomasa Dobashi, Public Works Research Center, Japan

ABSTRACT

The paper presents the results of three full-scale tests that were carried out to investigate the influence of transient flooding on the performance of multi-anchor reinforced soil (MAW) walls. The walls were constructed to a height of 6 m and flooded from the front of the structures to about mid-height and then drained in two to four stages. The walls were constructed with three different sand soils varying with respect to permeability, fines content and shear strength. The analysis of results showed that the wall facings were very permeable and thus prevented unbalanced hydrostatic or seepage forces from developing during drawdown that could increase anchor loads beyond drained condition values. The accuracy of the current Japanese design equation to estimate anchor capacity of MAW systems was demonstrated to vary widely depending on soil type and whether the soil was flooded or drained. However, on the load side, the method proposed by authors to predict anchor loads was judged to be more accurate than the current UK and Japanese methods.

1. INTRODUCTION

Reinforced soil walls constructed with metallic strips, geosynthetics and multi-anchor plates are now proven technologies. The first prototype multi-anchor test wall in Japan was built in 1980 (Fukuoka et al. 1980) and the first commercial structure was constructed in 1983 (PWRC 2002). There are now estimated to be more than 5000 multi-anchor walls (MAWs) in Japan. Figure 1 shows a schematic of the multi-anchor wall system.

Most MAW structures are not expected to be partially inundated during their design life. However, at the time of writing there are about 250 structures in Japan that have been built in shoreline areas where periodic flooding from the front of the wall occurs. These structures range from 3 to 25 m in height with the majority in the 5 to 9 m range. Three full-scale laboratory tests were carried out at the Public Works Research Institute (PWRI) in Japan to investigate the influence of transient flooding on the performance of multi-anchor reinforced soil walls (PWRC 1995). The 6 m-high walls were nominally identical but varied with respect to the backfill soil. This paper describes the experimental methodology and measurements recorded during cyclic transient flooding of these MAW structures based on the work of Miyata et al. (2010). The quantitative influence of flooding and draining on anchor loads is also presented. These measurements are compared to predictions using current PWRC (2002), BS8006 (1995) and the method proposed by Miyata et al. (2009) to compute anchor loads. The results of anchor pullout tests are also reported. Finally, implications to design and performance of multi-anchor reinforced soil walls in flooding environments are identified.

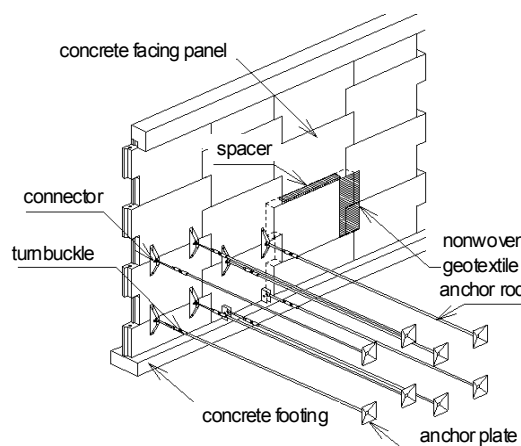


Figure 1: Detail of multi-anchor wall system.

2. EXPERIMENTAL PROGRAM

2.1. General arrangement and test method for full-scale walls

The laboratory test program involved three full-scale MAW structures constructed with different backfill soils. The 6 m-high walls were constructed in a concrete test pit 4 m wide, 4 m deep and 8 m long. The top 2 m of each wall was supported at the sides and back by a system of steel columns and concrete walls to allow each test wall to be extended above the top of the test pit facility. A cross-section of the general

arrangement for each test wall is given in Figure 2. Each wall was comprised of seven 4 m-long anchor rods and plates. The reinforced concrete panels were 1.5 m wide, 1 m high and 180 mm thick. Horizontal toe restraint was provided by frictional resistance between the bottom of the lower panel unit and the concrete floor of the test pit.

To simulate field construction practice for the MAW systems, there was no external support to the facing during construction. An impermeable strip of polyolefin foam was placed at the horizontal joint between facing panel units. A nonwoven geotextile was placed over the vertical panel joints at the back of the facing to prevent loss of soil. Pinned connections at the back of the facing panels were used to attach the anchor rods. The anchor rods are smooth circular bars with a 19 mm diameter. Each rod was attached to an anchor plate. The steel anchor plates used in this investigation were 300 mm by 300 mm.

The walls were instrumented with strain gauges bonded top and bottom to one column of anchor rods. Transducer-type earth pressure cells were embedded in the concrete facing units with the diaphragms flush with the concrete surface. Earth pressure cells were also placed at the base of the test pit. The free water level in front of the wall and within the backfill soil was monitored using pore water pressure transducers.

The walls were flooded and drained from the space in front of the wall. The maximum water level in front of the wall was about 3.5 m. Details of the flooding and draining history are described later. The target variable that was changed between tests was the backfill soil type. The soils varied from very permeable medium sand to less permeable silty fine sand.

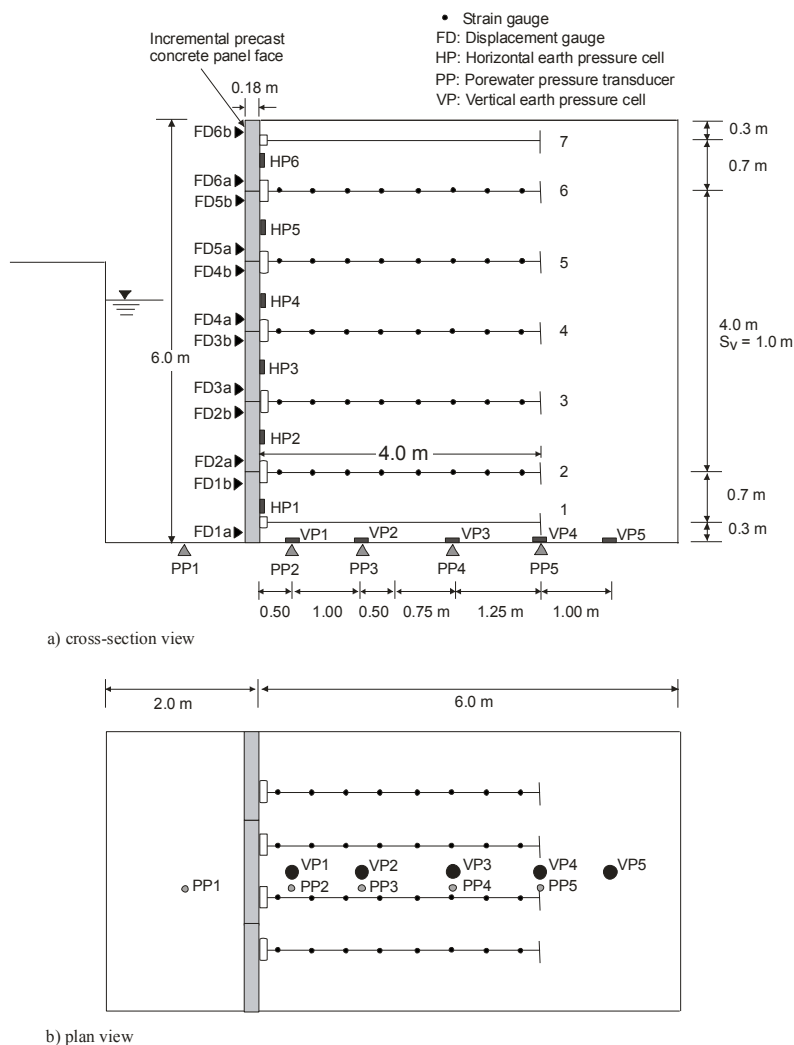


Figure 2: General test arrangement.

Table 1: Soil properties

	MAW-1	MAW-2	MAW-3
Soil Type	1	2	3
Natural water content w_n (%)	9.9	20.6	38.2
Fines content ^(a) (%)	6	19	42
D_{10} (mm)	0.13	0.019	< 0.001
D_{60} (mm)	0.62	0.16	0.16
Optimum water content w_{opt} (%)	8	20.9	N/A ^(d)
Dry unit weight (kN/m^3)	14.5	12.8	11.1
Triaxial test type ^(b)	CD	CU	CU
Cohesion, c (kPa)	0	2	4
Peak friction angle, ϕ (degrees)	36	30	11
Permeability, k (cm/s) ^(c)	7.8×10^{-3}	1.1×10^{-4}	2.8×10^{-5}

(a) Particle sizes by mass < 0.075 mm

(b) CD = consolidated-drained triaxial compression tests giving effective stress strength parameters. CU = consolidated-undrained triaxial compression tests giving total stress strength parameters

(c) Constant head test used for Type 1 and 2 soils. Tests carried out in accordance with JIS A2118 (1998). Permeability of Type 3 soil computed from particle size distribution using Kozeny-Carmen equation.

(d) N/A = not available

2.2. In-situ anchor pullout testing

Anchor pullout tests were carried out on selected anchors prior to and during Stage 1 flooding. The pullout test anchor rods were passed through the facing units. The end of the rod was threaded and a nut and reaction beam arrangement used. The free end of the anchor rod was loaded in steps using a hydraulic jack until a constant tensile load in the anchor rod was achieved. After the pullout test was completed, the anchor rod was put back into tension by tightening the nut on the front of the wall. All other anchor rods were attached at the back of the facing panel using the arrangement shown in Figure 1. The instrumented anchor rod in each layer was not used for pullout testing. Some disturbance to the anchor loads recorded in each instrumented anchor rod can be expected as a result of pullout testing. However, the average and spread in loads recorded in the instrumented anchor rods are included in the figures to follow and include loads before and after pullout testing. These data show that system disturbance due to the pullout tests likely added to spread in load data but not enough to change the conclusions reached later in the paper regarding the average quantitative effects of flooding and draining on anchor loads.

2.3. Material properties

The backfill soils were medium sand (SP) (Type 1), fine sand (SW) (Type 2) and silty fine sand SM (Type 3) for walls MAW-1, -2 and -3, respectively. Soil properties are summarized in Table 1. It is reasonable to rank Type 1 soil as the highest quality backfill soil in this investigation and Type 3 as the poorest. In each test wall the soil was placed in 250 mm-thick lifts and compacted to a target value of 90% of standard Proctor density. The soil was compacted in three passes using a walk-behind vibrating plate compactor.

An important requirement for multi-anchor wall construction is the use of a permeable drainage layer at the back of the facing panels (PWRC 2002). The material used in this study was a 4 mm-thick nonwoven polypropylene geotextile. The geotextile was placed in 420 mm-wide strips over each vertical joint. The geotextile was not placed against the horizontal joints since an impermeable polyolefin foam strip was placed between panels as noted earlier. In practice it is the unloaded vertical joints that are most important to protect against loss of backfill. No loss of material was reported through any facing joints in this study.

2.4. Flooding and draining histories

The flooding and draining history for Wall MAW-1 is shown in Figure 3a. The space in front of the wall was flooded and drained in four stages to a maximum depth of about 3.5 m. Flooding was carried out at 2.5 m/hour and the maximum flood depth held for 4, 1, 1 and 0.2 days for Stages 1, 2, 3 and 4, respectively. The drainage rates were 1 m/day and 2 m/day for Stages 1 and 2, respectively. Stages 3 and 4 were drained at 3 m/hour. Following Stages 1, 2 and 3, the walls were left in a drained state for 4, 2.5 and 0.5 days, respectively. The flooding and draining histories for Walls MAW-2 and MAW-3 are shown in Figures 4a and 5a, respectively. Note that for these two walls there were only two flooding and draining cycles. The flooding rates for Walls MAW-2 and MAW-3 were 2.5 m/hour for both stages. The drainage rates for Wall MAW-2 were the same as for Wall MAW-1. For Wall MAW-3 the two draining rates were 2 m/day and 3 m/day for Stages 1 and 2, respectively. Finally it should be noted that each initial flooding event (Stage 1) was continued until equilibrium was established between the internal phreatic surface and the free water level on the outside of the wall.

3. RESULTS

3.1. Behaviour of test walls

Figures 3b, 4b and 5b show the anchor loads recorded at one location on each monitored anchor. The load responses can be seen to match flooding and draining stages. Other measurements such as facing displacements and vertical earth pressures were also seen to change with changes in hydraulic boundary conditions. In this paper, lateral pressures acting on the wall and anchor loads are reported. These data were extracted at the end of each flooding and draining stage from continuous monitoring records. For more details of the response of these walls, the reader is directed to the paper by Miyata et al. (2010).

The plots in Figure 6 summarize net lateral pressures acting on the wall facing during Stage 1 and 2 flooding and draining. The symbols denote average drained and flooded pressure values while the range bars show maximum and minimum values recorded during the first two loading stages. These numbers are computed from multiple readings recorded during each stage. In all cases the net pressure acts outward. However, as expected the effect of submergence of the wall facing is (typically) reduction in the

net outward earth pressure (or load) on the wall below the flood level. The average net pressure values (or total outward wall force) for drained and flooded conditions can be seen to decrease in the order of walls with increasing cohesive shear strength component. As noted previously there were two additional flooding and draining cycles for Wall MAW-1 (Stages 3 and 4 in Figure 3a). The water level in front of the wall was lowered at a greater rate than for Stages 1 and 2 to simulate a rapid drawdown condition (about 3 m/h versus 2 m/day for Stages 1 and 2). However, there were no detectable increases in net lateral pressure (or load) against the back of the facing beyond those shown in Figure 6a (i.e. pressures were within the plotted range bars for each elevation). The reason for this is the porous facing formed by the nonwoven geotextile placed over the permeable joints of the concrete panels (Figure 1).

Figure 7 shows the maximum reinforcement axial load (T_{max}) recorded in each anchor rod along the height of the walls. The plots show a reduction in anchor loads below the flood elevation when the wall is flooded. This is consistent with the reduction in net lateral pressure acting on the back of the wall facing panels noted above. There is detectable smaller reduction in anchor loads above the flood level when the wall is flooded which can be ascribed to load redistribution in these redundant reinforced soil wall systems. Consistent with comments made regarding the lateral pressure response under rapid drawdown conditions, the maximum anchor loads during Stage 3 and 4 draining remained within limits recorded during Stage 1 and 2 loading. Rapid drawdown tests comparable to Stages 3 and 4 for Wall MAW-1 were not carried out for Walls MAW-2 and MAW-3 even though these walls were constructed with less permeable soils. It was concluded that since the same very permeable vertical drainage boundary was used for all three walls, unbalanced hydrostatic or seepage forces behind the concrete panels for Walls MAW-2 and MAW-3 would also not occur. The data collected from the horizontal earth pressure cells provides an opportunity to investigate at least qualitatively how the magnitude of total lateral earth force acting on the back of facing changes with draining and flooding and type of backfill, and how much of the lateral earth load is transferred to the anchor rods. To do this the average net pressure recorded by the earth pressure cells immediately above and below each anchor rod was computed and converted to horizontal force per unit running length of wall (F_h) at selected times during drained and flooded stages.

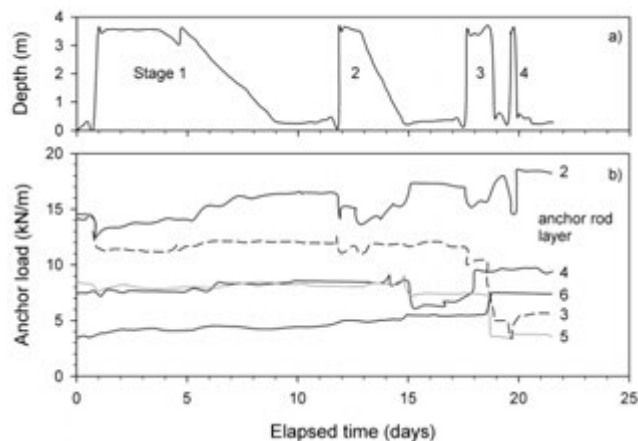


Figure 3: Flooding-draining history and anchor loads in MAW-1 (Soil Type 1)

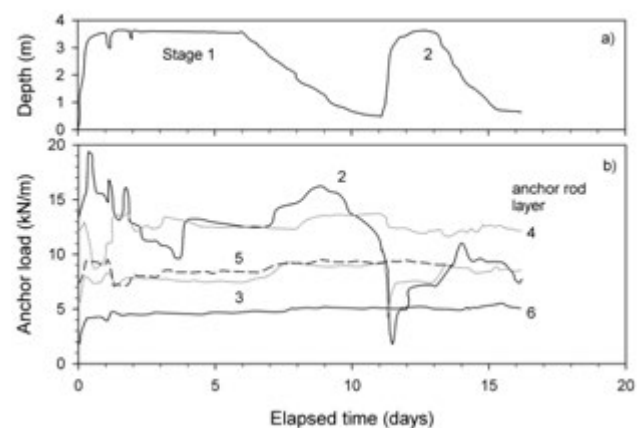


Figure 4: Flooding-draining history and anchor loads in MAW-2 (Soil Type 2)

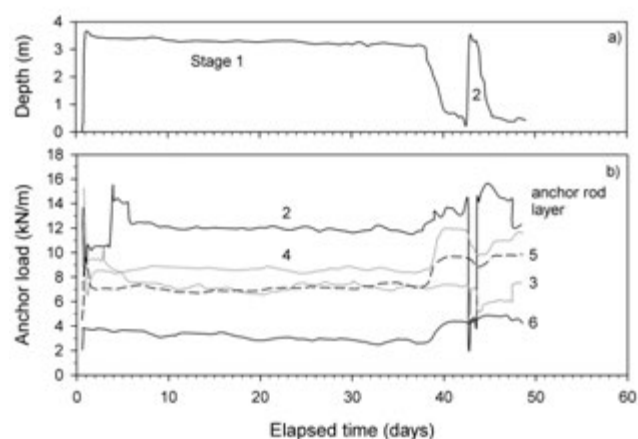


Figure 5: Flooding-draining history and anchor loads in MAW-3 (Soil Type 3)

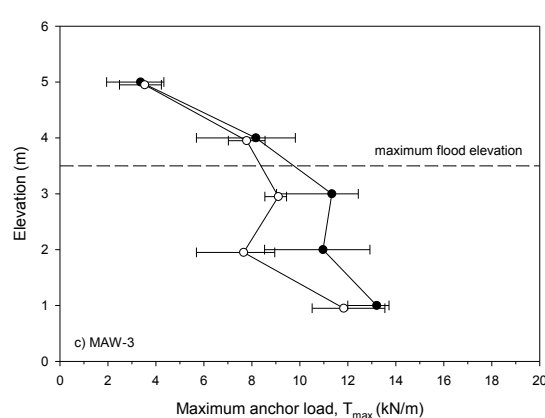
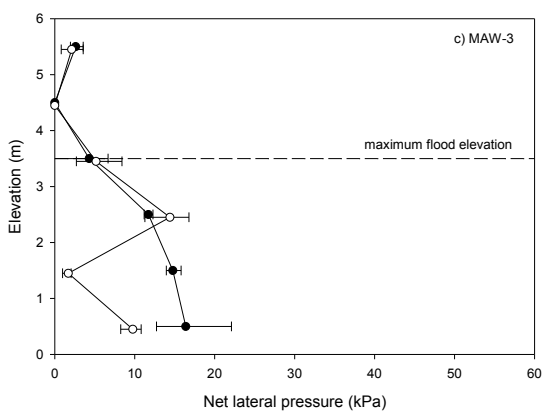
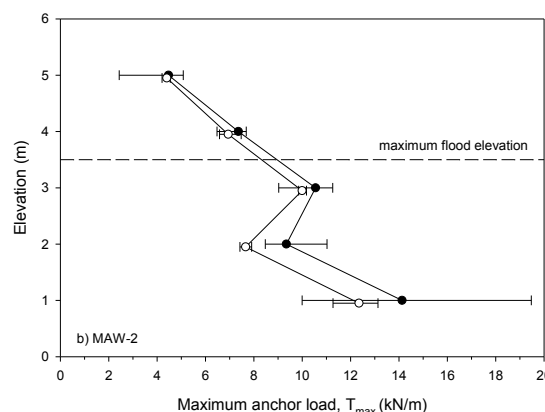
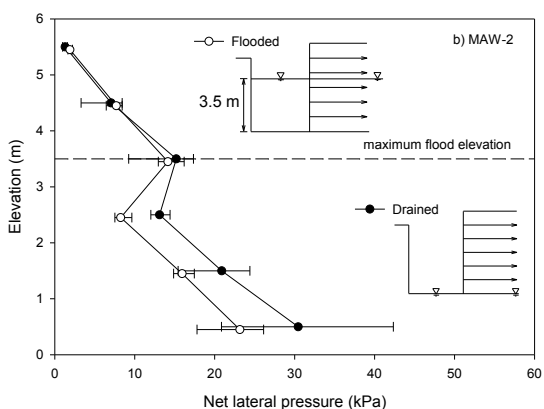
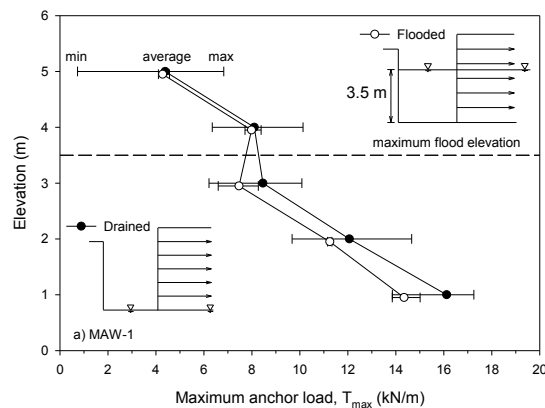
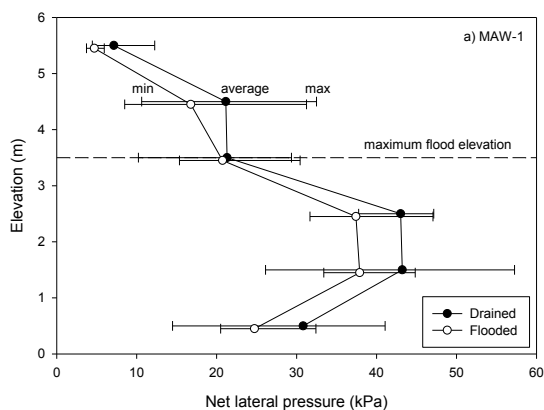


Figure 6: Net lateral pressure acting on wall facing units (data taken from first and second flooding and drainage stages).

Figure 7: Maximum anchor loads (data taken from first and second flooding and drainage stages).

The corresponding maximum tensile load recorded in each anchor rod (T_{max}) was then plotted against this value (Figures 8a, 8b and 8c). The plots in each figure show that there is no obvious visible difference between datasets for anchor loads corresponding to when the walls were drained and when they were flooded. For each wall (i.e. each soil type), most anchor loads are 15 kN/m or less. The consistent range of anchor load T_{max} regardless of soil type may be expected between walls using the proposed method by Miyata et al. (2009). In their method, anchor loads increase with decreasing friction angle but decrease with increasing cohesive shear strength component. The result is that on average the anchor loads for the three soil types in this investigation are reasonably similar between structures. Comparisons between predicted and measured loads using different analytical methods are examined later. An interesting observation from these plots is that while anchor loads vary over a narrow range, there is a clear reduction in earth forces in the order of Wall MAW-1, -2 and -3. This cannot be explained by classical active earth pressure theory which predicts the opposite trend for earth forces. However, consistent with current

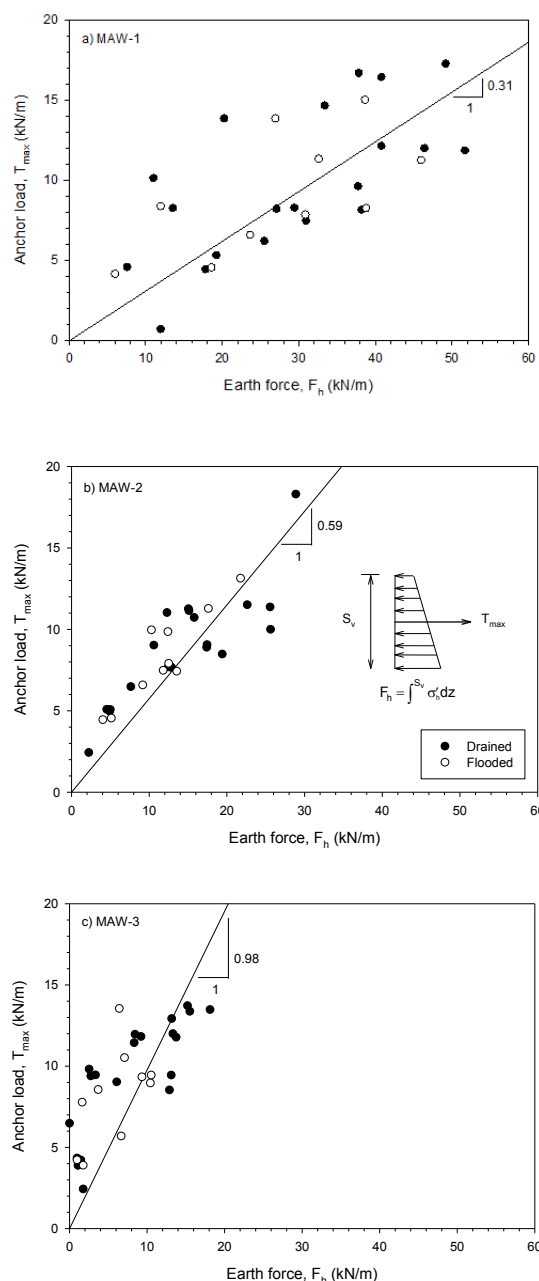


Figure 8: Comparison of maximum anchor loads and corresponding net lateral earth forces acting on the back of the facing. Notes: S_v = anchor vertical spacing; σ'_h = net horizontal earth pressure, and; z = depth.

constructed with relatively extensible (geosynthetic) reinforcement layers and a high quality frictional sand (SP) backfill, the restrained horizontal footing carried about 70% to 80% of the total earth force. For the same structure but constructed with a stiffer welded steel wire mesh reinforcement, the footing contribution was 50%. Hence, the argument that the walls in the current investigation may have developed significant load capacity at the toe of the wall may be expected. However, if it is accepted that the restrained toe of the walls in this investigation may mobilize load capacity, then Figures 8b and 8c, can be interpreted to demonstrate that proportionally more load is carried by the anchor rods (and less by the toe) as the quality of the backfill soil decreases. Nevertheless, it is not possible to know from the current investigation if the fraction of load carried by the toe will decrease with height of wall. There is some evidence from numerical modelling of hard-faced geosynthetic reinforced soil walls that this is the case (Huang et al. 2010).

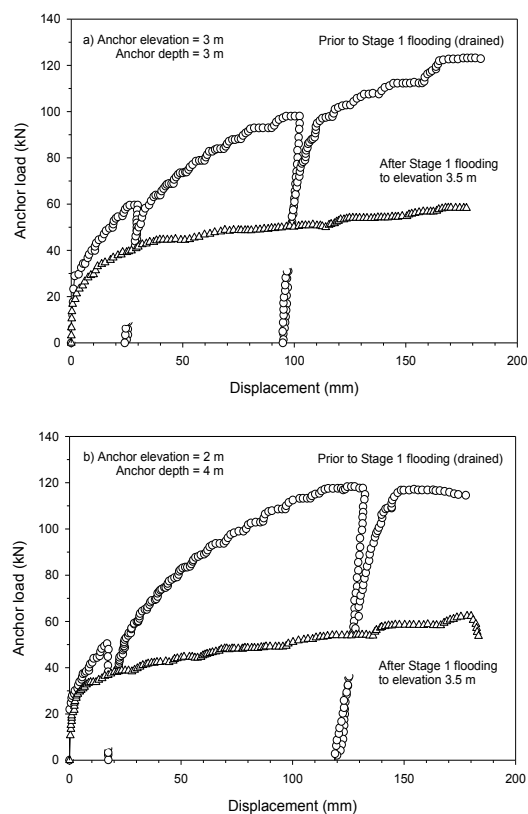


Figure 9: Example results of in-situ anchor pullout tests conducted on Wall MAW-1 in drained and flooded conditions.

design methods there is a generally linear trend of increasing anchor load with increasing net lateral earth force for each wall. However, the ratio of T_{max} to net lateral earth force (F_h) is roughly one third for Wall MAW-1, one half (say) for Wall MAW-2 and about one to one for Wall MAW-3. This implies that a large portion of earth load (i.e. perhaps two thirds) is carried by the concrete facing and transmitted to the toe for Wall MAW-1. An exact calculation is not possible because not all anchor rods were instrumented, nor was the horizontal toe reaction measured. The notion that a restrained horizontal toe at the base of a reinforced soil wall with a structural facing can carry a significant portion of the earth load in these systems under operational conditions has been reported by Bathurst et al. (2006). Bathurst et al. (2009) showed that for a series of 3.6 m-high modular block walls

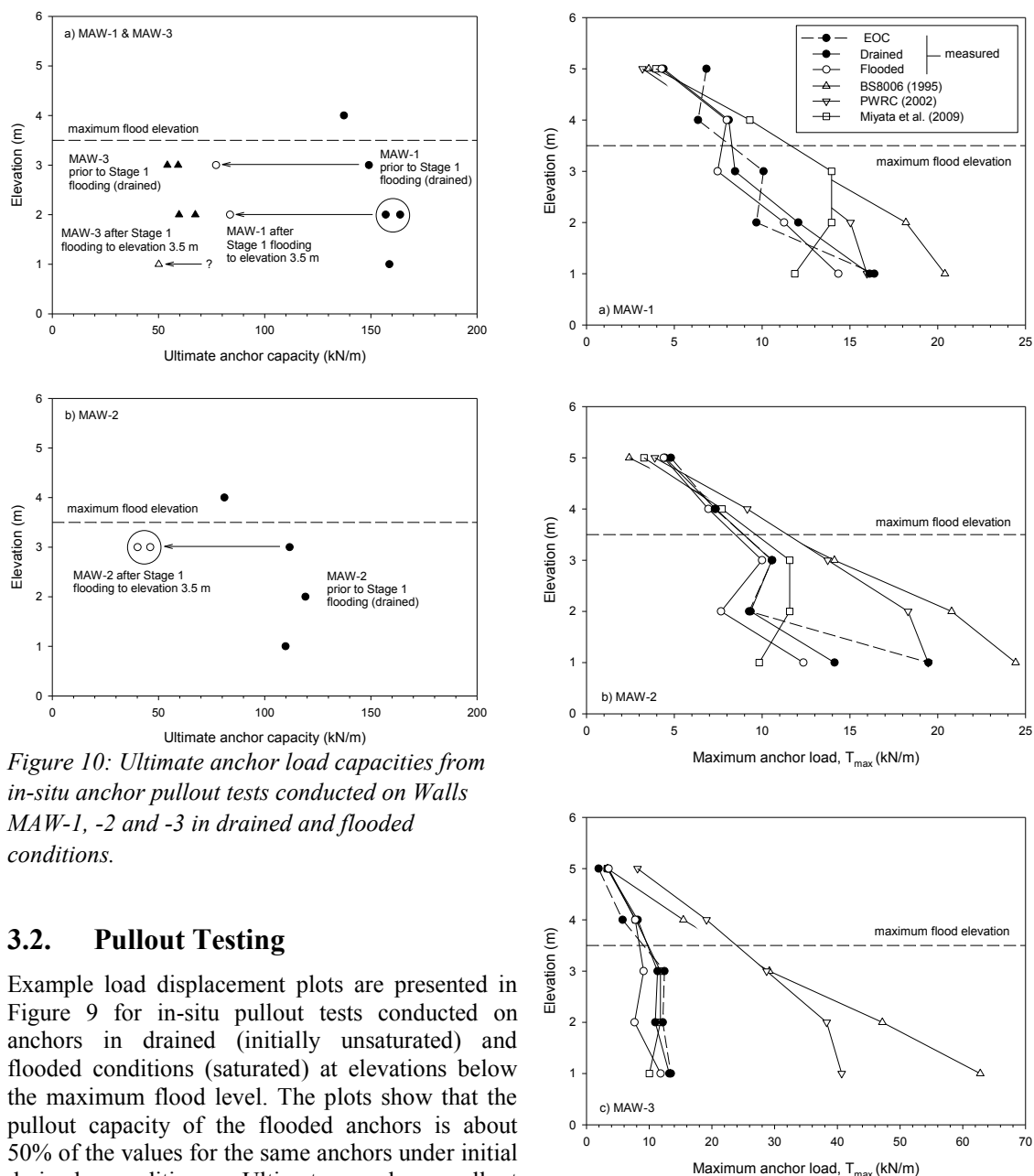


Figure 10: Ultimate anchor load capacities from in-situ anchor pullout tests conducted on Walls MAW-1, -2 and -3 in drained and flooded conditions.

3.2. Pullout Testing

Example load displacement plots are presented in Figure 9 for in-situ pullout tests conducted on anchors in drained (initially unsaturated) and flooded conditions (saturated) at elevations below the maximum flood level. The plots show that the pullout capacity of the flooded anchors is about 50% of the values for the same anchors under initial drained conditions. Ultimate anchor pullout capacities from all tests are summarized in Figure 10. The data shows that pullout capacity also reduces by about 50% for Wall MAW-2 and by about 30% (estimated) for Wall MAW-3 when the anchors are submerged.

4. IMPLICATIONS TO DESIGN

4.1. Anchor Loads

Miyata et al. (2009) investigated the accuracy of current and proposed anchor load design equations by comparing predicted loads with measured values. Their dataset included the three walls in the current study but prior to flooding and draining stages. Peak anchor load predictions (drained condition) using the same three different approaches reported by Miyata et al. (2009) are superimposed on measured anchor load data for drained and flooded cases in Figure 11. Load predictions for MAW-1 were carried out using effective stress strength parameters from CD triaxial tests since this wall was constructed with a cohesionless soil with relatively high permeability (good drainage properties). Total stress strength parameters were used for the other two walls that were constructed with cohesive-frictional soils with

Figure 11: Comparison of predicted and measured peak anchor loads. Note: EOC = end of construction.

lower permeability (relatively poor drainage properties). Hence, all analyses refer to short-term strength conditions that are consistent with the short duration of all physical tests in this study. The range bars on measured load values have been removed for clarity. The dashed lines in the plots correspond to anchor loads recorded at the end of construction (EOC) and were previously reported by the writers. There are detectable differences in these values and the values recorded just prior to flooding (the datum in this paper). This is believed to be the result of the disturbance caused by the initial set of pullout testing that was carried out between these two periods. Nevertheless, the overall trend in measured data and magnitude of anchor loads for MAW-1 at EOC and after pullout testing are judged to be similar. The discrepancies between initial load values for the other two walls are less.

The visual impression for the plotted data in Figure

11 is that of the two current design methods considered, the BS8006 (1995) method is typically more conservative (i.e. safer for design) than the PWRC (2002) method. The method recently proposed by Miyata et al. (2009) generally does better with the exception in some cases at the lowermost anchor. However, based on bias statistics the method of Miyata et al. is more accurate on average (i.e. mean bias statistics are close to one and the spread in bias statistics is much lower (Table 2)). Here, bias is defined as the ratio of measured to predicted load. Regardless of the design method, flooding increases predicted load conservatism (i.e. mean of bias values is reduced) consistent with observations made from the plotted data.

Table 2: Bias statistics for maximum anchor load, T_{max} .

Parameter	Method 1 BS8006 (1995)		Method 2 PWRC (2002)		Method 3 Miyata et al. (2009)	
	drained	flooded	drained	flooded	drained	flooded
n	30	15	30	15	30	15
Bias mean	0.77	0.76	0.77	0.77	1.07	1.20
Bias COV (%)	69	54	64	46	39	26

Notes: n = number of data points; bias = measured load/predicted load; coefficient of variation (COV) = standard deviation/mean

4.2. Anchor capacity

The current PWRC (2002) method for ultimate anchor plate capacity (R_p) is expressed as:

$$R_p = [cN_c + K_a \sigma_v (N_q - 1)] B^2 \quad (1)$$

Here, N_c and N_q = non-dimensional factors expressed as functions of soil peak friction angle, ϕ ; c = cohesion; K_a = active earth pressure coefficient; σ_v = vertical stress at the anchor elevation, and; B = height of the square anchor plate. The strength parameters used in Equation 1 were selected to be consistent with the values used to predict anchor loads in each matching wall.

Measured (R_m) versus predicted (R_p) anchor capacities are plotted in Figure 12 with black symbols. The data show that the measured anchor capacities are less than the predicted values for anchors in a flooded condition for Walls MAW-1 and -2. For Wall MAW-1, four out of five measured anchor capacities are less than predicted values. However, for Wall MAW-3 with the lowest quality backfill the measured anchor plate capacities are well in excess of predicted values for drained and flooded conditions. The wide range from under-predicted to excessively over-predicted anchor capacities illustrates that the anchor capacity model (Equation 1) is poor. However, PWRC (2002) recommends that a factor of safety of three be used for design. If this is done then the data points in Figure 12 shift to the left (see matching grey symbols) and all design anchor capacities are less than measured values which is a requirement for conventional working stress design.

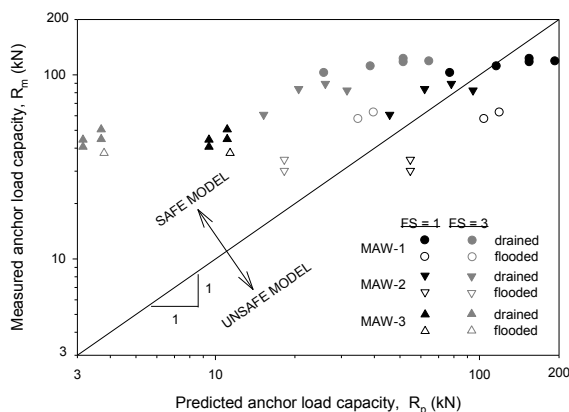


Figure 12: Measured anchor capacities versus unfactored ($FS = 1$) and factored ($FS = 3$) predicted capacities.

4.3. Anchor loads versus anchor capacity

Comparing the measured anchor loads in Figure 7 with the measured anchor capacities in Figure 12 suggests that the walls in this test program were very safe with no possibility of failure due to anchor pullout. Computed factors of safety using measured anchor loads and matching measured anchor capacities are summarized in Table 3 and confirm that this is indeed the case. The general impression from the numbers in this table is that the actual factor of safety against pullout failure decreases with decreasing quality of backfill soil and factors of safety are lower for the flooded case than for the nominal identical drained case. The range of factors of safety is from 18 to 2.8. The lower value is close to the recommended minimum factor of safety of 3 for these systems according to the PWRC (2002) design code. However, recall that there was only one anchor pullout test for MAW-3 in a flooded condition so the factors of safety for the flooded MAW-3 should be taken with some caution. Nevertheless, there appears to be a consistent trend in the data when all computed factor of safety values are examined together.

Table 4 reports computed factors of safety based on load predictions using three different models (BS8006 2005; PWRC 2002; Miyata et al. 2009) and anchor capacities using Equation 1. In all computations for flooded conditions the effective unit weight of soil below the flood elevation was used to compute anchor loads below the flood elevation. For Walls MAW-1 and -2, predicted factors of safety for the drained case fall within the range of measured values for all design methods (Table 3). For the flooded condition the predicted values are higher than measured factors of safety. For Wall MAW-3 the predicted factors of safety for the drained and flooded cases are well below measured values. In fact, Methods 1 and 2 predict failure for both flooded and drained conditions which clearly was not observed in the physical experiments. However, Method 3 predicts that this structure just satisfies a factor of safety of one. Based on all three methods it can be argued that the method proposed by Miyata et al. (2009) to compute loads gives a better prediction of collapse than current design methods using BS8006 (2005) and PWRC (2002) to compute anchor loads if Equation 1 (PWRC 2002) is used to predict anchor capacity.

Table 3: Computed factors of safety from measured loads and measured anchor capacities.

Wall	Drained				Flooded			
	n	Ave.	Max.	Min.	n	Ave.	Max.	Min.
MAW-1	5	10.7	18.0	6.90	2	6.66	8.76	5.54
MAW-2	4	7.90	10.6	4.23	2	3.24	3.51	2.96
MAW-3	4	4.05	5.92	3.27	1	3.18	2.78	3.58

Notes: n = number of in-situ anchor pullout tests

Table 4: Computed minimum factors of safety using predicted loads and predicted anchor capacities.

Wall	Method 1 BS8006 (1995)		Method 2 PWRC (2002)		Method 3 Miyata et al. (2009)	
	drained	flooded	drained	flooded	drained	flooded
	MAW-1	11.3 (2 m)	9.38 (2 m)	13.7 (3 m)	11.4 (2 m)	12.2 (3 m)
MAW-2	5.02 (2 m)	4.23 (2 m)	5.69 (2 m)	4.80 (2 m)	8.00 (3 m)	7.95 (3 m)
MAW-3	0.29 (1 m)	0.28 (1 m)	0.39 (2 m)	0.37 (2 m)	1.02 (4 m)	1.15 (3 m)

Notes: bold face factors of safety denote predicted failure; numbers in parentheses are corresponding anchor rod elevations

5. CONCLUSIONS

This paper is focused on the quantitative performance of three full-scale 6 m-high multi-anchor walls that were subjected to transient flooding and draining to about wall mid-height. The major conclusions from this study are:

1. The horizontal concrete panel joints in combination with a permeable nonwoven geotextile were adequate in this experimental program to prevent the development of unbalanced hydrostatic or seepage forces that could put additional load on the anchors during drawdown.
2. The net lateral earth pressures acting against the back of the facing panels and the anchor loads in the walls were observed to decrease during flooding. Hence, for design the critical anchor loads correspond to the drained condition. The total earth force acting on the back of the facing panels was observed to decrease with backfill soils having increasing soil cohesion. The fraction of horizontal earth load carried by the anchors was observed to increase with backfill soil having increasing soil cohesion.

3. The accuracy of the current PWRC (2002) analytical model to estimate anchor capacity of MAW systems was demonstrated to vary widely depending on soil type and whether the soil was flooded or drained. For the two highest quality backfill soils in this investigation, the anchor capacity model greatly over-estimated anchor capacity when the anchors were in a flooded condition. For the poorest quality (high cohesive strength component and fines content) soil, the anchor capacity model greatly under-estimated anchorage capacity for both drained and flooded conditions. However, using a factor of safety of three on anchorage capacity as recommended by PWRC (2002) was observed to result in safe estimates of anchorage capacity for all backfill types in flooded and drained condition.
4. The method proposed by Miyata et al. (2009) to predict anchor loads was judged to be more accurate than the current BS8006 (2005) and PWRC (2002) methods based on the mean and spread of bias statistics where bias is defined as the ratio of measured to predicted anchor load.
5. Anchor capacity was observed to decrease by up to about 50% when the anchors were tested in a flooded condition compared to a drained condition.

6. ACKNOWLEDGEMENTS

The work described here was carried out with funding awarded to the first author by the Japan Ministry of Education, Culture, Sports, Science and Technology (Grant-in-Aid for Scientific Research (B) No.21360229) and the Japan Ministry of Defense. The second author is grateful for support provided by the Public Works Research Center in Japan which allowed him the opportunity to work in Japan and complete the study described here.

REFERENCES

- American Association of State Highway and Transportation Officials (AASHTO). 2007. LRFD Bridge Design Specifications. 4th edition, Washington, DC, USA.*
- Bathurst, R.J., Nernheim, A., Walters, D.L., Allen, T.M., Burgess, P. and Saunders, D. 2009. Influence of reinforcement stiffness and compaction on the performance of four geosynthetic reinforced soil walls, Geosynthetics International, Vol. 16, No. 1, pp. 43-59.*
- Bathurst, R.J., Vlachopoulos, N., Walters, D.L., Burgess, P.G. and Allen, T.M. 2006. The influence of facing rigidity on the performance of two geosynthetic reinforced soil retaining walls, Canadian Geotechnical Journal, Vol. 43, No. 12, pp. 1225-1237.*
- British Standards Institution. BS8006. 1995. Code of practice for strengthened/reinforced soil and other fills, BSI, Milton Keynes, United Kingdom.*
- FHWA. 2001. Corrosion/degradation of soil reinforcements for mechanically stabilized earth walls and reinforced soil slopes. Federal Highway Administration, U.S. Department of Transportation, Washington, D.C. USA.*
- Fukuoka, M., Imamura, Y., Kudoh, K., Naitoh, S. and Fukahori, T. 1980. Research on Multi-anchor wall, In proceedings of 15th Japanese Geotechnical Society Annual Meeting, Hiroshima, Japan, pp. 1525-1528 (in Japanese).*
- Huang, B., Bathurst, R.J., Hatami, K. and Allen, T.M. 2010. Influence of toe restraint on reinforced soil segmental walls, Canadian Geotechnical Journal, Vol. 47, No.8, pp. 885-904.*
- Miyata, Y., Bathurst, R.J. and Konami, T. 2009. Measured and predicted loads in multi-anchor reinforced soil walls in Japan, Soils and Foundations, Vol. 49, No. 1, pp. 1-10.*
- Miyata, Y., Bathurst, R.J., Konami, T. and Dobashi, K. 2010. Influence of transient flooding on multi-anchor walls, Soils and Foundations, Vol. 50, No. 3, pp. 371-382.*
- PWRC. 1995. Technical report on rational design method of reinforced soil walls. Public Works Research Center, Tsukuba, Ibaraki, Japan, 278 p. (in Japanese).*
- PWRC. 2002. Design method, construction manual and specifications for multi-anchored reinforced retaining wall. Public Works Research Center, Tsukuba, Ibaraki, Japan, 248 p. (in Japanese).*

Laboratory study of displacements in a geogrid reinforced soil model under lateral earth pressures

Lissette Ruiz-Tagle, CSP-DSI, Chile, lruiz-tagle@csp-dsi.cl
Felipe Villalobos, Catholic University of Concepción, Chile, avillalobos@ucsc.cl

ABSTRACT

An experimental and numerical study is presented related to displacements and rotations of soil particles without and with geogrid reinforcement under the application of active lateral earth pressures. To this end, the measurement technique PIV has been used, with which digital images are processed to obtain displacement and rotation fields. The experimental earth pressure equipment has a transparent window which allows the recording of soil particle movements. The process and analysis of the measured soil particle movements allow the determination of yielded and not yielded soil areas. In this form, the position and geometry of the failure surface was determined and compared with the defined by plasticity theory of active Rankine states. This comparison is only possible for the case without geogrids since the presence of geogrids changes significantly the zone of soil yielding. Geogrids can reduce up to twice the volume of yielded soil due to the active lateral earth pressure. This conclusion related to the soil deformation is found to be in direct relation with the active lateral earth pressure reduction when geogrids are used as reinforced elements. In addition, a numerical analysis using the computational program Plaxis was performed to estimate horizontal displacements. The numerical results estimate reasonably well the horizontal displacements measured in terms of the general shape of the soil yielding area. However, they do not reproduce in detail the geometry of the failure surface.

1. INTRODUCTION

The contribution of geogrids to the improvement of strength capacity and deformation reduction of foundation soils and artificial fills has been recognised within Geotechnical Engineering (e.g. Giroud 1986; Koerner 1986; Müller-Rochholz 2008). Moreover, construction methods can be more attractive economically, versatile in installation and less time consuming than traditional gravity or cantilever retaining walls. They have a good seismic response, for instance, no major damage has been found during the 2010 Chile earthquake of magnitude 8.8. Additionally, it has been found that geogrid reinforced soils can have a lesser carbon footprint than traditional retaining wall structures (O’Riordan *et al.*, 2011).

The study of active lateral earth pressure of compacted and reinforced fills against retaining structures is based mainly on plasticity theory, applying the Rankine stress states (Jones 1984, 1996). However, results of horizontal stresses measured by Berg *et al.* (1986) in retaining walls of 4.65 m y 6 m high with geogrid reinforced soil, were lower than that determined by the plasticity theory. Furthermore, the use of geogrids can significantly change the linear earth pressure distribution with depth. Differences with the linear distribution theory have also been shown by Pachomow *et al.* (2007), who have presented results from lateral earth pressure tests carried out on a 3.5 m high wall with a geogrid reinforced soil, comparing the results with that collected from a large database. These differences have been reflected, in part, in an updated version of the EBGeo (2009) recommendations, where the lateral earth pressure acting on a geogrid reinforced wall is lower than that proposed in the previous 1997 version.

There is scarce information available in the technical literature about experimental results of displacements and rotations of soil particles in geogrid reinforced walls under constant overburden σ . The little information available has been obtained numerically by means of the Method of Finite Element MFE (e.g. Pachomow *et al.* 2007). For that reason this experimental work focuses mainly on the analysis of the displacement variation of the soil retained behind a vertical wall. To this end, the image treatment technique PIV has been used. Finally, numerical analyses are carried out using the computing program Plaxis.

1.1. Experimental set-up

The equipment used and shown in Figure 1, has been designed and built by Ruiken *et al.* (2010a, 2010b, 2011). Additional information about the experimental set-up, Marienberg sand preparation and geogrid

characteristics can be found in Ruiz-Tagle and Villalobos (2011). They analyse the stress distribution results for the same tests, but they do not consider displacement and rotations as presented in this article.

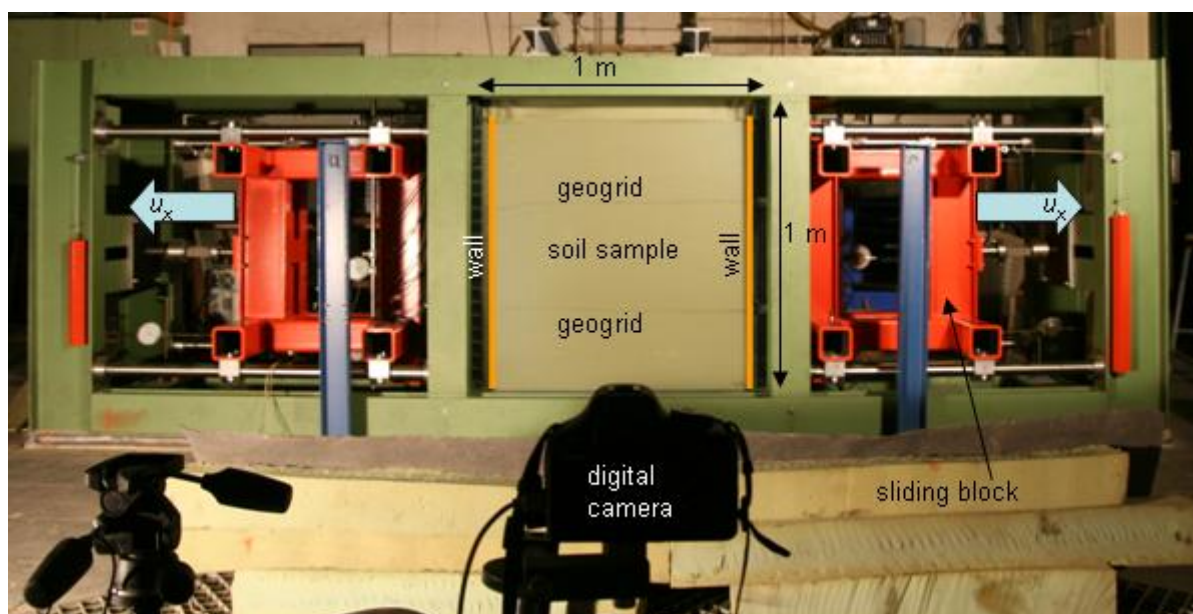


Figure 1: Experimental equipment for lateral earth pressure tests, showing the sample with two geogrids highlighted with black sand next to the glass window and the location of two digital cameras for PIV displacement analyses

The soil sample dimensions are 1 m high, 1 m long and 0.45 m wide (see Figure 1). There are two independent walls at each side which can be displaced manually by means of a block sliding along four horizontal bars. The active lateral earth pressure is obtained by the application of a block displacement u_x as shown in Figure 1. This set-up can model a scaled wall, but it can be also considered as a particular part of a wall as shown in a square in Figure 2.

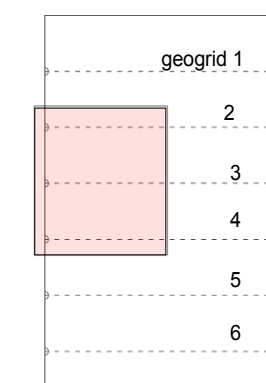


Figure 2: Retaining structure prototype with geogrid reinforced soil, showing the part studied in the laboratory

2. DETERMINATION OF THE SOIL DISPLACEMENTS

An optic method was used to study the soil displacement which is reinforced with geogrids. This method, known as PIV (Particle Image Velocimetry), allows the determination of movements and rotations of soil particles on a visible plane, usually behind a glass or a transparent material. A digital camera is required to capture every certain time intervals a focused and fixed frame, and in this form the movement of soil grains can be tracked. In this study sand grains move due to the active lateral earth pressure imposed by a sliding block inducing displacements u_x on a retaining wall in sequences of 0.1 mm until to reach a total u_x of 10 or 20 mm. The initial zero displacement allows the determination of the lateral earth pressure at rest. Ruiz-Tagle and Villalobos (2011) report that the active lateral earth pressure is completely developed

for a wall displacement u_x of 0.2 mm in a soil sample without reinforcement. This occurred when the measured horizontal stresses become similar to that calculated with the Rankine theory. Geogrid's positions were possible to observe with the assistance of dark sand, spread along the geogrid next to the window (see Figure 1 y 3). Figure 3 shows a detail of the soil settlement and geogrid distortion on the wall upper part.



Figure 3: Distortion detail of the geogrid and soil settlement

During the lateral earth pressure tests snapshots were taken to the whole sample and in some cases another camera was used to determine in more detail a particular area. In each test the location of the camera was the same, 0.7 m high from the floor to the objective centre allowed to capture the complete frontal area of the soil sample. Snapshots were taken for each interval of wall horizontal displacement $u_x = 0.1$ mm. Information about the PIV technique can be read in White *et al.* (2003) and White and Bolton (2004).

2.1 Results in soil without reinforcement

As a first stage in the study of active lateral earth pressure, measurements were performed without geogrid reinforcement. Figure 4 shows the displacement field and rotation variations of soil particles obtained after processing the PIV data for four levels of wall horizontal displacement $u_x = 0, 0.6, 3$ and 20 mm. The displacement and rotation fields are interpreted by means of displacement vectors and as clockwise or anticlockwise rotations, representing qualitative and relative parameters as shown by arrows and colours in Figure 4. For a wall displacement $u_x = 0.6$ mm, a slightly marked zone of soil can be hardly observed in movement. This establishes a difference with Ruiz-Tagle and Villalobos (2011) observation of active pressure development for $u_x = 0.2$ mm, from the stress distribution results. This difference might be related to the at rest pressure effect, which is higher than the active pressure, but without inducing displacements, *i.e.* it does not affect the displacement measurements.

For $u_x \geq 3$ mm the PIV results allow clear observation of the development of a zone where rotations are higher, defining a boundary or failure surface. According to plasticity theory a failure surface follows a straight line forming with the horizontal an angle $\theta = 45^\circ + \phi/2$. Since the sand was tested with a relative density of 93%, corresponding to a triaxial angle of friction $\phi_{tx} = 40^\circ$, results in $\theta = 65^\circ$. Some little adjustment can be done to correct the fact that a plane strain angle of friction ϕ_{ps} should be used. Thus, using $\phi_{ps} = 46^\circ$ according to Lee (1966), results in $\theta = 68^\circ$, still below $\theta = 75^\circ$, value obtained from the earth pressure test results shown in Figure 4. This means that a plastic equilibrium state or Rankine active state involves a larger area of plastified soil than that measured. It is worth noting that the failure surface tends to be vertical when reaches the upper part. This may be attributed to larger horizontal and vertical displacements (settlement) occurring in the upper part compared with the bottom part of the wall.

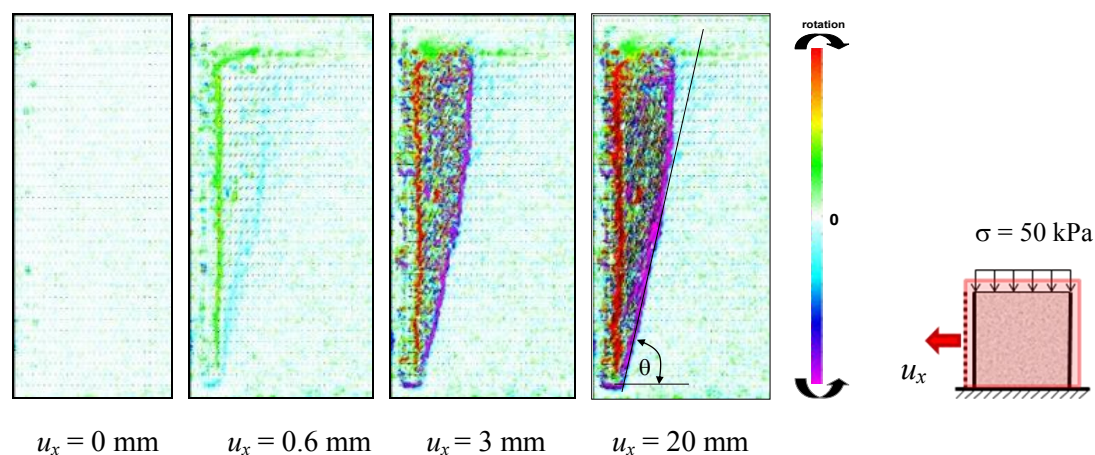


Figure 4: Rotation of soil particles for different wall displacements for an overburden of 50 kPa

2.2 Results in reinforced soil

The following results correspond to displacement and rotation fields of soil particles when geogrids were used as a reinforcement material in the soil behind a wall moved forward to generate an active earth pressure condition. The soil sample was reinforced with one, two, three and four geogrids, respectively. Inside the 1 m high sand sample, one geogrid was located in the middle, two geogrids were located from the top at 0.3 and 0.7 m, three geogrids at 0.2, 0.5 and 0.8 m and four geogrids at 0.1, 0.35, 0.65 and 0.9 m, respectively. Figure 5 shows the displacement field represented by vectors and rotation of particles represented by colours, after the wall has displaced 10 mm. It can be observed that geogrids restrain the failure surface to extend and involve more soil (see the horizontal black arrow on top to compare with the case without geogrid). The boundary between soil with and without movement, *i.e.* the failure surface, adopts a curve shape between geogrids. This change in shape also occurs in the horizontal stress distribution between geogrids as reported by Ruiz-Tagle and Villalobos (2011). They point out that the earth pressure reduction is related to the formation of stress arcs between geogrids. Then, this earth pressure reduction is taken in the form of a tension stress in the opposite direction by the geogrids.

Looking at the vector's directions in Figure 5, it is possible to observe that in general the vertical component predominates over the horizontal component of grain movement. The vertical movement of grains tends to be higher on the sample upper part and the horizontal component relative to the vertical tends to increase in grains next to the wall and closer to the wall base. Moreover, grains located closer to the wall undertake larger relative magnitude of movement. This relative movement of grains reduces with the distance from the wall towards the failure surface. Furthermore, the maximum rotations occur clockwise for soil grains next to the wall (red colour) and anticlockwise for soil grains in the failure surface (pink colour).

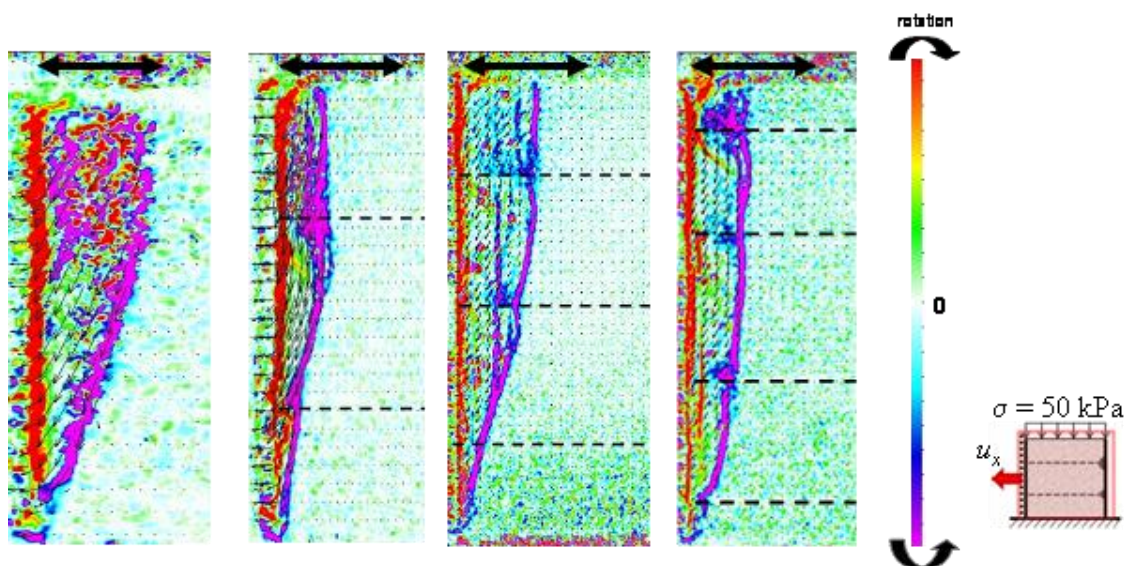


Figure 5: Displacement vectors and particle rotation in colours without and with two, three and four geogrids, overburden $\sigma = 50 \text{ kPa}$ and $u_x = 10 \text{ mm}$

In Figure 6, a detail of 0.3 m by 0.2 m located next to the wall and on the upper part, compares the cases without and with geogrid for $u_x = 10$ mm and an overburden $\sigma = 50$ kPa. The geogrid distortion due to settlement can be observed in Figure 6a. Horizontal displacement results obtained using the PIV technique with high resolution images (15 megapixels) are shown in Figure 6b for the cases without and with geogrid. The blue colour indicates the absence of displacements and the red colour represents the maximum values of horizontal displacement. These results also reveal that the geogrid reduces considerably the area of the soil yielding (red and yellowish zone). Furthermore, without the geogrid horizontal displacements vary uniformly from left to right (from red to green). Whereas with the geogrid, maximum horizontal displacements concentrate above the geogrid, hence, the gradual and uniform variation disappears.

In terms of displacement vectors, Figure 6c on the left shows the case without geogrid, where a unique and inclined failure surface develops. However, in the case with the upper geogrid (on the right hand side of Figure 6c and in terms of rotations), not only a main vertical failure surface is formed, but also another two almost parallel failure surfaces appear. Moreover, it is possible to observe the development of a failure line between the wall and the geogrid descending in 45° until it touches one of the parallel vertical failure surfaces. Despite the geogrid is not fixed to the wall, shear stresses are transmitted between the geogrid and the soil, which form a soil triangle above and below the failure line in 45° . The triangle above moves downwards, acting as an active wedge pushing the triangle below to the left. This follows observations pointed out by Ruiken *et al.* (2010b).

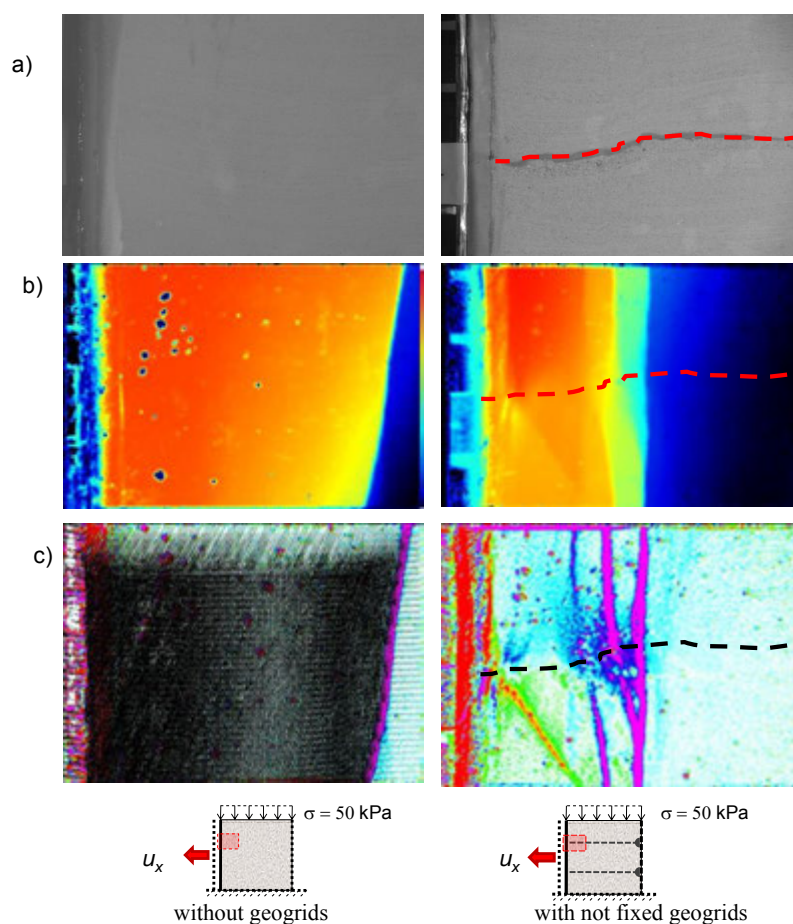


Figure 6: Details of the soil next and on top of the wall for $u_x = 10$ mm and $\sigma = 50$ kPa, a) distorted soil, b) horizontal displacements obtained with PIV and c) displacement vectors and particle rotation

2.3 Numerical analysis

The bi-dimensional finite element computing program Plaxis was used to study soil deformation. Modelling was performed for a plane strain condition with 15 nodes per element. It was considered that a medium mesh density with 98% accuracy was sufficient for the calculations. Fine and very fine meshes need higher computational resources and time to achieve a little accuracy increment. Boundary conditions were studied in order to simulate earth pressure laboratory tests. Soil-structure interaction effects were

taken into account, for the development of appropriate movements in the contact between the wall and the soil. However, in a finite element analysis, the use of continuous elements with displacement compatibility might not allow these movements in the soil. Consequently, when using the FEM a nodal compatibility condition has to be implemented to achieve coordinated movements among adjacent elements, *i.e.* without overlapping. To implement nodal compatibility Plaxis has the *interface* option for elements used in the modelling of contact surfaces, in this case between the wall and the soil. In this form, it was possible to modify the constitutive behaviour of contact surfaces (friction among different materials), and relative movements can be possible as well (sliding and separation).

Figure 7 shows a modelling result without using *interface*. Despite the active earth pressure applied, soil elements next to the wall do not settle, which is the opposite of that observed in the experiments (see Figure 3). This is due to the boundary conditions imposed in the modelling, *i.e.* a wall with too much friction does not allow the soil to slide and settle.

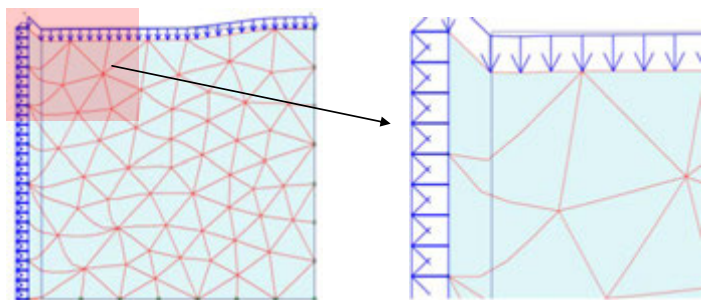


Figure 7: Deformed mesh without geogrid and not using interface

When a value of *interface* $R_{inter} = 1$ was used, the adherence effect between the soil and the wall disappear. However, this is not correct because a gap opens between the wall and the soil as shown in Figure 8, which does not reproduce the experimental results. Finally, in the computational simulations a value of $R_{inter} = 0.3$ was used in view of the better representation of the experimental interface angle of friction wall-soil of 2.6° . This value was also found to represent well the experimentally measured settlements. R_{inter} values lower than 0.3 are not recommended because the soil overlaps the wall, which is not real, resulting in deformation incompatibility.

The soil geotechnical parameter values used in the modelling are a dry unit weight $\gamma_d = 17.3 \text{ kN/m}^3$ and an angle of internal friction $\phi_{ix} = 40^\circ$. An elasticity modulus $E = 10^5 \text{ kPa}$ and a Poisson's ratio of 0.25 were assumed. The triaxial angle of internal friction was changed to 46° to take account of the plane strain condition according to Lee (1970). The geogrid stiffness value adopted was $EA = 2100 \text{ kN/m}$.

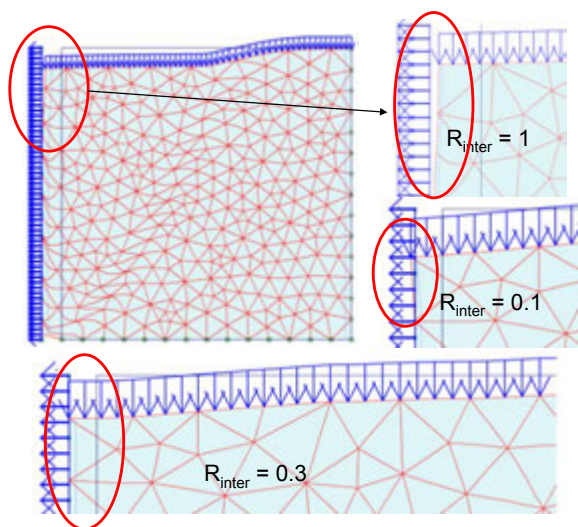


Figure 8: Deformed mesh for non reinforced soil, showing the boundary effect in the contact wall-soil in the upper part using interface $R_{inter} = 1, 0.3$ and 0.1

Figure 9a shows horizontal displacement results for the case without geogrids and Figure 9b shows the results for the case with two geogrids. It can be observed that the numerical results are able to simulate

the area reduction of soil yielding owing to the geogrid presence when active earth pressure is applied. Displacements arcs are also formed next to wall and between geogrids as observed in the experiments. When comparing Figure 9 with Figures 5 and 6 it can be noted that the numerical simulations are however not able to reproduce the steep slope of the failure surface at the upper part for both cases, without and with geogrids. This difference is probably due to small wall bending on the upper part, *i.e.* wall flexibility. Further research is needed to model numerically displacements and rotations caused by active earth pressure considering wall stiffness.

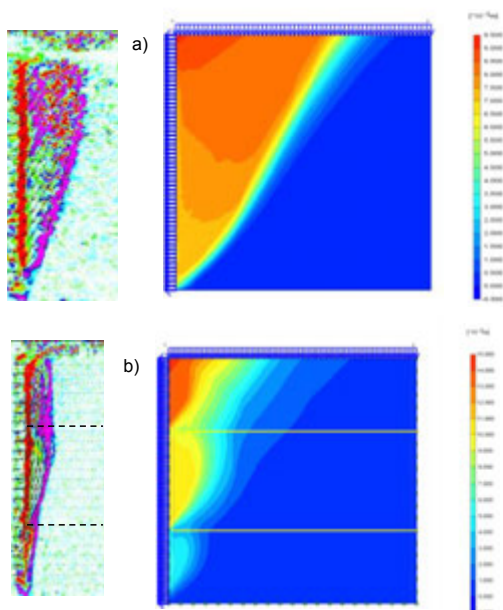


Figure 9: Soil horizontal displacements for $\sigma = 50$ kPa and $u_x = 10$ mm, a) without geogrid and b) with two geogrids (results from Figures 5 and 6 are shown for comparison)

3. CONCLUSIONS

Experimental results of soil particle displacements and rotations behind a retaining wall have been presented and analysed. This was possible by using the PIV technique which allows the definition of soil particle displacement and rotation fields. Analyses of relative displacements and rotations were performed qualitatively by means of displacement vectors and rotation directions, *i.e.* relative magnitudes were obtained without engineering units.

It can be concluded that the area of soil yielding is reduced significantly when geogrids are used. This reduction can reach up to half of the soil volume compared with the case without geogrid. This can explain the reduction of lateral earth pressure measured in the same equipment and reported by Ruiken *et al.* (2011) and Ruiz-Tagle and Villalobos (2011). This pressure reduction is transferred to the geogrids as a tension stress in the opposite direction. Thus, less lateral earth pressure is applied to the retaining structure because the volume of soil yielding is reduced.

A numerical analysis has also been presented using the computing program Plaxis. Initial numerical results are in a general agreement with the experimental results, in terms of the measured horizontal displacements without and with geogrids. However, there are differences related to the shape of the yielding zones. For instance, in the numerical results the yielding zone is wider and the slope of the failure surface on the upper part is much gentler than the almost vertical slope measured in the experiments. Further research is needed to improve numerical analysis.

4. ACKNOWLEDGEMENTS

The work presented in this paper was supported by the German Academic Interchange Service DAAD and the Catholic University of Concepción. The first author is grateful to the advice and supervision of Dipl.-Ing. Axel Ruiken and also appreciates the assistance of the Geotechnical Laboratory staff of the University RWTH-Aachen.

REFERENCES

- Berg, R.R., Bonaparte, R., Anderson, R.P. and Chouery, V.E. (1986). *Design, construction and performance of two geogrid reinforced soil retaining walls. Proceedings of the Third International Conference on Geotextiles, Vienna Austria, Vol. 2, 401-406*
- EBGEO (2009). *Empfehlungen für den Entwurf und die Berechnung von Erdkörpern mit Bewehrungen aus Geokunststoffen. Deutsche Gesellschaft für Geotechnik*
- Giroud, J.-P. (1986). *From geotextiles to geosynthetics: a revolution in Geotechnical Engineering. Proceedings of the Third International Conference on Geotextiles, Vienna Austria, Vol. 1, 1-18*
- Jones, C.J.F.P. (1996). *Earth reinforcement and soil structures. Thomas Telford*
- Jones, C.J.F.P. (1984). *Design and construction methods. Symposium on Polymer Grid Reinforcement in Civil Engineering. ICE London*
- Koerner, R.M. (1986). *Designing with Geosynthetics. Prentice-Hall*
- Lee, K. L. (1970). *Comparison of plane strain and triaxial test on sand. Journal of the Soil Mechanics and Foundation Division ASCE 96, No. SM3, 901-923*
- Müller-Rochholz, J. (2008). *Geokunststoffe im Erd- und Verkehrswegebau. Werner Verlag*
- O'Riordan, N., Nicholson, D., Hughes, L. and Phear, A. (2011). *Examining the carbon footprint and reducing the environmental impact of slope engineering options. Ground Engineering 44, No 2, 28-30*
- Pachomow, D., Vollmert, L. und Herold, A. (2007). *Der Ansatz des horizontalen Erddrucks auf die Front von KBE-Kronstruktionen. J. Geotechnik Sonderheft, 129-136*
- Ruiken, A., Ziegler, M., Vollmert, L. and Höhny, I. (2011). *Investigation of the compounded behavior of geogrid reinforced soil. Submitted to the Fifteenth European Conference on Soil Mechanics and Geotechnical Engineering, Athens*
- Ruiken, A., Ziegler, M., Vollmert, L. and Duzic, I. (2010a). *Recent findings about the confining effect of geogrids from large scale laboratory testing. 9th International Conference on Geosynthetics, Guarujá, Brazil*
- Ruiken, A., Ziegler, M., Ehrenberg, H. and Höhny, S. (2010b). *Determination of the soil confining effect of geogrids. XIVth Danube-European Conference on Geotechnical Engineering, Bratislava, Slovak Republic*
- Ruiz-Tagle, L. and Villalobos, F.A. (2011). *Experimental study of the lateral earth pressure on retaining structures in soils reinforced with geogrids. Submitted to Revista Ingeniería de Construcción*
- White, D. J., Take, W.A. and Bolton, M.D. (2003). *Soil deformation measurement using particle image velocimetry (PIV) and photogrammetry. Géotechnique 53, No. 7, 619-631*
- White, D. J. and Bolton, M.D. (2004). *Displacement and strain paths during plane-strain model pile installation in sand. Géotechnique 54, No. 6, 375-397*

Case studies on application of sandwich connection design for shored reinforced earth walls

John E. Sankey, PE, The Reinforced Earth Company, USA, jsankey@reinforcedearth.com
Susan Rafalko, The Reinforced Earth Company, USA, srafalko@reinforcedearth.com

ABSTRACT

Following a paper presented by the primary author at the 17th ICSMGE Conference in 2009, projects have been constructed using the concept presented on sandwich connection design for shored reinforced earth walls (SREW). SREW is a technology that combines the relative flexibility of a Mechanically Stabilized Earth (MSE) design in close proximity to an anchored or otherwise stabilized wall face with limited lateral space between. Rather than directly connecting the anchored wall face to the MSE section, a "Sandwich Connection" concept using overlapping reinforcements between the new wall fascia and existing stabilized face is employed. This paper presents case studies on three projects in the United States where the sandwich connection was used as a basis for design and construction. In two of the projects, connections were made to existing MSE walls where roadway widening was performed, and in a third project the connections were made to a conventional timber and H pile shored retaining wall. In all cases, the annular space between the existing and new retaining wall faces was less than 60% of the overall wall heights. The case studies will present several issues that were evaluated and resolved including selection and positioning of reinforcements and attachments, selection and installation of backfill, drainage, accommodating settlements and introducing seismic evaluations into design considerations using numerical modelling. A further finding in use of SREW near existing structures was the need to address extending upper reinforcing elements to prevent displacement and reflective cracking in the pavements supported by highway widening in the noted projects.

1. BACKGROUND

Mechanically stabilized earth (MSE) walls have been successfully used worldwide for over 40 years as retaining structures. The traditional concept for MSE walls is to establish a flat bench and then build the retaining structure upon it with a series of thin precast concrete fascia panels connected to steel or geosynthetic reinforcements combined in a matrix with compacted granular backfill as shown in Figure 1. Reinforcement lengths are typically a minimum of 2 meters long or 70% of the height of the wall, whichever is greater, with additional length added for stability against sliding, overturning or global stability. The density or number of reinforcements is developed based on pullout and tensile requirements required for internal stability.

The use of MSE walls has developed hand-in-hand with transportation-related projects where sufficient space is available to accommodate the full reinforced volume. More recently, however, there is a growing trend in the highway market for the construction of narrow-width walls that front either steep terrain or existing retaining walls where roadway widening is necessary. The resulting expanded structure is commonly referred to as a Shored Reinforced Earth Wall (SREW™).

Originally, SREW walls were constructed by connecting reinforcements directly from a shored cut face or existing retaining wall face to a new facing built along an expanded alignment as shown in Figure 2. The annular space between the original face and new face is typically filled with free-draining gravel alternated with the reinforcement connections. Such direct connection methods have offered an immediate solution to narrow space conditions, but at the same time reduces inherent flexibility of the combined wall system, which is a commonly desired property of MSE technology.

The purpose of this paper is to address a composite SREW system that provides overlapping reinforcements, where the annular space is not quite wide enough to accommodate full length MSE wall reinforcement and at the same time is still of adequate length to achieve overlapping of reinforcements that take advantage of pullout resistance beyond the active zone. A brief discussion of the overlapping or "sandwich" version of SREW technology will be described based upon design constraints, numerical modeling results and constructability considerations. The technology overview will then be followed with three case studies that demonstrate this innovative and effective approach to achieving internal stability while maintaining the flexibility of the combined wall system.

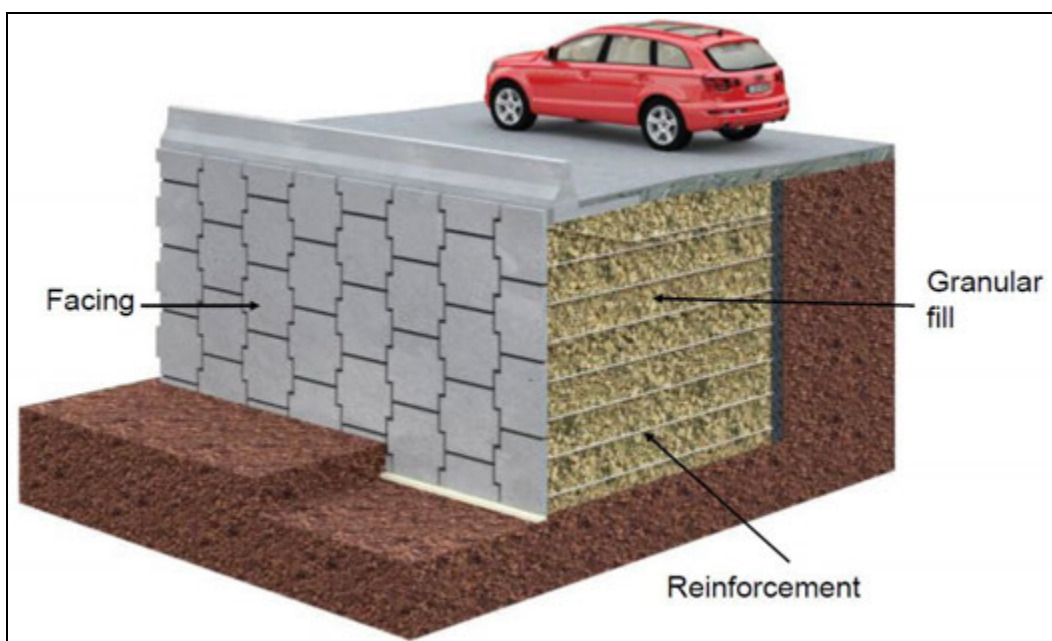


Figure 1: Typical section of a MSE wall.

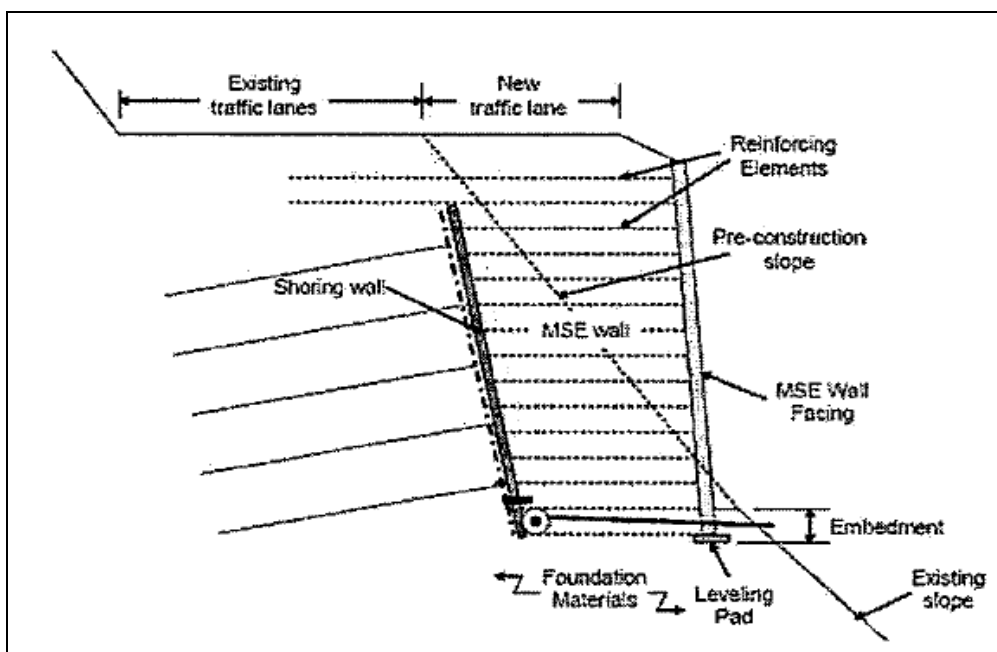


Figure 2: Generalized cross-section of shored MSE wall (Morrison et al., 2006)

2. TECHNOLOGY OVERVIEW

2.1. Design

For steep terrains in the United States, the basis for SREW design was developed using guidelines found in FHWA –CFL/TD-06-001 for Shored Mechanically Stabilized Walls (Morrison, et al, 2006). The main advantage was that the original shored face or MSE wall could be used to support the greater long-term lateral earth pressures as intended and any structural configuration added beyond only had to support the annular space. There were a number of considerations provided in the FHWA guidelines as follows:

- The wall needs to have a design life that matches the adjacent shored face or MSE wall.
- Drainage within the annular space needs to be addressed to make sure no additional lateral pressures due to hydrostatic conditions are incurred.

- The minimum length of the annular space needs to be $0.3H$ or 1.5 m, whichever is greater, where H is the height of the wall system.
- The upper two levels of reinforcements are recommended to extend to a length of at least $0.6H$ and at the same time to no less than a minimum of 1.5 m behind the existing shored or original MSE wall. The longer reinforcement will prevent the tendency of reflective cracking at the top of the wall near the interface of the adjacent added section. Such reflective cracking occurs where displacements in the respective wall volumes are dissimilar, and could in particular be an issue where roadway pavements are located.
- The guidelines are valid for static load conditions where seismic horizontal accelerations are less than $0.5g$; otherwise more detailed analyses are needed in more seismically active areas.

The FHWA guidelines go on to address critical failure surfaces for inextensible (steel) and extensible (geosynthetic) reinforcements, as well as other design criteria related to both internal and external stability. The FHWA guidelines are purposely generic to allow design users to develop more specific systems as project needs dictate. Specific elements related to connection of reinforcements between the original shored or MSE faces to the new expanded face are particularly left undefined.

The Reinforced Earth Company (RECO) first addressed consideration of SREW applications in South Africa as far back as 2001 (Smith, et al, 2001). The project in South Africa was located in the Eastern Cape Province and involved wire faced MSE walls with steel reinforcements attached directly to soil nails at the back cut face (Figure 3). The slope stability program Talren was used to evaluate the stability of the structure including loading placed on the soil nails by the adjoining MSE wall section. Not only did the composite wall system allow widening of the existing roadway as intended, it also improved the marginally stable slope that existed along the roadway alignment before the widening.

Several variations of SREW systems have since been identified, mostly tailored to the prevailing site conditions and space restrictions encountered. A common element of the systems has been the direct attachment of reinforcements to the shored wall or original MSE wall backface. The disadvantage of such an approach is trying line up reinforcements to the existing backface attachment locations, which not only limits the flexibility of the overall SREW section, but also requires more survey and labor preparation to line up connections. To allow greater flexibility, say in the case of settlements between new and original wall sections, a sandwich connection system was introduced to allow overlapping of front face and backface reinforcements in the SREW system (Tavakolian and Sankey, 2009). The sandwich connection consists of attaching short lengths of steel reinforcements anchored into the backface and overlapping these within the narrow annular space with short steel reinforcements attached to the new precast panel front face. Numerical modelling was used to evaluate and study the behaviour of the composite wall system.

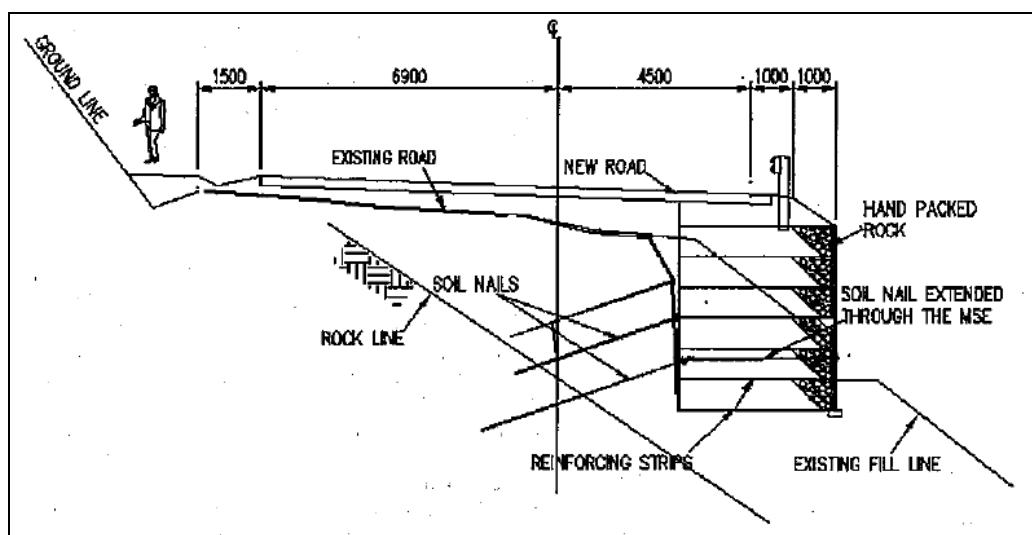


Figure 3: Cross-section of Kei Cutting wall, South Africa (Smith, et al., 2001)

2.2. Numerical Modelling

The use of a sandwich connection can be most effectively addressed in SREW designs where the available space between new face and shored or existing wall face is 30 to 60 percent of the wall height. The shorter space for reinforcements in the new wall section needs to be verified for internal stability

through adequate resistance for pullout and tensile capacity. Reinforcements in the more narrow space cannot as readily mobilize the full capacity of the reinforcements due to lengths being less than standard MSE design. By using the sandwich connection rather than direct connections, an increase in the number of reinforcements is needed at all levels of the wall height to obtain the needed pullout resistance. The increase in the number of reinforcements becomes more pronounced as the resistant zone beyond the active failure wedge decreases. A concept of the sandwich connection is shown in Figure 4.

Numerical modelling by use of FLAC has been performed to demonstrate that secondary reinforcements on the backside of the SREW system reduce the stress and strain from the failure wedge. In turn the tensile forces in the primary reinforcements connected to the front face of the SREW system are reduced as a result of the interaction with the secondary reinforcements (Figure 5). Additional FLAC modelling provided in the paper by Tavakolian and Sankey (2009) demonstrated that not only are the tensile forces redistributed between the primary and secondary reinforcements, but the resulting displacements are effectively controlled when using inextensible steel elements as the reinforcements.

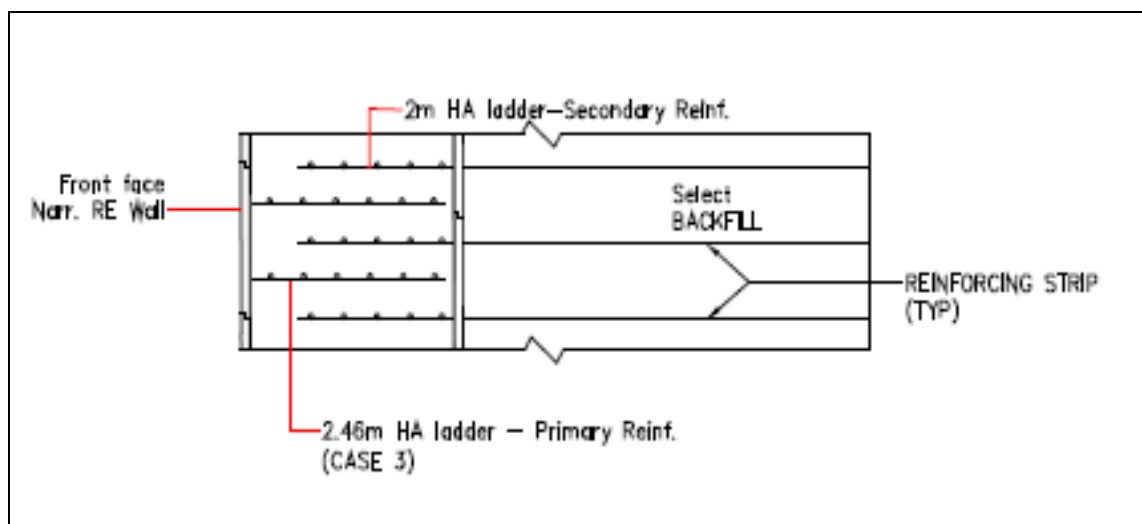


Figure 4: Sandwich connection concept

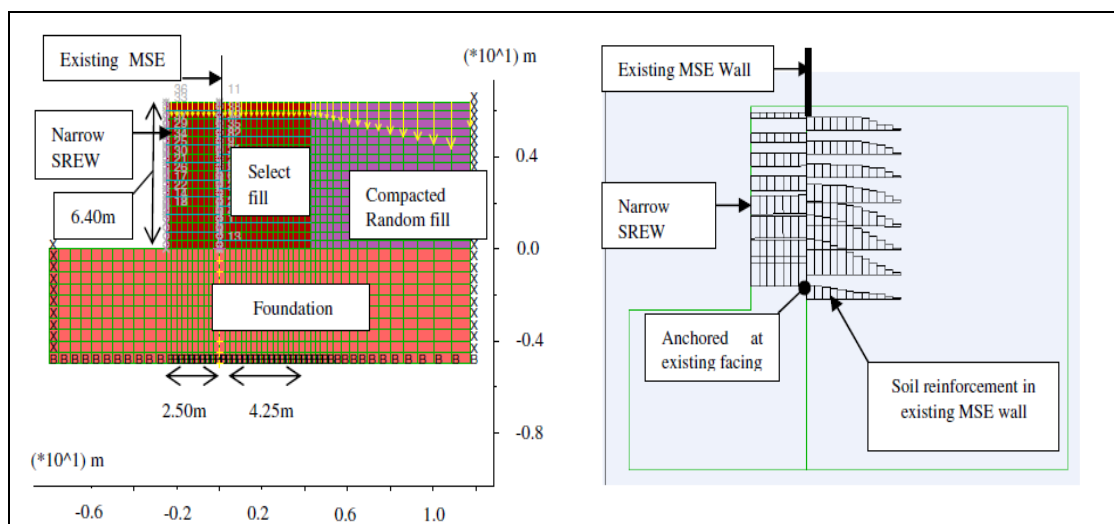


Figure 5: Typical FLAC model and distribution of tensile forces (Tavakolian and Sankey, 2009)

2.3. Constructability

In addition to the selection of steel reinforcements as an important element in the performance of the SREW system, there is the equally important consideration of the connections themselves. The primary reinforcements of the sandwich connection can be readily attached to new facing in a manner similar to MSE walls, however, the positive attachment of the secondary reinforcements requires more careful consideration of the backface. Where the backface consists of a shored cut face composed of soil nails, the reinforcements may be positively connected to the nail head by use of an eye bolt fit to the thread of

the nail as shown in Figure 6 (TerraNail™). Alternatively, where the backface is an existing concrete face such as a MSE wall, steel angles may be anchored to the concrete in place by epoxy or expansion anchors then a bolted connection is made to the steel reinforcements. Obviously, the capacity of the soil nail or concrete face must be understood as part of the design for the SREW system.

The limited annular space requires that the SREW construction be done in a stepwise fashion. Aggregate backfill is commonly recommended for the annular space since it is readily placed and densified, while at the same time providing effective drainage. Overall, use of the sandwich connection and gravel backfill makes construction of the SREW system similar to the ease of building an independent MSE wall with the same inherent flexibility. Three case examples from projects located in the United States are provided as the remaining basis for this paper to further demonstrate the practical use of the sandwich connection.

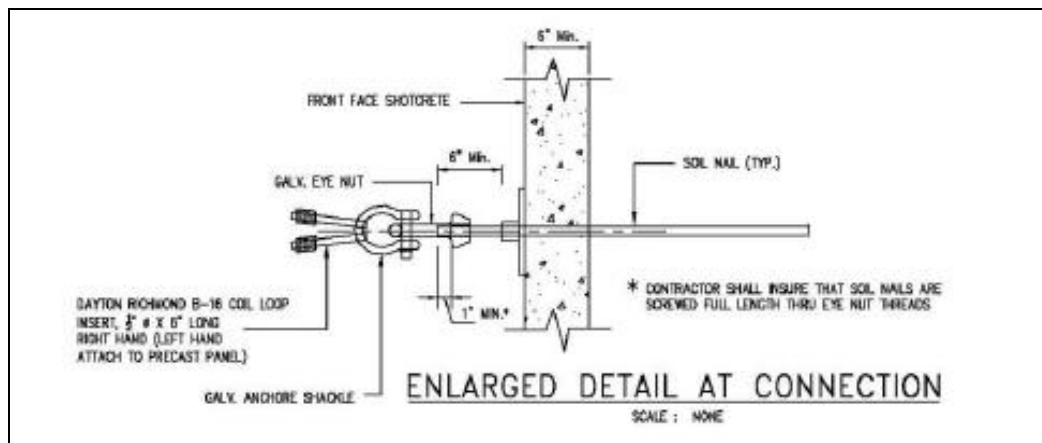


Figure 6: TerraNail connection at soil nail

3. CASE EXAMPLES

3.1. 148th Street Bridge, Omaha, Nebraska (USA)

The first example demonstrating use of the sandwich connection on a project in the USA was actually a composite design that incorporated elements of both MSE back-to-back wall and SREW designs. The project involved installation of walls immediately adjacent to two abutments where cuts were made and retained by steel sheet pile shoring. Though the retained cut faces only extended approximately 8 m beyond the outward edges of the abutments, space between the sheetpiling and new MSE face alignment was approximately 3.5 to 4.5 m which resulted in an equivalent annular space of $0.4H$ (where H is the height of the MSE wall). Beyond the limits of the shored wall, the MSE wall alignment had sufficient space to extend reinforcements to satisfy the minimum $0.7H$ length required in AASHTO national codes (2010).

The presence of sheetpiling prevented the direct attachment of connections to the backface cut, since it was considered inadvisable to weld connections directly on to the steel facing. Instead, free standing wire mesh was installed against the sheetpiling and steel hairpin connections were attached at regular intervals to short length ribbed steel strips. At the front face, cruciform MSE panels nominally measuring 1.5 m by 1.5 m and 140mm thick had similar short length ribbed steel strip attachments which overlapped the backface strips as shown in Figure 7a. Strictly speaking, the design of the resulting bin wall is very similar to standard back-to-back MSE walls constructed in the United States. However, the limited annular space does not comply with FHWA practice found in Publication No. NHI-09-083, so the use of sandwich connection evaluations in a SREW application was used instead to justify the design.

The SREW portions of the construction were readily carried out as shown in Figure 7b. Note that the upper portions of the wall were able to accommodate 2 rows of reinforcements to a length of $0.6H$ and drainage collection at the top was provided to reduce potential for hydrostatic pressures in storm events. In standard MSE wall applications, drainage would normally be adequately handled by the open joint spacing in the MSE fascia panels and large reinforced volume composed of freely draining granular soils. However, greater attention to drainage needs to be considered where a confined backface may inhibit free drainage away from the reinforced volume.

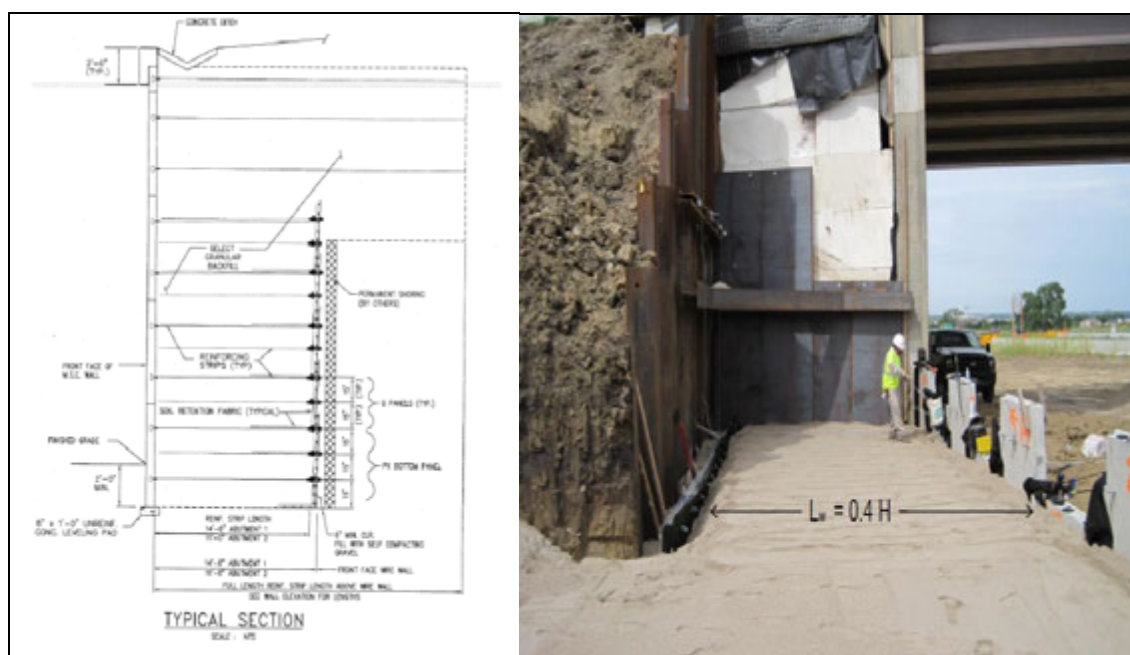


Figure 7: 148th Street, Nebraska (a) typical section and (b) during construction

3.2. Interstate 895 Connector, Richmond, Virginia (USA)

The Interstate 895 project was actually the first stand alone use of the sandwich connection in the USA. The intention of the project was to add a new lane to the existing roadway alignment. Existing return walls to abutments for a bridge were of MSE construction in place for approximately 10 years. The addition of the new lane presented geometry limitations to project whereby wall heights needed to be approximately 10 m and the available horizontal space was only 3.5 m (or 0.35H). Knowledge regarding the original MSE wall face and the space limitations for the road widening made this portion of the project ideal for the application of a SREW sandwich connection.

Primary and secondary reinforcements in the case of this project used high adherence narrow steel ladders. The selection of narrow ladders was considered over ribbed steel strips since greater pullout capacity could be realized to minimize the number of reinforcements. The secondary or backface reinforcements were connected into the existing MSE fascia panels which required the location of existing reinforcements to be avoided and was the reason that knowledge of the original wall design was necessary. Reinforcements were attached to the existing wall using field-installed epoxy anchors and steel clip angles as shown on the section view in Figure 8a.

Though vertical overlap between secondary reinforcements at the backface and primary reinforcements at the front face is commonly thought to be needed; a horizontal overlap is just as satisfactory and allows ease of placement as shown in Figure 8b. The main advantage of a horizontal overlap is that construction may proceed more efficiently with uniform layers of compacted backfill. Field connections to the existing MSE wall backface have to be located by survey at the start of construction so that primary reinforcements may be properly overlapped with the secondary reinforcements.

Construction proceeded quickly as shown in Figure 9 though much of the work was performed in a confined space limiting access by equipment. Heavy construction equipment should be limited anyway, since final fascia alignment may be affected by loading the SREW volume before sufficient overburden is installed for pullout resistance of reinforcements. The upper approximately 1 m portion of the existing MSE wall was removed to allow full length extension of the top 2 layers of reinforcements to 0.6 H from the newly installed fascia. The existing MSE wall and SREW sections ultimately function independently, maintaining overall flexibility and allowing the SREW section to settle as needed during construction.

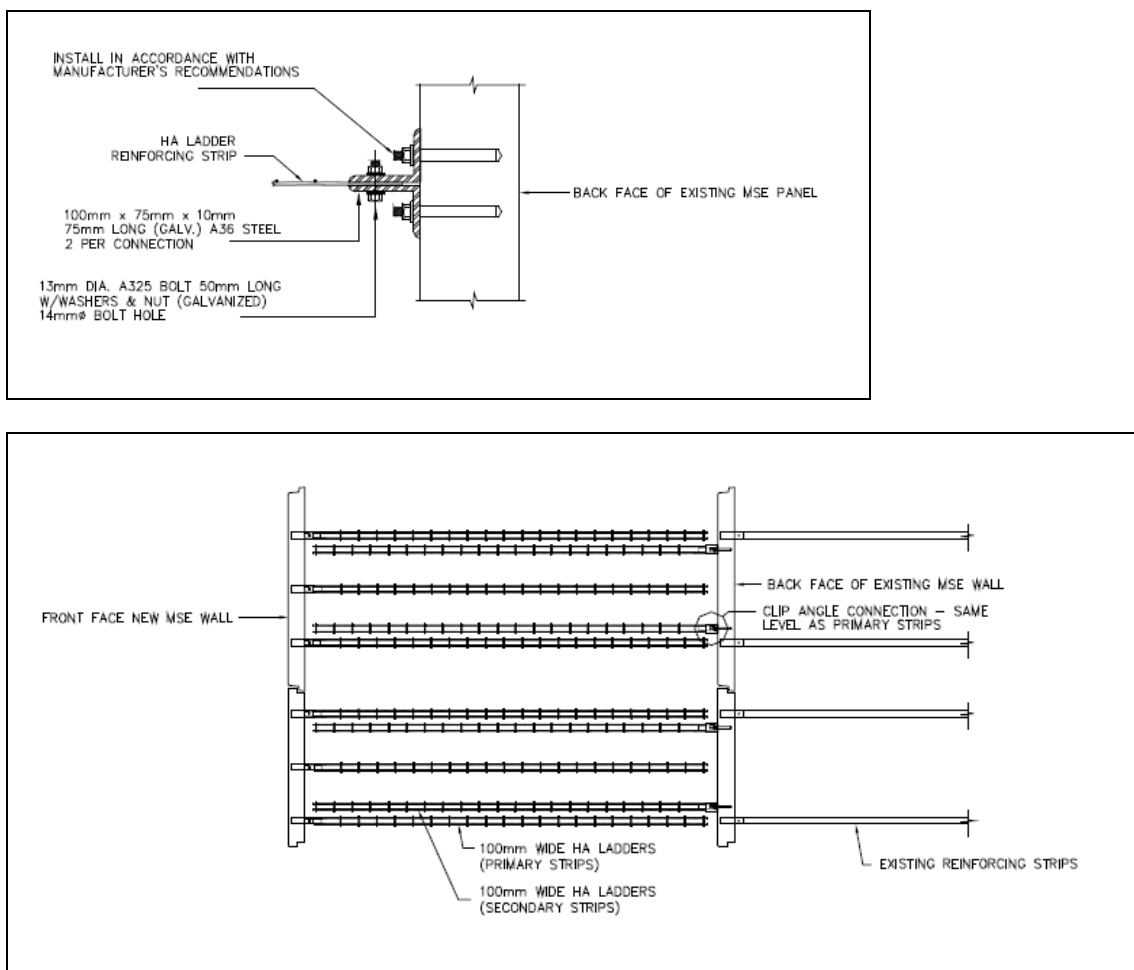


Figure 8: Details showing (a) clip angle connection to existing MSE panels and (b) plan view of soil reinforcement layout (Tavakolian and Grien, 2011)

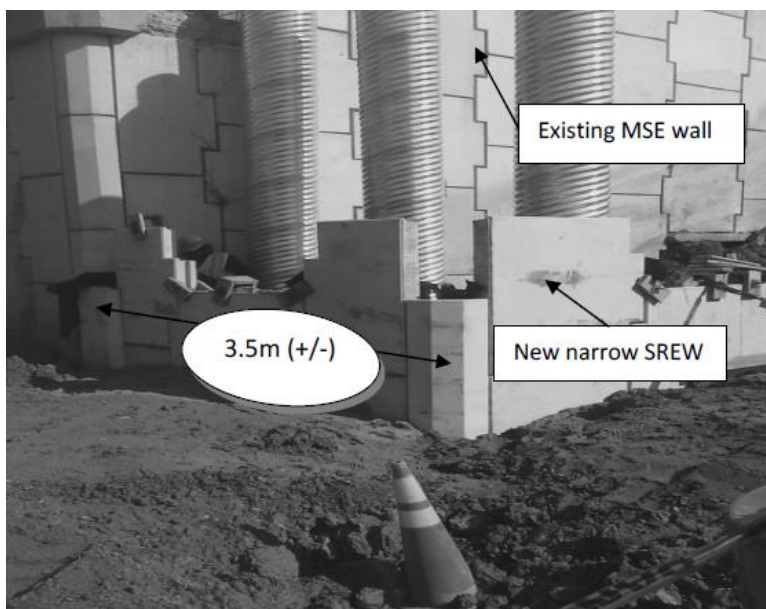


Figure 9: Construction of new section for Interstate 895 Connector, Virginia (Tavakolian and Grien, 2011)

3.3. Interstate 215 On-Ramp to Interstate 15, Utah (USA)

Widening of an existing steel grid reinforced MSE wall on Interstate 215 in Utah not only required consideration for installing a SREW system with sandwich connection, but also needed to consider high seismic loading. Again, knowledge of the existing MSE wall construction and use of steel narrow ladders in the sandwich connection was considered for the project. The orientation of the narrow ladders for the project is shown on Figure 10. The width to height ratio for the SREW section varied from 0.35H to 0.55H with wall heights up to 11m.

Unique features of the project included design for seismic acceleration of 0.4g. Both the static and seismic design calculations for the wall were performed using Load Resistance Factor Design methods found in AASHTO codes for MSE walls. The seismic design was further substantiated by a FLAC numerical analysis. The greater pullout capacity afforded by the narrow ladders allowed for an decreased number of reinforcements and increased resistance in the SREW section to withstand dynamic loading.

Other features of the design included incorporating an inlet within the SREW section. Though incorporating utilities in the SREW section is usually discouraged, the limited length of wall where SREW was necessary needed to continue utility alignments along the greater portion of the overall road widening project. Steel angles were used to allow offsets of the primary reinforcements near the inlet and still provide satisfactory overlap to the secondary reinforcements connected to the backside of the SREW section. It is noted that joining fascia with steel angles does limit its flexibility, so such accommodation to utilities does need to be kept limited.

A final unique feature of the project was the lack of space at the top of the SREW section that prevented two levels of full length (0.6H) reinforcements being installed as normally recommended. In this case, the upper level of reinforcements in the SREW section were connected from the back of the new fascia to the front of the existing fascia using anchored clip angles, thereby providing continuity across the annular space to the existing MSE wall volume. Construction of the SREW section with enhancements was readily and successfully performed during night time hours to accommodate local traffic conditions.

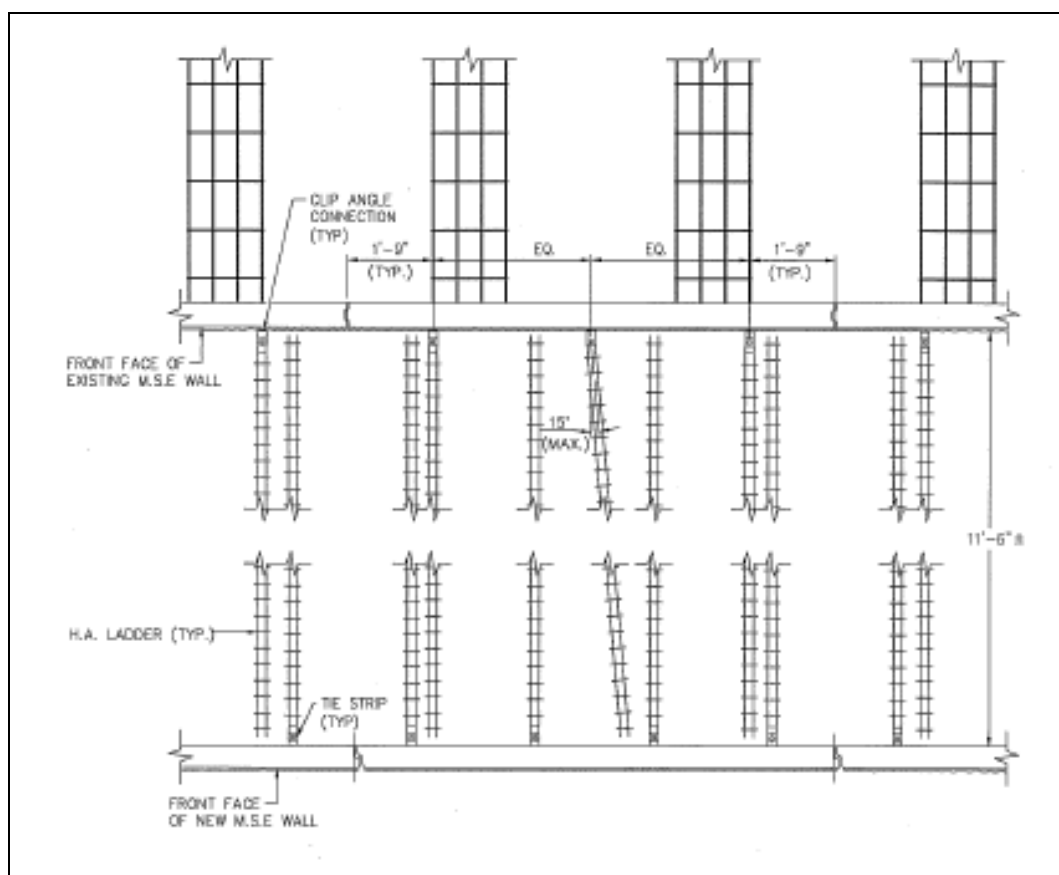


Figure 10: Layout of SREW section fronting steel grid-reinforced MSE wall

4. CONCLUSIONS

The construction of the SREW system using the sandwich connection demonstrates that it is a viable approach to building in limited spaces while still maintaining the flexibility that is normally associated with MSE walls. Design methods used to define the failure wedge, and corresponding numerical analyses, have transitioned into practical designs that can now be implemented in construction. The introduction of horizontal overlapping of reinforcements and the use of high adherence steel narrow ladders substantially reduces the horizontal stress and accommodates pullout resistance in the narrow SREW section. The contribution of the secondary reinforcements extending from the backface is influenced by several factors including the distance between the two faces, composition of the original wall or cut face, overlap length between primary and secondary reinforcements, vertical and horizontal spacing between reinforcements, type of reinforcement and relative geometry of the original and SREW portions of the wall.

It is noted that although the case examples given in this paper concentrated on sheetpile or MSE walls at the backface, it is possible to consider a similar sandwich connection for other stable retaining wall or anchored facings. Knowledge of the existing retaining wall or anchor construction is a necessary part in assuring the integrity of the SREW section. It is anticipated that the use of the sandwich connection, and indeed the larger use of the SREW system as a whole, will gain wider acceptance particularly with anchored faces. Attachments such as Terranail can be fit over anchor heads for soil or rock anchors, which in turn may be used to support precast concrete fascia meeting the increasing aesthetic demands along highways. On-going development and application of the SREW system is sure to evolve over time.

REFERENCES

AASHTO LRFD Bridge Design Specifications, AASHTO, 2010 (Fifth Edition)

Morrison, K.F., Harrison, F., Collin, J.G., Dodds, A. and Arndt, B., 2006, Shored Mechanically Stabilized Earth (SMSE) Wall Systems Design Guidelines. Federal Highway Administration Report, FHWA-CFL/TD-06-001.

Smith, A.C.S., Price, G.V. and Muhajer, A., 2001, Innovative solution for a Kei Cutting Problem. Landmarks in Earth Reinforcement, Fukuoka, Japan: 697-702.

Tavakolian, R. and Grien, M., 2011, Narrow Shored Reinforced Earth Wall with Friction-Based Reinforcing Strip Connection as an Innovative Solution to Expand Urban Highways. Geo-Frontiers 2011, ASCE, Dallas, Texas, USA:3469-3477.

Tavakolian, R. and Sankey, J., 2009, Sandwich connection for shored reinforced earth walls. 17th ISSMGE Conference, Alexandria, Egypt: 1441-1444.

Study of shored mse walls (smse) in high earthquake

Kim Truong, PE, ktruong@reinforcedearth.com
 John Sankey, PE, ASCE GeoInstitute, jsankey@reinforcedearth.com
 James Sullivan, PE

ABSTRACT

Widening of existing roadways supported by conventional Mechanically Stabilized Earth (MSE) can be readily performed when available space offers more than 0.7 of the aspect ratio. However, in rugged steep terrains such widening is a challenge for conventional wall installations due to space, safety and cost limitations. The preferred solution to the challenge of limited space is consideration of Shored MSE walls (SMSE), since it can accommodate very low aspect ratios. Although the US Federal Highway Administration had provided a comprehensive study and guideline on SMSE wall technology, its behaviour during a seismic event is virtually unknown. This paper will study the SREW wall system (an SMSE wall system developed by the Reinforced Earth Company) using a) the direct connection type and b) the sandwich connection type. Supported by numerical analyses, it will provide a better understanding of the behavior of SREW during and after a seismic event, leading to the best choice of connections when dealing with moderate to high seismic conditions.

1. DESCRIPTION OF SHORED REINFORCED EARTH WALLS (SREW)

1.1. TYPES OF SREW WALLS CONSIDERED IN THIS STUDY.

The most common SREW systems front existing MSE walls (SREW Type A), soil nail shoring (SREW Type B) or on top of buttresses (SREW Type C).

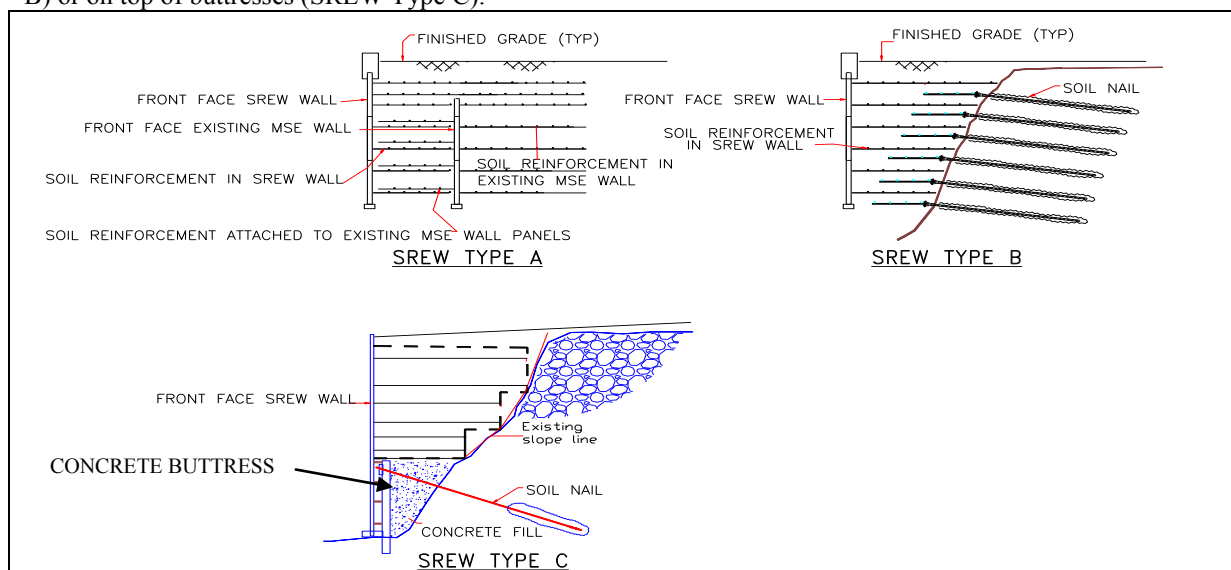


Figure 1: Common SREW walls configurations: Type A for SREW in front of a MSE wall, Type B for SREW in front of existing soil nail shoring, Type C SREW fronting a concrete fill buttress.

The soil reinforcement used for the evaluation in this study is high adherence ribbed steel strips measuring 50mm x 4mm in cross section. The facing is constituted of precast concrete panels 140mm thick.

1.2. TYPES OF REINFORCEMENT CONNECTIONS

This study focuses on SREW Type A only. Although Type B SREWs have been designed and built, it will not be considered in this study. Figure 2 shows the current types of steel strip connections for SREW: 1) direct connection where the soil reinforcements connect the new and existing walls and 2) sandwich connection where the primary soil reinforcement from the new wall and those secondary extended from the front face of the existing wall are separate and overlap each other.

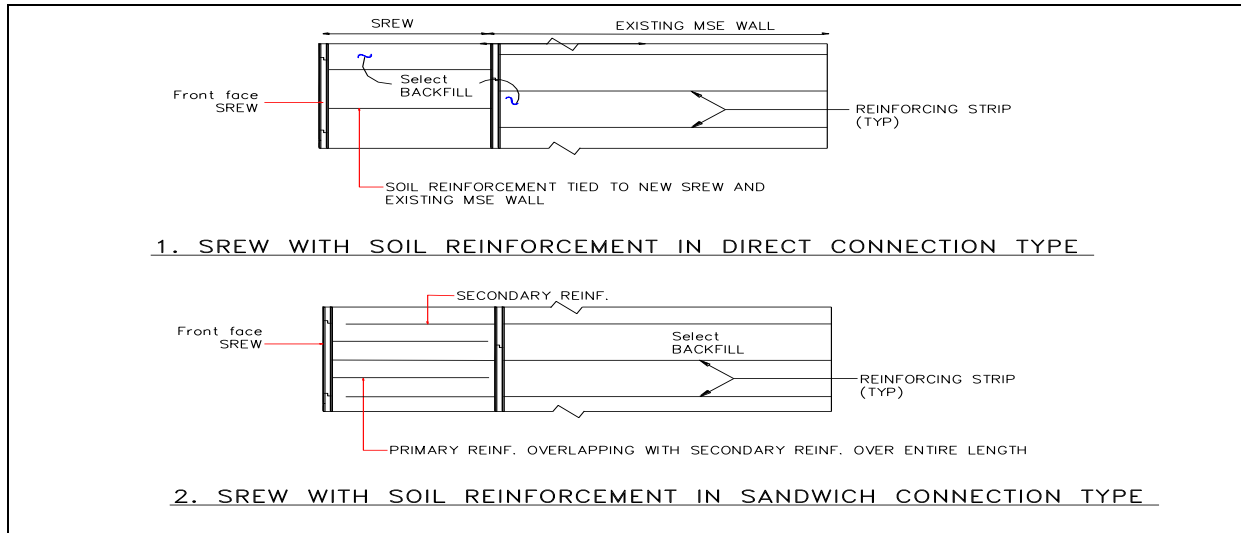


Figure2 :Two types of soil reinforcements configuration within the SREW wall: 1) DIRECT connection and 2) SANDWICH connection

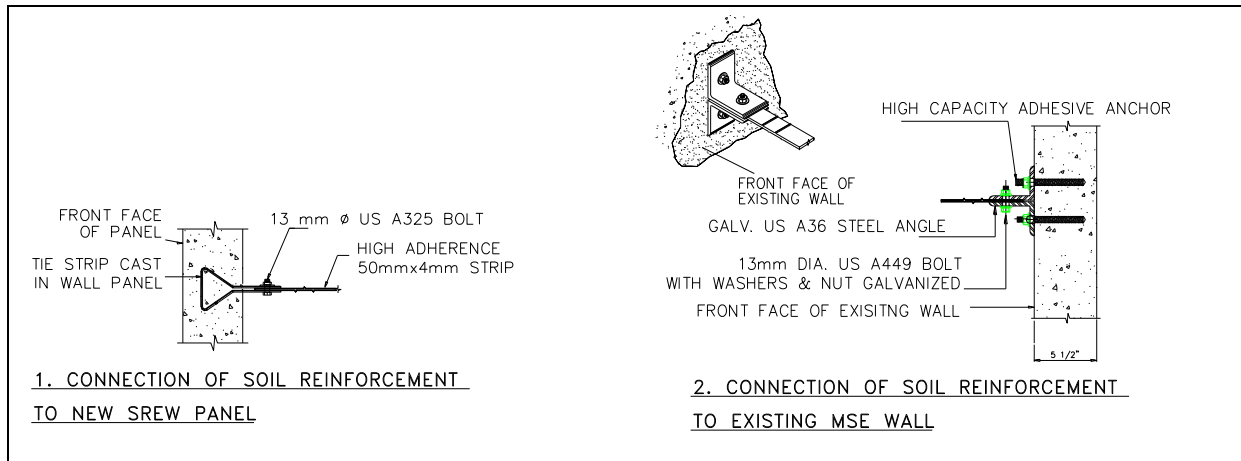


Figure3 : left to right : 1) connection of steel strips to facing of SREW; 2) connection of strips to facing of existing MSE wall

2. DESCRIPTION OF THE NUMERICAL ANALYSIS MODEL

2.1. Geometry of the model.

The aspect ratio (width to height) of a SREW ranges from 0.3H minimum to 0.6H maximum, as per the U.S.Federal Highway Administration Manual CFL/TD-06-001 (2006). This study focuses on SREW with aspect ratios of 0.3H and 0.4H. For each case, 2 models were created: one with the direct connection in the SREW and one with the sandwich connection.

Numerical analyses used the software FLAC (Fast Lagrangian Analysis of Continua). The model created comprises:

- An existing MSE wall 7.5m high with 5.3m long steel soil reinforcement, reinforcement vertical spacing set at 0.75m typically, reinforcement horizontal spacing at 0.6m for the lowest layer and 0.75m for the remainder.
- A SREW in front of the MSE wall described above, 9m high with steel reinforcement length of 3.6m long for an aspect ratio of 0.4H . The reinforcement vertical and horizontal spacings are typically 0.75m. The top 2 levels of reinforcement are extended past the facing of the existing MSE wall to prevent reflective tension cracks in the roadway at the top of wall .

An identical model is created for a SREW with an aspect ratio of 0.3H with 2.70m long reinforcements. The horizontal spacing of soil reinforcements are 0.5m on centers.

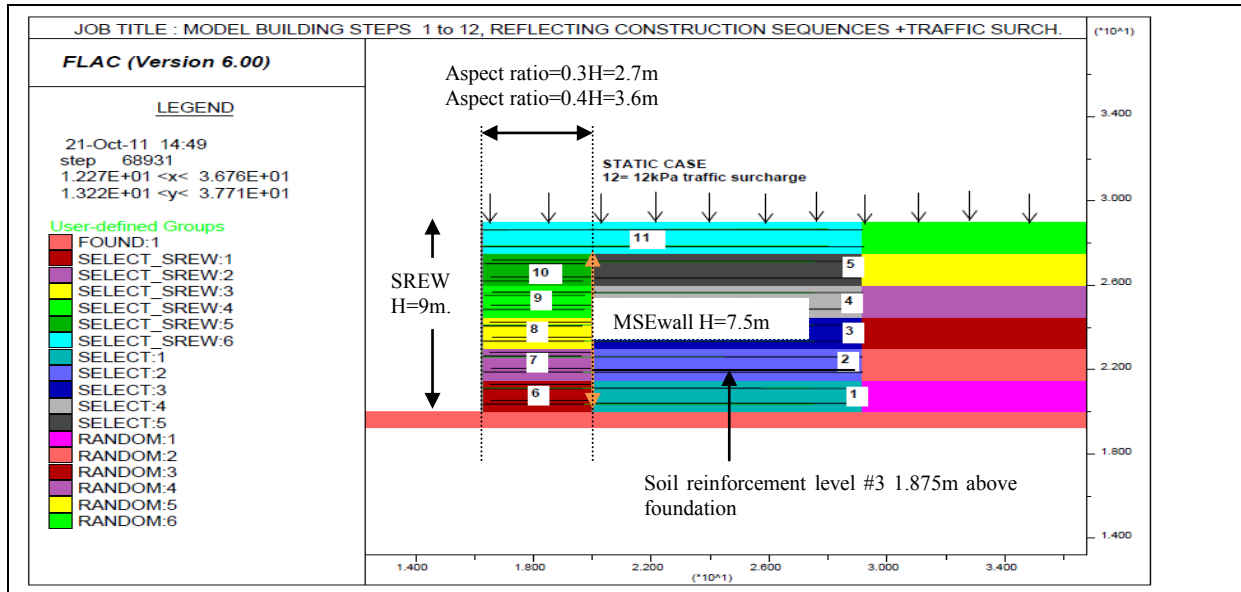


Figure 4:FLAC model- construction sequences. Notice the location of soil reinforcement level #3 in existing MSE wall where history of tensile force was recorded

2.2. Properties of materials

In high seismic areas, the quality of the random fill behind the existing MSE wall and that of the foundation soil must be investigated and identified, as their properties contribute greatly to the deformation and behaviour of the new SREW wall.

Table 1 :Properties of fills

Parameters	MSE fill	Random fill behind MSE volume	SREW fill	Foundation Soil
Modulus of Elasticity	60 MPa	40 MPa	60 MPa	463 MPa
Poisson's ratio	0.33	0.33	0.33	0.29
Internal Friction Angle	34°	30°	40°	NA
Dilation angle	4°	0	4°	NA
G Shear modulus in static phase	22.6 MPa	15 MPa	22.6 MPa	180 MPa
Constitutive model in static phase	Mohr Coulomb	Mohr Coulomb	Mohr Coulomb	Elastic
Constitutive model in dynamic phase	UBCHYST	UBCHYST	UBCHYST	UBCHYST
f^* = Apparent coefficient of friction at top surface	2.00	NA	2.00	NA
f^* at 6m depth	0.67	NA	0.67	NA
Confining pressure	120kPa	NA	120kPa	NA
Density	2040kg/m ³	1950kg/m ³	2000kg/m ³	2200kg/m ³

The foundation selected was a firm ground, defined as very dense material with shear wave velocity between 360m/s to 760m/s.

Table 2 :Properties of concrete facing

Modulus of Elasticity	2.5 x 10 ⁴ MPa
Poisson's ratio	0.20
Thickness	140mm
Density	2500kg/m ³

Table 3 :Properties of steel strips (as soil reinforcement)

Modulus of Elasticity	21.5 x 10 ³ MPa
Poisson's ratio	0.30
Section Area at time zero (50mm x 4mm)	200mm ²
Section Area at end of 75 year service life	130mm ²
Yield Strength	440 MPa
Strain at rupture	0.20
Allowable tensile capacity for service load	32kN/strip
Allowable tensile capacity for seismic load	43kN/strip
f* =Apparent coefficient of friction at top surface	2.00
f* at 6m depth	0.67
Confining pressure	120kPa
Density	8100kg/m ³

Table 4 :Properties of interface between concrete facing and select fill material

Modulus of Elasticity	2.5 x 10 ⁴ MPa
Poisson's ratio	0.20
Thickness	140mm
Density	2500kg/m ³

2.3. Constitutive models.

The foundation soil was brought to equilibrium using a static model basis. Using the Mohr-Coulomb constitutive model, the walls in the model were then built in steps of 1.5m until the SREW was entirely constructed. The steps used are shown on Figure 4. A traffic surcharge of 12kPa was applied as a final step over the entire top grade. The model was brought to equilibrium at each step.

From the beginning of the dynamic analysis , a switch to the UBCHYST (version 5) constitutive model was carried out. UBCHYST was created by the University of British Columbia, Canada for dynamic analysis. It generates non-linear stress-strain response and hysteretic loops under cyclic loading. The shear modulus is decreased and damping (hysteresis loop area) is increased as the stress path approaches the failure envelop. Large strain and 1% Rayleigh damping were implemented. Free field was set for the side boundaries of the model.

The earthquake record CHICHI-NS-2475year return period was selected for the dynamic analysis. The outcrop horizontal ground motion was input into the program SHAKE2000. The respective with-in ground motion at the base of the FLAC model was derived. A with-in earthquake horizontal velocity of 0.60m/s was applied at the base of the model over a duration of 75 seconds , typically for all models in this study.

3. RESULTS AND FINDINGS FROM THE NUMERICAL ANALYSIS MODELS WITH ASPECT RATIO OF 0.40H

3.1. FINDINGS DURING CONSTRUCTION OF SREW MODEL

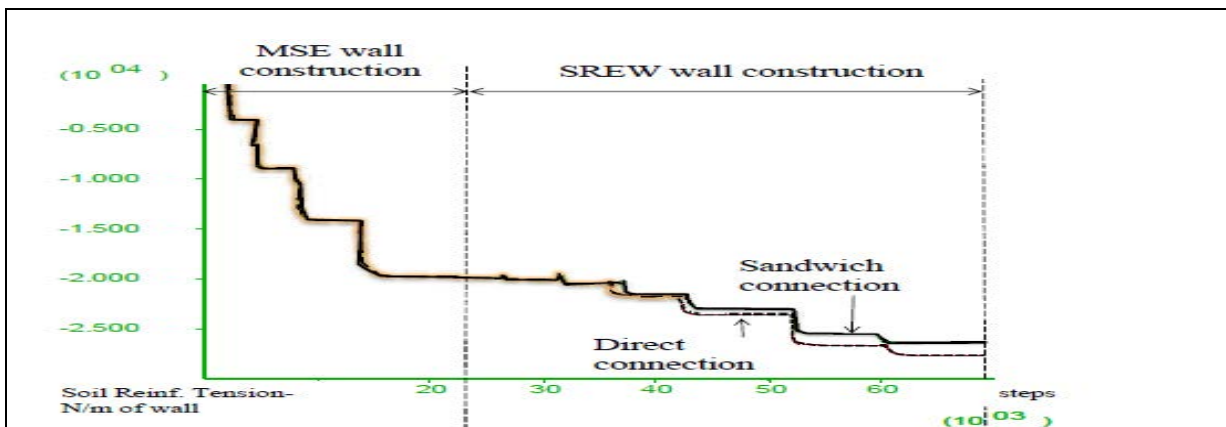


Figure5 : History plot of tensile force in soil reinforcement level #3 in existing MSE wall 1)during construction of MSE wall and 2)during construction of SREW in front of it

The FLAC model reveals that the construction of the SREW in front of the MSE wall increases the tensile force of the soil reinforcements inside the existing wall. As is the usual case, the existing MSE wall was designed and built several years ago and all the structural components were designed to capacity. Therefore investigations on the capacity of the existing MSE wall must be carried out prior to designing the new SREW in front, to ensure that the existing reinforcements are not overstressed by the construction of the new SREW.

It is also observed that the direct connection type of SREW generates a larger increase of tensile force (in the existing soil reinforcement) than the sandwich connection type. With the direct connection type, the panels of the SREW are tied to those of the existing wall and the connection mobilizes the at-rest earthpressure K_0 while with the sandwich connection the panels are not tied across and therefore active earthpressure K_a is mobilized.

3.2. BEHAVIOR OF SREW WALL DURING AN EARTHQUAKE WITH PGA OF 0.8g

3.2.1. Acceleration recorded at bottom of SREW

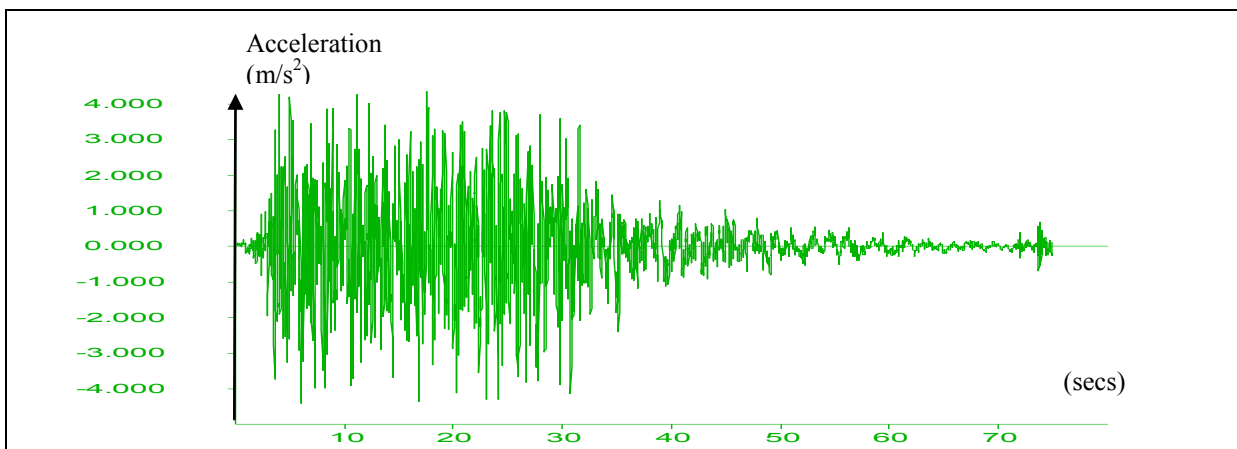


Figure 6 :Time History of input motion in FLAC (horizontal acceleration). X-axis=time, Y-axis acceleration- m/s^2

At the toe of the SREW, the maximum acceleration recorded is $4m/s^2$. If we consider this value as the product of the seismic factor γ_{EQ} of 0.5 by the Peak Ground Acceleration (PGA), as recommended by the U.S. AASHTO Standard Specifications, the equivalent design PGA is $8m/s^2$ (0.815g). Such PGA value is considered to be significant. Figure 6 shows that the acceleration gets dampened and starts to decrease gradually after 30 seconds of shaking. At 70 seconds, it is reduced almost to zero.

3.2.2. Horizontal displacement of wall at base and deformations of wall at top

Figure 7b shows that in the sandwich connection model, the top outer corner of the SREW experiences a horizontal displacement of 400mm, larger than 300mm recorded with the direct connection model in Figure 7a.

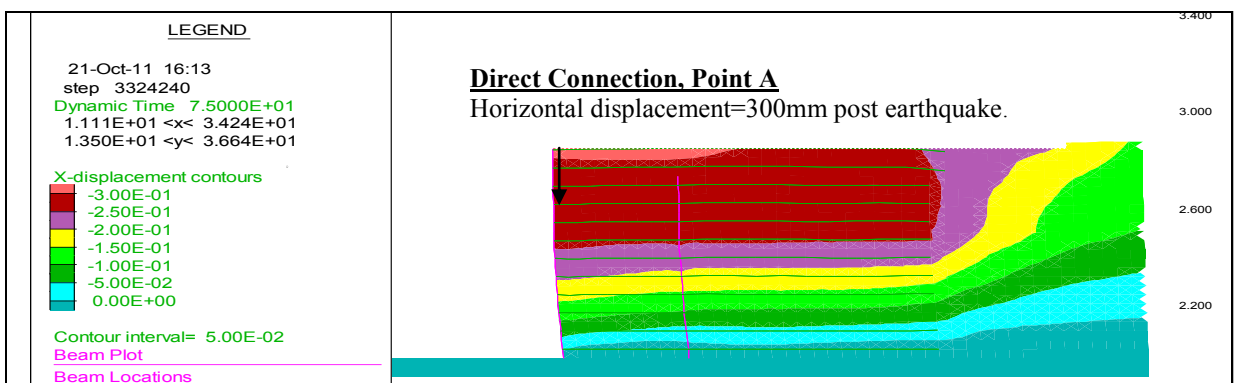


Figure 7a :Post earthquake contours of horizontal displacement of Point A (top outer corner of SREW wall) with DIRECT connection

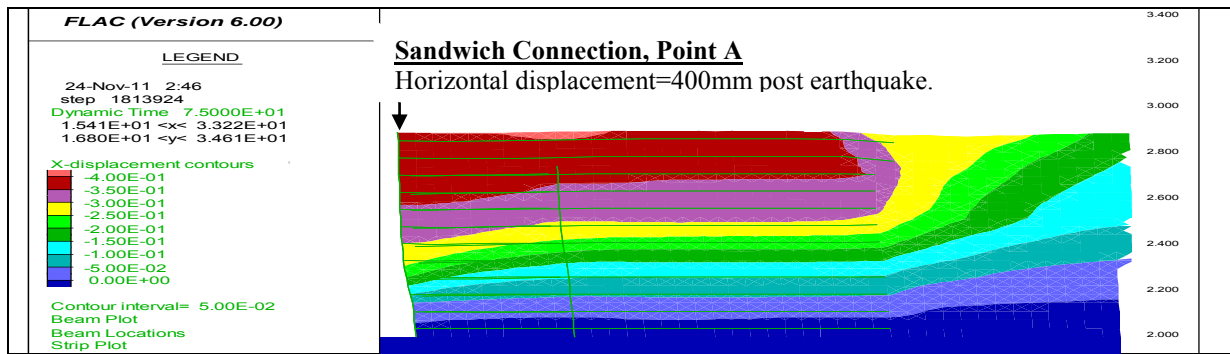


Figure 7b : Post earthquake contours of horizontal displacement of Point A (top outer corner of SREW wall) with SANDWICH connection

The larger displacement of the SREW with the sandwich connection is due to the reduced frictional resistance of the strips with the surrounding fill. During an earthquake, this frictional resistance is decreased by 20%, as per AASHTO specifications. This loss in frictional resistance causes the SREW panels to displace outward more than those with the direct connection, where the strips work purely in tension and do not rely on any frictional resistance with the surrounding soil. The displacement contours also show that the SREW and the existing MSE wall behave as a single structure with total aspect ratio of 1.1H (0.7H for MSE wall plus 0.4H for new SREW). Compared to studies done earlier by various consultants, the displacement recorded is lesser than that of a single MSE wall, which can be explained by the equivalent larger volume of 1.1H to mobilize.

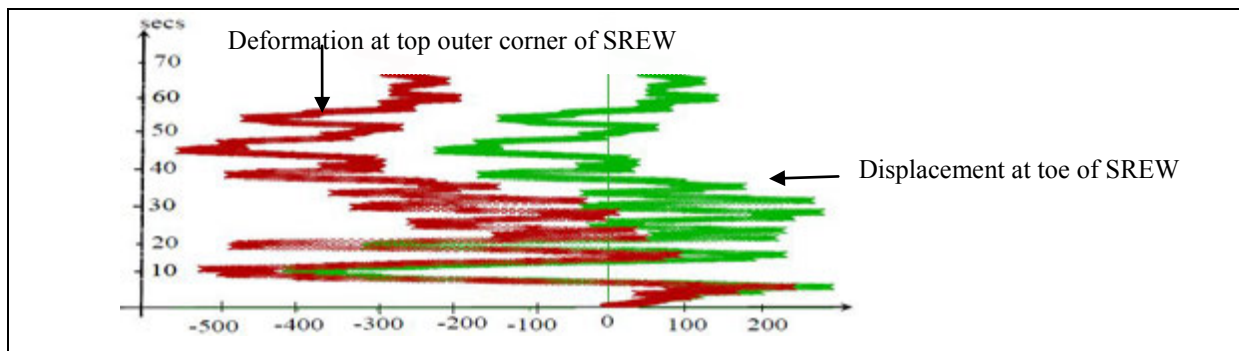


Figure 8 : Time history of horizontal deformation at top of SREW and horizontal displacement at toe of SREW

Figure 8 shows the time history of the horizontal displacement at the top outer corner of the SREW wall and that at the toe. The former reaches a maximum of 550mm during the first 50 seconds, reducing down to 300mm post earthquake mode. The toe of the wall moves in tandem with the top, however at a lesser magnitude and returns to almost the original location after 75 seconds

3.2.3. Vertical displacement at top of wall.

As shown in Figures 9a and 9b, the vertical deformation is maximum behind the existing MSE wall volume where there is no soil reinforcement. This proves again that the SREW and the existing MSE wall form an integral structure and move in tandem during an earthquake. The outward horizontal displacement causes a slight depression behind the integral reinforced earth volume.

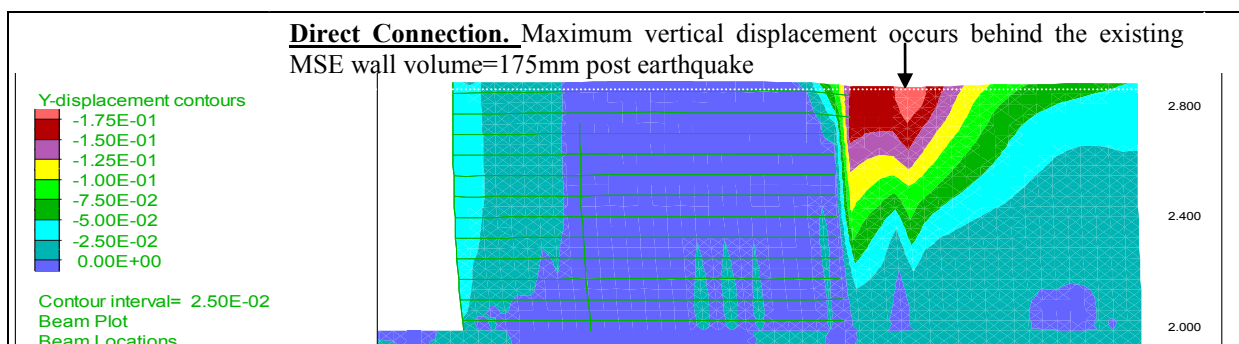


Figure 9a : Post earthquake vertical displacement behind the soil reinforced volume with DIRECT connection within the SREW wall

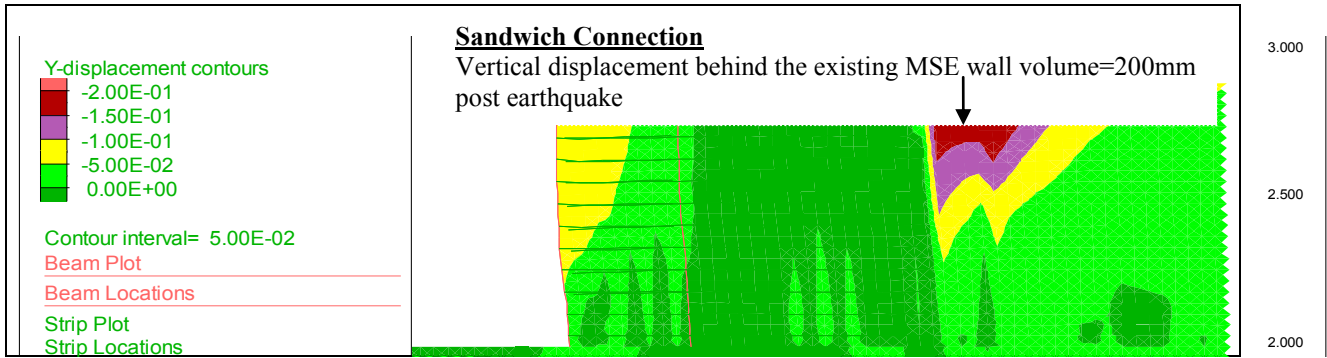


Figure 9b : Post earthquake vertical displacement behind the soil reinforced volume with the SANDWICH connection within the SREW wall.

As a general observation, the vertical deformation is small in both connection cases. It is 14% higher with the sandwich connection (200mm) than that with the direct connection (175mm). Both connection models appear stable after the earthquake event. In light of these results, the traffic at the top of wall may be resumed after post earthquake inspection. However the wall appearance may be aesthetically altered and may require cosmetic repair.

3.2.4. Increase of tensile forces in soil reinforcement during an earthquake

Figure 10a and 10b show recorded time histories of soil reinforcement tensile forces in models with both connection types. With the sandwich connection model, the tensile force in the soil reinforcement at level 3 (see figure 4 for location) in the existing MSE wall is 26.4kN/m before earthquake. It increases to 55kN/m during earthquake. This value remains within the allowable tensile capacity of the strips. This large increase is due to the high PGA of 0.815g.

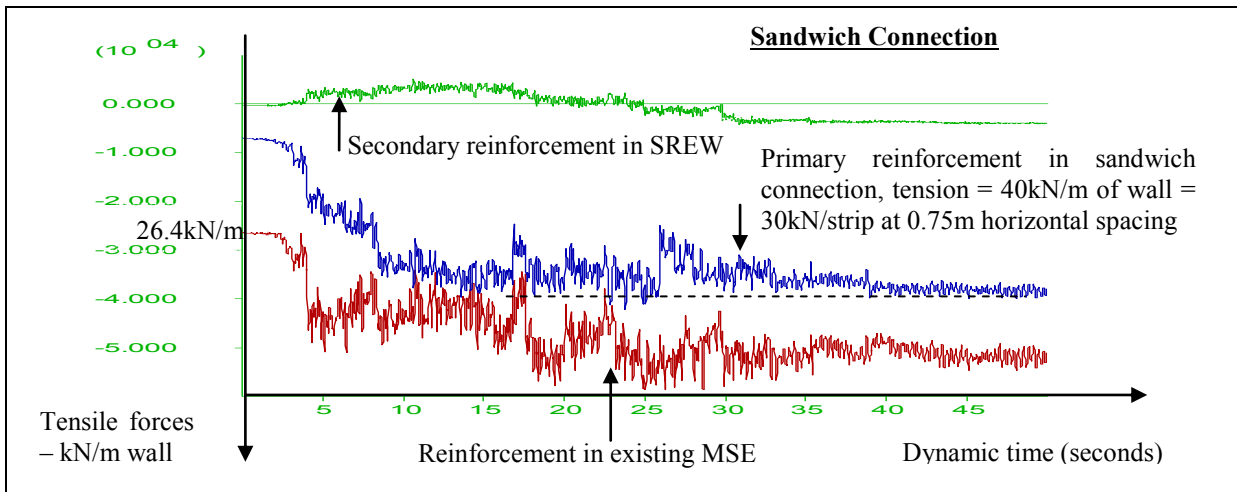


Figure 10a :History of tensile forces(in N/m) in soil reinforcements versus time in a SREW with the Sandwich connection

Figure 10a also shows that the secondary reinforcements attached to the face of the panels of the existing MSE wall experience very little tensile stress. The primary reinforcement for the facing of the SREW records a maximum force of 4×10^4 N/m or 30kN/strip which is lower than the maximum allowable of 32kN (Table 3).

In the direct connection model (Fig 10b), which has the same reinforcement densities, the maximum force recorded is 5.5×10^4 N/m or 41.3kN/strip; 38% higher than that in the primary reinforcement in the sandwich connection. However this tension value is still within the allowable tensile capacity of 43kN for seismic loading case (Table 3).

An SREW wall with the sandwich connection requires twice the amount of reinforcement as does an SREW with a direct connection. However the direct connection requires careful fitting, therefore more time during construction to ensure that the tension is fully mobilized. Furthermore, the sandwich connection appears to provide both better flexibility and better tensile loading while maintaining stability.

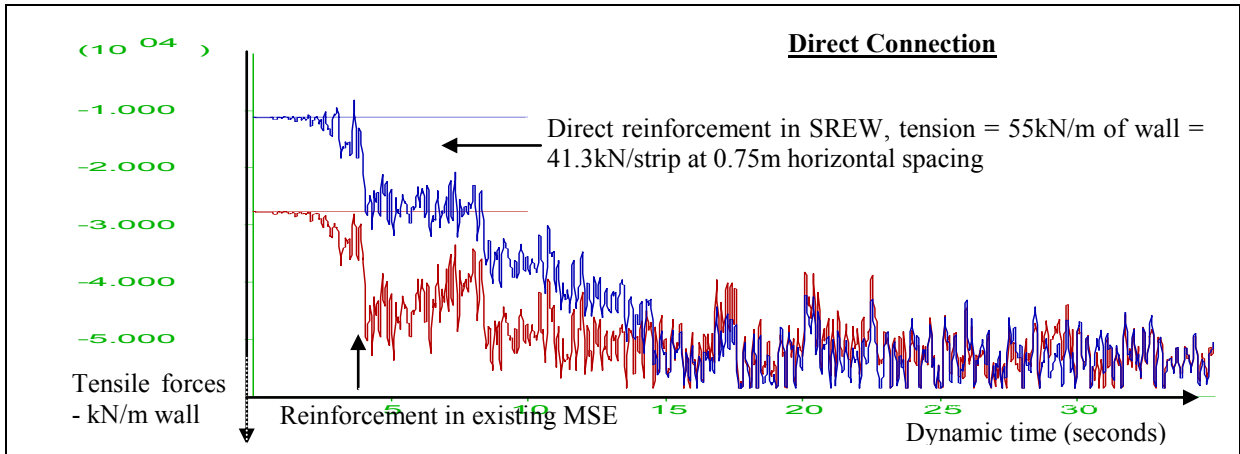


Figure 10b: Time history of tensile forces (in N/m) in soil reinforcements in a SREW with the Direct Connection

3.2.5. Strain in soil reinforcement during an earthquake

Figure 11a shows that with the sandwich connection, only two levels of soil reinforcement in the existing MSE wall experience strains past yield, ranging between 0.01378mm/mm to 0.01276mm/mm. However they are less than 10% of strain at rupture (0.215mm/mm, see Figure 12 next page). All the soil reinforcements in the SREW remain in elastic range during the earthquake. The walls are internally stable post earthquake mode.

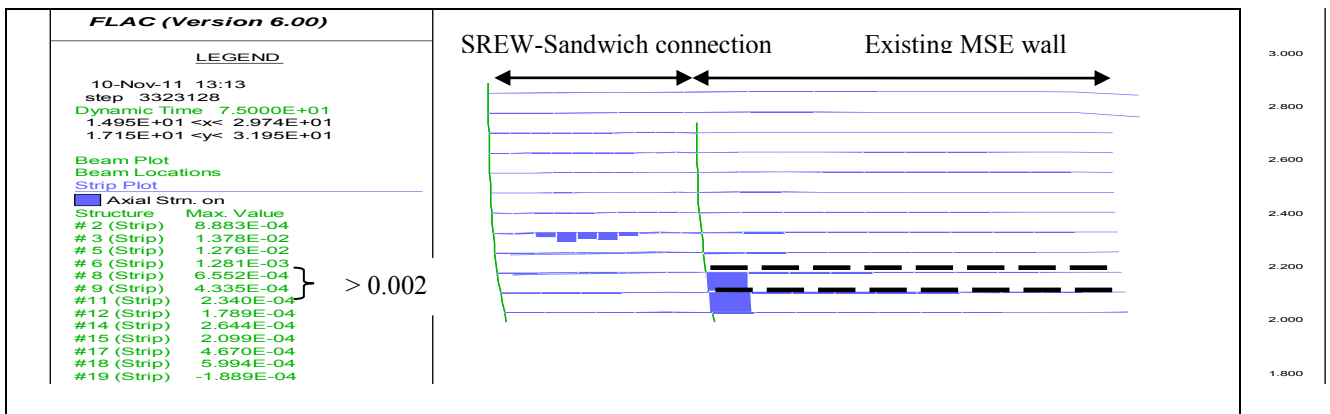


Figure 11a: Strain in soil reinforcement in existing MSE wall SREW with Sandwich connection. The strips with strain beyond the elastic limit are shown in bold dotted line

Figure 11b shows that with the direct connection, three levels of soil reinforcement in the existing MSE wall and three strips in the SREW experience strains past yield, ranging between 0.0022mm/mm to 0.02092mm/mm, which are higher than those with the sandwich connection stated above. However, they are again a fraction of the strain at rupture. These strains past yield are in the lower part of the walls and as expected with the high seismic loading



Figure 11b: Strain in soil reinforcement in existing MSE wall SREW with Direct Connection. The strips with strain beyond the elastic limit are shown in bold dotted line

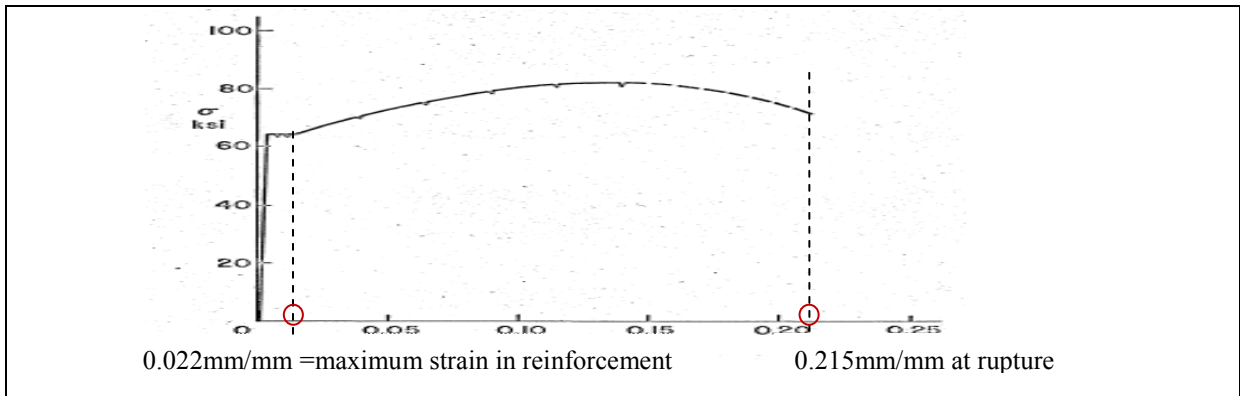


Figure 12: Typical strain-stress curve for soil reinforcement A572 (grade 448MPa) steel. 1Ksi=6.895MPa

Figure 13 shows that the post earthquake maximum compressive stress of 1.1MPa in concrete panels is much lower than the allowable limit of 24Mpa. The service level performance is therefore achieved.

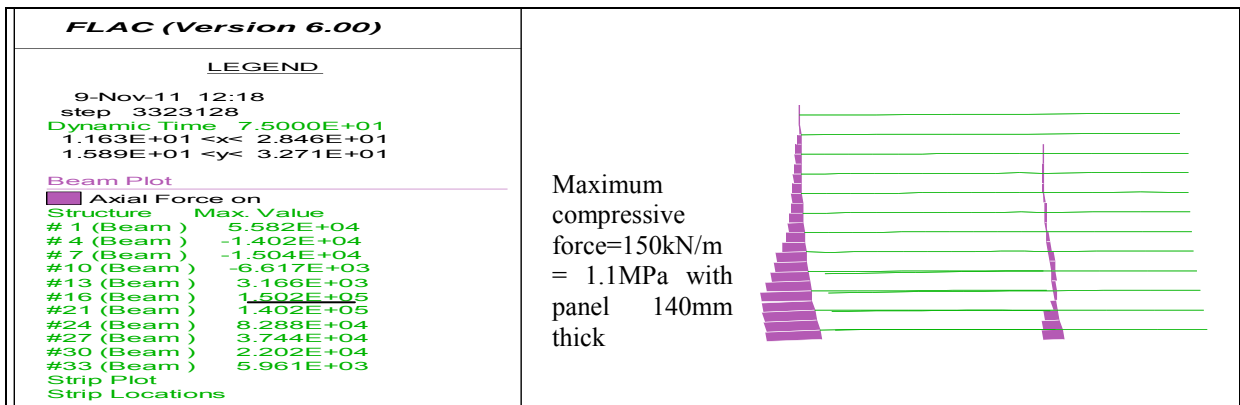


Figure 13: Compression forces in concrete panels- kN/m.

As a general observation, all the wall models with both connection types are internally stable in post earthquake mode. They satisfy to the criterion of non-collapse during a severe earthquake.

4. NUMERICAL ANALYSIS MODELS WITH ASPECT RATIO OF 0.30H

Figure 15 shows that for both connection types, the deformation at the top corner in SREWs with an aspect ratio of 0.3H are higher than those with an aspect ratio of 0.4H. The recorded horizontal displacement at the top corner of the SREW with the direct connection is 350mm (compared to 300mm in 0.4H SREW), an increase of 17%. However the horizontal displacement of the SREW with the sandwich connection reaches 600mm (from 400mm in 0.4H SREW), an increase of 50%. This large increase is due to the lower frictional resistance associated with shorter strips; a 20% reduction during earthquake and a lower total aspect ratio of 1.0H (0.7H plus 0.3H).

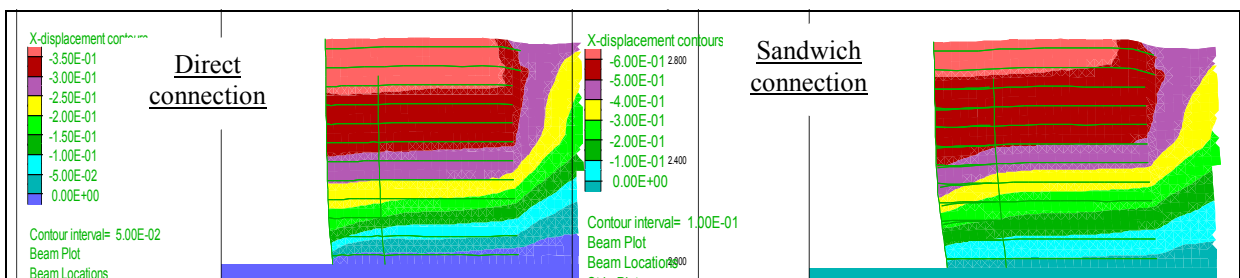


Figure 15: Contours of horizontal deformation at top corner of a SREW wall with aspect ratio of 0.3H.

Figure 16 shows a comparison of the tensile forces in reinforcements between the direct and sandwich connections. With the sandwich connection, the primary reinforcement experiences a tensile force of 22.5kN/strip, a 25% decrease from 30kN/strip with the 0.4H aspect ratio. This is due to the high deformation of the SREW with the sandwich connection stated above, which relieves partially the earthpressure within the

SREW. With the direct connection the strips experience a tension of 42.5kN/strip, almost equal to 41.2kN tensile force (Figure 10b) for strips in a SREW with an aspect ratio of 0.4H. For both aspect ratios of 0.3H and 0.4H, the tension values are within the allowable tensile capacity of 43kN for seismic loading (see Table 3).

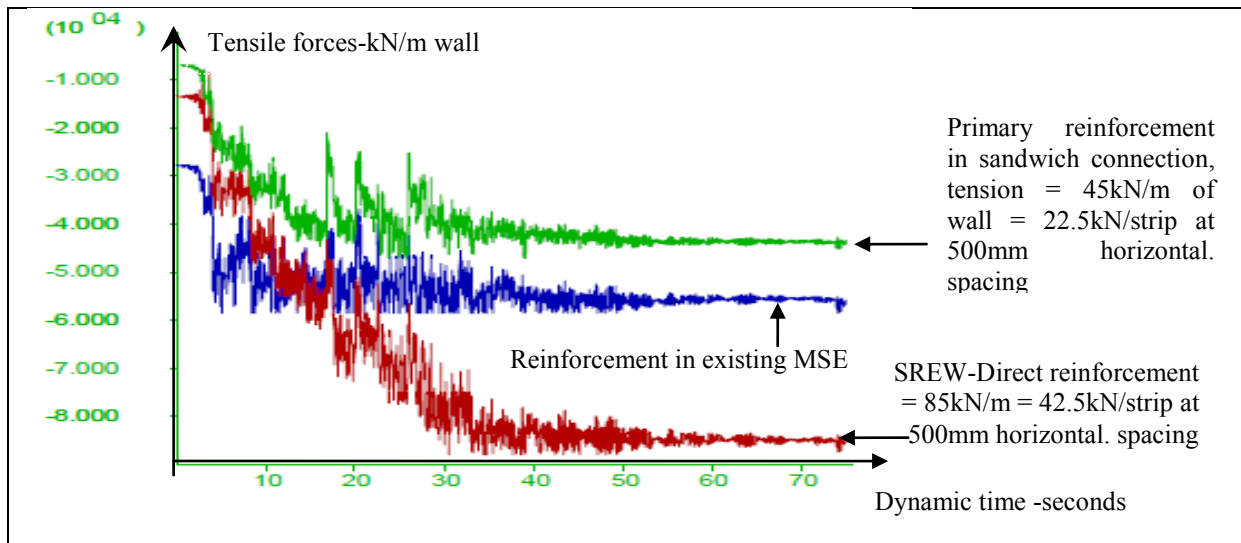


Figure 16: Time history of tensile forces in primary reinforcement of a sandwich connection and direct connection in SREW wall with an aspect ratio of 0.30H

5. CONCLUSIONS

The study above is based on specific material properties. For SREW (or SMSE) in high seismic areas, it is recommended that numerical analyses be performed with the actual soil material and structural components properties. Prior to designing an SREW, investigations on structural capacity of the existing MSE wall or soil nail shoring wall must be carried out as the new SREW (or new SMSE) will affect their structural performance.

Narrow SREW walls (with aspect ratios of 0.3H to 0.4H) maintain their internal stability and functionality after moderate to severe earthquakes; satisfying the criteria of non catastrophic collapse. The deformation of the wall and stresses in the existing wall and the new SREW section depend upon the type of connections for the soil reinforcement, the backfill quality, the foundation soil quality, the intensity and duration of earthquake.

As a general observation for SREWs, the smaller the aspect ratio, the larger the deformation. Despite the higher deformation in a SREW with the sandwich connection, it is the preferred connection type because of its flexibility, ease of construction and better structural performance during moderate to severe earthquakes.

REFERENCES

1. Ali Amini, Ernest Naesgaard, Naesgaard Geotechnical Ltd, *Dynamic Analysis of MSE Walls for Reinforced Earth Company, PMH1 Project, Vancouver, BC.*
2. *Shored Mechanically Stabilized Earth (SMSE) Wall Systems Design Guidelines. Publication No FHWA - CFL/td -06-001*
3. R. Tavakolian, J. Sankey. *Sandwich Connection design for Shored Reinforced Earth Walls, 17th ICSMGE Conference (2009) Alexandria, Egypt.*
4. *2100 American Association of State Highway and Transportation Officials Codes.*

Ice-Soil Composites Created by Method of Cryotropic Gel Formation: A preliminary report of direct shear and permeability tests

Vasiliev Nicolai, The B. E. Vedeneev VNIIG Inc., Saint Petersburg, Russia, nicolaivasiliev@hotmail.com
Ivanov Andrei, The B. E. Vedeneev VNIIG Inc., Saint Petersburg, Russia, andreialekseevich@gmail.com
Sokurov Vladimir, The B. E. Vedeneev VNIIG Inc., Saint Petersburg, Russia, SokurovVV@vniig.ru
Shatalina Irena, The B. E. Vedeneev VNIIG Inc., Saint Petersburg, Russia, ShatalinaIN@vniig.ru
Vasilyev Konstantin, Halcrow Group Ltd, Swindon, United Kingdom, VasilyevK@halcrow.com

ABSTRACT

This paper considers strengthening of both frozen soils and soils after thawing in ice-soil composites generated by the method of cryotropic gel formation. The properties of the frozen soils (ice-soil composites) have to be improved for example in order to create the reliable materials with low filtration factor for building weirs and other hydro engineering constructions, which operate under a wide range of temperatures, including positive temperatures. The application of this method is very promising in terms of creation of almost impermeable curtains for hydro engineering structures in cold regions. It is very important that such elements are safe in both frozen and thawing condition. The aqueous solutions of polyvinyl alcohol are used for the formation of cryogels. This paper shows that the ice-soil composites, obtained by using the method of cryotropic gel formation, are sufficiently strong and watertight during thawing. Experimental data are given.

1. INTRODUCTION

During the latest years many research groups focused their attention on the study of cryogels obtained by the methods of cryotropic gel formation (CGF) [Lozinsky, 2002; Altunina et al., 2006; Vasiliev et al., 2009]. Cryogels are considered as potential materials for solving practical problems. Especially it concerns cryogels based on polyvinyl alcohol (PVA). The range of domains of cryogels application is increasing [Lozinsky, 2002]. An example of cryogel application is the creation of reliable materials for building weirs and other hydro engineering constructions. The material created with using the method of CGF has a low-filtration factor and can be used in a wide range of temperatures including positive. An example of such application is the full-scale experiment of production of moisture-proof coating for the bottom of the ash disposal of Magadan heat and power plant. The method of CGF consists of the formation of strong hydrogels from aqueous solution of polymers such as PVA and some others by means of freezing and thawing process. In brief, the PVA solutions are frozen at -5 to -20 °C. Then they are allowed to thaw to positive temperature. PVA is a polymer with exceptional properties such as water solubility, biocompatibility, non-toxicity and non-carcinogenicity that possesses the capability to form hydrogels by chemical or physical methods. PVA is a non-expensive and versatile polymer, adaptable to various needs with minor modifications of the synthetic procedures. PVA has been applied to road and airfield construction and for strengthening of sands of barchan type [Bezruk, 1971] and against soil erosion [Eliseev A.V., Cheverev V.G. 2008]. Water is the only practically available solvent for PVA. PVA is a crystalline polymer obtained by hydrolysis of polyvinyl acetate. Molecular mass of the polymer is 10,000 – 1,000,000. More than 10 types of PVA with different molecular mass are available on the market. Water resistance of PVA is obtained by addition of substances of boron (tincalconite or boric acid) to the solution (Fig.1).

PVA has some foam stabilizing properties. PVA is also capable of improving strength of ice which is one of the components of frozen soils.

The experiment which confirmed the advantages of the method was carried out in the beginning of the 1990s. The local ash covered with cryogel coating has been used as a disperse material (for one m² of the surface of the coating the PVA expenditure was 0.3 kg). This polymer was the basic and most expensive component of the frozen soil coating. At present more than ten different brands of this polymer are sold at quite low prices. These brands vary according to the levels of solubility in water and their viscosity. The lower degree of hydrolysis of the polymer leads to the lower solubility of the polymer.

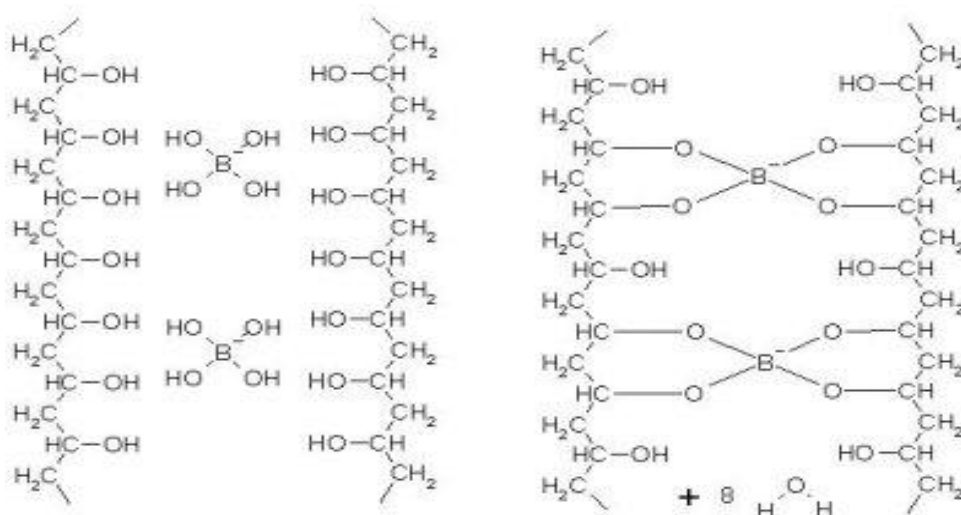


Figure 1: The reaction that forms the water resistance of PVA. The borax crosslinks the PVA

The higher molecular weight leads to a higher viscosity of the solution of the polymer. In 2003–2004 the cryotropic gels were successfully applied during the pilot tests. These tests were aimed at sealing a leaking interval at the base of the dam at the Irelyakh hydrosystem [Altunina, 2006].

The unique structure of cryogels appears to be useful in many spheres and the application of this method is very promising in various structures: docks, quays, dams, cells to contain waste products etc.

This paper considers possibilities of the CGF method for strengthening and improvement of impermeable properties of frozen soils during thawing. Such actions are necessary for the creation of reliable impermeable elements of dams and other constructions operating in a wide range of temperatures. The aqueous solutions of polyvinyl alcohol (PVA) are used for cryogel formation. The main reasons for application of PVA are excellent mechanical and thermo physical properties of the cryogels and their availability.

Strengthening action of additives of PVA is explained by formation of a continuous grid of a plastic polymeric phase in ice. Ice composites on the basis of PVA and their comparison with other types of water-soluble polymers have been studied in [Vasiliev, 1988]. This paper shows that due to the presence of small amounts of the PVA in ice (especially if a plastificator for PVA such as glycerine has been added), the resistance to cracks and the strength of ice doubles (Table 1).

Table 1: Relative strength k at bending of ice composites depending on various additives of water-soluble polymers (at temperature -20°C) (Vasiliev, 1988)

The type of polymer	Weight content, %	Relative strength, k
Polyethylene Glycol	4	0.85
Carboxymethylcellulose	4	0.25
Oksyethylcellulose	4	0.40
Methylcellulose	1	0.85
PVA	4	1.35
PVA with Glycerine weight content 0.5%	4	2.00

In cold regions the technology of using the frozen soils can include the following procedures: obtaining some coarse grained frozen soil by blast-hole drilling; grinding it with different types of machines; converting it into the plastically-frozen state, placing it into water (a polymer solution); the soil compaction. For example, the technology of a dam construction with local frozen soils placed into water is quite effective [Pechovich and Razgovorova, 1979].

This technology allows one to avoid such labour intensive actions as thawing of the frozen soils, then arranging their storage and insulation. The advantage of this technology proves the fact that the soils can be used in plastically-frozen condition instead of having to thaw the soils.

2. DESCRIPTION OF EXPERIMENTS

Two types of soil samples have been tested:

1. The ice-soil composite samples obtained by means of CGF (cryogel with sand);
2. The control soil samples prepared in the conditions identical to the first samples without using the methods of CGF (frozen wet sand without cryogel).

In order to prepare the samples of the first type the mixture of disperse soil and 10 % water solution of PVA with addition of 1.0 % of boric acid by weight was used. The PVA solution was obtained at the temperature 70 - 80 °C in a dry oven. When freezing samples were kept at negative (- 20° Celsius) temperatures for at least 4 hours, they were thawed at room temperature and if necessary were cooled again to the test temperature. It is important to note that there are types of PVA which can be dissolved at low temperatures. Higher molecular mass leads to higher viscosity, and lower degree of hydrolysis leads to lower solubility. At 5 % acetate group content the PVA swells in cold water and dissolves in water at temperatures 70 - 90°C. At the 10 - 15% acetate group content the polymer dissolves in cold water, but precipitates at temperatures more than 40°C. The control samples were prepared by means of mixing. They contained the same quantities of dispersed soil and water as the cryogel samples. The dispersed soil has been represented by a friable fine sand where the fractions of diameter 0.1 – 0.25 mm prevailed. All cryogel samples were tested after one cycle of freezing – thawing. Three series of tests were carried out at room temperature on both types of soils at normal pressures varying between 100-300 kPa and deformation speed of 5.0 mm/min. The normal pressures and the rate were chosen in the range as advised by the Russian standard (GOST 12248-96). This rate of shearing was taken to represent an undrained loading condition. All the tests were run immediately after the placement and compaction of soil in the shear box. Such situation represents mainly in-situ conditions. The diameter and height of the shear box were 63.5 mm and 20 mm correspondingly. The tests were conducted on computer controlled shear box equipment using different load and deformation transducers. Six twin-specimens were tested. The statistical data manipulation was done in accordance with the Russian standard (GOST 20522-96) using the method of applying all σ - τ couples obtained. The experiments have been carried out using the one-plane shear method on the shear machine 27-WF2180. The experimental set up and data-logging systems are shown in Fig. 2. Some tests were performed at different temperatures. The results of them are shown in Fig. 3.

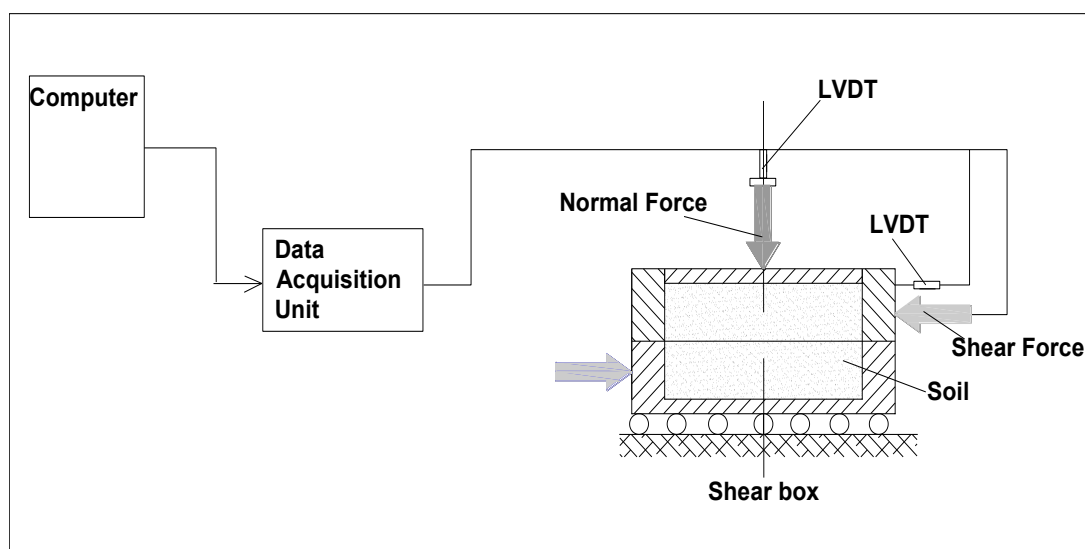


Figure 2: Computer controlled experimental setup of the direct shear test

3. DISCUSSIONS AND RESULTS

The undertaken laboratory research showed that the frozen technogenic soils obtained by means of CGF on the basis of PVA retain the properties of a solid body during thawing even after one cycle of freezing-thawing (Fig. 3).

In addition, after only one cycle of freezing-thawing the shear parameters of ice-soil composites are improved in comparison with the ones of the control soil: for the control soils the angle of internal friction is $\varphi = 25^\circ$ and cohesion is $C=0.0$ and for the ice-soil composites obtained by means of CGF: $\varphi = 36^\circ$ and C

= 0.05 MPa [Vasiliev et al., 2009]. It was proved that the strength parameters of cryogels after several cycles of freezing-thawing become better [Lozinsky and Damshkaln, 2000; Lozinsky, 2002]. It is obvious that shear strength parameters of ice-soil composites are not getting worse. It is important as the freeze-thaw cycling is a weathering process that frequently occurs in cold regions.

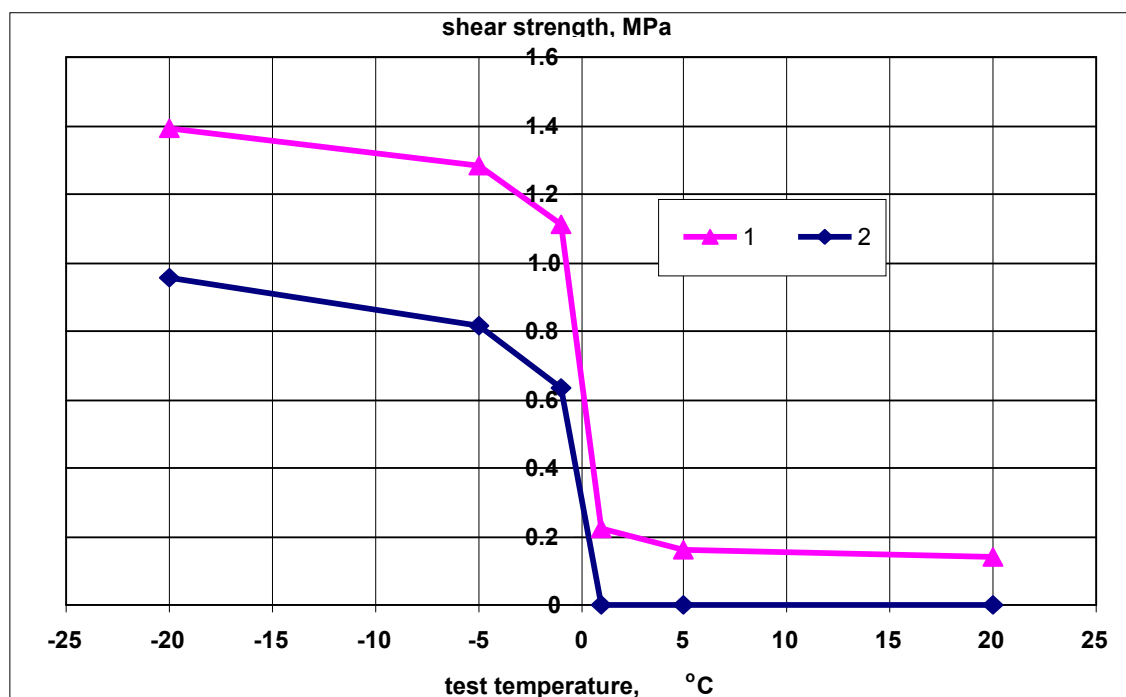


Figure 3: Shear strength of the ice-soil composite (1) and control soils (2) vs. test temperature during and after one cycle of freezing and thawing

The shear tests diagrams representing the shear loading versus horizontal displacement at various vertical pressures (Fig. 4) show that the ice-soil composites are stronger than control soil samples (they require higher shear pressure for the same value of horizontal displacement). In addition, the experiments carried out show that the plasticity of the soils obtained by means of CGF is noticeable. Even at the general deformation of shear exceeding 5-10 mm and more, no crack between the two halves of the sample were observed. It is also shown that the properties of the soils obtained by means of cryotropic gel formation (in our case cryogel with sand) are very different from the properties of the control soils. After thawing the samples of cryogel are extremely plastic at positive temperatures. It is also known [Vasiliev, 1988] that at negative temperatures the cryogel samples are more plastic than frozen ice. This is due to the fact that the icy form of PVA solution is more plastic than normal ice. Therefore the method of CGF is very promising in solving the problems occurring in freezing-thawing contact zone of hydro engineering structures.

The permeability factor K_f of the soil from the control samples reached 2.0 m/day, obtained at the drop of pressure 10kPa/m (hydraulic gradient for the sample 10 cm long is equal 1) in a device KF 00M according to the normatives of the Russian standard (GOST 25584-90). Currently a number of tests with different cryogel thawing composites are being performed in triaxial cells. After placing a sample in a cell, pore pressure is slowly increased up to 95% of the compression stress. If there is no filtration for some time higher compression stress needs to be applied in order to increase pore pressure as well. For example, the 10 cm long cylindrical ice-soil composite samples were generated with the help of cryogel solution and contained 10% PVA and 1% boric acid. These samples showed some filtration when the compression stress was 320 kPa, pore pressure 300 kPa and drop of pressure 3 MPa/m (hydraulic gradient for the sample 10 cm long is equal 300). After stabilization the permeability factor K_f was less than 10^{-5} - 10^{-6} m/day. For some tests 1.6% of glycerine was used, as plasticizer, which improved impermeable characteristics of the composites. The results of the tests to define the permeability factor are provided in Fig. 5. It is noted that when a small quantity of glycerine is added to the solution, the permeability factor is decreased.

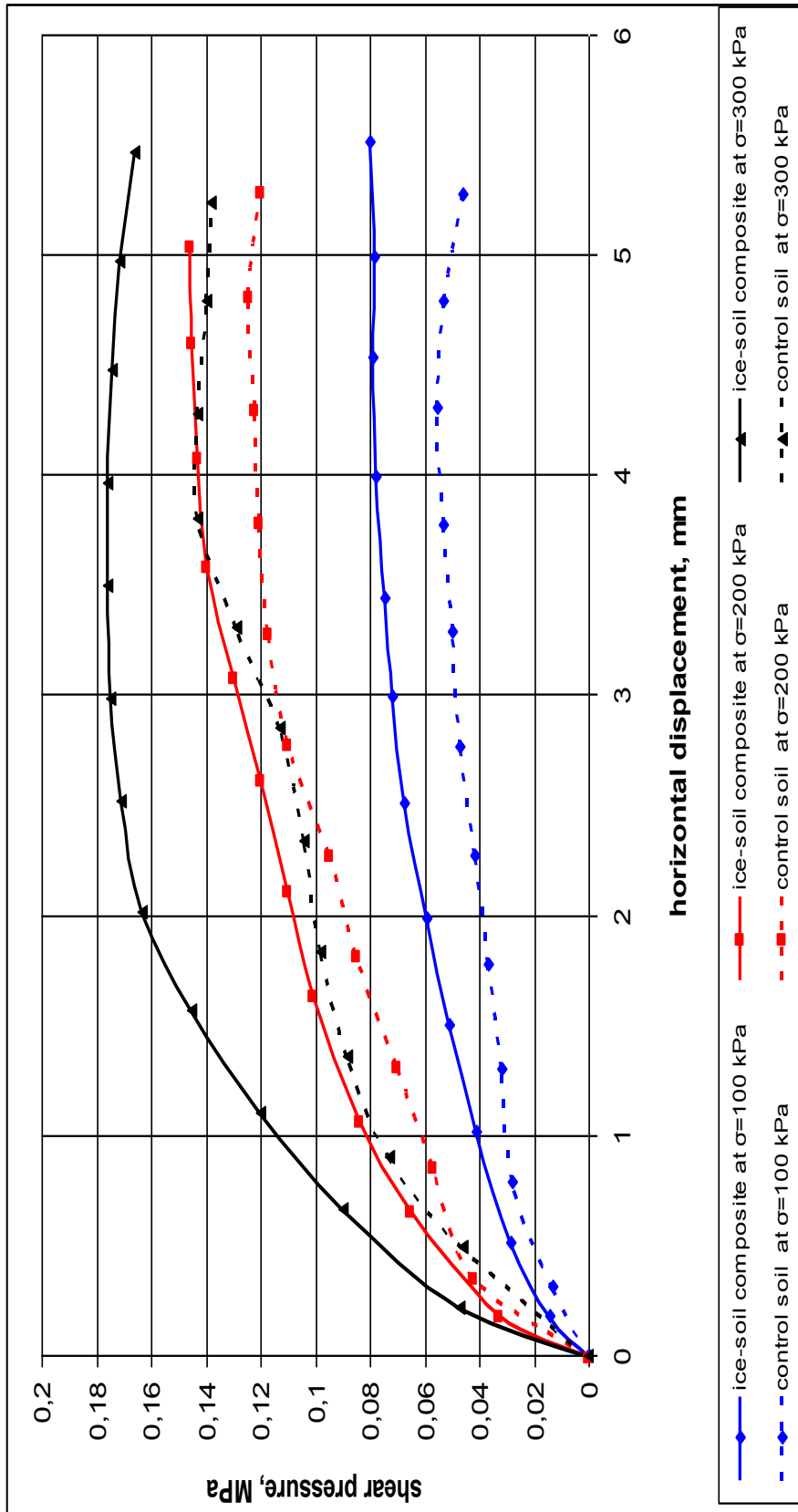


Figure 4: The shear diagrams at the positive temperature (+20° C) for different soils at various σ - normal pressure : the ice-soil composite or in this case cryogel-soil composites samples obtained by method of CGF and the control soil samples

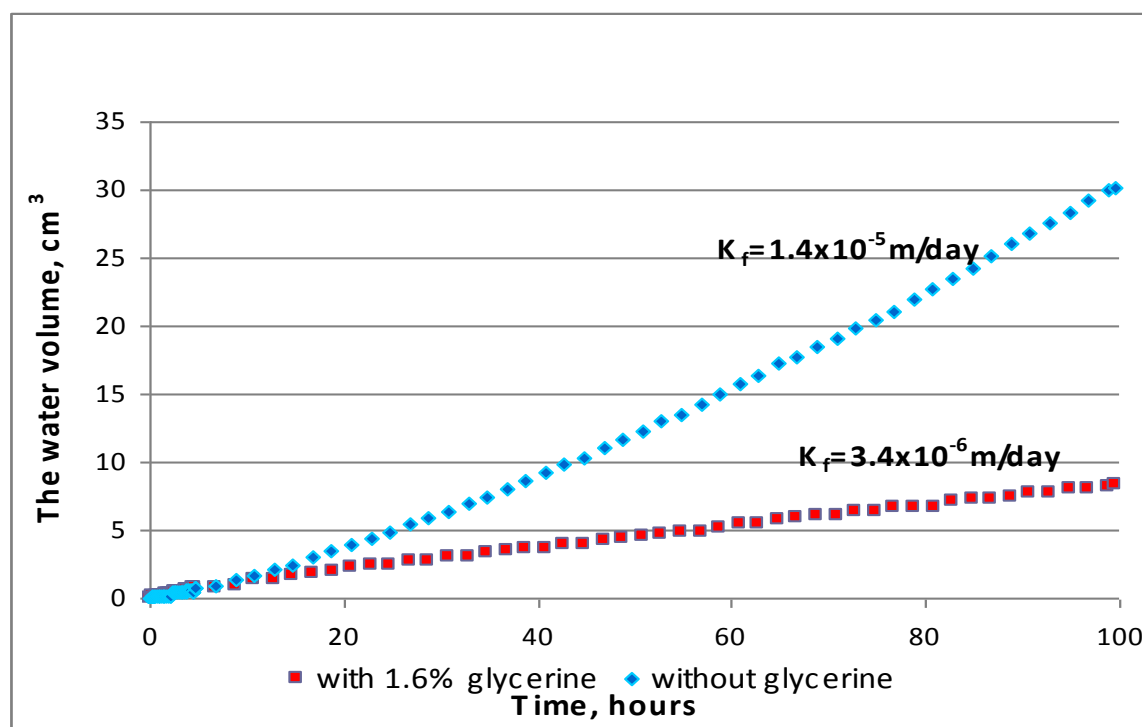


Figure 5: The water volume through a sample of ice-soil composites obtained by method of CGF with addition of plasticizer (glycerine) and the composites without addition of glycerine at positive temperature and at compression 320 kPa, hydraulic gradient 300

The technology of strengthening of a frozen soil by means of the method of cryotropic gel formation for construction of anti-filtration elements in weirs is protected by patents of the Russian Federation N 1600406 and N 2342484. The advantages of this method are: high efficiency of erection of impermeable elements for both fresh and sea types of water. This high efficiency is explained by many factors: the properties of foam generating installations with ejectors and also by the fact that the formed elements are waterproof, nontoxic, flexible (in the wet conditions they are capable of “selfcuring” the cracks), dissolvable in water and are very strong.

Also it has been noticed that the more cycles of freezing-thawing in which cryogel participates there have been, the greater cohesion and the friction angle of the soils are. Porous specimen obtained with the help of foamed cryogels have quite low thermal conductivity which is less than 0.3 W/m °C. Tests were performed by the method of thermal probe.

4. CONCLUSION

- The experimental data show that the ice-soil composites, obtained by using the method of cryotropic gel formation, are sufficiently strong and watertight during thawing.
- The method is quite new and needs further research. The influence of different factors on strength, permeability, durability, elasticity, heat insulation and other properties of the soils with gel can be explored further.
- It is also necessary to develop procedures of using the method in practice.

REFERENCES

- Altunina L.K., Kuvshinov V.A., Dolgikh S.N., 2006. Cryogels – promising material for underground works in permafrost. *Advances in Geological Storage of Carbon Dioxide*. Ed. By S. Lombardi, L.K. Altunina, S.E. Beaubien. – NATO Science Series.IV.Earth and Environmental Sciences. Springer.V. 65. p. 103-110.
- Bezruk V.M., 1971. *Strengthening of Soils in Road and Airfield Building Transport*. Moscow (in Russian).
- Eliseev A.V., Cheverev V.G. 2008. *Method of erosion protection of the dispersed soil*. *Earth's Cryosphere*. Vol. XII, N 3, p.36-40.
- Lozinsky V.I. and Damshkaln L.G., 2000. *Study of cryostructuration of polymer systems. XVII. Poly(vinyl alcohol) cryogels: Dynamics of the cryotropic gel formation*. *Journal of Applied Polymer Science.*; 77(9), pp.2017-2023.
- Lozinsky V.I., 2002. *Cryogels on the Basis of Natural and Synthetic Polymers: Production, Properties and Domains of Application*. *Uspekhi Khimii*. Vol. 71, pp. 559 – 585 (in Russian).
- Patent of the Russian Federation N 1600406. Vasiliev N.K., Shatalina I.N., Razgovorova E.L., Portnyagin L.G., Sidorov M.P., 1990. *Method of the Erection of a Soil Weir of a Frozen Type* (in Russian).
- Patent of the Russian Federation N 2342484. Vasiliev N.K., Sokurov V.V., Ivanov A.A., Shatalina I.N., Razgovorova E.L., 2008. *Method of Creation of a Water-resistant Screen in the Soil Materials of the Elements of a Hydrotechnical Structure* (in Russian).
- Pechovich A. I. and Razgovorova E. L.,1979. *Investigation of frozen soil compaction after putting them into water*. *Izvestiya of the B.E. Vedeneev VNIIG*. vol. 130. pp. 92-99 (in Russian).
- Vasiliev N.K., 1988. *The Research on Strengthening of Ice Using Water-Soluble High-Molecular Substances*. *Izvestiya of the B.E. Vedeneev VNIIG*. Vol. 205, pp. 45- 48 (in Russian).
- Vasiliev N.K., Davidov M. G., Sokurov V.V., Shatalina I.N., 2009. *Strengthening of Frozen Soils by the Method of Cryogenic Gelation*. *Izvestiya of the B.E. Vedeneev VNIIG*. Vol. 253, pp. 49- 54 (in Russian)

Realisation of integrated steep landscape slopes within existing railway embankments

Jan Verstraelen, TUC RAIL, BELGIUM, jve@tucrail.be
Lejeune Colombine, TUC RAIL, BELGIUM, ljc@tucrail.be
Eric De Clercq, TUC RAIL, BELGIUM, eric.declercq@tucrail.be

ABSTRACT

Within the framework of the regional express network around Brussels, two new railway tracks will be added besides two existing ones. It was decided to limit as much as possible any new expropriations, which leads to challenging design constraints. This article discusses several possible solutions (flexible and semi-flexible) to enlarge these existing embankments while keeping the railway line in service at all times. Within urban areas, the affected communities demanded also that the construction posses a "green" character. It was left to the designers to fill in this demand within a certain framework for the final appearance.

The chosen solutions consist of deep foundations supporting a concrete structure which has to be partially covered or hidden. To realise these foundations, a working platform needs to be created, for which a soil nailing of the existing embankment is used. Special attention will be given to the design impact of lateral loading on the foundation, as well as to the permanent or temporary use of soil nails.

1. INTRODUCTION

This article describes 4 different systems as they are currently being used in the development of the regional express network around Brussels. The overall project aims to enlarge the train capacity in and around Brussels by extending the existing railway tracks from 2 to 4 lines. A common problem or difficulty faced within the project is the need to create steeper slopes or retaining walls from within current embankments. These existing embankments usually have a slope around 6/4 and a toe very close to the property line.

Since expropriations lead to high costs, all the presented solutions aim to stay within existing property lines. Due to the urban nature of the surroundings, all the solution also need to present a green character. Different site characteristics and local requirements led to the described 4 different solutions, which all deal with similar problems in a different manner. First, these common problems will be underlined and put into context. Next, the ways in which these are solved will be explained as well as the inherent assumptions and consequences.

2. DIFFICULTIES AND LIMITATIONS

A common difficulty for all of the presented solutions is the need to create a wall or slope which possesses a green character, while maintaining a steep slope.

In general, the here presented systems can be divided into two subcategories:

- ▲ Green terraces: a stepped embankment is created with stacked concrete facing elements, with flat terraces between each element. Vegetation is allowed to grow on flat surfaces with a reasonable amount of available arable soil. The slope angle is usually at about 45°, but higher angles are also possible by decreasing the distance between the elements and thus the available vegetated surface area. Depending on the type and height of vegetation, a part of the concrete facing remains visible.
- ▲ Green walls: walls with a continuous slope and full surface vegetation. Slope angles are generally very steep and up to 70°. Different commercial systems exist, which use geogrids or concrete frames which are stacked together. The design of these walls is left to the general contractor within a certain limit set by the general designers. Vegetation on these walls is more difficult and may have an impact on the overall stability of the system.

The four systems presented here consist of 2 green terraces and 2 green walls.

A common difficulty is the foundation design of these retaining walls. Due to the small available surface area and high concentrated loads, piled foundations are usually necessary. The pile groups are especially subjected to high lateral loads.

Depending on the size of the chosen foundation, a retaining wall for the current embankment is chosen to create space to realise the latter. Since the existing tracks need to remain in service at all times and due to the small available workspace, soil nailing was chosen in all of the presented solutions. In some cases, these soil nailing will have a permanent function, namely to reduce the earth pressure on the newly constructed slopes.

Finally, the available work space sometimes calls for a less than ideal pile geometry due to the absence of raking piles or the use of less suitable pile types.

3. OVERVIEW OF THE DIFFERENT SYSTEMS

Table 1 shows an overview of the different systems with their category (terrace or wall), height, slope, type of retaining system (permanent or not), specific drawbacks and general cost per surface area.

Table 1: Comparison between different systems

Nr.	Location	Type	Height	Slope angle	Soil nailing	Specific	Cost
1	Ternat	terrace	10 m	45°	temporary	cemented backfill	1.800 €/m ²
2	Anderlecht	terrace	10 m	45°	permanent	geogrids	670 €/m ²
3	Anderlecht	wall	11 m	70° - 6/4	temporary	VHP grout anchor	1.020 €/m ²
4	Watermaal-Bosvoorde	wall	9 m	70°	permanent	shaft foundation	1.030€/m ²

When evaluating these different systems, and more specific the pricing, the assumptions and specific requirements need to be taken into account.

4. SYSTEM 1 – GREEN TERRACE WITH LARGE PILED FOUNDATION AND CEMENTED BACKFILL

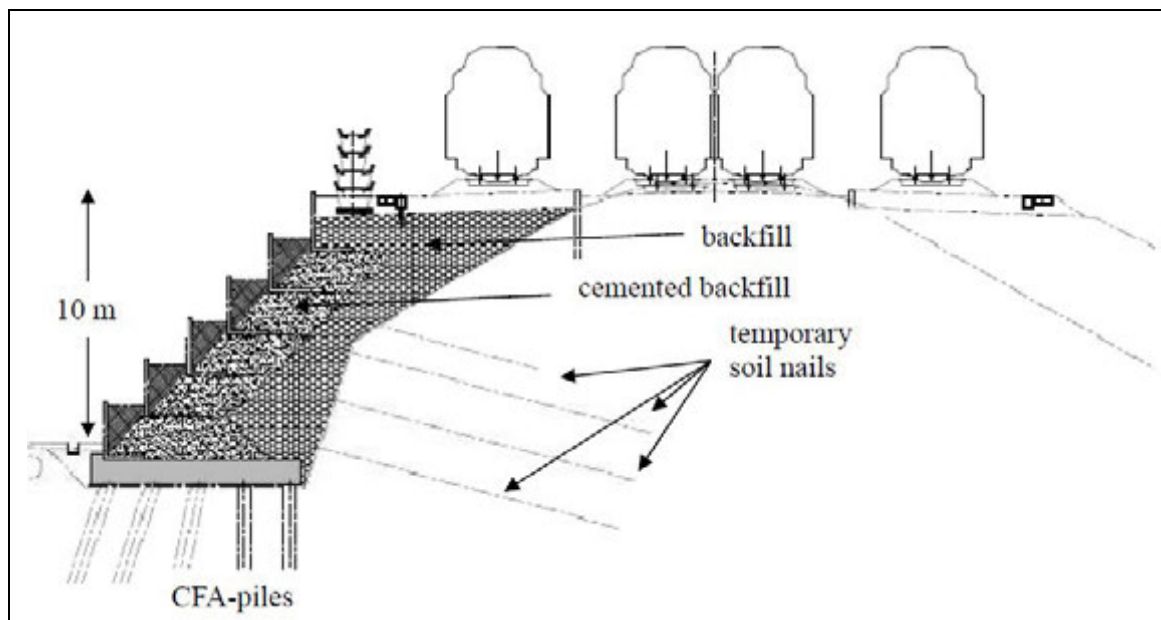


Figure 1: Green terrace with piled foundation and cemented backfill

In this system, the required space to install raking piles is at least temporarily available. Still, the embankment height and practical limit in raking angle, leads to a considerable number of piles which are still accompanied by considerable bending moments in the pile head and cap. Due to the local presence of alluvial deposits up to 7 m thick, piles are generally long and have to be heavily reinforced. The design of the piled foundation is carried out with analytical methods ([1], [2]) as well as finite element models in Plaxis and FLAC ([3], [4]).

Since the piled foundation is rather large, a high temporary retaining wall is needed to create a working platform. The retaining system, in this case soil nailing, has no permanent function what so ever. The green terraces which come on top of the foundation are stabilised by using a cemented backfill. Sand is mixed with cement in an installation to create a monolithic bloc containing the small cantilever walls. The cantilever walls hardly have any retaining function, and serve just to hold the arable soil.

4.1. Advantages

The foundation is a rigid structure with a common and relatively cheap pile type (i.e. CFA-piles). Execution is straight-forward. The type of wall as green terrace allows for a large variety of possible vegetation which can easily be maintained and even neglected, since it has no structural function. The soil nailing has a purely temporary function, so there is no need to address nail corrosion issues.

4.2. Disadvantages

The system relies heavily on the cemented backfill acting as a monolithic bloc. During the design, a number of shearbox tests were carried out on sand mixtures with different cement content, as well as shear box tests on concrete-backfill interfaces (table 2). In the latter case, tests were carried out on smooth precast surfaces as well as roughened surfaces, to present a cast-in-situ character.

Table 2: Lab results from direct shear tests on cemented backfill (sand treated with cement)

	c' intact	φ' intact	c' residual	φ' residual
50kg/m³ cement	116,5 kPa	48,1°	21,1 kPa	41,6°
100 kg/m³ cement	266,9 kPa	38,9°	96,1 kPa	26,7°
200 kg/m³ cement	247,0 kPa	74,0°	46,3 kPa	47,9°
150 kg/m³, roughened	38,7 kPa	38,7°	0,0 kPa	39,8°
150 kg/m³, smooth	3 kPa	42,3°	0,0 kPa	40,4°

In the backfill with concrete interface tests, the backfill was allowed to harden before bringing it into contact with the concrete segments. The roughening was performed by hammering a concrete surface to create an irregular surface with 1 to 2 mm asperities. From table 2 one can notice, in comparison to the roughened variant, that there is hardly any adhesion between the smooth concrete and cemented backfill, with similar intact and residual properties. Furthermore, it can be seen that the addition of the cement has mainly an impact on the rise in intact cohesion of the base material (i.e. sand).

In practice, an additional surplus in thickness of the cemented layer was foreseen in the design. During execution of the works, a number of plate load tests and UCS tests were carried out in situ and in the laboratory. To make sure that there are no interfaces between different lifts of backfill, it was specified to rip the surface of the hardened backfill before adding the next lift.

Photos 1 and 2 show soil nailed wall and pile heads, as well as a finished section of the retaining system.



Photo 1: Excavated pile heads and soil nailed wall



Photo 2: Finished green terrace, with temporary wild vegetation

5. SYSTEM 2 – GREEN TERRACE WITH GEOGRIDS AND PERMANENT SOIL NAILS

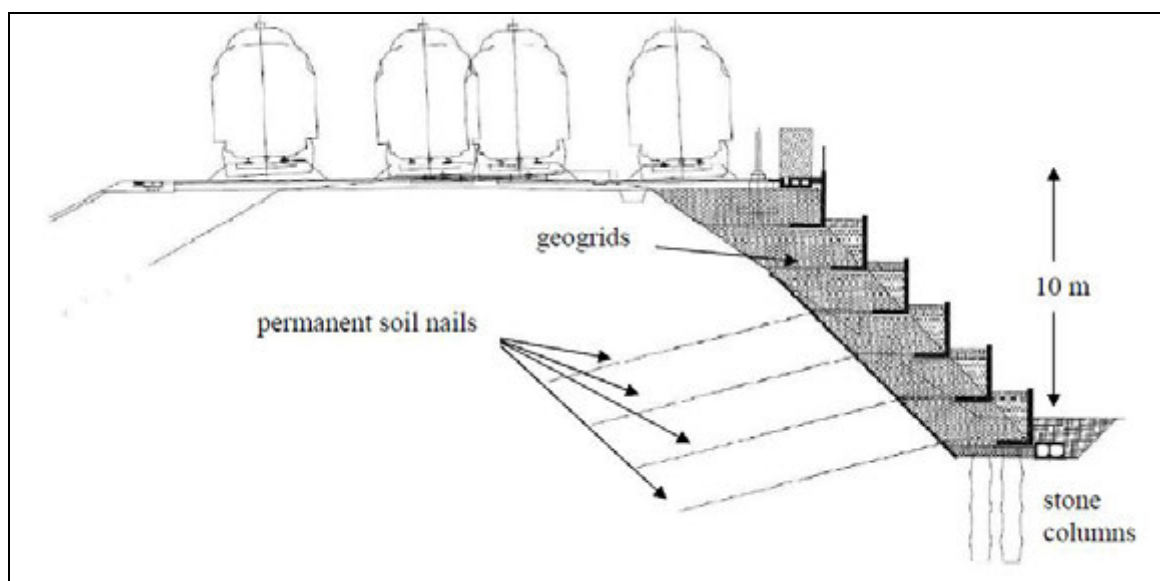


Figure 2: Green terrace with geogrids and permanent soil nails

The design and performance testing of this type of retaining wall is discussed in detail in ref [5]. This system starts from the design of the green terrace as a mechanically stabilised earth wall by anchoring a geogrid in the base slab of cantilever walls. In turn, some of the geogrids are connected to soil nails which provide the necessary stability for deep sliding. As a consequence, the added overload is relatively small and a small foundation area is sufficient. Due to the type of wall as being semi-flexible, the use of stone columns as foundation elements was selected, even though alluvial deposits up to 10 m thick were present.

5.1. Advantages

The type of wall as green terrace allows for a large variety of possible vegetation which can easily be maintained and even neglected, since it has no structural function.

The geogrids connect the rigid parts of the wall, being the cantilever walls and soil nails and they act together with the added soil to transfer the loads. As, in practice, the different levels of soil nails and cantilever elements never correspond, the tolerances have to be taken up with the geogrid. Therefore, the flexibility of the geogrids and their installation is very useful.

The stiffness of the geogrids was selected to limit displacements of the facing elements but remains low in comparison to structural components. Only the critical bottom elements are anchored to soil nails, the top elements have a free run-out geogrid anchor.

In addition, the soil nails which act as a temporary retaining wall turn into permanent nails for the geogrids, although permanent loads might even be smaller than temporary loads. The possibility to install the soil nailing under a gentler slope (45° instead of the more general 70°) also provides less stability issues or settlements of the existing embankment.

A foundation of stone columns is relatively cheap and quick to install.

5.2. Disadvantages

The system is semi-flexible, so some displacement has to be allowed. Due to the choice of very stiff geogrids this can be limited.

Also Mechanically Stabilised Earth-walls tend to exhibit creep, which needs to be avoided since this will lead to settlements and thus track maintenance. For this system, PVA-geogrids were selected due to their high stiffness (8000 kN/m in this case) and low tendency for creep. The demand for a high stiffness automatically leads to a large allowable difference between the short term and long term ultimate tensile strength. In this case, there is a factor of 7 difference between short term tensile strength and service load level. These geogrids are more costly than typical lower strength types of geogrids, but remain cheap in relation to the other systems discussed in this article.

However, the connection of the geogrid to the base slab at such high loads was an unknown factor, as well as the connection to the soil nails. The connection to the base slab was left to the general contractor, who had to perform lab tests to demonstrate their proposed solution. These tests showed a reduction in ultimate strength of up to 2 or 3, depending on the type and geometry of the geogrid. However, due to the general level of safety, these differences could be factored in.

Also, the laboratory tests were very susceptible to the test conditions, since different strands were not always loaded equally while testing in mid air. Furthermore, some damage seemed to occur at the exit of the geogrid from the element, since all tests showed rupture at this exact same location (photo 3). The results seemed to lead to the introduction of an extra installation factor, which needed to be added to those generally taken for the design of geosynthetics, such as biomechanical degradation, creep and installation damage [6]. The question remains if this is a realistic reduction factor or only dependant on the unrealistic laboratory conditions. In this regard, it can be noticed that factory tensile tests on geogrids generally never yield their design strength and fail at lower strengths at the geogrid-test clamp connection.

The connection with the soil nails also remains an issue to address. In this case, the soil nails have circular rings at the nail head, through which a steel tube is slid (photo 4). The geogrid is wrapped around the tube and anchored freely as wrap-around in the backfill. To avoid corrosion, the tubes are galvanised and coated. Since the design was made with finite element models, some ULS cases were checked in which the connection between geogrid and nail was removed.

The soil nails have a permanent function as to provide anchorage for the geogrids and to provide the necessary stability against deep sliding. The soil nails were subjected to performance testing to check their rupture load, and were designed with a sacrificial corrosion thickness according to Eurocode 3, part 5. As an added extra, the last 1,5 m of the steel bars were galvanised and coated.

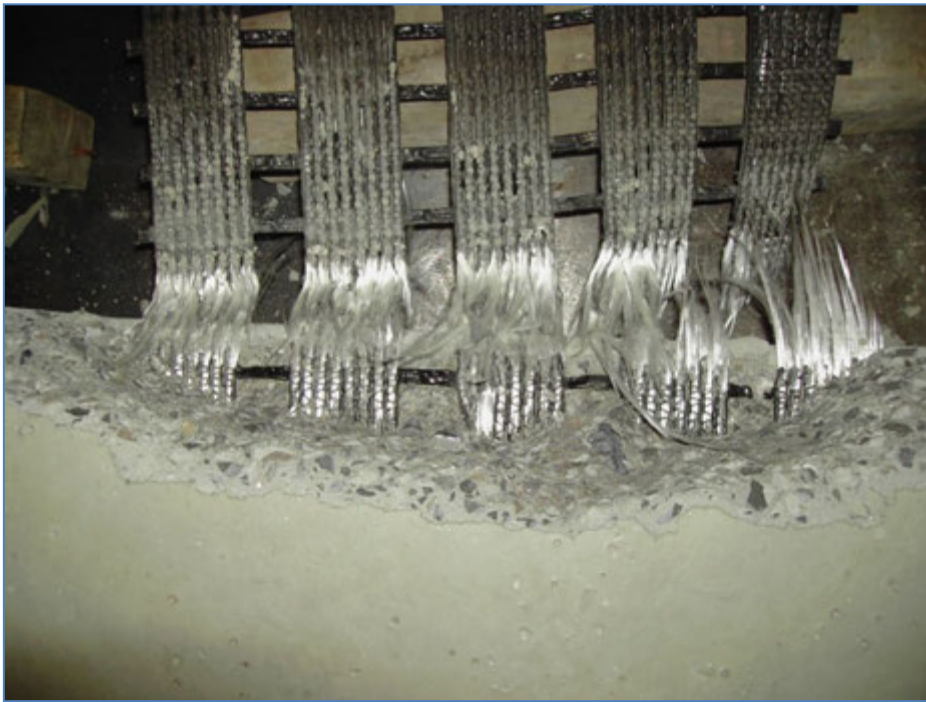


Photo 3: Load test on geogrid-base slab connection, showing tensile failure at the interface and concrete spalling of unreinforced part of base slab



Photo 4: Soil nails with shotcrete and nail heads with rings to connect tube and geogrid

6. SYSTEM 3 – GREEN WALL ON ANCHORED PILED FOUNDATION

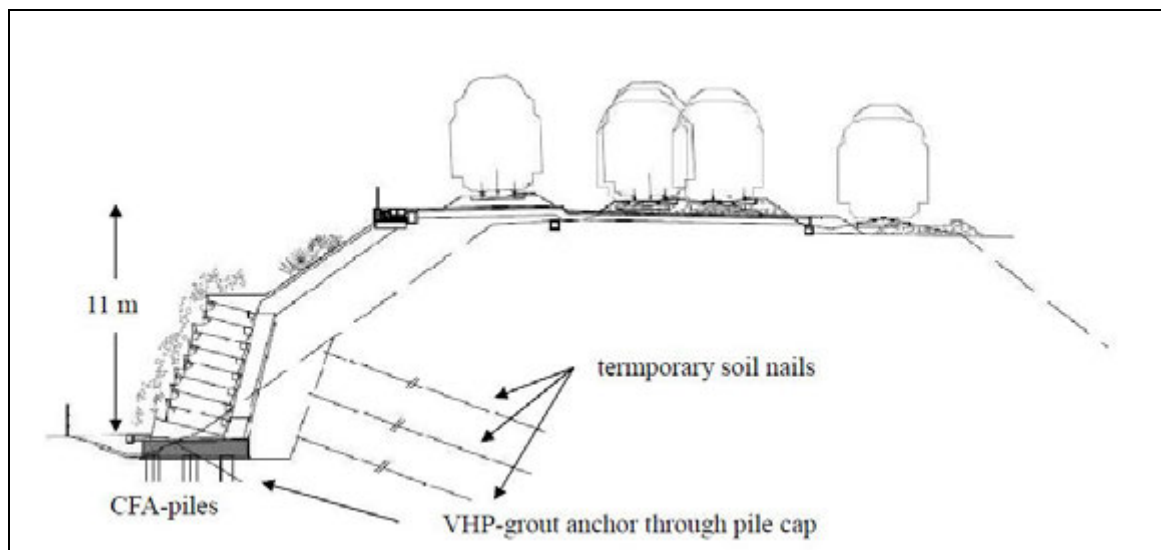


Figure 3: Green wall on anchored piled foundation

In this solution, a green wall is constructed on top of a piled foundation. Due to the limited available space, only vertical piles are used (i.e. CFA-piles). To limit the lateral loading on the piles, the pile cap is anchored with prestressed jetgrout anchors. The prestressed anchors halved the moments that occurred in the pile heads. The design of the green wall on top of the foundation is left to the contractor, but consists of a system of concrete frames that are stacked and contain arable soil. These elements need to eliminate long-term erosion and act as reinforcing elements to create a gravity wall. The subsoil is very similar to that of system 2, and consists of very weak alluvial deposits of up to 10 m thickness.

6.1. Advantages

The green wall is supported by a rigid foundation. The width of the foundation could be limited by the use of an active anchor instead of raking piles. The retaining system, in this case soil nailing, has no permanent function.

6.2. Disadvantages

The slope of the green wall is 70°, and thus difficult to allow for vegetation to grow.

The pile cap is anchored with a permanent grout anchor. The anchor is a very high pressure (> 200 bar) grout anchor with a diameter of minimum 30 cm and installed through reservations in a concrete base slab. This type of anchor is very susceptible to execution parameters (pressure, flow rate, advance rate, rotational speed ...). Since the grout anchors had to be anchored in alluvial soils, a large number of rupture load tests was carried out on test anchors to check the design assumptions and execution parameters.

The risk of corrosion of the steel anchor bar is limited due to the large diameter of the grout anchor. Still, a sacrificial corrosion thickness is added on the net steel section. While prestressing the anchors, a short test of the bearing capacity is performed.

Photo 5 shows a cross-cut of an excavated grout anchor, to check for the actual diameter. Figure 4 shows the results of a load test on the anchor up to more than twice the design load of 400 kN. A logarithmic creep limit of 2 mm between 15 and 60 minutes is passed at 720 kN.



Photo 5: Cross-section of excavated VHP grout nail of 30 cm diam

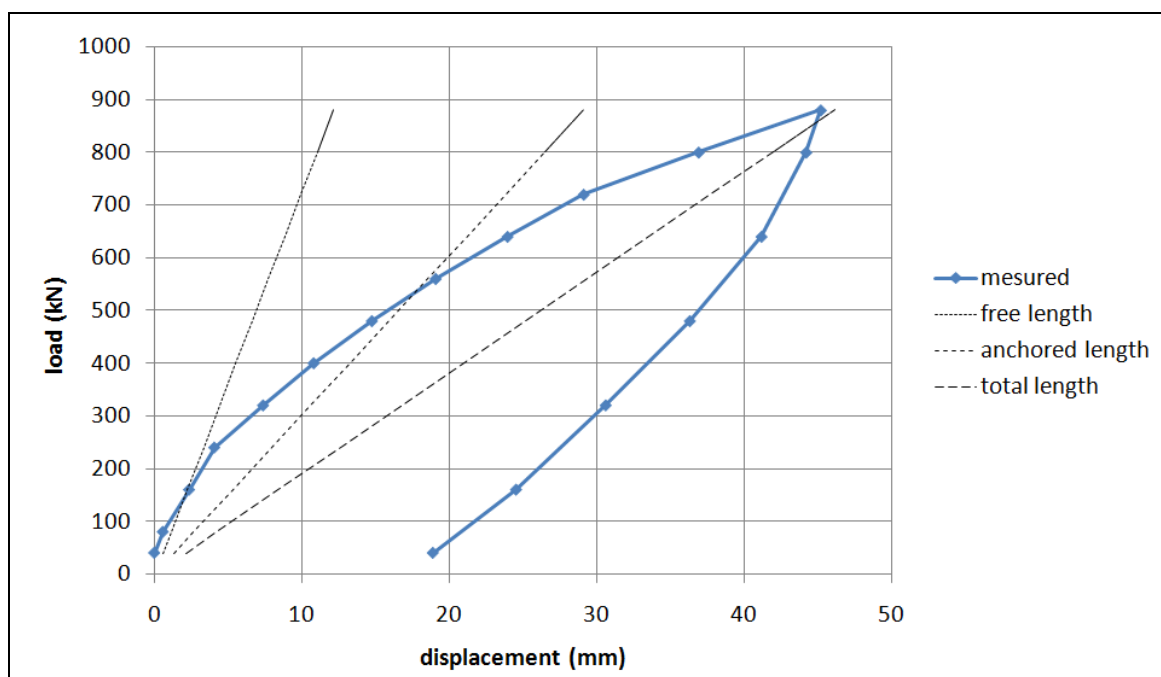


Figure 4: Result of load test on VHP grout anchor, showing load displacement curves together with theoretical elasticity of free length, anchored length (half the bonded length) and total length

7. SYSTEM 4 – GREEN WALL ON SHAFT FOUNDATION WITH SEMI-PERMANENT ANCHORS

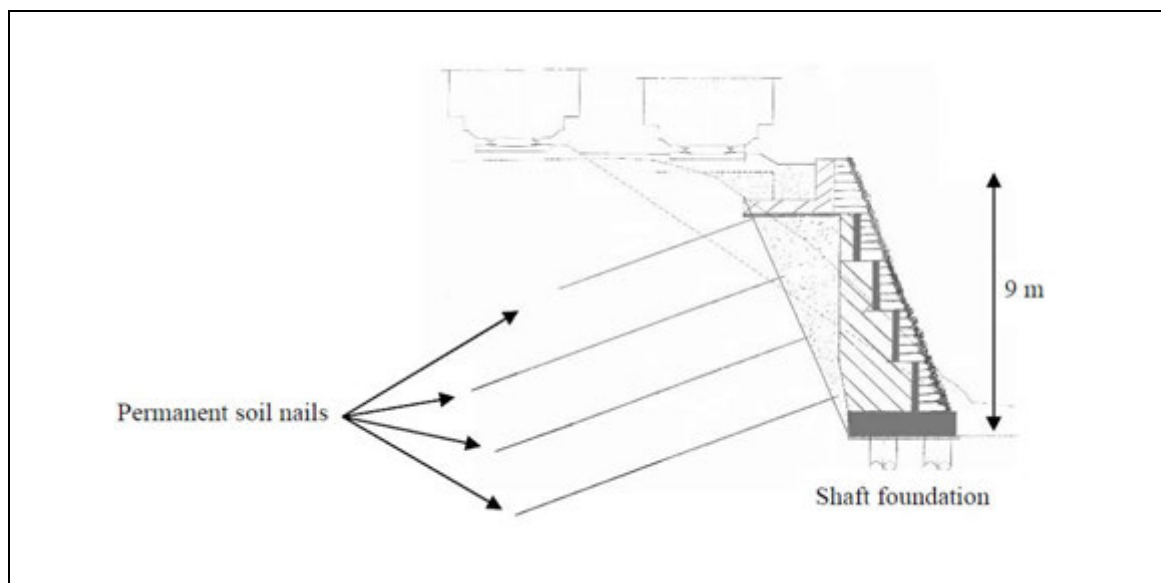


Figure 5: Green wall on shaft foundation with permanent soil nails

The last system described in this article is a rigid structure on a shaft foundation. The shafts, which are 90 cm in diameter and up to 7 m deep, are excavated by standard excavators with a temporary casing which supports the excavated hole. This technique was chosen due to the narrowness of the working platform (the size of the machines was limited to 3 meters wide).

The upper structure is designed by the general contractor and consists of beams and trusses connected to the pile cap. Three verifications were done for designing the shafts: the bearing capacity of the piles, the passive soil strength retaining the piles and the global stability of the embankment. The spacing and depth of the shafts were optimized to mobilise the full passive soil resistance. The shafts were reinforced to function as solid inclusions that stabilise the slope against deep sliding.

A system of geosynthetics, containing arable soil, was attached to this upper structure. This will make the slope “green”.

The retaining wall is a soil nailing similar to the other systems (photo 6). In this case, the soil nails have a semi-permanent character: the nail heads are allowed to corrode and are considered as unattached to the shotcrete, which itself is completely temporary. The effect of the free-headed soil nails is a rise in apparent cohesion of the existing embankment (from 2 to 20 kPa), and thus lowering the remaining earth pressure on the slope.

The subsoil in this case consists of moderately compact loam to dense sand, and can be considered to be more favourable compared to the other 3 systems.

7.1. Advantages

The major advantage of the shaft foundations is that this technique can be used on small working platforms and is relatively cheap. Bearing capacity for this type of foundation is limited, but due to the large diameter, the shafts can be reinforced to sustain high lateral loads.



Photo 6: Finished soil nail wall



Photo 7: Execution of shaft foundations

7.2. Disadvantages

A major disadvantage of the use of shaft foundations is their limitation in execution depth (7 m) and the impossibility to excavate beneath groundwater level. The temporary casing follows the drill and descends solely by its weight; it cannot be drilled or vibrated (photo 7).

8. CONCLUSION

Different systems to realise a steep slope that possess a green character were discussed and compared, presenting their different advantages and shortcomings. Given the building permit requirements and the available space for each zone, one of the above solutions was selected.

All of these systems had their particularities and difficulties, which were taken into the account or became obvious during execution of the works. With this added information, and the here presented back-analysis, future systems will be refined, adapted or new systems will be developed.

REFERENCES

- [1] M. Tomlinson, 2008, *Pile design and construction practice*, Taylor & Francis.
- [2] K. Fleming, 2009, *Piling engineering*, Taylor & Francis.
- [3] Plaxis, *2D geotechnical finite elements*, Plaxis bv.
- [4] FLAC, *Fast Lagrangian Analysis of Continua v5*, Itasca Consulting Group Inc.
- [5] J.Verstraelen, 2011, *Green terraces for the regional express network in Brussels*, EYGEC Rotterdam.
- [6] Koerner, 2005, *Designing with geosynthetics*, Pearson.

SESSION 7
BIOGROUT & OTHER GROUTING METHODS

Numerical Studies on the Design of Compaction Grouting

Antonios Anthogalidis, Faculty of Civil Engineering and Geodesy, Technische Universität Darmstadt, Germany,

anthogalidis@iwmb.tu-darmstadt.de

Ulvi Arslan, Faculty of Civil Engineering and Geodesy, Technische Universität Darmstadt, Germany,

arslan@iwmb.tu-darmstadt.de

Oliver Reul, Department of Civil Engineering, University of Applied Sciences Darmstadt,

Germany, oliver.reul@h-da.de

ABSTRACT

Compaction grouting is a well established ground improvement technique, which can be applied in various geological strata and from shallow to large depths. The effects of compaction grouting include not only compaction of soil but also controlled heave, pre-consolidation or filling of voids in a large range of geological materials such as rock with sinkholes or normally to over-consolidated soils.

In contrary to the large field of application in engineering practice the theoretical understanding of the mechanical behavior is not well established. In practice the planning is based on empirical data because detailed analytical or numerical models are not available yet.

Numerical approaches for simulating compaction grouting have to model large deformations and a soil constitutive model with pressure dependent soil properties such as density or stiffness is required. Early finite element modelling was carried out with modified Cam-Clay models. Other adequate models are Hardening Soil models or Hypoplasticity models, respectively.

In earlier investigations a finite element model for the process of compaction grouting and further for the process of deformation due to building loads was developed with the finite element program Tochnog 8 (FEAT, 2011). In the scope of this paper a parametric study was performed with Tochnog 8 for the design optimisation of compaction grouting.

1. PRACTICE OF COMPACTION GROUTING

Primarily compaction grouting was applied for the controlled uplifting of buildings with excessive settlement. Due to the developments in compaction grouting, especially regarding pump technique, the range of applications has been broadened during the past years, e.g. soil improvement applications such as dam remediation or consolidation settlement control, to mention only a few. Figure 1 shows the main aspect of compaction grouting:

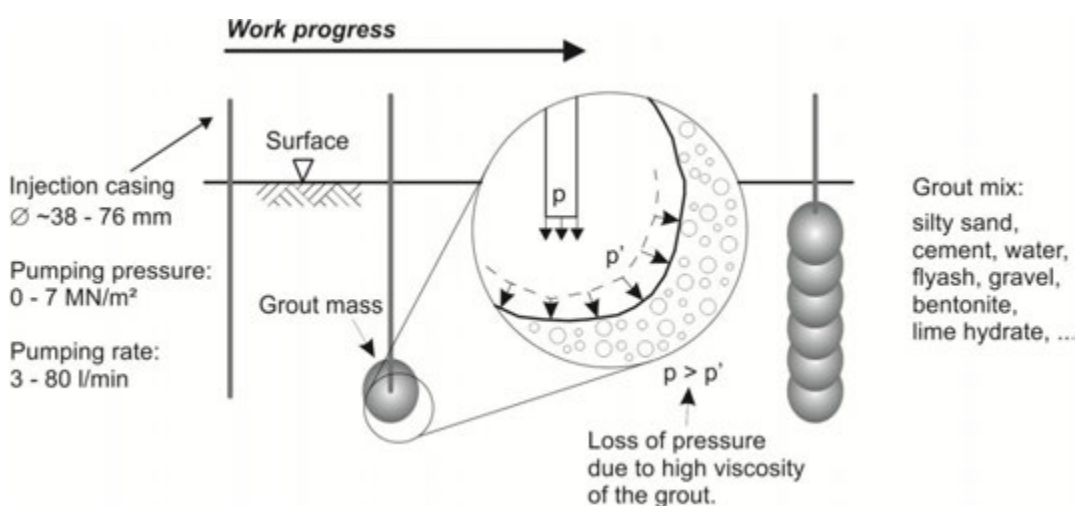


Figure 1: Main aspects of compaction grouting.

The two main effects intended by compaction grouting are:

- Compaction of surrounding soil,
- Controlled uplift of buildings or ground surface.

These two effects can be achieved separately or in combination. Additionally the purpose of compaction grouting depends on building conditions and soil conditions. Thus, the range of applications can be defined as follows:

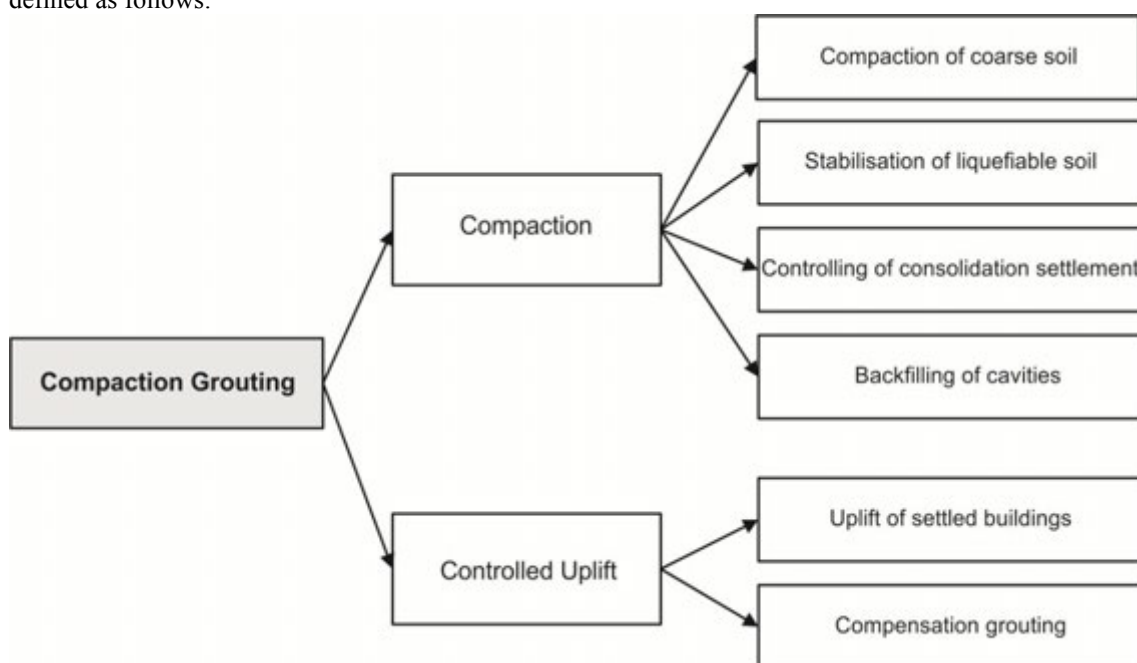


Figure 2: Categories of compaction grouting.

The planning of compaction grouting is mainly based on empirical data. Hence, field tests are usually carried out to determine the parameters of grouting, grid patterns and abort criteria. Typical abort criteria are the maximum grout pressure, planned grout volume and incorrect uplift of buildings or ground surface.

At the beginning of the process the amount of compaction has to be defined. Therefore the difference between explored and required compaction is an approximated value, assuming that reduction of pore volume in soil is equal to the grout volume. The grout volume usually lies between a few percent up to 20 % or more of the total volume of the compaction grouting area (Baker, 1985). The grid spacing can be approximately two- or three-times of the grout bulb diameter (ASCE/GI Standard 53-10, 2010). A triangular grid pattern with primary, secondary and tertiary grout locations is advisable. The grid spacing for primary grout points typically lies between 2.5 m and 3.7 m. The typical vertical spacing between two grouting points is approximately 60 cm.

Compaction grouting can be carried out in a top-down procedure or in the more common bottom-up procedure. Under consideration of the development of grout pressure soil properties can be estimated (Brown, Warner, 1973). A constant development of grout pressure over time yields a homogeneous soil. otherwise heterogeneous soil can be assumed. The difference between the peak of grout pressure and relaxation is an indication for the amount of compaction.

The quality control to check the obtained amount of compaction is carried out for example by means of cone penetration tests or large-scale loading tests before and after grouting. Furthermore, monitoring is performed during the grouting process including the recording of pressure, grout volume and uplift measurements. A standardised correlation of these measured parameters with the amount of compaction does not exist until now.

2. MODELLING OF THE GROUTING PROCESS

Compaction grouting constitutes a compact volume of grout mass without mixing it with the surrounding soil. The grout mass can be unsteadily formed. In case of isotropic, homogeneous soil conditions the grout mass has an approximately cylindrical or spherical volume. Around the grout mass a complex system of radial and tangential stresses develops, with maximum stresses close to the grout mass. The stresses decreases with growing distance from the grout mass. With increasing grout pressure the zone of influence grows. In vicinity of the grout mass shearing and plastic deformation occur. In a larger distance where stresses due to compaction grouting are smaller than stresses due to soil-weight elastic deformations are caused.

With increasing grout volume the grout pressure increases until uplift occurs, preventing further compaction, (Graf, 1969). Hence, the ability of compaction depends on the weight of the conical soil body above the grout mass (Figure 3).

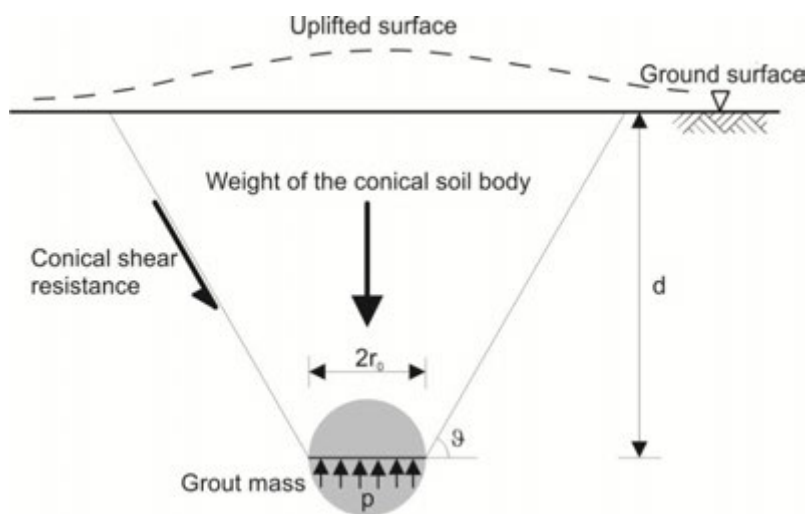


Figure 3: Conical shear failure (El-Kelesh et al., 2001).

Analytical solutions for the grouting process are based on the cavity expansion theory. Uplift is modelled by a state of failure condition like the conical shear failure (Graf, 1969). The closed-form solutions exist for cylindrical and for spherical, displacement-controlled cavity expansion in an infinite, homogeneous, isotropic continuum under isotropic stress state (Au et al., 2006). These assumptions lead to a 2-dimensional and symmetric analysis.

The boundary conditions are given by the stresses and strains at the border of soil and grout mass as well as at an infinite distance to the grout mass. The constitutive stress-strain law for soil is elastic-plastic applying a failure criteria such as Mohr-Coulomb or Cam-Clay. (Vesic, 1972) assumes a plastic zone around the grout mass and behind a radial distance of R_p an elastic behaviour (Figure 4).

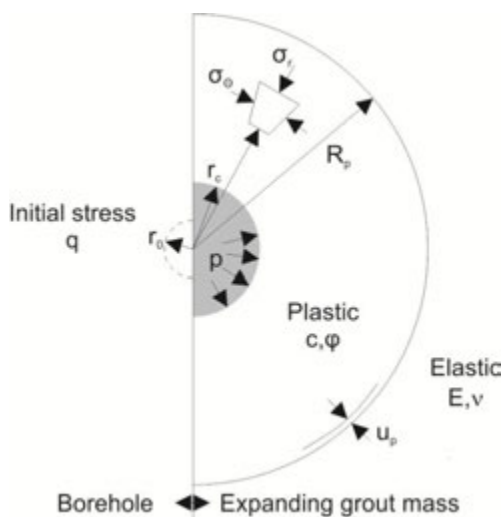


Figure 4: Stress and strain (Vesic, 1972).

The stress distribution at the the border of soil and grout mass is constant. The expansion of grout mass is modelled as a cavity expansion. At the border of the cavity (border of soil and grout mass, respectively) the constant pressure p is applied. The grout volume (current radius r_c) expands spherically or cylindrically from the initial radius r_0 . For a cylindrical expansion under drained conditions (Vesic, 1972) Figure 5 shows the distribution of radial stresses σ_r and tangential stresses σ_θ in dependency of the radial distance r to the grout volume. The assumed constitutive law for the soil is elastic-plastic applying the Mohr-Coulomb failure criteria.

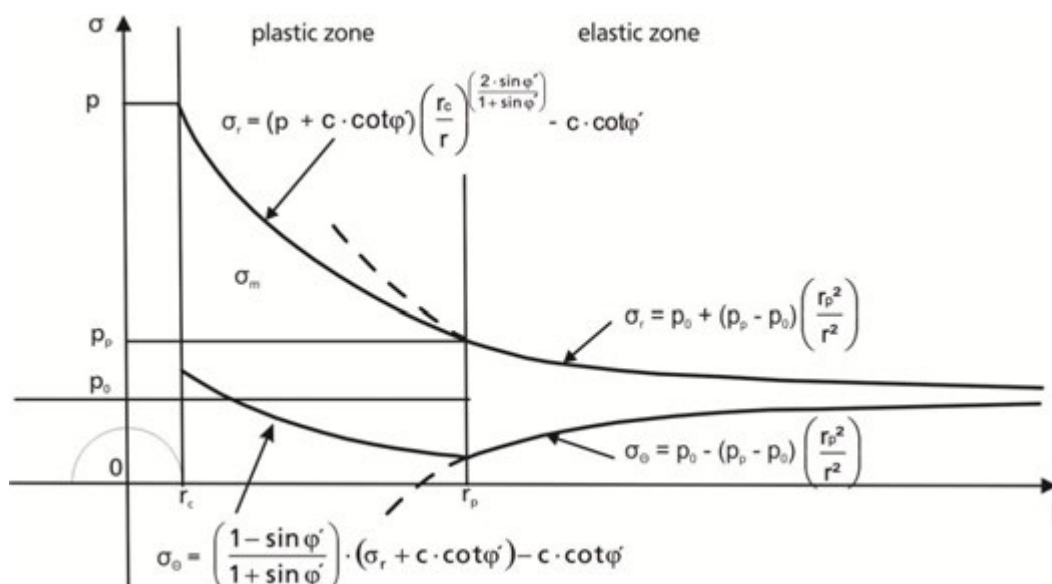


Figure 5: Drained stress distribution according to (Vesic, 1972).

Calculated maximum grout pressure applying the conical shear failure criterion in combination with the analytical solution by (Vesic, 1972) is smaller than the measured grout pressure (El-Kelesh, 2001). This is because the analytical solutions do not take the pre-compaction due to neighbour grout masses into account.

In addition to the analytical solution by (Vesic, 1972) other solutions exist for cylindrical or spherical expansion under drained or undrained conditions for different soil constitutive laws. An overview of cavity expansion theory in geomechanics is given by (Yu, 2000). Various analytical solutions based on the cavity expansion theory are listed in the following Table 1:

Table 1: Analytical solutions for cavity expansion in soil

Paper/Report	Analytical approach	Soil constitutive law
Chadwick, 1959	spherical cavity expansion	elastoplastic (Mohr-Coulomb) associated flow rule
Vesic, 1972	cylindrical/spherical cavity expansion, drained/undrained	elastoplastic (Mohr-Coulomb)
Baligh, 1976	cylindrical/spherical cavity expansion, drained	elastoplastic (Mohr-Coulomb, extended)
Davis et al., 1984	cylindrical cavity expansion, undrained	elastoplastic (Cam Clay)
Carter et al., 1986	cylindrical/spherical cavity expansion, drained	elastoplastic (Mohr-Coulomb)
Collins et al., 1992	cylindrical/spherical cavity expansion, drained	elastoplastic (Critical-State-Model)
Collins, Yu, 1996	cylindrical/spherical cavity expansion, undrained	elastoplastic (Cam Clay)
Bolton, Whittle, 1999	cylindrical cavity expansion, undrained	non-linear elastic/perfect plastic (user defined)
Cao et al., 2001	cylindrical/spherical cavity expansion, undrained	elastoplastic (Modified Cam Clay)

Numerical approaches for simulating compaction grouting have to satisfy the requirement of large deformations and need a soil constitutive model with variable soil properties such as density or stiffness. Early finite element modelling was carried out with modified Cam-Clay models (Table 2).

Table 2: Numerical modelling of compaction grouting

Paper/Report	Subject	Soil	Soil constitutive law	FE-program
Au et al., 2006	Grouting test	clay	elastoplastic (Cam Clay)	ABAQUS
Elmi, Favre, 2004	Cone penetration test	diff.	elastoplastic (own law)	n/a
Iagolnitzer, 2000	Comp. grouting test area	sand	elastoplastic	ABAQUS
Jafari et al., 2000	Grouting test	clay	elastoplastic (Cam Clay)	ABAQUS
Komiya et al., 2001	Grouting test	clay	elastoplastic (Cam Clay)	n/a
Kovacevic et al., 1996	Compensation grouting	clay	elastoplastic (Mohr-Coulomb)	ICFEP
Kummerer, 2003	Compensation grouting	sand	elastoplastic (Hardening Soil)	PLAXIS 3D

The main purpose of compaction grouting is to change void ratio. Hence, a stress dependent soil constitutive model with variable soil properties such as density, stiffness or - of course - void ratio itself is preferable. Additionally numerical approaches have to satisfy the requirement of large deformations. First finite element modelling was carried out with elastoplastic models. By the use of Cam Clay or Hardening Soil, (Table 2) the requirement for a modelling of densification behavior was satisfied.

In the current work the numerical modelling was carried out with a hypoplastic soil model (Kolymbas, 1988) which is suitable for granular soils since the void ratio is one of the model parameters.

3. NUMERICAL STUDIES

The aim of the numerical studies was to investigate the behaviour of soil in dependency of the grid spacings and the height of the overlying strata above the grout columns. 12 different grid patterns with spacings between 2.0 m and 14.0 m and 3 different heights of overlying strata between 2.0 m and 6.0 m were investigated. The grid patterns were assumed to be quadratic. The model boundary was placed 12 m below the bottom of the columns, to minimize the influence on the results (Figure 6).

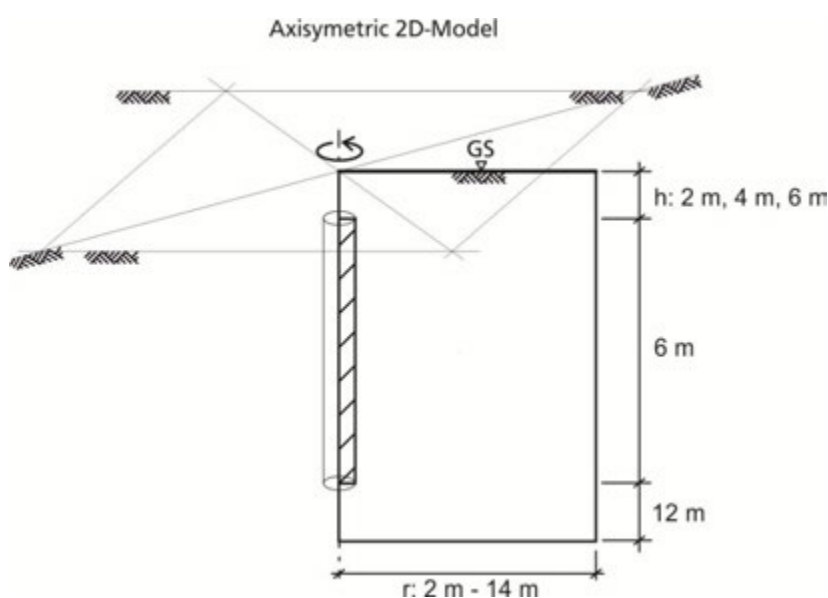


Figure 6: Dimensions of the model.

The numerical simulation was carried out for a single column expansion up to 1 m in diameter with a finite element program Tochnog 8 (FEAT, 2011). The representative column expansion for all columns of the various grid patterns were modelled. Therefore axisymmetric finite element models with up to 4359

nodes and up to 4215 linear quadrilateral elements were designed with the program. The cylindrical volume of the modelled area represents the size of the various grid spacings. The ratio of the grout volume to the compacted soil volume is called the relative grout volume a_s . In Table 3 the representative model-radius r_{model} for the various grid spacings a and the corresponding grout volume a_s are listed.

Table 3: Representative radius r_{model} for various grid spacings a and relative grout volume a_s respectively.

a [m]:	2.0	2.2	2.4	2.6	2.8	3.0	3.2	3.4	3.6	7.0	10.0	14.0
a_s [%]:	18.5	15.3	12.9	11.0	9.5	8.2	7.2	6.4	5.7	1.5	0.7	0.4
r_{model} [m]:	1.1284	1.2412	1.3541	1.4669	1.5797	1.6926	1.8054	1.9182	2.0311	3.9493	5.6419	7.8987

Boundary conditions were determined assuming that the representative column only causes soil displacements inside the grid spacing width. Thus, the horizontal displacements on the radial boundary of the model were set to zero. They are illustrated in Figure 7. On the one hand this assumption implicates a radius of the model too small in case of a primary grout column. On the other hand the further assumption of no preload due to adjacent grout column is underestimating the initial stress conditions in case of a secondary grout columns. After all the combination of these two assumptions represent the average boundary conditions of grout columns in or near the center of a compaction grouting area.

The grouting process was simulated volume-controlled based on the Eulerian description for the continuum. Hence, the grout mass expands convectively and cylindrically over a mesh, fixed in space (Figure 7).

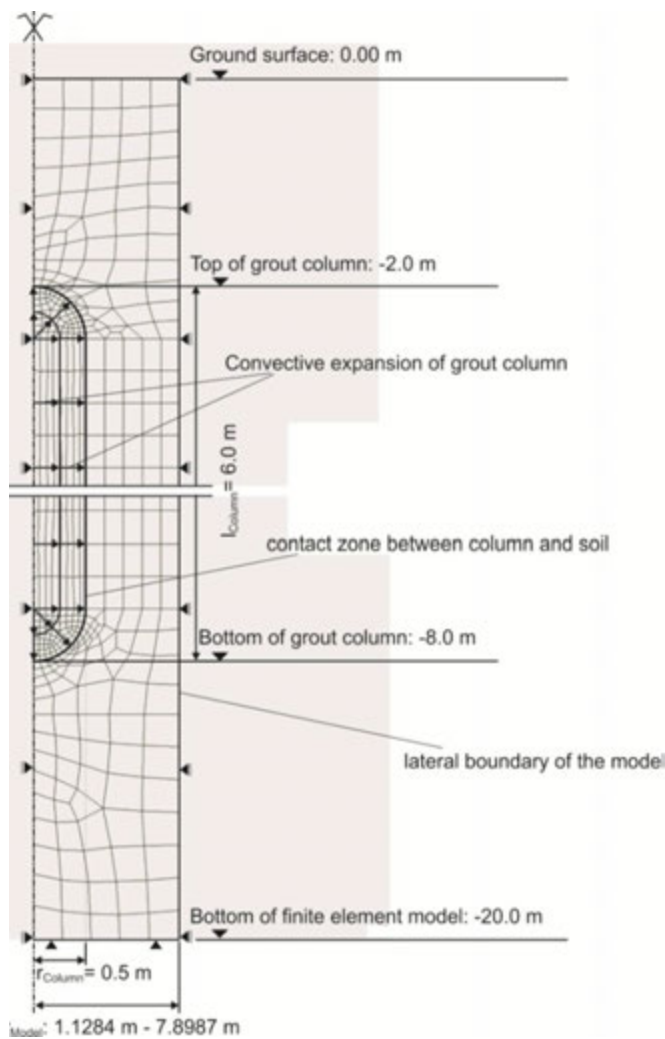


Figure 7: Finite element model.

The stress-strain dependency of the soil was modelled with the hypoplastic model by (Kolymbas, 1988), extended by (von Wolffersdorff, 1996), where the void ratio e is pressure dependent. Figure 8 shows the relationship between the void ratio e and the mean pressure p in case for the used hypoplasticity law in comparison with the Cam Clay model. The critical void ratio e_c approximately corresponds with the state of the least compacted soil. The void ratio e_i is a theoretical maximum value in case of perfectly isotropic compaction. The shape of the hypoplastic curve can be controlled by the granular hardness h_s and its exponent n .

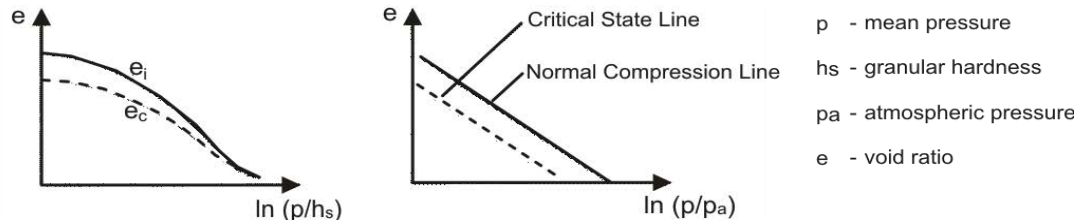


Figure 8: Void ratio – pressure dependency, (left) hypoplastic relation, (right) Cam Clay, (Bauer, 1996).

The soil was assumed to be Schlabendorf-Sand. This sand has a coefficient of uniformity of $C_U = 3.09$. The initial void ratio of the sand was assumed to $e_{ini} = 0.75$, corresponding to a bulk density of $D = 0.2$, i. e. a loose density. According to e_{ini} the initial specific weight was $\gamma_{Sand} = 15.1 \text{ kN/m}^3$. The hypoplastic parameters of Schlabendorf-Sand were determined by (Herle, 1997). They are listed in Table 4.

The grout columns were modelled linear elastically with an increasing Young’s modulus. The final Young’s modulus was set to $E = 10 \text{ MN/m}^2$.

Table 4: Hypoplasticity parameter – Schlabendorf-Sand

φ_c [°]	h_s [MN/m ²]	n [-]	e_{c0} [-]	e_{d0} [-]	e_{i0} [-]	α [-]	β [-]
33	1600	0.19	0.85	0.44	1.00	0.25	1.0

4. RESULTS

For grid spacings between $a = 2.0 \text{ m}$ and $a = 3.6 \text{ m}$ the sand was simulated to be compacted from a loose soil to a mainly mediumdense soil. The bulk density D after the complete injection was analysed for the lateral area of the column. The average values over the full length of column l_{column} (2 m to 8 m depth) was determined for the contact zone between column and soil and for the lateral boundary of the axisymmetric model (contact zone and lateral boundary are shown in Figure 7). The results are plotted in the following diagram in Figure 9.

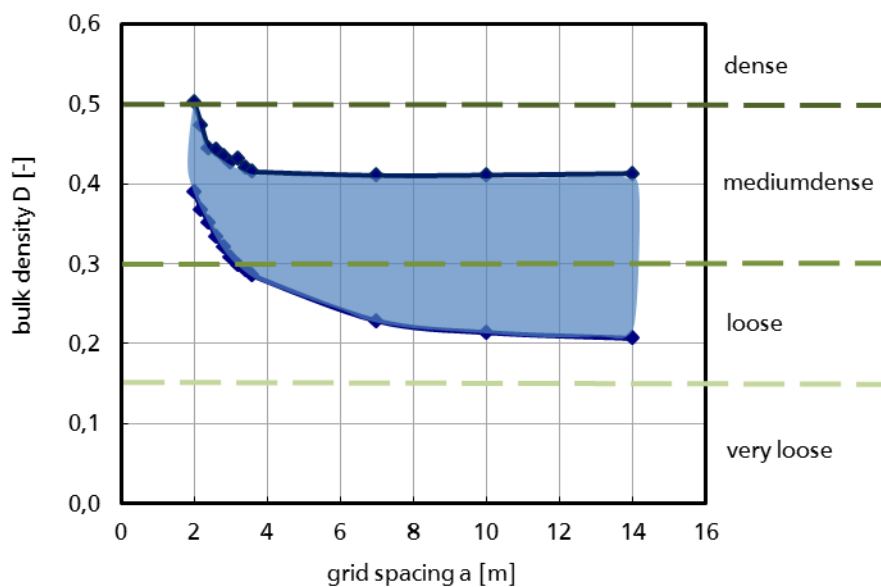


Figure 9: Average bulk density D vs. grid spacing a .

The bulk density in the contact zone depends significantly on small grid spacings of $a = 2.0$ to $a = 3.6$ m. Grid spacings of $a > 4$ m show no influence on the bulk density in the contact zone. The bulk densities at the lateral boundary show a different behaviour. They are also considerably dependent on small grid spacings but they also depend less clearly on grid spacings of $a > 4$ m.

Figure 10 shows the dependency of the lateral stress after the compaction on the grid spacing. For this purpose the average horizontal stresses at the lateral boundary of the model were determined from a depth of 2 m to 8 m.

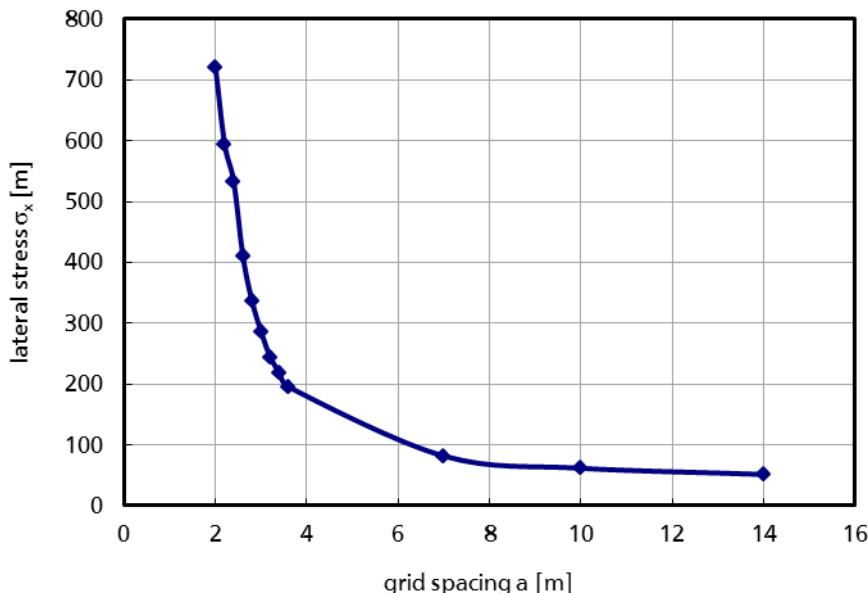


Figure 10: lateral stress σ_x vs. grid spacing a .

The curve characteristic of the lateral stress is the same as for the bulk density. The significant dependency is between $a = 2.0$ m and $a = 3.6$ m. The maximum horizontal stresses at the contact zone was between $\sigma_x = 420$ kN/m² for a grid spacing of $a = 14.0$ m and $\sigma_x = 2000$ kN/m² for $a = 2.0$ m. Thus, the ratio of the lateral stresses at the model boundary to the lateral stresses at the contact zone, $\sigma_{x, \text{boundary}} / \sigma_{x, \text{contactzone}}$ is considerably bigger for $a = 2.0$ m than for $a = 14.0$ m.

In contrast to the lateral stresses the coefficient of earth pressure k_0 at the model boundary does not depend on the small grid spacings between $a = 2.0$ m and $a = 3.6$ m. To illustrate this, Figure 11 presents not the dependency of k_0 on the grid spacing a but on the relative grout volume a_s . Between $a_s = 5.7\%$ ($a = 3.6$ m) and $a_s = 18.5\%$ ($a = 2.0$ m) k_0 is nearly constant.

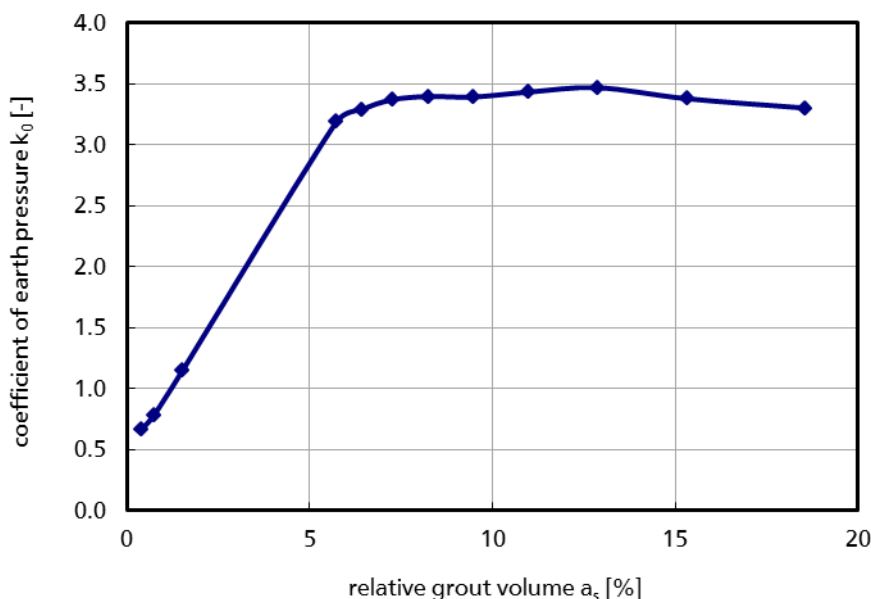


Figure 11: Coefficient of earth pressure k_0 vs. relative grout volume a_s .

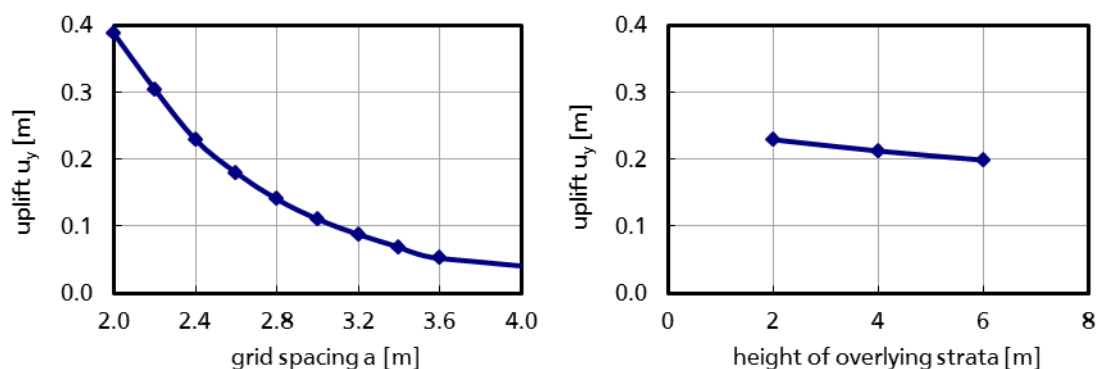


Figure 12: Uplift of ground surface u_y vs. grid spacing a and uplift u_y vs. height of overlying strata.

Finally, Figure 12 shows the uplift u_y of the ground surface depending on the grid spacing (left side) and on the height of the overlying strata (right side), respectively. For large grid spacings $a > 7$ m the ground surface settles. With decreasing grid spacings $a < 4$ m u_y increases exponentially. The dependency of u_y on the height of the overlying strata was calculated for a grid spacing of $a = 2.4$ m. The detected dependency was much less significant than the dependency on grid spacing.

5. CONCLUSION

The suitability of the used finite element model with hypoplasticity law was already tested by a numerical back-analysis (Anthogalidis et al., 2011) of a compaction grouting laboratory test (El-Kelesh et al., 2009). The intention of the current analysis was to extend the model for simulation of a practical compaction grouting application and further to investigate the dependence of design parameters on compaction and on uplift.

The detected curve characteristic of the relation between the bulk density and the grid spacing show that a reduction of soil void ratio over the total area occurs up to a certain maximum grid spacing. This certain grid spacing for the loose Schlabendorf-Sand is $a = 3.6$ m. If the grid spacing is larger, there will be no homogeneous reduction of soil void ratio over the whole area. If the grid spacing is chosen lower than the certain maximum grid spacing, the bulk density increases significantly but also a significant increase in uplift can be expected. Hence, when compaction is the primary purpose the range of the optimal grid spacings is very small.

As also determined in laboratory tests (Liao et al., 2006) and in field tests (Wong et al., 1996) the radius of influence of the grout column is 3 to 4 times the radius of the column.

For small grid spacings of $a = 2.0$ m to 3.6 m a maximum compaction was reached with a considerable uplift at the ground surface. Because of the mainly horizontal direction of the compaction effect, the variation of the height of overlying strata has no considerable influence on the uplift. In contrast to that, the grid spacing influences the uplift behaviour significantly.

Further investigations are currently carried out to study the influence of loading of overlying structures, grout volume, radius of injection casing, initial bulk densities and hypoplastic parameters on the compaction effect, on the uplift and on the reduction of settlement-potential.

REFERENCES

- Anthogalidis, A., Arslan, U., Reul, O. (2011). Numerical Back-Analysis of compaction grouting with a hypoplastic soil model. *XV European Conference on Soil Mechanics and Geotechnical Engineering*, 12.-15.09.2011, Athens, Greece
- ASCE (2010). *Compaction Grouting Consensus Guide (ASCE/G-I 53-10)*, edited, ASCE.
- Au S.K.A., Yeung A.T. und Soga K. (2006). „Pressure-controlled cavity expansion in clay.” *Canadian Geotechnical Journal*, No. 43, pp. 714-725.
- Baker W.H. (1985). „Embankment Foundation Densification by Compaction Grouting.” *Issues in Dam Grouting*, Proc. of the Session sponsored by the Geot. Eng. Div. of the ASCE, Denver, Colorado, pp. 104-122.
- Baligh, M.M. (1976). Cavity Expansion in Sands with Curved Envelopes, *Journal of the Geotechnical Engineering Division*, 102(11), 1131-1146
- Bauer, E. (1996). „Calibration of a comprehensive hypoplastic model for granular materials.” *Soils and Materials*, 36(1), pp. 13-26.

- Bolton, M.D., Whittle, R.W. (1999). A non-linear elastic/perfectly plastic analysis for plane strain undrained expansion tests, *Geotechnique*, 49(1), 133-141.
- Brown D.R., Warner J. (1973). Compaction Grouting. *Journal of the Soil Mechanics and Foundations Division*, Vol. 99, No. 8, Journal Paper, pp. 589-601.
- Cao, L.F., Teh, C.I., Chang, M.F. (2001). Undrained cavity expansion in modified Cam clay I: Theoretical analysis, *Géotechnique*, 51(4), 323-334.
- Carter, J.P., Booker, J.R., Yeung, S.K. (1986). Cavity expansion in cohesive frictional soils, *Géotechnique*, 36(3), 349-358.
- Chadwick, P. (1959). The quasi-static expansion of a spherical cavity in metals and ideal soils, *The Quarterly Journal of Mechanics and Applied Mathematics*, 12(1), 52-71.
- Collins, I.F., Pender, M.J., Yan, W. (1992). Cavity expansion in sands under drained loading conditions, *International Journal for Numerical and Analytical Methods in Geomechanics*, 16(1), 3-23.
- Collins, I.F., Yu, H.S. (1996). Undrained Cavity Expansions in Critical State Soils, *International Journal for Numerical and Analytical Methods in Geomechanics*, 20(7), 489-516.
- Compaction Grouting Consensus Guide Committee of the Geo-Inst. of the ASCE. (2010). *Compaction Grouting Consensus Guide*, ASCE/GI Standard 53-10.
- Davis, R.O., Scott, R.F., Mullenger, G. (1984). Rapid expansion of a cylindrical cavity in a rate-type soil, *International Journal for Numerical and Analytical Methods in Geomechanics*, 8(2), 125-140.
- El-Kelesh, A.M., Matsui, T., Tokida, K.-I. (2009). Calibration chamber investigation of confirming pressure on mechanisms of compaction grouting, *Proceedings of the 17th International Conference on Soil Mechanics and Geotechnical Engineering*, 19-22.
- El-Kelesh, A.M., Mossaad, M.E., Basha, I.M. (2001). Model of Compaction Grouting, *Journal of Geotechnical and Geoenvironmental Engineering*, 127(11), 955-964.
- Elmi, F., Favre, J.L. (2004). „Cylindrical cavity expansion modeling for interpretation of cone penetration tests.” *Proceedings ISC-2 on Geotechnical and Geophysical Site Characterization*, pp. 897-903.
- FEAT (2011). Tochnog Professional Version 8, *Finite Element Program*.
- Graf E.D. (1969). „Compaction Grouting Technique and Observations.” *Journal of the Soil Mechanics and Foundations Division*, Proc. ASCE, SM 5, pp. 1151-1158.
- Herle I. (1997). „Hypoplastizität und Granulometrie einfacher Konrgerüste.“ Veröffentlichungen des Institutes für Bodenmechanik und Felsmechanik der Universität Fridericiana in Karlsruhe; Heft 142
- Iagolnitzer, Y. (2000). A Comparative Field Experiment on Compaction Grouting, *Mitteilungen des Instituts und der Versuchsanstalt für Geotechnik der Technischen Universität Darmstadt; Heft Nr. 52*, 75-85.
- Jafari, M.R., Au, S.K.A., Soga, K., Bolton, M.D., Karim, U.F.A., Komiya, K. (2000). Experimental and Numerical Investigation of Compensation Grouting in Clay, *Proceedings of GeoEng 2000*.
- Kolymbas D. (1988). „Eine konstitutive Theorie für Böden und andere körnige Stoffe.“ Veröffentlichungen des Institutes für Bodenmechanik und Felsmechanik der Universität Fridericiana in Karlsruhe, Heft 109.
- Komiya, K., Soga, K., Agaki, H., Jafari, M.R., Bolton, M.D. (2001). Soil Consolidation Associated with Grouting during Shield Tunnelling in soft clayey Ground, *Geotechnique*, 51(10), 835-846.
- Kovacevic, N., Potts, D.M., Vaughan, P.R. (2000). „The effect of the development of undrained pore pressure on the efficiency of compaction grouting.” *Geotechnique*, Vol. 50 No. 6, pp. 683-688.
- Kummerer, C. (2003). „Numerical Modelling of Displacement Grouting and Application to Case Histories.“ Gruppe Geotechnik Graz, Institut für Bodenmechanik und Grundbau, Heft 19.
- Liao, H.-J., Su, S.-F., Chen, W.-L. (2006). Ground improvement piles induced shear strength increase in normally consolidated clay, *Anglais*, 29(1), 9.
- Vesic A.S. (1972). „Expansion of Cavities in Infinite Soil Mass.” *Journal of the Soil Mechanics and Foundations Division*, Proc. of the ASCE, pp. 265-290.
- von Wolffersdorff P.-A. (1996). „A hypoplastic relation for granular materials with a predefined limit state surface.” *Mechanics of cohesive-frictional materials*, Vol. 1, pp. 251-271
- Wong, L.W., Chau, M.C., Chen, H.T. (1996). Compaction Grouting for Correcting Building Settlement, *Proceedings of IS-TOKYO'96, The Second International Conference on Grouting and Deep Mixing*, 231-236.
- Yu, H.-S. (2000). *Cavity Expansion Methods in Geomechanics*, Kluwer Academic Publishers; Dordrecht, Netherlands.

Grand Carré de Jaude: an exceptional building site of soil treatment by jet-grouting in the middle of a volcano

Patrick Berthelot, Bureau Veritas, France, patrick.berthelot@fr.bureauveritas.com)

Frédéric Durand, Fugro Géotechnique, France, f.durand@fugro.com

Olivier Madec, Botte Fondations, France, olivier.madec@vinci-construction.fr

Alexandre Reynaud, Fugro Géotechnique, France, a.reynaud@fugro.com

ABSTRACT

In the center town of Clermont-Ferrand, the building of real estate complex with 2 basement levels needed complicated substructure works. Because of the special geology and hydrogeology due to the volcano and its filling, the building designers were obliged to find very specific constructive solutions. During the stage of works the perimetral wall has been carried out from metal sheeting piles down a mixing-ground trench. In stage of use this wall has been reinforced by a concrete wall.

To assure the bearing capacity, the equilibrium of the deep excavation and the retaining structures during scope of works and scope of services, a 3 meter thick injected bottom with secant jet-grouting columns and jet-grouting load-transfer columns has been realized. To assure the 3 conditions of soil improving (bearing pressure, watertightness, increase of passive pressure) a specific target in terms of deformation unit, permeability and compression resistance, has been defined during the conception stage. At the begin of works, many testing boards have been used to confirm the type and characteristics for the concrete, diameters, resistance and deformation characteristics of the columns, according to the types of soils (sandy, slity-clayey with some organic materials...).

A program of works follow-up and control (compressive resistance, dilatometer, inclinometer, topography, water test, static loading test...) has been set up during the whole execution stage to achieve the earthworks and all substructure works.

1. INTRODUCTION

One of the most important real estate projects has been launched in France in 2010. This project has a size on ground of more than 11 000m² and is situated at Clermont-Ferrand, in the Centre of France and in edge of the main place in the city centre : place of Jaude.

Several 6 or 7-level buildings with flats, offices and functional structures must be realized on two levels of shops and 2 levels of basement.



Photo 1: presentation of the project

The achievement of such a project in the city centre requires a perfect control of the deformations of the project itself but also of the neighbouring works.

To the north of the project the nearby buildings are located at less than 15 meters. The other buildings around are located at a distance between 5 and 10 meters from the project.

The main difficulty of this project is to realize the 2 basement levels with an under-water excavation with the water table that is near the naturel ground and could be artesian locally.

2. PRESENTATION OF THE SITE

2.1. Geology: the Jaude maar

The site is geologically atypical because it is on an ancient maar. An old volcanic chimney with a cylindrical or conical shape has stamped out the pre-eruptive substratum from Marls and marl-limestone. On about one hundred meters, the central depression has been filled up by water then by lake sediments (silts and sands) and probably by river sediments (coarse sands, silts and soft clays).

The Fugro Géotechnique campaign of geotechnical investigations confirmed that the site was situated on the ancient maar filled up by recent sediments.

Under the 3 meters of backfill, the following layers have been found:

- Limons from old volcanic griffins whose gaseous release were rich in CO₂
- Soft upper silts which are excessively compressible and organic in some places
- Fine sands to coarse sand which are more or less compact
- Lower consolidated silts which constitute the main deposit of the maar.

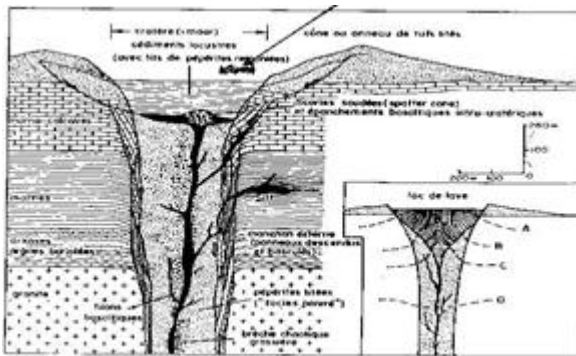


Figure 1: geological cut

2.2. Geotechnic

The geological campaign consisted in 44 static penetrometer tests with piezoconic head and about 10 core drillings (between 15 and 30 meters deep) to define precisely the stratigraphic cuts, the identification characteristics and the soil mechanics.

With the piezocone tests we can separate the different soils : sandy soils and silt or clay soils.

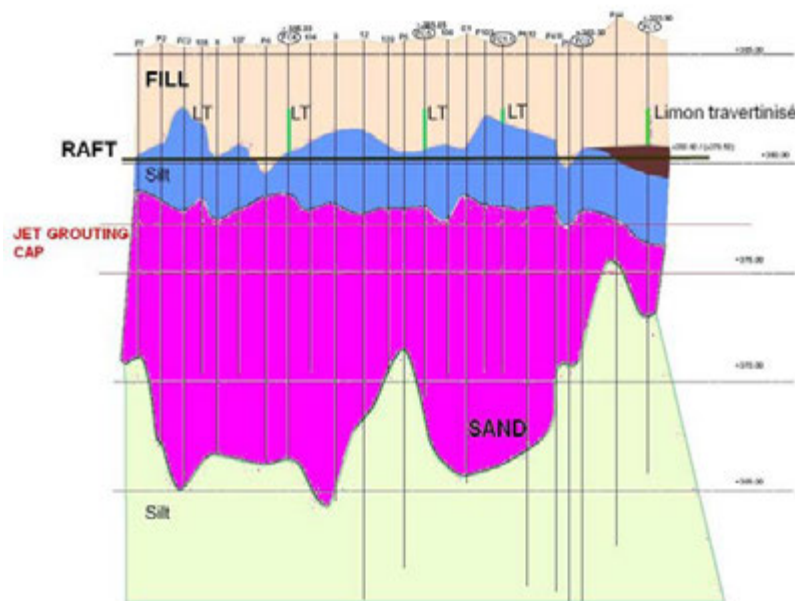


Figure 2: west-east overall cut

We remark that the upper silt layer is less thick at the west end.

At the east end, which is also the maar end, the sand layer is less and less thick depending on the raising of the lower silt roof.

In the central part, the sandy materials are thicker, so the lower silts are deeper.

Laboratory Tests :

According to the laboratory tests the upper and lower silts have a high water content, respectively 90% and 50% in correspondance with weak dry contents, respectively 15kN/m^3 and 17kN/m^3 .

The CU + U shear tests realised by triaxial equipment show high shearing resistance ($\Phi=36^\circ$) obtained with deformations too high to be compatible with work deformation in urban site.

The maximum shear characteristics have been voluntarily limited at deformations lower or equal to 2%, which force us to calculate shear resistance on a maximum angle of friction of 25° .

About the silt compressibility we took into account the compressibility parameters $C_c/(1+e_0)$ calculated in the range of the work sollicitations and not the compressibility parameters in the high stress range.

Artesianism :

Under this ancient volcano, some “chimneys” have ascending water currents charged with carbonic gas, called “griffon”. The static penetration tests with U measure and the selective piezometers have permitted to measure the deep pore fluid pressure higher to the simple hydraulic charge, which means pressions like $(1+i)\cdot\gamma_w\cdot h$, rather than $\gamma_w\cdot h$.

On the surface, water table is located towards 3meters depth. On the other hand, towards 15meters depth, the artesianism could locally reach charges higher than the natural ground charges (around 3 meters above the natural ground).

3. PRESENTATION OF THE PROJECT

3.1. General principle

Several buildings with 6 or 7 levels and 2 levels of shops and 2 basement levels are planned.

For the 2 basement levels, an under-water excavation with a specific artesianism is needed.

The zero level of the project was fixed at +386.10NGF, which is slightly above the original ground. The final underground levels were fixed at -5,7m compared to the zero level of the project and at some places at -6,60m, so respectively the final levels at the following heights +380,4NGF and +379,5NGF.

The under-water excavation obliges to realize a vertically and horizontally permeable work to isolate the parcel from the rest of the site. This work should include :

- A perimetric wall,
- An injected deep excavation.

A perimetric wall with descending sheeting piles (to avoid beating problems in urban site) in the mortar wall already drilled must be set up.

The injected deep excavation will be made with secant columns of jet-grouting.

Otherwise the general principle of the work foundation consists in realizing a compensated foundation, which means that the removed soil weight is almost equal to the work global weight deduced from Archimedes' buoyancy.

The building foundation is made up of a concrete foundation raft to report charges on the jet-grouting transfer columns anchored in the injected deep excavation. The aim is to obtain a homogeneous stress on the injected deep excavation base.

The deep excavation made of jet-grouting columns has 3 functions :

- watertightness function during the provisional phase
- cross brace function to block sheeting piles bases
- stress distribution function on the injected deep excavation base to complete the concrete foundation raft and the transfer columns.

3.2. Perimetric wall (530ml – 5 950m²)

Because of the locally artesianism risk, the selected execution principle is a wall with grout pre-drilling and sheeting piles. The slurry wall solutions must be avoided because of the bentonitic mud needed to hold the drilling wall.

The usual density of this mud is equal to $10,2\text{kN/m}^3$, so the risk is to get instability when a pannel is open if it is situated on a “griffon”.

The supporting and relative watertightness are obtained by the sheeting piles. The grout pre-drilling allows to cross hard bolster benches and to fix the sheeting piles without beating or high vibration. During the final stage we planned reinforced concrete veil.

As an alternative to the grout drilling, the company proposed a soil mixing solution which minimizes the evacuation of materials and allows a better control in case of “griffon”.



Photo 2: soil mixing principle

3.3. Jet grouting injected deep excavation (42 000m³)

Because of the nature of the materials (sand, silt and soft limon) the injected deep excavation could not be done as usual by a grout injection. So it has been made of secant jet-grouting columns.

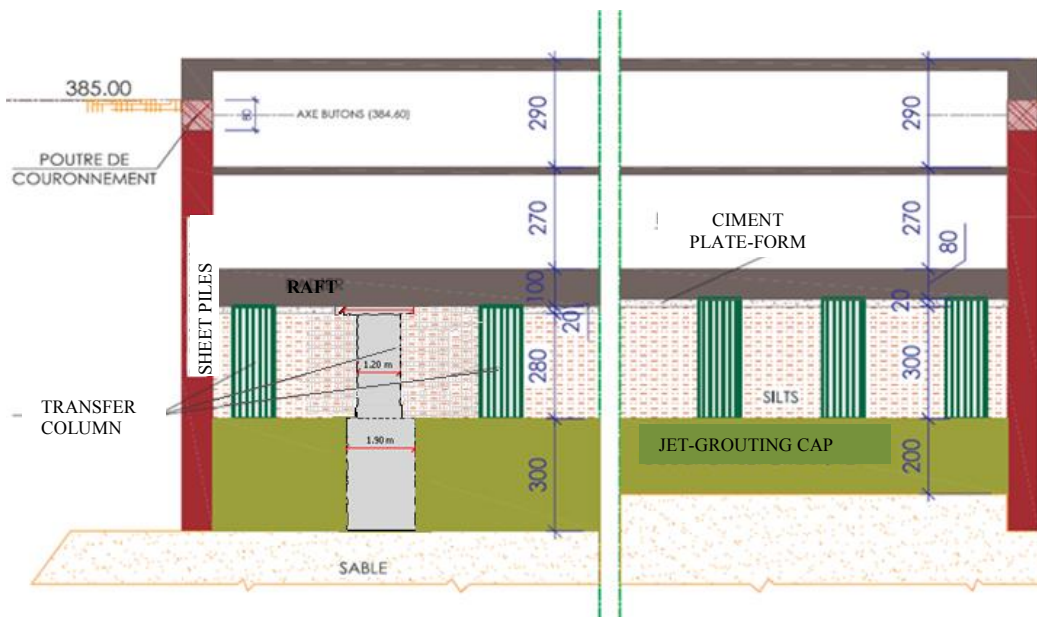


Figure 3 : infrastructure cut

Because of the global conception of the project, the injected deep excavation and the transfer columns have 3 functions, which oblige to define efficient characteristics for the calculations :

- A injected deep excavation thickness between 2 and 3 meters depending on the loading zones brought by the building,
- An E Young modulus superior or equal to 2 000MPa. We need to obtain a modulus at least equal to 2000MPa because of the modelling results and the relative settlements which must have a maximum slope of 1/500,

- A compressive strength equal or superior to 6MPa. The higher compression zones are situated in the transfer columns and also in contact with the injected deep excavation.
- A pulling resistance (tensile strength) worthless in the modulus to take into account the procedure to realize the columns which could be done with a primary phasing secondary or fresh,
- A permeability lower than 10^{-7} m/s to minimize flow of exhaustion and make the project hydraulically independent of the exterior,
- A column diameter in accordance with the planned objectives to ensure that the injection deep excavation device is secant,
- A transfer column diameter also in accordance to ensure a perfect load transfer between the concrete foundation raft base and the injected deep excavation roof.

Moreover we can recall the complementary stress for this project:

- The transfer columns are mainly situated in the upper silts whereas the injected deep excavation columns are mainly in the sands, which makes it easier to reach the specific target in the deep excavation rather than in the transfer columns.
- The columns must be realized from the naturel ground but after the realisation of the perimetric wall to remain confined into the project and avoid the grout linking by breakdown outside the site
- The transfer columns must be perfectly in contact with the the deep excavation columns. That is why the company chose an uninterrupted realization between the transfer columns and the deep excavation columns, which imposed a specific calpinage for the transfer columns and a change in the jet grouting parameters.
- For the important traficability problem in the deep excavation due to a 90% water content in the upper silts, the jet grouting columns must be ended by a platform with thickness of 50cm virtually continuous jet.

To resist to the uplifts, the jet grouting cap must have a continuous horizon with minimal thickness. Taking into account the surface (more than 11 000m²) and realization method (more than 6000 columns), the cap thickness has been optimized according to the foundation raft position.

The deep excavation has a variable thickness between 2 and 3 meters and the position of the deep excavation must ensure its stability during the digging stage.

Consequently the jet-grouting deep excavation is at various altimetrical levels depending on the different zones. The drawing below shows the different cases of the project.

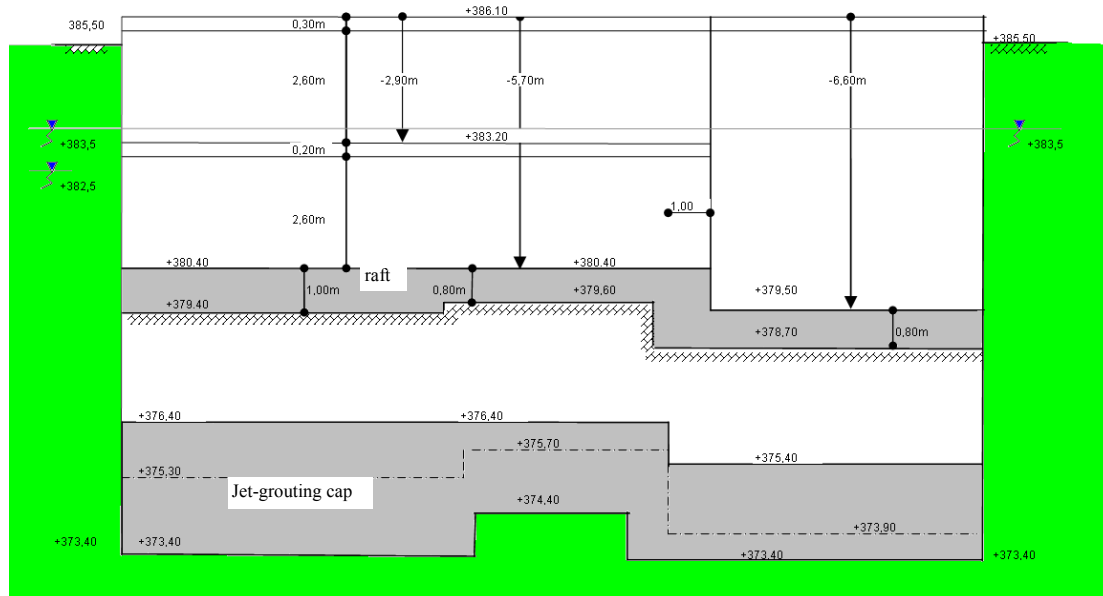


Figure 4 : position of the jet-grouting cap

To check the deep excavation equilibrium, we take into account :

- An uplift due to a groundwater head at +383.50
- An equilibrium within the deep excavation (dotted line on the drawing above).

To secure the work in case of griffin or high pressure, have been realized some events that cross the deep excavation and go up to the level +383.50.

3.4. Realization of the jet grouting columns

3.4.1. Injected deep excavation

When the building site started, the deep excavation columns were realized with a primary and secondary phasage and with a pre-cutting operation with water. But the quantity of spoils to deal with was a delicate problem of this work. So, after some tests, the company went over its phasage and implemented a fresh execution and without water pre-cutting. The nature of the cement has also been changed to ensure a better grout setting.

3.4.2. Transfer columns

Between the foundation raft base and the deep excavation roof, some jet-grouting columns are planned to transfer loads. The transfer column diameters were adapted to respect a maximal stress acceptable to the ELS at 1.8MPa, so $0.3f_c$ and, depending of the loading distribution, 3 transfer column diameters have been retained :

- $Q_{ELS} (Max) \leq 1410 \text{ kN}$ for a diameter of 1.00m
- $Q_{ELS} (Max) \leq 2030 \text{ kN}$ for a diameter of 1.20m
- $Q_{ELS} (Max) \leq 2750 \text{ kN}$ for a diameter of 1.40m.

The following drawing shows an extract of the setting up plan for the jet-grouting columns with the deep excavation columns (in transparency) and the transfer columns (highlighted) that are up in the excavation. We can notice that for all columns the jet-grouting operations are made at the deep excavation level to ensure the implementation of a jet-grouting platform.

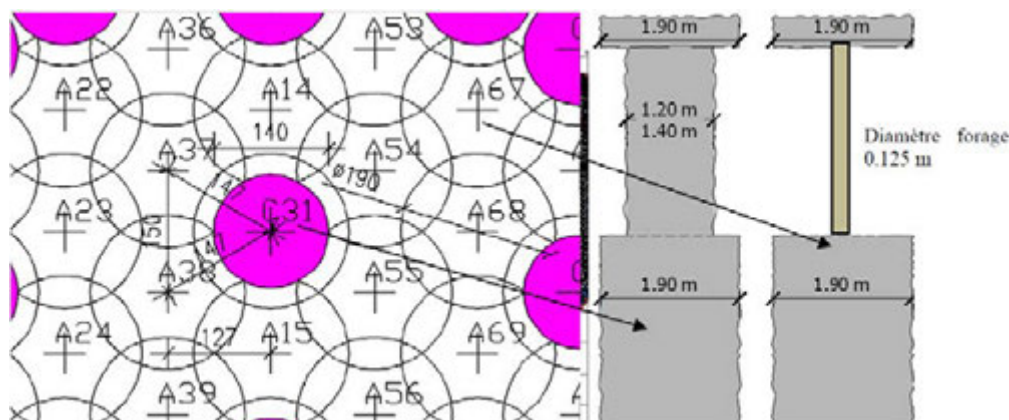


Figure 5 : implementation principle of the various columns

On a surface of 11 400m², the whole deep excavation has needed more than 1600 jet-grouting columns (more than 42 000m³ of jet-grouting).

We can see on the drawing above the traces of the transfer columns on both sides of the supporting grout curtain and piles in a symmetrical way. The first point to check was the columns implementation in Y and X and the altimetry in the drilling beginning in Z.

For that, the company set up an automatic acquisition in X, Y, Z. The number of columns to achieve obliges to set up a minimal automatic acquisition. Some controls by geometrical surveys were made regularly and we had one implementation control for about 60 columns. The variations were lower than 7cm compared to the values planned to ensure a sufficient crosscheck of the deep excavation columns. In altimetry the variations were lower than 10cm, which is a satisfactory value.

When the building site started, a test block has been planned to check the execution of the jet-grouting columns with the following targets :

- A sufficient diameter for the columns,
- The necessary mechanical characteristics at the triple point (meeting point of the 3 jet-grouting columns).

4. THE DIFFERENT STAGES OF THE JET-GROUTING WORKS

4.1. The testing boards

The test block has been done on about 20 jet columns. The target was to check :

- The diameter of the column on the deep excavation, of the transfer columns and of the platform layer,
- The bearing pressure of the transfer column linked to the deep excavation by a static loading global test
- The mechanical characteristics at the triple point of the deep excavation.

To control the diameter of the jet-grouting columns, the company proceeded to several types of tests :

- a feed of pantograph type : this feed was not effective because the tools get stuck at the level of the facies variations
- the release of the columns heads : this check-up was limited because it could be done at about 3 meters depth only and out of water and mainly above the future deep excavation,
- a geophysical method with an electric cylinder. This check-up gave some satisfactory results but their interpretation was difficult.
- A method by static penetration test in the column before setting. This test allows to show that the diameters obtained were superior to the diameters planned with feeds linked to the jet-grouting parameters.

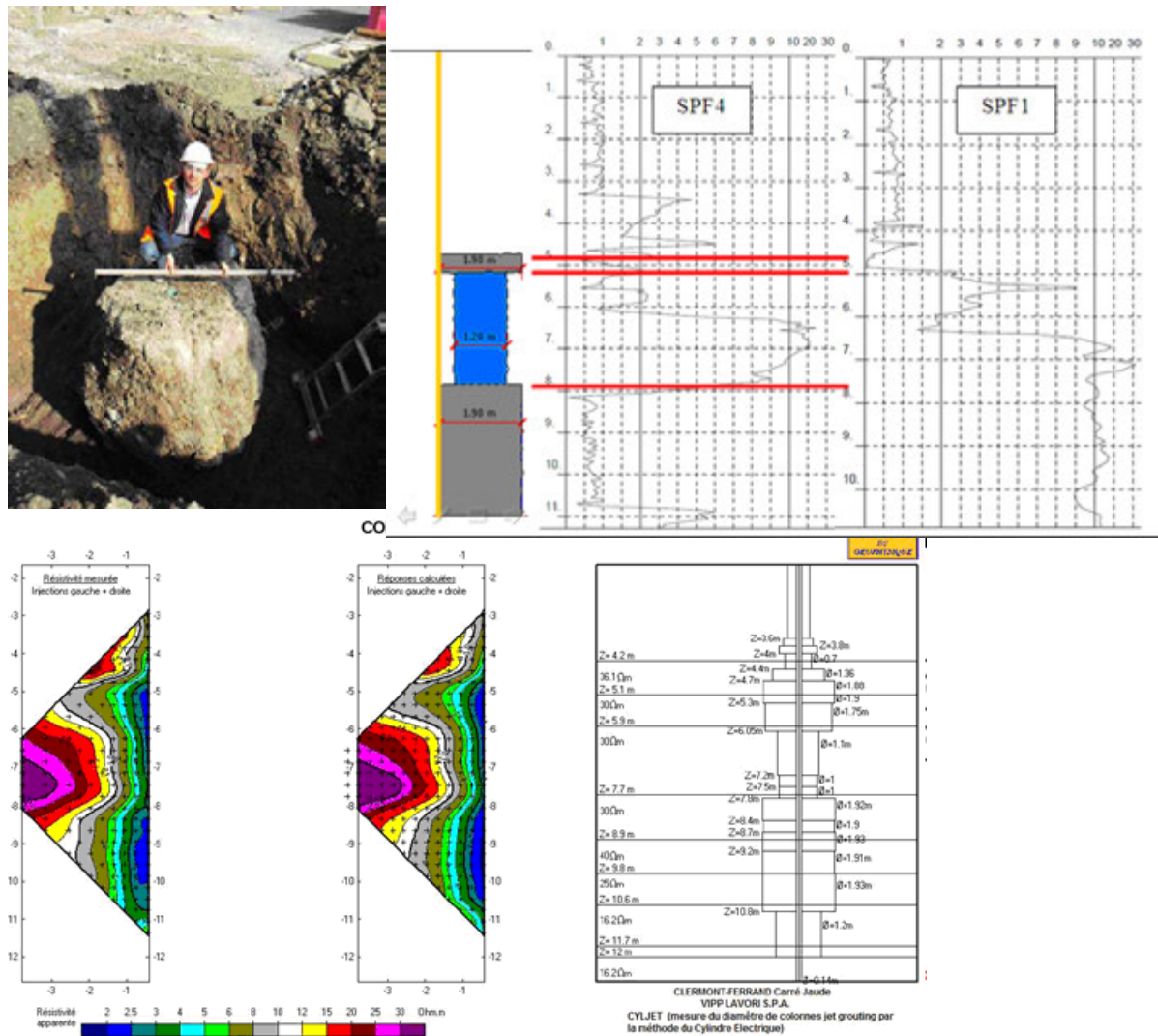


Figure 6: diameters controls

For the static load test, a transfer column with a tubed head was used to avoid parasitic frictions in the upper part and a several jet-grouting columns to simulate the injected deep excavation. The reaction was obtained by sealed bars in the jet-grouting columns.

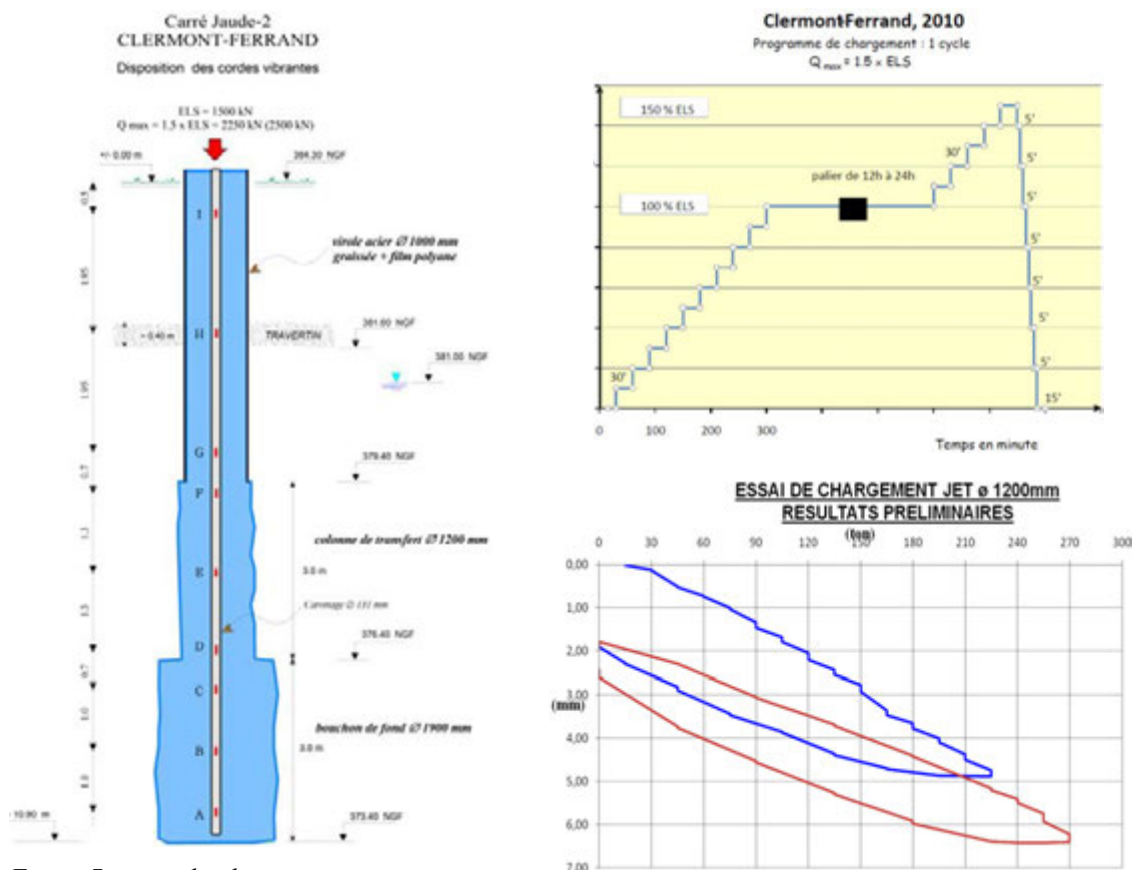


Figure 7 : static load test

The static load test results were especially positive because the bearing pressure was amply reached : at the 2700 kN-charge for 1500 kN ELS the settlement in the column heads was limited to 6mm with less than 3mm of permanent residual deformation.

A digital modeling of the test has showed that the Young modulus of 2000MPa was amply exceeded.

On the other hand the deformation sensors in the jet-grouting column did not allow to examine the deformation distribution in depth.

The characteristics of shear in unconfined compression ($RC \geq 6\text{MPa}$) were checked by test-tubes taken in coring.

The deformation modulus ($E_y \geq 2\,000\text{MPa}$) were checked in different ways. By samples taken in coring and axial compression, the recompression modulus was taken into account and not the first loading modulus to avoid the problems linked to the installation of the samples. Also, the Young modulus have been checked by dilatometer tests and using the unloading and recharging modulus not to include the problems linked to installation of the probe.

We did not retain the Menard pressiometer tests because their precision was not good enough to ensure the measuring in the range of modulus.

We must recall that, in this project, the only guarantee of the compression strength was not enough to ensure a good behaviour of the work foundations.

The first testing boards realized proved that the cement setting was too slow and that the procedures of execution and the cement proportionings must be changed to especially ensure the deformation modulus.



Figure 8: example of reports of control tests

For the dilatometer tests we used stress stages limited at 1.5, stress stages deduced from the calculations of the higher sollicitations. To interpret the test we took into account the thickness of the jet in containment around the columns. For example, if the thickness of the jet-grouting in containment around the probe is superior or equal to 3 meters, the corrector coefficient of the modulus is 1 ; on the other hand, if the thickness of the jet-grouting is limited to 0,90 meters – which is only one column – the corrector coefficient is equal to 0,40. The adjustment of the corrector coefficient was made thanks to the adjustment of the dilatometric tests with axisymetrics finite elements and taken into account the double-layer around the probe what has an unsteady thickness.

4.2. The execution stages

4.2.1. Number of tests

The target is to work on the fractiles to obtain more than 95% of the values higher than the agreed limit.

Table 1: number of axial compression tests

Typology	Coring		Compression tests Rc		Young Modulus on test-tubes		Dilatometer	
	Transfer	Cap	Transfer	Cap	Transfer	Cap	Transfer	Cap
Stage 1	8	20	20	33	13	27	0	8
Stage 2	16	28	45	57	13	20	0	20
Stage 3	11	25	35	29	0	4	0	23
Total	35	73	100	119	26	51	0	51

4.2.2. Compressive strength

The target is to obtain a jet with compressive strength higher than 6MPa.

Table 2: results of axial compression tests of the cap

Average	Min (MPa)	Max (MPa)	Standard variation (MPa)	Number of tests	Number of tests with results lower than 6MPa
9,57	4,97	25,36	3,87	128	8

Table 3: results of axial compression tests of the transfer column

Average	Min (MPa)	Max (MPa)	Standard variation (MPa)	Number of tests	Number of tests with results lower than 6MPa
8,00	4,5	11,5	2,24	90	8

94% of the compressive strength values are higher than 6MPa at the cap level.
 90% of the compressive strength values are higher than 6MPa at the transfer-column level.

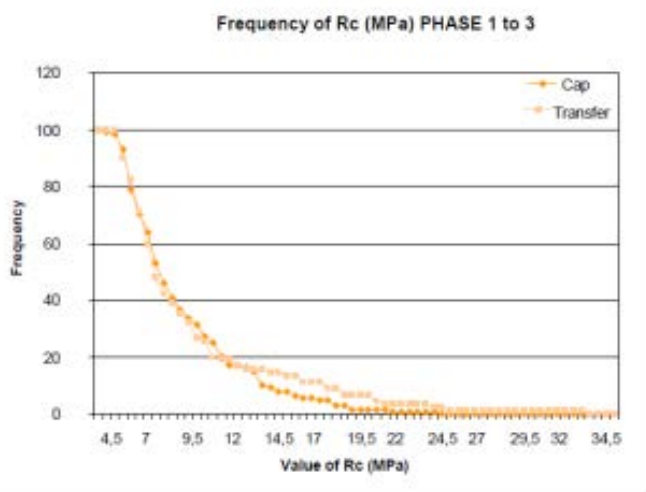


Figure 9: frequency of Rc

4.2.3. The dilatometric tests

Table 4: number of dilatometer tests

	Dilatometer		Measures of modulus
	Transfer	Cap	
Total of stage 1	0	9	80
Total of stage 2	0	15	80
Total of stage 3	0	23	295

Table 5: results of the dilatometer tests

	Stage 1	Stage 2	Stage 3
Number of tests	80	80	295
Maximal value (MPa)	11681	7465	17045
Minimal value (MPa)	1743	1635	1454
Average (MPa)	3402	3514	4625
Median (MPa)	2885	3465	3924
Standard variation (MPa)	1807	1055	2589

96% of the dilatometric modulus values are higher than 2000MPa.

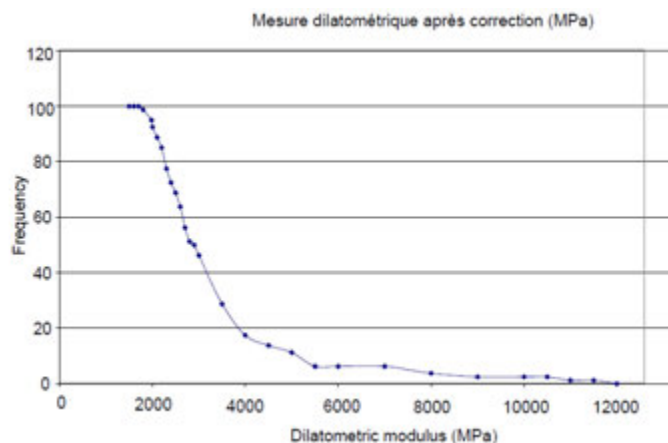


Figure 10: frequency of the dilatometer results

4.2.4. The jet density

Table 6 : results of the density values

Average (t/m ³)	Min (t/m ³)	Max (t/m ³)	Standard variation (t/m ³)	Number of tests
1.85	1.31	2.13	0.14	61
1.9	1.576	3.611	0.4	122
1.8	1.53	3.7	0.28	63

96% of the jet density values are higher than 1.6T/m³.

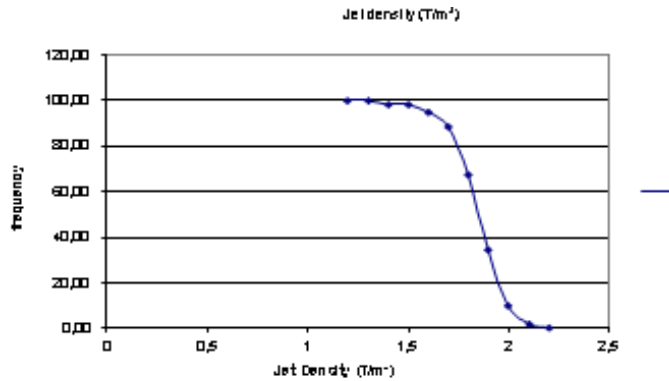


Figure 11: frequency of the density values

5. CONCLUSIONS

The project has been defined precisely at the second stage of the project study to fix a specific target to achieve this work.

The testing boards highlighted the possible difficulties to realize the jet-grouting in such materials and the adapted solutions to meet the goals.

The follow-up and the controls during the execution stage have allowed to achieve the work without technical problems.

The strong reactivity of all companies and participants involved in the building project contributed to the successful infrastructure realization.

A large diameter jet grouting method for arrival of shield tunnelling machine

S. H. Cheng, Department of Construction Engineering, National Taiwan University of Science and Technology, Taipei, Taiwan, shcheng@mail.ntust.edu.tw

Ricky K. N. Wong, Taipei Branch, Sanshin Corporation Ltd., Taipei, Taiwan

H. J. Liao, Department of Construction Engineering, National Taiwan University of Science and Technology, Taipei, Taiwan, shcheng@mail.ntust.edu.tw

ABSTRACT

This paper reports a case study of jet grouting project which involves constructing a watertight grouted zone under a drainage culvert as part of the arrival process for shield machine. An improved jet grouting method which consisted of a modified jet nozzle and an increased flow rate and jet grouting pressure (=360 L/min and 35 MPa respectively) was adopted for this project. This method can produce a large diameter grout pile with less slime. Among the 38 grouting holes of 20m deep drilled in this project, 10 were drilled through the culvert. All grout piles are expected to have a nominal diameter of 3.5 m, which was verified later with sound detectors during jet grouting. The design strengths of grout pile are equal to 1.2 MPa for the silty clay and 2 MPa for silty sand. Cored specimens were recovered to obtain the unconfined compressive strength of jet grouted piles (= 2.36 MPa for silty clay and 3.25 MPa for silty sand). Test results indicate that the strength and diameter of jet grouted piles constructed with the reported jet grouting method can meet the design specifications. The entire jet grouting project of 1750 m³ in cement grout volume (W/C=1.22) was finished in 105 days, within schedule.

1. INTRODUCTION

Underground construction in urban areas has been a long time problematic issue for engineers. Taking Taipei MRT for example, more than 2/3 of construction was built underground over the past two decades. Following the continuing development of modern cities, the depth of tunnel and underground station has become deeper and deeper and subjected to a more restricted construction condition. Moreover, the underground construction may be very close to the existing underground facilities such as foundation, drainage culvert, utility networks etc. and make the situation more complicated. In the last decade, jet grouting method has been widely used in the construction of Taipei MRT for more than 20 years to ensure the stability and waterproof needed for the arrival and departure of shield tunnelling machine and the construction of underground station. Recently, the increasing complexity of underground construction environment and limited construction space has pushed the need to improve the current jet grouting method further.

This paper will report a case study of large diameter jet grouting project, which involves the construction of a water tight grouted zone under a drainage culvert, for the arrival of shield machine at the Dingpu Station of Taipei MRT. To minimize the number of grouting hole drilling in a congested street, a large diameter jet grouting method was adopted. This study will present how the large diameter jet grouting technology was carried out in the field and the measures taken to ensure the quality of jet grout piles installed by the aforementioned jet grouting method.

2. SUBSOIL CONDITIONS UNDER THE CONSTRUCTION SITE

Tucheng extension line (Yongning Station→Dingpu Station) of Taipei MRT is located in the southern part of Taipei Basin. The depth of shield tunnel ranges from 9.58 m to 19.82 m below ground surface. Its subsoil condition varies from silty clay, silty sand to weathering sandstone. Along the Tucheng extension line, four sites are considered to have high risk potential, namely the departure site of shield machine (at Dingpu station), the arrival site (at Yongning station) and two cross-passage sites between shield tunnels (Figure 1a). Double packer (DP) grouting method and jet grouting method are used to improve the mechanical properties and water tightness of soil near the high risk sites. To better understand the subsoil properties of the sites, a thorough geological investigation was carried out at each ground improvement site. The SPT-N values, grain size distribution and physical soil properties profiles are shown in Figure 2. The subsoil condition near Yongning Station (arrival site of shield tunnel), the groundwater level at site is 3.7 m below surface, The upper 12.5m of silty clay layer has some drifted wood embedded. It has the undrained shear strength (S_u) about equal to 30 KPa. Between the depth of 12.5m to 22 m, it is a silty

sand layer (friction angle $\phi' = 28^\circ \sim 30^\circ$) embedded with large number of drifted wood. Below the depth of 22 m, it is mostly loosely cemented weathering sandstone and with the unconfined compressive strength (q_u) equal to 5~20 MPa.

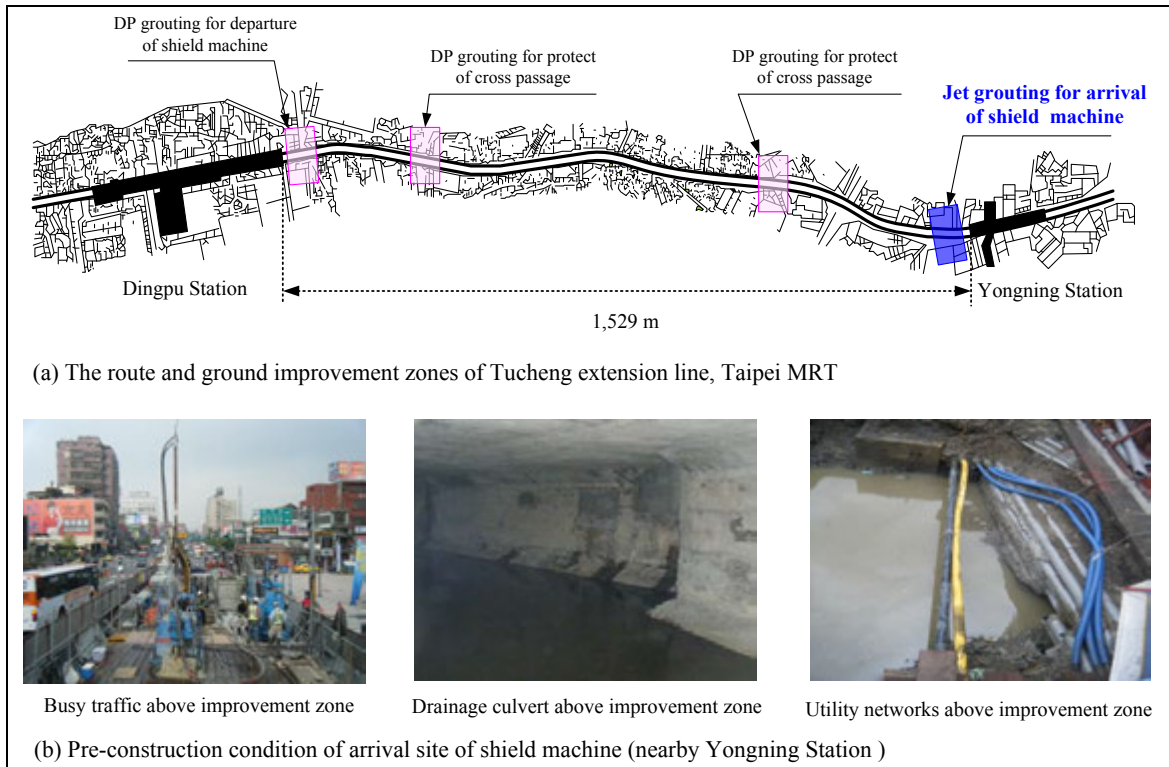


Figure 1: The route, improvement zones and photos of pre-construction condition of Tucheng extension line, Taipei MRT

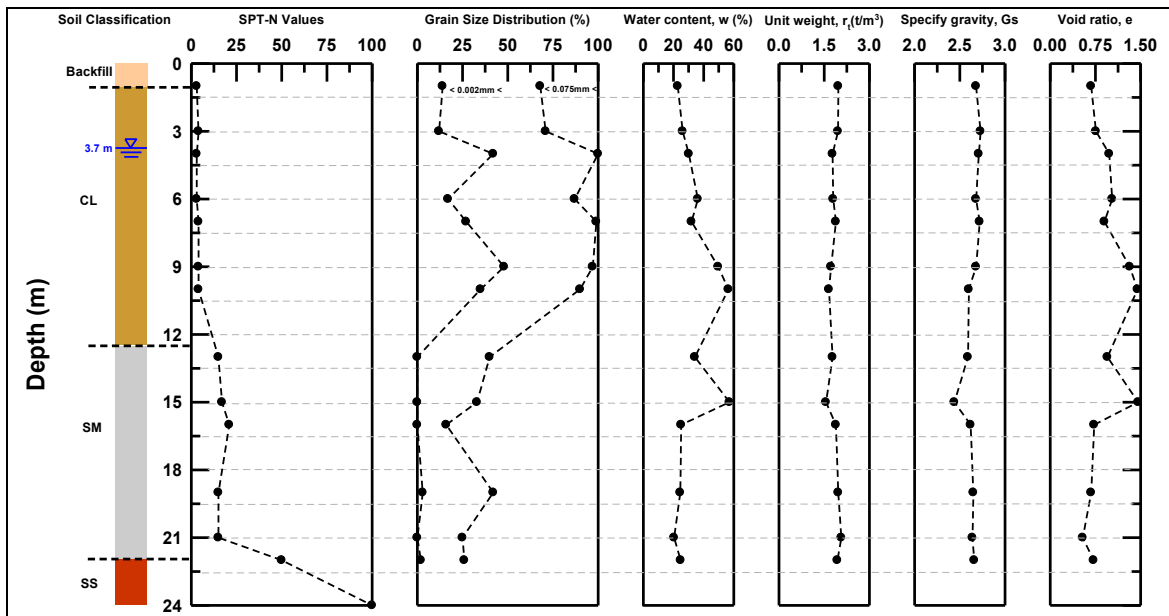


Figure 2: The SPT-N values, grain size distribution and soil properties profiles of arrival site (at Yongning Station)

3. DESIGN AND GROUTING METHODS REVIEW

The zone to be grouted for the arrival of shield tunneling machine is equal to 2,426 m³ [approximate dimension of 24m (L) X 10m (W) X 10m (H)]. The arrival site is located under a busy main street of Tucheng city and is near the residential area also. The traffic and noise problems are two main concerns

for this jet grouting project. In addition, the zone to be grouted was in conflict with the nearby utility network and the drainage culvert (Figure 1b). Due to the complexity of the project, it is necessary to have a detailed study on the construction methods in advance before carrying out the grouting job to minimize the risk involved. Evaluation on the design and grouting methods taken before construction are illustrated as follows:

3.1. Design evaluation

Since there is a drainage culvert located between ground surface and shield tunnels, trial layouts of drilling holes was adopted before jet grouting. Both the inclined holes and vertical holes layouts were used to study the optimum drilling plan and grout pile diameter for this jet grouting job. As shown in Figure 3a, if the grout pile with the diameter equal to 1.2 m is adopted and the drainage culvert needs to be avoided, totally 345 grout holes are needed. It includes 161 inclined grout holes with dip angles varying from 18° to 36°. Alternatively, Figure 3b shows the grout hole layout without inclined holes. But it needs to drill 92 grout holes through the drainage culvert. It is concerned that drilling so many holes through the drainage culvert may have a bad effect on the integrity and function of the culvert. Especially, it may result a serious leaking problem for the drainage culvert. So, the grout holes layouts shown in Figures 3a and 3b are not adopted. Instead, the grout hole layout of Figure 3c was used to reduce the number of grout holes to 38 and only 10 holes must be drilled through the culvert. It certainly can maintain a better function of the drainage culvert and consequently minimize the risk involved in the jet grout practice. To carry out the grouting job of Figure 3c, the designed diameter of grout pile must be more than 3.5 m. So the jet nozzle of the monitor and the grouting parameters such as flow rate, grouting pressure, and rod withdraw rate and rotation rate are needed to be modified accordingly.

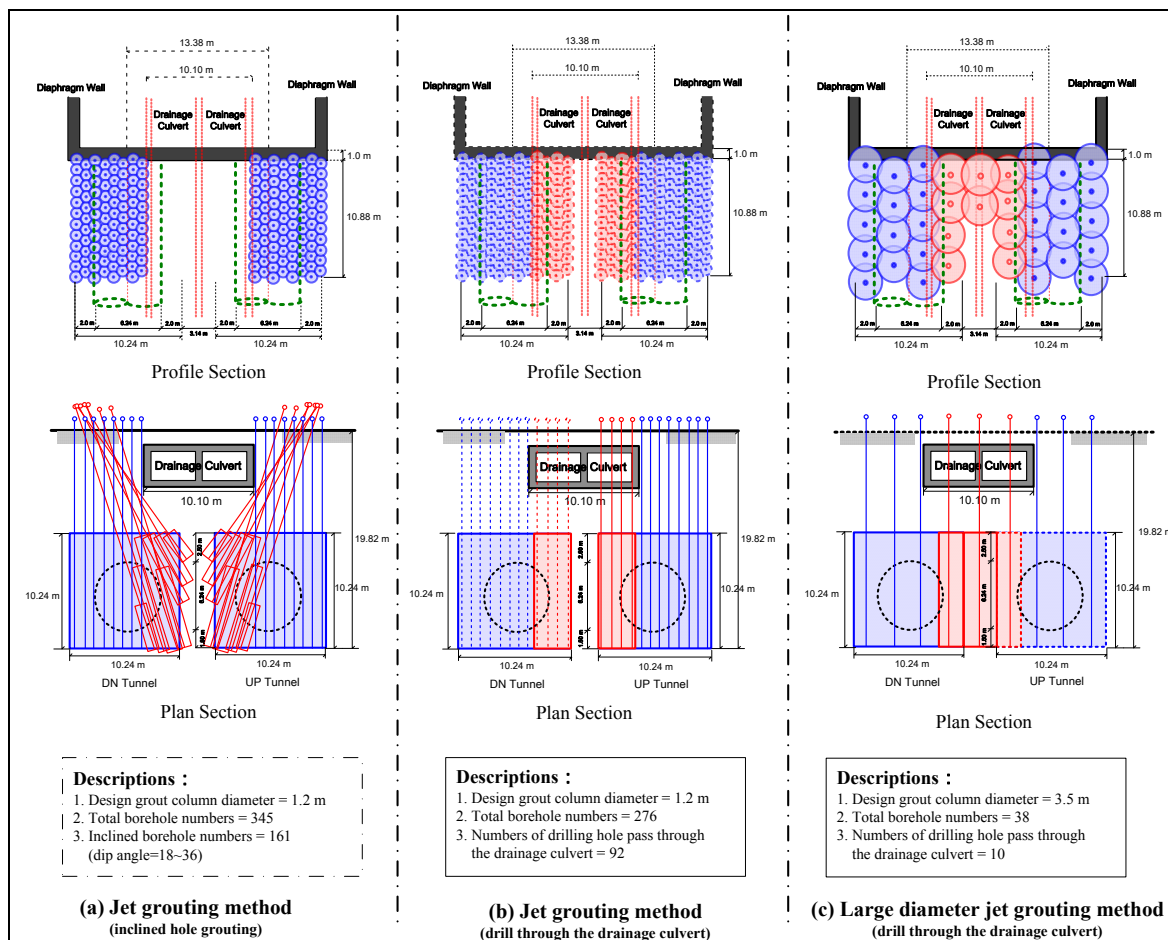


Figure 3: Proposed jet grouting layouts for the arrival site

3.2. Outlines of large diameter jet grouting

Similar to the commonly used JSG method, the large diameter jet grouting method uses a double-tube grouting system with two nozzles on the opposite side of the monitor. The latter also uses air and jet

stream to cut and mix the in-situ soil with grout. A larger nozzle diameter of 3~4.2 mm is used to allow for a larger grouting rate. The grouting parameters used here are as follows: grouting pressure = 33~37 MPa, grouting rate = 180 or 360 L/min, and rod rotation and withdrawal rate = 2~5 rpm and 10~18 min/m. Using these parameters, the grouting capacity can be increased to 35.3 m³/hr. So, it can rapidly install a grout pile with a diameter up to 2.5~4.5 m at a depth up to 50 m below ground surface. More details of the large diameter jet grouting method and comparison with existing grout methods are illustrated in Table 1.

Table 1: Comparison of different jet grouting methods (after Yong et al., 1996; Yoshida et al., 1996)

Method		Jet Special Grout (JSG method)	Column Jet Grout (CJG method)	Rodin Jet Pile (RJP method)	Large Diameter Jet Grouting
Effective diameter		ϕ 1.0 ~ 2.0 m	ϕ 1.2 ~ 2.0 m	ϕ 2.0 ~ 3.0 m	ϕ 2.5 ~ 4.5 m
Geological condition	Sand	SPT-N \leq 50	SPT-N \leq 200	SPT-N \leq 100	SPT-N \leq 100
	clay	SPT-N \leq 4	SPT-N \leq 9	SPT-N \leq 5	SPT-N \leq 5
Design strength	Sand	2 ~ 3 MPa	2 ~ 3 MPa	2 ~ 3 MPa	2 ~ 3 MPa
	Clay	0.3 ~ 1 MPa	0.3 ~ 1 MPa	0.3 ~ 1 MPa	0.3 ~ 1 MPa
Drill hole diameter		0.12 ~ 0.15 m	0.14 ~ 0.25 m	0.14 ~ 0.25 m	0.14 ~ 0.25 m
Drill rod diameter		0.06 m (double-tube)	0.06 m or 0.09 m (triple-tube)	0.09 m (triple-tube)	0.06 m or 0.09 m (double-tube)
Number of nozzles use		1	2	2	2
Jet grouting	material	Binder	Water	Water	Binder
	total pressure	18 ~ 22 MPa	35 ~ 40 MPa	20 MPa	33 ~ 37 MPa
	total flow rate	60 L / min	70 L / min	50 L / min	180 or 360 L / min
Total air pressure		0.6 ~ 0.7 MPa	0.6 ~ 0.7 MPa	0.7 ~ 1.05 MPa	0.7 ~ 1.05 MPa
Binder	total pressure	—	2 ~ 5 MPa	40 MPa	—
	total flow rate	—	140 ~ 180 L / min	190 L / min	—
Rod rotation		<10 rpm	<6 rpm	<6 rpm	2~5 rpm
Withdrawal rate		16 ~ 40 min/ m	16 ~ 25 min/ m	15 ~ 20 min/ m	8 ~ 16 min/ m
Grouting capacity		4.0 m ³ / hr	11.8 m ³ / hr	18.5 m ³ / hr	35.3 m ³ / hr
Binder consumption		0.9 m ³ / m ³	0.9 m ³ / m ³	0.6 m ³ / m ³	0.5 m ³ / m ³
Amount of sludge		1.3 m ³ / m ³	1.8 m ³ / m ³	1.0 m ³ / m ³	0.7 m ³ / m ³

4. CONSTRUCTION

During construction, in order to proceed ground improvement, it is required to prevent the nearby soils from collapsing or water and sand gushing while the closed shield machine was arriving Yonging Station to pass through diaphragm wall in order. Within limited space and under the condition of obstacle of drainage culvert and utility networks, large diameter jet grouting method is applied in construction according to design evaluation. After improvement, the compressive strength of silty clay layer is set to increase to 1.2 MPa, while that of the silty sand layer is set to increase to 2.0 MPa and the permeability of the improved zone is set to less than 1×10^{-5} cm/sec.

To avoid causing traffic problem on the busy road, this grouting project was carried out in three different stages: (1) Find out the underground obstacles and remove them. Carry out the pilot grouting test. Complete 14 grout piles on the southern side of the drainage culvert. (2) Drill 10 grout holes through the culvert. Seal the annular space between drill rod and bored hole on the upper and lower slab with water seal box. Construct the grout piles beneath the drainage culvert. (3) Complete 14 grout piles on the northern side of the drainage culvert. The details of the jet grouting work are shown in Table 2 and Figure 4.

4.1. Grouting parameters

To speed up the construction process of the large diameter jet grout piles, the flow rate of grouting needs to be increased by increasing the number of jet nozzles and by parallel connection of high pressure slurry pumps during grout injection. As shown in Table 1, the number of nozzle adopted for the large diameter jet grouting was 2 and the flow rate was 360 L/min compared to 1 nozzle and 60 L/min flow rate used for traditional JSG method. Meanwhile, the rod rotational rate was decreased to 2-5 rpm to allow the grout jet to cut deeper into the soil. But the overall grouting time was not slow down because the rod withdraw rate was increased to 12 min/m to compensate the slower rotation rate. Totally, 38 jet grout piles (diameter = 3.5 m, grouted depth varied from 9.58 to 19.82 m below grout surface) were installed at the arrival site of shield machine. Grout material used in this jet grouting project was slag cement with the water-cement ratio equal to 1.22. Table 1 summarizes the grouting parameters adopted in this project and the comparison with existing grout methods.

Table 2: Details of jet grouting work at different stages

Work stage	Work days*	Number of grout pile	Length of grout pile	Volume improved
1 st stage	38	14	10.24 m	1140.85 m ³
2 nd stage	37	10	10.24 m	144.69 m ³
3 rd stage	30	14	10.24 m	1140.85 m ³

* Work days include traffic re-routing, trial pit excavation, protection and restoration of utilities lines at each stage.

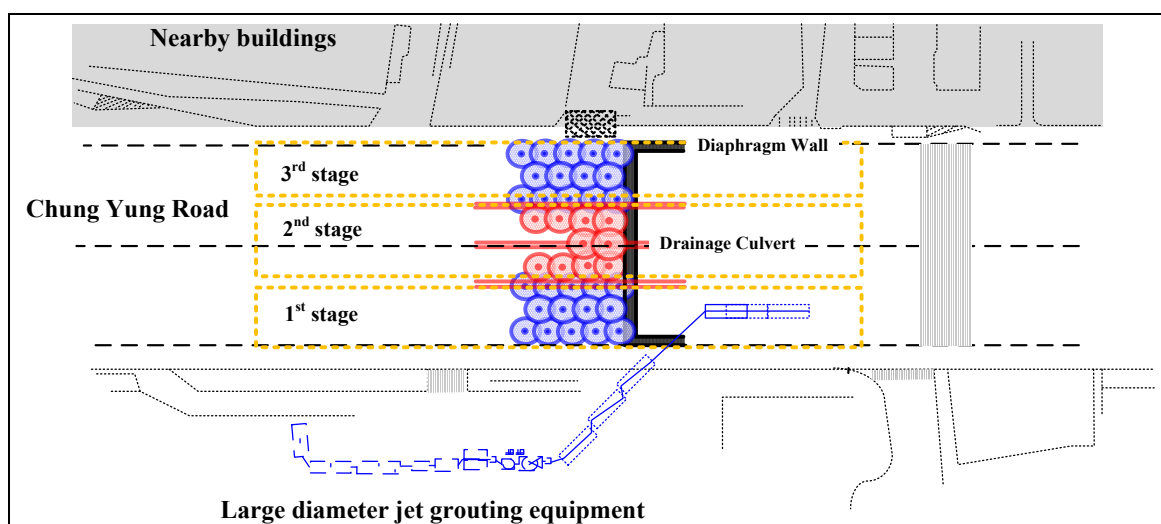


Figure 4: Improvement zones and layout of grouting equipment at different stages

4.2. Pilot test and effectiveness of grout work

To verify the pile diameter constructed by the large diameter jet grouting method under various grouting parameters and in different soil conditions (silty clay layer and silty sand layer), sound detectors were installed to confirm the pile diameter before the first stage construction was carried out. As Figure 5 demonstrates, the tube and sound detectors were installed at distances of 3.2m, 3.5m, and 3.8m from the grouting point respectively. In general, the drilling alignment of the grouting hole was satisfactory. There was less than 10 cm off the alignment over a drilling depth of 17 – 20 m. All the sound detectors located at different locations could pick up the sound of jet stream. It verified the design pile diameter of 3.5m had been achieved successfully. Using the unconfined compressive strength and the falling head permeability test on specimens cured for 10 days, it can be shown that grouting parameters set for the large diameter jet grouting practice are adequate to construct the grout piles with compressive strength varying from 3 to 6.5 MPa. Such a strength is considerably higher than the design strength of 1.2 and 2 MPa for silty clay and silty sand, respectively (Figure 6).

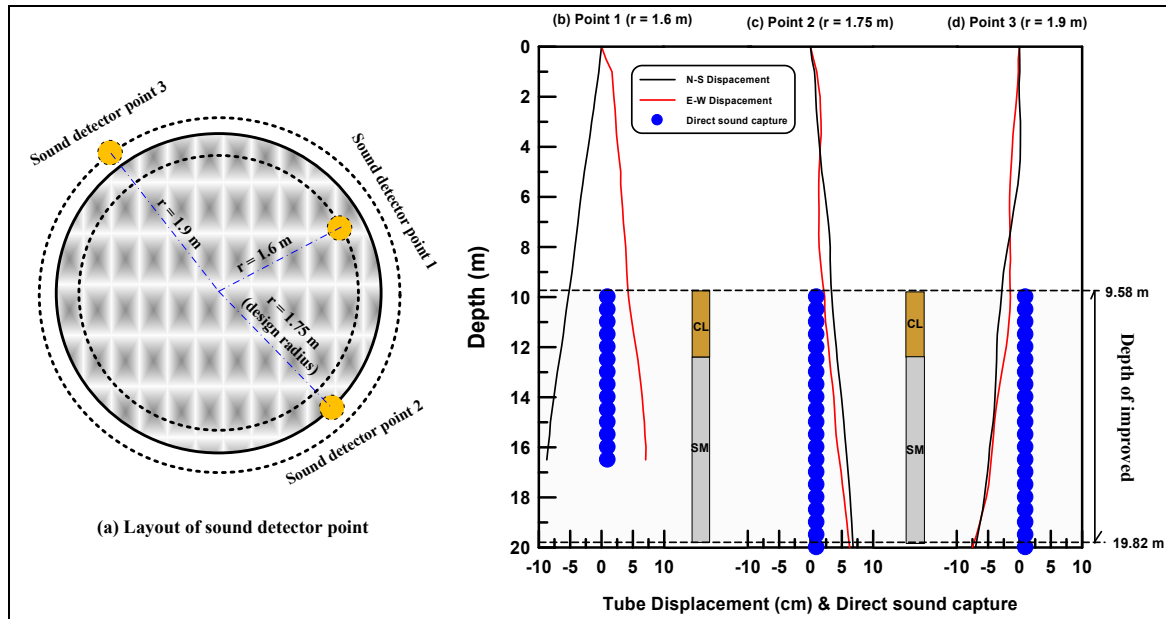


Figure 5: Layout and results of sound detecting test

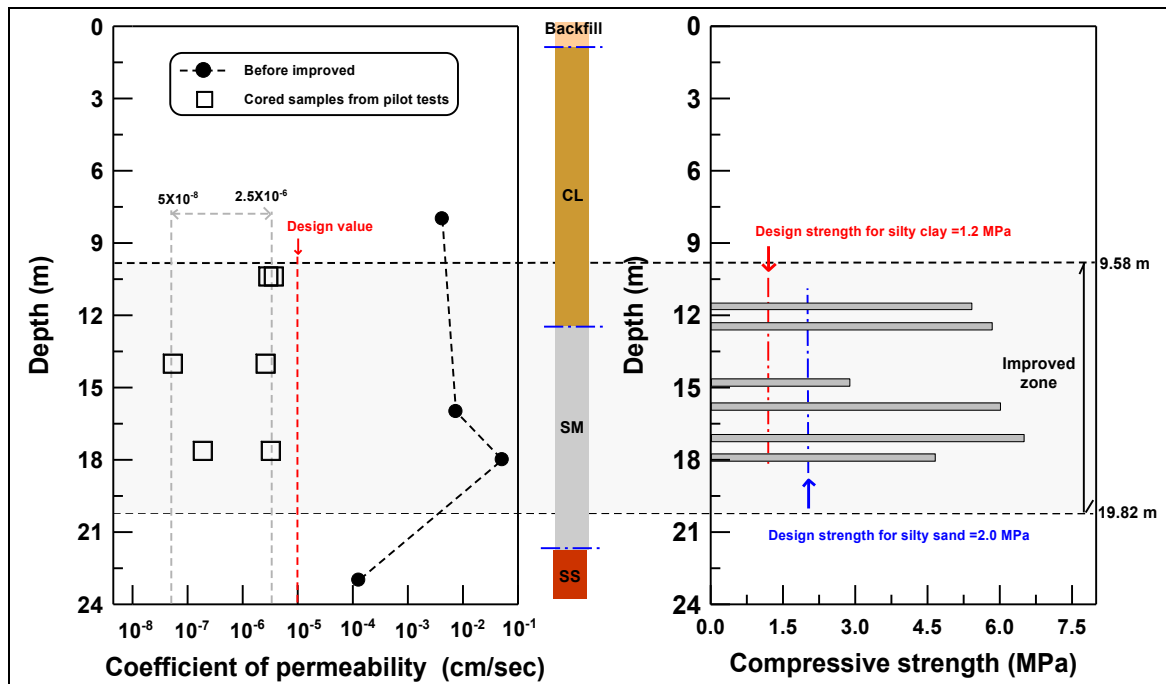


Figure 6: In the pilot test, permeability and compressive strength of grout piles in silty clay/silty sand layer (cured 10 day)

4.3. Construction procedure

To maintain the function of drainage culvert during and after the jet grouting practice, the construction procedure taken for this grouting project is illustrated in Figures 7 and 8:

1. Excavate the soil cover of the drainage culvert. Position the drill rig. Drill the casing pipe (diameter = 300 mm) through the upper slab and stop at the lower slab.
2. Install the water seal box outside the casing pipe to stop groundwater flowing in from the bottom of the culvert. Replace the casing pipe with a double pipe (diameter = 200 mm) with the monitor mounted at the tip to continue drilling to the design depth.
3. Start jet grouting and withdraw the double pipe. Let the slime overflow through the casing to the surface. Jet grouting stops at some distance below the bottom of the culvert. Withdraw the double tube drilling rod.

4. Insert a 40 mm grout pipe to inject the slag cement + sodium silicate grout at an injection rate of 15 L/min and grouting pressure of 0.8~1 MPa to strengthen the soil between the top of jet grout pile and the bottom of culvert.
5. Seal the holes on the upper and lower slab of the culvert with no shrinkage cement and steel plate.

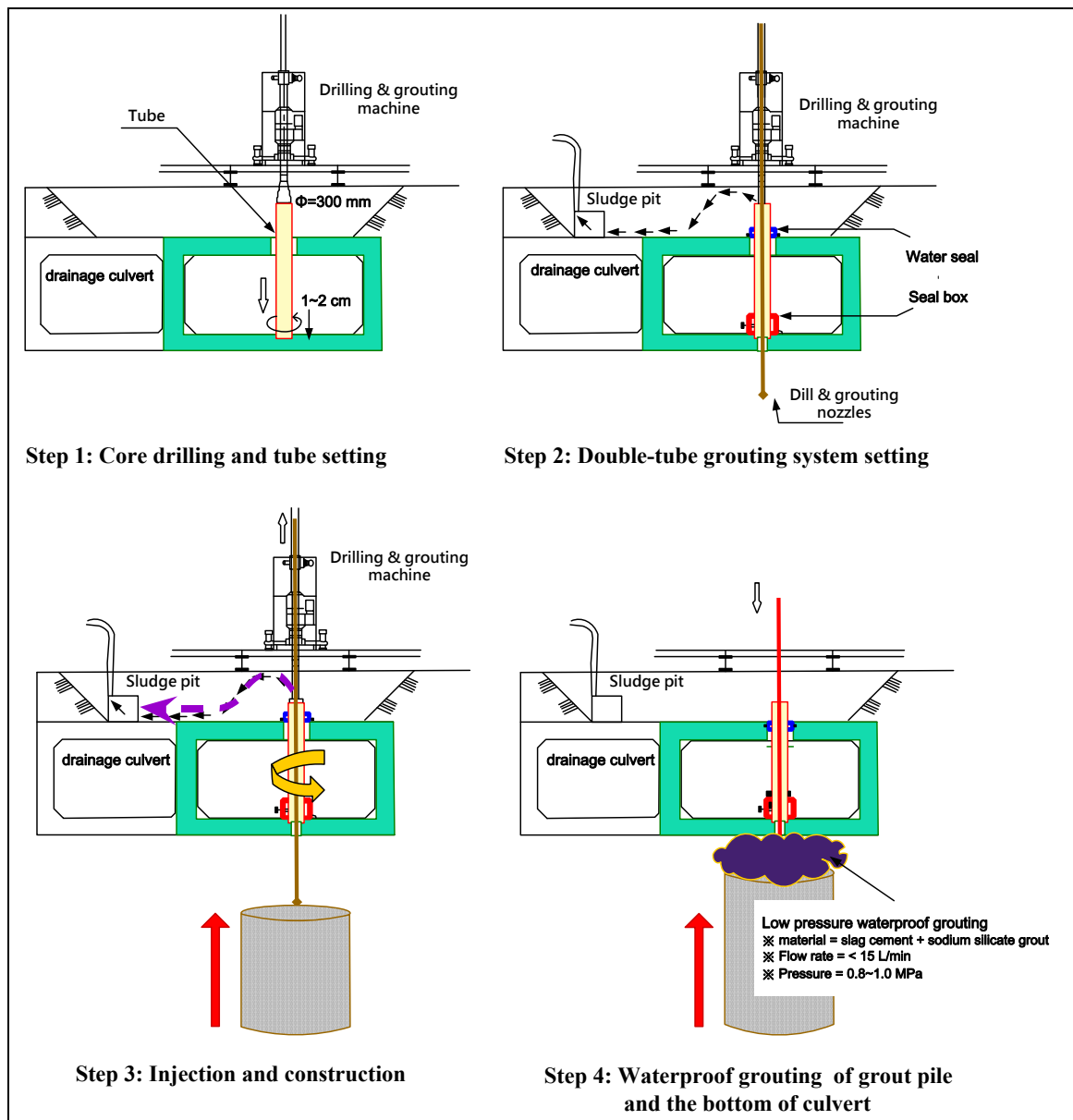


Figure 7: The procedures of jet grouting under drainage culvert and treatment for culvert

4.4. Quality assurance

To monitor the ground movement associated with this grouting project, 15 settlement marks were installed to measure the ground settlement during grouting. The monitored results showed that the settlement was well within the values set by the designer ($\pm 5 \text{ mm}$) (Figure 9). 28 days after the completion of grouting, 2 grout piles were randomly chosen from 38 grout piles for the quality check. Cored samples were taken from the piles and inspected following the evaluation method for high pressure injection mixing piles proposed by the Japan Society of Civil Engineers (Takashi *et al.*, 2003). The core samples are shown in Figure 10 and all are rated acceptable. Besides, from the consolidated undrained triaxial test run on cored samples, the effective shear strength parameters are increased to $c = 50 \sim 70 \text{ KPa}$, $\phi = 50^\circ \sim 63^\circ$ for silty sand layer and $c = 200 \sim 960 \text{ KPa}$, $\phi = 28^\circ \sim 55^\circ$ for silty clay layer. Also, the compressive strength and permeability of cored samples can meet the design requirement (Figure 11).

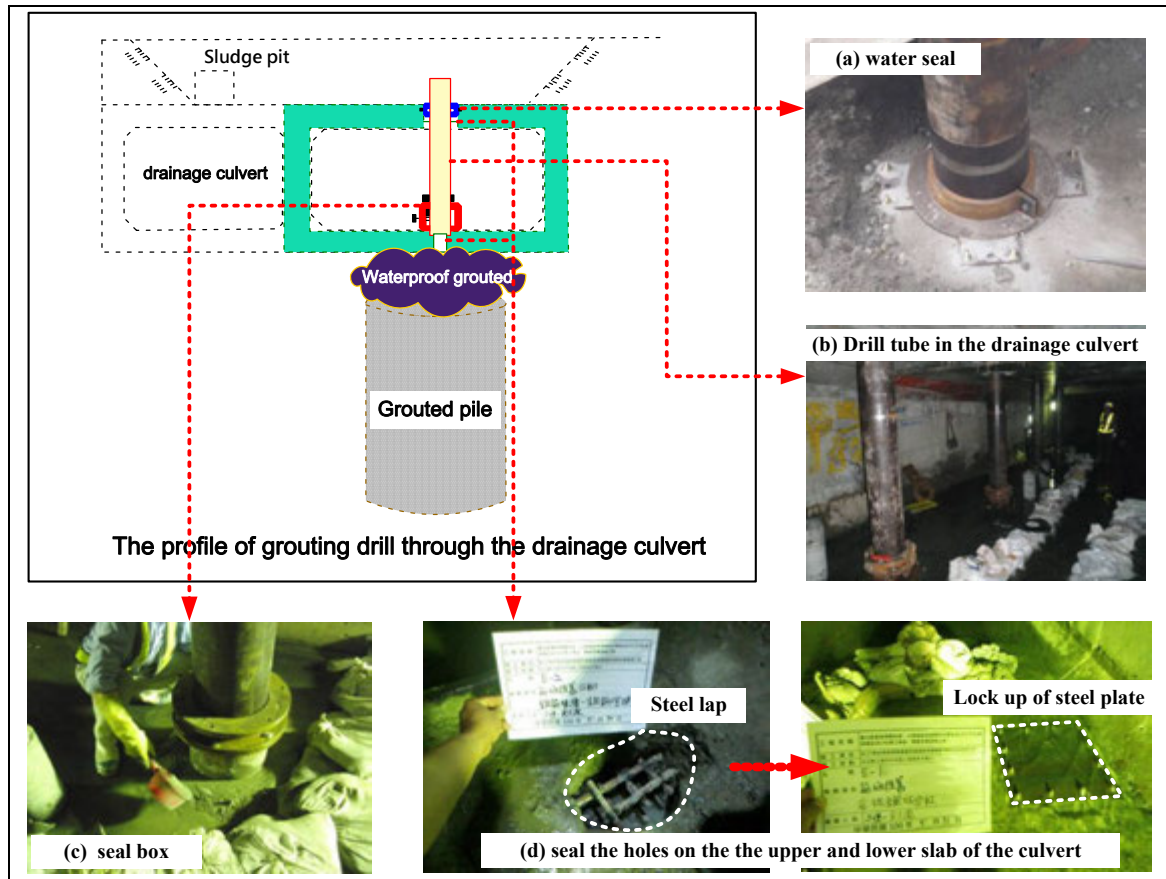


Figure 8: Photos of treatment condition during jet grouting under drainage culvert

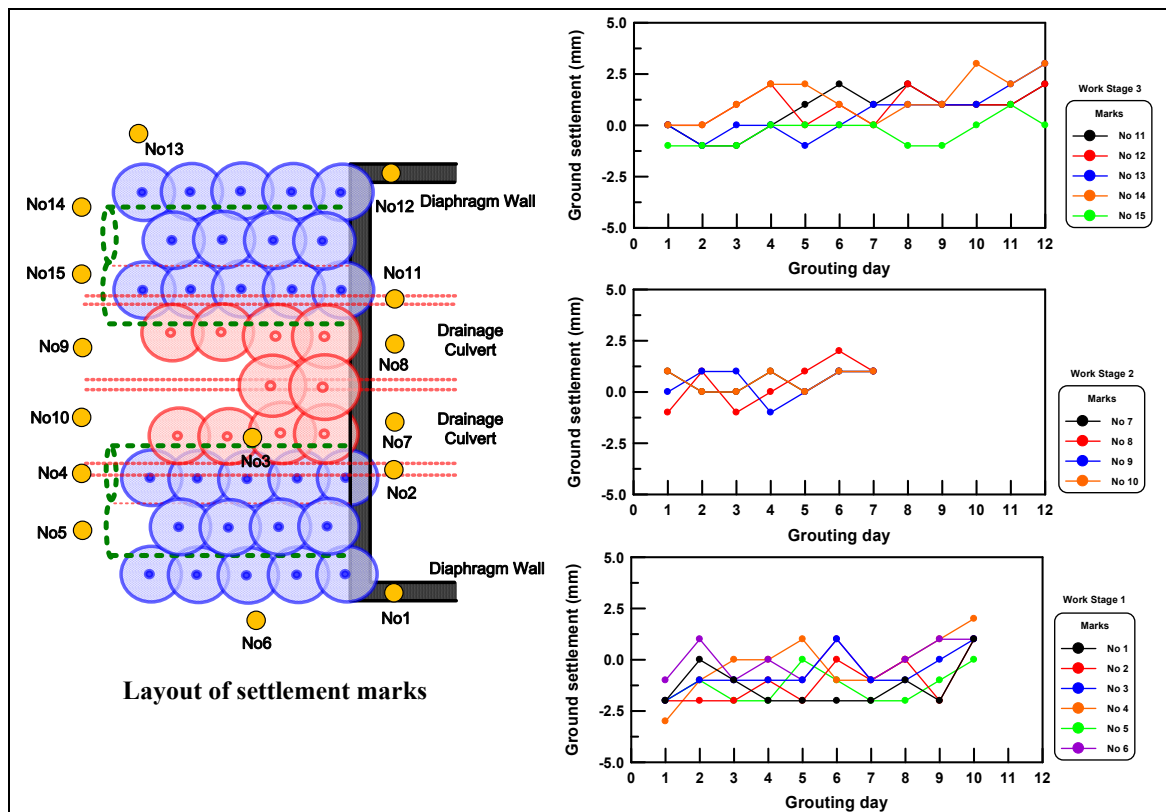


Figure 9: Layout of settlement marks during grouting and monitored settlement

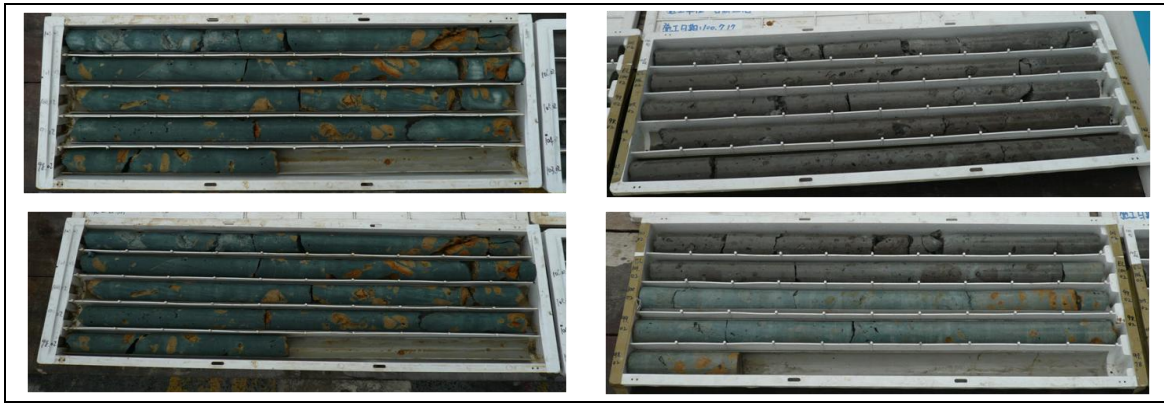


Figure 10: Cored specimens from improved zone

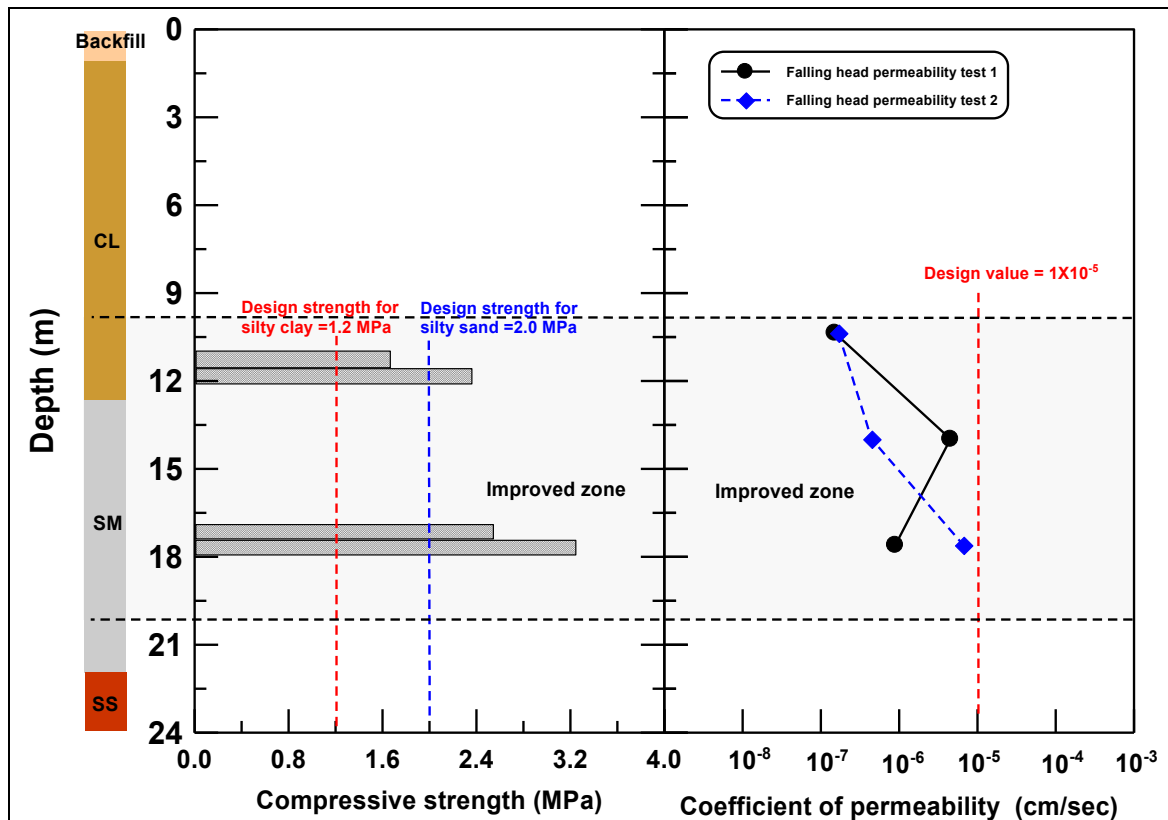


Figure 11: Permeability and compressive strength of grout piles in silty clay/silty sand layer (cured 28 day)

5. CONCLUSIONS

Jet grouting was carried out as the ground improvement work for the arrival of shield machine in Yongning Station of Taipei MRT. Located in between ground surface and shield tunnel, there was a drainage culvert in the way for this grouting project. This paper reports the experience learned from the practice of large diameter jet grouting project under such a difficult condition. The following conclusions were drawn from the findings of this project:

1. By minimizing the number of grouting holes (either vertical or inclined one), large diameter jet grouting method can facilitate the grouting job in the congested area or under the busy road. As a result, the quality of the grout piles and the overlapping portion between neighboring piles can be improved.
2. The drainage culvert located between ground surface and shield tunnels was the obstacles of this grouting project. 10 grout holes must drill through the drainage culvert. By proper arrangement of casing drilling, groundwater sealing and jet grouting practice, the function of the drainage culvert can be not influenced during and after jet grouting.

3. The ground improvement project in urban area is often carried out very close to the neighboring buildings. Excess ground movement associated with jet grouting is a common phenomenon. So it is very important to constantly monitor the ground movement to minimize the jet grouting induced damage to the neighboring structures.

6. ACKNOWLEDGMENTS

The Authors are indebted to the following organizations: Sanshin Corporation (Taipei Branch) for carrying out the field work of the large diameter jet grouting; the Moh and Associate Inc. and the Central District Project office of Department of Mass Rapid Transit, Taipei city government for providing valuable construction records for the writing of this paper.

REFERENCES

Yong, D. M., Hayashi, K. and Chia, B. H. (1996). "Jet grouting for construction of a RC canal in soft marine clay." Grouting and deep mixing: Procds., IS Tokyo 96, 2nd International conference on Ground Improvement Geosystems Tokyo, Japan, pp. 375-380.

Yoshida, H., Jimbo, S. and Uesawa, S. (1996). "Development and practical applications of large diameter soil improvement." Grouting and deep mixing: Procds., IS Tokyo 96, 2nd International conference on Ground Improvement Geosystems Tokyo, Japan, pp. 721-726.

Takashi, M., Ikeda, A., Akira, Y., Yuukiti, T. and Nakagawa, K. (2003). "Evaluation method of soil improvement effect of high-pressure injection mixing method." Japan Society of Civil Engineers, No. 735 (VI-59): 215-220.

Prediction of jet grouting efficiency and columns average diameter

Croce Paolo, University of Cassino, Italy, croce@unicas.it
Flora Alessandro, University of Napoli "Federico II", Italy, flora@unina.it
Lirer Stefania, University of Napoli "Federico II", Italy, stelirer@unina.it
Modoni Giuseppe, University of Cassino, Italy, modoni@unicas.it

ABSTRACT

Even though jet grouting technology has noticeably progressed since the first applications, and treatment efficiency has accordingly improved, there is still a great level of uncertainty on the results of treatment, in terms of both column diameter and mechanical properties of cemented material.

This paper focuses on the estimate of the average diameter, which is by far the most important geometrical parameter of jet grouted columns at the design stage: it is fundamental for overlapping of adjacent columns in linear barriers and massive treatments, but plays a still important role in reinforcements made with isolated columns. In principle, the diameter of a column is strongly dependent on the characteristics of the injected fluids and on the physical and mechanical properties of soils, being the result of a very complex interaction between these two elements. Comprehensive analyses of these mechanisms have been rarely attempted, but several studies can be found in the literature trying to establish relations, on empirical or sound theoretical basis, between diameters and injection parameters or soil properties. In the attempt to establish more rational and complete design correlations, in the paper the evidence gained from a large number of experimental data collected in time by the authors have been compared with the simulations provided by a theoretical model of the formation of jet grouting column, for the case of single fluid jet grouting. The analyses and observations reported in the paper represent a preliminary step towards the production of reliable charts for the design of jet grouting treatments.

1. INTRODUCTION

Jet grouting is adopted to waterproof or strengthen subsoil in a variety of geotechnical structures as impermeable barriers, foundations, earth retaining structures, provisional support of tunnels. Most of the success of these applications relies upon the achievement of an adequate size of columns, which is generally important in the case of isolated columnar reinforcements, and becomes fundamental when continuity of structures must be ensured by overlapping of adjacent columns to provide strengthening and/or waterproofing functions. Cut-off walls, sealing of excavations and tunnel canopies are the most frequent examples of these structures.

In principle, the diameter of jet grouting columns is the result of the interaction between the erosive action of jets and the resistance of soils to cutting. Therefore, a desired diameter should be obtained by properly selecting the injection technique (single, double or triple fluid) and by calibrating the operational parameters (number and diameter of nozzles, injection pressure and/or flow rate, lifting speed of the monitor and grout mix composition). In practice, these parameters are initially assigned on the basis of previous experiences (e.g. Davie, 2003) and then tuned by checking the effectiveness of treatments with the so-called field trials.

In an effort to reduce subjectiveness, at least in the preliminary design of treatments, several authors have proposed empirical correlations to estimate columns diameter, expressed in the form of tables, charts or formulas among diameter of columns, treatment system and/or soil properties (Table 1). Some of these correlations (e.g. Xanthakos, 1994; Botto, 1985; Bell 1993; Kutzner, 1996; Tornaghi and Pettinaroli, 2004; Flora and Lirer, 2011; AGI, 2011) subdivide soil types into broad categories and provide for each of them ranges of diameters that can be obtained with typical sets of injection parameters. Some others (e.g. J.J.G.A., 2005) point out the role of soil resistance to cutting and establish relations between columns diameter and soil index properties obtained from in situ and laboratory tests.

Most of these correlations do not explicitly take into account treatment parameters, reference being simply made to the different injection techniques. Some authors (e.g. Tornaghi, 1989, Croce and Flora, 2000, Tornaghi and Pettinaroli, 2004, Flora and Lirer 2011) propose more comprehensive relationships including the combined effect of soil properties and injection parameters.

Tornaghi (1989) is the first to explicitly introduce the specific energy (i.e. the energy supplied at the pump per unit length of column) as a meaningful variable to summarise all treatment parameters, expressed (in MJ/m) as:

$$E_p = \frac{p \cdot Q}{v_s} \quad (1)$$

where p is the injection pressure of the mixture, Q the flow rate, v_s the average monitor lifting speed.

Table 1: List of some correlations available in literature.

Reference	Form of correlation	Soil classification	Injection type and parameters
Botto (1985), Bell (1993)	Chart	Soil type	Single, double, triple fluid with typical parameters
Miki and Nakanishi (1984) Shibazaki (1991)	Chart	Coarse grained N_{spt}	Single, double, triple fluid with typical parameters
Xanthakos et al. (1994)	Table	Fine – coarse grained	Single, double, triple fluid with typical parameters
Kutzner (1996)	Table	Soil type	Single, double, triple fluid and pressure
Tornaghi (1989)	Chart	Coarse grained N_{spt} Fine grained c_u	Single, double, triple fluid Specific energy at the pump
J.J.G.A. (2005)	Table	N_{spt}	Single, double, triple fluid with typical parameters
Tornaghi and Pettinaroli (2004) Flora and Lirer (2011)	Chart	Soil type	Single, double, triple fluid Specific Energy at the pump
AGI (2011)	Table	Soil type	Single, double, triple fluid with typical parameters
Modoni et al. (2006) Croce et al. (2011)	Chart	Coarse grained ($\sigma'_v \cdot \tan\phi'$) Fine grained (c_u)	Single fluid considering all treatment parameters

Croce and Flora (2000) argue that the effective energy must be evaluated at the nozzles, and the concentrated and distributed energy losses occurring from the pump to the nozzles must be discounted. For this reason, they propose to use the kinetic energy per unit length of column as the reference parameter. By manipulating the well know expression of kinetic energy, the specific energy of the jet at the nozzle (in MJ/m) can be written as:

$$E_n = \frac{\pi}{8} \cdot \frac{\rho_g \cdot M \cdot d_o^2 \cdot v_o^3}{v_s} \quad (2)$$

where ρ_g is the density of the grout, M and d_o are the number and the diameter of nozzles, v_o the average speed of the mixture at the nozzle. Eq. (1) is usually preferred because of its simplicity and because it expresses the total energy spent to perform treatments, which is directly related to the cost of treatment. On the other side, the energy calculated by eq. (2) represents the contribution effectively given at the nozzle and is thus more suitable to predict diameters. The differences between E_p and E_n are obviously related to the energy losses. For well-designed facilities and short distances between pumps and nozzles, it is reasonable to assume:

$$E_n \approx 0.9 \cdot E_p \quad (3)$$

i.e. with an energy loss equal to about 10% of E_p (AGI, 2011).

As an alternative to empirical equations, theoretical models able to describe the hydrodynamic mechanisms taking place during the diffusion of submerged jets and the impact on the soil can be adopted. Examples for single fluid jet grouting are provided by Chu (2005) and Modoni et al. (2006). The theoretical approach has the advantage of performing an analysis of the phenomena on sound mechanical basis, of taking explicitly into account the role of each variable (either soil property or injection parameter) and of establishing logical and thus general relations between these latter and columns diameter.

However, it must be pointed out that due to the complexity of the phenomena induced by jet grouting, models are necessarily simplified and not totally free from empiricism, since their calibration is obtained by a comparison with experimental results.

In practice, all the above mentioned approaches lack of completeness, the empirical ones because their validity is confined to the case histories from which they are derived, the theoretical ones because require a sufficient number of experimental data to be calibrated. The research activity described in this paper

was then started to mix the benefits of theory and empiricism into a unique approach leading to the most general and accurate prediction of the average diameter of jet grouted columns.

2. JET GROUTING EFFICIENCY

The use of efficiency parameters is typical in all mechanical processes. In jet grouting production, efficiency can be defined by considering the ratio between the obtained benefit, which is for instance the volume of the column per unit length, V_C , expressed in m^3/m , and a parameter representing the cost sustained to obtain it, represented by the treatment specific energy E (either E_p or E_n , eqs. 1 or 2, expressed in MJ/m) or by the volume of injected grout per unit length of column, V_G , expressed in m^3/m . As a consequence, the two following parameters can be alternatively introduced:

$$\lambda_E = \frac{V_C}{E} \quad \text{energetic efficiency (m}^3/\text{MJ)} \quad (4)$$

$$\lambda_V = \frac{V_C}{V_G} \quad \text{volumetric efficiency} \quad (5)$$

It is simple to demonstrate that, by expressing the energy via eq. (1), the two efficiencies are linked by the following expression:

$$\lambda_E = \frac{1}{p} \lambda_V \quad (6.a)$$

If the energy is expressed using eq. (2) a slightly more complicated expression is obtained:

$$\lambda_E = \frac{1}{\gamma_g \frac{v_o^2}{2g}} \lambda_V \quad (6.b)$$

in which γ_g is the volume unit weight of the grout. Assuming that eq. (3) holds, however, it is simple to pass from one to the other expression of the specific energy. In practice, the energetic efficiency is often considered via its reciprocal $1/\lambda_E$, called volumetric specific energy E'_s (Tornaghi and Pettinaroli, 2004). The authors have collected a number of well documented case histories of single and double fluid jet grouting treatments, for which the parameters needed to quantify the efficiency of treatment were all available (Monda, 2010), from which some general considerations can be drawn: first of all, the values of the efficiency parameters λ_E and λ_V depend on the adopted injection system and on soil grading and state. Typically, finer and consistent soils require larger treatment energies and, as a consequence, jet grouting in these soils is less effective. Cost effectiveness suggests therefore that finer soils should be better improved by using alternative techniques (for instance, deep mixing). The larger efficiency of jet grouting in sands and sandy gravels also implies that the amount of grout spoil is the lowest for them, as experimentally confirmed by several authors (e.g. Covil e Skinner, 1994). A second interesting consideration is that even though the energies to be used on site may vary in a wide range, depending on the desired columns diameter, the efficiencies vary in a much narrower range, mostly related to soil properties. Then, efficiencies may be conveniently adopted (and often are in practice) as a simple mean for a preliminary estimate of the cost of jet grouting. Tabs. 2 and 3 summarize, for the Italian practice, typical values of the energetic efficiency λ_E for the cases of single and double fluid jet grouting respectively. In practice, values external to the ranges reported in the tables may be possible, due either to the adoption of non traditional jet grouting systems (any hydrodynamic improvement of the injection system will obviously result into a larger energetic efficiency) or to the need to solve specific peculiar problems (for instance, the need to create columns in clays may require an unusually large treatment energy, and as a consequence a small energetic efficiency).

Table 2: Characteristic values of the energetic efficiency λ_E and of its reciprocal $1/\lambda_E$ (volumetric specific energy) for a well conceived single fluid jet grouting treatment in different soils (after Flora and Lirer, 2011).

Soil		Energetic efficiency λ_E (m ³ /MJ)	$1/\lambda_E$ (MJ/m ³)
Sandy gravel		0.067÷0.100	10÷15
From gravelly sand to silty sand			
		Coarse	15÷30
From sandy silt to clayey silt (low consistency)		0.020÷0.033	30÷50
From sandy silt to clayey silt (high consistency)			
		Fine	>50
		<0.020	

Table 3: Characteristic values of the energetic efficiency λ_E and of its reciprocal $1/\lambda_E$ (volumetric specific energy) for a well conceived double fluid jet grouting treatment in different soils (after Flora and Lirer, 2011).

Soil		Energetic efficiency λ_E (m ³ /MJ)	$1/\lambda_E$ (MJ/m ³)
From sandy gravel to silty sand	Coarse	0.077÷0.125	8÷13
From sandy silt to clayey silt (low consistency)	Fine	0.077÷0.025	13÷40
From sandy silt to clayey silt (high consistency)		<0.025	>40

It is convenient to recall that the information on treatment efficiency retrieved from well documented case histories (Tabs. 2 and 3) are a first, immediate mean to predict the average diameter of jet grouted columns, simply by associating to each class of soils a typical range of efficiencies and, therefore, a range of diameters. Tornaghi and Pettinaroli (2004) and Flora and Lirer (2011) have in the last years suggested this approach. As a matter of facts, combining eqs. (5) and (6) the average diameter of the jet grouted column can be written as:

$$D = 1.128 \sqrt{p \cdot V_G \cdot \lambda_E} \quad (7)$$

in which, for dimensional consistency, the pressure p must be expressed in MPa, the volume of injected grout V_G in m³/m and the energetic efficiency λ_E in m³/MJ. Eq. (7) has been used with some possible values of the injection parameters and of the energetic efficiency to draw the chart reported in Fig. 1.

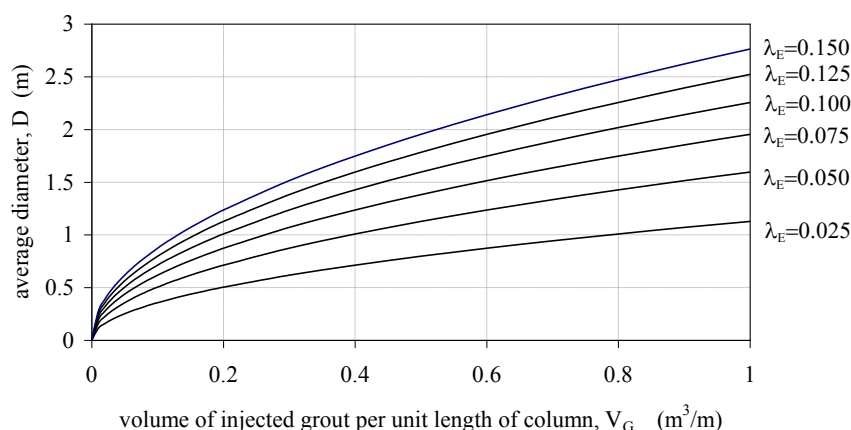


Figure 1: Average diameter of the column versus the volume of injected grout per unit length of column V_G , for different values of the energetic efficiency λ_E (see Tabs. 2 and 3) and for $p=40$ MPa.

It may be worth noting that this chart does not need to define the soil properties and the jet grouting system to be used, being such information directly related to the value of the energetic efficiency λ_E . Once the latter has been estimated on the basis of Tabs. 2 or 3, a reference average diameter of the jet grouted column can be estimated too.

3. THEORETICAL APPROACH – SINGLE FLUID JET GROUTING

Modoni et al. (2006) calibrated the theory of turbulent submerged jets formulated by Hinze (1949) with the experimental data from De Vleeshauer and Maertens (2000) to analyze the diffusion of a single fluid jet in the annular space between the injection rod and the ground. Assuming a Gaussian distribution of the fluid threads velocities in each cross section and imposing the conservation of momentum, the cross section velocity profiles of the single fluid jet can be calculated as functions of the distances from the nozzle, the rheological properties of the injected fluid (density and viscosity, both dependent on the water-cement ratio of the grout), the characteristics of the system (nozzle diameter and injection rate).

The advancing rate of the erosion front is then considered to be proportional to the difference between the average velocity of the jet threads V and a limit velocity V_L (i.e. the minimum velocity of jet threads causing erosion) according to the relationships experimentally found by Dabbagh et al. (2002), Bergscheider and Walz (2003) and Stein and Grabe (2003). The limit velocity V_L is calculated by

assuming that jet threads partially penetrate into sandy materials, reducing the effective stresses and the soil resistance to cutting, while an undrained collapse is assumed for fine grained materials. As a result, for sandy material V_L is a function of the drained shear strength $\sigma'_v \tan \phi'$, where σ'_v is the effective overburden stress and ϕ' the soil friction angle; for clayey-silty soils, V_L is a function of the undrained shear strength s_u .

By iteratively integrating the speed of the advancing front during the time when the jet acts in a single direction, the column diameter is eventually obtained. Therefore, once the model has been calibrated with a set of experimental results, it is able to quantify the role of all variables involved in the jet grouting process, extrapolating the experimental information to new scenarios. However, its numerical implementation requires a non trivial computational effort, which makes it somehow cumbersome for practical applications.

In order to reduce this complexity, Croce et al. (2011) have recently proposed a simple non linear dimensional analytical regression of a large number of model outputs, in which the diameter D of the columns is given as a power function of two variables: one (s) represents soil resistance to cutting (therefore, $s=s_u$ for fine grained soils, $s=\sigma'_v \tan \phi'$ for sandy materials); the other (J) comprehensively summarising the effects of all treatment parameters. Then, the diameter of the columns is:

$$D = A_j \cdot s^{\alpha_j} \cdot J^{\beta_j} \tag{8}$$

where

$$J = v_0 d_0 \left(\frac{M}{v_s} \right)^{0,77} (0,72 W^2 - 1,52 W + 4,07) \text{ (for clayey silty soil)} \tag{9.a}$$

$$J = v_0 d_0 \left(\frac{M}{v_s} \right)^{0,50} (1,16 W^2 - 2,06 W + 3,55) \text{ (for sandy soil)} \tag{9.b}$$

in which the variables v_0 , M , d_0 and v_s have been previously defined (eq. 2), and W is the water-cement weight ratio of the injected grout.

The best fitting dimensional parameters A_j , α_j and β_j of eq. 7 are given in Table 4.

A step forward towards the applicability of the proposed theoretical model is a further simplification, which assumes that the comprehensive parameter J be represented by the specific energy at the nozzle E_n (eq. 2).

$$D = A_{E_n} \cdot s^{\alpha_E} \cdot E_n^{\beta_E} \tag{10}$$

Table 4: Values of A_j , α_j and β_j for single fluid jet grouting (after Croce et al., 2011). v_0 and v_s expressed in meters per second (m/s), and the diameters D and d_0 in meters (m).

Soil type	A_j	α_j	β_j
clay-silt	0,11	-0,26	0,55
sand	0,54	-0,39	0,66

By recalling eq. (3), eq. (9) can be even more conveniently expressed as:

$$D = A_{E_p} \cdot s^{\alpha_E} \cdot E_p^{\beta_E} \tag{11}$$

Since quite often times the shear strength of coarse grained soils is obtained from in situ tests, and specifically from Standard Penetration Tests (SPT), in both eqs. (10) and (11) the variable s relative to sandy soil has been replaced by the number of blows N_{SPT} . The conversion has been based on the relation between N_{SPT} and the drained shear strength ($\sigma'_v \tan \phi'$) derived from literature (De Mello, 1975). For fine grained soils, s is the undrained shear strength s_u . The coefficients A_{E_n} (eq. 10), A_{E_p} (eq. 11), α_E and β_E (eqs. 10 and 11) are given in Tab. 5.

Table 5: Values of A_E , α_E and β_E for single fluid jet grouting (modified after Croce et al., 2011). In eqs. (10) and (11), D expressed in meters (m), energies in MJ/m, s_u in kPa.

Soil type	A_{En} (10)	A_{Ep} (eq. 11)	α_E	β_E
clay-silt	0,98	0,96	-0,26	0,225
sand	1.24	1,21	-0,39	0,250

4. ESTIMATING DIAMETER AND ENERGETIC EFFICACY

In the previous sections, an empirical and a theoretical approach for the prediction of the average diameter of jet grouted columns has been presented. Neither one can be considered fully comprehensive, but both may help in the prediction by imposing their mutual consistency.

As a first step to check mutual consistency, the values of the energetic efficiencies λ_E calculated using eq. (10) with typical values of the energy E_n for single fluid jet grouting have been plotted in Fig. 2, along with the limit characteristic values of λ_E retrieved from field trials and reported in Tab. 2. Generally speaking, the figure indicates that the empirical and the theoretical predictions are mutually consistent for both sandy and silty-clayey soils, thus confirming the capability of the model to catch the main features of the interaction between the jet and the soil. Furthermore, the model correctly predicts that, for a given soil and a given energy E_n , the efficiency reduces as shear strength increases (denser or more consistent soils). It may be worth noticing that even in a homogenous sandy soil, having a constant friction angle to the maximum depth of treatment – which is a rather common situation – the shear strength (and N_{SPT}) increases with depth because the effective stresses increase. Then, what Fig. 2 says is that the efficiency of jet grouting will not be constant for a given column if the input energy is kept constant, and it will tend to reduce with depth, as already pointed out and measured in a field trial by Croce and Flora (1998).

In Fig. 3, the diameter of the column computed with eq. 10 (single fluid jet grouting) is plotted versus soil shear strength (represented as in Fig. 2 by N_{SPT} or s_u) for the same specific energies at the nozzle (E_n) considered in Fig. 2. As well known, the figure shows that single fluid jet grouting is generally more effective in sandy than in clayey soils. The model correctly predicts a reduction of diameter with depth from the ground level for normally consolidated clays or sands having a constant friction angle. This is a potential and dangerous source of error in guessing column diameter in field trials, because most times columns are exposed only in the upper part, and an overestimate of the average diameter is likely to take place.

The figure also shows that diameters large enough to be economically convenient can be produced in very loose sands ($N_{SPT} < 10$) and soft clays ($c_u < 50$ kPa) even with relatively low energies (5-10 MJ/m). Larger energies, or more efficient systems (double or triple fluid jet grouting, or other ground improvement techniques) must be adopted for larger shear strengths.

Even though Fig. 3 indicates that, as expected, by increasing the energy E_n larger diameters are produced, Fig. 2 points out that this increase in diameter is obtained with a lower energetic efficiency, that is with a larger cost per unit volume of column. Furthermore, the absolute reduction in efficiency with increasing values of E_n is more pronounced for the larger values of the diameter. This result, which is consistent with experimental evidences, is generated by the theoretical model because the erosive effectiveness of the jet reduces with the distance from the nozzle; as a consequence, an increase in the energy (caused by an increase of the grout pressure and/or the flow rate, by a reduction of the monitor lifting speed or by the increase of the number of nozzles), produces a slower and slower progression of the erosion front as it moves out in the soil, with a simultaneous increase of ineffective, wasted grout flowing upwards (spoil) along the borehole.

This peculiar characteristic of the hydrodynamic process that gives rise to the jet grouting columns clearly points out the usefulness of considering the efficiency parameter λ_E (or λ_v) in the design of jet grouting: the best jet grouting system and the best set of treatment parameters should be chosen both considering the desired effect (column diameter D) and trying to maximise the efficiency.

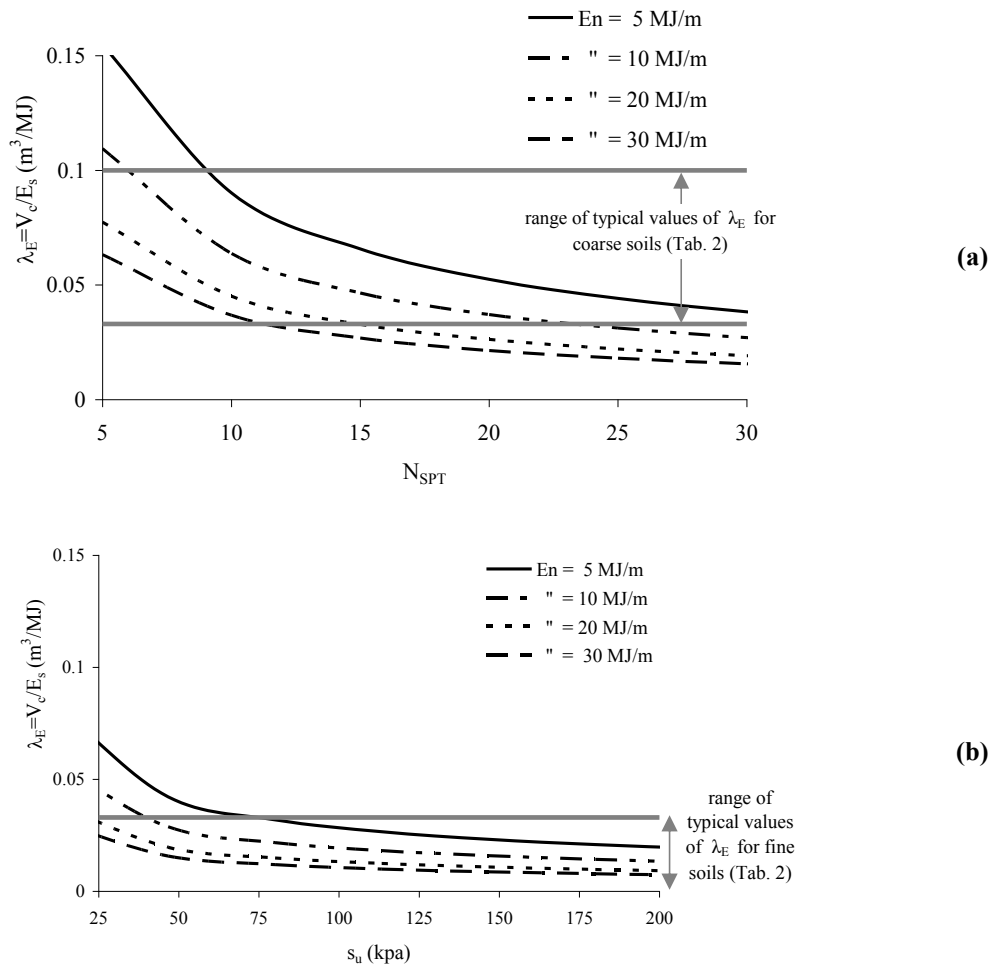
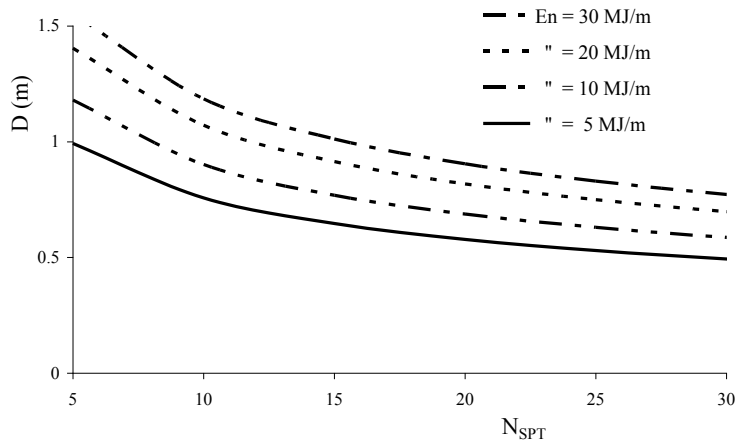
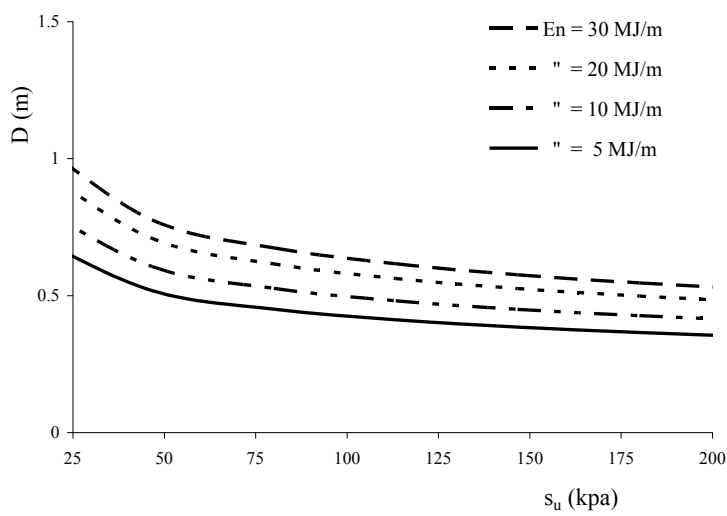


Figure 2: Single fluid jet grouting. Energetic efficiency λ_E computed with eq. (10) for sandy (a) and silty-clayey (b) soils.

Fig. 4, finally, reports the comparison between the diameter computed with the model (eq. 10) (for the single value of the specific energy $E_n=10$ MJ/m) and that obtained via eq. 7 for the two bounding values of the energetic efficiencies λ_E shown in Tab. 2, pertaining to the case of single fluid jet grouting in sandy soils. Again, the diameter predicted by the theoretical model is consistent with the range empirically suggested in Tab. 2.



(a)



(b)

Figure 3: Single fluid jet grouting. Diameter of the column computed with eq.(10) for sandy (a) and clayey-silty (b) soils

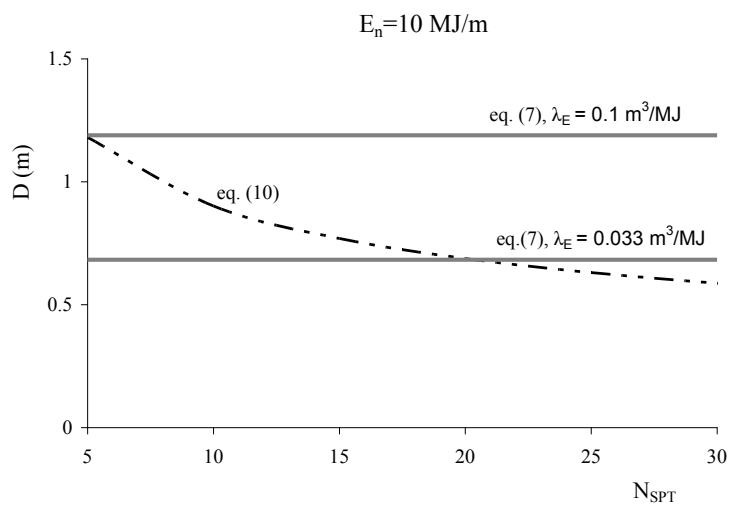


Figure 4: Single fluid jet grouting. Diameter of the column computed with eq. (7) and (10) for sandy soils and a given value of the specific energy at the nozzles $E_n=10$ MJ/m.

5. CONCLUSIONS

Jet grouting is a ground improvement technique which is nowadays widespread, and contributes to the solution of a large number of geotechnical problems. Yet, large uncertainties still exist on the true shape and position of the columns, and often the effectiveness of jet grouting is stated in a vague way and eventually checked during the execution of the main work. Obviously, repair or integration of partially or completely non effective jet grouting in this construction stage is by far more expensive than putting greater attention and care at the design stage. Then, cost effectiveness requires for rational jet grouting design criteria much more than for novel techniques. This is the reason why in the last 10 years the authors have concentrated on the design of jet grouted structures.

It is clearly recognized that the reliable prediction of columns average diameter is one of the key factors to be considered in the design of jet grouted structures, along with the estimate of the deviation of column axis and of the statistical dispersion of both diameter and position distributions (Croce et al., 2004, AGI, 2011).

As far as the average diameter is concerned, the amount of experimental information gained so far allows an empirical estimate of the ranges of possible values for the different jet grouting techniques. In the paper, it was argued that in order to calibrate treatment parameters to make jet grouting cost effective it is convenient to define an efficiency parameter, and two possible expressions were given for it (eqs. 4 and 5). Values of efficiency relative to single and double fluid jet grouting inferred from field trials have also been reported.

Since empirical data by themselves lack of completeness, being unable to take into account in a quantitative way the effect of the resistance to erosion of the soil, a theoretical model may be of great help, once it is carefully calibrated on trial field results. In the paper, such a calibration and comparison is shown. It is demonstrated that the theoretical model adopted (Modoni et al., 2006) is able to catch the main features of jet grouting treatment, even though it is necessarily simplified. By combining the theoretical and the experimental information, the final goal of this activity is to draw simple yet reliable design charts for the different jet grouting techniques.

6. REFERENCES

- AGI (2011), *Jet grouting guidelines*, Associazione Geotecnica Italiana Ed (in Italian).
- Bell, A.L. (1993). *Jet grouting*. In *Ground Improvement*, M.P. Moseley editor, Blackie, 149-174.
- Bergschneider B. and Walz B., (2003), *Jet grouting – range of the grouting jet*, Proc. of the XIII Europ. Conf. on soil Mech. And Found. Engng., Vanicek et al. eds Prague, 2003, 53-56.
- Botto, G. (1985). *Developments in the techniques of jet-grouting*. XII Ciclo di Conferenze di Geotecnica, Torino, reprint by Trevi.
- Chu, E. H., (2005), *Turbulent fluid jet excavation in cohesive soil with particular application to jet grouting*. PhD thesis, Massachusetts Institute of Technology.
- Croce P. and Flora A., (1998), *Jet-grouting effects on pyroclastic soils*, Rivista Italiana di Geotecnica, N.2, Patron Ed., Bologna, 5-14.
- Croce P., Flora A. and Modoni G. (2004), *Jet grouting –Tecnica, progetto e controllo*, Hevelius Ed, Benevento, 221 p. (in Italian).
- Croce P., Modoni G., Carletto M.F.W., (2011), *Correlazioni per la previsione del diametro delle colonne di jet grouting*, Proc. of the XXIV National Conference of Geotechnical Engineering 'Innovazione tecnologica nell'Ingegneria Geotecnica', AGI Ed., pp.423-430 (in Italian).
- Dabbagh A.A., Gonzalez A. S. and Pennington A.S. (2002), *Soil erosion by a continuous water jet*, Soils and Foundations, Vol.42, No.5, 2002, 1-13.
- Davie, J.R. (2003), *Jet Grout Columns Support Major Power Plant Structures*, In: XII Pan American Conference on Soil Mechanics and Geotechnical Engineering, ASCE Geoinstitute, Cambridge.

De Vleeshauwer H. and Maertens G., (2000) *Jet-grouting: State of the art in Belgium*, Proc. of the Conference 'Grouting – Soil improvement - Geosystem including reinforcement' Finnish Geotechnical Society, Helsinki, pp. 145-156.

Flora A., Lirer S., (2011), *Interventi di Consolidamento dei Terreni, Tecnologie e Scelte di progetto*, Proc. of the XXIV National Conference of Geotechnical Engineering 'Innovazione tecnologica nell'Ingegneria Geotecnica', AGI Ed., pp.87-148 (in Italian).

Hinze J.O., (1975), *Turbulence*, 2nd edition, McGraw-Hill, New York, 1975.

Japanese Jet Grouting Association, (2005), *Jet Grouting Technology – JSG method, Column Jet Grouting method, Technical Information*, 13th edition (English translation), 80 p.

Kutzner C. (1996), *Grouting of Rock and Soil*, Balkema Ed., Rotterdam.

Modoni, G, Croce, P., Mongiovì, L. (2006), *Theoretical modelling of jet grouting*, Géotechnique 56 (5) 335-347.

Monda M. (2010), *Analysis of jet grouting field trials and probabilistic design of jet grouted massive impermeable barriers*, Master Course Thesis, University of Napoli Federico II, Napoli, Italy (in Italian).

Stein J., Grabe J., (2003), *Jet grouting tests and simulation*, Proc. of the XIII ECMSGGE, Vanicek et al. Ed., Prague, pp. 899-902.

Tornaghi R., Pettinaroli A., (2004), *Design and control criteria of jet grouting treatments*, ASEP GI.
Tornaghi, R. (1989). *Trattamento colonnare dei terreni mediante gettiniezione (jet-grouting)*. XVII National Conference of Geotechnical Engineering, Taormina (in Italian).

Xanthakos, P., Abramson, L.W., Bruce, D. A., (1994), *Ground control and improvement*, John Wiley & Sons inc.

Offshore Jet Grouting - A Case Study

Turan DURGUNOGLU (ZETAS), Fatih KULAC (ZETAS), Selim IKIZ (ZETAS),
Ogan SEVIM (ZETAS), Onder AKCAKAL (ZETAS)

ABSTRACT

Having high budgets and construction difficulties, offshore structures serve sensible and attractive solutions with an expanding application area all over the world. Because of the marine sediment layers, generally offshore structures subject to be constructed on unfavorable soil conditions. A similar problem was encountered in the scope of an offshore plaza structure in Doha Port, Qatar. Since marine sediments exist with a thickness varying between 3 m to 12 m on the Simsima Limestone bedrock, soil improvement was recommended prior to plaza construction. Some locations of the site were filled and as a result dredging of the made ground was required before soil improvement works. Sea bed was dredged at a depth of -6.00 m and a flat platform was formed prior to soil improvement works. For soil improvement, offshore jet grouting technique is designed and implemented in accordance with the soil conditions and structural surface loadings. Ø80 cm diameter jet grout columns are constructed to a depth of bedrock. System is modeled in Plaxis 3D Foundation and checked in order to fulfill the settlement criteria considering embankment and superstructural loadings. For jet grouting applications a spud barge and a cantilever platform which is carried with a crane are mobilized to the site. Jet grouting is operated on this barge and cantilever platform simultaneously, in order to meet the tight construction schedule. After the soil improvement works, the seabed is dredged and plaza blocks are placed on a granular capping layer which is placed on the jet grout columns. In the scope of the quality control works core samples are taken from the jet grout columns and uniaxial pressure tests are performed to determine the modulus and strength of soilcrete. Since application difficulties and tight schedule of the constructions as in Doha Port, selection of a proper soil improvement method has provided important benefit to the project. It is again proved that, jet grouting is a convenient method because of versatile equipment, high production rate and a reliable output with a sufficient quality control for offshore soil improvement works.

1. INTRODUCTION

Off-shore structures are frequently demanded in shorelines of cities to serve various missions. The unfavorable soil conditions are one of the biggest challenging difficulties encountered during off-shore constructions. Beside bearing capacity problems, in some projects strict settlement constraints come forward in accordance with the importance of the structure. An off-shore sculpture plaza was planned to be constructed at the Museum of Islamic Art, Doha. Due to strict settlement criteria of the sculpture plaza, soil improvement works are designed and implemented carefully and presented in this interesting case study.

2. PROJECT DESCRIPTION

The Museum of Islamic Art is located on the south side of Doha's Corniche on a man-made island sixty meters from the shore. A C-shaped peninsula provides protection from the Persian Gulf on the north and from unsightly industrial buildings on the east. (<http://www.arcspace.com>, 2009) In the scope of the Museum of Islamic Arts Project an offshore sculpture plaza is planned to be constructed by Qatar Museums Authority. Sculpture which is approximately 24.5 m high is designed by the well known artist Mr. Richard Serra. Sculpture is planned to be placed on an off-shore plaza which is on the edge of the C-shaped peninsula (Photos 1 and 2).



Photo 1: The Museum of Islamic Art and Sculpture (<http://islamicartsmagazine.com>, 2011)



Photo 2: Off-Shore Sculpture Plaza (<http://islamicartsmagazine.com>, 2011)

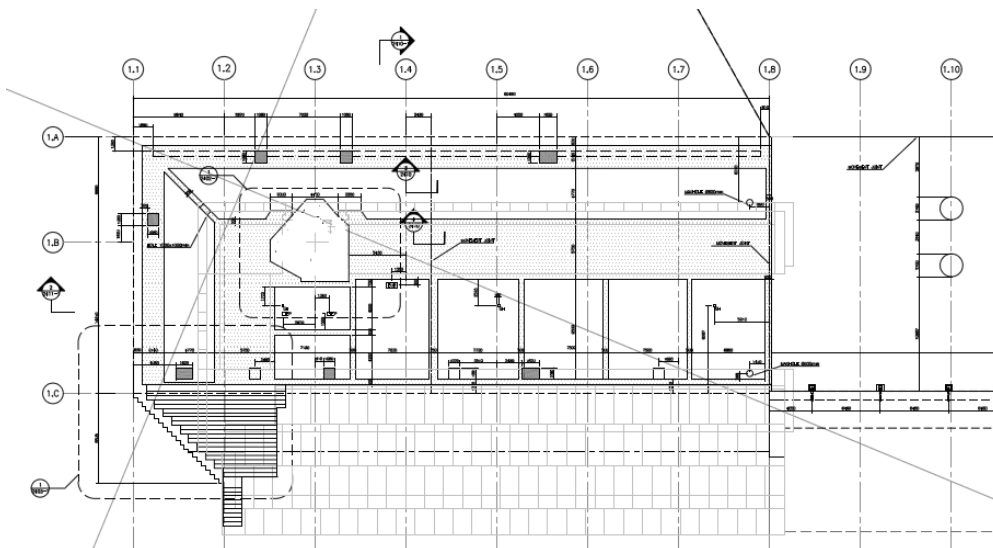


Figure 1: Plan view of the Plaza (COWI, 2010)

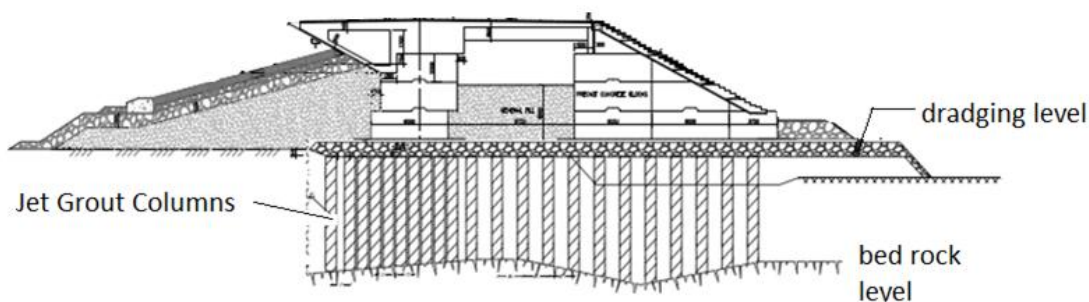


Figure 2: Section view of the Plaza (COWI, 2010)

Plaza is designed as standing on a rectangular area having dimensions approximately 60 m and 38 m. (Figure 3) Plaza is constructed by means of the precasted concrete blocks as given in section view below. (Figure 2)

Precasted concrete blocks and sculpture plaza were designed by engineering group, COWI and the loads under the sculpture plaza were submitted as given Figure 3. Under core part of the plaza block type soil improvement was requested to bear maximum 300 kPa load and under remaining parts wall type soil improvement was requested to bear maximum 150 kPa load.

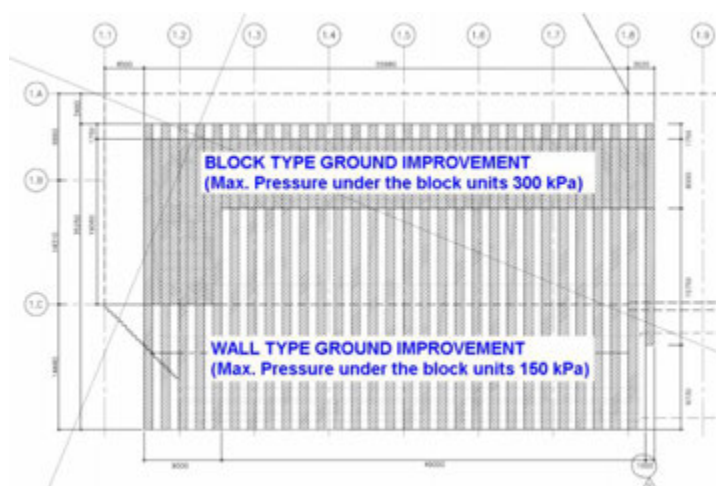


Figure 3: Loads under the Sculpture Plaza (COWI, 2010)

To minimize the settlements under the sculpture four bored piles with 100 cm dia. are implemented. Piles are embedded to base rock minimum 3.5 m. Sculpture is designed as standing on a separate foundation.

3. SOIL PROPERTIES

As stated in the soil investigation report prepared by Fugro Peninsular in 2010, two boreholes were performed on the plaza construction area. Boreholes were operated on the made ground which will be excavated and replaced with concrete blocks and back-fill.

Soil profile is given in the soil investigation report as; (Fugro Peninsular, 2010)

- For the top 12.00-13.50 m, **made ground** represented mostly by boulders, cobbles and gravel in a medium dense state.
- For the layer which has a variable thickness between from 3.40m thick in BH-01 to 10.7m thick in BH-02, **marine sediments** represented by a coarse grain sequence at the top and a fine grain unit at the bottom.
- And the **base rock** which represented by the geological formation Simsima Limestone, represented by a moderately strong and strong fine grained limestone, with numerous pockets of greenish-grey attapulgitic clay.

Soil profile is also illustrated as given in Figure 4.

4. SETTLEMENT LIMITS

It is stated in the specification issued by the Client Qatar Petroleum that ground improvement shall minimize the settlements of the block walls and ensure that the long term total settlements are kept within 25 mm. And special care shall be taken to ensure that the differential settlements shall be less than 15 mm over a length of 10 m.

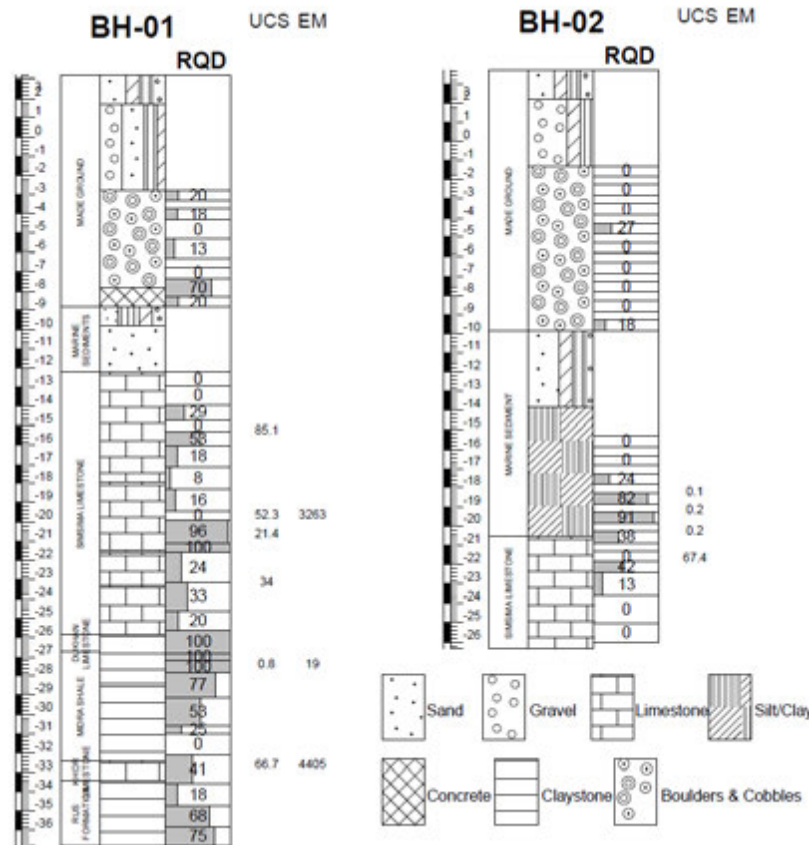


Figure 4: Soil Profile (Fugro Peninsular, 2010)

5. JET GROUTING DESIGN

Because of the existence of made fill and marine sediments, soil improvement is planned to be implemented under the sculpture plaza. Made fill and marine sediments under the seabed will be improved with a suitable method which will be operated on a platform in the sea.

Jet grouting is selected as a convenient method because of the less weight of its equipment, high production rate and a reliable output with a sufficient quality control.

Jet grout columns are designed based on with the section capacity of the columns.

In accordance with the experiences in similar projects, Ø80 cm diameter jet grout columns with 475 kg/m³ cement dosage will be suitable for this project with 1265 kPa estimated section capacity. Jet grout section capacity is calculated in Equation 1.

$$F_{jg} = \frac{A_{jg} \cdot \sigma_{jg}}{FS}, F_{jg} = \frac{0.5m^2 \cdot 1265kPa}{1.5 \times 1.1} = 383kN \cong 380kN \quad (1)$$

A value of 1.1 partial factor of safety is considered for soilcrete section capacity calculations beside the general factor of safety which considered as 1.5.

Measured water soluble sulphate (SO₄) values are 960mg/l for BH1 and 2280mg/l for BH2. As per BRE SD1-2005 the cement should be comply with CMIV/B in accordance with BS EN 197:2000.

Both design of wall and block type jet grout applications are given below

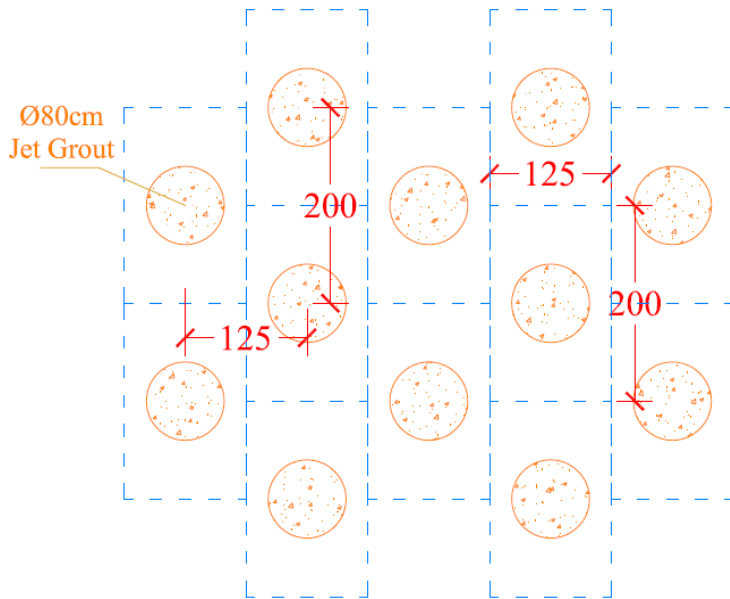


Figure 5: Jet Grout Settlement (Type 1 Area)

Bearing capacity of Type 1 area (wall type) calculated in Equation 2.

$$\frac{380KN}{1.25m \cdot 2.0m} = 152kPa \quad (2)$$

$$152kPa > 150kPa$$

Jet grout settlement given in the Figure 4 will suffice to bear 150 kPa load under wall type (Type1) soil improvement area

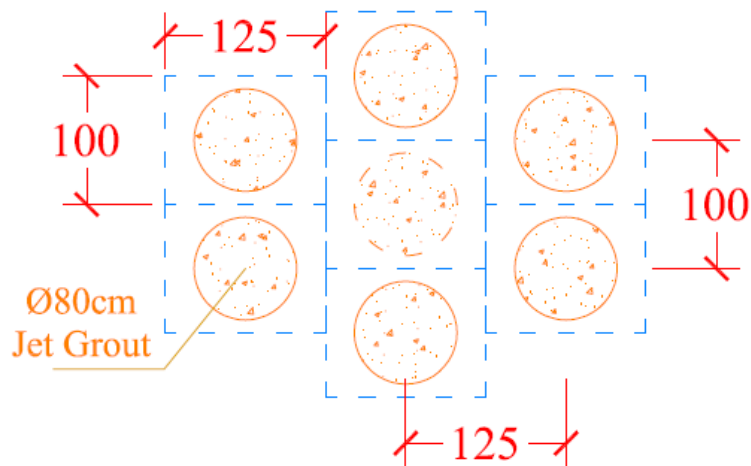


Figure 6: Jet Grout Settlement (Type 2 Area)

Bearing capacity of Type 2 area (block type) calculated in Equation 3.

$$\frac{380KN}{1.25m \cdot 1.0m} = 304kPa \quad (3)$$

$$304kPa > 300kPa$$

Jet grout settlement given in the Figure 3 will suffice to bear 300 kPa load under block type (Type2) soil improvement are

Total jet grouting quantity to be implemented is calculated as 9,283 m.

6. SETTLEMENT CALCULATIONS

Since the loads will be transferred to the base rock with jet grout columns, preliminary calculation for expected settlements is considered as elastic settlement of the jet grout columns. Preliminary calculation for settlement is given in Equation 4.

$$\delta_{total} = \frac{P \cdot L}{E \cdot A} = \frac{380kN \cdot 14m}{750000kN/m^2 \cdot 0.5m^2} = 0.014m = 14mm \quad (4)$$

To simulate the settlements under the plaza more accurately, system is modeled in Plaxis 3D Foundation. Model boundaries and 5 critical points are determined as given in the Figure 7.

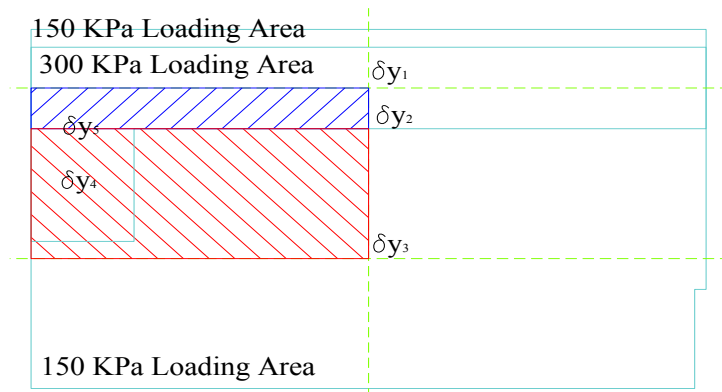


Figure 7: Model Boundaries and Critical Settlement Points

First model is quarter part of the 150 kPa loading area which contains 300 kPa loaded part as an unfavorable situation. Second model is quarter part of the 300 kPa loading area. Described models are illustrated in the Figures 8 and 9.

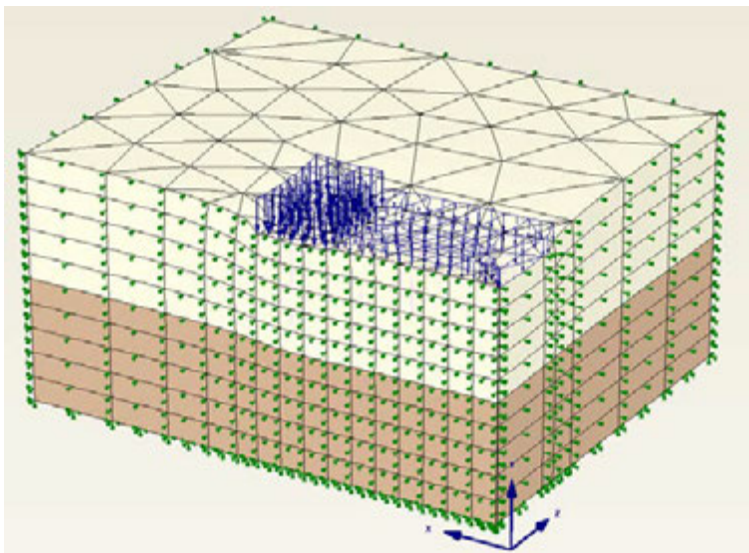


Figure 8: Model 1

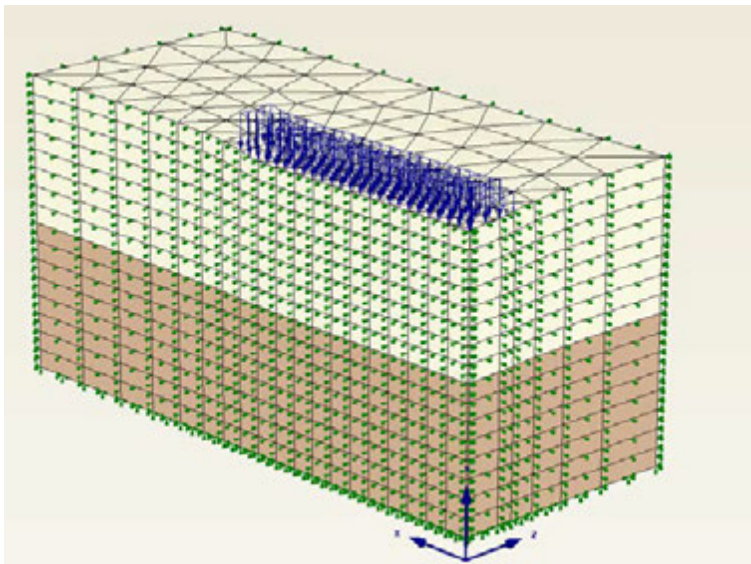


Figure 9: Model 2

In both two models bedrock depth is modeled at 15 m. 15 m jet grouts are modeled under the loaded areas. Calculated settlements for Model 1 are given in the Figures 10, 11 and 12.

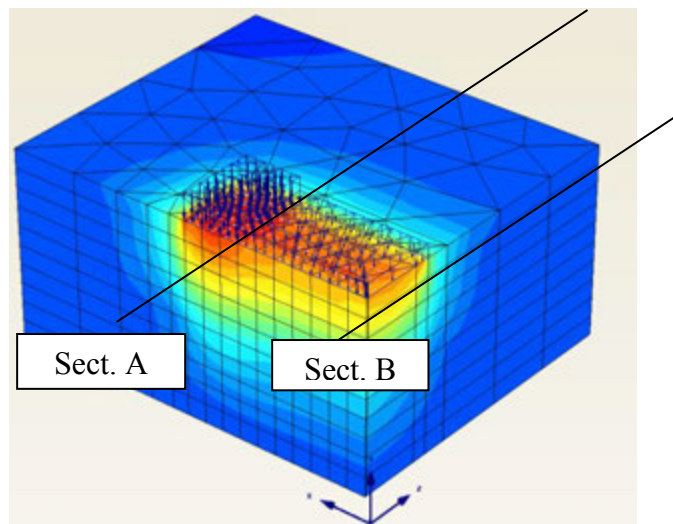


Figure 10: Model 1 Settlement Distribution

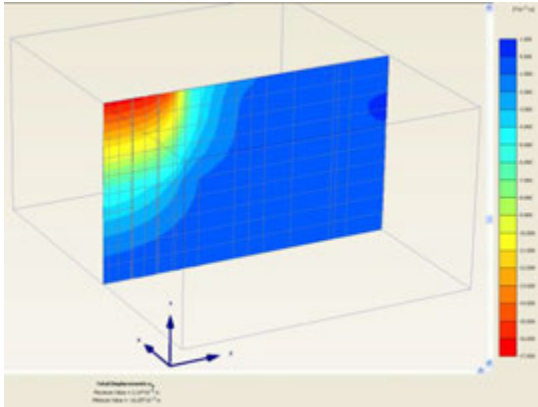


Figure 11 Section A – Max Settlement 16.65 mm, Settlement on the edge 11 mm

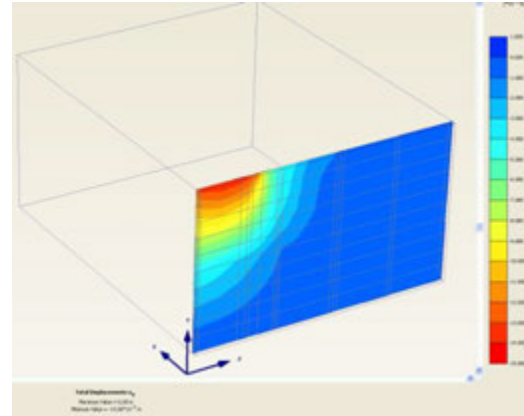


Figure 12 Section B – Max Settlement 14.06 mm, Settlement on the edge 9 mm, Settlement under midpoint of neighbor area 4 mm

Calculated settlements for Model 2 are given in the Figures 13, 14 and 15.

7. SUPERPOSED SETTLEMENTS UNDER CRITICAL POINTS ARE CALCULATED AS GIVEN IN TABLE 1.

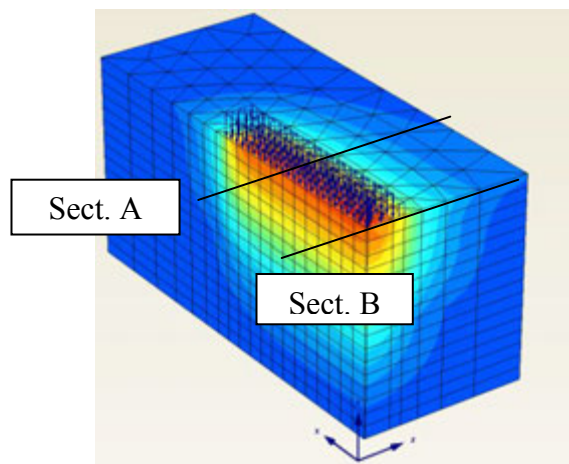


Figure 13: Model 2 Settlement distribution

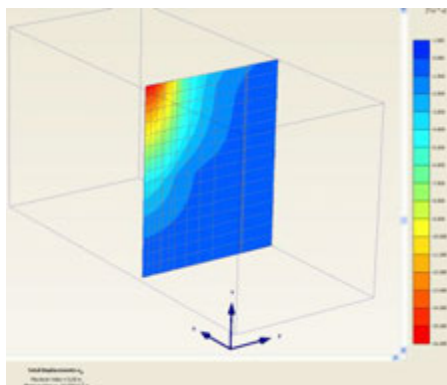


Figure 14: Section A – Max Settlement 15.85 mm, Settlement on the edge 9 mm, Settlement under midpoint of neighbor area 4 mm

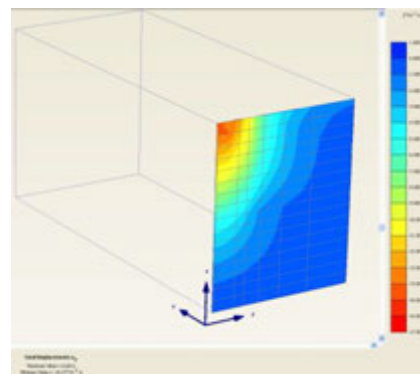


Figure 15: Section B – Max Settlement 16.27 mm, Settlement on the edge 8 mm, Settlement under midpoint of neighbor area 3 mm

Table 1: Superposed Settlements

Critical Points	Settlements, mm		Superposed Settlements, mm
δy_1	16.3	4.0	20.3
δy_2	9.0	8.0	17.0
δy_3	14.1	3.0	17.1
δy_4	16.7	4.0	20.7
δy_5	11.0	9.0	20.0

Settlement values calculated are under the limits of total settlement value 25 mm and differential settlement value 15 mm /10m as specified in the specification.

8. OFF-SHORE JET GROUTING APPLICATION

Prior to soil improvement works sea bed was dredged at the depth of -6.00 m and a flat platform was formed. Off-shore jet grout columns planned to be implemented with two different methods simultaneously within this project in order to meet the tight construction schedule. Total approximately 9,300 m Ø80cm dia. jet grouting have been implemented in 60 days reaching to a rate of 155 m/day. One is the jet grouting on the spud-barge mobilised to the application site (Photo 3), the other is the jet grouting on a cantilevered platform which is carried by a crane (Photo 4).



Photo 3: Jet Grouting on Spud-Barge



Photo 4: Cantilevered Platform Carried by Crane

IPC 830B model drilling machine is used on the cantilevered platform because of its low weight and versatility. (Photo 5) The cantilevered platform is designed and fabricated specially for this project by Z Makine a sister company of Zetas. (Photo 6)



Photo 5: IPC 830 B

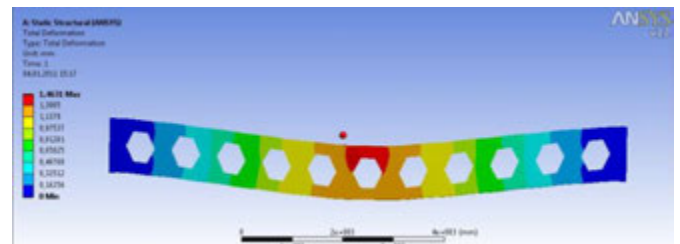


Photo 6: Distribution of stresses on Cantilevered Platform Considering IPC 830B weight

After the off-shore jet grouting works for leveling the sea bed clamshell grab is used before placing the fill and precasted concrete blocks.

9. QUALITY CONTROL TEST

Compression tests of the core samples taken from the jet grout columns are performed in the scope of the quality control applications. Assumptions on the material properties of the soil-crete columns such as section capacity and modulus were checked and approved.

10. CONCLUSIONS

Because of the unfavorable soil conditions and strict settlement criteria, soil improvement is implemented under the off-shore sculpture plaza in Doha Port. Regarding the soil conditions and structural surface loadings off-shore jet grouting technique is considered as a proper solution for soil improvement. Variable base bedrock depth is encountered during the soil investigation and jet grout columns are implemented to the depth of rock stratum. System is modeled in Plaxis 3D Foundation and checked in order to fulfill the settlement criteria. Jet grouting is performed on spud barge and a cantilevered platform which is carried with a crane. In order to meet the tight construction schedule jet grouting is operated on this barge and cantilevered platform simultaneously. Core samples are taken from the jet grout columns and uniaxial compression tests are performed, in the scope of the quality control works. With off-shore jet grouting, soil improvement works implemented successfully in a very tight schedule and provided important benefit to the project. In this case study it is again proved that, even working on an off-shore project, jet grouting provides a reliable and a quick solution because of versatile equipment, high production rate and a reliable output with a sufficient quality control.

11. ACKNOWLEDGEMENT

We would like to extend our great appreciation to all the individuals involved in various stages during the realization of this challenging project. Special thanks are due to BAYTUR and QP ASTAD.

REFERENCES

- BRE, 2005, Concrete in Aggressive Ground, The third edition of BRE Special Digest 1*
- BS EN 197-1, 2000 Cement Composition, specifications and conformity criteria for common cement*
- FUGRO PENINSULAR, 2010, State of Qatar Geotechnical Investigation Museum of Islamic Art – Sculpture Plaza Doha*
- COWI A/S, 2010, Sculpture Plaza Structures Ground Improvement, Drawing No. 2763-2210 Rev. D*
- COWI A/S, 2010, Sculpture Plaza Structures Main Cross-Section, Drawing No. 2763-2202 Rev. E*
<http://www.arcspace.com>, 2009
<http://www.islamicartsmagazine.com>, 2011

Construction of the Bellinzona Portal Ceneri Base Tunnel, AlpTransit Gottard Tunnel

Robert D. Essler, RD Geotech Ltd, United Kingdom, robert.essler@rdgeotech.co.uk
Francesco M. Rossi, G.Dazio&Associati SA, Switzerland, rossi@dazio.com

ABSTRACT

The Alptransit project is part of the Swiss railway system that will also serve as part of the European high speed railway line between Milan and Zürich. The railway line will cross through the Alps and provide an alternate method of transportation to Italy. The new Alptransit line will generate the so called "flat high speed railway line" across the Swiss Alps by drilling 3 main tunnels: the Gotthard Base Tunnel (57km), the Zimmerberg Tunnel (20km) and the Ceneri Base Tunnel (15km). There are a number of portals along the route where the railway enters and exits from the mountains.

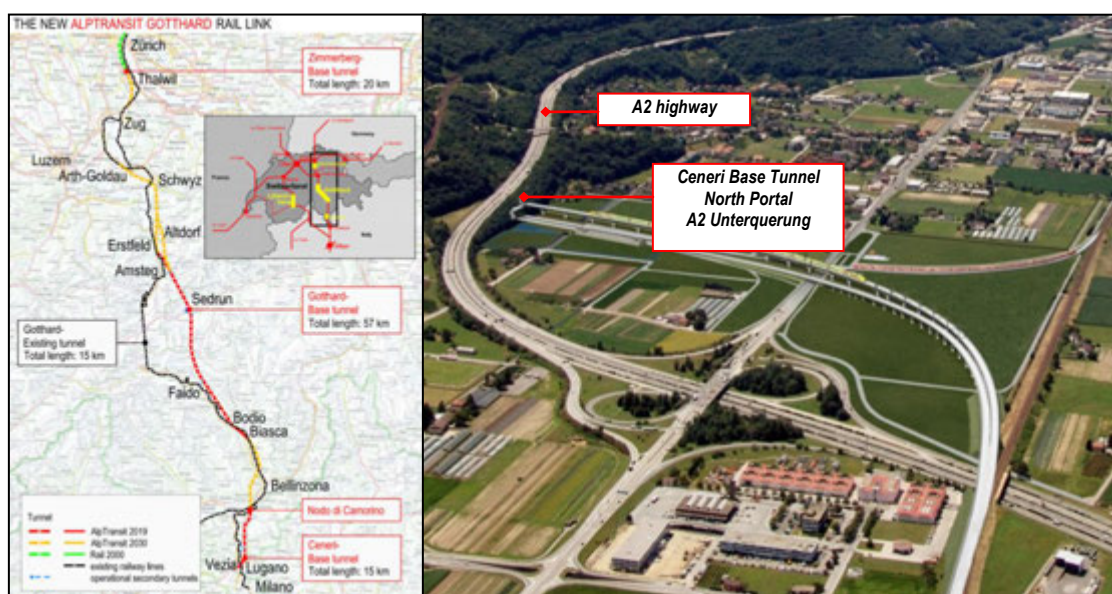


Figure 1: New European Alptransit Gotthard Rail Link and perspective view of the Nodo di Camorino

At Bellinzona the North portal of the Ceneri Base Tunnel passes immediately below the A2 motorway with a cover of only 8m in soft ground. Because there could be no disruption to the overlying motorway, the portal had to be very carefully constructed to minimise movements. At this location the motorway is constructed on a granular fill embankment and thus the tunnel portal passes through fill material into rock debris and finally rock. The completed tunnel has a total width of 28m and a height of 16m and thus has a very low cover compared to its size.

The construction solution adopted was to drill two side tunnels with the crown supported by a canopy of horizontal jet grouting and a central cavern spanning between and supported by the two side tunnels also with a horizontal jet grouted canopy and face spiles. Inside the two side tunnels, massive concrete beams are supported on a series of vertical jet grout columns extended through weak natural ground to bedrock.

The paper describes the method of construction in detail with associated design and demonstrates that a very large excavation can be safely constructed at a shallow depth in variable ground.

1. INTRODUCTION

1.1. General

The Ceneri Base Tunnel is part of the Alptransit project that allows crossing the Swiss Alps from Zürich to Lugano with a new railway line. The system allows the creation of a flat high speed railway line that, thanks to 3 main tunnels, shortens travel time from the northern part of Switzerland to the Southern part. The Ceneri Base Tunnel has a total length of 15km and connects the capital city of the Canton Ticino, Bellinzona, to the economic center Lugano in the south part of Switzerland.

The north portal of the Ceneri Base tunnel is the subject of this paper and the most difficult part of the entire project. The first 50 meters are characterized by crossing the A2 motorway with a 350m² cavern excavated in soft soil made partially of the A2 motorway dam built in the early '70s. The excavation has a cover of only 8 meters from a five lane highway which had to be always fully operational during all construction phases.



Figure 2: Aerial view of the north portal of the Tunnel during construction with the A2 motorway. Source: Alptransit SA Bellinzona

Figure 2 shows a view of the construction site at an early stage where two nailed walls have been constructed to prepare the excavation under the A2 highway. The first nailed wall has a height of 18m and a width of 30m in order to accommodate the 350m² cavern that is excavated under the highway with a cover of 8m from the traffic operational during all construction stages. The second nailed wall is smaller in size and accommodates one railway line. Finally the tunnels will allow the passage of 4 railway lines under the existing motorway.

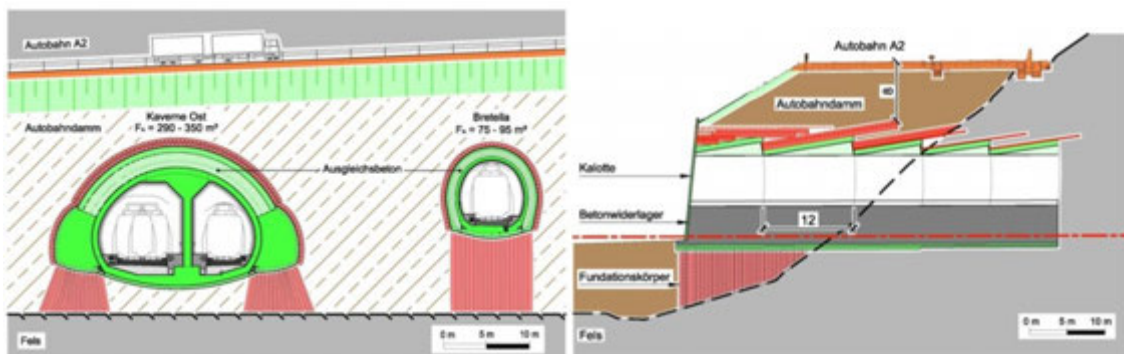


Figure 3: Schematic view of the excavation. Source: CIPM – Consorzio Ingegneri Piano di Magadino

1.2. Geology

The geology is characterized by the manmade embankment of the motorway built in the early '70s. The natural slope has been covered by a 23m high embankment compacted in layers to form the new platform for the 5 lane highway. The geotechnical values of the layers composing the soil were evaluated with extensive site investigation and have been summarized in a geological report. Most of the excavation of the Cavern in soft soil is made through the embankment material that has an internal friction of 40 degrees, and an elastic modulus ranging from 35 to 50 MPa and a cohesion $c=0-5kPa$. The embankment is founded on layers of the original ground surface with similar geotechnical characteristics to the embankment and below it lies a moraine layer of thickness 1-3 meters which overlies the rock. The geologic formation below the embankment is typical in the region of the Swiss Alps where the glaciers shaped the valleys.

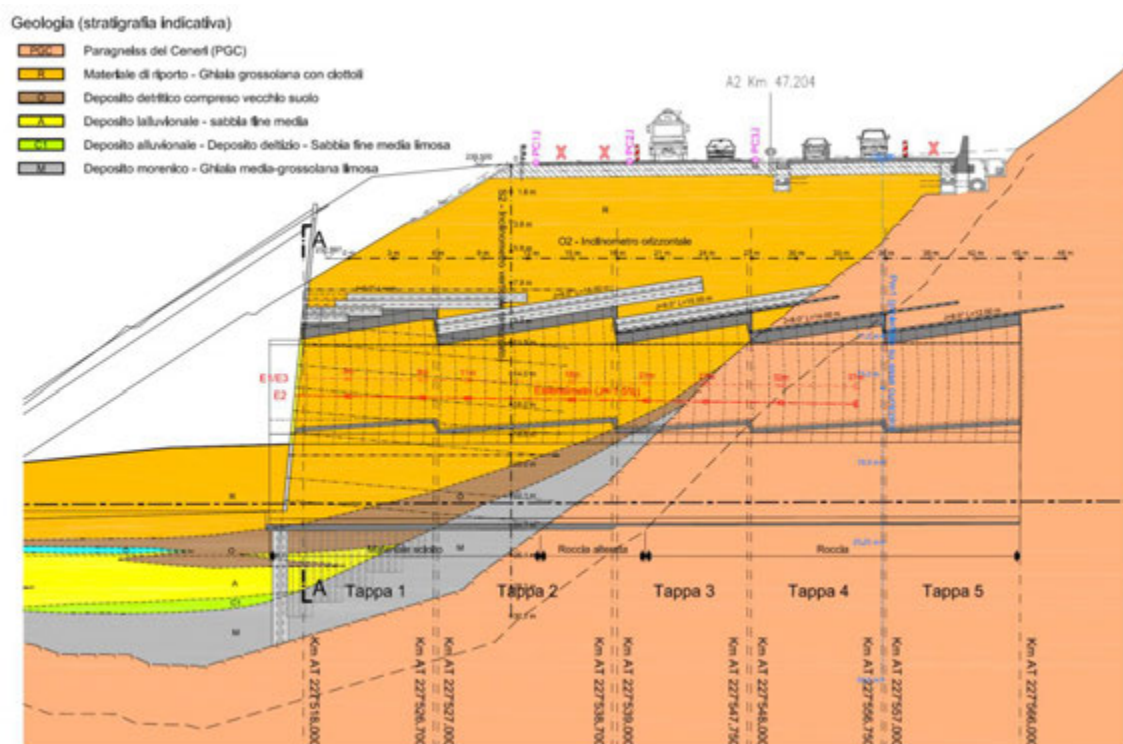


Figure 4: Geological longitudinal section. Source: CIPM – Consorzio Ingegneri Piano di Magadino

2. DESIGN

2.1. Conceptual design

The conceptual design was developed by Professor Kalman Kovári. The main objective is to minimize the settlements on the A2 highway.

The large cavern of more than 20m is constructed in phases. In the first phase two side tunnels each of about 60m² were excavated using the protection of a jet grouting umbrella, jet grouting columns reinforced with steel piles for the front face stability and the installation of a reinforced sprayed concrete liner. The 48 meter excavations to cross the highway was carried out in 5 main steps of 9m, 12m, 9m, 9m, 9m. Each step being excavated in 1 meter per day in order to install a protective lining of sprayed concrete on the front face of the excavation and carry out the operations for installing the steel truss girders and the concrete lining. At the end of phases 1, 2 and 3 a new jet grouting canopy and front face reinforcement were installed for the next excavation phase. In phase 3 and 4 an additional grouted steel bar canopy was provided for the support for the transition between soft soil and rock.

After the excavation of the two side tunnels, vertical jet grouting in the first phase (9m) assured the transfer of load from the concrete beams to the rock. The concrete beams are poured into the side tunnels and have a height of more than 6m, a variable width of 2-3.5m and a length of the excavated tunnels of 48m. These two supports had the task to transfer the loads coming from the cavern arc to the rock and in the first phase from beam to jet grouting and then finally to rock.

The top cavern excavation has a height of 8m and a width between 20 to 24 meters with only 8m soft soil cover from the A2 highway. After completing the top cavern excavation the tunnel can be excavated in bench between the 2 side tunnels and the invert is therefore connected to the concrete beams.

The conceptual design is a solid solution that has the following strong points:

- It is an easy static solution;
- It guaranties a stiff structural system;
- It requires demanding jet grouting works;
- Allows an easy construction method; and
- Reduces the residual risks.

2.2. Finite Element Analysis

In the next figures are shown schematically the various levels of ground improvement using jet grouting and the effect on the settlements and steel bar reinforcement of the 70cm thick concrete lining of the cavern.

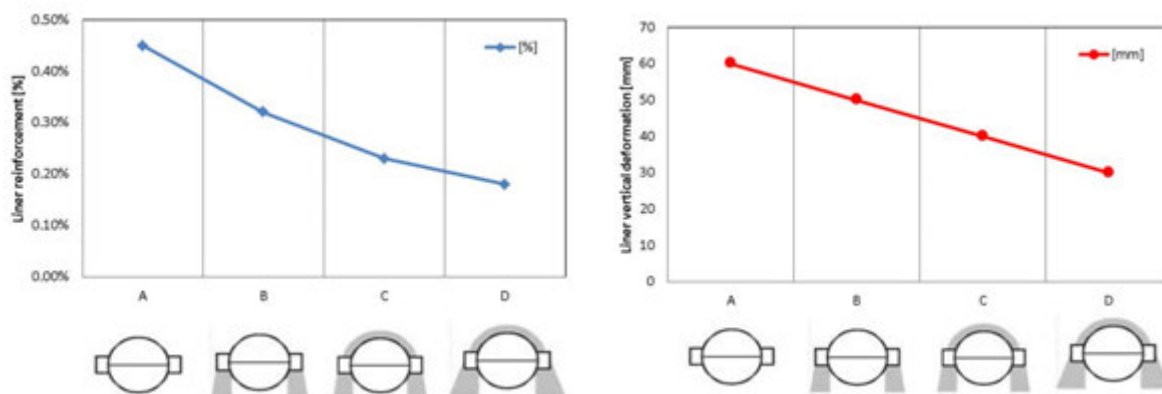


Figure 5: levels of jet grouting improvements. More jet grouting, less settlements and less reinforced steel bars in the 70cm thick liner

The case **A** is the first shown in the diagram and represents the cavern's excavation carried out without jet grouting. Of course this is impossible to realize and is only theoretically investigated to show the effect of ground improvement on the system. In case **B** the jet grouting is provided under the concrete beam foundations to transfer the loads to the rock. In case **C** it modeled the jet grouting umbrella and finally in case **D** it can be seen the effect of more jet grouting on the sides of the concrete beams in order to bring even more stiffness to the system.

The reinforced steel needed in the 70cm thick lining is also reduced from $\rho=0.45\%$ to $\rho=0.20\%$ thanks to the installation of jet grouting columns. Also settlements are greatly reduced with a higher level of ground improvements so that traffic on the A2 highway can be operational during all construction phases.

The settlements shown in the diagram do not include the influence of the nailed wall, the excavation of the side tunnels, the effect of jet grouting operations and creep and shrinkage.

The front face stability, in phase 2 of excavation length 12m, is guaranteed by installing reinforced jet grouting columns in the front face. The horizontal jet grouting columns have a length of 18m and inside of them is installed a steel bar of 40mm in diameter.

2.3. Final Design Solution

The solution designed is shown in the next figures where the details of the construction phases are supported by pictures taken during the execution. The safety of the excavation in soft ground relies on the single fluid jet grouting canopy placed on the external perimeter of the tunnel. The columns have a diameter of 60cm, length of 18m and are installed with a spacing of 45cm to form an arc of treated ground. The minimum required mechanical properties of the treated ground were:

Density	22kN/m ³
Elasticity modulus	3000MPa
Compressive strength	5MPa
Poisson value	0.30
Cohesion	1000kPa
Friction angle	45°

The values were verified with local field tests in advance of excavation.

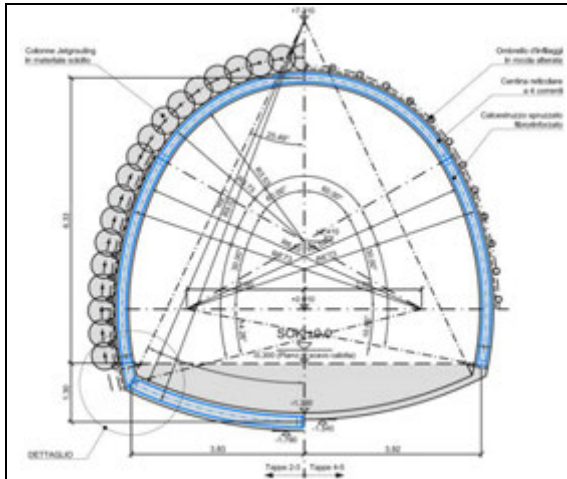


Figure 6: side tunnels cross section



Figure 7: Excavation of the 2 side tunnels

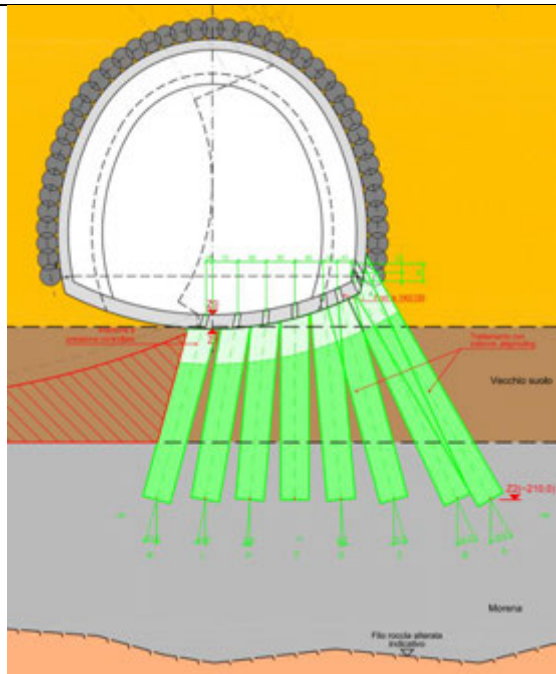


Figure 8: vertical jet grouting in the side tunnels



Figure 9: vertical jet grouting under the concrete beams in the first 9 meters of the tunnel

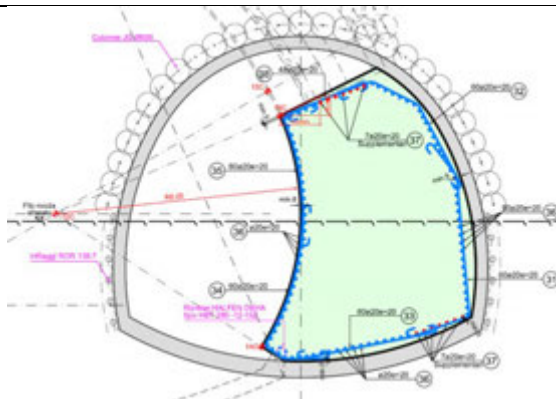


Figure 10: cross section of designed concrete beams inside the side tunnels



Figure 11: construction of the 48 meters long concrete beams inside the tunnels

A significant amount of very careful horizontal and vertical jet grouting was required to enable the construction and some details of this are shown in the following figures.

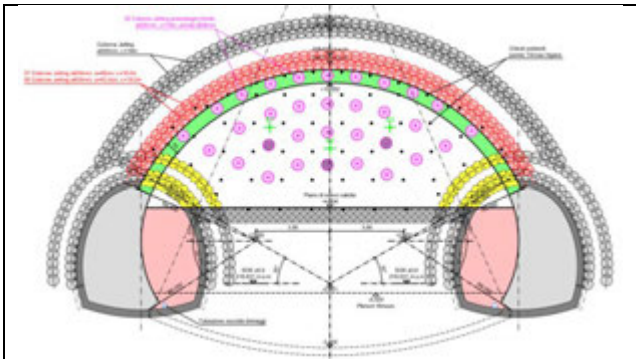


Figure 12: reinforced horizontal jet grouting for tunnel face stability



Figure 13: top cavern excavation

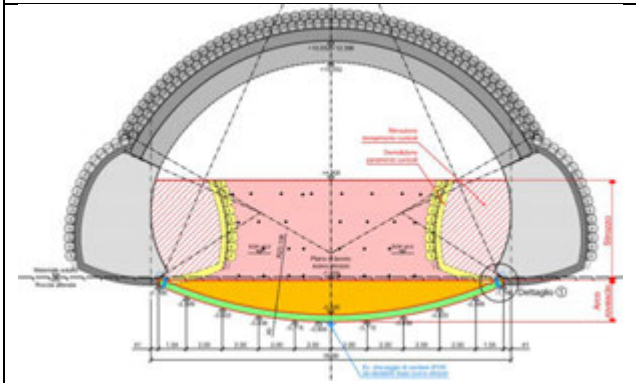


Figure 14: cross section of cavern bench and invert excavation



Figure 15: cavern bench excavation

3. JET GROUTING

The jet grouting, carried out by Rodio CH, caused initially settlement greater than expected. In the course of installation of jet grouting columns, especially in the original ground layer, a consolidation process takes place causing the compaction of the original soil between the moraine and the manmade embankment. The volume loss of the layer, compressed by the weight of the embankment, produces a localized vertical settlement (Figure 16). This has been found to be the main reason for the unexpected settlements but movements may also have been produced by the jet grouting methods applied by Rodio CH.

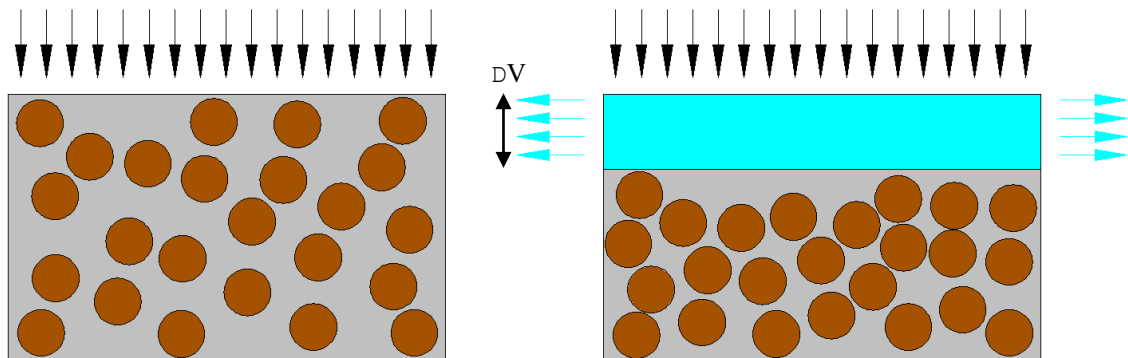


Figure 16: vibro compaction effect during installation of jet grouting

Because of the importance of the top cavern excavation (20-24m large excavation in soft ground) and the sensitive interface with the overlying motorway, movements had to be minimized and hence the jet grouting process was reviewed by the consultant who appointed a specialist in jet grouting (RD Geotech).

The initially findings of the specialist was that the hole deviation was greater than designed and this could be causing problems with the stiffness of the arch. A review of the drilling for the jet grouting was carried out and the ground characterized by the drilling energy, reported by the Lutz jet grouting instrumentation. This is shown on Figure 17. The drilling energy was divided into three zones and the canopy plotted to show where the weak zones existed. This indicated that on the western side of the works the ground was potentially weaker and needed more care in the jet grouting approach.

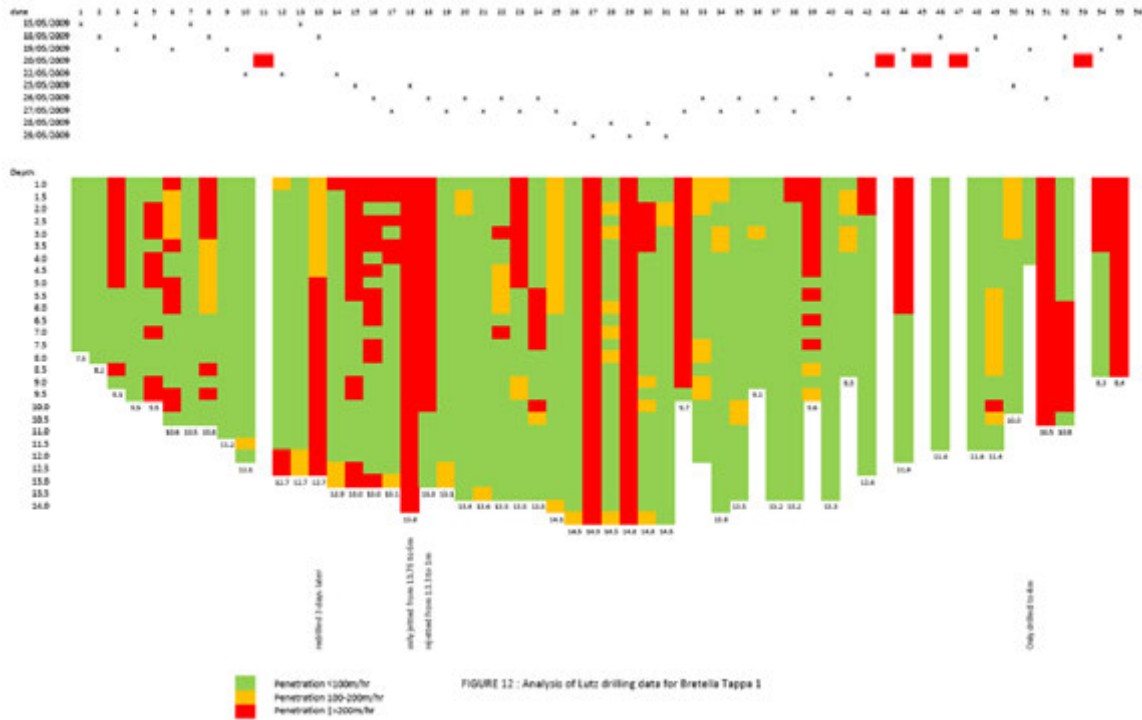
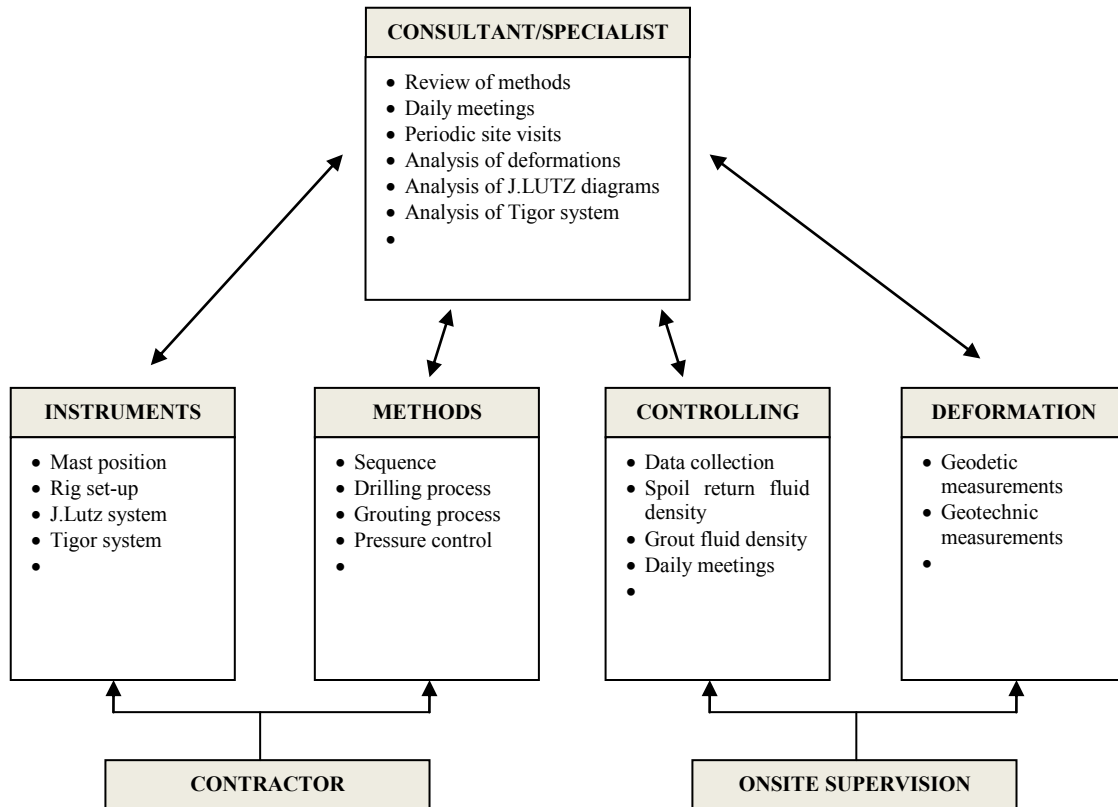


Figure 17: Drilling energy for one of the jet grouted canopies

After an initial review of the previous jet grouting works, the specialist has introduced organizational and operational improvements and refinements in order to assure the quality of the remaining jet grouting for the large cavern.



The following main refinements were investigated:

- The set up of the drill rig was improved as shown in Figure ;
- Initial commencement of each column was accomplished by overdrilling by around 200mm to 300mm and gradually applying the high grout pressure to avoid “shocking” the ground; and
- The jetting sequence was revised to ensure that the face columns and canopy were jetted “top down” to ensure that spoil could not contaminate adjacent columns.

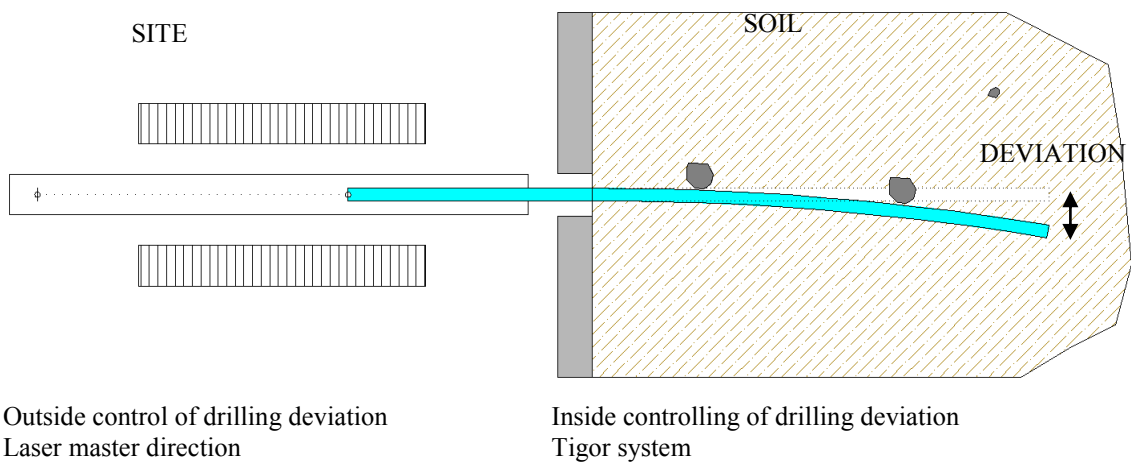
Column and nail deviations

The deviation of the columns was found to be much greater than the allowed in the design (0.50% of the column length). The rig set up has been improved by attention to mast position controlled continuously with a laser pointer during drilling. This assures that no deviation occurs based on positioning. Each column is surveyed during drilling by the use of the TIGOR system and the deviations have been calculated. In general we find that most columns deviate in a similar direction which is often found for soils (in clays holes deviate downwards, in sands and gravels they deviate upwards).

For the first stage of drilling the average and maximum deviation was respectively <0.6% and <1% and for the 2nd stage the drilling has been reported <0.50% based on the Tigor measurement. However the columns in the front face of the tunnel have shown excessive deviations (>5% of drill depth which is not acceptable) and the Tigor system proved to be not reliable in this case. Following advice by RD Geotech, the excavation was temporarily stopped by the consultant and additional nails were installed for the front face stability of the top cavern. The as built positions were reviewed and a number of additional columns were installed subject to final review by the contractor. These have been jet grouted with normal parameters to fill any gaps potentially present. Figure 18 shows the position of a bar installed in a column illustrating the deviation that could take place.



Figure 18: deviation of pile within jet grout column



Outside control of drilling deviation
Laser master direction

Inside controlling of drilling deviation
Tigor system

Figure 19a: Planview. Bending of the rod inside the ground

It has been calculated that a steel pipe with an outer diameter of 95mm and a thickness of 10mm could bend inside the ground; it can bend up to 10% of the length and have stresses lower than 200MPa allowing elastic movements of the rod in the soil without detecting deviations from the measurements of the mast outside the ground. Only a correct and reliable instrumentation can detect the inside the ground position of the rod. However even the Tigor has shown difficulties detecting the real position of the column.

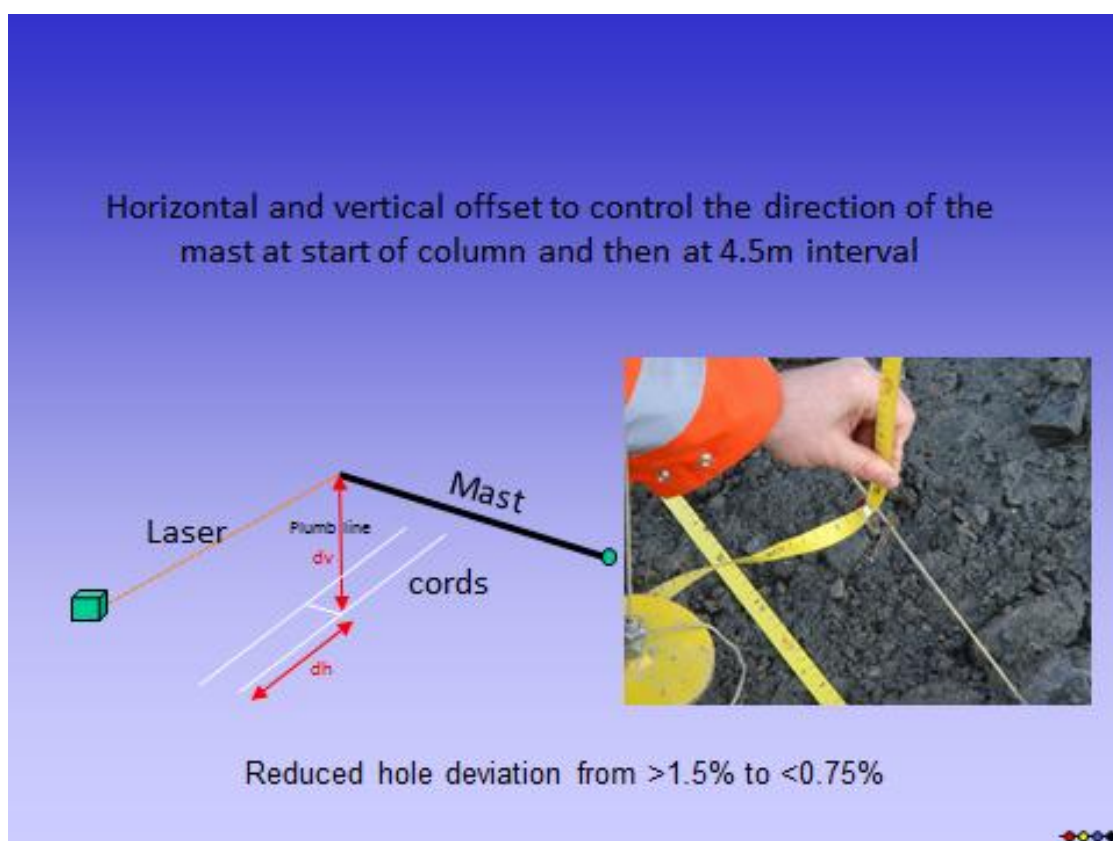


Figure 19b: improvement in rig setup by attention to mast position

Drilling and grouting operations

The question of maintaining spoil return is always important. Settlement has been caused rather than heave which would be a result of over pressurisation so this has not been a problem on the project, more the reverse. The specialist suggested that two changes be made to the jet grout process.

- 1) The column should be drilled 30cm deeper and a phased commencement of jet grouting increasing the pressure in steps of 100 bar should be carried out to reduce any hydraulic shock to the ground
- 2) Some holes at the start of a shift should be drilled with grout to assess whether this improves the situation.

A trial of phased pressure start up was carried out and appeared to be successful in maintaining spoil return and have be implemented for the remaining jet grouting needed. As a final check destructive borings have been carried out after each phase. The positions of these holes have been assessed based on the Lutz instrumentation, movements and as built positions.

Jetting sequence

The jetting sequence has been revised by the specialist to ensure that the face columns and canopy were jetted “top down” to guarantee that spoil could not contaminate adjacent columns. The operations have been planned using contemporarily 2 machines on the east and the west side of the jet grouting arc of the second phase.

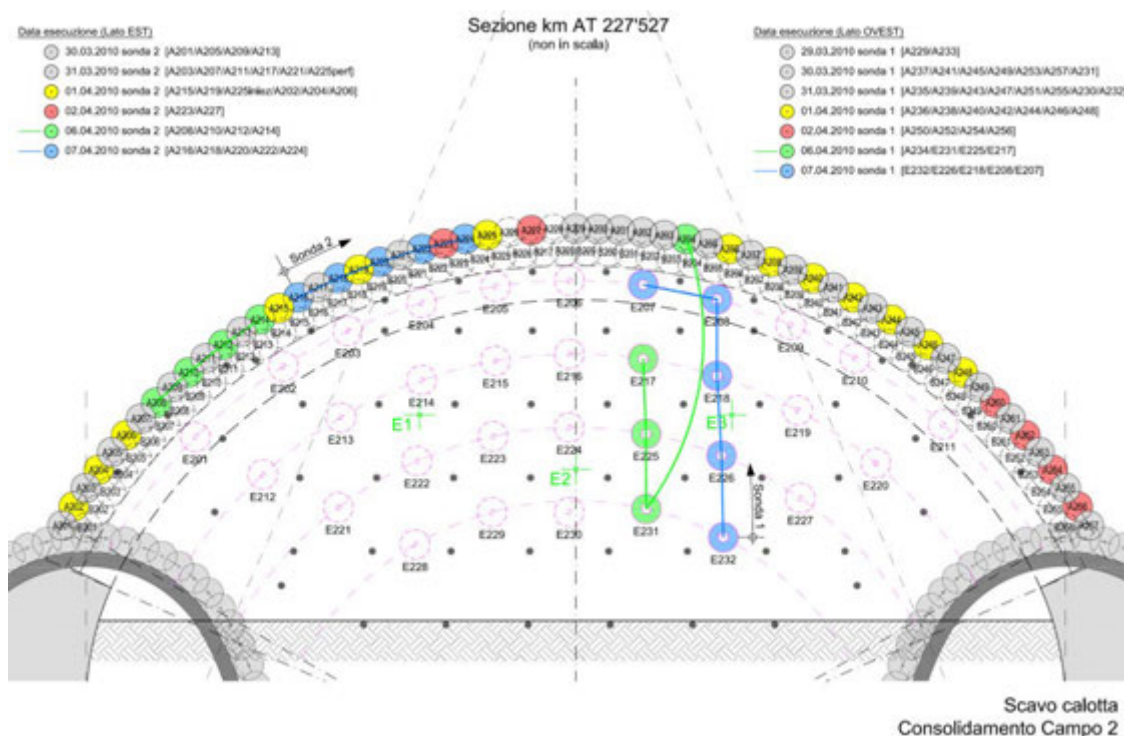


Figure 20: jetting sequence. Daily drawings and review

Following these improvements the first jet grouting phase of the cavern did produce only 5mm heave. Later the phases 2 and 3 showed again localized settlements caused by the injection of the layer of original ground that has not affected the first phase. The settlement was in the last jet grouting much smaller compared to the initial settlements and the cavern was excavated completely into the soft rock.

4. CONCLUSIONS

The main conclusion from the project was that a very large cavern could be safely constructed beneath a live motorway without causing excessive settlements. Additionally it was also demonstrated that the horizontal jet grouting could be improved by improvements to the rig set up, jetting methodology and sequence.

Modelling of Jet Grouting and its interactions with surrounding soils

José M. Gesto

Universitat Politècnica de Catalunya and INGESTAR Technologies, Spain, jose.manuel.gesto@upc.edu,
jmgesto@ingestar.net

Antonio Gens and Marcos Arroyo

Universitat Politècnica de Catalunya, Spain, antonio.gens@upc.edu, marcos.arroyo@upc.edu

ABSTRACT

The versatility of Jet-Grouting as a soil improvement technique has made this procedure to be widely used in geotechnical engineering practice. In this work we discuss some aspects related to the THMC coupling phenomena that may arise when the Jet-Grouting technique is employed. Namely, we describe some basic constitutive models that may be appropriate to simulate the response of the surrounding soils and that of the Jet-Grouted soil itself while those interactions take place.

1. INTRODUCTION

Jet-Grouting has become one of the most widely used soil improvement techniques. It is applied, for instance, to create provisional earth retaining and waterproofing slabs and walls in excavations or supporting arches of cemented soil ahead of the face of shallow tunnels. Jet-grouted soil generally has better strength and permeability than the original soil, thus providing with safer work conditions and reducing soil displacements and surface settlements; in particular, such benefits may be exploited in urban environment to avoid damage on pre-existing infrastructures and buildings.

Standard jet-grouting treatments are formed with assemblies of overlapped columns of cemented soil. Advances in jet grouting technology permit nowadays the installation of high diameter (several meters) jet columns. The fast pace of injection that is possible requires a careful design of grouting schemes to avoid pitfalls during construction, with particular attention to the relative location of fresh columns within the treatment, see for instance Pichler et al. (2003). The high energy associated with jet installation almost always results on a fluid material that solidifies (“sets”) as cement hydration takes place. Hydration is not only a strongly exothermic reaction, but also one whose rate depends on the temperature. Hydration heat does not remain confined within the treated zone but it is also transferred to surrounding soils (SS). This, according to their specific thermomechanical properties, might have mechanical or hydraulic consequences.

Clearly, the application of jet-grouting treatments results into complex thermo-hydro-chemo-mechanical (THMC) interactions that, in particular, may have substantial effects regarding to the estimation of movements and water fluxes which have not been properly studied yet. These sophisticated interaction phenomena are not covered by the current design practice for jet-grouting treatments, which is mostly based on empirical rules. A better understanding of the THMC couplings involved in the application of this soil improvement technique would lead to a more rational use of it.

A framework for the study of the jet-grouting hydration reaction and of the associated THMC interactions with the surrounding soils has been developed in the Department of Geotechnical Engineering and Geosciences of the Universidad Politècnica de Catalunya. In this work, we give a brief description of some basic models proposed for the jet-grouted soils (JGS) and the SS in the context of plasticity theory for saturated soils. More details and models will be presented in further publications, which will also be devoted to the analysis of the state equations governing the coupled problem.

2. NOTATION

Here we focus on the case in which the SS is saturated, and hence we assume that its behavior is governed by the following variables: displacements, temperature and water pressure. As for the JGS, it is necessary to introduce new state variables to account for the effects of the hydration reaction. A variable commonly used in this context is the *degree of hydration*, defined as the mass of hydrates formed by unit volume divided by the respective mass at the end of the hydration process, see Brandstätter et al. (2005).

Table 1 gathers some of the symbols used hereafter and a brief description of each one of them. Bold will be used for tensors and matrices and italic for scalar variables. We will use no mark to distinguish between total or effective stresses and parameters; this distinction will be clear from the context.

Table 1: some symbols used in the paper and their description

Symbols	Description
x, y, z, t	Cartesian spatial coordinates and time
$(\bullet), (\dot{\bullet}), f_{(\bullet)}$	A generic variable, time derivative of a generic variable, derivative of function f with respect to a generic variable (sub-indexes are also used with other purposes) and the operator nabla
\mathbf{u}, T, p_w, ξ	Displacements of the solid skeleton with respect to a fixed reference system, temperature, water pressure and degree of hydration at a material point (positive water pressures mean compression)
$\boldsymbol{\sigma}, \boldsymbol{\varepsilon}, \boldsymbol{\varepsilon}^T, \boldsymbol{\varepsilon}^E, \boldsymbol{\varepsilon}^P$	Stresses, total strains, elastic thermal strains, shrinkage strains and plastic strains (positive stresses and strains mean compression)
$\sigma_i, \varepsilon_i, \varepsilon_i^P, i=1,2,3$	Principal stresses, principal strains and principal plastic strains
$p, J, \theta, \varepsilon_v, \varepsilon_v^P$	Classical stress and strain invariants: mean stress, deviatoric stress, $J = \sqrt{((\sigma_1 - \sigma_2)^2 + (\sigma_1 - \sigma_3)^2 + (\sigma_2 - \sigma_3)^2)}/6$, Lode's angle, total volumetric strain, plastic volumetric strain
π_1, π_2	Auxiliary coordinates for π -planes: $\pi_1 = \sqrt{2}J \cos \theta, \pi_2 = \sqrt{2}J \sin \theta$
$\mathbf{r} = [1 \ 1 \ 1 \ 0 \ 0 \ 0]^T$	Auxiliary matrix
$E, \nu, K, G, \Lambda, \kappa$	Young's modulus, Poisson's ratio, bulk and shear elastic moduli, loading and unloading-reloading moduli (in a curve $\ln p \leftrightarrow \varepsilon_v$)
$F, G, \mathbf{n}, \mathbf{m}, \zeta, H$	Yield and potential functions, derivatives of the yield and potential functions with respect to the stresses, plastic parameter, plastic modulus
$\mathbf{D}_{el}, \mathbf{d}, \mathbf{D}_{ep}$	Elastic tangent matrix, auxiliary matrix, elasto-plastic tangent matrix: $\mathbf{d} = \frac{\mathbf{D}_{el} \mathbf{m}}{H + \mathbf{n}^T \mathbf{D}_{el} \mathbf{m}}, \mathbf{D}_{ep} = \mathbf{D}_{el} - \mathbf{d} \mathbf{n}^T \mathbf{D}_{el}$
$\alpha_{SS}, \lambda_{JGS}, E_{JGS}, c_{JGS}$	Linear thermal coefficient for the SS (negative values indicate expansion), thermal conductivity of the JGS, internal energy and specific heat capacity of the JGS
$l_\xi, \tilde{A}, E_a, \chi, R$	Latent heat of hydration per unit volume, chemical affinity, activation energy and shrinkage coefficient (negative means expansion) of the JGS, universal constant for ideal gases
$\theta_i, i=1, \dots, 6$	Auxiliary angles: $\theta_1 = \theta \quad \theta_2 = \frac{2\pi}{3} + \theta \quad \theta_3 = \frac{4\pi}{3} + \theta \quad \theta_4 = \frac{\pi}{3} - \theta \quad \theta_5 = -\frac{\pi}{3} - \theta \quad \theta_6 = \pi - \theta$
$\hat{b}, g, \mathcal{H}, \mathcal{T}, h_c, w, \hat{w}$	Auxiliary functions and coefficients: $\hat{b}(\xi, r_1, r_2) = \ln(\exp(r_1 r_2) + \exp(2r_1(\xi - 0.5))) / r_1$ $g(\theta, \varphi) = \cos \theta + \sin \theta \sin \varphi / \sqrt{3} \quad \mathcal{H}(\theta, \varphi) = \ln \left(\sum_{i=1}^6 \exp(p_{\mathcal{H}} g(\theta_i, \varphi)) \right) / p_{\mathcal{H}}$ $\mathcal{T}(\theta) = (\cos^{p_T} \theta + \cos^{p_T}(\pi/3 - \theta) + \cos^{p_T}(\pi/3 + \theta))^{1/p_T}$ $h_c(\varphi) = h(-\pi/6, \varphi) \quad w(\varphi) = g(-\pi/6, \varphi) / h_c(\varphi) \quad \hat{w} = 0.5\sqrt{3} / \mathcal{T}(-\pi/6)$

3. BACKGROUND

It is well-known that the hydration reactions of cement are exothermic, and hence that of the cemented soil that constitutes the jet-grouted mass at the beginning of its placement. Figure 1a, for instance, displays the temperature rise measured by Catharin (1978) in adiabatic tests for cement samples. Ulm & Coussy (1995) proposed the following law of Arrhenius type for the variation of the degree of hydration:

$$\dot{\xi} = \tilde{A}(\xi) \exp(-E_a / RT) \quad (1)$$

In Pilcher et al. (2003) it is showed how the equation of energy balance can be integrated in adiabatic

conditions to obtain, by means of a regression analysis based on Catharin's experiments, an expression for the chemical affinity \tilde{A} as a function of the degree of hydration, see Fig. 1b. Recently, they have been presented more complex models for Portland cements and blended cements involving four degrees of hydration, referring to each one of the main clinker phases, which, in particular, may produce curves with several cycles of heat generation, as they are observed in practice, see Meinhard & Lackner (2008) and the references therein.

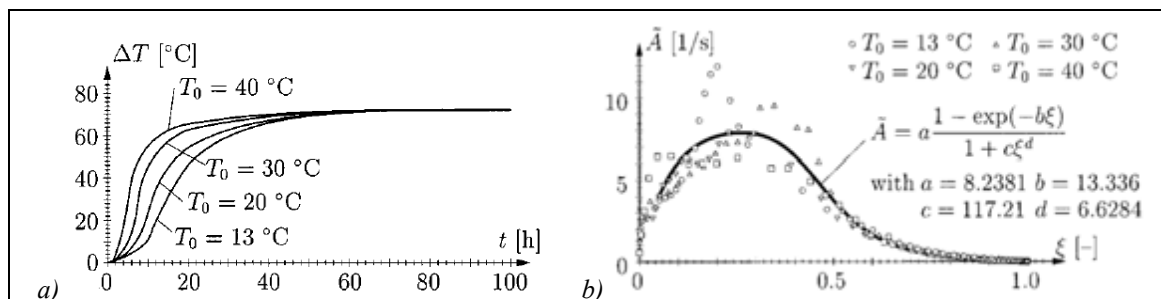


Figure 1: a) increment of temperature in adiabatic tests for cement CEM I 32.5 according to Catharin (1978); b) intrinsic chemical affinity for the same cement and affinity function obtained by regression as appears in Pichler et al. (2003)

A number of experimental results are also available with regards to the evolution of the strength and stiffness of the JGS as the hydration reaction takes place. Brandstätter et al. (2002) showed that the increase of Young's modulus and of the uniaxial compressive strength with the degree of hydration may be approximated by bilinear functions, see Figs. 2a and 2b. These results are particularly appropriated to be integrated within THMC coupled analysis, as they are presented in terms of intrinsic variables.

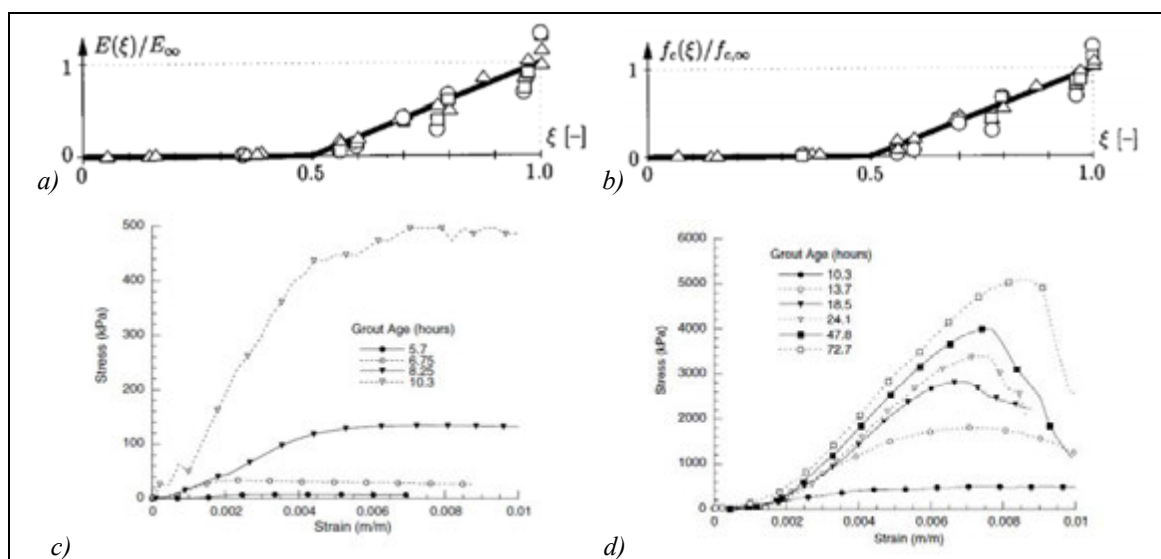


Figure 2: intrinsic material functions for a) Young's modulus and b) compressive strength of soil improved by means of cement grout (CEM I 32.5, water/cement ratio=1.0) according to Brandstätter et al. (2002); stress-strain curves recorded for unconfined compressive tests for grout at various times for c) less than 10.5 h and d) greater than 10.5 h according to Coulter & Martin (2006)

Coulter & Martin (2006) performed a series of laboratory tests to determine the Young modulus, compressive strength, tensile strength (Brazilian tests) and shear strength (vane tests) of a grout with a composition similar to that found in the construction of jet-grouting columns at different stages of the hydration process. Their results are presented as a function of time; in particular, they observed that 6 h are necessary to measure significant Young's modulus and strength values, and that the tensile strength development with time had a similar shape as the unconfined compressive strength development, being the average ratio of both magnitudes of 0.133. They also observed that approximately 10.5-11 h after the beginning of the hydration reactions the rates of strength, stiffness and temperature increase reach peak values; at this time the unconfined compressive strength tests show that the material behavior changes from plastic to brittle, see Figs. 2c and 2d.

After their placement, the effects of the presence of JGS on the surroundings is mainly associated to the release of hydration heat, which is transmitted through the soil by conduction and transported by advection due to the flux of water. In this respect, knowledge of the thermomechanical behavior of the SS is essential to carry out a THMC analysis of the interactions between JGS and SS. As it is claimed in Gens (2010), one of the most interesting observations concerning temperature effects on mechanical soil behavior was presented by Baldi et al. (1991). They applied cycles of heating and cooling to saturated Boom clay samples with different overconsolidation rates. They observed that, whereas the heavily overconsolidated samples dilated upon heating and contracted during cooling in an almost reversible way, the normally consolidated samples undergone very large compression strains on heating and additional smaller compression strains during cooling, see Fig. 3a. From these and other experimental results, it has been adopted the assumption that the size of the yield surface reduces with increasing temperature, see Fig. 3b, extracted from Uchaipichat & Khalili (2009).

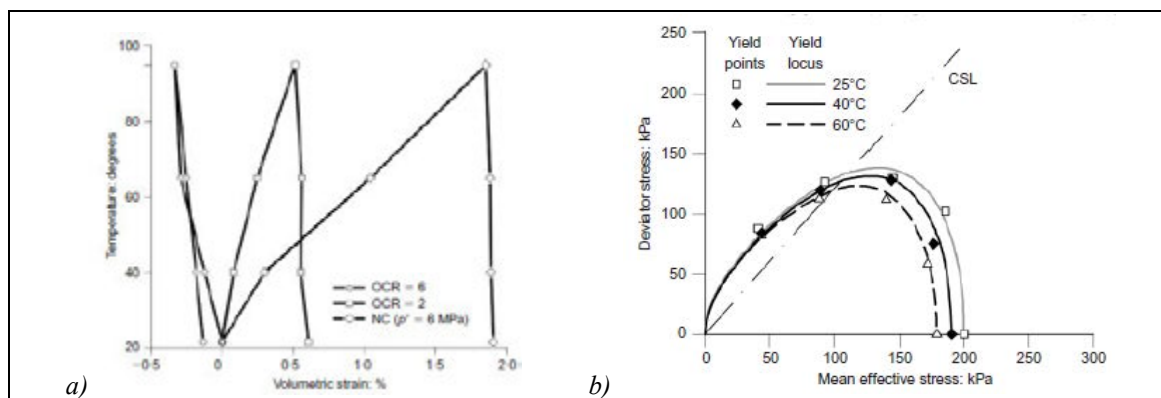


Figure 3: a) Variation of volumetric strain with temperature observed in heating-cooling tests on samples of saturated Boom clay with different overconsolidation ratios (OCRs) according to Baldi et al. (1991); b) Evolution of yield locus with temperature for null suction according to a study on Bourke silt reported by Uchaipichat & Khalili (2009)

4. MODELS FOR THE JET-GROUTED SOIL

In this Section 4 and in Section 5 we describe some basic models that have been developed to simulate the behavior of JGS at early ages and that of the SS within the framework of THMC analyses. For the JGS we will work in total stresses, as we treat the mixture soil-cement-water like a single phase referred to by means of the sub-index JGS. The models presented here fall within the framework of classical plasticity theory; phenomena like dislocation-like processes within the hydrates or microdiffusion of water in the capillary pores between the hydrates, which may appear in cement-based materials producing long-term or short-term creep strains -Pichler et al. (2003)-, are not considered at this stage of the analysis.

4.1. Stress increments

Within the elastic domain, we assume that the increment of stresses may be obtained from the expression $d\boldsymbol{\sigma} = \mathbf{D}_{el}(d\boldsymbol{\varepsilon} - d\boldsymbol{\varepsilon}^T - d\boldsymbol{\varepsilon}^{\xi})$, where the thermal strains and the shrinkage strains are given by $d\boldsymbol{\varepsilon}^T = \alpha_{JGS} dT$, $d\boldsymbol{\varepsilon}^{\xi} = \chi d\xi \mathbf{r} = \chi \dot{\xi} d\mathbf{t}$. On the other hand, the variation of the hardening parameters of the material is assumed to be controlled not only by the generation of plastic strains -plastic parameter ζ - but also directly by the degree of hydration, so the yield and potential functions read $F(\boldsymbol{\sigma}, \boldsymbol{\kappa}(\zeta, \xi))$ and $G(\boldsymbol{\sigma}, \boldsymbol{\eta}(\zeta, \xi))$, respectively. Hence, under plastic loading, the application of the consistency condition leads to the expression $d\boldsymbol{\sigma} = \mathbf{D}_{ep}(d\boldsymbol{\varepsilon} - d\boldsymbol{\varepsilon}^T - d\boldsymbol{\varepsilon}^{\xi}) - F_{\xi} \dot{\xi} d\mathbf{t}$ for the computation of the stress increments.

In general, all the constitutive parameters involved in the previous expressions may depend on the hydration ratio and other factors as for instance the cement content in the JGS, the water/cement ratio, etc.

4.2. Release of hydration heat

For the JGS, the equation of balance of energy is written as $c_{JGS} \rho_{JGS} \dot{T} - (\lambda_{JGS} T) = l_{\xi} \dot{\xi}$, where the latent heat of hydration may be assumed to be proportional to the product of the density of the JGS and

the % by weight of cement within the jet-grouted mass. Fig. 1b, extracted from Pilcher et al. (2003), display the results of a regression analysis based on Catharin's (1978) experiments; by taking as a reference the expression (1) for the rate of change of the degree of hydration, the following expression is proposed for the intrinsic chemical affinity:

$$\tilde{A}_0(\xi) = a \frac{1 - e^{-b\xi}}{1 + c\xi^d} \quad (2)$$

In spite that equation (2) adjusts reasonably well the experimental data, some of its features do not seem satisfactory, namely: $\tilde{A}_0(0) = 0, \tilde{A}_0(1) \neq 0$. The former equation implies that the rate of change of ξ (and hence the rate of change of the temperature in adiabatic conditions) is null at the beginning of the hydration process; the latter inequality implies that the rate of change of ξ is not null as time grows. Both facts seem to disagree with the experimental results obtained by Catharin, and result in some conceptual and numerical problems. An expression without such problems is given by:

$$\tilde{A}(\xi) = B\tilde{A}_0(\xi) + B_1 - [B_1 + \tilde{A}_0(1)B_2]\xi \quad (3)$$

Figure 4 displays the corrected affinity curve for $B_1 = 1, B_2 = 0.90625$ as well as a comparison between the results obtained by Catharin and those produced by equation (1) by using the affinity function (3).

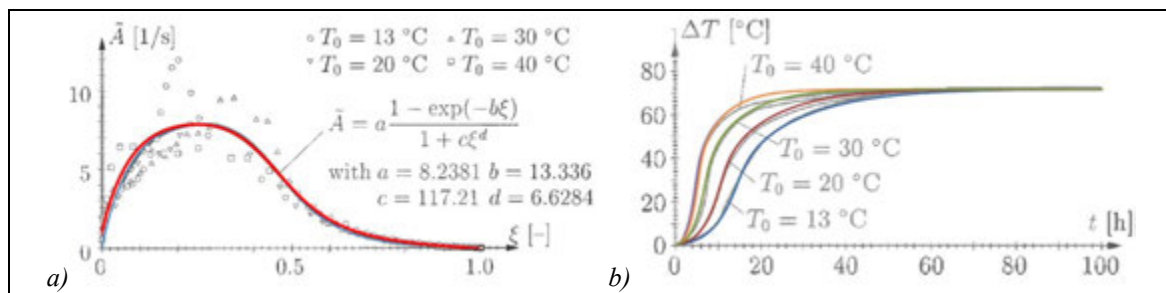


Figure 4: a) corrected intrinsic chemical affinity function for cement CEM I 32.5 (red); b) comparison between the results observed for this cement by Catharin (1978) and the curves obtained by combining equations 1-3

4.3. Elasticity

To describe the elastic behavior of the JGS we start by recalling Fig. 2a, extracted from Brandstätter *et al.* (2002). According to this figure, the Young modulus of the JGS varies with the degree of hydration approximately in the form $E/E_\infty = \max\{0, 2(\xi - 0.5)\}$, where E_∞ stands for the value of the Young modulus at the end of the hydration process (the sub-index ∞ will be used from now on to denote values of parameters at the end of the hydration process). We obtain a complete (isotropic) elastic model by using the following expressions:

$$E/E_\infty = \beta, \quad K/K_\infty = s, \quad \nu = (s - \beta[1 - 2\nu_\infty])/2s, \quad G/G_\infty = \beta(1 + \nu_\infty)/(1 + \nu), \quad (4)$$

The last two expressions may be readily obtained according to elasticity theory. On the other hand, it is easy to check that $s \geq 1 \rightarrow 0 \leq \nu \leq 0.5$.

An immediate choice for functions β, s consists in taking $\beta(\xi) = \max\{0, 2(\xi - 0.5)\}, s = 1$, in such a way that the results of Fig. 2a are reproduced by the model and it is assumed that the bulk modulus of the material does not depend on the hydration ratio. Nevertheless, it may be argued that, as the behavior of the grout at the beginning of the hydration process is basically that of a viscous fluid and it changes to be that of a brittle material, its bulk modulus could vary from an initial value K_0 to the final smaller value K_∞ . The introduction of function s in the formulation allows us to contemplate this possibility, which would need to be corroborated by experimental results. Finally, let us observe that the function β above has a corner at $\xi = 0.5$; although this fact does not represent a problem in this context, we may use the technique by Gesto *et al.* (2011,2012) to obtain a smoothed version of this function. Figures 5a and 5b, for instance, display the variation of ν, G with ξ according to the following expressions:

$$\beta(\xi) = \hat{b}(\xi, p_\beta, 0), \quad s = \frac{K_0}{K_\infty} + \left(1 - \frac{K_0}{K_\infty}\right) \hat{\beta}, \quad K_\infty \leq K_0, \quad \hat{\beta}(\xi) = \hat{b}(\xi, p_{\hat{\beta}}, 1) \quad (5)$$

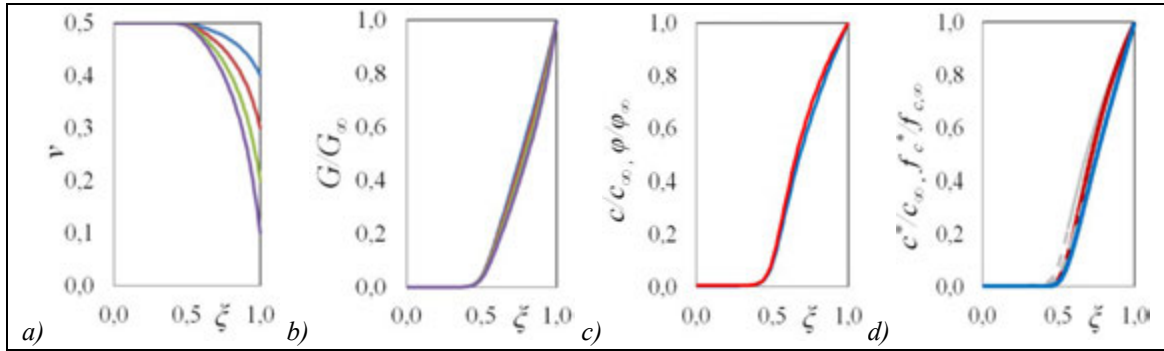


Figure 5: variation of a) Poisson's ratio and b) shear modulus with hydration ratio according to equations 4 and 5 in the case $K_0 / K_\infty = 3$ for $v_\infty = 0.1, 0.2, 0.3, 0.4$ with $b = 0, p_\beta = p_\beta = 15$; c) variation of c / c_∞ (blue) and φ / φ_∞ (red) with the hydration ratio according to model 6-8 with $c_\infty = 2\text{MPa}, \varphi_\infty = 35^\circ, d = 2 \cdot 10^{-3}, p_\delta = 15$; d) variation of the actual cohesion c^* (red) and the actual uniaxial compressive strength f_c^* (blue) according to the model described by equations 6-8 with the parameters used for c) and $r = 2 \cdot 10^{-3}, p_\rho = 15$

4.4. Plasticity

As a first approximation, we will assume Mohr-Coulomb perfect plasticity with null dilatancy for the JGS. Under these hypotheses, the application of the smoothing technique described in Gesto *et al.* (2011, 2012) leads to the following plasticity model:

$$\begin{cases} F(p, J, \theta, c(\xi), \varphi(\xi), \varepsilon(\xi)) = \ln(e^{f_1} + e^{f_2}) \\ G_{(\cdot)} = (g_1)_{(\cdot)} \hat{w}_1 + (g_2)_{(\cdot)} \hat{w}_2 + (g_3)_{(\cdot)} \hat{w}_3 \\ H = 0 \quad F_\xi = F_c c_\xi + F_\varphi \varphi_\xi + F_\varepsilon \varepsilon_\xi \end{cases} \quad (6)$$

Where $f_1 = (J\mathcal{H}\omega - p \sin \varphi - c \cos \varphi) / k_1$, $f_2 = -(J\mathcal{H}\omega + p \sin \varphi + c \cos \varphi) / k_1$, $g_1 = \mathcal{T}\hat{\omega}J / \hat{k}_1$, $g_2 = -\mathcal{T}\hat{\omega}J / \hat{k}_1$, $g_3 = -p / \hat{k}_3$, and $k_1 = \hat{k}_1 = \varepsilon c \cos \varphi / \ln 2$, $k_3 = k_1 / 5$, $\hat{k}_3 = k_1 / 2$, $\omega = \omega(\varphi_\infty)$, $\hat{w}_i = e^{f_i} / (e^{f_1} + e^{f_2} + e^{f_3})$, with $f_3 = -(p + (1 - \varepsilon)a) / k_3$.

As usual, φ stands for the internal friction angle. Parameter ε is an auxiliary variable that the employed smoothing technique introduces in the formulation and that allows us to control the tensile strength independently of the rest of the parameters. More precisely, the tensile strength is computed as $(1 - \varepsilon)c \cot \varphi$. Parameters c, f_c represent the cohesion and the unconfined compressive strength before the smoothing; after that, the actual cohesion –value of the tangential stress at the intersection of the yield surface with the axis $\sigma = 0$ in the plane σ, τ - and unconfined compression strength are denoted by c^*, f_c^* , and c, f_c become parameters without physical meaning.

To complete the model it is necessary to define the way the parameters c, φ, ε vary with the degree of hydration, which may be made according to multiple criteria. For instance, if we assume that

$$\frac{c \cos \varphi}{c_\infty \cos \varphi_\infty} = \frac{\sin \varphi}{\sin \varphi_\infty} = C, \text{ then we may propose}$$

$$\begin{cases} f_c / f_{c,\infty} = \delta \quad \delta(\xi) = b(\xi, p_\delta, d) \\ C = \frac{f_{c,\infty} \delta}{2c_\infty \cos \varphi_\infty + f_{c,\infty} \sin \varphi_\infty \delta} \quad \frac{c}{c_\infty} = \frac{C \cos \varphi_\infty}{\sqrt{1 - C^2 \sin^2 \varphi_\infty}} \quad \varphi = \sin^{-1}(C \sin(\varphi_\infty)) \\ \varepsilon = 1 - (1 - \varepsilon_\infty)\rho \quad \rho(\xi) = b(\xi, p_\rho, r) \\ \varphi_\xi = \varphi_c C_\delta \delta_\xi \quad c_\xi = c_c C_\delta \delta_\xi \quad \varepsilon_\xi = (\varepsilon_\infty - 1)\rho_\xi \end{cases} \quad (7)$$

It may be checked that with this approach it holds

$$c^* = \frac{\varepsilon c \omega}{\omega \ln 2} \cosh^{-1} \left(2^{\frac{1}{\varepsilon}-1} \right), \quad \frac{f_c^*}{\sqrt{3}} = \frac{\varepsilon c \cos \varphi}{h_c \omega \ln 2} \cosh^{-1} \left(2^{\frac{f_c^*+3a}{3\varepsilon a}-1} \right), \quad a = c \cot \varphi = c_\infty \cot \varphi_\infty \quad (8)$$

Figures 5c, 5d and 6 display some aspects of the described model, which admits many other variants. For the smoothing of the Mohr-Coulomb and Tresca functions in planes π , we have taken $p_H = 12, p_T = 8$

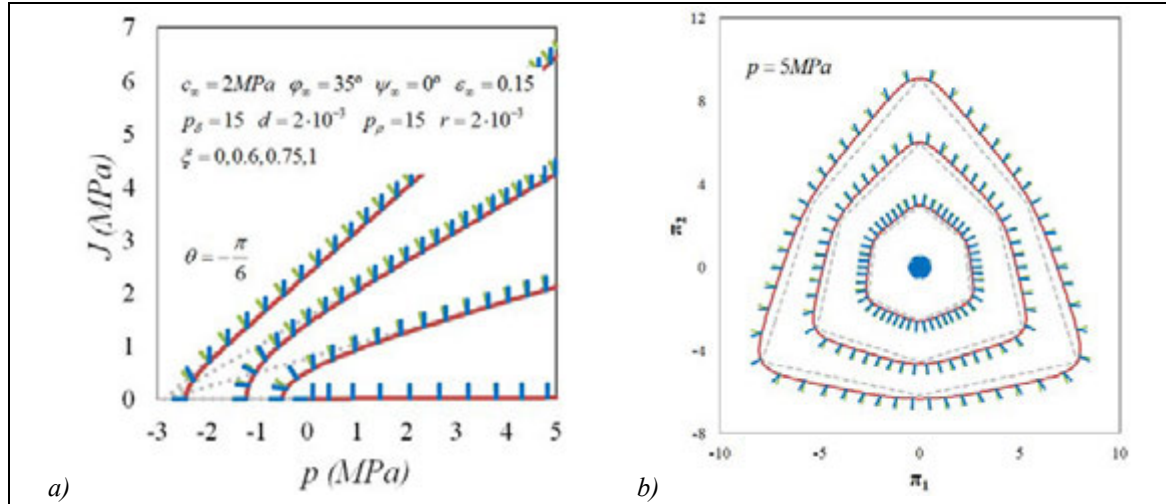


Figure 6: yield surfaces (red) and directions of \mathbf{n} (green) and \mathbf{m} (blue) according to the model described by equations 6-8 for different values of the hydration ratio a) in plane p, J for triaxial compression states and b) in a plane π_1, π_2

5. MODELS FOR THE SURROUNDING SOIL

For the SS we will work in effective stresses and assume saturated conditions, in such a way that Terzaghi's effective stress principle holds. As for the JGS, the models are developed in the context of classical plasticity theory.

5.1. Stress increments

The elastic increment of total stresses reads $d\boldsymbol{\sigma} = \mathbf{D}_{el} (d\boldsymbol{\varepsilon} - d\boldsymbol{\varepsilon}^T) + \mathbf{r} dp_w$, where $d\boldsymbol{\varepsilon}^T = \alpha_{SS} dT \mathbf{r}$. In this case, the role that the degree of hydration played for the JGS is now assumed by the temperature, in such a way that we may write $F(\boldsymbol{\sigma}, \boldsymbol{\kappa}(\zeta, T))$ and $G(\boldsymbol{\sigma}, \boldsymbol{\eta}(\zeta, T))$, and the consistency condition gives the equation $d\boldsymbol{\sigma} = \mathbf{D}_{ep} (d\boldsymbol{\varepsilon} - d\boldsymbol{\varepsilon}^T) - F_T dT \mathbf{d} + dp_w \mathbf{r}$ for the computation of the total stress increments. In general, all the constitutive parameters involved in the above expressions may depend on temperature.

5.2. Elasticity

For the elastic parameters of the SS we will take as a reference that the bulk modulus is proportional to the mean effective stress, as it is typically observed in unloading-reloading curves of triaxial tests. For the rest of the elastic parameters there are of course many possible choices. For instance, we may suppose the Poisson ratio to be constant -this could lead to non-conservative models, an irrelevant problem at this stage of the analysis-.

On the other hand, we will assume that the position of the yield locus is governed by a single volumetric hardening parameter p_0 which for elastic loading only varies if temperature does. The magnitude of the derivative of p_0 with respect to the temperature is taken proportional to p_0 , and the magnitude of this derivative for a certain reference value of the hardening parameter, Ψ_{ref} , is the basic coefficient that controls the thermal variation of the yield surface.

Summarizing the above considerations, we may propose the following basic elastic model:

$$\left\{ \begin{array}{l} K = \max\left(\frac{p}{(1-\phi)\kappa}, K_{\min}\right) \quad v = \text{constant} \quad G = \frac{3(1-2\nu)}{2(1+\nu)}K \quad E = 2G(1+\nu) \\ dp_0 = \frac{\partial p_0}{\partial T} dT \quad \frac{\partial p_0}{\partial T} = -p_0 \frac{\Psi_{ref}}{(p_0)_{ref}} \end{array} \right. \quad (9)$$

According to this formulation, the size of the yield locus reduces with increasing temperature and grows with decreasing temperature in a fully reversible way if no plastic strains are generated.

5.3. Plasticity

As a basic model for the SS we will take a volumetric hardening cap depending on parameter p_0 combined with a shear failure envelope of Mohr-Coulomb type by means of the same smoothing technique mentioned in previous Sections. The Mohr-Coulomb failure surface cut the part of the cap corresponding to highly overconsolidated states. The non-thermal variation of the hardening parameter will depend on the part of the volumetric plastic strains associated to movements of the cap according to the usual volumetric hardening law. A general formulation of such a model may be

$$\left\{ \begin{array}{l} F(p, J, \theta, c, \varphi, p_0(\zeta, T)) = \ln(e^{f_1} + e^{f_2} + e^{f_3}) \\ G_{(\square)} = (g_1)_{(\square)} \hat{w}_1 + (g_2)_{(\square)} \hat{w}_2 + (g_3)_{(\square)} \hat{w}_3 + (g_4)_{(\square)} \hat{w}_4 \\ \frac{\partial p_0}{\partial (\varepsilon_v^p)_3} = \frac{p_0}{(1-\phi)(\Lambda-\kappa)} \quad \frac{\partial p_0}{\partial \zeta} = \frac{w_3 (g_3)_p p_0}{(1-\phi)(\Lambda-\kappa)} \quad H = -w_3 \frac{\partial f_3}{\partial p_0} \frac{\partial p_0}{\partial \zeta} \\ dp_0 = \frac{\partial p_0}{\partial \zeta} d\zeta + \frac{\partial p_0}{\partial T} dT \quad \frac{\partial p_0}{\partial T} = -p_0 \frac{\Psi_{ref}}{(p_0)_{ref}} \quad F_T = \frac{\partial F}{\partial p_0} \frac{\partial p_0}{\partial T} \end{array} \right. \quad (10)$$

For an associated modified Cam-Clay cap with a Mohr-Coulomb dependency on Lode's angle, and assuming that the dilatancy is null on the failure Mohr-Coulomb surface, we may choose the functions

$f_1 = (J\mathcal{H}\omega - p \sin \varphi - c \cos \varphi) / k_1$, $f_2 = -(J\mathcal{H}\omega + p \sin \varphi + c \cos \varphi) / k_1$, the modified Cam-Clay cap

function $f_3 = (3(\mathcal{H}J)^2 - (h_c M)^2 (\mu a + p)(p_0 - p)) / k_3^2$ and $g_1 = \mathcal{T}\hat{\omega}J / \hat{k}_1$, $g_2 = -\mathcal{T}\hat{\omega}J / \hat{k}_1$,

$g_3 = (3(\mathcal{H}J)^2 - (h_c \hat{M})^2 (\mu a + p)(p_0 - p)) / \hat{k}_3^2$, $g_4 = -p / \hat{k}_4$, where $k_1 = k_4 = \hat{k}_1 = \varepsilon c \cos \varphi / \ln 2$,

$k_3 = \hat{k}_3 = \eta(p_0 + \mu a)$, $\hat{k}_4 = 5k_4 / 2$, $\omega = w(\varphi)$, $a = c \cot \varphi$, $M = \hat{M} = 6 \sin \varphi / (3 - \sin \varphi)$,

$w_i = e^{f_i} / (e^{f_1} + e^{f_2} + e^{f_3})$ and $\hat{w}_i = e^{f_i} / (e^{f_1} + e^{f_2} + e^{f_3} + e^{f_4})$, with $f_4 = -(p + (1 - \varepsilon)a) / k_4$.

Figure 7 shows the shape of the yield surface and the direction of the plastic vectors for planes containing the hydrostatic axis and perpendicular to it and for the following set of parameters $c = 25 \text{ kPa}$, $\varphi = 30^\circ$, $\psi_{shear} = 0^\circ$, $\psi_{cap} = \varphi$, $\varepsilon = 0.2$, $\eta = 0.15$, $\mu = 1.3$, $p_0 = 100 \text{ kPa}$.

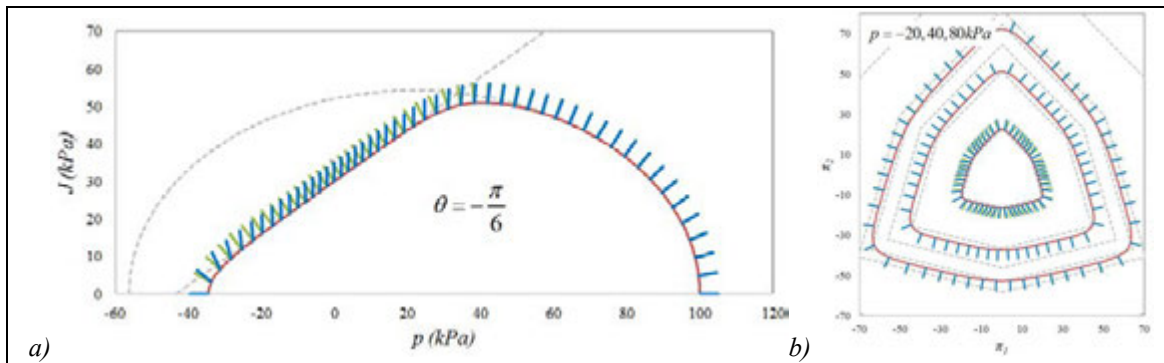


Figure 7: yield surfaces and directions of \mathbf{n} (green) and \mathbf{m} (blue) according to the model described by equations 10 for $p_0 = 100 \text{ kPa}$ a) in plane p, J for triaxial compression states and b) in planes π_1, π_2 for different values of the mean stress

Figure 8 displays the performance of the above model under the loading-unloading and heating-cooling paths imposed for the thermomechanical experiments of Baldi *et al.* (1991) whose results are depicted in Fig. 3a. The parameter set was: $\Lambda = 6.42 \cdot 10^{-2}$, $\kappa = 1.28 \cdot 10^{-2}$, $\nu = 0.3$, $K_{\min} = 5 \text{ MPa}$, $\alpha_{SS} = -10^{-5} \text{ K}^{-1}$, $\Psi_{ref} = 1.3 \text{ kPa} / \text{K}$, $(p_0)_{ref} = 200 \text{ kPa}$. As it may be observed, the behavior of the normally consolidated and highly overconsolidated samples is well reproduced by the proposed thermoplastic cap mechanism. Nevertheless, in the context of classical plasticity, one finds that the first phase of cooling for the slightly overconsolidated sample implies dilatation, as elastic thermal strains take place, which does not agree with the observations. In any case, to our purpose of understanding the main mechanisms related to the THMC interactions between JGS and SS, the proposed approach seems to maintain a reasonable equilibrium between simplicity and predictive capacity.

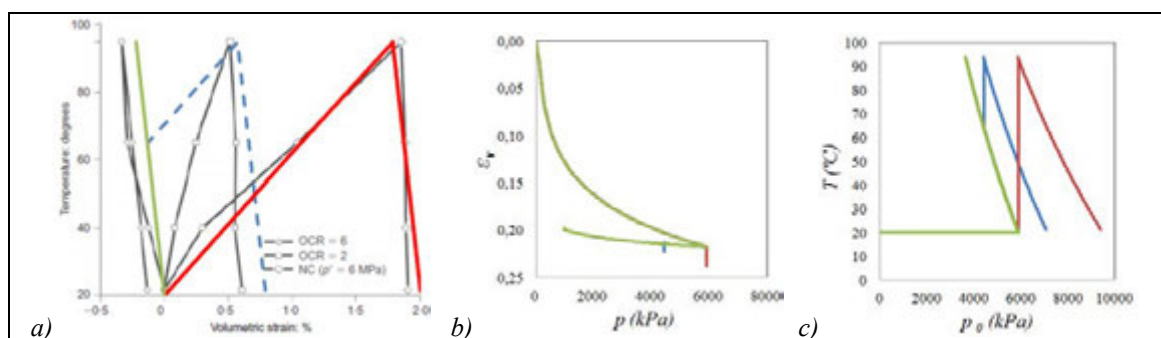


Figure 8: a) comparison between the results observed by Baldi *et al.* (1991) and the model described by equations 9 and 10 – the blue dashed curve correspond to $OCR = 1.3$ and not to $OCR = 2$ -; the same paths are represented in planes b) p, ε_v and c) p_0, T

6. CONCLUDING REMARKS

We have presented some basic models designed to simulate the behavior of JGS and SS at early ages of the cement added to the soil. In this stage of the application of the treatment, the release of heat due to the hydration reactions that take place within the jet-grouted mass is strongly linked to the evolution of the strength and stiffness properties of the JGS and may induce deformations and changes in the hydraulic conditions of the SS. The presented models fall within the framework of plasticity for saturated soils, and we have shown how they are able to reproduce many of the main features highlighted by the available experimental results. In spite of the intricate appearance of the formulation of the models, they have been obtained by combining simple and well-known constitutive models by following systematic algebraic procedures to obtain smooth functions.

The proposed models admit a great number of variants and improvements which will be described in further publications. The developed models have been implemented within a FEM program based on CODE_BRIGHT, a code developed in the Department of Geotechnical Engineering of the UPC for the modelization and analysis of complex thermo-hydro-mechanical interactions in geotechnical problems. This FEM program is being used to study the interactions JGS-SS in a fully coupled THMC context. For more details on the formulation of this kind of coupled problems, see for instance Olivella *et al.* (1994) and Gens (2010).

7. ACKNOWLEDGEMENTS

This work was supported by the Ministry of Science and Innovation of Spain through grant BIA2008-06537.

REFERENCES

Baldi, G., Hueckel, T., Peano, A. & Pellegrini, R., 1991, *Developments in modeling of thermo-hydro-geomechanical behaviour of Boom clay and clay-based buffer materials*, Report 13365/2 EN., Luxembourg: Publications of the European Communities.

Brandstätter, C., Lackner, R. & Mang, A., 2002, *Bestimmung von Materialeigenschaften zementgebundener Werkstoffe mittels Temperaturmessungen: Anwendung in Rahmen des Düsenstrahlverfahrens (Evaluation of properties of cementitious materials by means of temperature measurements: Application to jet grouting)*, *Bauingenieur*, 77, N° 2, 51-57.

Brandstätter, C., Lackner, R. & Mang, A., 2005, *In situ temperature measurements provide new insight into the performance of jet grouting*, *Ground Improvement*, 9, N° 6, 163-167, Thomas Telford Ltd.

Catharin, P., 1978, *Hydratationswärme und festigkeitsentwicklung (Hydration heat and strength evolution)*, *Forschungsinstitut des Vereins der österreichischen Zementfabrikanten, Vienna, Technical Rep. 31.*

Coulter, S. & Martin, C.D., 2006, *Single fluid jet-grout strength and deformation properties*, *Technical note, Tunnelling and Underground Space Technology*, 21, 690-695.

Gens, A., 2010, *Soil-environment interactions in geotechnical engineering*, *Géotechnique*, 60, N°1, 3-74.

Gesto, J.M., Gens, A & Vaunat, J., 2011, *Smoothing of yield surfaces and a reformulation of multi-surface plasticity*, *XI International Conference on Computational Plasticity. Fundamentals and Applications, COMPLAS XI*, E. Oñate, D.R.J. Owen, D. Peric and B. Suárez (Eds).

Gesto, J.M., Gens, A & Vaunat, J., 2012, *A smoothing technique with applications in Plasticity, in preparation.*

Meinhard, K & Lackner, R., 2008, *Multi-phase hydration model for prediction of hydration-heat release of blended cements*, *Cement and Concrete Research*, 38, 794-802.

Olivella, S., Carrera, J., Gens, A. & Alonso, E., 1994, *Non-isothermal multiphase flow of brine and gas through saline media*, *Transp. Porous Media*, 15, N° 3, 271-293.

Pichler, Ch., Lackner, R & Spira, Y., 2003, *Thermochemomechanical Assessment of Ground Improvement by Jet Grouting in Tunneling*, *J. Eng. Mech.*, 129, N° 8, 951-962, ASCE.

Uchaipichat, A. & Khalili, N., 2009, *Experimental investigation of thermo-hydro-mechanical behaviour of an unsaturated silt*, *Géotechnique*, 59, N° 4, 339-353.

Ulm, F. & Coussy, O., 1995, *Modelling of thermochemomechanical couplings of concrete at early ages*, *J. Eng. Mech.*, 121, N° 7, 785-794, ASCE.

Laboratory investigations on groutability of the alluvial used in ground improvement for construction metro tunnels

M. Gharouni Nik, *Iran University of Science and Technology (IUST), Iran, gharouni@doctor.com*
M. Esmaeili, *Iran University of Science and Technology (IUST), Iran, m_esmaeili@iust.ac.ir*
H. Hosseinpour, *Iran University of Science and Technology, (IUST), Iran, hoseinpour@hotmail.com*

ABSTRACT

One of the methods for improving the ground for excavation underground spaces is grouting in order to minimize permeability and increase strength of loose materials at the time of construction. This ground improvement enables people to excavate tunnels and underground spaces in safe environment. Considering the increase in constructing subway lines and underground spaces in Iran and the necessity of passing through loose formations, it is essential to study the groutability of alluvial soils which compose the main part of urban regions.

In the present paper, Laboratory investigation has been conducted on several soil mixtures, distribution of which is in accordance with Tehran alluvial as hosting material of many parts of Tehran metro. Cylindrical specimens of these materials with different percentages of compaction were prepared. Grouting with different ratio of w/c and various pressures were applied on these specimens which were encapsulated in a glassy cell. Therefore, groutability of the material is traced clearly during grouting procedure. Finally, a numerical criterion for groutability of Tehran alluvial has been presented using the results of the experiments.

1. INTRODUCTION

One of the challenges of tunnel excavation in urban areas is the weak geological conditions and high level of underground water. At the same time, controlling soil settlement for minimizing the movement of neighboring buildings and installations is considered as an important aspect for designing and constructing urban tunnels and underground spaces. During the construction, underground water flows are one of the biggest challenges for the successful completion of tunneling projects. Failures endanger safety, results in difficulties in excavation and tunnel support, sensitivity of surrounding residents to the impact, settlement of ground surface and increase of costs. An appropriate grouting program before drilling can be beneficial for the contractor and owner through decreasing risk likelihood and controlling project costs and delays [1].

The problem of groutability of granular soils (N) has been investigated for some years. First, the solutions were developed only based on the grain size of soil and cement (Burwell 1958, Bell 1993, Incecik and Ceren 1995) while the large-scale experiments showed that an exact solution for predicting the N of granular soils is in direct relationship with different parameters of soil and grout (Kutrner 1996, Akbulut 1999) [2], [3].

Depending on the effects of different parameters of soil, it is a complicated issue to exactly predict grout-taking in granular soils. It is well known that these parameters include grain size of soil and cement-based grout, relative density and fine-grained content of soils, water-to-cement ratio of the grout and grout pressure, which directly affect the grout -taking of soil media. However, relative density, contents of fine-grained soil, water-to-cement ratio and grout pressure are rarely considered in predicting grout -taking [2], [3].

By studying the effects of these parameters on grout -taking, an empirical relation was introduced (Akbulut and Saglamer 2002) for estimating grout -taking of granular soils which was confirmed by the experimental results obtained from the sand grout-taken samples with different densities [2], [3].

The aim of this study was to investigate the soil's groutability in Tehran C Alluvium considering the initial parameters such as pressure, cement-to-water ratio, grain size and percent of soil compaction and to extract a relation for predicting the groutability and increasing resistance. The study was undertaken by compressing the soils with determined grain size in transparent cylindrical cells and grouting with different water-to-cement ratios at various pressures [4].

2. REVIEWING AVAILABLE RELATIONS FOR DETERMINING GROUTABILITY RATIO IN GROUTING GRANULAR SOILS [5]

It is very difficult to estimate soil groutability in grouting performance and many parameters should be evaluated for determining it. Soil groutability has been studied for a long time and some fundamental relations have been presented between the grain size of soils and suspended particles in the grout admixtures. Cambefort believed that the permeability domain of grouted materials is limited by the aggregation of that soil in a soil sample. In his following studies, he presented a criterion based on the size of void spaces between soil particles which were filled by the cement particles. Hendron and Lenahan determined that the amount of permeability of grouted materials was limited by the soil aggregation. According to this study, if more than 10% of particle sizes of a soil passed through a 200 mesh sieve, that soil is not grout able. Akbulut and Saglamer believed that the groutability ratio essentially depends on the aggregation of soil and particles of the grout admixture and the groutability ratio can be increased by the particle size of grouting material for any kind of soil with different aggregation.

3. EXPERIMENTS [4]

3.1. Introduction

In order to perform the experiments, first, four different soil aggregation types were prepared which indicated all the properties of the soils within the aggregation of Tehran C Alluvium. Compressive strength of the soil samples was achieved by compacting it inside the transparent cylindrical cells with two compaction percents of 50% and 70%. Moreover, to investigate the effect of pressure increase on the grout operation and grout-taking rate, the pressures were used 2, 4 and 6 times during the performance. Another parameter investigated during the experiments was the water-to-cement ratio (w/c) of the cement grout which was entered into the sampling with two amounts of 1 and 2. In Table (1), the general plan of preparing the samples related to each soil aggregation is given.

Table 1: The plan of preparing cylindrical samples from each aggregation

	S1	S2	S3	S4	S5	S6	S7	S8	S9	S10	S11	S12
R %	70	70	70	70	70	70	50	50	50	50	50	50
P (bar)	2	4	6	2	4	6	2	4	6	2	4	6
w/c	1	1	1	2	2	2	1	1	1	2	2	2

3.2. Soil Characteristics

The soil used in the experiments was made based on the aggregation diagrams obtained from Tehran C Alluvium at different points considering a specific aggregation area for making the desired soil. As can be observed in Figure (1), all the aggregation diagrams were placed at a specific area which ranged from extremely fine-grained to coarse-grained soil diagrams. Since the diagrams on the left were extremely fine-grained, the aggregation area was divided into two parts and the right side area was covered by four aggregation diagrams (Figure (1)). Because of the small dimensions and limited diameter of the cell, all the soils were passed through the 3/8 mesh sieve in order to get the maximum aggregation size of about 10 mm. Therefore, in the aggregation diagram, the soils with the aggregation numbers of 2, 3 and 4 at the point equivalent to the diameter of 3/8 percent of mesh sieve had 100% passing rate and corresponded to each other. Table (2) presents the properties of soils applied in this experiment.

3.3. Cement

Portland II cement was selected to be applied in these experiments and its aggregation diagram is given using the hydrometric experiment (Figure (2)). Considering this diagram, the d_{90} of the applied cement was equivalent to 0.039mm.

3.4. Experimental Equipment

The experimental equipment included a transparent cylindrical cell, in which the soil was compacted, metal caps with rubber gaskets for sealing and a pressure gauge. Moreover, the input and output required for doing the grouting performance and permeability experiments were embedded on the caps.

Compressed pumping of the cement grout was done using a manual grouting pump (grouting bin). In Figure (3), the construction and grouting equipment of the samples is demonstrated.

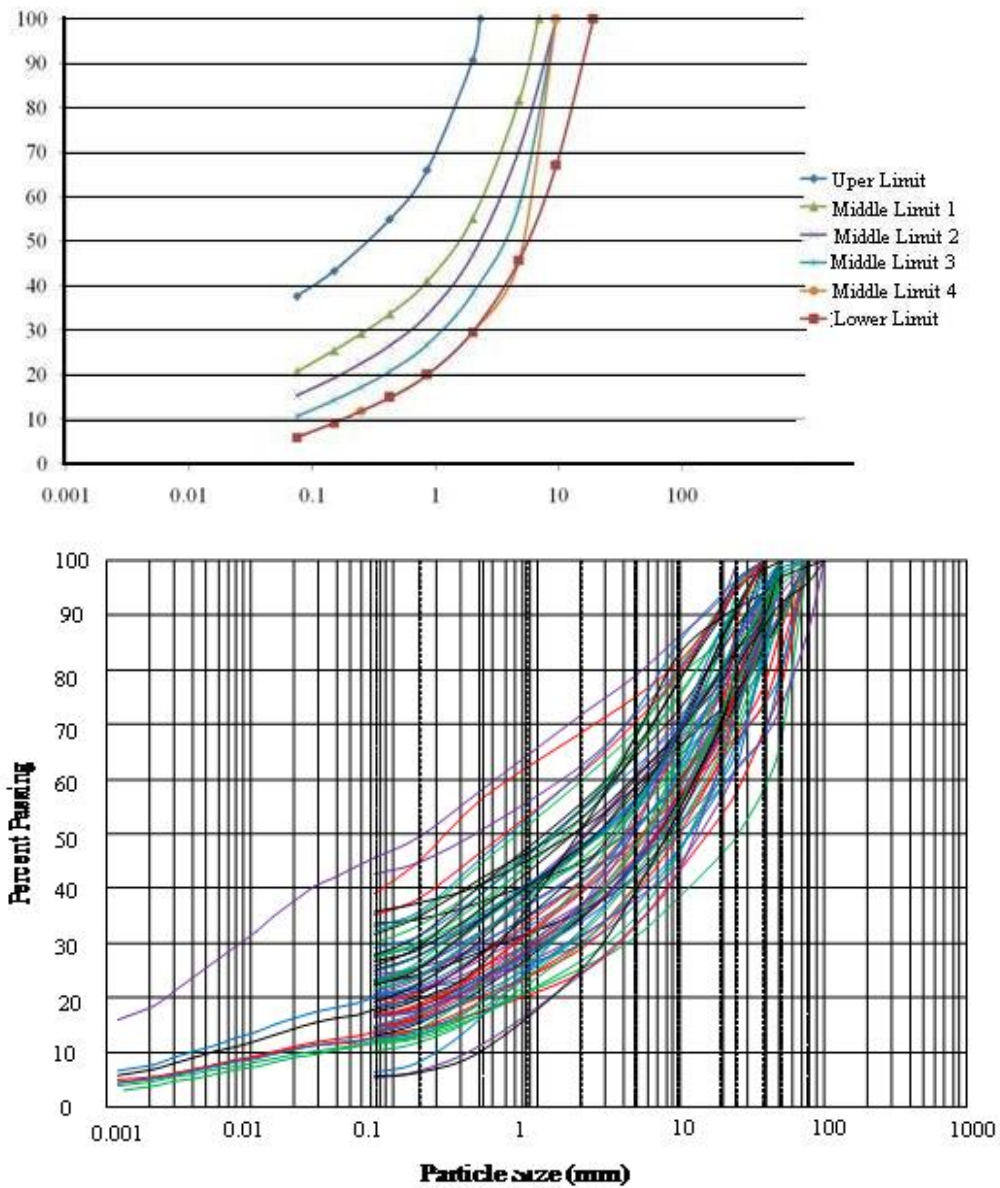


Figure 1: Aggregation of the soils used in the experiments

Table 2: The properties of the soils used in the experiments

Soil Sample	γ_{dmax} (ton/m ³)	LL	PL	PI	Cc	Cu	Soil
1	1.89	35.81	21.55	14.26	3.57	204	SC
2	1.91	36.7	23.41	13.29	2.69	74.88	SC
3	1.95	34.86	20.89	13.97	2.4	48.56	SW-SC
4	1.96	45.63	22.65	22.98	2.27	37.66	GW-GC

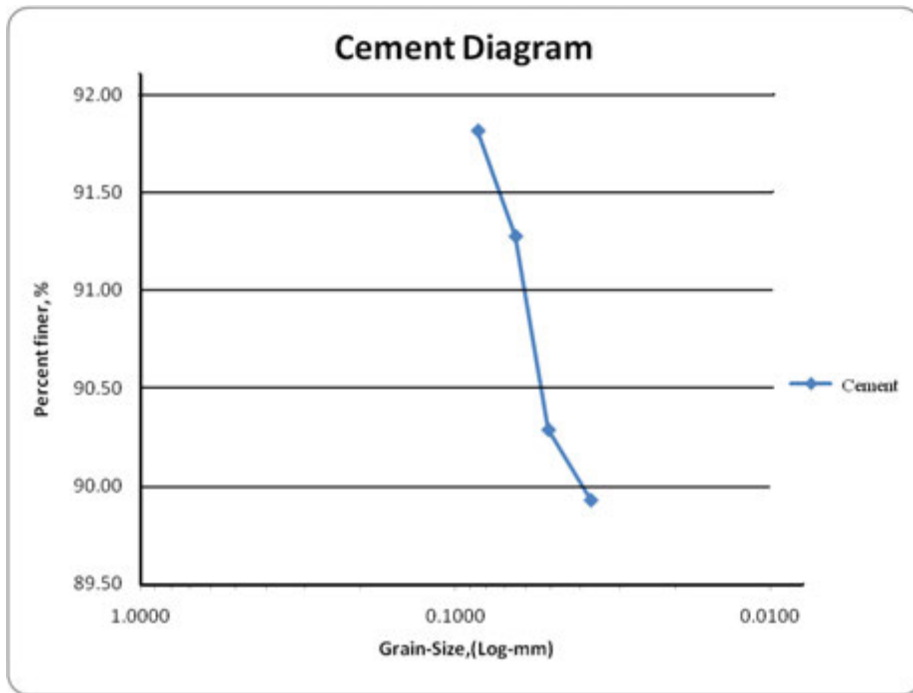


Figure 2: Aggregation diagram of the used cement

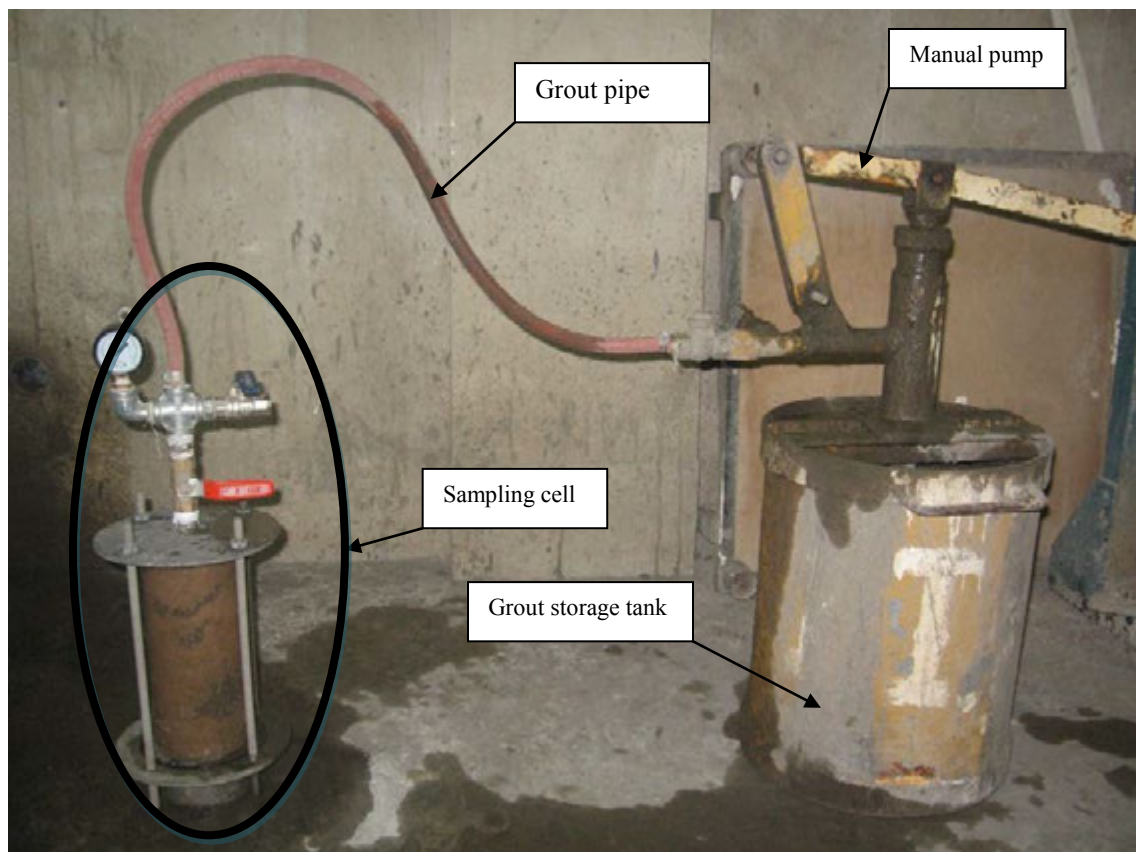


Figure 3: General view of the grouting and sampling equipment

3.5. Preparing Soil Samples

In order to prepare the cylindrical samples, the soil was uniformly placed into the transparent cell and was compacted in layers in order to reach the desirable compaction percent. After soil compaction, the weight of soil inside the cell was measured using the difference between the soil weight before and after grouting in order to measure compaction percent and obtain the grout-taking rate of the soil.

The diameter of the cells was 10 cm and their height was 25 cm; the first 5 cm of the sample was cut after the grouting performance and taking the sample out of the cell (while conducting the capping performance). This was done in order to remove non-uniformities in the upper part of the sample which were caused by the grouting performance and to create the proportion of 2 to 1 between the samples' height and diameter.

3.6. Grout

According to Table 1, two kinds of cement grouts with the water-to-cement ratio of 1 and 2 with no additives were used for grouting the samples in order to investigate the effect of increasing the amount of water on the grout-taking amount of the samples.

3.7. Experimental Programme

As mentioned in the beginning of the section, sampling was conducted for each soil with specified aggregation. Three cylindrical samples of soil were prepared each time and the grouting was performed according to the program with different water-to-cement ratios and pressures. Twelve cylindrical samples were made from each soil so that, first, the samples with 70% compaction were prepared and grouted at 3 different pressures of 2, 4 and 6 bars with the water-to-cement ratio of 1. Then, the samples with 70% compaction with the same pressure of 3 and with the different water-to-cement ratio of 2 were grouted. Then, the samples with 50% compaction were prepared and grouted at different pressures with the water-to-cement ratios of 1 and 2.

According to the instructions presented for the grout pressure in Section 2 and the requirement of lower grout pressure in the soil compared with the rock, the maximum pressure applied in these experiments was considered equal to 6 bar and it was observed that the grout pressure of 4 bar was sufficient for conducting a successful grouting in most of the conducted samplings. In cases in which the result of the performance was recorded as inadequate or unsuccessful despite the increase in the grout pressure, the grout pressure did not exceed 6 bar due to the constraints of the system for bearing the pressure; in one of the first cases of the sampling performance, increase in the pressure to 10 bar led to the burst of the transparent sampling cell and stop of the grouting performance.

3.8. Data Recording

After discharging the grouted soil from the cells, the weight of the grouted sample was measured using the weight difference of the soil sample before and after grouting in order to obtain the grout-taking rate of the soil. Also, the visual observations of the results of the grouting performance were recorded using three titles of successful, inadequate and unsuccessful (Figure (4)). Based on these results, a relation is presented in the following section in order to predict the results of the grouting performance based on the parameters before the grouting such as pressure, compaction percent, fine-grained content of soil, water-to-cement ratio and so on. Table (3) demonstrates the characteristics of the prepared samples along with the results of the grouting performance.



Figure 4: The schematics of grouting results of the three samples: successful, inadequate, and unsuccessful

4. INTERPRETATION OF RESULTS [4]

The grout-taking rate of each soil sample was obtained using the weight difference of the sample before and after grouting and its numerical values are given in Section 4. One of the most important parameters which affected the grout-taking rate of the soil was the grout pressure; according to the results, the grout-taking rate of the soil increased with the increase in the grout pressure P (Figure (5)).

In this figure, the grout-taking average equivalent to the applied compaction was separately drawn for the samples with the compaction percent of 50 and 70 against the pressure. The results of the grouting of samples with 70% compaction were mainly recorded as inadequate and unsuccessful, based on which the slope of the curve was more in the diagram fitted to these points, meaning that the samples were not saturated completely and it was possible for the samples to take more grout with the increase in the grout pressure. On the other hand, the slope of the curve fitted to the points with the compaction of 50% was less, which was the result of their mainly successful grouting; this showed more saturation of the limited area of the sample and lack of grout-taking as a result of increase in grout pressure.

Furthermore, another important parameter which affected the grout-taking rate of soil and, consequently, the result of the grouting performance was the compaction percent of the soil; the experimental observations while doing the tests showed this parameters as the most effective factor for the results of the grouting performance and, as mentioned in the previous paragraph, the grouting results of most samples with 50% pressure was recorded as successful.

Figure (6) indicates that the grout-taking rate of the soil decreased considerably with the increase in the compaction rate of the soil.

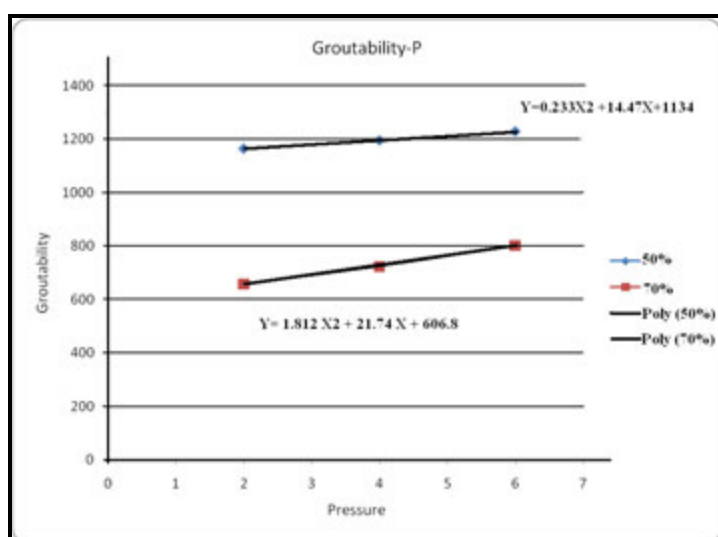


Figure 5: Changes of grout-taking rate against the increasing pressure

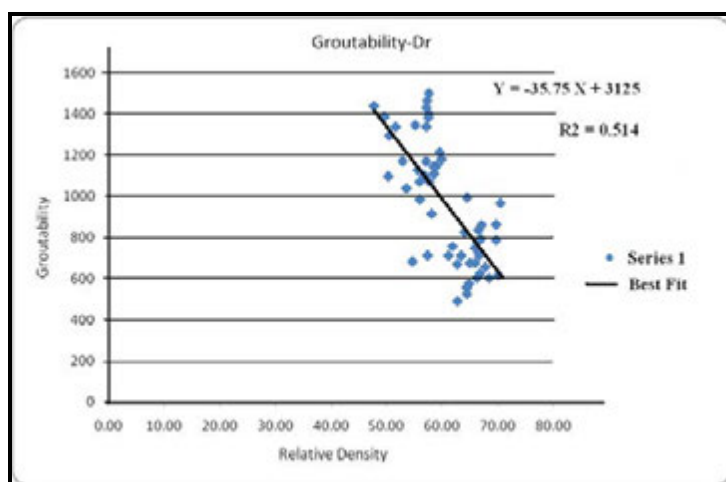


Figure 6: Changes of soil grout-taking against the compaction percent of soil samples

Table 3: Characteristics of the constructed samples along with the results of the experiments

Sample Name	R%	Grout Pressure (bar)	w/c	Grout Result	FC%	D10(Soil)	D90 (grout)	Grout Take (gr)	Ultimate Strength (kg/cm ²)
S 1-1	70	2	1	Inadequate	39.57	0.010	0.039	710	1.23
S1-2	70	4	1	Unsuccessful	39.57	0.010	0.039	755	0.14
S1-3	70	6	1	Unsuccessful	39.57	0.010	0.039	655	1.70
S1-4	70	2	2	Inadequate	39.57	0.010	0.039	792	0.23
S1-5	70	4	2	Successful	39.57	0.010	0.039	914	0.35
S1-6	70	6	2	Successful	39.57	0.010	0.039	994	0.40
S1-7	50	2	1	Inadequate	39.57	0.010	0.039	1097	1.10
S1-8	50	4	1	Unsuccessful	39.57	0.010	0.039	682	1.19
S1-9	50	6	1	Unsuccessful	39.57	0.010	0.039	711	1.35
S1-10	50	2	2	Successful	39.57	0.010	0.039	1295	1.41
S1-11	50	4	2	Inadequate	39.57	0.010	0.039	1400	0.36
S1-11*	50	4	2	Successful	39.57	0.010	0.039	1387	0.61
S1-12	50	6	2	Successful	39.57	0.010	0.039	1438	0.81
S2-1	70	2	1	Successful	29.86	0.043	0.039	674	1.54
S2-2	70	4	1	Successful	29.86	0.043	0.039	720	2.02
S2-3	70	6	1	Successful	29.86	0.043	0.039	786	1.21
S2-4	70	2	2	Inadequate	29.86	0.043	0.039	782	0.13
S2-5	70	4	2	Successful	29.86	0.043	0.039	862	1.32
S2-6	70	6	2	Successful	29.86	0.043	0.039	967	0.26
S2-7	50	2	1	Successful	29.86	0.043	0.039	1148	0.65
S2-8	50	4	1	Successful	29.86	0.043	0.039	1215	0.49
S2-9	50	6	1	Successful	29.86	0.043	0.039	1180	0.56
S2-10	50	2	2	Successful	29.86	0.043	0.039	1038	0.35
S2-11	50	4	2	Successful	29.86	0.043	0.039	1339	0.56
S2-12	50	6	2	Successful	29.86	0.043	0.039	1383	0.65
S2-2P	70	4	1	Successful	29.86	0.043	0.039	674	-
S2-9P	50	6	1	Successful	29.86	0.043	0.039	1170	-
S3-1	70	2	1	Unsuccessful	24.03	0.090	0.039	525	1.21
S3-2	70	4	1	Unsuccessful	24.03	0.090	0.039	601	0.95
S3-3	70	6	1	Inadequate	24.03	0.090	0.039	711	1.71
S3-4	70	2	2	Inadequate	24.03	0.090	0.039	748	0.33
S3-5	70	4	2	Inadequate	24.03	0.090	0.039	837	0.36
S3-6	70	6	2	Successful	24.03	0.090	0.039	860	2.04
S3-7	50	2	1	Successful	24.03	0.090	0.039	1070	1.11
S3-8	50	4	1	Successful	24.03	0.090	0.039	1101	0.46
S3-9	50	6	1	Inadequate	24.03	0.090	0.039	1146	0.69
S3-10	50	2	2	Successful	24.03	0.090	0.039	1345	0.51
S3-11	50	4	2	Successful	24.03	0.090	0.039	1465	0.76
S3-12	50	6	2	Successful	24.03	0.090	0.039	1500	0.89
S3-1P	70	2	1	Unsuccessful	24.03	0.090	0.039	616	-
S3-2P	70	4	1	Successful	24.03	0.090	0.039	601	-
S3-8P	50	4	1	Successful	24.03	0.090	0.039	1128	-
S4-1	70	2	1	Unsuccessful	17.16	0.201	0.039	489	0.49
S4-2	70	4	1	Unsuccessful	17.16	0.201	0.039	555	0.68
S4-3	70	6	1	Unsuccessful	17.16	0.201	0.039	623	1.22
S4-4	70	2	2	Inadequate	17.16	0.201	0.039	668	0.28
S4-5	70	4	2	Inadequate	17.16	0.201	0.039	710	0.84
S4-6	70	6	2	Inadequate	17.16	0.201	0.039	825	0.91
S4-7	50	2	1	Successful	17.16	0.201	0.039	984	0.86
S4-8	50	4	1	Successful	17.16	0.201	0.039	1070	1.08
S4-9	50	6	1	Inadequate	17.16	0.201	0.039	1108	1.37
S4-10	50	2	2	Successful	17.16	0.201	0.039	1337	0.52
S4-11	50	4	2	Successful	17.16	0.201	0.039	1171	0.35
S4-12	50	6	2	Successful	17.16	0.201	0.039	1431	0.71
S4-1P	70	2	1	Unsuccessful	17.16	0.201	0.039	573	-

Also in these experiments, the changes of water-to-cement ratio on the grout-taking rate of the soil cylindrical samples were investigated. To this end, two grouts with the water-to-cement ratios of 1 and 2 were used. In Figure (7), the average of grout-taking is drawn as equivalent to the two water-to-cement ratios against the water-to-cement ratio; as a result of the increase in this ratio, the groutability of the soil samples increased.

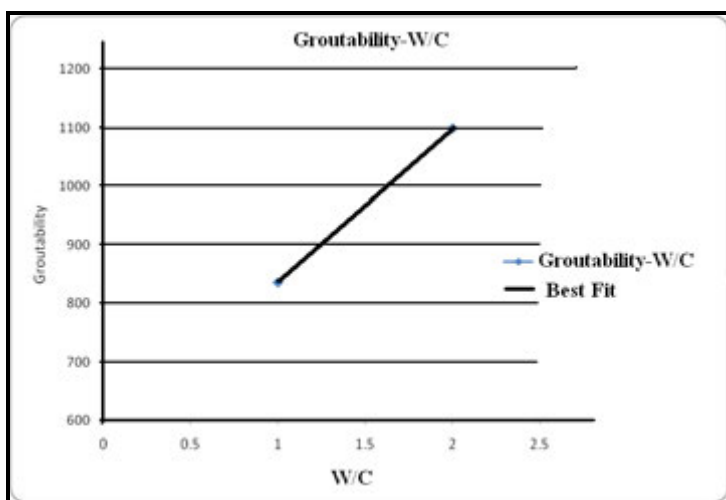


Figure 7: The effect of changes of water-to-cement ratio on the groutability

4.1. Prediction the Results of Grouting Performance

Considering the obtained experiences and recorded results during the experiments, it was determined that the grout-taking of the samples was an appropriate criterion for dividing the results of the grouting performance into two groups of successful and unsuccessful or inadequate ones. Accordingly, the grout-taking of the samples was drawn against the results of the grouting performance (Figure 8) which showed that the samples above the grout-taking border of 750 were mainly the samples which had successful grouting and the samples below this border were mainly located in the group of samples which had unsuccessful or inadequate grouting performance. The numbers placed on the horizontal axis of the diagram refer to the names of the samples and do not have numerical values.

Considering the table for constructing cylindrical samples in Section 4 (Table (3)), the parameters which were studied in this research included grout pressure P , water-to-cement ratio w/c , compaction percent of soil D_r and soil aggregation, the last of which was stated by two parameters of D_{10} and fine-grained content of soil. Also, the effect of cement aggregation on the grout-taking was entered into the equation as d_{90} .

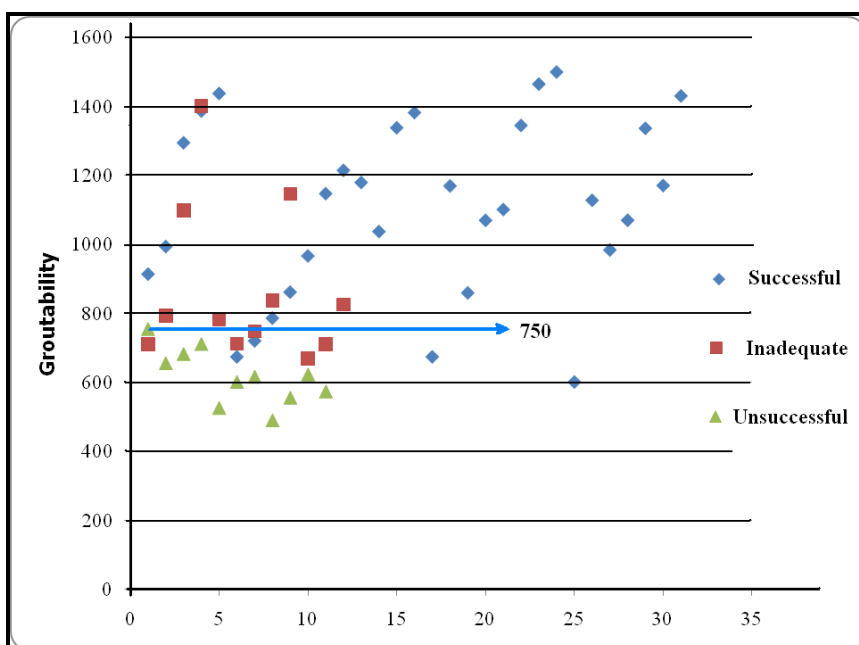


Figure 8: The samples' grout-taking against the results of the grouting performance

For the convenience of formulating the grout-taking equation and obtaining rational coefficients for the equation parameters, the results obtained for the samples' grout-taking were scaled through being divided by 30 so that the grout-taking border of 750 became equivalent to 25.

Accordingly, by doing a linear interpolation between the input parameters and output results (grout-taking) using the SPSS Statistical Software, the coefficients of the grout-taking equation were obtained as follows; consequently, the results of the grouting performance can be predicted:

$$GR = -18.59 \frac{D_{10}(\text{Soil})}{D_{90}(\text{grout})} + 1.29P \times \frac{w}{c} + 17.19 \frac{10^4}{R \times FC} - 36.08 \quad (1)$$

where the values of compaction percent R and fine-grained content of soil FC are in percent and the unit of pressure is bar. In order to normalize the equation, the coefficient of the second part of the equation is considered as 1/bar.

By putting initial parameters of the grouting performance of an actual project (grout pressure, water-to-cement ratio, etc.) in this equation, the result of grouting performance can be predicted. Therefore, if $GF > 25$, the result of the grouting performance is considered successful; otherwise, it is inadequate or unsuccessful grouting.

5. RESULTS AND SUMMARY

The aim of the present study was to investigate the groutability of Tehran C Alluvium considering the initial parameters of grouting such as pressure, water-to-cement ratio, aggregation and compaction percent of soil and to extract a relation for predicting groutability. The study was done by compacting the soils with specified aggregation in transparent cylindrical cells and using the cement grout with different water-to-cement ratios at different pressures.

Considering the presented diagrams, it was observed that groutability of soils is in direct relation with the grout pressure. Thus, for the soils with higher compaction percent, the grout-taking grouting increases considerably with the increase of grout pressure. To obtain a successful grouting result, the increase of grout pressure can be an appropriate solution. Another parameter for the soils' grout-taking rate is water-to-cement ratio; it was observed that increase in the water-to-cement ratio can increase the soil groutability; however, in the reverse situation, it has a negative effect on the increasing rate of soil resistance. Consequently, in an actual operation, first, the aim of grouting should be identified; then, decision should be made on the selection of initial parameters of the grouting performance. For instance, if the aim of grouting is only to prevent from water seepage into the tunnel, the grouting performance with the water-to-cement ration of 2 can be sufficient. If the tunnel is in the risk of failure due to the load of the surrounding structures, special care should be paid for selecting the water-to-cement ratio.

Moreover, in order to state the effect of materials and aggregation of soil and cement on the result of grouting performance, the parameters related to the soil and cement grain sizes and fine-grained content were entered into the grout-taking relation of the soil.

Compaction percent of soil had also a considerable effect on the result of grouting performance and it was demonstrated that main samples with successful grouting results had lower compaction percent. In order to increase the compaction percent of the soil for obtaining a successful grouting result, the effect of increasing grout pressure, increasing the water-to-cement ratio or both of them should be investigated.

The obtained relation of the soil groutability can be used for predicting the result of grouting performance in conducting actual projects. This issue can be effective for estimating the initial costs of grouting performances, which account for a considerable part of financial loads in tunneling projects. Also, considering that in general soil is evaluated as an unknown material in most construction projects and limited data are available on the actual conditions of soil in the location, this relation can be used for preventing from blind grouting and getting a general view of the result of grouting performance and selecting its initial parameters.

REFERENCES

- [1] *Engineering and Designing Grouting Technology*, 1984, U.S. Army Corps of Engineers Washington, DC, Engineer Manual (EM 1110-2-3506).
- [2] S. Akbulut and A. Saglamera , 2002, *Estimating the groutability of granular soils : a new approach , Tunneling and Underground Space Technology* 17 , 371–380.
- [3] M. Axelsson, G. Gustafson and Å. Fransson, 2009, *Stop mechanism for cementitious grouts at different water-to-cement ratios*, *Chalmers University of Technology, Tunneling and Underground Space Technology* , 24 390–397.

- [4] M. Esmaili, M. Gharouni Nik and H. Hosseinpour, 2011, *Evaluating Grouting Performance in Tunneling: Experimental Study of Tehran C Alluvium*, M.Sc. thesis (Railway Track and Structures), School of Railway Engineering, Iran University of Science and Technology.
- [5] A. Majdi, and M. Zahiri, 2006, *Mathematical Model for the Groutability Ratio of Granular Soils*, *Journal of Technical School*, Volume 40, Issue 2 (249- 237).
- [6] A. Cheshmi, A. Fakher and M. Khomeh Chian, 1999, *Geology of Tehran Alluvium and Evaluation of Ground Classification for Studying Engineering Geology*, *Journal of Sciences, University of Tehran*, Volume 34, Issue 2 (1-15).

The design and execution of Settlement Mitigation Measures for Bridge 404, North South Metro Project, Amsterdam

F.J. Kaalberg, Witteveen + Bos, Netherlands, f.kaalberg@witteveenbos.nl
R.D.Essler, RD Geotech Ltd, United Kingdom, robert.essler@rdgeotech.co.uk
R.Kleinlugtenbelt, Witteveen + Bos, Netherlands, R.Kleinlugtenbelt@witteveenbos.nl

ABSTRACT

The Amsterdam North/South Metro line is a challenging project in an adverse urban environment of very soft soil and historical buildings founded on wooden piled foundations close to the tunnels. Following successful full-scale trials, compensation grouting was selected as the most preferable method for mitigating movements. The shield driven tunnels are to be driven both from the north and the south and are approximately 7m in diameter. Bridge 404 is located south of the Ceintuurbaan station box where the tunnels are stacked, thus the two tunnels pass under the bridge at different depths in preparation for entering the station.

Bridge 404 is a historical bridge founded on brick abutments which in turn are supported on driven wooden piles approximately 13m deep. The two TBM's pass under the bridge from South to North with the Western tunnel at a depth of approximately 12m below the bridge foundations but the Eastern tunnel only has a clearance of 1.5 m below the pile toes.

In order to protect the bridge from unacceptable movements a combination of compensation grouting and ground improvement was carried out. Compensation grouting was used to protect the bridge during passage of the deep tunnel and compensation grouting in combination with ground improvement was used to mitigate the effects of the shallow tunnel. As the cover under the canal is reduced and the loads of the piles do have a significant impact on the stability of the bore front, advanced 3D numerical simulations were used to support the design of the mitigating measures.

The paper describes both the compensation grouting and ground improvement design in detail and presents the results of the works carried out to date.

1. INTRODUCTION

The Amsterdam North/south Metro scheme includes 3.8KM of twin tunnels of diameter 6.5m which pass through the centre of the city from Central station in the North to RAI in the south.

The tunnels are constructed using a Mixshield tunnel boring machine to reduce volume loss and disturbance to the environment. The previous section of the Amsterdam Metro was constructed in the 1970s through the city centre using cut and cover techniques and resulted in significant disruption and damage. The City Council was determined that the North-South section would be constructed with minimum environment disruption and so settlement mitigation was considered necessary for certain locations along the route.

Along the tunnel route exists in excess of 1000 historical buildings mainly all founded on wooden piles driven through the very soft clays to a sand layer. At locations where the tunnels are curving, volume loss would be expected to be higher and the design recognized that at these locations, despite the use of a very advanced TBM, mitigation of tunneling settlements would be needed (Kaalberg et al, 1999).

Design for the scheme commenced in 1995 and at an early stage (1999), compensation grouting was identified as a suitable solution to mitigate the settlements. In total seven locations required the use of compensation grouting to mitigate settlements. In general the crown of the TBM was in excess of 4m below the pile toes, however at Bridge 404, the crown of the east tunnel passes only 1.5 m below the pile toes and a special strategy needed to be developed.

2. GROUND CONDITIONS AT BRIDGE 404

The ground conditions relating to the tunneling and compensation grouting comprised the following strata (and thicknesses):

Fill (1m)

- Very soft clays (12m)
- 1st Sand layer (2m)
- Alleröd (3m)
- 2nd Sand layer (4m)
- Eem Clay (3 m)
- 3rd Sandlayer (to depth)

The Alleröd is a silty/clayey strata of variable composition. The general succession is shown on Figures 1 and 2. Groundwater is very close to ground level.

3. BRIDGE 404 CONSTRUCTION

Bridge 404 was constructed in 1920's and spans the Amstel canal. It comprises timber piled brick abutments supporting a steel-concrete composite deck. The bridge is a historical landmark because of the small towers of typical Amsterdam architecture at the four corners of the bridge. A photograph of the bridge is shown on Figure 1.



Figure 1: Bridge 404 looking east

The bridge has a composite steel beam and concrete deck with a span of 12m and a section from the original drawings is shown on Figure 2.

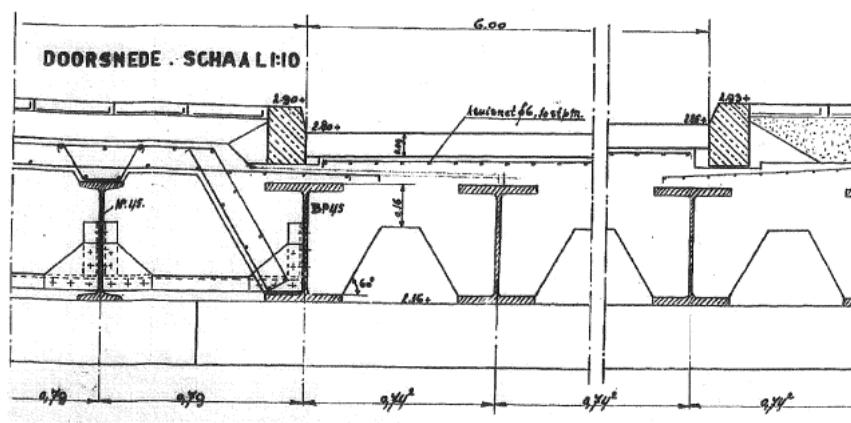


Figure 2: Section showing deck construction

4. GROUND IMPROVEMENT DESIGN

Bridge 404 is situated around 530m south of Ceintuurbaan station. This station is located within a narrow street and thus the tunnels are required to be stacked as they pass through the station. Because of this requirement, at Bridge 404, the west tunnel is relatively deep but the east tunnel is quite shallow as the two tunnels align for the station box. Figure 3 shows the cross-section of the bridge and the two tunnels.

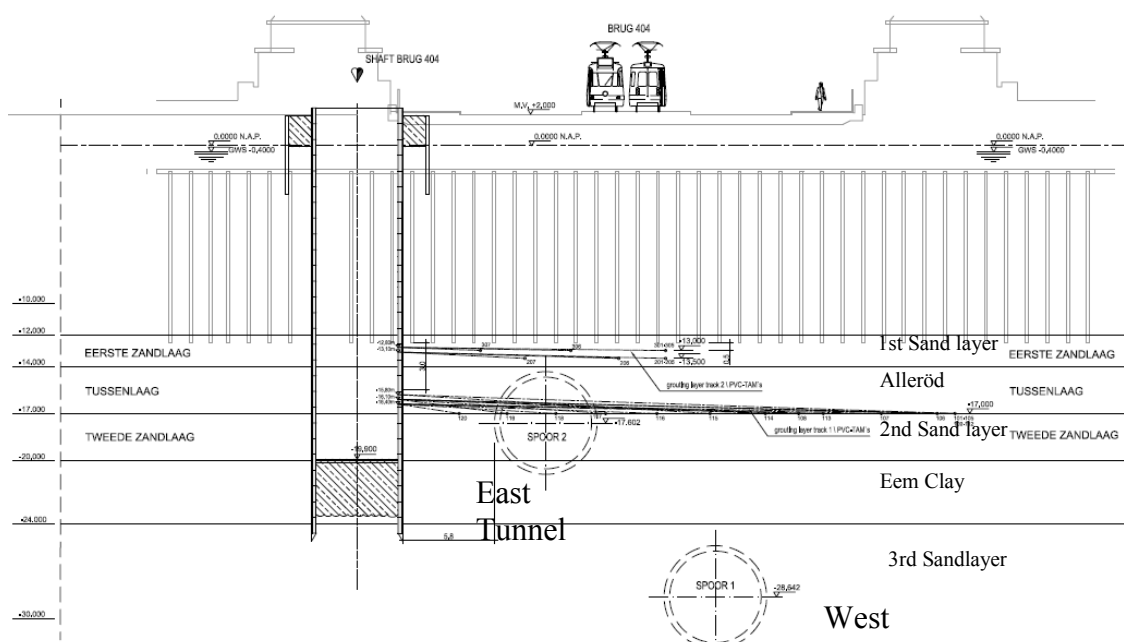


Figure 3: Cross-Section at Bridge 404 showing tunnel locations and compensation grouting pipes

Because of the difference in tunnel depths, the ground improvement strategy was evolved separately for each tunnel. Expected settlements for the bridge foundations (at pile toe level) assuming 0.5% volume loss were around 10 mm for the west tunnel but 40 mm for the east tunnel assuming greenfield conditions.

4.1. West Tunnel

Because of the depth of the west tunnel, conventional compensation grouting was planned. Figure 3 shows that the pipes were designed to be installed mainly in the Alleröd layer as there had been difficulties drilling and installing pipes in the very dense 2nd sand layer before and grouting efficiencies showed to be higher in the Alleröd layer. Also there was no space available as the TAM's for the east tunnel had to be positioned directly below the piled foundations. At the other locations the compensation grouting pipes are positioned mid way between the structure foundations and the tunnel crown according to the developed interception strategy (Kaalberg, Essler 2011), however for this location, the additional strengthening and face support from the installed pipes was felt to be beneficial in reducing movements further for the east tunnel passage.

As a consequence subsequent to the passage of the west TBM, the east TBM would need to bore through the compensation grouting pipes. Because of this, the normal steel injection pipes were substituted with thick walled PVC pipes. Because these had not been used before by the contractor, three holes were trialled at the Picoplein compensation grouting site to ensure well in advance of the programme that they could be successfully installed. In the event, no problems with drilling in the pipes were encountered at Picoplein.

A 5.5m internal diameter shaft was positioned to the north east of the bridge and outside the influence of the tunnel settlement.

Figure 4 shows the plan layout of compensation grouting pipes for the west tunnel. In accordance with the normal design, the pipe coverage extended 3m beyond the plan positions of the pile toes and provided coverage to the expected 5mm contour of settlement due to 1% volume loss. The spacing between pipes at the farthest limit was designed as 3m.

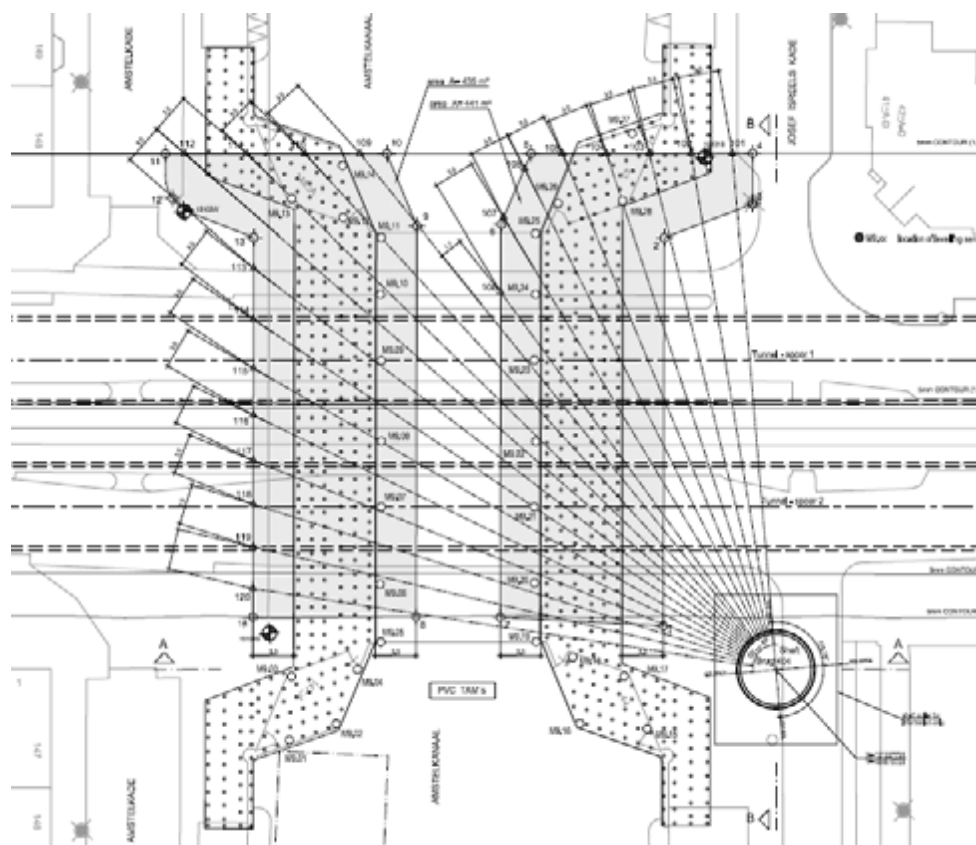


Figure 4: Layout of Compensation grouting pipes for the deep west tunnel

4.2. East Tunnel

The protection of the bridge during the east tunnel TBM passage presented a formidable challenge. The distance between the crown of the tunnel and the expected pile toes is less than 2m which means that any grouting during the passage would be problematic, due to potential interference with face pressure balance. Because of the initial imposition of a 3.5m exclusion zone by the contractor, SATURN, concurrent grouting during TBM transit was not envisaged (finally this was changed see section 7). The design therefore assumed that a treated block would be created around and above the TBM axis to stiffen the ground and reduce settlements. The following strategy was adopted :

Two rows of plastic TAMs were installed above the east tunnel and below the pile toes in accordance with the original design. The TAM spacing would have to be based on the minimum distance between exit points from the shaft (380mm). This gave variable spacing depending on distance of the TAM distal point from the shaft. The upper pipes were preinjected with a colloidal silica grout (MP325) and the lower pipes preinjected with an ultrafine cement (Mikrodur R-X). The MP325 would permeate even very fine sands and should be suitable for the 1st sand layer but would probably only achieve a strength of 0.4MpA. The ultrafine fine cement may not penetrate as well and may hydrofracture the ground but would achieve higher strengths. The upper layer was injected in advance of the lower layer to provide a barrier to the ultrafine cement fracturing through into the upper Holocene layer. The lower west tunnel pipes which were in the Alleröd were injected with microfine cement adopting low injection volumes, not exceeding 100 litres to provide further stiffening.

Injection was continued until a maximum allowable preheave of around 5mm achieved. Heave resulting from the MP325 and Microfine cement injection was to be limited to 2-3mm to allow the possibility of the injection of grout in the lower west tunnel pipes.

Figure 5 shows the section close to the east tunnel indicating details of the pipes installed and Figure 6 shows the plan layout of pipes in the upper two layers.

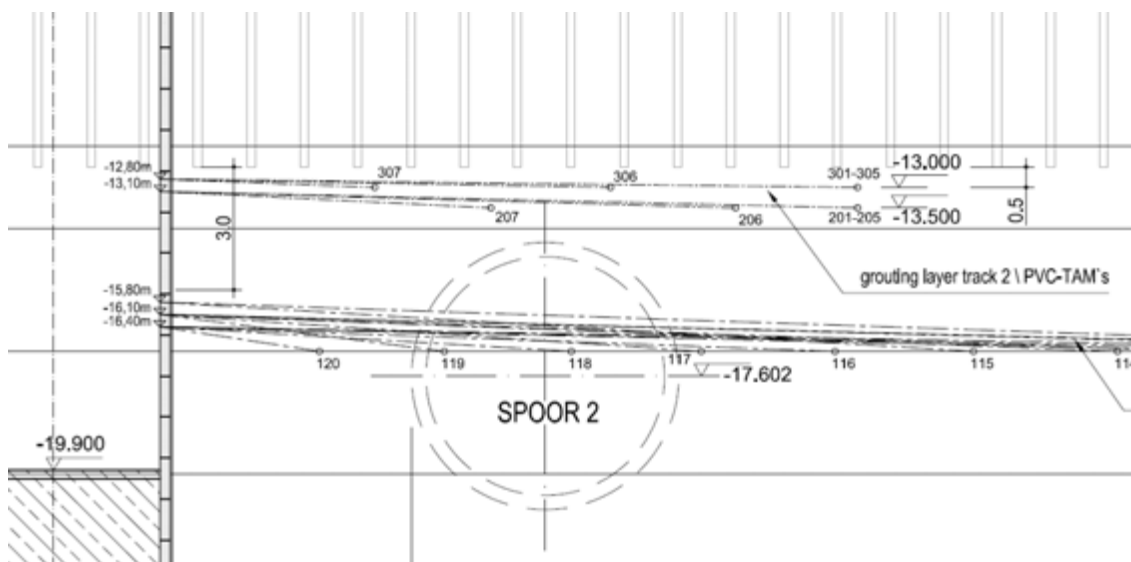


Figure 5: Section looking South showing East Tunnel and lower and upper injection pipes

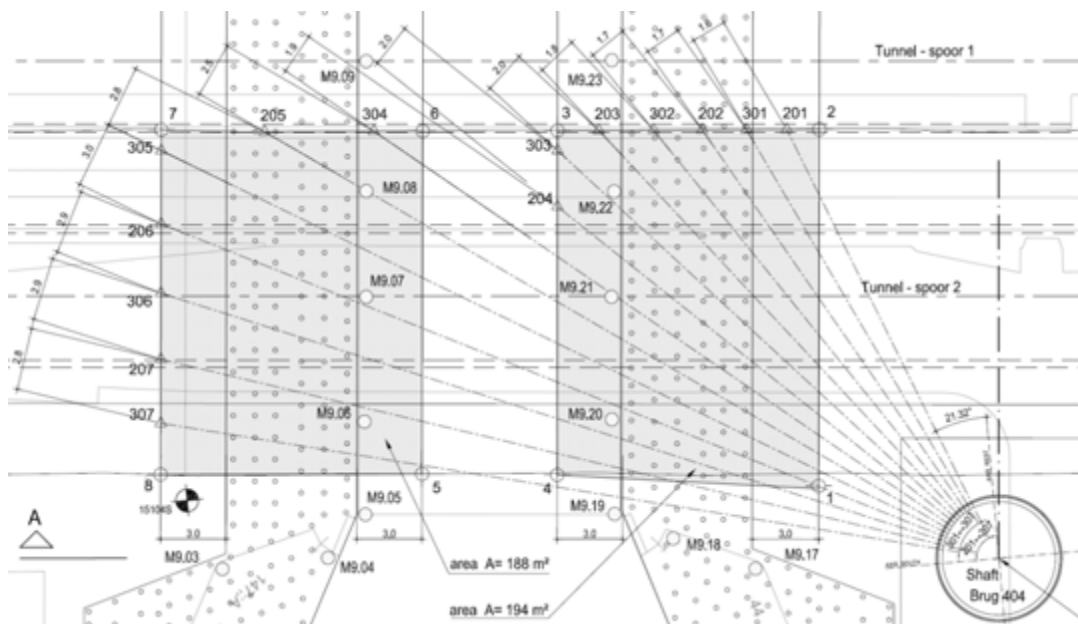


Figure 6: Plan layout of upper injection pipes for the shallow East tunnel

4.2.1. TBM Transit Situation

Three issues need to be resolved for the TBM transit at this location:

- Preventing structural bridge damage
- Preventing face instability (a normal requirement for TBM travel)
- Preventing surface blow out (a normal requirement for TBM travel)

There is an upper limit on the face pressure (P_{bo}) that prevents a blow out to the surface via ground fracturing. There is also a minimum face pressure (P_{fs}) required to maintain face stability. For Brug 404 because of the canal excavation (also under abutments) and the deep pile loadings, the minimum pressure P_{fs} is actually greater than P_{bo} , when applying the regular analytical face stability calculation methods. This creates a problem as, if the face pressure is reduced below P_{fs} , additional settlement and potential borefront collapse is created. Figure 7 illustrates this.

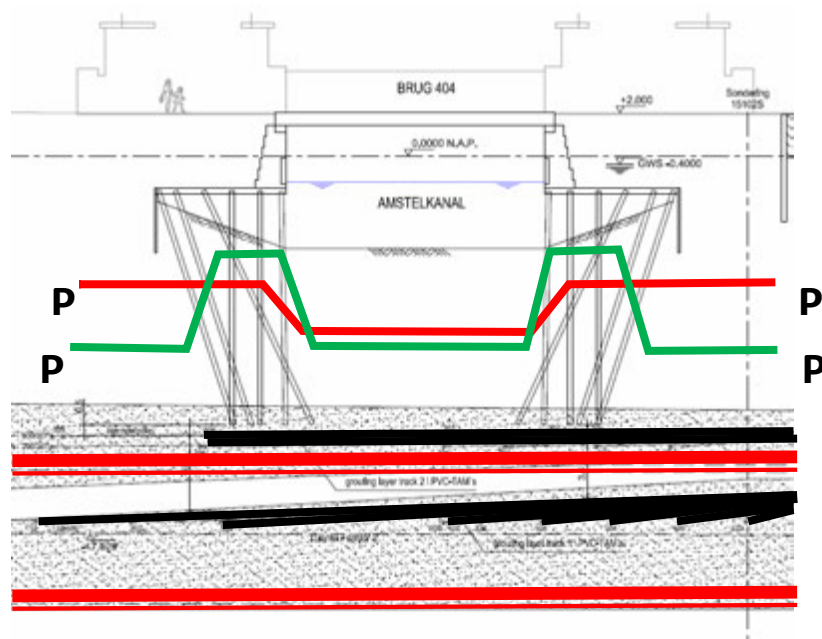


Figure 7: Schematic representation of blow out and face stability pressures based on analytical calculations

Therefore it is necessary to create conditions to be able to either increase P_{bo} to greater than P_{fs} or reduce P_{fs} to less than P_{bo} . The P_{bo} can only be increased if the ground is stiffened/homogenised and blow out risk is therefore reduced and P_{fs} can only be reduced if the ground is improved, or more advanced 3D design calculations are applied. Thus the use of the ground improvement not only deals with the settlement due to volume loss but also helps solve the problem of the inequality of blow out and face stability.

4.2.2. Numerical Analysis

A 3D numerical analysis using Plaxis 3D was carried out to determine more accurately the required minimum face pressure. Figure 8 show the layout adopted with the strata used. In the 3D numerical model a ϕ -c reduction analysis was performed in order to assess the safety factor on the front stability. Also the applied face pressure was gradually reduced until the borefront became (numerically) unstable.

The 3D numerical analysis showed that the original (pseudo 3D) analytical analysis appeared to be conservative, indicating that the actual minimum face pressure needed for stability was lower than originally calculated. In general this is common knowledge, however still topic of many publications as academic research regarding is still going on to validate these 3D numerical calculations. In this particular case however, it was necessary to quantify this difference and take it into account to make the bridge passage feasible. Based on a numerical parametric (both for soil parameters as front pressures) risk analysis it appeared to be possible to reduce P_{fs} . However, in order to minimise the required reduction of P_{fs} it was felt that it would be useful to mitigate the risk of blow out as well, by implementing extra measures to be able to raise the P_{bo} . Therefore, in order to prevent the bentonite escaping from the bore front to the canal bed, the area under the bridge deck and the abutments above the Eastern tunnel was injected with MP325 and microfine cement. In this way a small steering range for the TBM face pressures of 0.25 bar was achieved ($P_{bo} > P_{fs}$).

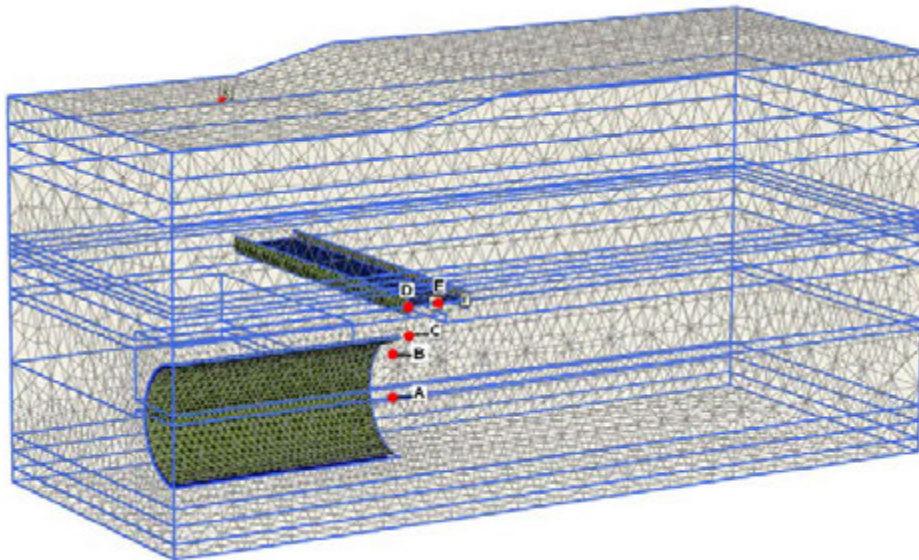


Figure 8: Three Dimensional model and points considered in safety analysis

It was investigated numerically as well if this ground improvement between tunnels and pile toes would contribute to the face stability, but his effect was not significant as the added stiffness to the subsoil was relatively low compared to the bridge loads. Also the contribution of the ground improvement at the borefront to the stability was numerically investigated. It appeared that ground improvement at the bore front did not significantly increase the factor of safety, although it was noticeable that settlements could be increased before the numerical model became unstable. It must be stated that the stiffness parameters for the ground improvement were taken conservatively, as it is rather difficult to assess the achieved in-situ stiffness and homogeneity of the injections.

Figure 9 shows the output of a part of the analysis showing the stress distribution from the TBM.

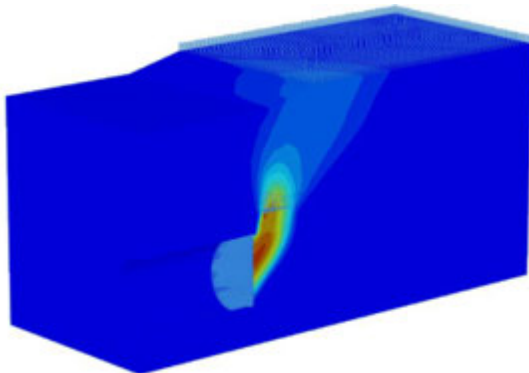


Figure 9: Stress distribution due to face instability.

In addition to the 3D analysis of the TBM face stability, further analysis was carried out to evaluate the soil structure interaction of the bridge abutments to determine if the predicted settlements would be reduced due to the structure interaction.

Figure 10 shows the three dimensional model adopted for this analysis.

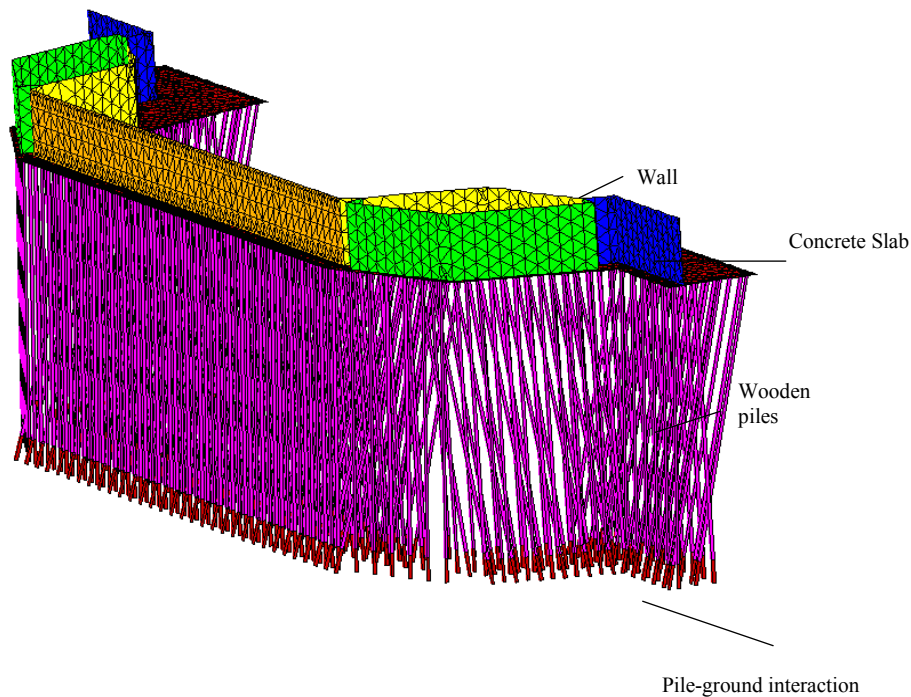


Figure 10: Soil-Structure interaction model

Initial calculations run with a flexible foundation indicated that the predicted settlements of the bridge abutments would reach the predicted 40 mm (virgin) subsoil settlement at pile toe level and thus provided some calibration to the model. When the pile stiffness and deck structure were introduced, settlements of the abutments were significantly reduced. Figure 11 shows the settlements at the top, middle and toe of the piles.

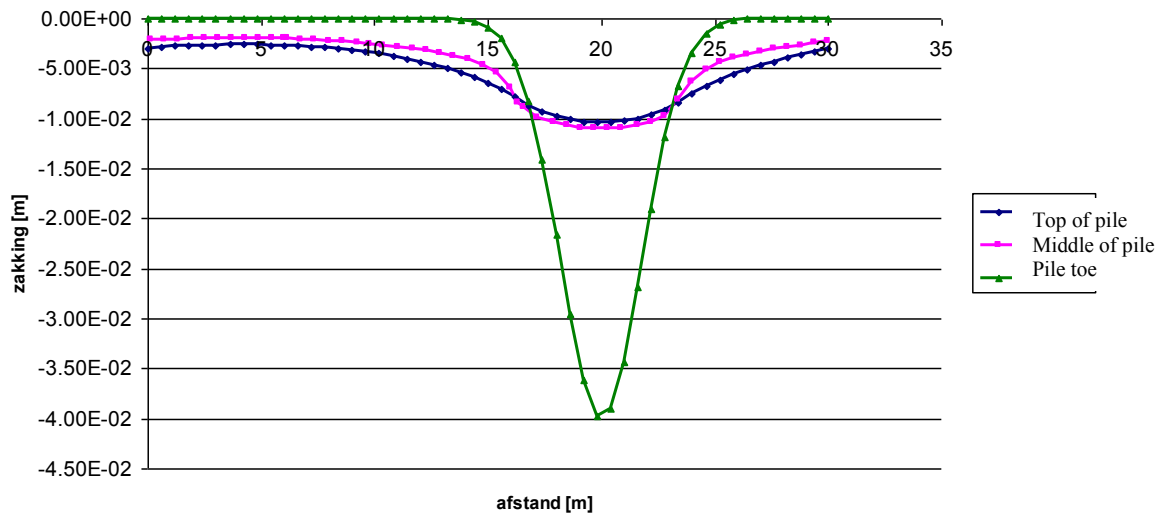


Figure 11: Predicted pile settlements

The reduction in settlement is achieved by a load redistribution within the piled foundations, due to the stiffness of the bridge abutment and this is shown on Figure 12. Varying the pile stiffness or the ground improvement had little influence on the settlements of the bridge abutment. Effectively the piles immediately above the TBM become unloaded and the bridge deck load is then transferred to the piles at either side of the TBM. At earlier full scale trials it was found out that wooden piles with end bearing capacity can settle more than the subsoil due to stress relieve around the pile toes (Kaalberg e.a., 2005).

As this is difficult to model, this effect was not incorporated in the above simulations. However, the improved ground assists this by an increased bearing capacity and creates a “frozen stress situation” which prevents stress relieve within the first sand layer, so this additional settlements were not incorporated in the predictions.

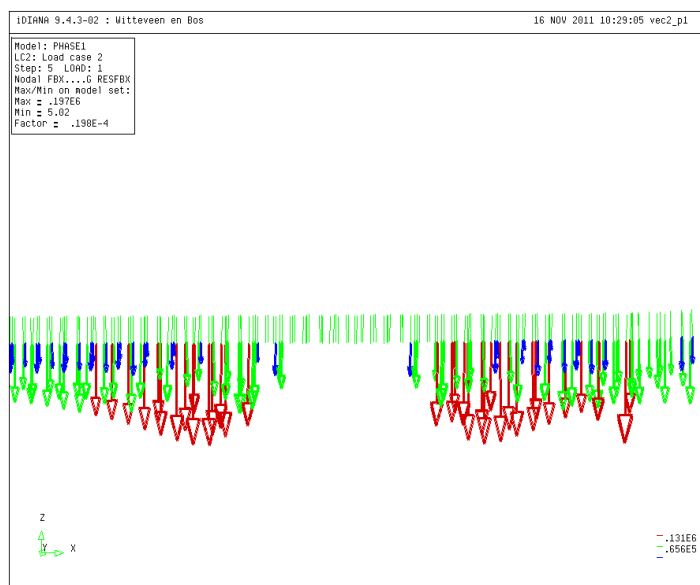


Figure 12: Predicted pile toe stresses during TBM passage

In a parametric analysis it was shown by the model that the bridge abutment would crack at 3 locations when the settlements would increase and the associated tensile strength of the bridge abutment exceeds its maximum capacity. Based on this result it was decided to abandon the original opinion that no concurrent grouting would take place and to start concurrent grouting as soon as possible after the passage of the TBM front.

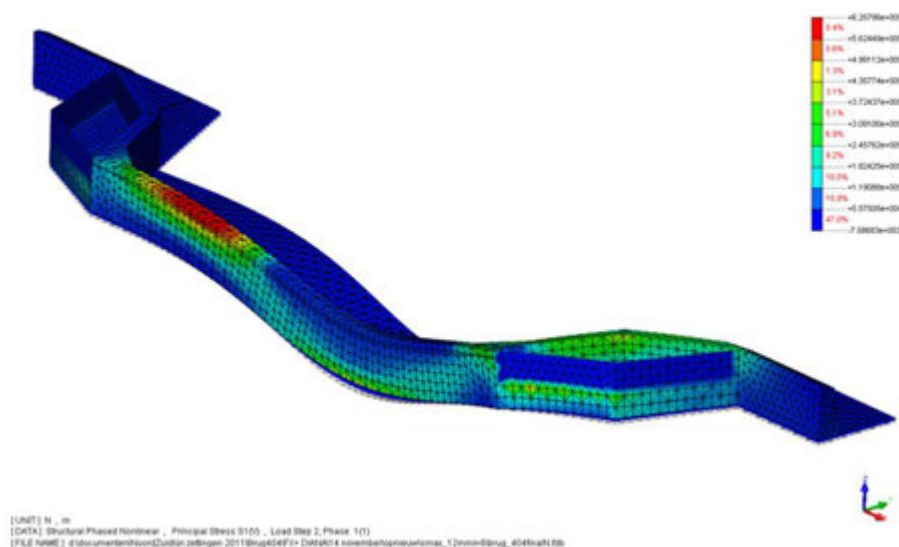


Figure 13: Example of principal stresses in bridge abutment during TBM passage

4.3. Monitoring

The bridge is extensively monitored by three systems:

1. Water settlement cells fixed to the north and south abutments and buildings
2. Total station prisms fixed to the four corner buildings and ends of the bridge abutment walls
3. Reflectorless surveying of the centreline of each TBM axis at 1m intervals of chainage.

Figure 14 shows the monitoring provided by the total stations and water settlement cells.

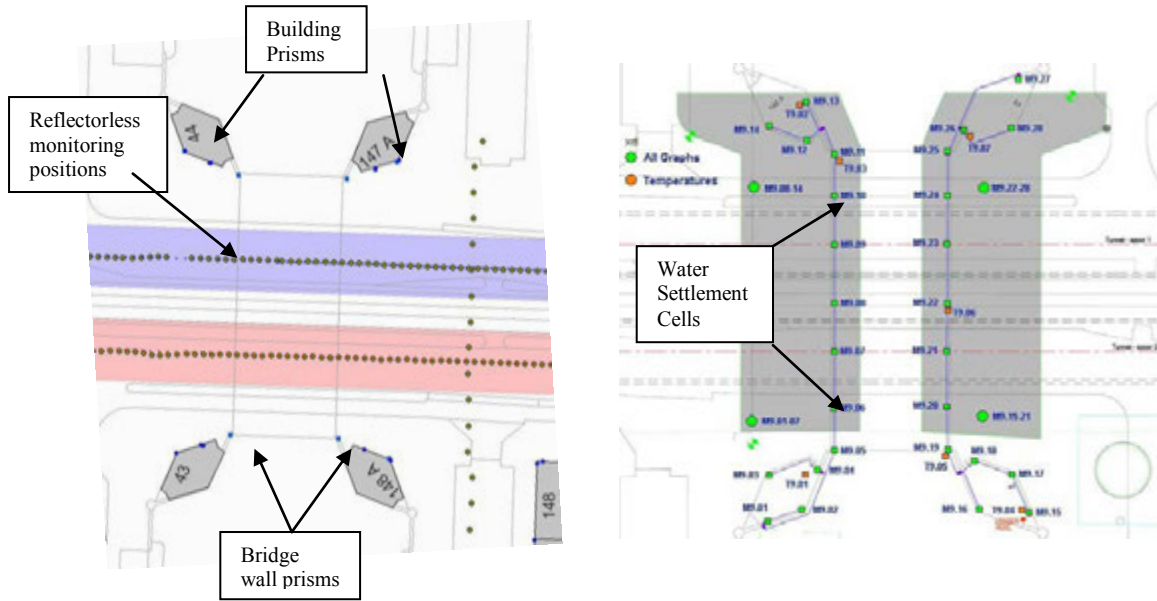


Figure 14: Total station monitoring and water settlement cell layout

Monitoring commenced in June 2008 prior to any drilling or grouting activity around the bridge. The shaft was remote enough not to provide concern and the building prisms were in any case already being monitored.

Figure 15 shows a comparison of the movement provided by the settlement cell 9 and the closest reflectorless measurement point at the bridge surface.

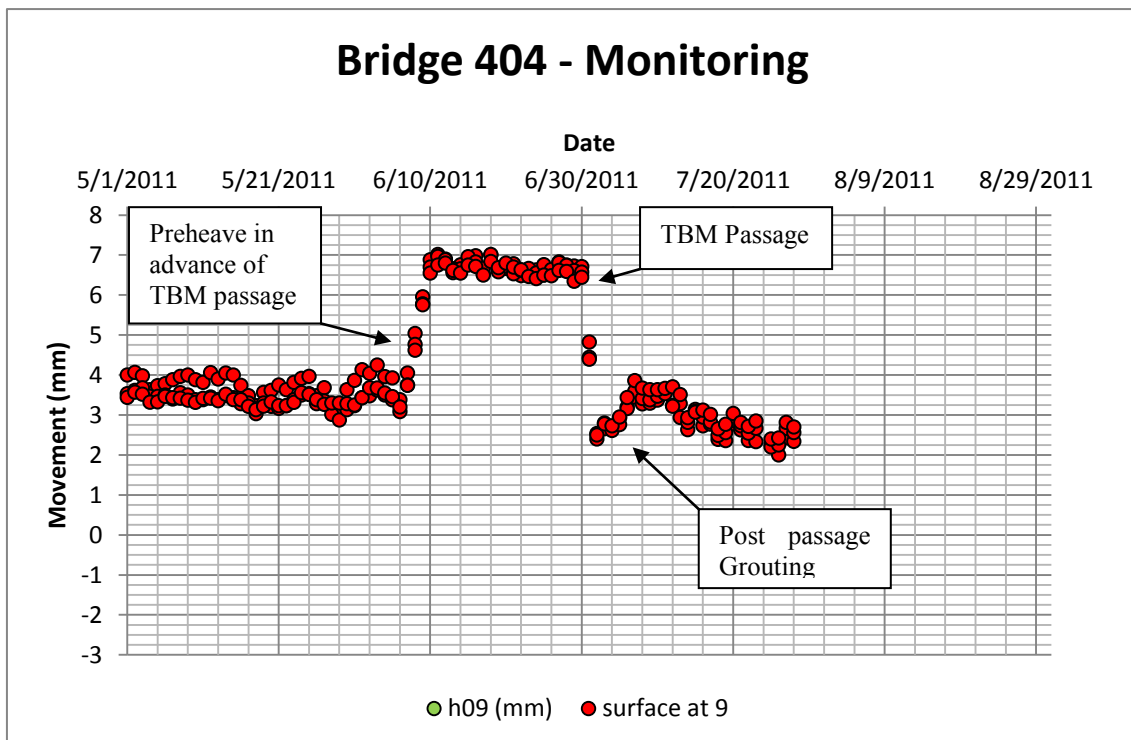


Figure 15: Comparison of surface and abutment monitoring during west TBM passage

In general there is close agreement between the settlement cell system and the total station system allowing both to be checked against the other.

5. CONSTRUCTION

5.1. Shaft Sinking

Shaft sinking took place in October 2008 and took about five weeks in total. The methodology adopted was that the bottom edge of the shaft was jacked ahead of the excavation within the shaft which prevented loss of ground and hence settlement being generated. Special precast concrete segments were used which allowed bentonite to be injected at the cutting edge through pipe channels that were aligned when the segments were bolted together. This provided a friction reduction and assisted the jacking process. In operation, the bottom edge would be jacked into the ground with the excavation being no closer than 0.5m above the base. The segments were 1m in depth, thus the jacking operation consisted of constructing a 5.2m internal diameter ring of nine segments, jacking and excavating 1m and repeating the process.

5.2. Drilling

Following completion of shaft sinking, a drill mounted on a rotating and jackable drill stand was installed within the shaft. The rotation allows the drill to be easily positioned for each drill hole and the jacking frame allows the drill to be simply moved up and down. In order to accommodate the drill and frame around 3m of space was required below the drilling level.

In order not to compromise the structural integrity of the shaft construction, special segments were installed during jacking at the levels of drilling. These segments allowed the drills to penetrate without cutting the reinforcement. In order to provide sufficient space between each drill hole, a number of entry levels had to be used.

Drilling was carried out using special preventers to deal with the 1.5 Bar water pressure. On completion of drilling, the steel injection pipe was installed and with the help of a seal between the injection pipe and the drill casing, the casing was withdrawn while grouting the hole under pressure.

5.3. Grouting

Pregrouting was carried out immediately after drilling. It was decided that it would be beneficial to incorporate a small tilt of the bridge away from the tunnel drive to compensate for the settlement during TBM passage. The control of the grouting was very precise and the tilt was applied to the bridge with 4mm at the line of the tunnel axis and 1mm remotely. The grout utilized was a preblended mix provided by Heidelberg known as Blitzdammer 750. The water solids ratio was set at 1.4.

Initially grouting was carried out in the lower layer of pipes to condition the ground for the west tunnel passage.

5.4. Movements

Movements during the drilling process were very small and if any movement took place, initial injection pipes would be injected to compensate for this.

Grouting was carried out as discussed above, initially in the lower pipes for the west tunnel drive and then the extensive grouting was carried out to improve the ground above the east tunnel drive. At the completion of grouting the bridge deck had been heaved by a maximum of 4mm over the line of the west tunnel.

6. TBM PASSAGE WEST TUNNEL

The west TBM transited the bridge in July 2011. Figure 15 shows the reaction of the bridge during TBM passage. Grouting was only implemented when the initial preheave values dropped to 50% of their initial values so that the bridge would not be left higher than necessary.

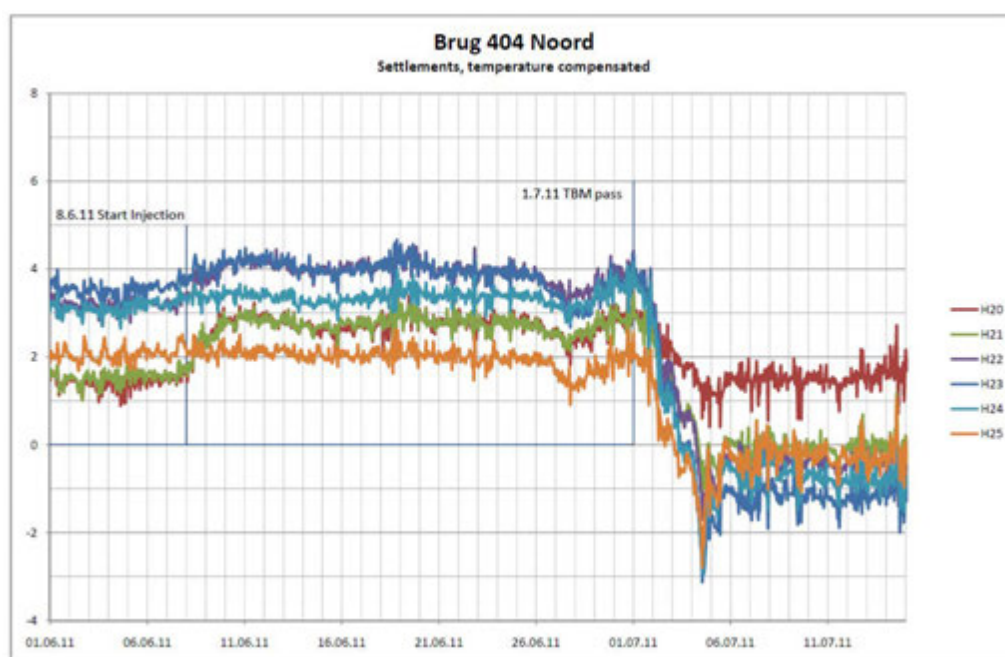


Figure 16: Bridge movements during west tunnel TBM transit

7. TBM PASSAGE EAST TUNNEL

Further grouting was carried out in December 2011 and January 2012 in preparation for the transit of the east tunnel. This involved the establishment of new heave levels above the axis of the east tunnel with a maximum of around 5mm. At this time the zone between the two bridge abutments was grouted with MP325 and ultrafine cement to create the necessary ground improvement for blow out protection.

Initial calculations were carried out by the client to assess the amount of ground treatment required. An assumption of 0.5% volume loss was taken together with a 15% grouting efficiency. These calculations showed that 1870 litres of grout was required to be injected for each ring advance. Following discussions with the contractor immediately before the eastern TBM passage, a 6m grouting exclusion zone back from the face of the TBM was agreed to mitigate the risk of grout entering the TBM slurry. No grouting was permitted in front of the TBM in order to avoid any face stability issues. Given that the client made no restriction to the TBM rate of progress, an advance rate of 1m/hour could be contemplated and thus the predictions showed 1870 litres of grout could be required in a short period of 90 minutes. Because this gave very little time for reaction and the potential rate of settlement was large, it was decided to agree a grouting sequence for each ring construction rather than wait for the monitoring system to signal the settlement trough and the software calculate the required grout quantities. In this way, the grouting sequence was designed and written down for each ring and was instigated as soon as the TBM communicated that the ring had been built.

This methodology provided a very efficient method of working for the grouting teams as there would be no delays between grout passes.

The TBM entered the southern grouting zone of bridge 404 on 31st January 2012 and grouting continued on a non stop, 24 hour basis until the 4th February 2012 when the TBM left the immediate area of the north abutment. The monitoring throughout was used to ensure that movements did not exceed the performance requirements. Figure 17 shows the change in bridge level with time as the TBM transits and it is clear that beyond the bridge foundations, the surface settles by about 7mm corresponding to around the 0.5% volume loss predicted, so it is likely that the predicted settlements at pile toe level were also according to predictions (still up to 40 mm see Figure 11). However, as can be noticed in Figure 17 the bridge abutments are maintained in position, by means of the compensating injections. The amount of grout needed in reality was close to the predicted values, so it can be concluded the developed compensation grouting strategy was very successful.

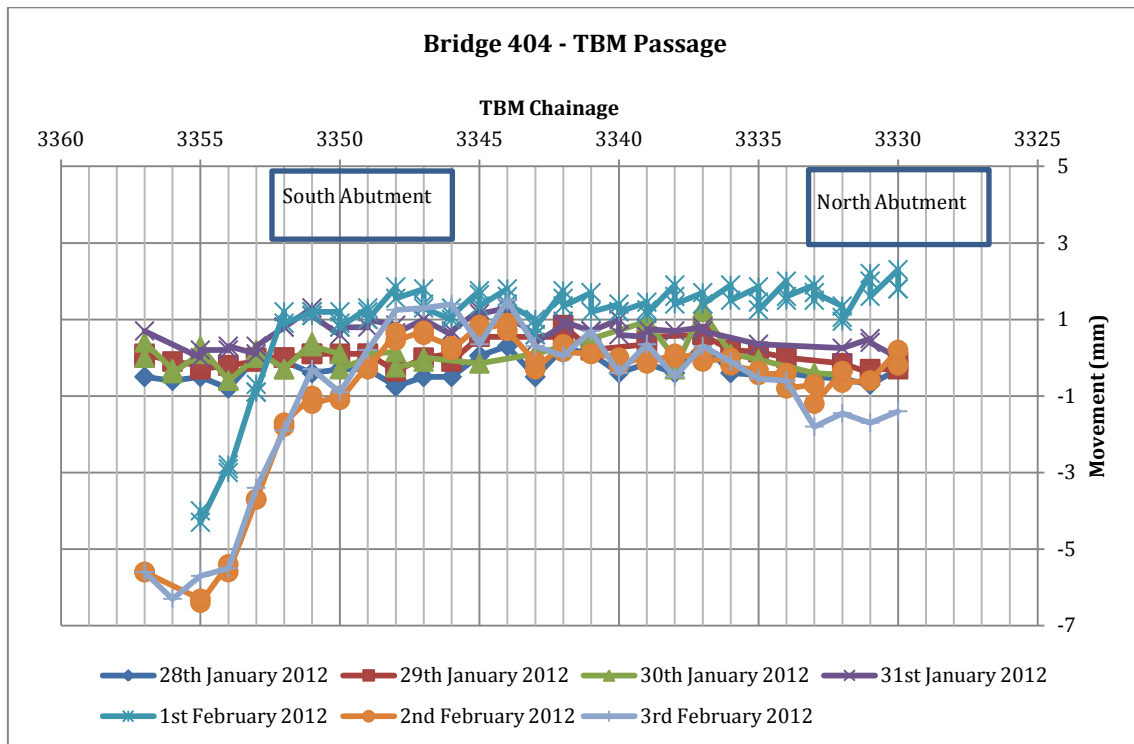


Figure 17: Change in bridge level as the TBM passes underneath

REFERENCES

Kaalberg, F.J. & Hentschel, V., 1999, *Tunnelling in Soft Soil with a High Water Level and Pile Foundations, Towards the development of settlement-oriented and settlement-minimizing TBM operation*, Proceedings of ITA World Tunnel Congress, Oslo.

F.J. Kaalberg, E.A.H. Teunissen, F. van Tol, J.W. Bosch, 2005, *Dutch research on influence of Bored tunneling on piled foundations*, ISSMGE-TC28 Conference Amsterdam.

F.J. Kaalberg, R. D. Essler, R. Kleinlugtenbelt, *Compensation grouting of piled foundations to mitigate tunneling settlements*, ISSMGE-TC 28 Conference 2011, Rome.

Jet grouting foundation under the overpass of the A27 in the polder construction sealed with a foil at Amelisweerd

ing. O.S. Langhorst, Movares Nederland BV, the Netherlands, onno.langhorst@movares.nl

ABSTRACT

The railway between Utrecht and Geldermalsen crosses the deepened highway A27 by means of a viaduct. The actual car overpass which runs parallel to this viaduct has to be retro-fitted for railway traffic. A new overpass for car traffic is therefore necessary. It is chosen to set this overpass on two land abutments and a centre pillar. The particularity of this location is that at Amelisweerd, the deepened A27 is laid out in a polder construction sealed off with a deep foil. After verification appeared that the expected sand layer that should have been above the foil was largely missing. The soil profile consists namely of clay and loose packed sand layers, which would make a traditional shallow foundation unsuitable. A ground improvement technique that could make this type of foundation possible was sought after. The implementation of jet grouting appeared to be the optimal solution.

1. INTRODUCTION

A new design for a car overpass over the deepened A27 was drafted in 2003. This new overpass will run parallel to the actual railway viaduct. The existing situation is given in photo 1. Therein is shown that the deepened A27 is set within a polder construction sealed by means of a foil. An impression of the supports of the new overpass is given in figure 1.

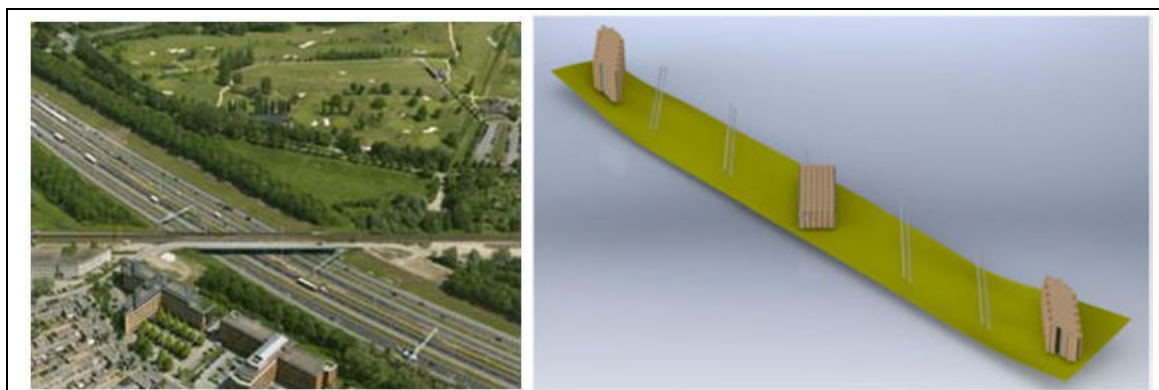


Photo 1: Existing situation

Figure 1: Impression of the new supports

The new overpass consists of a steel frame with a composite deck, that in order to keep the weight down. The assumption for this design was that during its construction, the polder was filled up with sand. However, after verification, it was clear that a significant volume of clay was incorporated in the backfill. Further studies have shown that mixed soil was returned to the fill site; this soil was the initial topsoil or originated from elsewhere and was transported to the site by means of hydraulic earthworks so as shown in figure 2.



Photo 2: Hydraulic earthworks

The consequence of this situation is that the amount of clay lenses is so large that the design of a shallow foundation for the new overpass without implementing additional measures was not possible anymore. The soil survey was subsequently extended to 3 core borings and 10 CPT's per support point. Because of the risk that the soil investigations could damage the foil, all investigations were limited to 1 meter above the construction level of the foil. The location of cross-sections I-I, II-II, III-III which were made at the centre pillar are given in figure 2. The brown areas in the cross-sections are the clay layers. The soil profile is given in figure 2.

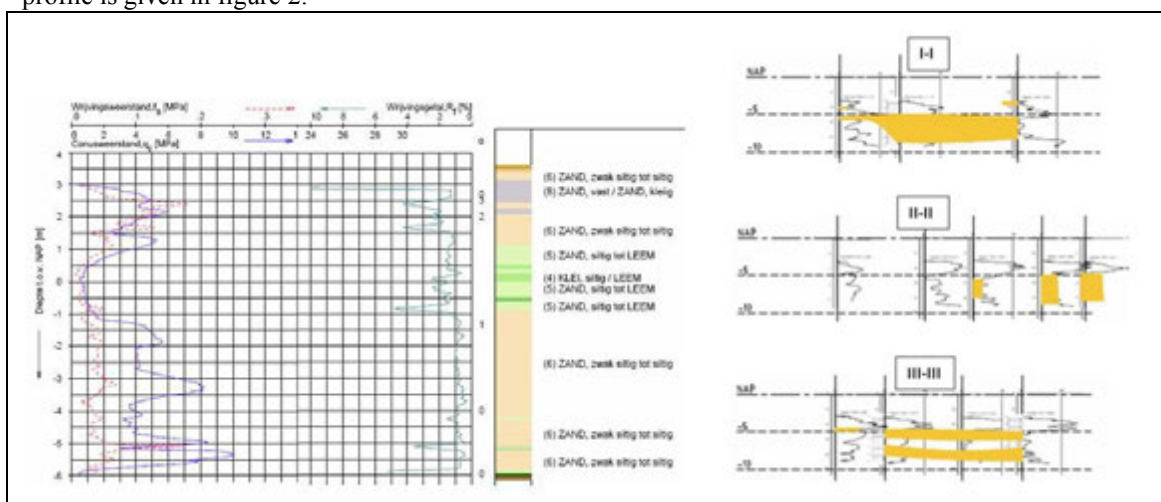


Figure 2: CPT, the soil profile and cross-sections I-I, II-II, III-III at the centre pillar

The foil construction consists of a PVC foil. The concrete slab underneath the middle pillar has for dimension 6m x 15m. By the land abutments, the dimensions of the concrete slabs amount to 5m x 10m. Mitigating measures must be taken under these foundations in order to generate sufficient bearing capacity and stiffness to carry a the overpass deck. The deck of the overpass consists of two spans with a total length of about 125m. To make the foundation of such a structure possible and due to the fact that at the building site the soil profile varies strongly with compressible clay lenses and sand layers with low cone resistance, a ground improvement technique has to be implemented.

2. GROUND IMPROVEMENT TECHNIQUES

The possibilities for implementing ground improvement techniques are dependent on the strongly varying soil profile encountered at this location. In addition, the ground improvement has to be implemented from natural ground level because the slightest excavation could lead to a burtsing of the polder construction. At the middle shoulder of the highway, accessibility also plays a major role in the carrying out the works. Finally, technical requirements such as limited increase in the forces and strains in the foil, risks of damage to the foil, settlements and differential settlement have to be taken into account. A simplified

representation of the assessments that were made regarding the possibilities of implementing soil improvement techniques is presented in table 1.

Table 1: Soil improvement techniques

Accepted techniques	Applicability *1	Constructive *2	Foil *3	Highway *4	Cables & ducts *5	Horizontal drainage*6	Conclusion
Jet grouting	+	+	+	+/-	+/-	-	+
Ground fracturing	+/-	-	+	-	+/-	-	-
Ground grouting (compaction)	+/-	-	+	-	+/-	-	-
Mechanical mixing	-	+/-	+	+/-	+/-	-	+/-

Whereby:

-: poorly applicable, +/-: moderately applicable, +: well applicable;

*1: In strong fluctuating soil profile consisting of clay/peat/loose packed sand;

*2: A bearing capacity of 100 kN/m² has to be achieved;

*3: Ground improvement must be brought to maximum 1 m above the foil because of the risk of damage to the foil;

*4: Because of accessibility/applicability issues in the middle shoulder of the highway, execution using light equipment must be taken into account;

*5/*6: Has to be excavated and derived before the start of the jet grouting.

On the basis of assessment tables, it can be concluded that jet grouting could provide a suitable solution to this challenge.

3. DESIGN ASPECTS

As a result of the jet grouting, the exerted forces are carried deeply below ground level and transferred in the underlying soil. This has for benefit that the bearing capacity of the soil increases and that less compressible soil layers are found under the construction level. The drawback of this construction method is that the stresses in the ground at the foil level are less spread out. Because of the critical function of the foil, it was decided to study this situation further by means of a 3D Finite Element Model (FEM, Plaxis). In the FEM-computations, a soil layer with a thickness of 1 m with variable mechanical properties is schematized above the foil. This variable layer is integrated and varied in the computations as a clay layer to a sand layer. The possibility that a silt layer was formed under the foil during the placing of the foil (under water) has to be taken into account; the thickness of this silt layer is estimated to be about 0,1 m. This variation in the soil conditions has led to four normative combinations which were calculated. The expected settlement at the centre pillar amounts maximal 5 to 6 cm (during 6 years) and at the abutments about 1 cm. The deformations at the centre pillar are given in the graphic in figure 3 below.

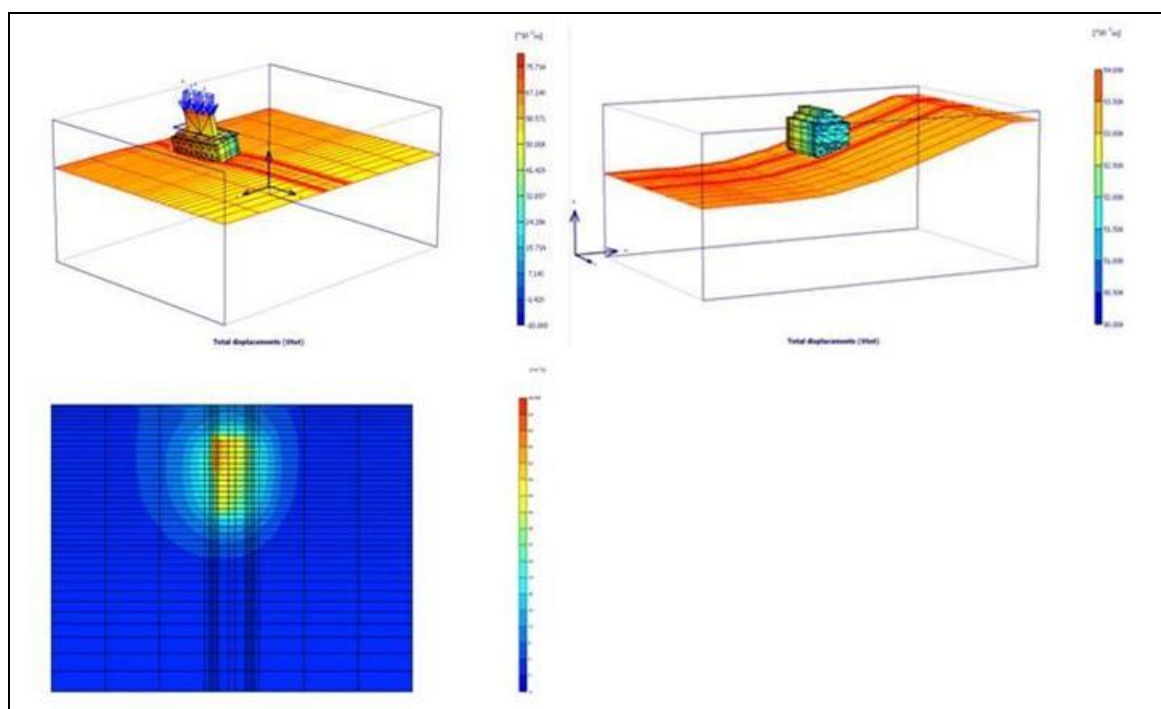


Figure 3: Deformations at the centre pillar and abutment

The results of the computations, give a maximum strain increase under the centre pillar of 4,9% in the ultimate state. For the design, it was decided, in agreement with the Client Rijkswaterstaat, that an increase in strain up to 10% could be acceptable. For the upper structure, a deck with three support points, it is planned that the settlement behavior of the intermediate support will be monitored and that the level of the bearings could be adjusted by means of jacks.

4. JET GROUTING

In the recent years, an extensive experience with jet grouting has been acquired whereby a large data set including values of strength, E-modulus, production parameters (speed of lifting out, rotation, pressure, flow rate, etc.) in relation to the soil type and diameter has been gathered. In the process, one has to make the distinction between one-, two- and three-phase (s) jet grouting, pre- and after cutting, cement content, etc. For the purposes of the intended foundation, the required characteristic compression strength of 100 kN/m^2 is of minor importance because in a similar soil profile consisting of clay and loose packed sand, values for the compression strength of 2000 to 10000 kN/m^2 can be easily obtained. However, the E-modulus deserves special attention because values between 1400 and 1600 kN/m^2 are not easy to achieve, that especially in cohesive ground layers. In order to reach these values, a cement content of about 300 kg/m^3 has to be met. With 2-phases jet grouting (with addition of air), large column diameters can be obtained, but a drawback of this method is that high water overpressures in the soil can be generated. This can lead to settlements by the highway surface and undesirable increase in stresses close to the foil. The process is better manageable by implementing a 1-phase jet grouting but this results in smaller columns diameters. The column diameter in sandy soil reaches about 1,1 to 1,3 m, in cohesive ground types is this usually about 50% less. In the building up of a jet grouting block, it is therefore crucial to control the variation of the columns diameters in the different soil layers and to choose a jet grouting pattern for which possible variations of the columns diameter will have a restricted effect on the risk of too small overlap or shadow working.

5. FROM DESIGN TO JET GROUTING TRIALS

In June 2010, a comprehensive jet grouting trial was carried out at the location of the north abutment. Hereby, 6 individual jet grouting columns and a mini jet grouting block consisting of 4 columns were executed. During this trial, variations of the speed of lifting out, grout composition, jet grouting monitoring and well/not pre-cutting were experimented. Furthermore and among others, in relation with the soil profile, the diameter and variations in diameter of the columns were investigated by using a so-called "column calliper" (see photo 3) en geo-electrical measurements (see figure 4). The geo-electrical

measurement method allows visualising the variation in diameter of the column over its entire height. The measurement methods can be calibrated and compared with one another through excavating the upper section of the columns on completion. In average, it has been found that these measurement methods were quite comparable. Normally, reduced diameters are expected in cohesive soils. This trial showed fairly similar diameters in the clay and the sand layers. This is because the soil at this location was hydraulically sprayed and that the clay especially is barely consolidated. The soils particles haven't developed much cohesion making the soil easy to cut and to mix. Strength and E-modules were determined on samples of the return slurry and the fresh columns (samples retrieved through core borings). The E-modulus from the samples from the core borings amounts to almost 4000 kN/m² with an acceptable 17,5% understepping van 1500 kN/m². This falls within the design tolerances.

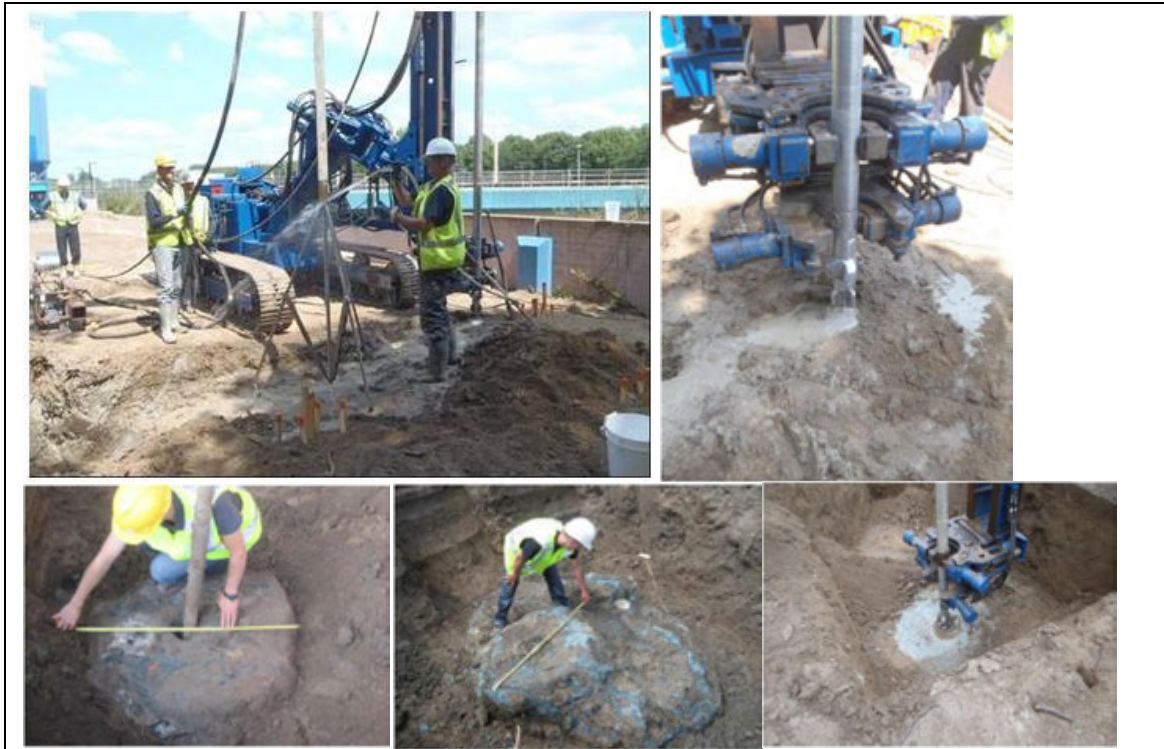


Photo 3: Above: column calliper measurements, beneath: diameter and variations in diameter

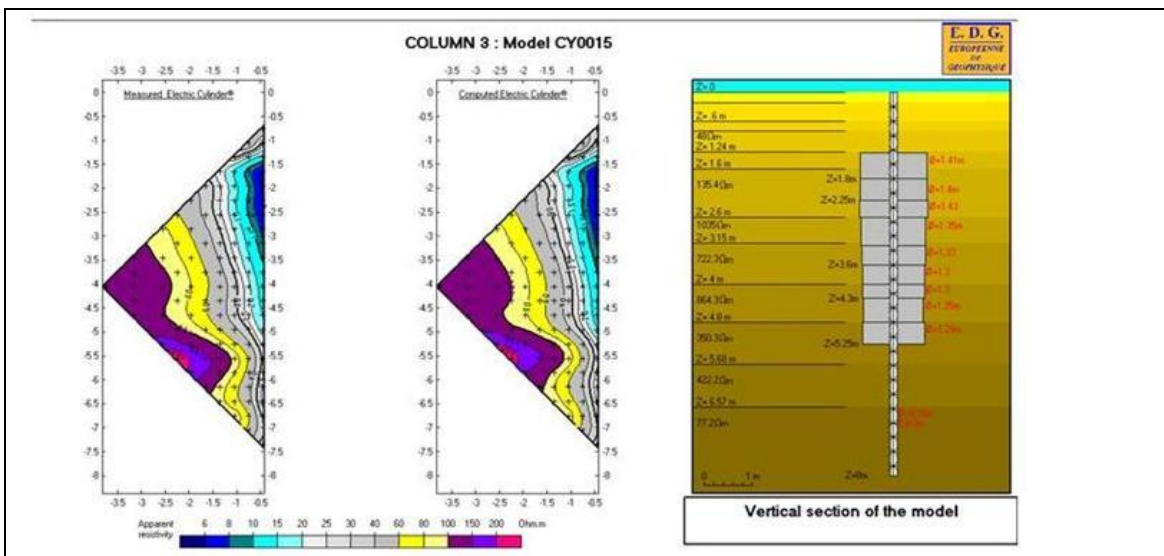


Figure 4: Geo-electrical measurements

6. RISKS

The technical risks regarding the jet grouting process are described and simplified in table 2.

Table 2: Technical risks

Risk/failure	Direct effect	Cause	Management measures
Imperfections in jet grouting block	Settlement too high, bearing capacity insufficient	Jet grouting strength too low, too large variations in jet grouting strength, discontinuities in the jet grouting body	Test columns, control strength properties, limitation of inclusions/holes < 30% (Design jet grouting pattern)
		Missing large volumes of jet grouting (shadow working, faulty borings, etc)	Control measurement implementation, flexible steering during execution
		Too narrow diameters, too large variations	Test columns, diameter in relation to the jet grouting parameters
		Too large deviations in verticality	Limited boring depths, measurement of the inclination (<1%), limitation of the boring velocity, boring with reduced top axial pressure.
Foil	Damage and leaks	Jet pressure, boring too deep, uneven load distribution	Stay 1 m above foil, material restriction on the jet grouting rig, Finite element computations (Plaxis)
Highway	Settlements and heaving of the road surface	Too high water overpressure, pressure build-up in the ground due to clogging of the borehole	1-phase instead 2-phase jet process, visual monitoring flow return slurry, if clogging et grouting process halted directly and clear/pre-cut boreholes
Cables and ducts	Damage, becoming defect	Boring	Excavated, temporarily deviated
Horizontal drainage	Damage, becoming clogged	Boring	Excavated, temporarily deviated

7. EXECUTION

The design is further detailed by the jet grouting contractor VSF. The jet grouting pattern is made up of primary jet grouting columns which are the first to be produced; then the secondary and tertiary (filling) jet grouting columns are executed. The target diameter of the primary and secondary jet grouting columns is set at 1,1 m and for the tertiary columns at about 1,3 m. The columns are executed in a triangular mesh whereby the centre to centre distance between each column is about 0,9 m. The height of the columns varies between 4,04 m and 4,73 m at the centre pillar, 9,95 m to 7,68m at the north abutment and 5,16 m to 6,21 m at the south abutment. Furthermore, the depth of the foil also varies throughout the cross-section. The pattern of the jet grout columns under the abutments en the centre pillar is given in figure 5. Throughout the works, the diameter of the quite a number of primary columns was controlled through the implementation of a column calliper. This was implemented mostly to check the columns diameters in heterogeneous soil profile. At the centre pillar, small adjustments to the execution method of the secondary and tertiary columns were made. The results of the measurements of the column diameters are given in figure 6. After completion of each foundation block, core borings were drilled for product control purposes. An impression of the execution operations at the centre pillar [situated in the middle shoulder of the A27] is given in photo 4.

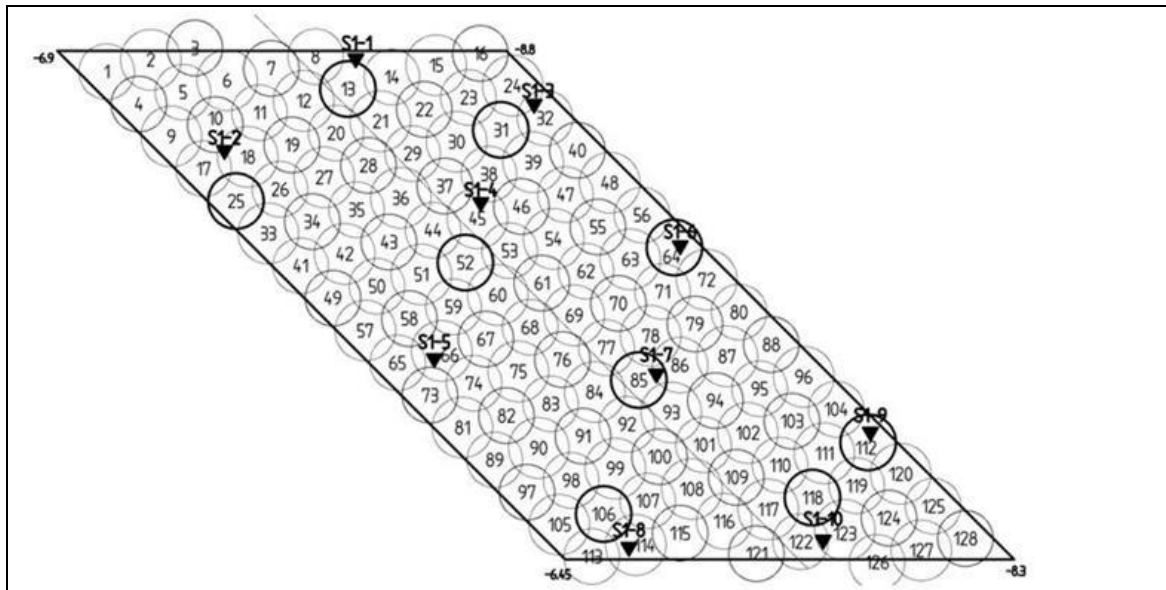


Figure 5: Pattern of the jet grout columns

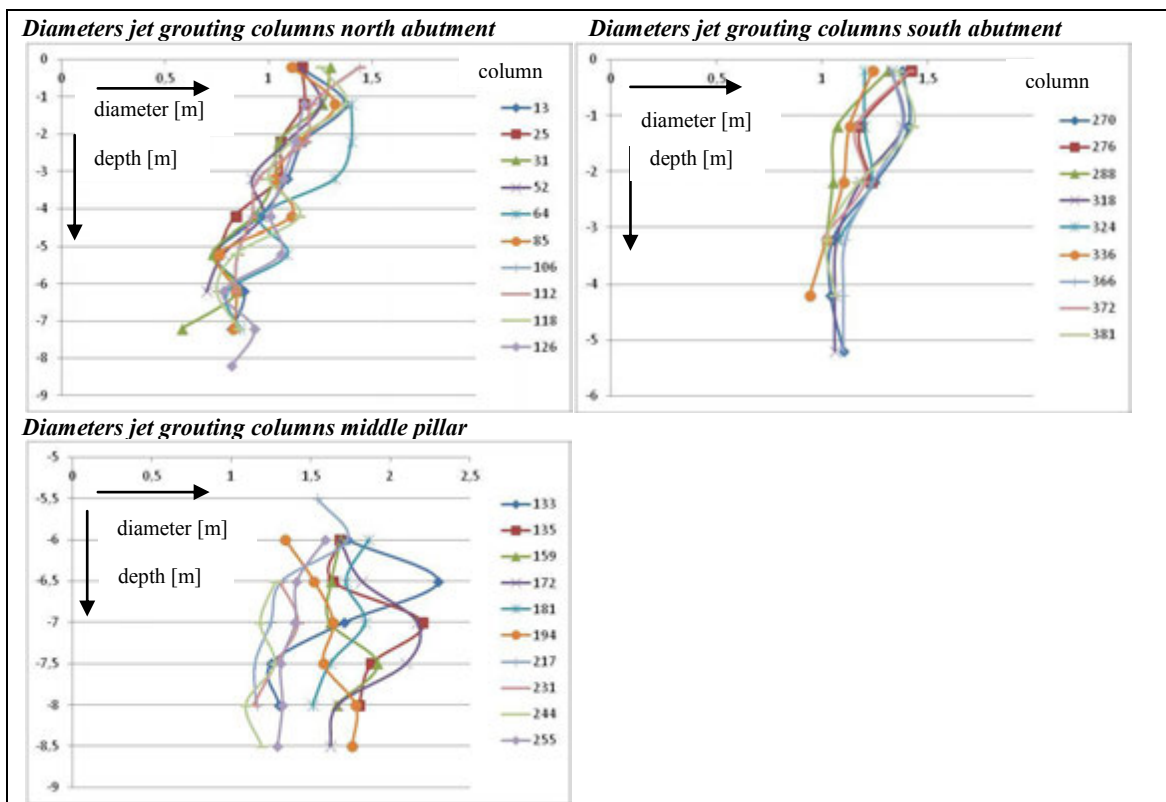


Figure 6: Measurements of the column diameters



Photo 4: An impression of the execution operations at the centre pillar

The implemented and measured parameters are summarized in table 3.

Table 3: Implemented en measured parameters

Implemented parameters	Unit	Primary en secondary jet grouting columns	Tertiary (filling) jet grouting columns
Cement content	kg/m ³	≥ 300	≥ 300
Cement type	-	Blast furnace CEM III B 42,5	42,5
W _{ef} (water/cement factor)	-	0,9	0,9
Speed of lifting out	cm/min	20	20
Pressure	bar	450	480

Measured parameters primary columns		Unit	Average	Standard deviation
Diameter	South abutment	m	1,19	0,13
	North abutment	m	1,03	0,20
	Pillar	m	1,55	0,18

Average values	Compression strength	Fission tension strength	E modulus
	kN/m ²	kN/m ²	kN/m ²
South abutment	15730	2,03	5692
North abutment	21470	2,46	6966
Pillar	9460	1,15	3196

8. CONCLUSION

Altogether, it can be concluded that a special foundation has been build in order to achieve sufficient bearing capacity in a heterogeneous and stirred soil above a foil sealing. Because of the choice of the Client to tackle this work within an integrated team, a partnership between all parties was established allowing the sharing of the knowledge of everyone which led to the achievement of the most optimum result. In a relative short time span, specialists from Movares Nederland BV, Heijmans Beton- en Waterbouw and Volker Staal en Funderingen have modified the original design and executed the works without any damage to the existing structures. At the location of the car overpass across the A27, a ground improvement technique such as jet grouting has proven to be a suitable alternative to execute a foundation above a foil sealing.

REFERENCES

- [1] O.S. Langhorst, G.M. Kaptein, B.J. Admiraal, G.A. van Zwieten, 2012, *Jetgroutfundering viaduct A27 in de polderconstructie van folie te Amelisweerd*, *Geotechniek*, april 2012, blz 22 - 27.
- [2] J.C.W.M. de Wit, P.J. Bogaards, O.S. Langhorst, B.J. Schat, R.D. Essler, J. Maertens, B.K.J. Obladen, C.F. Bosma, J.J. Sleuwaegen, H. Dekker, 2007, *Design and Construction of a metrostation in A'dam, challenging the limits of jetgrouting, Design and validation of validation of jetgrouting for the Central Station A'dam*, 14th European Conference on Soil Mechanics, Madrid.
- [3] B.J. Schat, A. Bots, O.S. Langhorst, 2007, *Innovative retaining wall with jetgrout for new metrotunnel underneath Amsterdam Central Station*, RECT te Toronto.
- [4] J.J. Sleuwaegen, H. Dekker, 2006, *Anwendung des Jetgrout Verfahrens unter dem Hauptbahnhof Amsterdam unter besonderen technischen und geologischen Randbedingungen*, 13e Darmstädter Geotechnik Kolloquium, Grundbautag Technische Universität Darmstadt.
- [5] J.C.W.M. de Wit, P.J. Bogaards, O.S. Langhorst, B.J. Schat, R.D. Essler, J. Maertens, B.K.J. Obladen, C.F. Bosma, J.J. Sleuwaegen, H. Dekker, juli 2006, *Uitvoering van de sandwichwand onder Amsterdam Centraal Station*, *Geotechniek*, nr 3, blz 28-33.
- [6] J.C.W.M. de Wit, P.J. Bogaards, O.S. Langhorst, B.J. Schat, R.D. Essler, J. Maertens, B.K.J. Obladen, C.F. Bosma, J.J. Sleuwaegen, H. Dekker, april 2006, *Ontwerp van de sandwichwand onder Amsterdam Centraal Station*, *Geotechniek*, nr 2, blz 26-31.
- [7] J.M. van Esch, A.F. van Tol, H.R. Havinga, A.M.W. Duijvestijn, B.J. Schat, J.C.W.M. de Wit, 2005, *Funcional analyses of jetgrout bodies base don Monte Carlo simulations*, 11th Int. Conf. On Computer Methods and Advances in Geomechanics, Torino, Italy.
- [8] A.M.W. Duijvestijn en B.J. Schat, 2001, *Een kanaal onder het Centraal*, *cement*, nr 3, blz 41-47.

Injections of microfine cement grouts into sand columns for penetrability and effectiveness evaluation

I.N. Markou, D.N. Christodoulou and A.I. Droudakis
Department of Civil Engineering, Democritus University of Thrace, Greece
imarkou@civil.duth.gr

ABSTRACT

A laboratory investigation was conducted in order to evaluate the influence of parameters pertinent to suspension composition and sand characteristics on the penetrability and effectiveness of microfine cement suspension grouts. Four gradations each from three different types of cement (CEM I, CEM II/B-M and CEM IV/B, according to EN 197-1) were used having nominal maximum grain sizes of 100 μm , 40 μm , 20 μm and 10 μm . The penetrability and effectiveness of cement suspensions with water to cement ratios of 1, 2 and 3 by weight were evaluated by conducting one-dimensional injections into five clean, uniform sand fractions with different grain sizes and into eight composite sands with different gradations, using a specially constructed device. Grouting effectiveness was quantified by conducting unconfined compression and constant head permeability tests on the resulting grouted sand specimens, after curing for 28 days. Microfine cement suspensions can penetrate satisfactorily into medium to fine sands. Penetrability predictions by groutability ratios are not always confirmed by laboratory injections because these criteria do not take into consideration factors, such as water to cement ratio and viscosity, which affect penetrability. Grouted sands obtained unconfined compression strength values of up to 14 MPa and permeability coefficients as low as $1.3 \cdot 10^{-6}$ cm/s or by up to 5 orders of magnitude lower than those of ungrouted sands. Water to cement ratio of cement suspensions and grain size of sands have a substantial contribution to the improvement of both strength and permeability of grouted sands and, therefore, they are considered as the most important of the investigated parameters for grouting effectiveness.

1. INTRODUCTION

The safe construction and operation of many structures frequently requires improvement of the mechanical properties and behavior of soils by permeation grouting using either suspensions or chemical solutions. The former have lower cost and are harmless to the environment but can not be injected into soils with gradations finer than coarse sands. The latter can be injected in fine sands or coarse silts but are more expensive and, some of them pose a health and environmental hazard. The design of structural grouting projects is based, among other factors, on the penetrability of suspensions, since this parameter controls the improvement degree of soil as well as the cost of the project. Therefore, the quantification of suspension penetrability and the investigation of the factors affecting it became the objectives of various research efforts worldwide. Furthermore, improvement of soil properties by means of microfine cement grouting has been practiced in last decades in order to extend the application range of ordinary cement grouts and to reduce the use of harmful chemical solutions. As a result, a number of microfine or ultrafine cements has been developed and manufactured. The behavior and the effectiveness of microfine cements in permeation grouting is also the objective of many ongoing research efforts.

The experimental investigation reported herein is part of an extensive research effort aimed toward the development of relatively fine-grained materials, suitable for permeation grouting, obtained by pulverization of ordinary cements produced in Greece. Scopes of this presentation are: (a) to evaluate the penetrability of suspensions prepared with these new materials, (b) to quantify the improvement of the strength and permeability of sands by grouting with these coarse- and fine-grained cements and, (c) to document the effect of cement type and fineness, suspension water to cement ratio and properties (viscosity or bleeding capacity) and sand grain size, gradation, relative density and degree of saturation prior to grouting, on the penetrability and effectiveness of these cement grouts.

2. MATERIALS

For the purposes of this investigation, three different cement types, each at four different gradations were used. Suspensions of these coarse- and fine-grained cements having water to cement (W/C) ratios of 1, 2 and 3, by weight, were tested. Five uniform, clean sands with different grain sizes were used alone or in various proportions to obtain eight additional soils, with different gradations, for grouting.

2.1. Cements

Three cement types (Portland, Portland – composite and pozzolanic cement), code-named CEM I, CEM II/B-M and CEM IV/B, respectively, according to European Standard EN 197-1, were selected because of production cost differences. The compositions of these cements are presented in Table 1 both in terms of oxides and in terms of the raw materials used for their production. The amount of clinker used for the production of the CEM I cement is significantly higher in comparison to the other cements which are more pozzolanic. The chemical analysis of the cements (Table 1) reflects the anticipated differences in oxide composition according to cement type.

Each ordinary cement was pulverized, using a special laboratory mill, to produce three additional cements with nominal maximum grain sizes (d_{max}) of 40 μm , 20 μm and 10 μm . Characteristic grain sizes and Blaine specific surface values for all cements are presented in Table 2. In terms of gradation, all cements with nominal $d_{max} = 10 \mu\text{m}$ can be considered as “microfine” since they satisfy the requirements of Standard EN 12715 ($d_{95} < 20 \mu\text{m}$ and specific surface over 800 m^2/kg) as well as definitions adopted by ISRM, ACI Committee 552 and PCA (Henn and Soule 2010). Also, cements with nominal $d_{max} = 20 \mu\text{m}$ have adequately small characteristic grain sizes to be considered, marginally, as “microfine”.

Table 1: Composition of cements.

Oxides (%)	Cement Type			Components (%)	Cement Type		
	I	II/B-M	IV/B		I	II/B-M	IV/B
SiO ₂	19.38	26.67	29.99	Clinker	90.3	63	58
Al ₂ O ₃	4.28	7.46	11.22				
Fe ₂ O ₃	3.24	4.30	3.83				
CaO	64.11	49.37	47.92	Pozzolan	0	13.5	20
MgO	3.43	3.54	2.14	Fly ash	0	10	18
SO ₃	3.09	3.07	2.60				
other	1.29	1.96	2.43	Limestone	4.7	8.5	2
LOI	3.73	6.06	2.56	Gypsum	5	5	2

Table 2: Gradation of cements.

Grain Sizes	Cement Type											
	CEM I				CEM II/B-M				CEM IV/B			
Specific Surface												
d_{max}^* (μm)	100	40	20	10	100	40	20	10	100	40	20	10
d_{95} (μm)	57.0	22.5	11.5	8.2	45.5	25.8	13.6	9.1	48.0	26.0	12.8	9.8
d_{50} (μm)	16.6	8.6	4.2	3.2	14.0	9.4	5.8	4.2	14.2	9.3	4.4	3.9
d_{10} (μm)	3.0	2.0	1.2	1.0	2.2	2.0	1.4	1.1	3.0	2.2	1.3	1.2
Blaine (m^2/kg)	384	529	710	920	466	591	735	942	452	582	715	923

* Nominal maximum cement grain size

2.2. Suspensions

All suspensions tested during this investigation, were prepared using potable water since it is considered appropriate for preparing cement-based suspension grouts. The suspension W/C ratio was set equal to 1, 2 and 3 by weight, in order to test both stable and unstable suspensions in terms of bleed capacity. A superplasticizer (patented new generation of admixture based on polycarboxylate chemistry), at a dosage of 1.4 % by weight of dry cement, was used to improve the suspension properties of the pulverized cements. The same dosage was applied to all cement suspensions, without optimizing the dosage for each specific suspension. All suspensions were prepared using high speed mixers, of the type used for the preparation of soil specimens for hydrometer testing, with a speed of 10000 rpm at no load. As recommended by the superplasticizer producer, the appropriate amount of cement and 70% of the required water were placed in the mixer together with the superplasticizer dosage and mixed for 5 min. Then, the rest of the water was added and mixing continued for another 5 min. The properties of suspensions were evaluated in terms of bleeding capacity, viscosity, setting times, early strength development by conducting pocket penetrometer tests and unconfined compression strength. The values of suspension properties presented in Table 3, indicate that microfine cement ($d_{max} = 20 \mu\text{m}$ and 10 μm) suspensions enhanced with superplasticizer can be used in permeation grouting for soil improvement.

Table 3: Properties of ordinary and microfine cement suspensions.

Cement		W/C Ratio	Apparent Viscosity* (cP)	Bleeding Capacity (%)	Setting Times (hours)		Early Strength# (hours)	Unconfined Compression Strength ^s (MPa)
Type	d _{max} (μm)				Initial	Final		
CEM I	100	1	86	29	5	8	7	13.1
		2	16	59	5	9	8	7.1
		3	9	68	6	11	10	4.6
	20	1	21	0	6	8	8	6.5
		2	6	37	7	9	10	1.8
		3	4	46	8	11	11	1.9
CEM II/B-M	100	1	220	16	9	14	13	9.0
		2	39	50	9	18	17	3.9
		3	17	64	10	37	18	2.7
	20	1	53	2	5	8	8	10.6
		2	12	35	7	12	13	2.8
		3	3	49	8	19	16	1.6
	10	1	114	2	4	6	6	9.7
		2	30	19	5	8	11	3.6
		3	5	38	6	8	12	1.5
CEM IV/B	100	1	160	27	9	17	18	11.4
		2	23	53	12	21	22	3.6
		3	10	65	14	25	25	2.5
	20	1	168	1	8	10	10	7.0
		2	8	26	15	> 48	46	2.5
		3	5	42	15	26	36	1.5

* Obtained at t = 30 min with viscometer rotation speed = 60 rpm

Time needed for pocket penetrometer strength value = 450 kPa

^s Specimen curing time = 28 days

2.3. Sands

A limestone sand with angular grains was used for the preparation of two types of soils, utilized for penetrability and effectiveness evaluation. With appropriate treatment (washing and sieving), five clean, uniform sand fractions (type I sands) with grain sizes limited between sieve sizes (ASTM E11) Nos. 5 and 10, 10 and 14, 14 and 25, 25 and 50, and 50 and 100, were produced. The properties of sand fractions, designated using the aforementioned sieve Nos., are presented in Table 4. Permeability coefficient values of the sands were obtained from constant head permeability tests in dense and loose specimens. Summarized in Table 5 are the compositions, selected gradation characteristics and permeability coefficient values (dense specimens) of the composite (type II) sands, prepared with the above-mentioned sand fractions. It can be observed that type II sands have different uniformity coefficients, which are also higher than the ones of type I sands (Table 4), and were tested in order to investigate the effect of sand gradation on the penetrability and effectiveness of microfine cement grouting.

The resulting eight composite sands are divided into four 5-50 and four 5-100 sands with grain sizes limited between sieve sizes (ASTM E11) Nos. 5 and 50, and 5 and 100, respectively, and grain size distributions presented in Figure 1. More specifically, 5-50 (1) and 5-100 (1) sands were prepared by mixing successive sand fractions in equal proportions and, as a result, they attained smoother gradations

Table 4: Properties of sand fractions.

Sand Fraction	Grain Size Limits (mm)	d ₁₅ (mm)	Uniformity Coefficient	Specific Gravity	Void Ratios		Permeability Coefficient ^s (cm/s)	
					e _{min}	e _{max}		
5-10	4.00 – 2.00	2.25	1.40	2.71	0.66	1.06	4.1*10 ⁰	2.3*10 ⁰
10-14	2.00 – 1.40	1.48	1.19	2.72	0.67	1.03	1.8*10 ⁰	8.0*10 ⁻¹
14-25	1.40 – 0.71	0.80	1.43	2.72	0.67	1.07	5.3*10 ⁻¹	2.2*10 ⁻¹
25-50	0.71 – 0.30	0.36	1.56	2.70	0.70	1.06	8.5*10 ⁻²	4.0*10 ⁻²
50-100	0.30 – 0.15	0.17	1.43	2.72	0.72	1.12	2.9*10 ⁻²	1.3*10 ⁻²

^s Left column: sands in loose condition (D_r = 32%), Right column: sands in dense condition (D_r = 96%)

Table 5: Composition and properties of composite sands.

Sand Designation	Contained Sand Fractions (%)					d_{15} (mm)	C_u	Permeability Coefficient ^s (cm/s)
	5-10	10-14	14-25	25-50	50-100			
5-50 (1)	25.0	25.0	25.0	25.0	0.0	0.50	3.77	$5.3 \cdot 10^{-1}$
5-50 (2)	26.7	26.7	26.7	20.0	0.0	0.57	3.63	$2.1 \cdot 10^{-1}$
5-50 (3)	28.3	28.3	28.3	15.0	0.0	0.71	3.26	$6.1 \cdot 10^{-1}$
5-50 (4)	30.0	30.0	30.0	10.0	0.0	0.79	2.51	$8.5 \cdot 10^{-1}$
5-100 (1)	20.0	20.0	20.0	20.0	20.0	0.25	6.67	$5.7 \cdot 10^{-2}$
5-100 (2)	26.7	26.7	26.7	10.0	10.0	0.46	5.57	$1.4 \cdot 10^{-1}$
5-100 (3)	28.3	28.3	28.3	7.5	7.5	0.71	4.33	$2.5 \cdot 10^{-1}$
5-100 (4)	30.0	30.0	30.0	5.0	5.0	0.80	2.51	$3.6 \cdot 10^{-1}$

^s Sands in dense condition ($D_r = 93\%$)

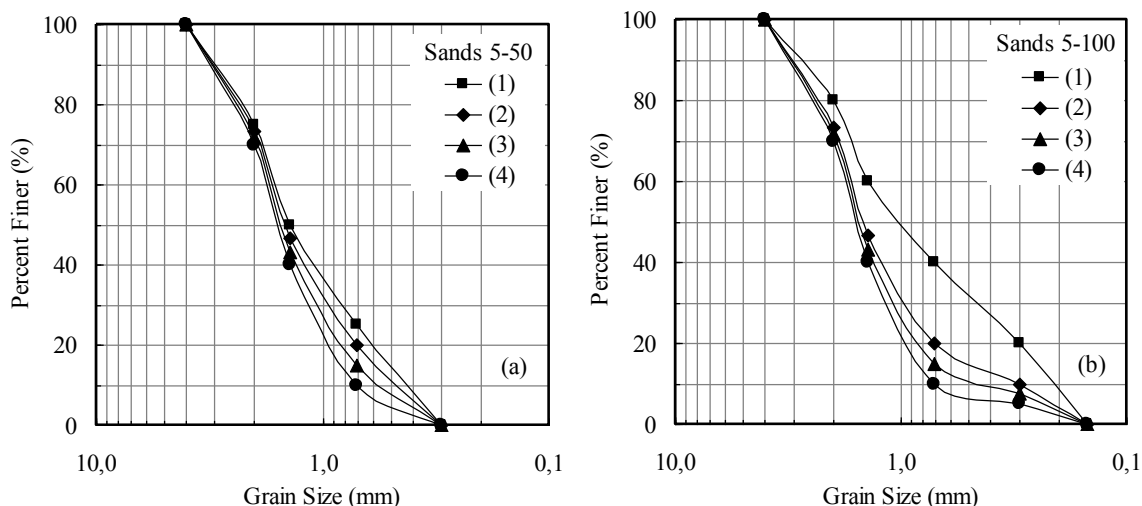


Figure 1: Grain size distributions of composite sands.

compared to the other equivalent sands (Figure 1). All the other composite sands were produced using a basic sand, easily groutable with microfine cement suspensions (5-25 sand), which was modified with the addition of a “tail” in three alternative total percentages (10%, 15% and 20%), containing all sand fractions (if more than one required) in equal proportions. For example, 5-100 (3) sand consists of 5-25 basic sand (containing equal proportions of sand fractions 5-10, 10-14 and 14-25) and 25-100 “tail” (containing equal proportions of sand fractions 25-50 and 50-100) in overall percentages of 85% and 15%, respectively. The term “tail” is derived from the gradation shape of these sands, which, as it is shown more clearly in Figure 1b, can be idealized as bilinear with a coarser portion represented by the basic sand and a finer portion represented by the “tail”. All sands were grouted in dense condition (mean value of relative density, D_r , $98 \pm 1\%$) and were dry prior to grouting. Sand 25-50 was also grouted in loose condition ($D_r = 41\%$) or was saturated prior to grouting in order to evaluate the effect of sand relative density and degree of saturation on the penetrability and effectiveness of microfine cement grouting.

3. EXPERIMENTAL PROCEDURES

The special apparatus shown in Figure 2a was used for injecting sand columns with cement suspensions. It allows for adequate laboratory simulation of the injection process, investigation of the influence of the distance from injection point on the properties of grouted sand, and evaluation of grout penetrability. The grouting column was made of PVC tube with an internal diameter of 7.5 cm and a height of 144 cm. Injection was stopped when either the volume of the injected grout was equal to two void volumes of the sand in the column or when the injection pressure became equal to 700 kPa. After curing for 28 days, the grouted columns were cut in alternating lengths of 16 cm and 9 cm. The resulting specimens with a length of 16 cm were tested in unconfined compression at an axial strain rate equal to 0.05 %/min. The specimens with a length of 9 cm were utilized for constant head permeability testing under water pressures ranging from 10 kPa to 200 kPa, using the specially constructed apparatus shown in Figure 2b, which allows for simultaneous, independent testing of two grouted sand specimens in their PVC tubes.

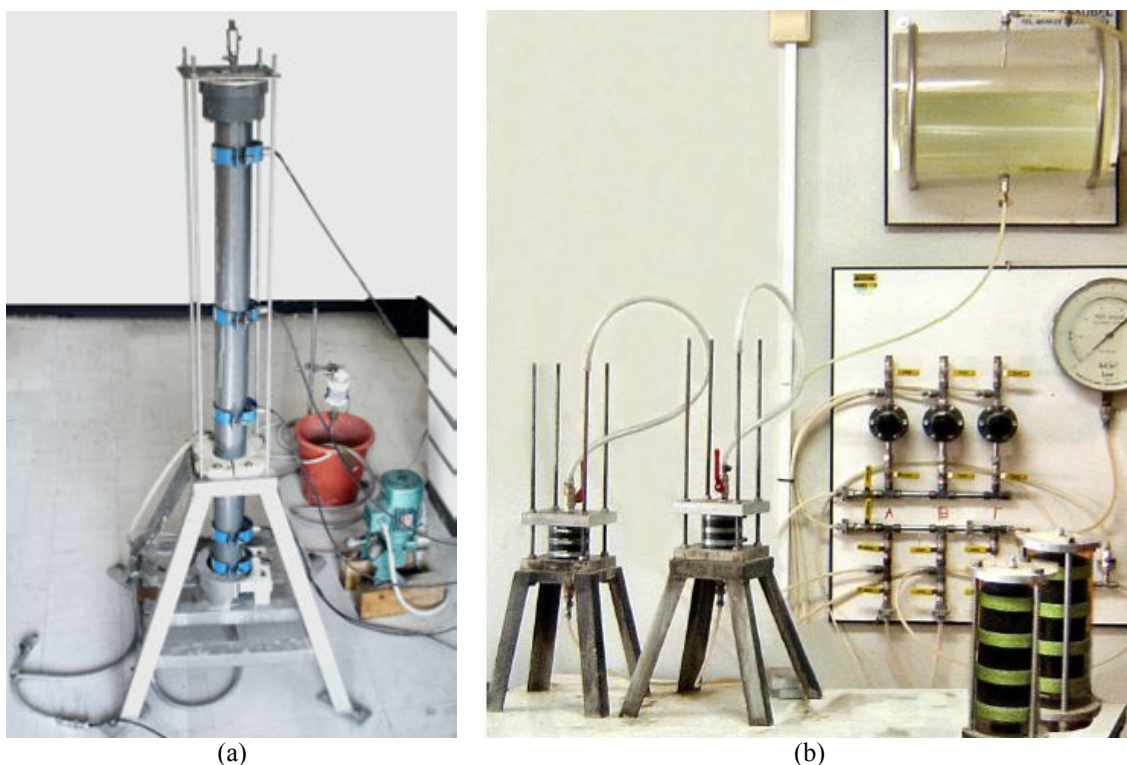


Figure 2: Laboratory equipment (a) for grouting sand columns and, (b) for the determination of permeability coefficient of grouted sands.

4. PENETRABILITY

The term “penetrability” was selected in the present research to describe qualitatively the permeation distance of a grout into the voids of a given soil that can be achieved under a predetermined maximum injection pressure. The results of the laboratory injections were characterized as “very good” when the predetermined quantity of grout (two void volumes of the sand column) was injected with a possible increase of grouting pressure, as “moderate” when the volume of injected grout was much less than the predetermined quantity and grout penetration length was higher than 60 cm under the maximum applied pressure (700 kPa), and as “poor” when grout penetration length was lower than 60 cm under the maximum applied pressure of 700 kPa. A preliminary evaluation of groutability was also made using as criteria the “groutability ratios” (Mitchell 1981) which are defined as $N_1 = (d_{15})_{\text{soil}} : (d_{85})_{\text{grout}}$ and $N_2 = (d_{10})_{\text{soil}} : (d_{95})_{\text{grout}}$. Grouting is considered possible if $N_1 > 25$ and $N_2 > 11$ and not possible if $N_1 < 11$ or $N_2 < 6$. If $N_1 \geq 50$, satisfactory permeation can be achieved.

Presented in Figure 3a are the results obtained from the penetrability tests together with the corresponding groutability ratio values, N_1 , for all cements, W/C ratios and sand fractions used in this investigation. For different cement types of the same d_{max} injected into a specific sand, small differences are obtained for the groutability ratio values which are due to differences in the d_{85} values of the cements. It can be observed that penetrability was “very good” in coarse sands, regardless of the W/C ratio of the suspensions. Penetrability in medium sands was, generally, “very good” for cement suspensions with groutability ratios $N_1 > 25$. The medium-to-fine sands were grouted satisfactorily with cement suspensions having, generally, $N_1 > 25$ and W/C=2 or 3. Penetration in fine sands was negligible for any cement suspension used. The effect of cement type on penetrability was not significant. In terms of observed performance, cement types I and II/B-M are rated as about equivalent and slightly superior to cement type IV/B. Values of the N_2 groutability ratio are presented in Figure 3b together with the results obtained from the same penetrability tests. For the cases investigated, predictions based on $N_2 > 11$ criterion are optimistic relative to those obtained by applying the $N_1 > 25$ criterion. As shown in Figure 3b, a “modified” criterion according to which grouting is considered possible if $N_2 > 22$, presents comparable prediction efficiency to the $N_1 > 25$ criterion (Figure 3a).

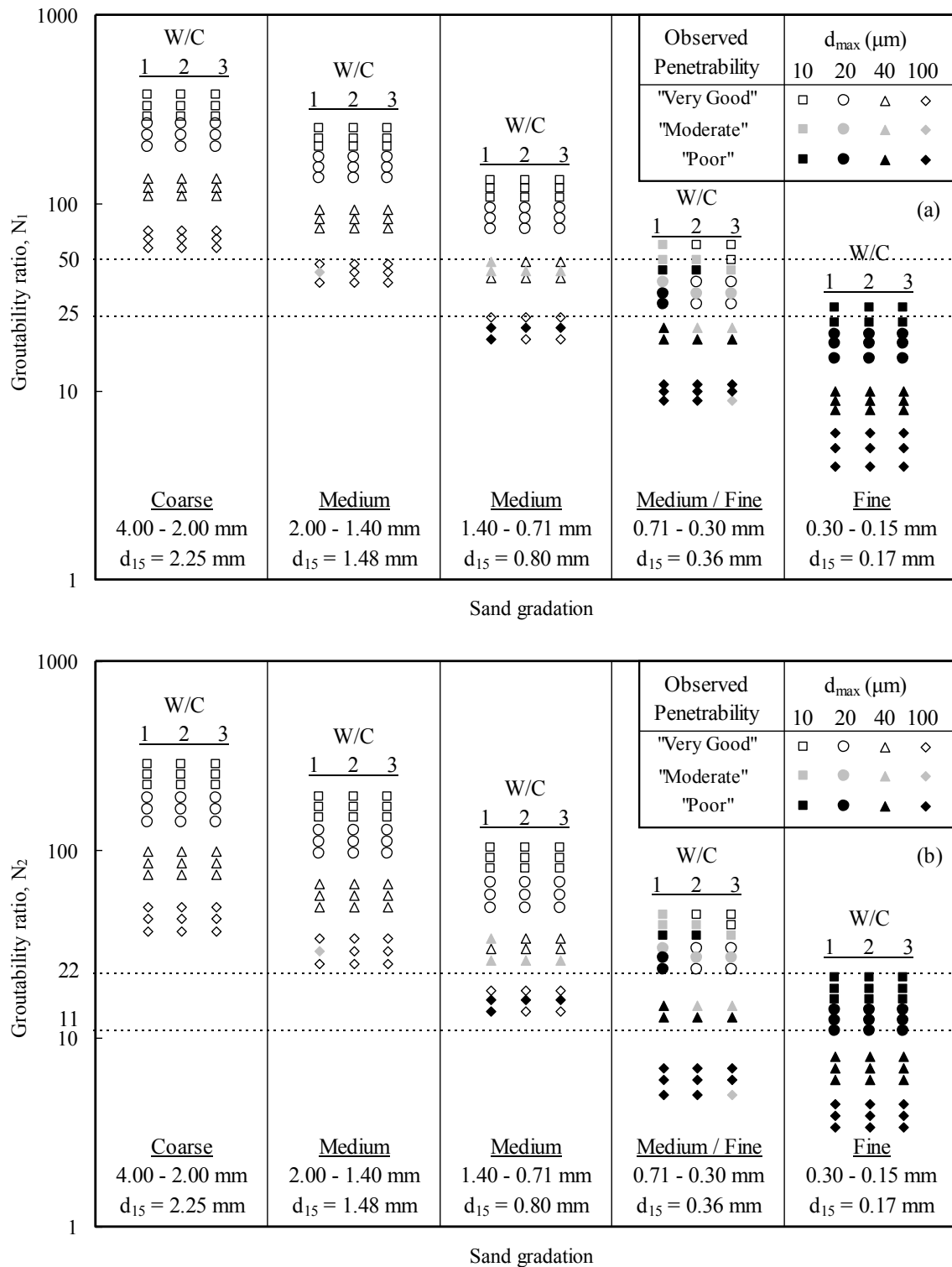


Figure 3: Effect of grout composition and sand grain size on the penetrability of cement grouts.

Table 6: Effect of sand relative density and degree of saturation on the penetrability and effectiveness of microfne cement grout.

Sand Fraction	Relative Density (%)	Degree of Saturation (%)	Maximum Pressure (kPa)	Penetration Length (cm)	Unconfined Compression Strength (MPa)	Permeability Coefficient (cm/s)
25-50	98	0	> 700	83	2.04	$2.1 \cdot 10^{-5}$
25-50	41	0	113	> 134	2.10	$2.6 \cdot 10^{-5}$
25-50	98	100	35	> 134	1.34	$1.2 \cdot 10^{-5}$

Table 7: Effect of sand gradation on the penetrability and effectiveness of microfine cement grout.

Composite Sand	Groutability Ratio Values		Void Ratio	Maximum Pressure (kPa)	Penetration Length (cm)	Unconfined Compression Strength (MPa)	Permeability Coefficient (cm/s)
	N ₁	N ₂					
5-50 (1)	66	47	0.52	131	> 134	1.41	2.8*10 ⁻⁵
5-50 (2)	75	51	0.50	583	> 134	2.92	3.0*10 ⁻⁵
5-50 (3)	93	58	0.51	177	> 134	1.54	3.5*10 ⁻⁵
5-50 (4)	104	78	0.55	68	> 134	0.88	3.7*10 ⁻⁵
5-100 (1)	33	23	0.41	> 700	75	4.26	2.4*10 ⁻⁴
5-100 (2)	61	33	0.47	> 700	90	2.43	1.8*10 ⁻⁵
5-100 (3)	93	44	0.50	> 700	> 134	1.89	2.1*10 ⁻⁵
5-100 (4)	105	78	0.53	60	> 134	1.88	1.9*10 ⁻⁵

For tests with the medium / fine sand ($d_{15} = 0.36$ mm) twelve different cement gradations were tested, with groutability ratio, N_1 , values ranging between 9 and 60 indicating the full range of possible predictions on the basis of this ratio. As shown in Figure 3a, the performance of the three suspensions of the original cements having nominal d_{max} of 100 μ m and yielding N_1 values between 9 and 11 was accurately predicted by the N_1 criterion. Suspensions of the three different cements with nominal d_{max} of 40 μ m have corresponding N_1 values 19, 19 and 22 which are in the range of 11 to 25 where the N_1 criterion suggests some positive possibility for grouting. The experimental results indicate moderate penetrability only for suspensions of the type I cement with W/C ratios equal to 2 and 3, where a relatively high N_1 value (22) was combined with low apparent viscosity values (2.2 cP and 1.6 cP, respectively) at preparation. Grouting with suspensions having nominal d_{max} of 20 μ m and 10 μ m should be possible according to the groutability criterion since $34 \leq N_1 \leq 60$. However, this was not always confirmed for the cases of suspensions with W/C = 1 which had an apparent viscosity value at the time of preparation ranging from 23 to 180 cP. Conditions were improved when the W/C ratio was increased to 2 yielding apparent viscosity values between 3 and 17 cP and even further improved for suspensions with W/C = 3 (apparent viscosity between 2 and 5.4 cP). This information indicates that although predictions based on the groutability ratio, N_1 , values and observations from laboratory injection tests are, mostly, in agreement, for a number of cases, these predictions are rather optimistic and are not confirmed experimentally. Similar prediction inefficiency has been documented in available literature (i.e. Zebovitz et al. 1989; De Paoli et al. 1992; Akbulut and Saglamer 2002) and is attributed to the fact that groutability ratios are based solely on characteristic grain sizes of grout and soil and do not take into consideration factors, such as W/C ratio and viscosity, which have an effect on penetrability.

The effect of sand relative density and degree of saturation prior to grouting was investigated by injecting the same suspension (cement: II/B-M, $d_{max} = 10$ μ m and W/C = 2) into initially dry 25-50 sand columns in dense ($D_r = 98\%$) or loose ($D_r = 41\%$) condition and into an initially saturated 25-50 sand column in dense condition. By comparing the relevant results presented in Table 6, it can be observed that the “moderate” penetrability obtained in dense and dry sand is turned into a “very good” one by reducing sand relative density or by saturating the sand prior to grouting. The improvement of penetrability due to the decrease of sand compaction degree has also been reported by other researchers (Akbulut and Saglamer 2002). The positive effect of sand saturation prior to grouting on the penetrability can be attributed to the absorption of a quantity of suspension water from the dry sand grains (Perret et al. 1997) leading to a decrease of suspension W/C ratio during injection into initially dry sand. The results obtained by injecting suspension of II/B-M cement with $d_{max} = 10$ μ m and W/C = 2 into dense and dry composite sand columns, are summarized in Table 7 and are, generally, in agreement with groutability ratio predictions. In 5-50 sands, although the modification in sand gradation has not affected penetration length, it has induced an increase of maximum injection pressure due to the decrease of sand void ratio. In 5-100 sands, the reduction of the proportion of 25-50 and 50-100 sand fractions (Table 5) has generated an improvement in suspension penetrability. This improvement results by taking into consideration both maximum injection pressure and penetration length and is attributed to the increase of sand void ratio (Table 7).

5. EFFECTIVENESS

The effect of cement type on the strength of grouted sand is quantified in terms of the unconfined compression strength ratio, defined as the ratio of the unconfined compression strengths of equivalent sand specimens, grouted with corresponding suspensions of different cement types. The results presented in Figure 4a, indicate a strength increase due to grouting with CEM I suspensions. The other two cement types give comparable but inferior results. The superiority of CEM I suspensions expands with increasing

W/C ratio of the grouts and can be attributed to the composition of the cements, since CEM I is a pure Portland cement consisting of a larger proportion of clinker in comparison with the other two cement types and does not contain pozzolanic materials (Table 1).

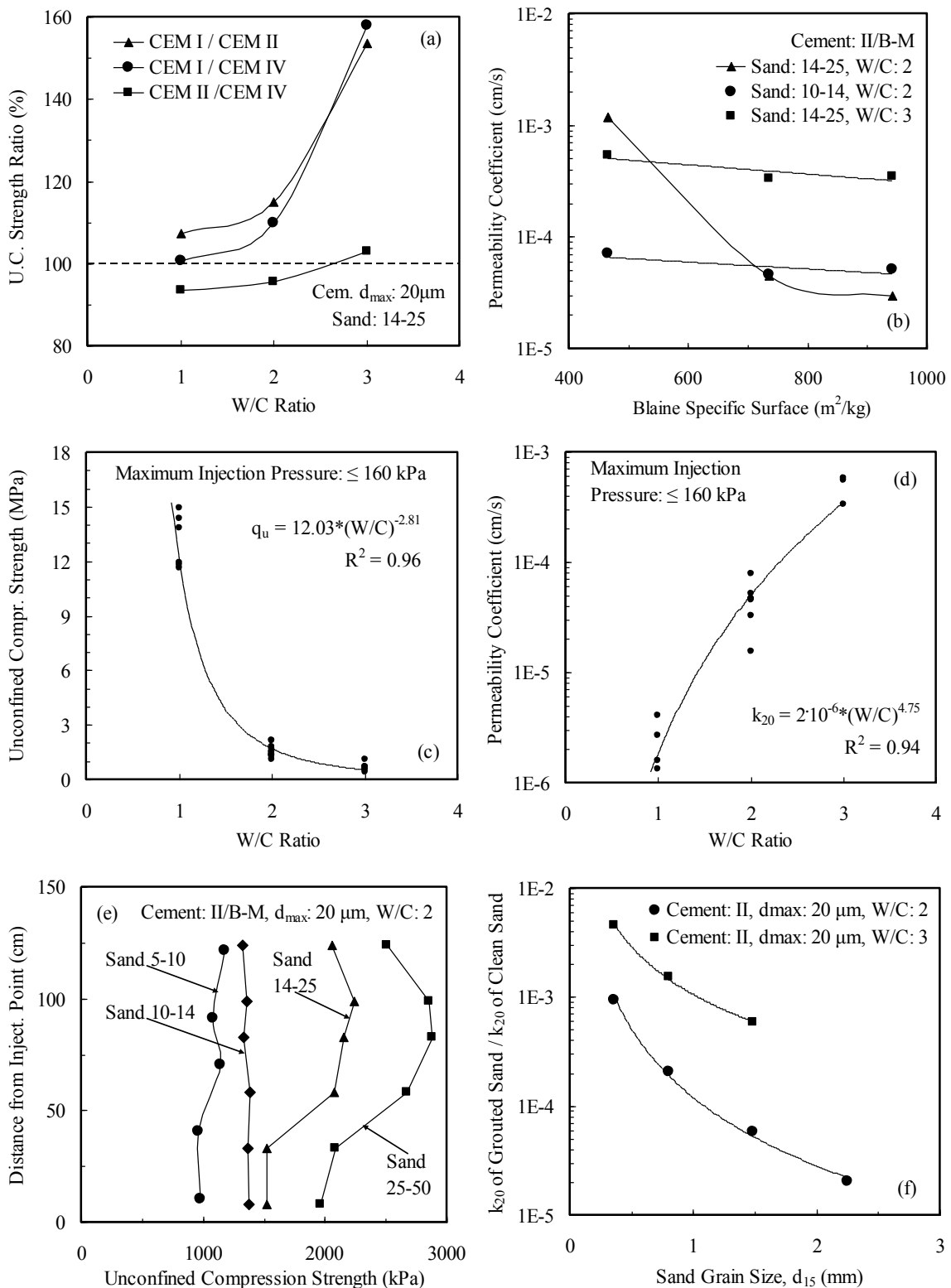


Figure 4: Effect of grout composition and sand grain size on the effectiveness of microfine cement grouts.

Table 8: Range of strength and permeability values of grouted sands in relation to suspension W/C ratio.

W/C Ratio	Unconfined Compression Strength (MPa)		Permeability Coefficient (cm/s)		Permeability Reduction (Orders of magnitude)	
	min	max	min	max	min	max
1	7.20	13.73	$1.3 \cdot 10^{-6}$	$8.5 \cdot 10^{-5}$	4	5
2	1.07	2.86	$1.1 \cdot 10^{-5}$	$7.2 \cdot 10^{-4}$	3	5
3	0.51	1.61	$1.7 \cdot 10^{-4}$	$1.4 \cdot 10^{-3}$	2	4

The effect of cement fineness, expressed as Blaine specific surface, on the permeability of sands grouted with CEM II/B-M suspensions, is shown in Figure 4b. It can be observed that permeability coefficient values decrease with increasing cement Blaine specific surface, in agreement with the observations of other researchers (De Paoli et al. 1992; Shibata 1996). The effect of cement fineness on the permeability of grouted sands is attributed to the lower bleeding capacity (total proportion of the volume of bleed water to the initial volume of suspension) of microfine cement suspensions (Table 3) which leads to the more effective filling of sand voids with grout solids. This justification is confirmed by the results of the present investigation since it was verified that permeability coefficient values of grouted sands decrease with decreasing bleeding capacity of the suspensions used in the injections (Markou and Droudakis 2011). Therefore, it is evident that the mechanism of permeability reduction is based on the reduction rate of soil voids induced by grouting, as it has also been stated by other researchers (Krizek and Helal 1992; Schwarz and Chirumalla 2007). On the contrary, the unconfined compression strength of grouted sands is not affected by cement fineness. It is known (De Paoli et al. 1992; Shibata 1996) that use of microfine cements can lead to higher unconfined compression strength values of grouted soil in comparison with ordinary Portland cements. This observation was not verified by the findings of the present research, possibly due to the high W/C ratios (equal to 2 and 3) of the suspensions used. However, it must be stated that suspensions with W/C ratio equal to 1 were not used because, in the case of cements with $d_{\max} = 100 \mu\text{m}$, they may present poor penetrability in 14-25 sand (Figure 3).

The results of permeability and unconfined compression tests conducted on specimens obtained from cement grouted sand columns, after curing for 28 days, are summarized in Table 8 in relation to W/C ratio of the suspensions. Unconfined compression strength of grouted sand increases and permeability coefficient of grouted sand decreases with decreasing W/C ratio of the suspensions and, as indicated in Figures 4c and 4d, respectively, a good correlation exists between unconfined compression strength or permeability coefficient of grouted sands and W/C ratio of suspensions, for sand columns grouted with relatively low injection pressures. The equation resulting from the correlation of unconfined compression strength with W/C ratio (Figure 4c), is of the same form with the one developed by Dano et al. (2004). As shown in Table 8, the permeability coefficient of sands grouted with suspensions of W/C ratio equal to 1 can be as low as $1.3 \cdot 10^{-6}$ cm/s indicating an improvement (reduction) of sand permeability by 4 to 5 orders of magnitude. The permeability reduction attained with these suspensions is by 1 to 2 orders of magnitude higher than the ones achieved using suspensions with W/C ratios equal to 2 and 3. The unconfined compression strength of sands grouted with suspensions of W/C ratio equal to 1 ranged from 7.2 MPa to 13.7 MPa and is generally up to 7 and up to 20 times higher than the ones obtained using suspensions with W/C ratios equal to 2 and 3, respectively. The ranges of strength and permeability values of grouted sands presented in Table 8 are in good agreement with values found in the literature for cement grouted soils (e.g. Zebovitz et al. 1989; De Paoli et al. 1992; Krizek and Helal 1992; Dano et al. 2004; Schwarz and Chirumalla 2007). Thus, the end effect of grouting with the suspensions used in this investigation is comparable to that obtained by grouting with other ordinary or microfine cement suspensions.

As shown in Figure 4e, the unconfined compression strength of grouted sand increases with decreasing sand grain size. This observation is attributed to the increased number of grain-to-grain contact points in a finer soil and, as a result, to the increased number of points available for cementation (Zebovitz et al. 1989). Although the permeability of grouted sand decreases with decreasing sand grain size in agreement with the results of other researchers (e.g. Zebovitz et al. 1989; Dano et al. 2004; Schwarz and Krizek 2006), the observed differences are considered as low since they, generally, do not exceed half an order of magnitude. Consequently, the ratio of permeability coefficient of grouted sand to the one of clean sand decreases with increasing grain size of the sand (Figure 4f) indicating a higher permeability improvement (reduction) as the grain size of sand increases.

The unconfined compression strength and permeability coefficient values of grouted, dense and loose 25-50 sands are compared in Table 6. As reported in available literature (Akbulut and Saglamer 2002; Dano et al. 2004), the relative density of sand has a minor effect on the unconfined compression strength of

grouted sand. This statement is verified from the results of present research (Table 6), not only for unconfined compression strength but also for permeability coefficient of grouted sand. The effect of degree of saturation of sand prior to grouting was investigated by injecting the same suspension into initially dry or saturated 25-50 sand columns, both in dense condition. By comparing the relevant results presented in Table 6, it can be stated that the degree of saturation of sand prior to grouting has an insignificant effect on grouted sand permeability. On the contrary, the unconfined compression strength of initially dry grouted sand is by 52% higher than the strength of initially saturated grouted sand, possibly due to the suspension compression as a result of the high injection pressure (> 700 kPa) and/or the absorption of a quantity of suspension water from the dry sand grains (Perret et al. 1997) leading to a decrease of suspension W/C ratio during injection into initially dry sand. The unconfined compression strength and permeability coefficient values of grouted, composite sands are summarized in Table 7. It can be observed that the effect of sand gradation on grouted sand permeability is not significant. The unconfined compression strength of grouted 5-50 sands (comparable penetration lengths) increases possibly due to the increase of suspension compression resulting from the increase of injection pressures.

6. CONCLUSIONS

Based on the results obtained and the observations made during this experimental investigation and within the limitations of the range of parameters investigated, the following conclusions can be advanced:

- The use of microfine cements, produced by grinding of common cements, improves the penetrability of cement suspensions rendering them effective for grouting of medium to fine sands. Suspension penetrability is also improved by increasing W/C ratio, decreasing viscosity, reducing sand relative density or saturating the sand prior to grouting and is affected by sand gradation.
- Predictions of penetrability based on the groutability ratio, N_1 , values and observations from laboratory injection tests are, mostly, in agreement, while predictions based on the groutability ratio, N_2 , values are rather optimistic and, usually, are not confirmed experimentally. Therefore, a “modified” criterion based on the groutability ratio, N_2 , values is proposed since it presents comparable prediction efficiency to the equivalent criterion based on the groutability ratio, N_1 , values.
- Unconfined compression strength of grouted sand increases when CEM I (pure Portland cement) suspensions are used, with decreasing suspension W/C ratio and sand grain size and when the sand is dry prior to grouting, is affected by sand gradation and is not affected by sand relative density.
- Grouted sand permeability decreases with increasing cement fineness, with decreasing suspension W/C ratio and bleeding capacity and is not affected by sand relative density, saturation degree prior to grouting and gradation. Permeability reduction increases with increasing grain size of the sand.
- Good correlations were found between unconfined compression strength or permeability coefficient of grouted sands and W/C ratio of suspensions, for sand columns grouted with low injection pressures.
- Unconfined compression strength values of grouted sands ranging from 7 MPa to 14 MPa and satisfactory reduction (4 to 5 orders of magnitude) of the permeability of sands can be obtained by grouting with cement suspensions having W/C ratio = 1.

7. ACKNOWLEDGEMENTS

The research effort reported herein is part of the research project (PENED-03ED527) which was co-financed by the E.U. – European Social Fund (75%) and the Greek Ministry of Development – GSRT (25%). The contribution of TITAN Cement Company S.A. was substantial for the selection, chemical analysis, pulverization and grain size analysis of the cements.

REFERENCES

- Akbulut, S. & Saglamer, A. 2002. *Estimating the groutability of granular soils: a new approach. Tunnelling and Underground Space Technology* 17: 371–380.
- Dano, C., Hicher, P.Y. & Tailliez, S. 2004. *Engineering properties of grouted sands. J. Geotech. & Geoenv. Engrg.* 130: 328–338.
- De Paoli, B., Bosco, B., Granata, R. & Bruce, D. 1992. *Fundamental observations on cement based grouts (2): Microfine cements and the Cemill^R process. Proc., Conf. on Grouting, Soil Improvement & Geosynthetics, New Orleans, ASCE, GSP No. 30, Vol. 1, 486–499.*
- Henn, R.W. & Soule, N.C. 2010. *Ultrafine cement in pressure grouting. ASCE Press, Reston, Virginia.*

Krizek, R.J. & Helal, M. 1992. Anisotropic behavior of cement grouted sand. *Proc., Conf. on Grouting, Soil Improvement & Geosynthetics, New Orleans, ASCE, GSP No. 30, Vol. 1, 541–550.*

Markou, I.N. & Droudakis, A.I. 2011. Effectiveness of microfine cement suspension grouting. *Proc., 15th ECSMGE, Athens, IOS Press, Vol. 1, 223–228.*

Mitchell, J.K. 1981. Soil improvement – state of the art report. *Proc., 10th ICSMFE, Stockholm, A.A. Balkema, Vol. 4, 509–565.*

Perret, S., Ballivy, G., Khayat, K. & Mnif, T. 1997. Injectability of fine sand with cement-based grout. *Proc., Conf. on Grouting: Compaction–Remediation–Testing, Logan, ASCE, GSP No. 66, 289–305.*

Schwarz, L.G. & Chirumalla, M. 2007. Effect of injection pressure on permeability and strength of microfine cement grouted sand. *Proc., Geo-Denver 2007, Denver, ASCE, GSP No. 168.*

Schwarz, L.G. & Krizek, R.J. 2006. Hydrocarbon residuals and containment in microfine cement grouted sand. *J. of Materials in Civil Engrg. 18: 214–228.*

Shibata, H. 1996. Study on long – term strength properties of suspension grouts with ultra-fine-grain materials. *Proc., Conf. on Grouting & Deep Mixing, Tokyo, A.A. Balkema, Vol. 1, 71–76.*

Zebovitz, S., Krizek, R. & Atmatzidis, D. 1989. Injection of fine sands with very fine cement grout. *J. Geotech. Engrg. 115: 1717–1733.*

Ground Improvement Solutions for the new Cruise Terminal in Lisbon

Alexandre Pinto, JetSJ Geotecnia Lda. – Portugal, geral@jetsj.pt,
Rui Tomásio, JetSJ Geotecnia Lda., Portugal
João Ravasco, Somague Engenharia S.A., Portugal

ABSTRACT

The “Terreiro do Trigo” dockyard, at the “Jardim do Tabaco”, was filled in order to allow the construction of the new “Santa Apolónia” Cruise Terminal in Lisbon, at the Tagus River right bank. A load transfer platform (LTP), founded over jet grouting columns, allowed the construction of a 4,2m height embankment, placed over a soft muddy alluvium layer (undrained shear stress lesser than 20kPa) with about 20m of average thickness. Vertical and horizontal full scale load tests were performed in order to assess the possibility to incorporate the jet grouting columns, reinforced with steel micropiles, as foundation solution for the new Cruise Terminal building. The design and execution criteria of the jet grouting columns, including the quality control and quality assurance, are presented, as well as the main results of the adopted monitoring and survey plan. The main results of the full scale load tests are pointed out. Finally, the technical and economic advantages of the adopted solutions, comparing with some more conventional ones, are presented.

1. INTRODUCTION

The first prize in International Competition for the Cruise Terminal in Lisbon, launched by the Lisbon Port Administration (APL), was attributed to the Portuguese architect João Luís Carrilho da Graça. The jury also distinguished the proposals by other architects such as Aires Mateus and Gonçalo Byrne, William Vazquez Consuegra, ARX Portugal and Zaha Hadid. The creation of the new “Santa Apolónia” Cruise Terminal provides the opportunity to address the interstitial space between the city and river. Designed from the architectural point of view as a simple volume that responds to the “desire of liberating the surrounding area”, the new Terminal will create a new public realm providing green spaces that can support varying activities for the city and adjacent neighbourhoods. One of the key points of the proposal was the maintenance of the existing dock’s structure, reaffirming its memory by keeping the void space and recovering the surrounding centenary masonry walls. The building of the new Terminal is a simple and compact design solution. The building is assumed towards the park and the city as a pavilion, an overflow system. It appears to be a floating volume, as it is broken, generating tension zones and inflections that suggest entry and exit points for the building. The building is wrapped by a series of paths which provide a mean to slowing “discovery of the surroundings while passing through the different facades. The path ends at the roof which assumes the features of a stage, relating with the river and the city without any obstacles (figures 1 and 2).



Figure 1: Site location and perspective of the new Cruise Terminal.

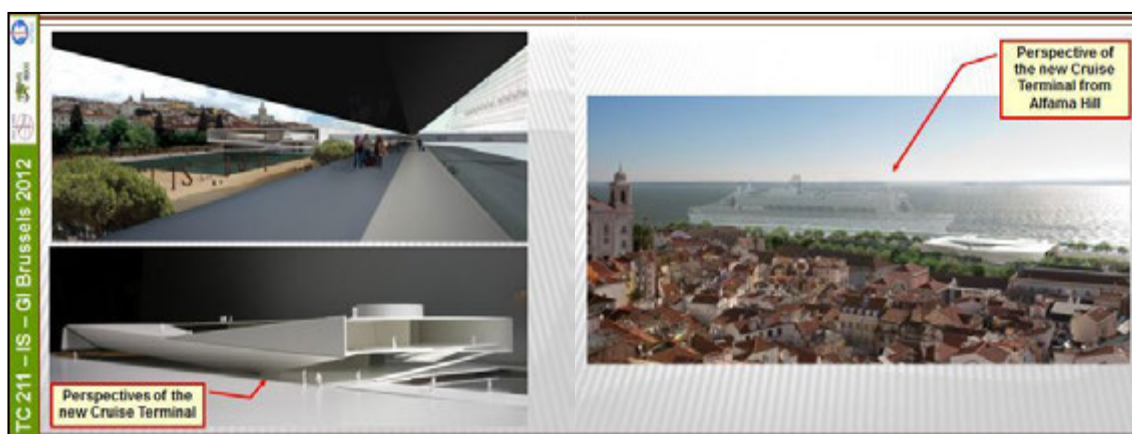


Figure 2: Perspectives of the new Cruise Terminal.

From the geotechnical and geological point of view, the new Cruise Terminal will be located on a complex zone, at the Tagus River right bank, demanding the use of versatile and flexible solutions, as for instance jet grouting and micropiles, for the filling of the “Terreiro do Trigo” dockyard, as well as for the refurbishment and underpinning of the centenary masonry walls. Taking account the described scenario in this paper is mainly presented the case of a load transfer platform foundation, where the jet grouting technology was applied with success on very complex conditions.

2. LTP FOR THE NEW CRUISE TERMINAL IN LISBON

2.1. Introduction

As already stated, jet grouting columns were used as solution for the foundation of the LTP under the fill of the “Terreiro do Trigo” dockyard, including the closing and refurbishment of the “Jardim do Tabaco” centenary quay walls, at the Tagus River right bank in Lisbon. A landfill with an area of about 290x56m² and 4,2m height, over soft alluvium soils (mud with Cu lesser than 20KPa) with about 20m of average depth, resting over the Miocene, was built with the purpose to allow the construction of the new Lisbon Cruise Terminal. Other main issues were the preservation of the stability of the adjacent old buildings and infrastructures, as well as the centenary quay walls integrity, including the compatibility with the new deck built over bored piles in the river, allowing the operation of big ships. In order to resist to the new landfill earth pressures and to confine the soft soils under the fill, the quay walls were previously refurbished and the dockyard gate previously closed (figure 3).



Figure 3: View of the dockyard before the filling works.

2.2. Adopted solutions for the landfill foundations

Taking into account the existent conditions, mainly the complex working area, as well as the works overall schedule (24 months), the landfill was built over a LTP, located also over jet grouting $\varnothing 1,5\text{m}$ columns on a $5,7 \times 5,7\text{m}^2$ mesh, used as both ground improvement and foundation solution, installed during low tide. Due to durability reasons, pozolanic cement was adopted, with a ratio of about 550kg/m^3 , in order to obtain an Unconfined Compression Strength (UCS) of about $3,7\text{MPa}$ and a Young Modulus of 1GPa . The LTP was formed by two layers of biaxial polypropylene geogrids (20 and 30kN/m of tension resistance) located under two layers of granular material. Due to the LTP level, below the high tide water level at the Tagus River, the jet grouting and geogrids works were performed only during low tide water level (figure 4).

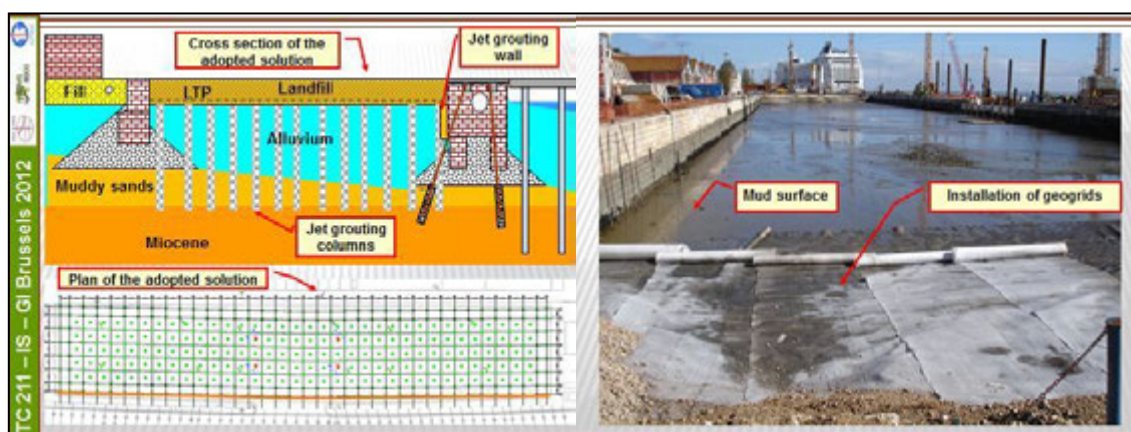


Figure 4: Adopted solution and view of the geogrids installation works.

2.3. Adopted solutions for the quay walls refurbishment and underpinning

The masonry centenary quay walls were previously refurbished and underpinned using inclined tubular self-drilling steel micropiles, capped by a grillage of reinforced concrete beams and slabs. In order to optimize its overall length, the self-drilling micropiles were sealed inside $\varnothing 0,6\text{m}$ jet grouting columns. The dockyard gate, with about 40m length, was also previously closed using a sheet pile wall, as well as bored piles, both capped by a reinforced concrete slab (figures 5 and 6). Those works, together with a jet grouting wall, $\varnothing 1,2\text{m}$ columns spaced $1,0\text{m}$, built at the quay wall internal face, allowed the previous horizontal confinement of the alluvium materials inside the dockyard. This confinement effect allowed also the decrease of the tides water level amplitude inside the dockyard, leading to the increase of the earth and jet grouting works performance.

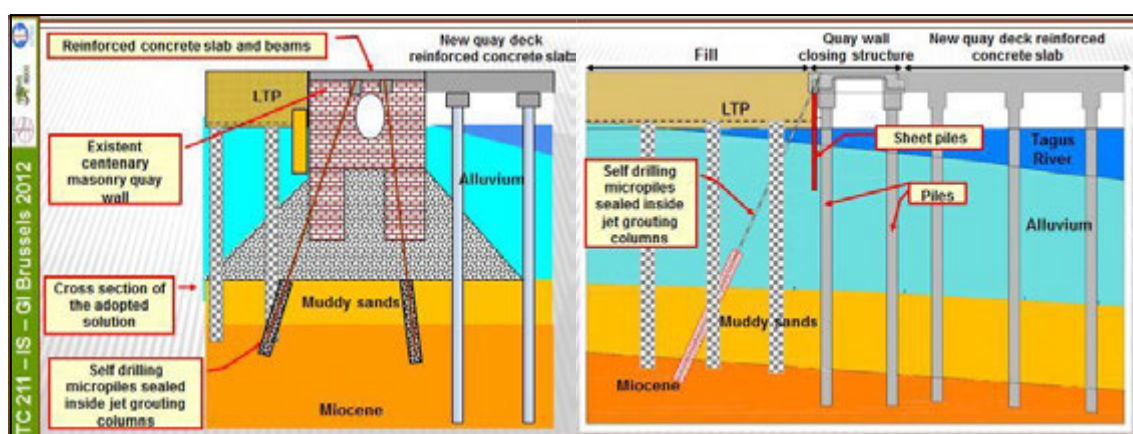


Figure 5: Quay wall refurbishment cross section and closing dockyard gate structure.



Figure 6: Quay wall underpinning and refurbishment works.

2.4. Design

For the design of the adopted solution a 3D FEM analysis was carried out, using Plaxis software. The maximum estimated vertical displacements at the top of the fill, after the conclusion of the earth works, were about 76mm. During the construction of the LTP and the landfill the maximum vertical displacements obtained at the topographic marks were about 350mm (figure 7).

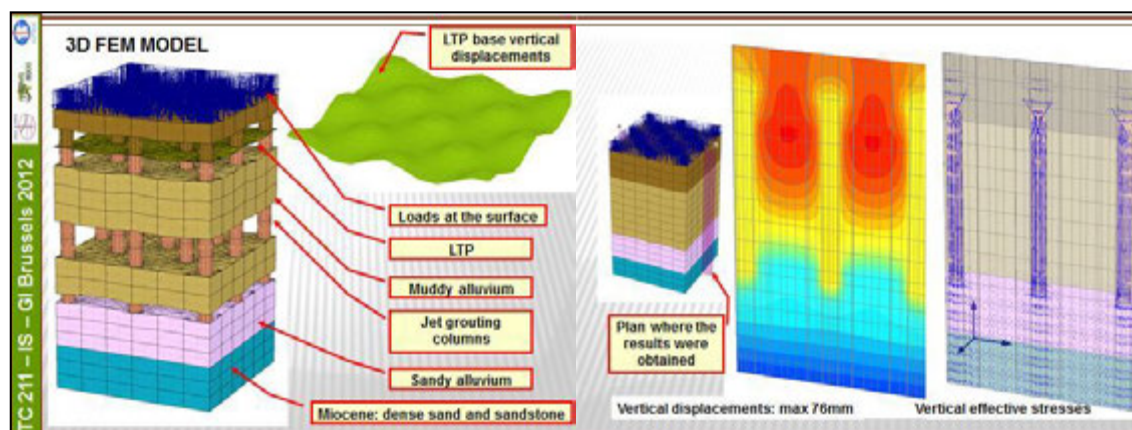


Figure 7: Adopted 3D FEM model and vertical displacements and stresses.

2.5. Monitoring and survey

The solution overall performance was assessed through a monitoring and survey plan during and after the jet grouting and earth works. The monitoring and survey plan comprised the installation of topographic marks at the landfill base, as well as rod extensometers at the LTP geogrids and pressure cells at the jet grouting columns head (figures 8 and 9). According to the analysis of the instrumentation devices it was possible to conclude that, in spite of the jet grouting columns had been design to resist to all the loads due to the landfill weight (3,7MPa of UCS), the majority of those loads was directly transferred to the mud and only after to the jet grouting columns shaft at a small depth, similar to half the distance between the columns, approximately 3m. The consolidation effect due to this situation was very small and occurred mainly during the construction phase, as the loaded mud layer was only 3m thickness and the mud overall bearing capacity increased also due to the 3D confinement effect, which could be explained by the following frontiers:

- a) At the top of the mud: due to the upper landfill;
- b) At the base of the mud: due to the Miocene layer;
- c) Horizontally: due to both jet grouting columns and peripheral quay and retaining walls.

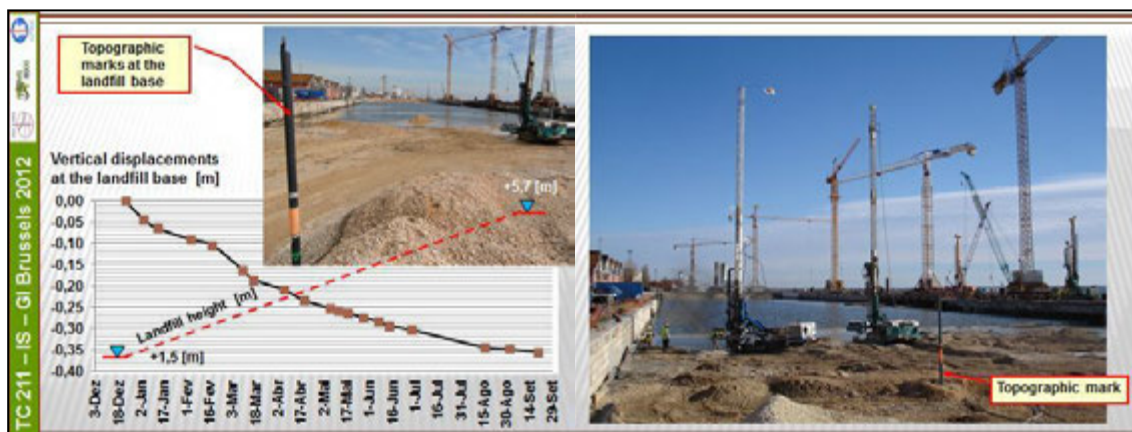


Figure 8: Topographic marks readings and view of a topographic mark.

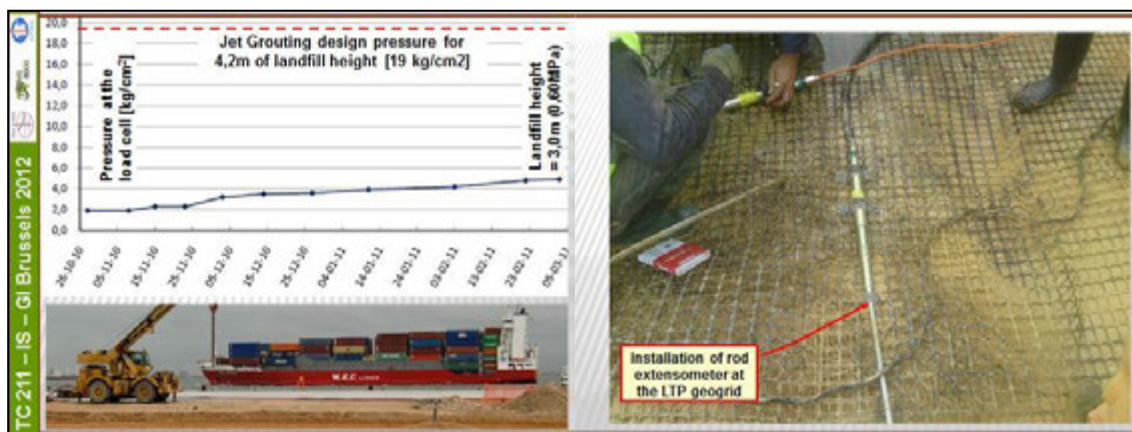


Figure 9: Pressure load cells readings and installation of rod extensometers.

2.6. Quality control and quality assurance

The execution of the jet grouting columns was also complemented by a tight quality control and quality assurance, allowing the confirmation of the resistance, deformability and geometry of the columns. For this purpose, test columns were built and full length cores from test and final columns were collected in order to access geometry and to perform laboratorial tests, mainly UCS and Young Modulus, at different ages. During the execution of the jet grouting columns a permanent registration of all the adopted parameters was also performed, allowing to confirm the columns overall length, mainly the columns toe at the Miocene sandstones and dense sands (figure 10).



Figure 10: Quality control and quality assurance of the jet grouting columns: core samples and parameters registration (LT3).

In spite of the very difficult conditions (figure 11), the adopted solutions allowed the fulfilment of all the main objectives: technical (low deformations at the landfill platform and at the neighbourhood structures and infrastructures) and control of both costs and construction schedule, confirming the good performance of the solution.



Figure 11: Views of the complex works inside the dockyard.

The adopted solution was tested with full scale vertical and horizontal load tests in order to confirm and calibrate their inclusion on the foundations solution of the new Cruise Terminal building. For this purpose, the jet grouting columns located under the building columns and walls will be reinforced with steel tubular micropiles in order to resist to about 2.500kN of axial service load, and capped by a stiff raft. The building structural mesh will be adapted to the jet grouting columns mesh. The results of the full scale load tests confirmed the possibility to include the jet grouting columns on the new Cruise Terminal building foundations due to its vertical and horizontal resistance and stiffness (figures 12, 13, 14 and 15).



Figure 12: Vertical full scale load test: reaction structure and load applying system.



Figure 13: Vertical full scale load test: main results.



Figure 14: Horizontal full scale load test: reaction structure and load applying system.

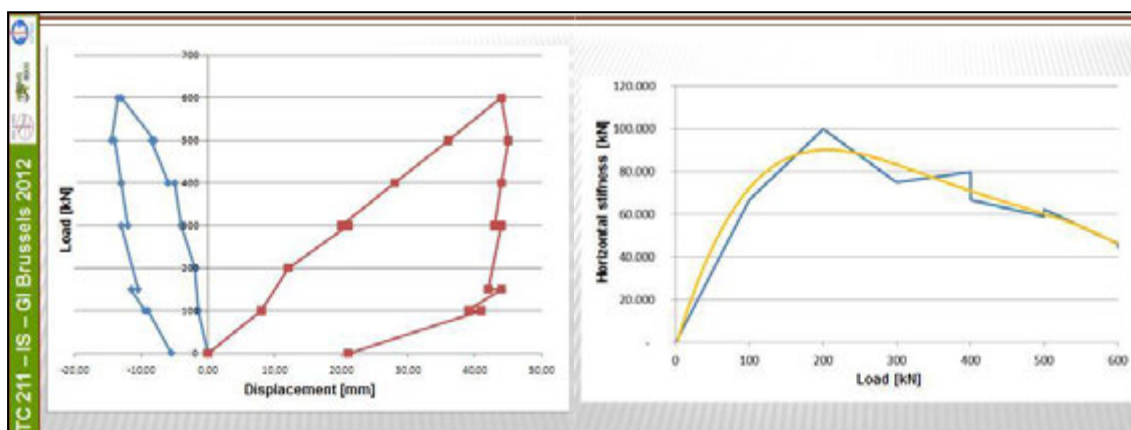


Figure 15: Horizontal full scale load test: main results.

2.7. Alternative solutions

It should also be stated that the adopted solution for the ground improvement of the landfill foundation was designed as an alternative to an initial stone columns solution, leading to the induced consolidation of the muddy soils, which would increase the vertical deformations to about 1,5m, including possible severe damages to the sensitive neighbourhood buildings and infrastructures, mainly the centenary quay walls, a water supply pipe \varnothing 1,0m and the Metro tunnel (figure 16).

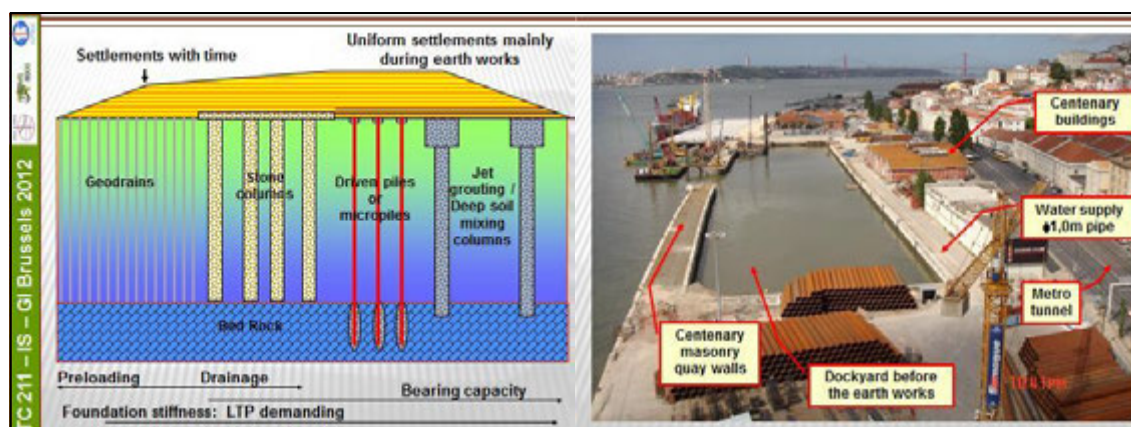


Figure 16: Differences between ground improvement solutions and dockyard neighbourhood conditions.

3. MAIN CONCLUSIONS

Taking into account the presented case history and comparing, it is possible to point out the following advantages of the jet grouting solutions, already stated by Pinto et al. (2011, 2009, 2007 and 2005):

- Possibility to be applied to almost every kind of soils, with low vibration, low-noise and strong but local ground perturbation;
- Small dimension and small weight of the jet grouting equipment, leading to big versatility, allowing the use of the technology on very complex scenarios;
- The ground is improved, using an hydraulic process, in order to be integrated on the final engineering solution with both economic and environmental advantages;
- The confinement effect on soft soils leads to the minimization of differential and total settlements, occurring mainly during the construction phases;
- No need for pre loading on soft soils. The consolidation effects are small and occur, in the majority of the situations, only very close from the surface and during the construction phase;
- Possibility to reinforce the columns with steel profiles, in order to better resist to shear and tension efforts due to bending moments, shear and tension loads, as well as to facilitate the connection to the stiffer capping and structural elements, as for instance slabs or beams;
- Complete execution control due to the sophisticated equipment, allowing in real time the assessment and correction of the main execution parameters.

As main limitations of the jet grouting technology, comparing with some more conventional solutions, the following ones could be point out:

- Production of spoil, which could however be reused or integrated on the earth works;
- Very demanding quality control and quality assurance, as happens with the majority of the ground improvement techniques.

The presented case history of ground treatment for foundations can be considered as an example how the jet grouting technology can be used on wide and complex geological and geotechnical scenarios, proving its technical and economic advantages, as well as the importance of the execution control on site, before and during the construction of the final elements.

4. ACKNOWLEDGMENTS

The authors thank to the Owner of the described case history, Lisbon Port Administration (APL), its permission for the writing and presentation of this paper. The presented works were successfully performed by a general contractor group, including: Somague, SETH and OFM. The geotechnical works were performed by Hagen (micropiles and jet grouting) and Teixeira Duarte (bored piles). The supervision was done by TPF – Planege. The main design, including the new quay deck over bored piles, was developed by WW and STA.

REFERENCES

Simon, B. (2009). "Projet national de recherche et développement. Amélioration des sols par inclusions verticales rigides." *Travaux n°862*, pp. 65-72.

Pinto, A.; Tomásio, R.; Ravasco, J.; Marques, G. (2011) "Fill of the Terreiro do Trigo Dockyard in Lisbon over Alluvial and Hard Soils". *15th European Conference on Soil Mechanics and Geotechnical Engineering, September 2011, Athens, Greece, Part 2 – 3.1 – Shallow Foundations*, pp. 787 – 792.

Pinto, A.; Pereira, A.; Cardoso, D.; Sá, J. (2009). "Ground Improvement solutions at Sana Vasco da Gama Royal Hotel". *17th International Conference on Soil Mechanics and Geotechnical Engineering, Alexandria, Egypt, Volume 3 - 4A - Ground Improvement, Grouting and Dredging*, pp. 2180 – 2183.

Pinto, A.; Tomásio, R.; Cruz, S.; Carvalho, B. (2007). "Special Foundations for an Urban Viaduct in Lisbon." *14th European Conference on Soil Mechanics and Geotechnical Engineering, September 2007, Madrid, Spain*, pp. 475 – 480.

Pinto, A.; Falcão, J.; Pinto, F.; Melo Ribeiro, J. (2005). "Ground Improvement Solutions using Jet Grouting Columns." *16th International Conference on Soil Mechanics and Geotechnical Engineering, September 2005, Osaka, Japan*, pp. 1249 – 1252.

Analysis of soil solidification with the help of “jet grouting” method when constructing a municipal collector

A.B. Ponomaryov, Perm National Research Polytechnic University, Russia, andreyfab@mail.ru
A.L. Novodzinsky, Perm National Research Polytechnic University, Russia,
A.V. Zakharov, Perm National Research Polytechnic University, Russia,

ABSTRACT

The emergency analysis when sinking the shaft of the main municipal collector in the city of Perm is considered. For groundwater protection and engineering service lines maintenance in the course of construction, the use of a watertight diaphragm made from secant soil-cement piles by “jet-grouting” method was provided. To analyze this situation additional engineering-geological survey and numerical simulation of the collector using PLAXIS 2D and PLAXIS 3D Foundation software packages were carried out. As a result, the cause of the emergency situation was determined. The soil and hydrological conditions and construction methods used for this project were analyzed.

1. BRIEF DESCRIPTION OF THE PROBLEM HEADING

In accordance with the development plan of the city of Perm the construction work of the main discharge manifold is being done. The geological structure in this area of work to a depth of 41 m is represented by the deposits of Ufa stage of the Upper Permian formation which consist of argillite, sandstone, and rarely of siltstone. They are overlapped by a thick layer of quaternary alluvial-diluvial deposits represented by loam of various consistency – from fluid to solid, with interlayer’s and lenses of sand, clay sand and gravel ground at the bottom. The bedrock was uncovered at the depths of 15.2 – 17.5 m. Filled-up ground occurred from the surface to the depths of 1.4 – 2.0 m.

Groundwater was found in alluvial-diluvial clay deposits, in alluvial sand and gravel ground and the Upper Permian deposits. In the upper part of the quaternary section ground water was attributed to very soft and fluid loam with the filtration coefficient of 0.012 m /day. Ground water level was 2.2 – 4.1 m from the surface. Tight-plastic loam was as a waterproof layer . Groundwater was of free-flow and fed by atmospheric precipitation and leakage from service lines. Groundwater in gravel and sand soil is sporadic and confined to the lenses of gravel and sand soil, which lie at the base of Quaternary deposits. The main source of supply is atmospheric precipitation, groundwater of the Upper Permian deposits. Water is pressured. Pressure head reaches 11m. The average permeability coefficient for gravel soil is 9.05 m / day. Groundwater of the Upper Permian deposits is confined to argillite and sandstone, which are characterized by various degrees of weathering and fracturing. Practically the entire exposed thickness of the Upper Permian deposits is water-encroached. The main source of supply is atmospheric precipitation and water of Quaternary deposits. Water of the Upper Permian deposits is pressured. Pressure head is 7.5 – 21.5 m. Filtration coefficient is 3.7 m /day.

Work on the collector driving is done using the method of shield tunneling at a depth of 30 ÷ 40 m under existing historic urban development conditions. Furthermore, construction of shafts along the full length of the collector was provided for the technological service and removal of the soil excavated during the construction.

From the constructive point of view, shafts represent sunk reinforced concrete monolithic wells circular in plane. The inner diameter of the shaft is 5.5 m, the wall thickness is 400 mm. Well sinking is carried out at the expense of its own weight, with the soil being extracted by a grappeler. In order to reduce the friction of the shaft walls, the application of bentonitic drilling mud is provided by technology.

To protect against groundwater and to maintain engineering service lines, the construction of a watertight diaphragm made from secant soil-cement piles to a depth of 29.5 m., carried out with the help of “jet-grouting” method, is provided for the entire period of construction. The pile diameter is 1,000 mm, the spacing parameter is 650 mm into the perimeter of the shaft. Water lowering with the help of holes bored to bedrock is also provided for the whole period of work fulfillment.

Washout of the wall and sloughing of ground accompanied by traffic-bearing surface sagging of the city main occurred periodically when sinking one of the shafts to a depth of about 20.1 m. The magnitude of roadway sag was 25 cm. The subsidence of concrete floors of a shopping centre located nearby and pillar displacement of the building framework were also registered.

2. NUMERICAL SIMULATION OF SHAFT CONSTRUCTION

In order to analyze the situation, additional engineering geological investigations and numerical simulation of the collector and shaft sinking were carried out. Numerical modeling was performed with the use of software package PLAXIS 2D and PLAXIS 3D Foundation. For the analysis, a typical cross-section going through the axis of the shaft perpendicular to the city main, on which there was a subsidence of the roadway, was considered. A design finite-element scheme, adopted in PLAXIS 2D is shown in Figure1. A design finite-element scheme, adopted in PLAXIS 3D Foundation is shown in Figure2.

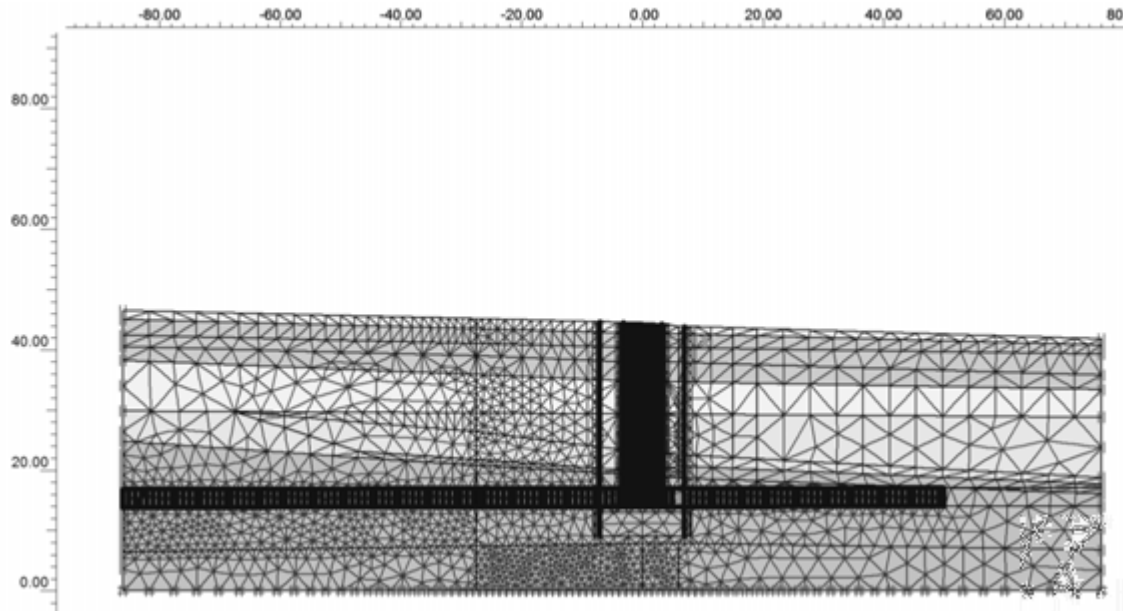


Figure 1: Design finite-element scheme in PLAXIS 2D for the cross section under study

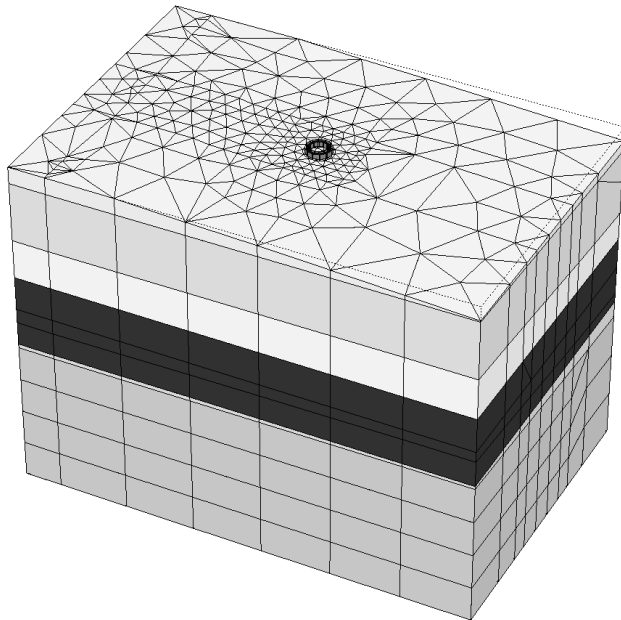


Figure 2: Design finite-element scheme of the ground mass around the shaft in PLAXIS 3D Foundation

For a more detailed analysis of obtained settlement some points on the soil day surface were allocated. As an example, there were given data for the most characteristic point at the distance of 10 m \approx to the "right" from the axis of the shaft in that part of the city main roadway where the largest subsidence of day surface was registered. Consideration was given to ground development and vertical-sliding support sinking at the following characteristic stages:

- stepwise ground development and vertical-sliding support sinking to a depth of 7 m without water lowering;
- stepwise ground development and vertical-sliding support sinking to a depth of 18.2 m with water lowering by means of pumping water from the wells with discharge of 20 m³/day;
- water conduit accident under the city main;
- stepwise ground development and vertical-sliding support sinking to a depth of 20.1 m with water lowering by means of pumping water from the wells with discharge of 7 m³/day (168 m³/day).

Graphical results of PLAXIS 2D calculation are shown in Figures 3 – 5, calculation results in PLAXIS 3D Foundation are shown in Figures 6 – 8. The numerical values of the characteristic point settlement are given in Table 1.

Table 1: Settlement of the characteristic point on the day surface:

	point settlement, mm
PLAXIS 2D	-217.5
PLAXIS 3D Foundation	-225.8
in-situ measurement	-250

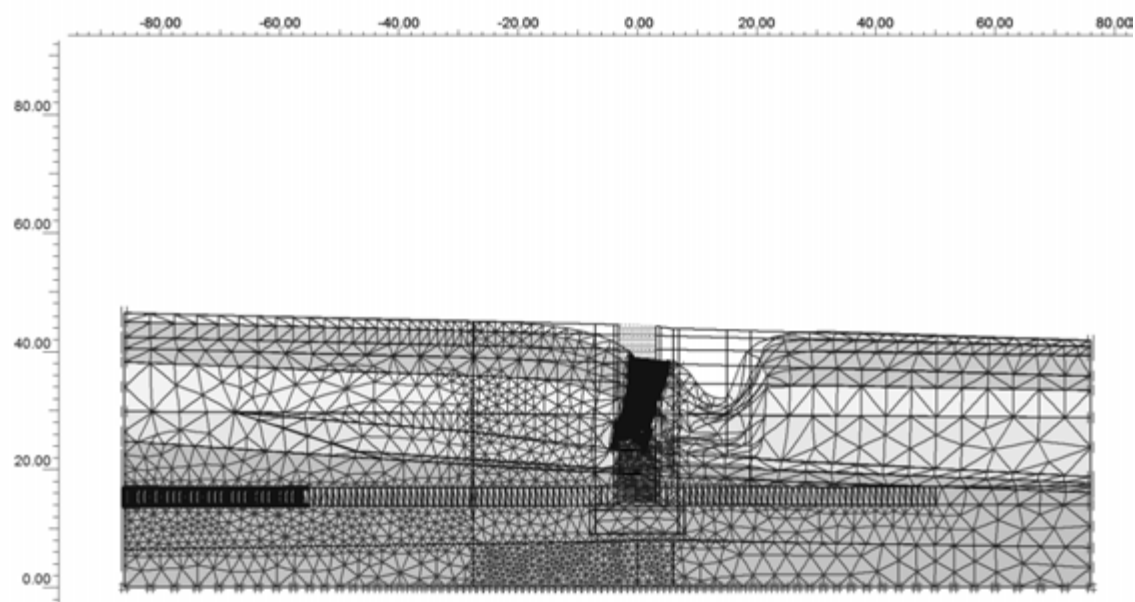


Figure 3: Deformation cross-section scheme in PLAXIS 2D when developing ground and sinking a vertical-sliding support to a depth of 20.1 m

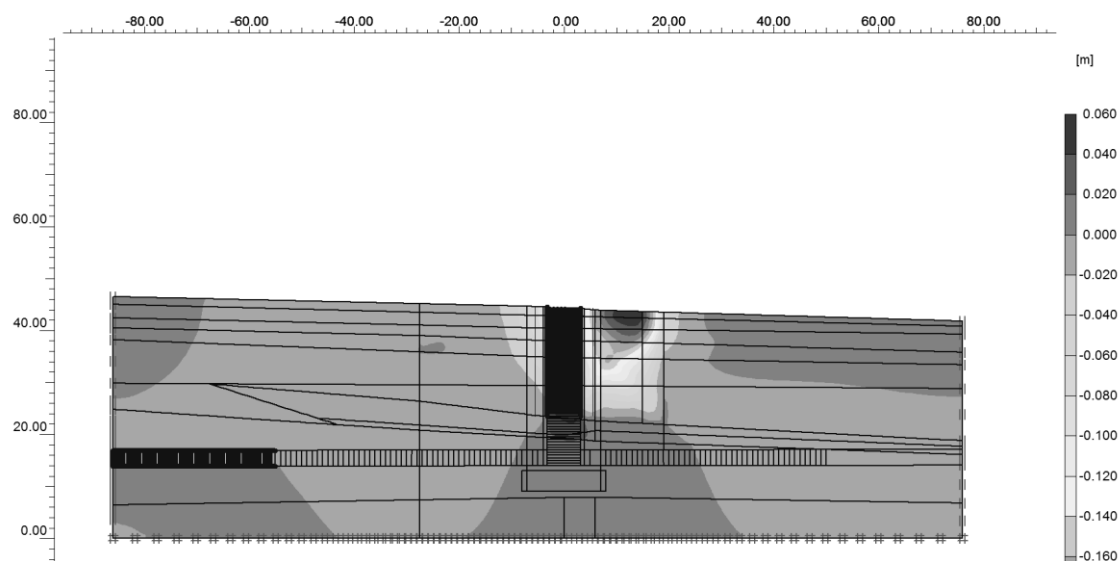


Figure 4: Lines of vertical displacement of foundation soil in cross-section in PLAXIS 2D when developing ground and sinking a vertical-sliding support to a depth of 20.1 m.

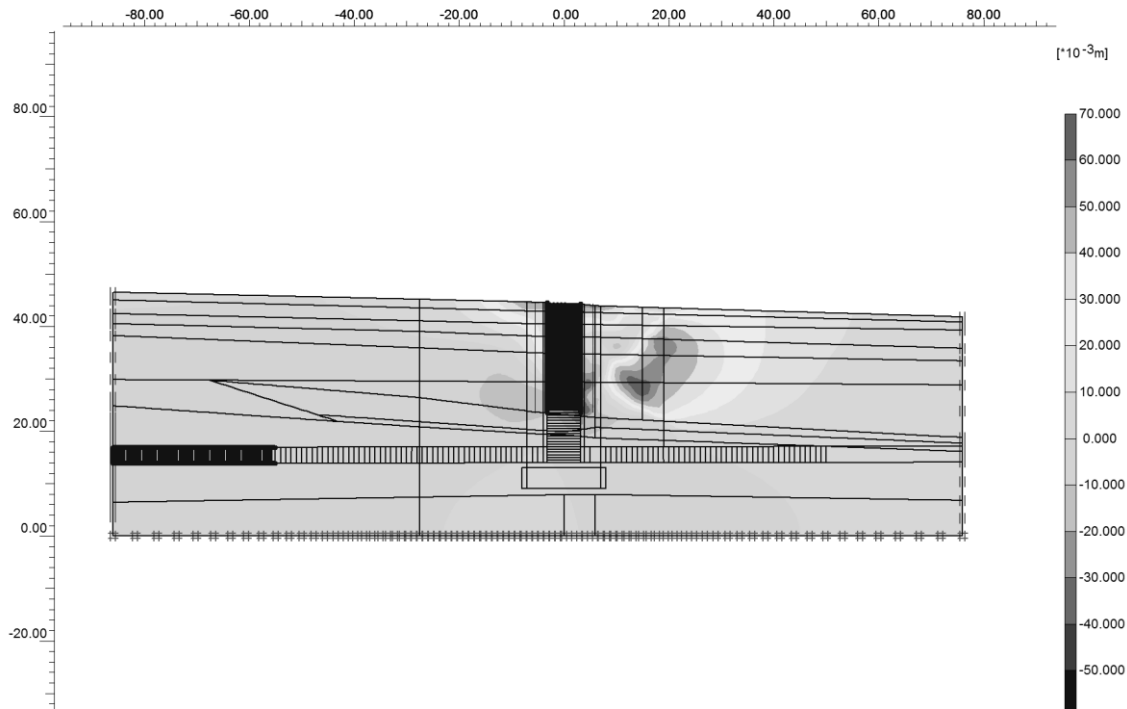


Figure 5: Lines of horizontal displacement of foundation soil in cross section in PLAXIS 2D when developing ground and sinking a vertical-sliding support to a depth of 20.1 m

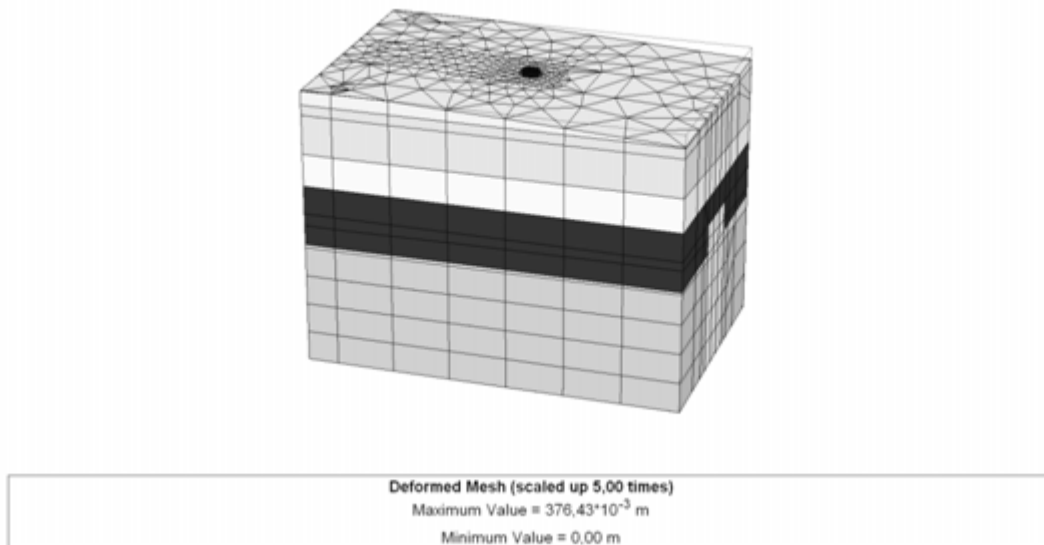


Figure 6: Deformation scheme of foundation soil in PLAXIS 3D Foundation when developing ground and sinking a vertical-sliding support to a depth of 20.1 m

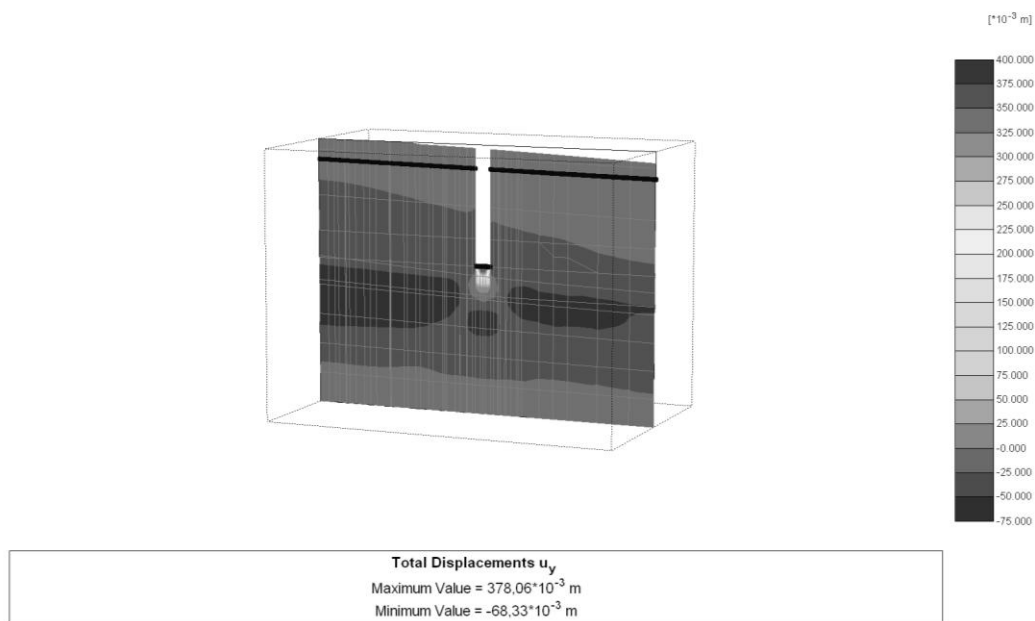


Figure 7: Lines of vertical displacement of foundation soil in cross section in PLAXIS 3D Foundation when developing ground and sinking a vertical-sliding support to a depth of 20.1 m

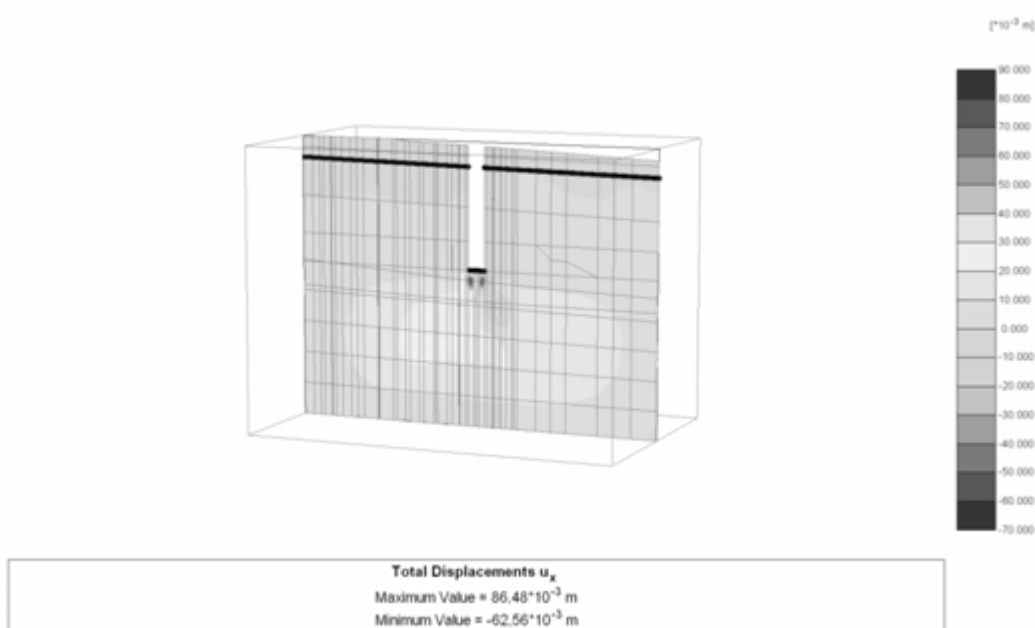


Figure 8: Lines of horizontal displacement of foundation soil in cross section in PLAXIS 3D Foundation when developing ground and sinking a vertical-sliding support to a depth of 20.1 m.

3. ANALYSIS OF THE RESULTS OF NUMERICAL SIMULATION AND ENGINEERING – GEOLOGICAL SURVEY

As the investigations showed, the most significant factor that had influenced the existing situation was the presence of pressured groundwater related to the Quaternary base and the Upper Permian deposits. That fact was not taken into account when developing the technology of shaft sinking. The project work specified the construction of a watertight diaphragm made from soil-cement piles with the help of “jet-grouting” method. The diaphragm was provided only into the perimeter of the shaft, i.e. protection against pressured groundwater of the Upper Permian deposits (from the bottom of the shaft) was not designed. Furthermore, the watertight diaphragm construction started only after the shaft sinking at a depth of 18.2 m.

Complex hydrogeological conditions in the presence of pressured groundwater in conjunction with the soils having a high rate of filtration and well-fractured bedrock did not allow to construct with due quality a solid watertight diaphragm of 29.5 m deep using “Jet grouting” technology.

The absence of a watertight diaphragm alongside with the work on water lowering led to day surface settlement that were recorded, deformation of utilities located nearby and breaking of the water conduit. That, in its turn, resulted in water-saturation of soil, washout and deterioration of physical and mechanical soil properties. What is more, it worsened the general hydrogeological situation.

Numerical simulation results proved that assumption. For further ground development and vertical-sliding support sinking, an alternative of cold application for building a temporary ice-soil enclosure as a waterproof barrier into the perimeter and at the shaft base was proposed.

Application of a sensitivity analysis procedure to interpret uniaxial compressive strength prediction of jet grouting laboratory formulations performed by SVM model

Joaquim Tinoco, University of Minho, Portugal, jabtinoco@civil.uminho.pt
António Gomes Correia, University of Minho, Portugal, agc@civil.uminho.pt
Paulo Cortez, University of Minho, Portugal, pcortez@dsi.uminho.pt

ABSTRACT

Jet Grouting (JG) technology is one of the most widely used soft-soil improvements methods around the world. When compared with other methods, JG versatility is highlighted, since it can be applied to several soil types, creates elements with different geometric shapes and, normally, is less expensive. However, due to inherent geological complexity of soil and high number of variables involved in JG process, JG design is a hard task. Nowadays, its design is essentially based on empirical rules that are often too conservatives, compromising the economy and the quality of the treatment. In the present study, data mining (DM) techniques, particularly the high learning capabilities of support vector machines (SVM) algorithm were used to predict uniaxial compressive strength (UCS) of JG laboratory formulations over time. Furthermore, and by performing a detailed sensitivity analysis, some important information was extracted based on the learned model. The high performance achieved by SVM algorithm in UCS prediction is summarized showing the high predictive accuracy reached ($R^2=0.93$). In addition, after apply a one- and two-dimensional sensitivity analysis, an important explanation of the model is given in terms of what are the key variables and its effect on UCS estimation, as well as the interaction level between input variables. Hence, it is shown that age of the mixtures, cement content and the relation between mixture porosity and volumetric content of cement have a high influence in strength behavior of JG laboratory formulations. Furthermore, was also possible to observe that water/cement ratio is the variable with higher interaction with age of the mixture and cement content.

1. INTRODUCTION

For constructions purposes the soil foundation should presents suitable geotechnical properties. However, due to increased urbanization and industrialization the availability of soils with such requirements is increasingly scarce. As a result, there is a growing demand for construction on soft soil, which is characterized by high plasticity, high fraction of fines and void ratio, low strength and high compressibility (Liu et al., 2008). In these cases, deep mixing methods are currently applied to improve soil properties, where powder cement or slurry cement is injected into the natural soil. Nowadays there are several soil improvements methods (Nikbakhtan et al., 2010) where Jet Grouting (JG) is highlighted. JG technology was first introduced by Yamakoda brothers in 60's decade and since them has been widely applied (Xanthakos et al., 1994). Such technology has aroused interest within the geotechnical community due to it great versatility. JG enable to improve mechanical and physical properties of different types of soil (ranging from coarse to fine-grained soils), obtain different geometries shapes (columns, panels), just require few equipments for its application and is economically attractive when compared with other similar methods.

The concept behind JG technology is to produce a soil-cement mixture, often termed as *soilcrete*, with an enhancement in terms of mechanical characteristics (strength and stiffness) and permeability. The new material is obtained by injecting grout, with or without other fluids (e.g. air or water) at high pressure and velocity into the sub soil. The fluids are injected through small nozzles placed at the end of a rod that, after introduced at the intend depth, is continually rotated and slowly removed up to the surface. Depending of the number of fluids injected, three systems are currently in use (Xanthakos et al., 1994). Single fluid system, where is only injected grout at high pressure and velocity; double fluid system is very similar to the single system but with the addition of an air shroud to the nozzle; and finally the triple fluid system, which differs from the single and double systems in that the erosion of the ground is carried out by a high pressure water jet shrouded with air with an additional low pressure grout line. In addition to these three systems there is also the Xjet system, also known as cross-jet or collided jetting that consists of a pair of intersecting air-shrouded water jets with separate grout jets and is designed to cut a nominal 2m diameter column in any ground (Shibazaki, 2004).

JG technology has been applied for different purposes, namely in the improvement of foundation soils, slope stabilization, and underpinning (Welsh and Burke, 1991). Furthermore, was also used as a method of performing block stabilization of contaminated soils as well as for the formation of barriers for the control of contaminant migration in the environmental field (Gazaway and Jasperse, 1992). In spite of being widely used, JG design lacks of rational approaches to predict its physical and mechanical properties. Indeed, even in large scale works, JG design is essentially based on empirically methods, as illustrated in Figure 1 and supported by knowhow of JG companies. The main reasons for such absence are related to the number of variables involved in JG process, which present complex or even nonlinear relationships, as well as due to inherent heterogeneity of the natural soil. As a result, and since such empirical rules are often too conservative, the quality and cost of the treatment can be compromised. Hence, and bearing in mind the high versatility of JG technology and its role in important geotechnical works, there is need to develop rational and reliable methods to estimate accurately JG mechanical and physical properties.

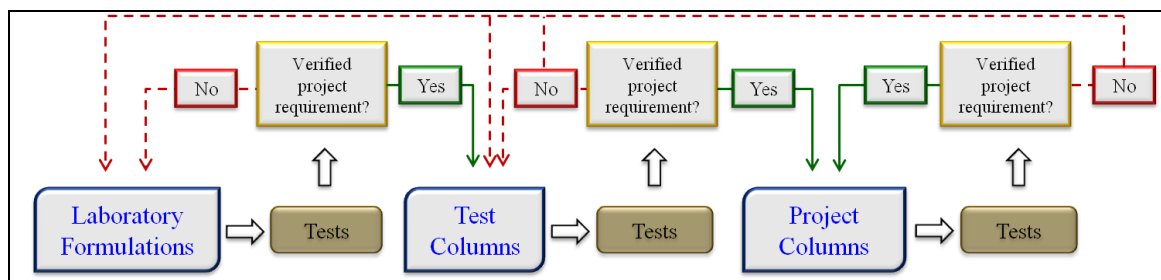


Figure 1: Empirical design of JG treatment.

One of the best ways to deal with high number of variables with complex relationship is to use an automate processes using artificial intelligent tools that analyze the raw data and extract useful knowledge. These tools can be seen as a good alternative to the traditional statistical approaches, which are unable to deal with such information, leading to poor results. Knowledge Discovery in Databases (KDD) (see Figure 2) is an iterative process that consists of several steps, where Data Mining (DM) is just one step (although crucial), aiming at the extraction of useful patterns from the observed data. According to CRISP-DM methodology, the following steps should be followed (Chapman et al., 2000): 1 - business understanding; 2 - data understanding; 3 - data preparation; 4 - modeling; 5 - evaluation; and 6 - deployment.

Two important DM tasks, classification and regression, require a supervised learning, where a model is adjusted to a dataset of examples that map I inputs (independent variables) into a given target (the dependent variable). There are several DM algorithms, each one with its own proposes and capabilities. Some of the most interesting supervised learning DM models are Artificial Neural Networks (ANNs) and Support Vector Machines (SVMs), characterized by their flexibility and nonlinear learning capabilities. In the Geotechnics field, there are some successful applications of DM to different kinds of problems. Miranda et al. (2011) propose a new alternative regression models using ANNs for the analytical calculation of strength and deformability parameters of rock masses. Goh and Goh (2007) used SVMs to assess seismic liquefaction. Erzin (2007) studied the relationship between the swell pressure and soil suction behavior in specimens of Bentonite–Kaolinite clay mixtures with varying soil properties using ANNs. Tinoco et al. (2011b) applied SVMs and ANNs to predict deformability properties of JG laboratory formulations over time.

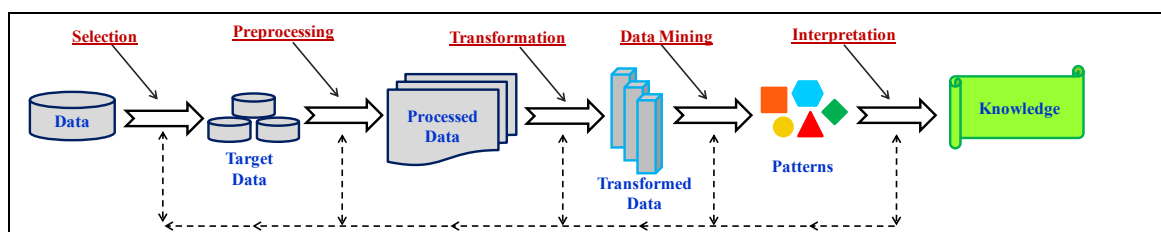


Figure 2: Steps of KDD process (adapted from Fayyad et al., 1996).

In the present work, a first step was made, by proposing a rational approach to predict Uniaxial Compressive Strength (*UCS*) of JG laboratory formulations (JGLF) over time, which is the mechanical properties currently used to measure the bearing capacity of foundations. For such purpose, an SVM was trained with *UCS* data collected from JGLF samples, in order to predict its strength over time. The main

results are here summarized and interpreted. Furthermore, an interpretability of SVM model is given by performing a detailed sensitivity analysis procedure. Such analysis allow us identify what are the key variables in UCS prediction of JGLF as well as a better understanding of the effect of each one in such prediction. In addition, was also measured the interaction between variables and interpreted its means and effect on UCS prediction.

2. METHODS AND DATA

2.1. Support Vector Machines

For regressions tasks there are several DM algorithms that can be applied, each one with its own advantage and limitations. The present study focuses on SVM algorithm that has been shown high learning capabilities even when working with complex data (Tinoco et al., 2011c). Support Vector Machines (Chen and Councill, 2003) are a very specific class of algorithms, based on statistic theory, characterized by use of kernels, absence of local minima during the learning phase and capacity control obtained by acting on the margin, or on number of support vectors. When compared with other types of base learners, such as the multilayer perceptron (the most popular neural network type), SVM represents a significant enhancement in functionality. The supremacy of SVM lies in their use of nonlinear kernel functions that implicitly map inputs into high dimensional feature spaces. In this feature spaces linear operations may be possible that tray to find the best linear separating hyperplane ($y_i = \omega_0 + \sum_{i=1}^m \omega_i \phi_i(x)$), related to a set of support vector points, in the feature space. Thus, although SVMs are linear learning machines with respect to feature spaces, they are in effect non-linear in the original input space (see Figure 3). These attractive features and promising empirical performance are responsible for its popularity.

SVM was initially proposed for classification problems by Vladimir Vapnik and his co-workers (Cortes and Vapnik, 1995). Later, after the introduction of an alternative loss function proposed by Vapnik (Smola et al., 1996), called ε -insensitive loss function, was possible to apply SVM to a regression problems (Smola and Schölkopf, 2004).

When working with SVM, it is well known that SVM generalization performance (estimation accuracy) depends on a good setting of meta-parameters C , ε and the kernel parameters. The problem of choosing a good parameter setting in a learning task is the so-called model selection. The problem of optimal parameter selection is further complicated by the fact that SVM model complexity (and hence its generalization performance) depends on all three parameters. Parameter C controls the trade-off between complexity of the machine (flatness) and the number of non-separable data points and may be viewed as a “regularization” parameter (Goh and Goh, 2007). Parameter ε controls the width of the ε -insensitive zone, used to fit the training data. The value of ε can affect the number of support vectors used to construct the regression function. Hence, both C and ε values affect model complexity (but in a different way). Selecting a particular kernel type and kernel function parameters is usually based on application-domain knowledge and should reflect distribution of input (x) values of the training data (Cherkassky and Ma, 2004). In the present work was adopted the popular Gaussian kernel, since it presents less parameters than other kernels (e.g. polynomial):

$$K(x, x') = \exp(-\gamma \cdot \|x - x'\|^2), \gamma > 0 \quad (1)$$

For model selection, several approaches have been proposed (Huang et all, 2007; Momma and Bennett, 2011; Frohlich and Zell, 2005) in order to find the best set of parameters with less effort (time and computing consuming). In the present work, we adopt the heuristics proposed by Cherkassky and Ma (2004) to set the complexity penalty parameter, $C=3$ and the size of the insensitive tube $\varepsilon = \hat{\sigma}/\sqrt{N}$, where $\hat{\sigma} = 1.5/N \times \sum_{i=1}^N (y_i - \hat{y}_i)^2$, \hat{y}_i is the value predicted by a 3-nearest neighbor algorithm and N the number of examples. The most important SVM parameter, the kernel parameter γ , was set using a grid search within $\{2^{-15}, 2^{-13}, \dots, 2^3\}$, under an internal (i.e. applied over training data) 10-fold cross validation (Hastie et al., 2009).

All experiments were implemented in R tool (R Development Core Team), using rminer library (Cortez, 2010), which is particularly suitable for SVM training through use advanced functions (particularly “mining” and “fit”). Before fitting the SVM model, the data attributes were standardized to a zero mean and one standard deviation and before analyzing the predictions, the outputs post-processed with the inverse transformation (Hastie et al., 2009).

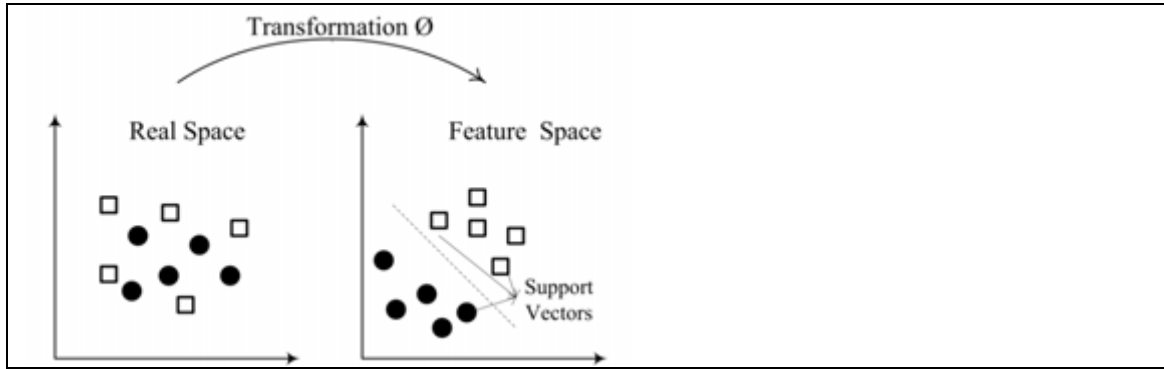


Figure 3: Example of a SVM transformation (adapted from (Cortez, 2010)).

In a regression problem, the main goal is to induce a model that minimizes an error measurement between observed and predicted values considering N examples. For this purpose, three common metrics were calculated: Mean Absolute Deviation (MAD), Root Mean Squared Error (RMSE) and Coefficient of Correlation (R^2). These metrics are defined as:

$$MAD = \frac{\sum_{i=1}^N |y - \hat{y}|}{N}; \quad RMSE = \sqrt{\frac{\sum_{i=1}^N (y - \hat{y})^2}{N}}; \quad R^2 = \left(\frac{\sum_{i=1}^N (y - \bar{y}) \times (\hat{y} - \bar{\hat{y}})}{\sqrt{\sum_{i=1}^N (y - \bar{y})^2 \times \sum_{i=1}^N (\hat{y} - \bar{\hat{y}})^2}} \right)^2 \quad (2)$$

If the first two metrics show lower values and R^2 is close to the unit value, this means high predictive capacity of the model. The main difference between RMSE and MAD is that former is less sensitive to extreme values. The regression error characteristic (REC) curve, which plots the error tolerance on the x -axis versus the percentage of points predicted within the tolerance on the y -axis (Bi and Bennett, 2003) was also adopted during the analysis of model performance.

The overall generalization performance of the trained model was accessed by using 20 runs under Leave-One-Out approach (Hastie et al., 2009), which is special suitable for small databases (e.g. lower than 100 examples). Under this scheme, one example at a time is used to test the model, and the remaining data is used to fit the model. At the end all data are used for training and testing. Yet, this method requires approximately N times more computation, because N models must be fitted. The final generalization estimate is evaluated by computing the MAD, RMSE and R^2 metrics for all N test samples.

Besides obtaining a high predictive performance it is also important to extract human understandable knowledge from the data-driven model. This is precisely the main drawback of such models. One of the best ways to “open” a DM model is to apply a sensitivity analysis procedure (Cortez and Embrechts, 2011). Such procedure is carried out after the training phase and analyzes the model responses when a given input is changed. This procedure can be applied to any supervised DM model and allows to quantify the relative importance of each input parameter and also to measure the average effect of a given input on the target variable. Such quantification is determined by successively holding all inputs at a given baseline (e.g. their average values), except one input attribute that is varied through its range of values ($x_a \in \{x_1, \dots, x_l\}$), with ($j \in \{1, \dots, L\}$) levels. The obtained responses ($\hat{y}_{a,j}$) are stored. Higher response changes indicate a more relevant input. In particular, following the results achieved in (Cortez and Embrechts, 2011), we adopt the gradient measure (S_a) to access the input relevance (R_a) of the attribute x_a (the higher the gradient, the higher is the input importance):

$$R_a = S_a / \sum_{i=1}^L S_i \times 100(\%), \quad \text{where } S_a = \sum_{j=2}^L |\hat{y}_{a,j} - \hat{y}_{a,j-1}| / (L - 1) \quad (3)$$

For more input influence details, the Variable Effect Characteristic (VEC) curve was plotted (Cortez and Embrechts, 2011). For a given input variable, the VEC curve plots the attribute L level values (x -axis) versus the sensitivity analysis responses (y -axis). In this paper, we set $L=12$. Furthermore, aiming to achieve a more realistic interpretation of the model a two-dimensional sensitivity analysis was performed. Here, two variables are changed simultaneously and the response is measured. With the stored values it is possible to plot the VEC surface or VEC contour (Cortez and Embrechts, 2011).

2.2. Jet Grouting Data

During the learning phase of SVM algorithm was used a dataset with 175 records assembled from a laboratory experimental program, carried out at University of Minho, with the purpose of analyzing the influence of several variables in mechanical behavior of JG laboratory mixtures. Should be stressed that the acquisition of each data example requires considerable cost and amount of time, demanding laboratory work and material (e.g. cement). All records can be grouped in 9 different formulations characterized by its values of Water/Cement ratio (W/C), cement content (mass of cement/mass of

soil+mass of cement)) (C), cement type (s) and soil properties, i.e., percentage of sand ($\%Sand$), percentage of silt ($\%Silt$), percentage of clay ($\%Clay$) and percentage of organic matter ($\%OM$). The input variables were chosen based on expert knowledge related to soil-cement mixtures (Shibazaki, 2004) and authors' experience (Tinoco et al., 2011a). Thus, additionally to the seven variables previously enumerated, the relation between mixture porosity and volumetric content of cement ($n/(C_{iv})^d$) as well as the age of the mixture (t , days) were also chosen as input variables of the model. The main statistics of the input and target variables of UCS dataset are shown in Table 1. For a physical characterization of the natural soil, some samples were collected and tested in laboratory. Although all soils were of clayed nature, they have different percentages of sand, silt, clay and organic matter. A detailed description of the distinct soil types can be found in Table 2. In the table, the first column denotes the construction site, while the third column shows the number of records that contain such soil. All laboratory formulations were prepared with cement type CEM I 42.5R ($s=0.20$), CEM II 42.5R ($s=0.20$) and CEM IV/A 35.5R ($s=0.25$).

Table 1: Summary of the input and output variables in UCS dataset

Variable	Maximum	Minimum	Mean	Standard Deviation
t	56	3.00	21.60	19.24
C	0.75	0.24	0.47	0.15
$n/(C_{iv})^d$	74.26	48.83	62.59	7.26
W/C	1.12	0.68	0.88	0.16
s	0.25	0.20	0.21	0.02
$\%Sand$	39.00	0.00	13.57	11.53
$\%Silt$	57.00	33.00	50.49	5.49
$\%Clay$	45.00	22.50	35.89	7.74
$\%OM$	8.30	0.40	2.71	1.81
UCS	13.19	0.76	5.20	2.73

Table 2: Soil types present in the collected data

Site	Soil type	Frequency	$\%Sand$	$\%Silt$	$\%Clay$	$\%OM$
A	Lean clay (CL)	10	39.0	33.0	27.0	8.3
B	Organic lean clay (OL)	5	6.0	57.0	37.0	1.8
C	Fat clay (CH)	85	7.0	53.0	40.0	3.2
D	Silt Clay (CL-ML)	20	25.0	52.5	22.5	0.4
E	Lean clay (CL)	15	0.0	55.0	45.0	3.9
F	Silt Clay (CL-ML)	20	32.5	43.5	24.0	1.2
G	Lean clay (CL)	20	10.5	48.5	41.0	1.0

3. RESULTS AND DISCUSSION

SVM algorithm was able to learn with high accuracy the complex relationships between UCS of JGLF and its contributing factors. Figure 4 shows visually the excellent performance achieved by SVM model in UCS estimation of JGLF over time (all points are very close to the diagonal line), which is proven (mean value and 95% confidence intervals) by metrics $R^2=0.93\pm 0.00$, $MDA=0.55\pm 0.00$ and $RMSE=0.73\pm 0.00$. Furthermore, REC curve (dotted line) show a fast improvement on model accuracy. For example, SVM model can predict 90% of the records with an absolute deviation lower than 1.5MPa. When evaluating a DM model, we should consider not only predictive accuracy but also try to understand how model works. In the present paper, model interpretability was measured by quantifying what are the key input variables in UCS estimation and its effect in such prediction. For such purpose was applied a detailed sensitivity analysis.

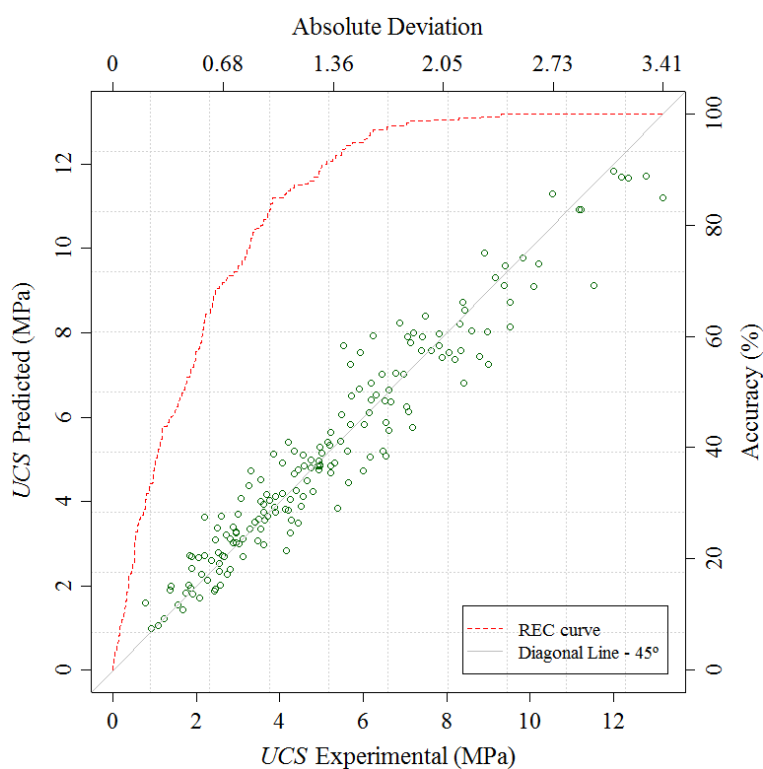


Figure 4: Relation between UCS experimental versus UCS predicted by SVM model (the dashed line represents the REC curve and should be read on top horizontal and right vertical axis).

The averaged relative importance of each input variable and the correspondent t-student 95% confidence interval for all 20 runs performed was quantified by one-dimensional sensitivity analysis. Figure 5 (left side) shows such results and allow to point out some important conclusions. One the one hand, the key variables that control the mechanical behavior of JGLF, in terms of strength, are the age of the mixture with an impact around 19%, followed by cement content (18%) and $n/(C_{iv})^d$ (16%). One the other hand, and based on t-student values, SVM algorithm is very consistent for all 20 runs performed. Furthermore, this relative importance ranking is in agreement with the empirical knowledge related with soil-cement mixtures. It is well known that t has a strong influence in such mixtures behavior, mainly if we take in account the range of t variable in the dataset used during the learning phase, i.e. $t \leq 56$ days time of cure. On the other hand, make all sense that C shows high impact when we are study soil-cement mixtures (Horpibulsuk et al., 2003). In addition, the mixture porosity it is also considered throughout $n/(C_{iv})^d$ variable. The W/C ratio and cement type have a less impact in strength behavior of JGLF, with an relative importance around 12% and 10% respectively. Finally, maybe seem strange the lower influence of soil properties. However, this observations can be explained if we take in account that all soils are very similar, i.e., all soil were classified as clayed nature, just differing on its sand, silt, clay and organic matter content.

Based also on one-dimension sensitivity analysis, the effect of the four key variables on UCS estimation was quantified and is depicted in Figure 5 (right side). The first observation we can draw is that all four variables have a nonlinear effect on UCS behavior of JGLF. Second, and as expected, t and C have a positive impact in such prediction. On the other hand, increasing $n/(C_{iv})^d$ and/or W/C the strength of the mixture decrease. VEC curve of t shows a convex shape which means that age effect is more pronounced for early ages of cure and trend to stabilize for advanced ages (up to 45 days time of cure). It is also interesting to observe the shape of C VEC curve. In this case, C improves considerably UCS for values higher than 45%. Lastly, it is also possible to observe that $n/(C_{iv})^d$ and W/C VEC curves have a very similar effect (concave shape) on UCS prediction.

All previous results were obtained by performing a one-dimensional sensitivity analysis, i.e., holding all variables at its mean values and range only one at each time. As we know, such conditions rarely or even never happen in the real word. Hence, and keeping in mind a more realistic and detailed analysis, in the next lines we present and discusses some important observation taken from a two dimensional sensitivity analysis, i.e., when two variables are changed simultaneously. Thus, was measured the interaction level of all variables with t and C and plotted the VEC surfaces for: t and W/C ; t and $n/(C_{iv})^d$; C and W/C and C and t .

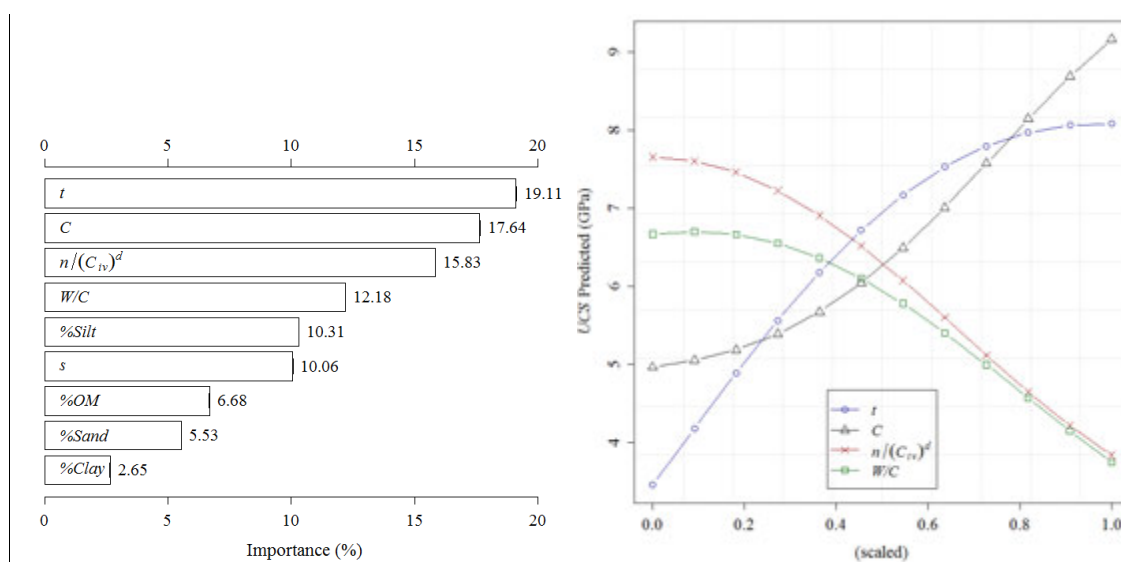


Figure 5: Relative importance of each input variable (left side) and VEC curves of t , C , $n/(C_{iv})^d$ and W/C variables, according to SVM mode, quantified by one-dimensional sensitivity analysis.

Figure 6 shows the relative interaction between all variables with t (left side) and C (right side), i.e., the first two key variables. In both situations the highest interaction is observed for W/C , with an relative importance around 14%. This observation shows that in spite of W/C being the fourth variable with more impact in UCS prediction, based on a one-dimensional sensitivity analysis, it should be taken in account in JGLF behavior since it has a strong interaction with other variables, namely with t and C . The highest interaction of W/C with t can be explained if we consider that the gain of strength is related to the decreasing of free water in the mixture (hardness process). This means that when is used a high W/C ratio we will need to wait more time to obtain the same strength than for a lower W/C ratio. Then, we can conclude that to obtain a fast hardness process, the mixture should be prepared with lower values of W/C ratio. The high interaction between C and W/C explain the cement content effect. Normally, mixtures with high C are prepared using grout with lower W/C ratio. Therefore, is clear that C and W/C has a strong interaction. Another interest observation from Figure 6 is related with the soil properties. Again this input shows low impact on UCS estimation of JGLF.

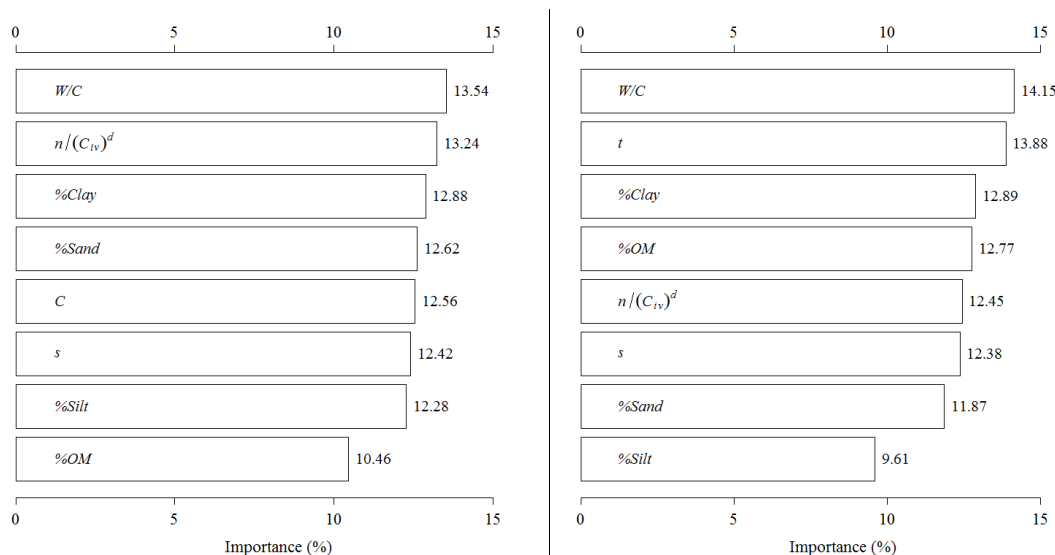


Figure 6: Interaction level of all variables with t (left side) and C (right side), according to SVM model, when a two-dimension sensitivity analysis is applied.

Plotting the interaction effect between t and W/C in UCS prediction, we obtain the VEC surface shown in Figure 7 (left side). This surface shows precisely the high effect of the interaction between these two variables, evidenced by the high range of UCS values for different combinations of t and W/C (since 2 MPa to 9MPa). Furthermore, it is also possible to observe that mixtures with high W/C ratios trend to

stabilize for ages more early. Based on VEC surface for t and $n/(C_{iv})^d$ (Figure 7, right side), we can see the high impact interaction that these two variables also have in UCS estimation of JGL (UCS range from 2MPa to 9MPa). In addition, the effect of t on UCS is more pronounced for lower values of $n/(C_{iv})^d$ than for higher values. This means that when we have a mixture with high porosity (or lower cement content) the UCS will just slight increase over time.

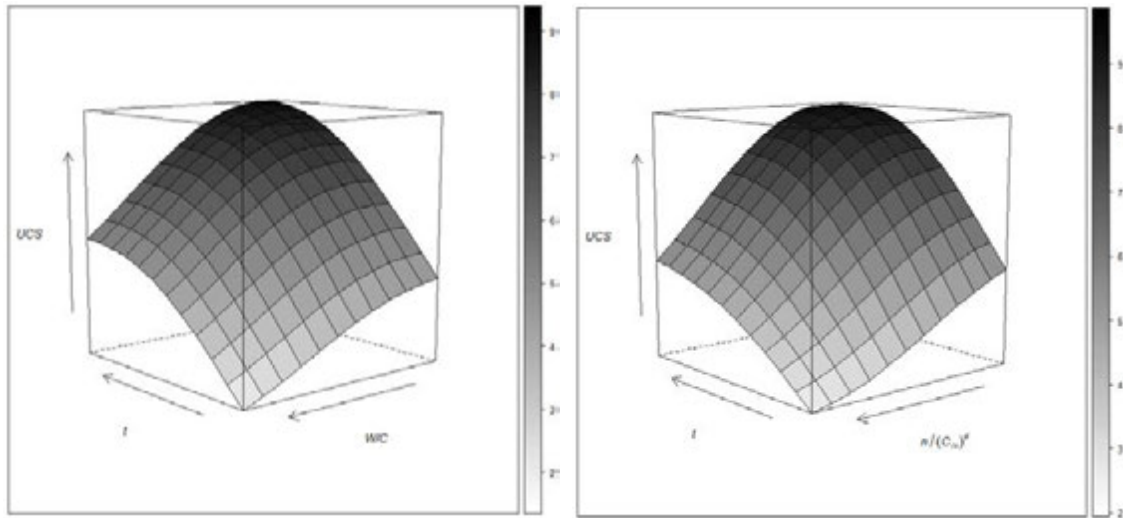


Figure 7 : VEC surface for t and W/C (right side) and t and $n/(C_{iv})^d$ (left side) in UCS prediction, according to SVM model, quantified by two-dimensional sensitivity analysis.

Figure 8 shows the VEC surfaces for C and W/C (left side) and C and t (right side). In these pictures we can see the high impact interaction of both W/C and t (UCS range from 3MPa to 11MPa). The VEC surface of C and W/C (left side of Figure 8) shows a fast increasing of UCS for higher values of C when W/C decrease. This behavior can be explained by the high amount of cement in such condition (high C and low W/C ratio). Observing the VEC surface of C and t (right side of Figure 8) we can see an almost linear effect of C for advanced ages.

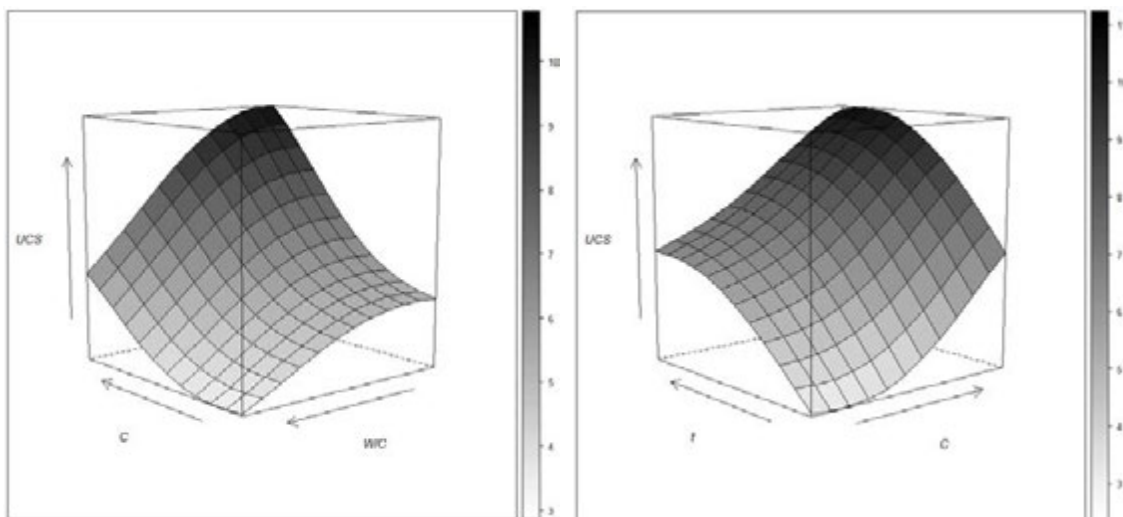


Figure 8: VEC surface for C and W/C (left side) and C and t (right side) in UCS prediction, according to SVM model, quantified by two-dimensional sensitivity analysis.

4. CONCLUSION

In the context of Jet Grouting (JG) technology the main drawback is related with the absence of rational design models to predict mechanical properties of JG mixtures, namely its Uniaxial Compressive Strength (UCS). Nowadays, this task is essentially performed considering the results of laboratory tests and empirical models. However, in the preliminary stages of design, mainly in smaller geotechnical works, the decision regarding the parameter values is based on limited information. Thus, the use of data from past projects can be seen as a good solution to overcome this problem. The application of Data Mining (DM)

techniques to well organized data gathered from large geotechnical works can provide a strong framework to the development of models that can be very useful in future projects.

In the present work, a rational model has been proposed to predict *UCS* of jet grouting laboratory formulations (JGLF) over time using DM techniques. The proposed model is able to accurately predict *UCS* of JGLF mixtures from 3 to 56 days in advance (i.e. the range values for variable age) prepared with clayed soils containing different percentage of sand, silt, clay and organic matter. Furthermore, some important observations were pointed out by performing a detailed sensitivity analysis. Age of the mixture (t), cement content (C) and the relation between mixture porosity and the volumetric content of cement ($n/(C_v)^d$) were identified as key variable in *UCS* prediction of JGLF. These three variables have a nonlinear effect on *UCS* estimation according to exponential laws. In addition, the Water/Cement (W/C) ratio shows a strong interaction with the first two key variables on *UCS* prediction.

Moreover, and since the proposed model are in agreement with the empirical knowledge related to JGLF, it can be conclude that such model can be used to describe rationally the actual empirical knowledge related to this material. All obtained knowledge can be seen as an important advance for geotechnical civil engineering works since contribute for a better understanding of JG mixtures behavior, which will allow to significantly reduce the number of laboratory formulations need to be prepared. At the end, the economy and the quality of the treatment will be improved.

As future works, the same methodology, i.e. DM techniques will be applied in order to develop rational models to estimate deformability properties of JGLF. In addition, the same tools will be also used to define predictive model for strength and stiffness of real JG columns as well as its diameter.

5. ACKNOWLEDGEMENTS

The authors wish to thank to “Fundação para a Ciência e a Tecnologia” (FCT) for the financial support under the strategic project PEst-OE/ECI/UI4047/2011 and the doctoral Grant SFRH/BD/45781/2008. Also, the authors would like to thank the interest and financial support by Tecnasol-FGE.

REFERENCES

- Bi, J. and Bennett, K., “Regression Error Characteristic Curves”, *Twentieth International Conference on Machine Learning (CD-ROM)*, AAAI Press, 40-50, 2003.
- Chapman, P., Clinton, J., Kerber, R., Khabaza, T., Reinartz, T., Shearer, C. and Wirth, R., “CRISPDM1.0: Step-by-Step Data Mining Guide”, *CRISP-DM consortium*, 2000.
- Chen, Y. and Councill, I., “An Introduction to Support Vector Machines: A Review”, *AI Magazine*, AAAI Press, 24(2):105-107, 2003.
- Cherkassky, V. and Ma, Y., “Practical Selection of SVM Parameters and Noise Estimation for SVM Regression”, *Neural Networks*, Elsevier, 17(1):113-126, 2004.
- Cortes, C. and Vapnik, V., “Support Vector Networks”, *Machine Learning*, Springer, 20(3):273–297, 1995.
- Cortez, P., “Data Mining with Neural Networks and Support Vector Machines Using the R/rminer Tool”, *Advances in Data Mining – Applications and Theoretical Aspects 10th Industrial Conference on Data Mining (ICDM 2010)*, *Lecture Notes in Artificial Intelligence 6171*, Springer, 572-583, 2010.
- Cortez, P. and Embrechts, M., “Opening Black Box Data Mining Models Using Sensitivity Analysis”, *2011 IEEE Symposium on Computational Intelligence and Data Mining (CIDM 2011)*, IEEE, 341-348, 2011.
- Erzin, Y., “Artificial Neural Networks Approach for Swell Pressure versus Soil Suction Behavior”, *Canadian Geotechnical Journal*, NRC Research Press, 44(10):1215–1223, 2007.
- Fayyad, U., Piatetsky-Shapiro, G. and Smyth, P., “The KDD Process for Extracting Useful Knowledge from Volumes of Data”, *Communications of the ACM*, ACM, 39(11):27-34, 1996.
- Frohlich, H. and Zell, A., “Efficient Parameter Selection for Support Vector Machines in Classification and Regression via Model-Based Global Optimization”, *Neural Networks*, IEEE, 3:1431-1436, 2005.

Liu, S., Zhang, D., Liu, Z. and Deng, Y., "Assessment of Unconfined Compressive Strength of Cement Stabilized Marine Clay", *Marine Georesources & Geotechnology*, Taylor & Francis, 26(1):19-35, 2008.

Gazaway, H. and Jasperse, B., "Jet grouting in Contaminated Soils", *Grouting, Soil Improvement and Geosynthetics (GSP 30)*, ASCE, 206-214, 1992.

Goh, A. and Goh, S., "Support Vector Machines: Their use in Geotechnical Engineering as Illustrated using Seismic Liquefaction Data", *Computers and Geotechnics*, Elsevier, 34(5):410-421, 2007.

Hastie, T., Tibshirani, R. and Friedman, J., "The Elements of Statistical Learning: Data Mining, Inference, and Prediction", Springer-Verlag, 2nd Edition, 2009.

Horpibulsuk, S., Miura, N. and Nagaraj, T., "Assessment of Strength Development in Cement-Admixed High Water Content Clays with Abrams' Law as a Basis", *Geotechnique*, Thomas Telford, 53(4): 439-444, 2003.

Huang, C., Lee, Y., Lin, D. and Huang, S., "Model Selection for Support Vector Machines via Uniform Design", *Computational Statistics & Data Analysis*, Elsevier, 52(1):335-346, 2007.

Miranda, T., Gomes Correia, A., Santos, M., Sousa, L. and Cortez, P., "New Models for Strength and Deformability Parameter Calculation in Rock Masses Using Data-Mining Techniques", *International Journal of Geomechanics*, ASCE, 11:44-58, 2011.

Momma, M. and Bennett, K., "A Pattern Search Method for Model Selection of Support Vector Regression", *Proceedings of the SIAM International Conference on Data Mining*, Philadelphia: SIAM, 261:274, 2011.

Nikbakhtan, B., Ahangari, K. and Rahmani, N., "Estimation of Jet Grouting Parameters in Shahriar Dam, Iran", *Mining Science and Technology*, Elsevier, 20(3):472-477, 2010.

R Development Core Team, "R: a Language and Environment for Statistical Computing", R Foundation for Statistical Computing, Vienna, Austria, <http://www.R-project.org>.

Smola, A. and others, "Regression Estimation with Support Vector Learning Machines", Master's Thesis, Technische Universit at Munchen, 1996.

Smola, A. and Schölkopf, B., "A Tutorial on Support Vector Regression", *Statistics and Computing*, Springer, 14(3):199-222, 2004.

Shibazaki, M., "State of practice of jet grouting", *Grouting and Ground Treatment: 3rd International Specialty Conference on Grouting and Ground Treatment*, ASCE, 198-217, 2004.

Tinoco, J., Gomes Correia, A. and Cortez, P., "Application of Data Mining Techniques in the Estimation of the Uniaxial Compressive Strength of Jet Grouting Columns over Time", *Constructions and Building Material*, Elsevier, 25(3):1257-1262, 2011a.

Tinoco, J., Gomes Correia, A. and Cortez, P., "Using Data Mining Techniques to Predict Deformability Properties of Jet Grouting Laboratory Formulations over Time", *Progress in Artificial Intelligence*, Springer, 491-505, 2011b.

Tinoco, J., Gomes Correia, A. and Cortez, P., "Uniaxial Compressive Strength Prediction of Jet Grouting Columns using Support Vector Machines", *The 2011 European Simulation and Modeling Conference, EUROSIS*, 326-330, 2011c.

Xanthakos, P., Abramson, L. and Bruce, D., "Ground Control and Improvement", Wiley-Interscience, 1994.

Welsch, J. and Burke, G., "Jet Grouting – Uses For Soil Improvement", *Geotechnical Engineering Congress (GSP No. 27)*, 334-345, 1991.

Innovative monitoring tools for on line monitoring of excavations. A monitoring test site

Gauthier Van Alboom, Geotechnics Division Flemish Government (FG), Belgium,
gauthier.vanalboom@mow.vlaanderen.be

Leen De Vos, Geotechnics Division FG, Belgium, leen.devos@mow.vlaanderen.be

Koen Haelterman, Geotechnics Division FG, Belgium, Koen.haelterman@mow.vlaanderen.be

Wim Maekelberg, TUC RAIL n.v., Belgium, Wim.maekelberg@tucrail.be

ABSTRACT

A project was launched to monitor a building excavation, consisting of a tangent grout pile wall with HEB profiles and 5 rows of nails.

Three selected firms were invited to develop and perform online monitoring for an excavation, measuring and logging deformation of the wall (x,y,z), maximum moment in the wall, deformation of the soil (z) behind the wall and anchorage forces for anchors/nails. Proposed monitoring techniques consist of optical fiber technology, Microelectromechanical Systems (MEMS) sensors, vibrating wire anchor load cells and electrical beam sensors.

Verification monitoring is performed, using as well traditional inclinometer, topographical measurements, anchor load cells as Brillouin Optical Time Domain Reflectometry (BOTDR) and Draw Tower Grating (DTG) fiber optics. The paper gives a description of implemented monitoring tools and a first comparison of test results.

1. INTRODUCTION

1.1. General context of the project

The government agency for Innovation by Science and Technology (IWT) helps Flemish companies and research centers in realizing their research and development projects. IWT also supports the Flemish Government in its innovation policy and the Flemish administration in realizing their innovative projects.

The project “Innovative monitoring of building excavations” was initiated by the Geotechnics Division (GEO) of the Flemish Government. The project is partially funded by the Flemish Government (through IWT) allowing the set-up of a pilot test phase.

After notification and tendering, three selected firms were invited to work out and implement a monitoring scheme for on line monitoring of a building excavation of a TUC Rail regional network project around Brussels (Maekelberg et al. 2012) :

- FOS&S (Belgian firm specialized in fiber optic sensing), recently taken over by FBGS
- Inventec (Dutch firm specialized in advanced measuring and monitoring systems)
- OSMOS (Belgian affiliate of a French firm specialized in permanent monitoring of constructions and buildings)

GEO in cooperation with Cambridge University (CU), the Belgian Building Research Institute (BBRI) and the General Technical Support Division of the Flemish Government perform verification monitoring, using as well traditional deformation as fiber optic measurements.

A technical committee consisting of representatives of GEO, CU, BBRI and TUC Rail is established for the scientific follow-up of the project.

1.2. Main objectives of the project

The main aim of the project is to promote interactive design by active on line monitoring. The monitoring scheme consists of measuring, logging and deriving:

- deformation of the wall (x,y,z)
- maximum bending moment in the wall
- deformation of the soil (z) behind the wall
- anchorage forces for 2 nails

Due to the nature of the pilot project site (no excavation beneath groundwater level) monitoring of groundwater level was omitted.

The monitoring results were to be monitored digitally and sent to a server for data processing. In order to have full access to all data at all times, the data which are measured continuously are sent to an ftp server and the data are gathered and processed in real time in the cloud. The data are accessible through an internet site of the Flemish Government.

The main goal of the project is an evaluation of monitoring results and suitability of proposed monitoring schemes for application in an interactive design method. This implies that accuracy, installation possibilities, reliability and cost are important aspects to be considered.

2. SITE DESCRIPTION

The monitoring site is located in Belgium, Anderlecht (Brussels), where an extra railway track will be constructed alongside of the existing tracks. The construction pit, installed with monitoring equipment is situated at the Brussels side of the bridge. Photo 1 gives a view on the location before the works. For the deep foundation of the new bridge, a nailed jet grout wall is to be installed next to the existing railway. By doing so, the soil can be excavated vertically and the foundation can be realised in from street level. The excavation depth is 10m and the HEB profiles which are inserted in the jet grout wall have a length of 21m. Five rows of nails are installed over the excavated depth. Figure 1 shows a drawing of the HEB jet grout wall and the nails.



Photo 1: Pictures of the local situation prior to installation

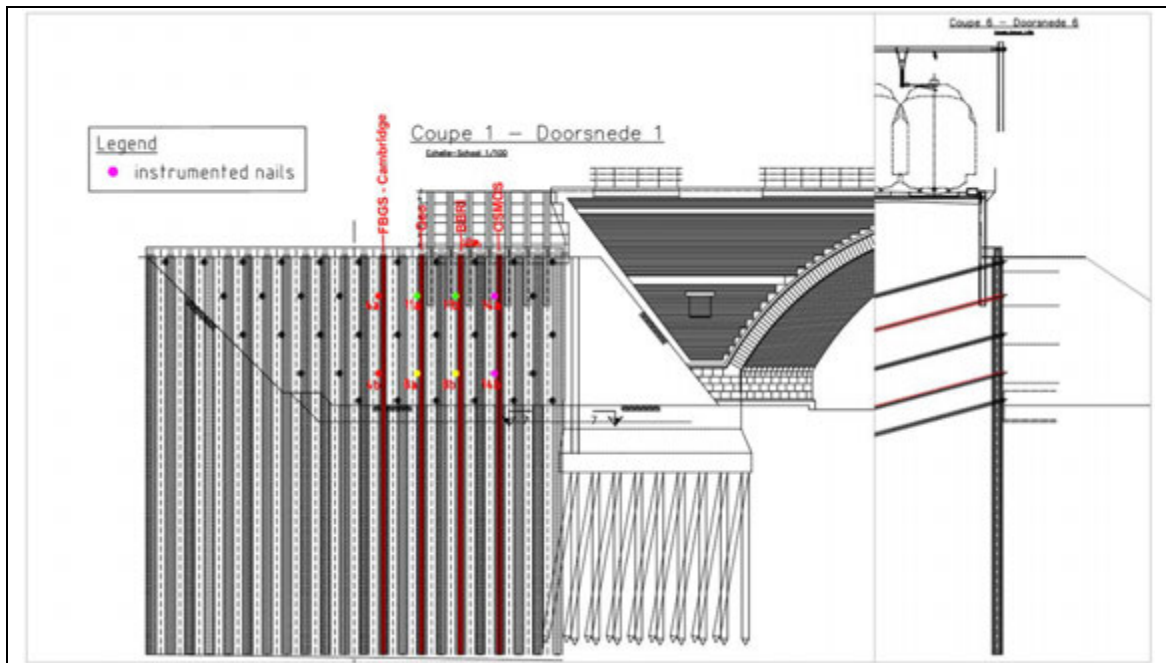


Figure 1: Plan of nailed HEB jet grout wall (front view and side view).

3. MONITORING EQUIPMENT

As described above, monitoring equipment is installed to measure and derive the deformations and moments in the jet grout wall, the deformations of the rail track behind the jet grout wall and the forces and force distribution in the nails. In this section, a description of the installed equipment is given.

3.1. Deformation and moments in the jet grout wall

In order to measure the deformations and derive the moments in the jet grout wall, 2 different techniques are used:

- An inclinometer technique in which the inclination over the height of the HEB profile, placed inside the grouted wall. The inclination is measured at well-known intervals. Both a continuous inclinometer (SAAF) and a traditional inclinometer system (with an external inclinometer which is lowered in an inclinometer casing), are used. Both systems measure the inclination every 0.5m. The SAAF (Shape Accel Array Field) consists of an articulated chain of sensor elements (segments) each 0.5m long. The segments are joined together in such a manner that they can move in relation to each other in all directions. Each segment contains a multi-axial MEMS-chip accelerometer. This makes the segment act as an inclinometer, determining the angle of inclination in both X and Y direction.
- Optical fiber technology, which is used to measure strain and temperature along the HEB profile inside the wall. Optic fibers are small in size, offer a great variety in measurable parameters, to be insensitive to external perturbations, and offer the possibility of remote monitoring. They also have the ability to multiplex many sensors using only one optical fiber, driving down the cost of complex control systems.

By measuring the strain at discrete points or continuously along one continuous fiber deformations of the profile can be detected. The used fiber optic sensor techniques are:

- o Fiber Bragg Grating (FBG) is a type of distributed Bragg reflector constructed in a short segment of optical fiber that reflects particular wavelengths of light and transmits all others. This is achieved by creating a periodic variation in the refractive index of the fiber core, which generates a wavelength specific dielectric mirror. FOS&S uses a fiber optic Anchor Strain Chain, containing different strain segments in series. Each strain segment contains a single strain sensor in between two anchoring points. A relative displacement between the two anchor points is transferred into a change in the strain of the segment. The standard length of a segment ranges from 0.5 m to 5 meters.
- o Draw Tower Grating is an application of FBG offering high mechanical strength, spliceless arrays, direct fixation, high operating temperature range and relative low cost. This fiber optic sensor technique was used by BBRI.
- o The Brillouin optical time-domain reflectometer (BOTDR) used by CU is a distributed optical fiber strain sensor whose operation is based on Brillouin scattering. BOTDR equipment has been developed for practical use in the field of civil engineering. This equipment can measure continuous strain along an optical fiber over long distances up to 10 km.
- o The light attenuation optic fiber sensors of the optical strands used by OSMOS are based on the principle of intensity modulation using analogue measurement: if a fiber optic cable is bent, it loses some of its light where the bending takes place. With the aid of light attenuation measurements, this loss can be measured. The sensor effect is based on the correlation between the changes in attenuation, or light intensity, on the one hand and changes in the length of the fiber optic cable on the other. The Optical Strand is a long-basis deformation detection line, which standard lengths are 2, 5 and 10 meters. This sensor spans a length which is representative of the whole structural element and cumulates averaged information.

Table 1 (section 4) summarizes the different techniques which are applied by the different partners, including the information on installation of the equipment. Figure 2 shows the location of the equipment installed on the HEB profiles. In total, 4 profiles are equipped with monitoring instruments. Almost all instrumentation is installed over the full length of the HEB profile (20m), by either welding or gluing it onto the HEB profile. When necessary, protective casings were placed over the monitoring equipment for protection during installation.

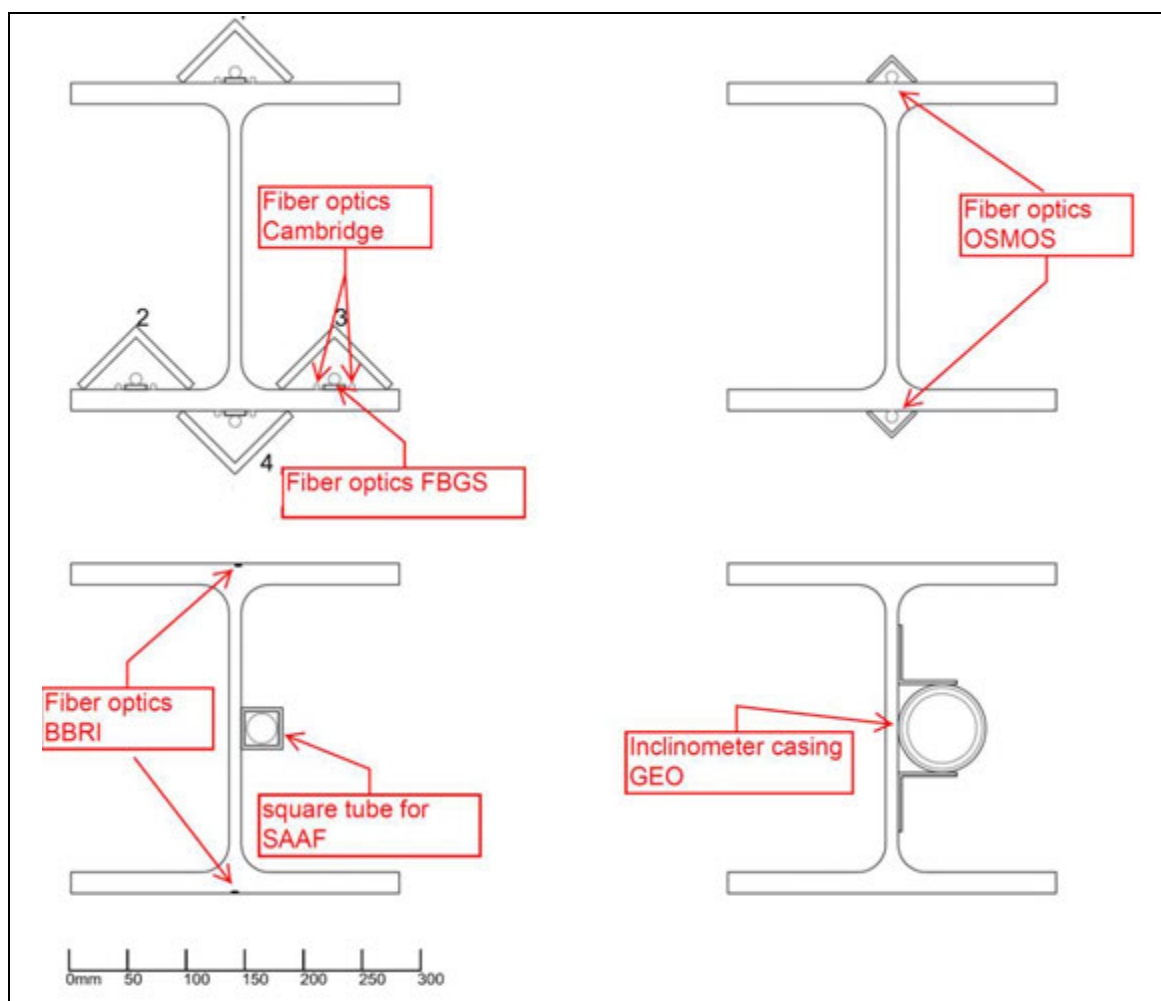


Figure 2: Details of installed equipment along the HEB profiles

3.2. Deformations behind the jet grout wall

As one of the main concerns during an excavation are the settlements of the soil (and inherently the infrastructure) in the vicinity of the excavation, vertical deformation is one of the important parameters which are monitored. In this project specifically, deformations of the railroad track are to be avoided.

The deformations behind the wall are measured:

- with two horizontal inclinometers (a traditional one and a continuous SAAF inclinometer) which are placed perpendicular to the wall in the ballast underneath the rails and thus measure the deformation profile behind the grout wall (Photo 2a).
 - topographically: the rails are marked and vertical deformations are measured by topographic levelling at different stages of the project (Photo 2b).
 - with electrical beam sensors placed on the railway sleepers (Photo 2c); the beam sensor consists of an electrolytic tilt sensor attached to a rigid metal beam. The tilt sensor is a precision bubble-level that is sensed electrically as a resistance bridge. The bridge circuit outputs a voltage proportional to the tilt of the sensor. The beam, which is one to two meters long, is mounted on anchor bolts that are set onto the sleepers. Movement of the railway track changes the tilt of the beam and the output of the sensor. The voltage reading from the sensor is converted to a tilt reading in mm per meter. Displacements are then calculated by subtracting the initial tilt reading from the current reading and multiplying by the gauge length of the sensor (the distance between anchors). When sensors are linked end to end, displacement values can be accumulated from anchor to anchor to provide a profile of differential movements or settlement.
 - with an optical strand with protective casing placed on the railroad tracks (Photo 2d);
- Photo 2 shows some pictures of the different monitoring equipment measuring the deformation.

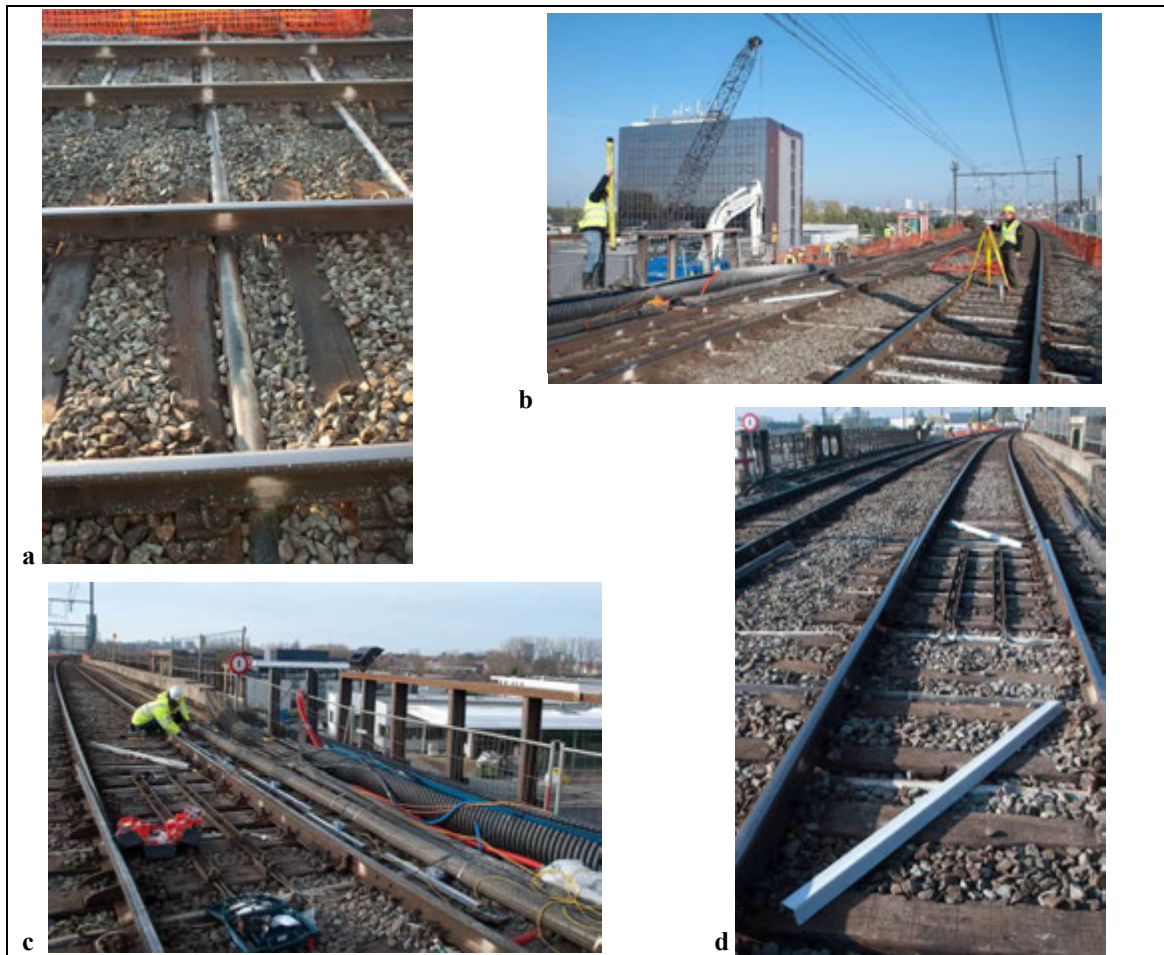


Photo 2: Pictures of the monitoring equipment, measuring the settlements behind the excavation

3.3. Anchor forces

The forces in the nails are expected to be distributed as shown in Figure 3. The maximum force will normally be found along the nail length, depending on the excavation depth. The forces in the nails are measured with different techniques:

- The stress distribution in the nails is measured by means of an optical FBG fiber, which is placed along the full length of the nail.
- The stress is measured with an optical strand near the location where the maximum force is expected (see Figure 3).
- The force transition at the wall is measured with load cells. To have an idea of the difference between the maximum force in the nail and the force which is measured near the wall, two different lengths of the nail are made free (2m and 9m).

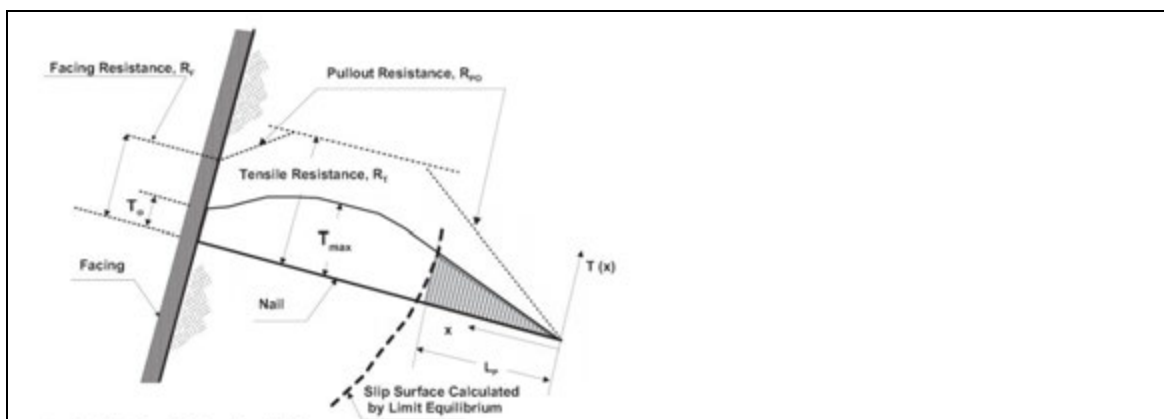


Figure 3: Force distribution in a nail (Lazarte et al., 2003)

4. INSTALLATION

The installation of the equipment was performed in several stages. At first, (almost) all instrumentation monitoring the deformation and strains in the jet grout wall were mounted on the HEB profiles. In total 4 HEB profiles are equipped with instrumentation (Figure 2).

The HEB profiles have a length of 21m and are placed in full length in a fresh bore hole, filled with grout. Except for the one HEB profile that could only be inserted in the grout over a length of about 19m.

Table 1 gives more detailed information on each monitoring equipment and photo 3 shows some pictures which are taken prior to installation. Figure 4 gives some more information on the location of the instrumentation. Figure 4 gives the location of each instrumentation of the different partners.

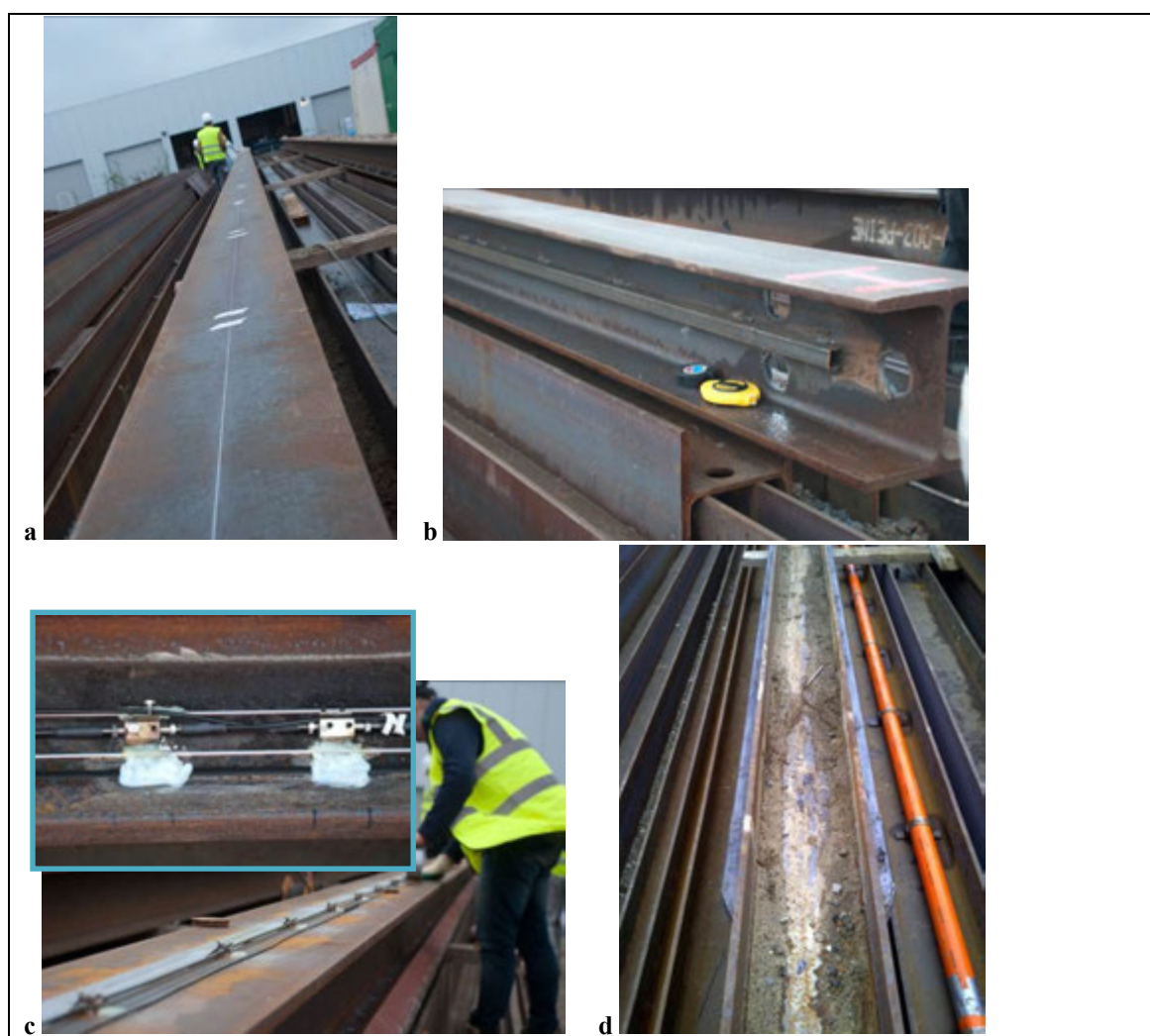


Photo 3: pictures taken during installation of the equipment:

a) optic fiber of BBRI, glued in a thin slit in the HEB flange;

b) square tube for SAAF (Inventec), welded to the HEB profile;

c) centrally an optical fiber from FBGS, fixed with screws in a welded anchor every 0.5m to 2m; next to the optical fiber from FBGS, optical fiber for BOTDR, glued every 0.5 to 2m.

d) on the left protection casing for optical strands of OSMOS, on the right, inclinometer casing for the traditional inclinometer

Table 1: details of the installed equipment

Reference number on Figures 2 and 4	Subcontractor	Measured parameter	Monitoring equipment	Installation	Details
1	CAMBRIDGE UNIVERSITY	Strain on the HEB profile in the jet grout wall	optical fiber using Brillouin Optical Time Domain Reflectometry (BOTDR)	The fiber is prestressed and glued to the HEB profile.	The strain is measured along the full length of the fiber. Discontinuous measurement.
2	FBGS international	Strain on the HEB profile in the jet grout wall	Optical fiber using Fiber-Bragg-Grating Sensors (FBG)	4 optical fibers are mounted in brackets (anchors) which are welded to the HEB profile. A protective casing is placed over the fibers for protection during installation.	The strain is measured over a length of 20m. The anchors are placed every 0.5 m at the upper 7m of the HEB profile and every 2m at the lower part. Continuous measurement.
3		Inclination of the crossbeams the rails	Electrical beam sensor	The equipment is fixed on beams which are bolted on the railway sleepers	An end to end string (10m in total) of different beams is made. The rotation of each beam is measured. The first beams are secured to sleepers on the bridge, which is assumed to be a fixed point. Discontinuous measurement.
4		Strain in the nails	Optical fiber using Fiber-Bragg-Grating Sensors	The fiber is placed in a hollow nail.	The fiber is fixed on a steel pipe, which is placed inside a hollow nail. The hollow nail is filled with grout after installation of the fiber. Continuous measurement.
5	Flemish Government	Deformation of HEB profile in the jet grout wall	Traditional inclinometer	Inclinometer casing attached to the web of a HEB profile	Discontinuous measurement made at each important stage during the building process. The measurements are made every 0.5m.
6		Deformation of the soil behind and perpendicular to the jet grout wall	Traditional horizontal inclinometer	Inclinometer casing placed in the ballast underneath the rails, perpendicular to the jet grout wall	Discontinuous measurement made at each important stage during the building process. The measurements are made every 0.5m.
7		Deformation of the top of the jet grout wall and of the rails behind the wall	Topographical measurements	Total station + levelling	Discontinuous measurements
8		Anchor force	Load cell	Two load cells are placed on two nails between wall and bolt. A free length of 2m and 9m is used over the last part of the nail.	Discontinuous measurement. The total force which is exerted on the nail is measured.

Reference number on Figures 2 and 4	Subcontractor	Measured parameter	Monitoring equipment	Installation	Details
9	INVENTEC	Deformation of HEB profile in the jet grout wall	Vertically placed continuous inclinometer (Shape Accel Array / Field)	The SAAF is lowered after installation of the HEB profiles inside a square tube, which is welded to the web of the HEB profile.	Continuous measurements of the inclination are made every 0.5m (x and y direction). The deformation profile is determined based on the inclination measurements.
10		Deformation of the soil behind and perpendicular to the jet grout wall	Horizontally placed continuous inclinometer (Shape Accel Array / Field)	The SAAF is placed in a tube, which is placed in the ballast underneath the rails, perpendicular to the jet grout wall	Continuous measurements of the inclination are made every 0.5m (z direction). The deformation profile is determined based on the inclination measurements.
11		Anchor force	Load cell	Two load cells are placed on two nails between wall and bolt. A free length of 2m and 9m is used over the last part of the nail.	Continuous measurement. The total force which is exerted on the nail is measured.
12	OSMOS	Strain on the HEB profile in the jet grout wall and inclination of the top of the HEB profile	Optical strands	Two 10m long optical strands are attached to the upper part of the HEB profile. An inclinometer is placed on top of the HEB profile	The optical strands are installed under tension. Extension or compression of the strands are measured at two sides of the HEB profile. The difference between the two measurements indicates bending of the profile. The direction of the bending is indicated by the inclinometer.
13		Deformation of the rails behind the grout wall	Optical strands	Two 2m long optical strands are fixed on the sleepers	The optical strands are installed under tension. Extension or compression of the strands are measured, indicating differential movement between two crossbeams.
14		Strain in the nails	Optical strand	The strand is placed on an extra steel bar, placed next to the nail.	The strand has a length of 2m and is prestressed and fixed to a steel bar, which is placed immediately beside a nail. Continuous measurement.
15	BBRI	Strain on the HEB profile in the jet grout wall	Optical fiber	4 optical fibers are mounted in brackets (anchors) which are welded to the HEB profile. A protective casing is placed over the fibers for protection during installation.	The strain is measured along 20m. The anchors are placed every 0.5 m at the upper 7m of the HEB profile and every 2m at the lower part. Continuous measurement.

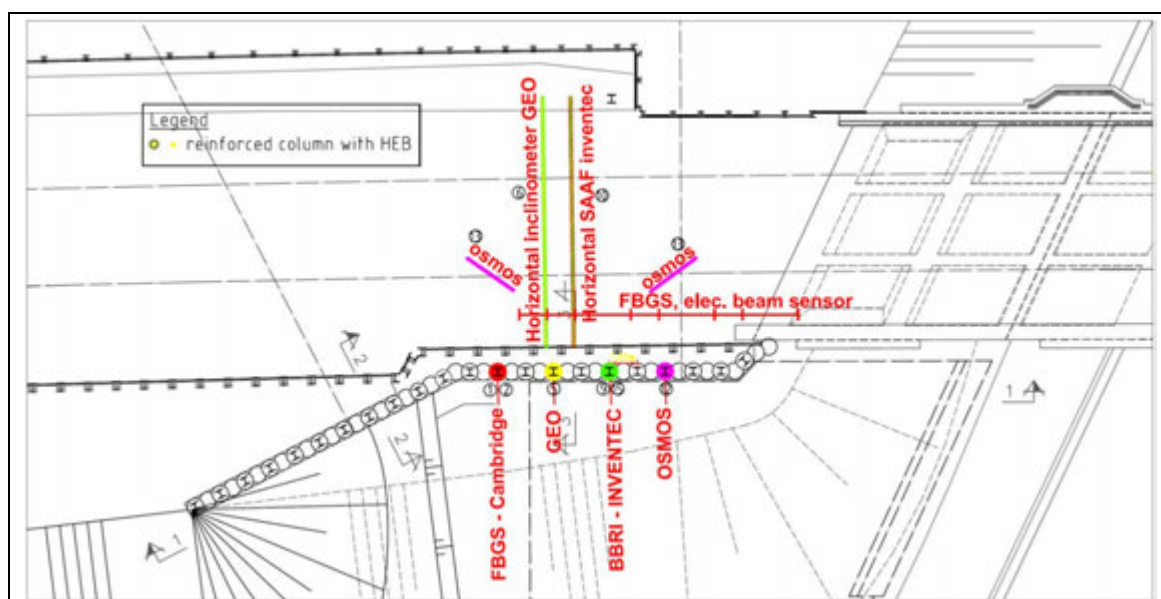


Figure 4: location of the instrumentation (top view)

5. FIRST RESULTS

For the moment, the excavation is still ongoing and not all instrumentation has been installed yet. Also the measurements have not been completed or have not been completely analyzed. Therefore, only the first results of the measurements inside the jet grout wall and the deformations behind the jet grout wall are presented.

Table 2 gives some information on timing of installation and progress of the works.

Table 2: information on timing of the excavation and installation of monitoring

Date	Information
22-23/10/2011	Installation of the instrumented HEB profiles in the jet grout wall
03/11/2011	Excavation up to 1m below the top of the jet grout wall
06-09/11/2011	Installation of the first row of nails
06-07/12/2011	Excavation up to 3m below the top of the jet grout wall
08-12/12/2011	Installation of the second row of nails
10-11/01/2011	Excavation up to 5m below the top of the jet grout wall

5.1. Deformation of the jet grout wall

Figure 5 shows the measurements which are made over the length of the HEB profile with the FBG sensors (a), with the traditional inclinometer (b) and the continuous inclinometer (c). Plot (a) shows the strain which is measured over 1 of the 4 strain chains, while the other two show the deformation measured with the inclinometers in the direction of the largest movement. Some difference can be seen within the measurements of the traditional and the continuous inclinometer. For example, the depth at which the maximum displacement is measured differs, but in fact, the SAAF is placed on a HEB profile which could not fully penetrate in the jet grout wall and thus extends 2m above the top of the wall. In addition to this, the HEB profile is also twisted and the flanges do not stand perpendicular to the wall, probably due to the presence of a stone during installation. The location of higher strain, measured with the FBG sensors is comparable to the location of deformation measured with the traditional inclinometer (upper 6m). It should be mentioned that the data before 25/11/2011 is not temperature compensated and that at this date, the data has been reset to zero strain. At the beginning, large strains were measured due to the heating in the fresh grout.

Figure 6 plots the strain which is measured with the optical strains from Osmos. Two strain chains are placed, 1 on each flange. At the moment that there is a difference between the two chains, this is due to bending of the HEB profile.

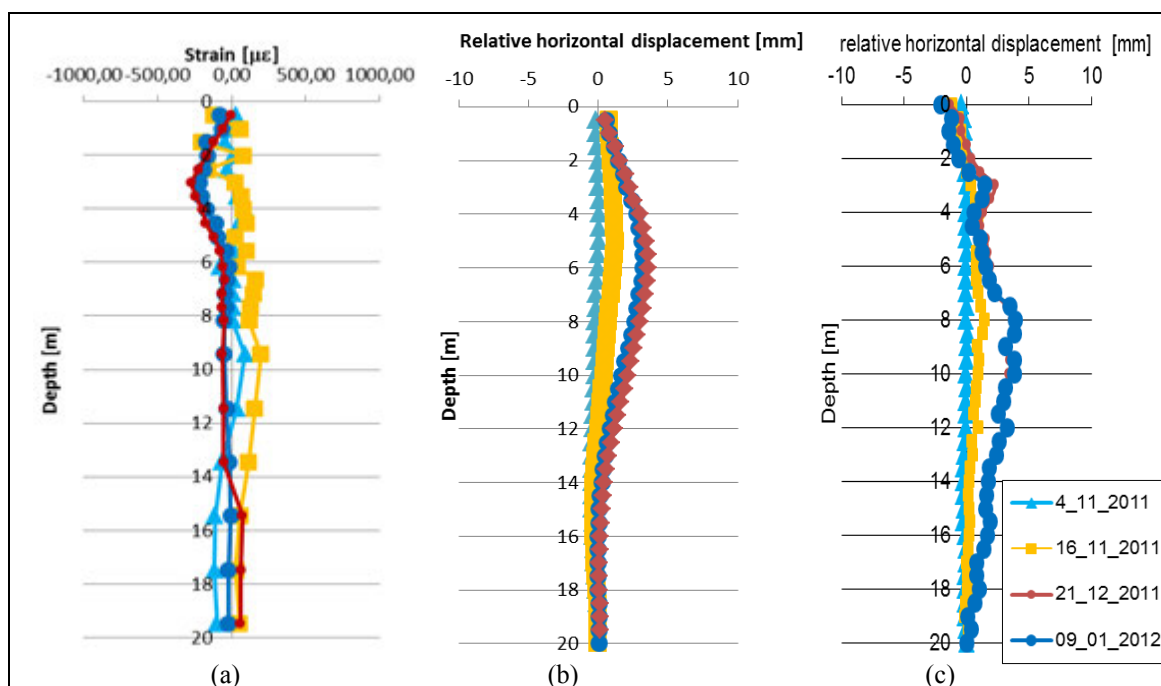


Figure 5: (a) strain (FBGS) and (b), (c) respectively deformation measured with a traditional inclinometer and the SAAF along the length of the HEB profiles

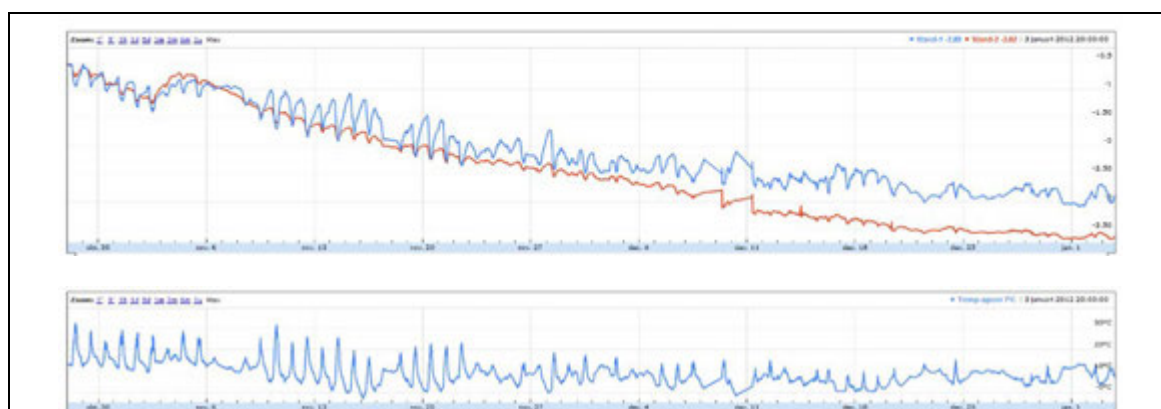


Figure 6: strain measured with the optical strands from OSMOS: top: strain, bottom: temperature

5.2. Deformations of the rails

Figure 7 gives the results of the topographical measurements which are made along the length of the rails on 11/12/2011 (reference measurements were made on 22/10/2011). The measurements made over a distance of 0 to 20m are located at the opposite side of the bridge, where a similar excavation is made. The old railway bridge (which is founded on piles) is located between 20m and 60m from the reference point (0m) and the excavation which is monitored is located approximately between 60 and 70m. The red line represents the rail track located nearest to the excavation, while the blue line represents the rail track located at the opposite side. At some time, the rail track at the opposite side had to be lifted at the location of the excavation, as it had encountered too large displacements. This can be clearly seen in the measurements. The maximum change in level, which is measured topographically on the sleepers is somewhat less than 4mm when the excavation had a depth of about 3m.

Figure 8 shows the measurements of the horizontal inclinometers, which are located perpendicular to the jet grout wall. They show a maximum settlement of approximately 10 mm at a distance of 8m behind the jet grout wall.

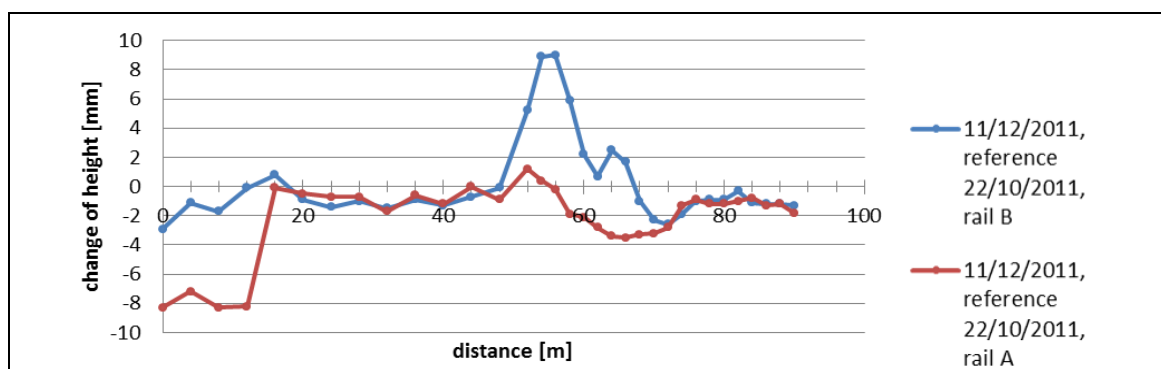


Figure 7: topographical leveling on 11/12/2011, with reference reading taken at 22/10/2011

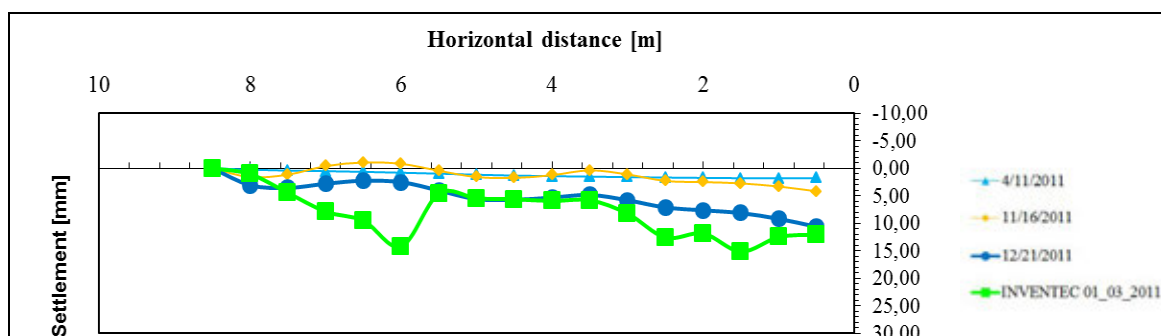


Figure 8: Comparison between settlements measured with the SAAF and a traditional inclinometer..

6. EVALUATION

As mentioned above the monitoring project is still in progress and therefore only some preliminary conclusions can be drawn. It has however already become clear that:

- All proposed monitoring techniques proved to be applicable within a construction site environment. A good cooperation between monitoring organization, project owner and contractor is essential for successful monitoring. It is therefore desirable to incorporate monitoring activities in the project specifications.
- Notwithstanding a close follow-up one should always account for unforeseen events (e.g. an instrumented HEB profile that could not be inserted to the proposed depth, tilting of the profile). Therefore redundancy of instrumentation and instrumented structural elements is essential.
- Online data transfer is successfully achieved, with however some practical problems. Despite the provision of a separate container for data acquisition and data transfer with secured power supply, the monitoring team has been confronted with several power cuts. During planning, special attention should be given to electricity supply.
- It is advised to incorporate a (limited) traditional set of monitoring tools parallel to innovative monitoring tools. They might not offer the same possibilities as new technologies but have a proven status of reliability and give additional information for interpretation of the results.

Comparison and evaluation of monitoring results cannot be substantially performed in the present stage of the project, but will be dealt with in a subsequent paper.

7. ACKNOWLEDGEMENTS

The authors would like to acknowledge the IWT for its' funding.

REFERENCES

A Carlos, A. Lazarte, Victor Elias, David Espinoza, Paul J. Sabatini, 2003, Report FHWA0-IF-03-017, GEOTECHNICAL ENGINEERING CIRCULAR NO. 7 3 Year, Soil Nail Walls.

Maekelberg, W., Verstraelen, J., De Clercq, E., 2012, Realization of a railway enlargement in unstable excavations alongside the existing line at Dilbeek (Belgium), ISSMGE – TC211

Preservation of Panorama Mesdag, The Hague

A.E.C. van der Stoel, CRUX Engineering BV & University of Twente, Netherlands, vanderstoel@cruxbv.nl
M. de Koning, CRUX Engineering BV, Netherlands, dekoning@cruxbv.nl

ABSTRACT

This paper deals with the preservation of the Panorama Mesdag, a cylindrical painting, more than 14 meters high and 120 meters in circumference. The vista of the sea, the dunes and Scheveningen village was painted by one of the most famous painters of the Hague School, Hendrik Willem Mesdag. It is the oldest 19th century panorama in the world in its original site and a unique cultural heritage. About three years ago the building, which is a uniquely complex structure, was damaged by a nearby excavation.

In the years to follow a series of measures have been taken of which the compensation grouting of the foundation is the most extensive from a geotechnical point of view.

This paper outlines the history of the damage, the construction of the building and most importantly the extents of the compensation grouting and the result of the grouting and the extensive monitoring. The effectiveness of the grouting is determined and conclusions have been drawn for the still to be performed excavations and construction activities.

1. INTRODUCTION

For the realization of a two layered underground parking garage at the Mauritskade in The Hague a 6m deep building pit had to be constructed. This parking garage is situated between the Museum Panorama Mesdag, the The Hague Hilton hotel, the gardens of the British Embassy and the Maurits Canal. The museum's *Rotonde* building, with the historical *Mesdag* painting inside, is particularly at short distance of the building pit. To prevent damage to the building and the painting due to possible vibrations caused by installing sheet piles by vibrating, the decision was made to realize this side of the building pit constructing a secant piled wall. In Figure 1 and Figure 6 and 11 an overview is given of the project location and the location of the secant piled wall.

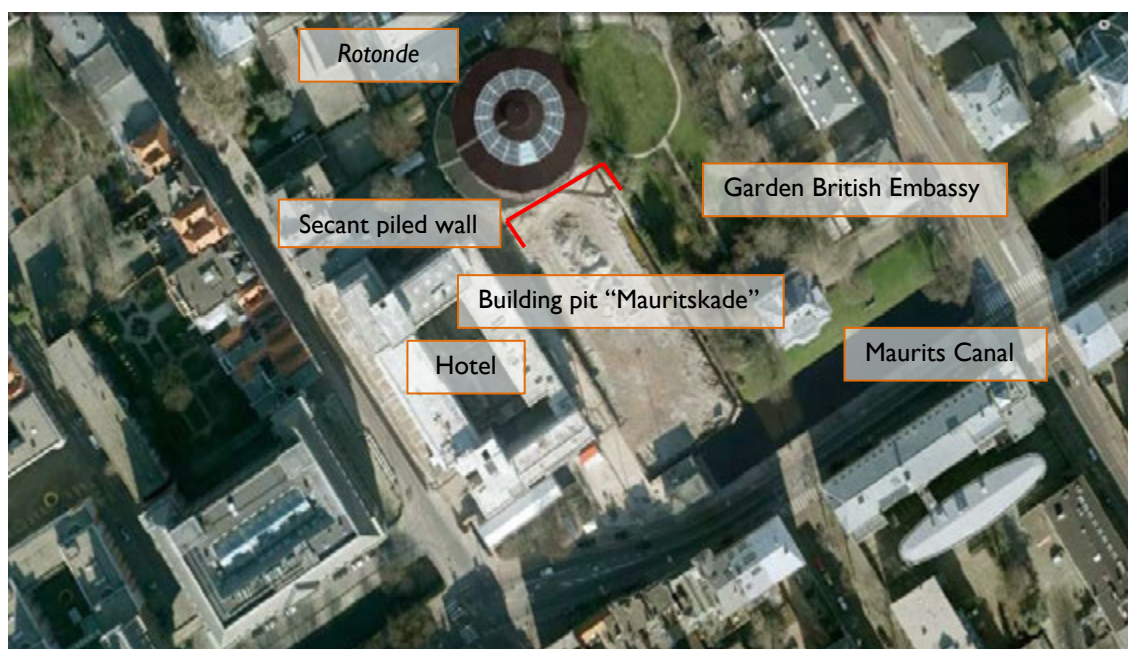


Figure 1: Overview of location Museum Panorama Mesdag and the building pit (source: Google Earth)

Although the *Rotonde* building is now a monument by itself, deformation of the building may cause severe tension in the painting, which is attached to its walls.

During the construction of the secant pile wall significant deformations were observed at the *Rotonde* building. After these observations the work on the building pit was stopped and several investigations were started to find the possible cause of the deformations and to determine the structural stability of the

building. The conclusion of these investigations was that the building had insufficient structural stability and that mitigating measures needed to be executed. These measures consisted on the one part of strengthening the construction of the building and on the other on stabilizing the foundation and partly compensation of the vertical movement of the building by conducting *compensation grouting*. This paper deals with the geotechnical part of the compensation grouting measures that are taken.

2. ROTONDE BUILDING

The *Rotonde* is built in the eighties of the 19th century and has a regular hexadecagon shape. The construction of the building can be characterized by its simplicity. The columns at each of the 16 corners are made of steel and are connected with concrete footings. Between the columns the spacing is filled with plastered brickwork. The roof of the building consists of cast iron construction which carries its own weight. The building is founded on a shallow foundation. In Figure 2 a cross section of the building is shown.

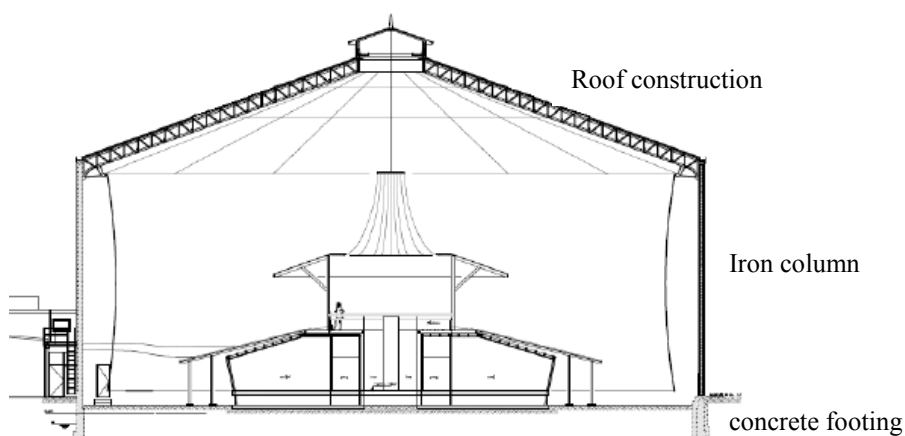


Figure 2: Cross section of the Rotonde building

3. SOIL CONDITIONS

Before the work started several cone penetration tests (CPTs) were executed at the construction site. Several of these CPTs were located near the secant pile wall. In Figure 3 a typical CPT of the construction site is shown. The greenfield is at a level of about 0,6m above NAP (NAP is the reference level used in the Netherlands)

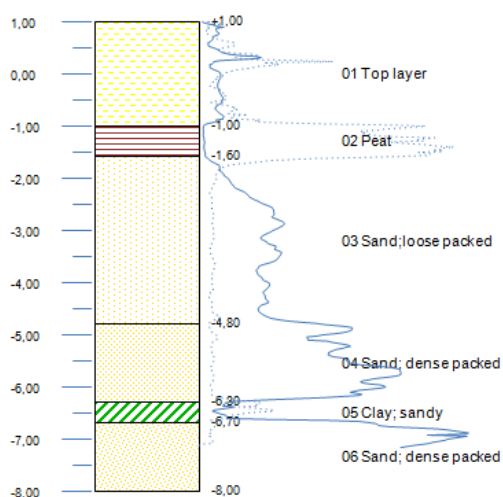


Figure 3: Typical CPT construction site The Hague

From the CPT it can be concluded that beneath the sandy top layer, at a depth of about 1,5m below greenfield, a Holocene peat layer is found with a thickness of about 1m. Below this layer sand layers are found varying from a loose density to dense. From a depth of about 6,5m below the greenfield thin sandy clay layers can be found between the sand deposits.

4. MONITORING

Before the start of the construction work, in 2007 a comprehensive monitoring system was installed inside the *Rotonde*. The system consists of an automatic leveling system with a sensor placed at each column at foundation level, 16 sensors in total, as well as in the roof construction. In Figure 4 an overview is given of the sensors positioned at foundation level. Figure 5 shows the total station used for the measurements and a detail of a deep CPT that was used as an absolute reference level. The deformations of the building were measured in three directions, the vertical direction and the longitudinal and transversal horizontal direction.

Due to the large amount of sensors the time interval between two measurements of an identical sensor was about 60 minutes. This could be speeded up to about every 15 minutes if the sensors in the roof construction and at the back of the building, sensors no. 90 until 160, on foundation level were neglected. This means that only the sensors directly linked to construction works thus of particular interest, the sensors directly next to the building pit no. 10 until 80, were measured.

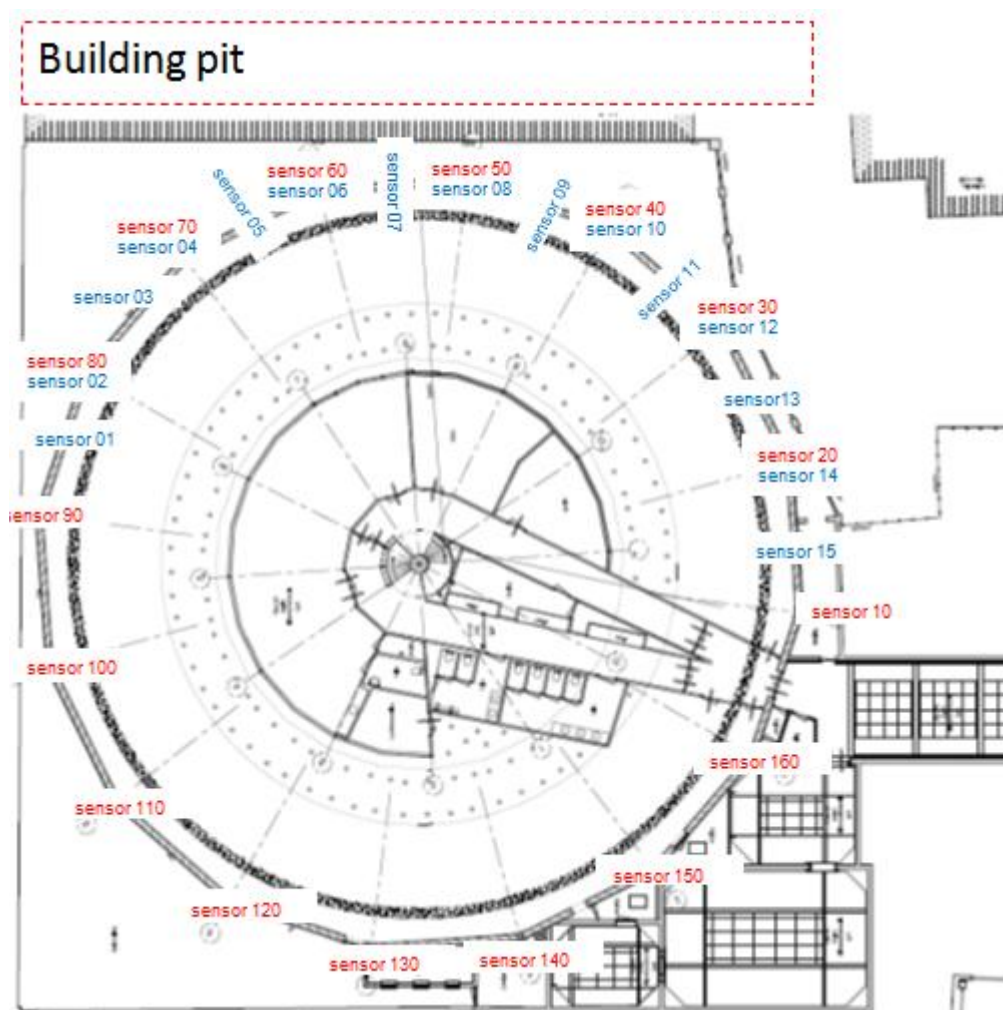


Figure 4: Overview measuring points at foundation level

During all stages of the work, the deformations of the *Rotonde* in both the horizontal as well as the vertical plane were continuously monitored. To register the vertical displacements during compensation grouting a faster and more accurate measurement system was needed.

Therefore, to monitor the grouting process and compare the strict requirements for the distortions with the measured distortions, a hydrostatic leveling system was installed as a secondary system. This system records realtime the vertical displacements at 15 sensors, which were located on the foundation footings and the wall between the footings.

Before the start of the compensation grouting a comprehensive analysis was made of the deformations of the *Rotonde* that occurred during the installation of the secant pile wall. The analysis was based on the measured displacements in vertical and horizontal direction using the automatic leveling system. Based

on the measured deformations the rotation (α) and relative angular distortion (β) in both vertical and horizontal direction were determined. This analysis was executed to determine the maximum rotation (α) and relative angular distortion (β) which has occurred in the past. The analysis was used to compare the deformations during the compensation grouting with the historic deformations.

Based on the measured data in the past the natural movements, for example due to temperature change and groundwater fluctuations, of the *Rotonde* were also analyzed. From this analysis it could be concluded that the building shows a natural vertical displacement of about $+ / - 0.3$ mm per day.

The Municipality of The Hague specified a *limit* value of 2mm of vertical deformation for each sensor during the installation of the compensation grouting. The *alarm* value was set to be 1mm. If the alarm value was exceeded the involved parties were warned by means of a text message. Also for the rotation (α) and relative angular distortion (β) in both vertical as well as horizontal direction a limit value of 1:1200 was set by the Municipality.

Considering the natural movements of the building and the accuracy of the measurement system the requirements for the deformation were considered to be very strict.



Figure 5a: Part of Mesdag's painting and Rotonde roof



Figure 5b: Total station at foundation level and part of Mesdag's painting ; detail: deep CPT for absolute reference level

To be able to determine and evaluate the rotation and relative angular distortion of the building on the fly, a special spreadsheet has been prepared which, based on the direct measurements, directly calculates all the rotations and relative angular distortions.

Prior to the compensation grouting it has been determined that the measured displacements on July 26, 2010 would serve as a reference for comparing the measured displacements during the compensation grouting works.

5. COMPENSATION GROUTING

Compensation grouting offers the possibility to lift the foundation of the *Rotonde* as well stabilize the ground underneath the building, this method is found to be the most appropriate mitigation measure. The horizontal fixation of the building level is ensured by installing a structural horizontal fixation using a sort of *spokes* at foundation level to connect the outer wheel of the *Rotonde* to the core of the structure.

The compensation grouting was carried out according to the Soilfrac® principle as developed by Smet-Keller. With this technique specific grout injections are made to increase the effective stress in the ground. With the increase of the effective stress cracks are created around the injection valve and the grout suspension can flow into the soil. By filling the soil with the grout suspension the soil above the injection valve will finally be lifted, so the occurred settlement during the construction will be (partially) compensated.



Figure 6: Overview of the site; left Hilton Hotel, middle PM & compensation grouting equipment

The injection work consisted of three phases:

1. Initial injections, to fill the pores in the soil.
2. Contact injections which equals the horizontal effective stress to the vertical effective stress.
3. And finally the injections that will lift the foundation of the building.

In Figure 7 the Soilfrac® principle is shown.

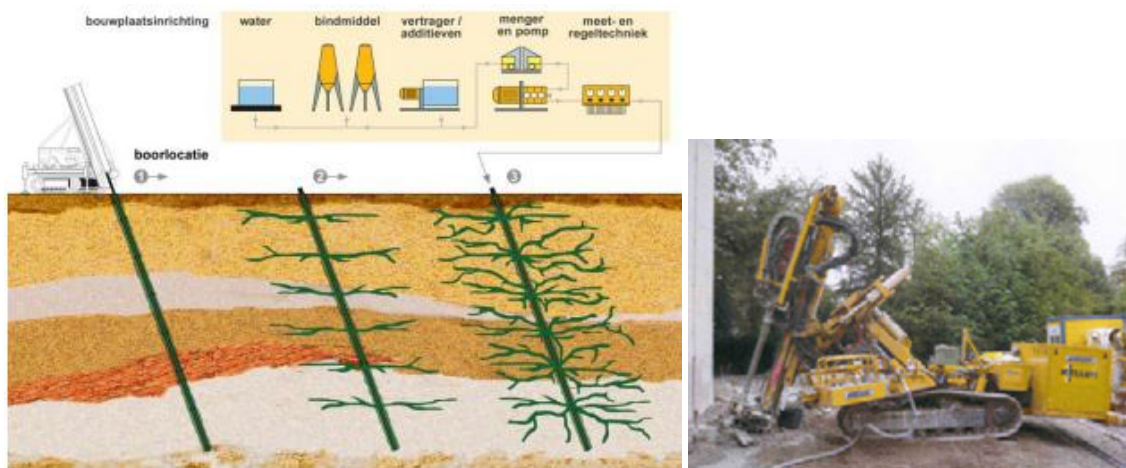


Figure 7: Compensation grouting by means of Soilfrac® Principe (source: Keller Funderingstechnieken b.v.)

In August 2010 the work was started by installing Tubes-à-Manchette's (TAMs) into the ground to a depth of approximately NAP -7m. A total of 64 TAMs including 32 vertical and 32 diagonal TAMs were installed in a period of two weeks (see Figure 8). The vertical TAMs were placed at a distance of approximately 0.6m from the *Rotonde*. The top of the diagonal TAMs was located approximately 1.6 m from the façade. The diagonal TAMs passed the foundation footings of the *Rotonde* at a depth of about

NAP -2.5 m. To reduce the deformation of the building during the installation process as much as possible, the TAMs were installed using a cased drilling system. During the installation process of the TAMs the borehole was kept stable using a drilling fluid. After pulling the inner tube the TAM was inserted.

During the installation of the TAMs the limit value of the vertical displacement was set to be ± 2 mm. An initial alarm value was determined at a measured vertical displacement of ± 1 mm. This alarm value was increased to ± 1.5 mm at several sensors during the installation process, because it was the expectation that the 2mm boundary would not be reached at these points. This increase was necessary because at several sensors the alarm value was exceeded. During the last two days of the installation of the TAMs the limit value of ± 2 mm was exceeded at the final installation points / sensors. A maximum vertical displacement was measured of about -2.5mm at the *Rotonde* footing which was at the shortest distance of the secant piled wall. In consultation with all the involved parties it was decided to allow this exceedance if the rotation and the relative angular distortion in both vertical as well as horizontal direction did not exceed the limit value 1:1200. These requirements were met at all sensors.

To perform the necessary grout injections, double packers are placed inside the TAMs. The TAMs have injection valves with a centre to centre distance of approximately 500 mm. Through the injection valves the grout is injected under a high pressure (>5 bar) into the soil. To compensate pressure losses in the pipes a higher initial pressure is applied. The pressure losses in the pipes are particularly depending on the applied water-cement ratio (liquidity) of the grout and are determined on the basis of proofs.

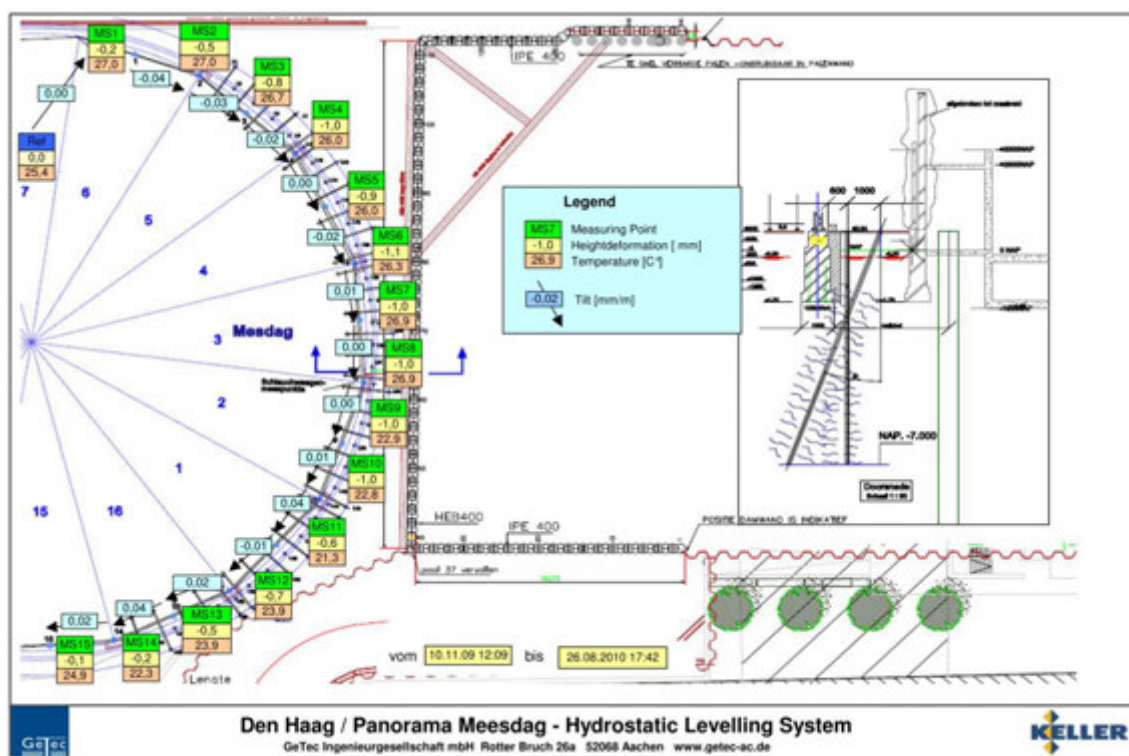


Figure 8: Vertical deformations during compensation grouting process

Before the start of the compensation grouting the decision was made to end the *initial* and *contact* injection after a arbitrarily chosen lift of the building of 0.3mm. After the first two days of initial grouting the measured lift at several sensors already exceeded 0.3mm indicating a high efficiency of the injections. The reaction of the ground was so good that at the same time the pores were filled and the vertical- and horizontal stress were leveled. This meant that the first two stages of the injection process were effectively executed at the same stage. This can be explained by the fact that during the drilling process the pores of the sand were already being filled with drilling fluid so less grout was needed to fill the pores than initially assessed.

On the third day of grouting, it was decided to adjust the lift criterion from 0.3mm to 0.5mm and possibly adjust the injection volumes. After one week of initial grouting and contact grouting all sensors reached the lift criterion of 0.5mm. After a 3-day 'resting' / consolidation period it could be decided that the

amount reached lift was permanent.

After this the actual to lift the *Rotonde* injections could be started. By alternately grouting the vertical TAMs a wall was created around the foundation of the *Rotonde*. By grouting the lower injection valves of the diagonal TAMs a kind of footing was placed below the walls. The remaining non-grouted injection valves were than alternatively used for controlled lifting of the foundation/building.

The required amount of lift can be divided into three components, being:

1. lift to compensate for subsidence as a result of installing the TAMs;
2. lift to reach the desired net lift at each footing;
3. lift to compensate for plastic shrinkage ("bleeding") of grout (volume reduction by bleeding occurred, the efficiency of the grouting was approximately 90%, which is very high!).

For lifting the foundation footings by compensation grouting the maximum net lift was set to be about 4mm for the footing closest to the secant pile wall (point 50). The lift for the other footings was a linear reduction from the maximum lift to about 0.5mm for the footings which are located at the edges of the building (point 10 and 80).

After reaching the desired lift a consolidation period of two weeks considered of the *Rotonde* was sufficiently stable / settlement free.

In Figures 8 and 9 an overview is given of the measured vertical displacements during the compensation grouting process.

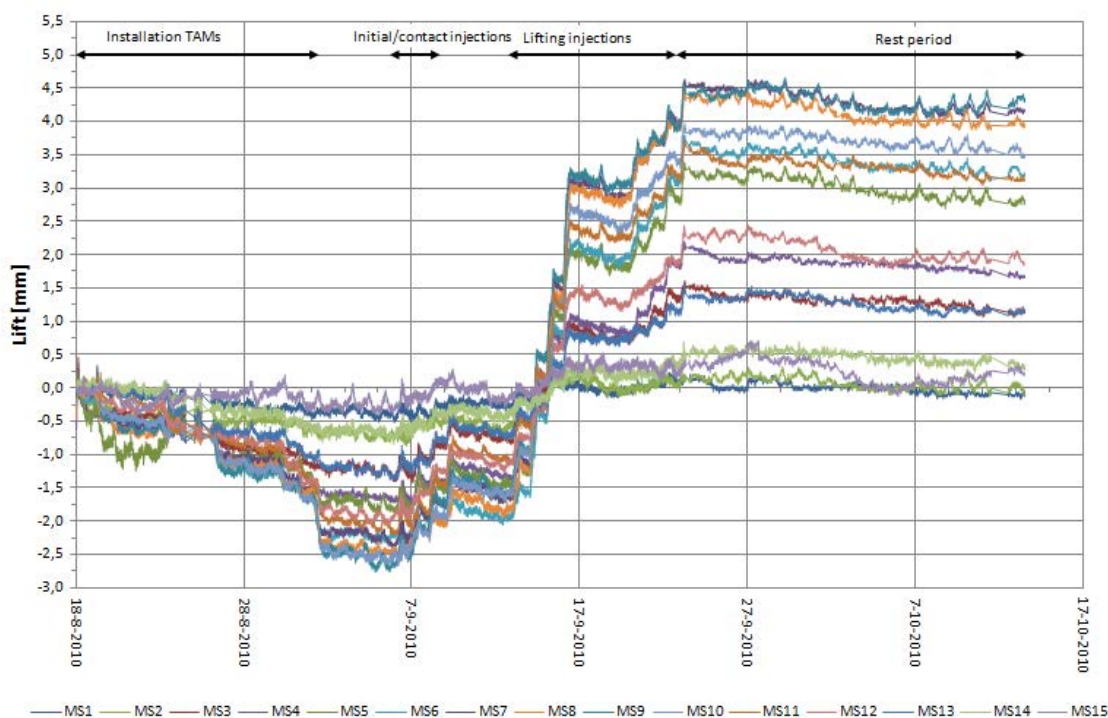


Figure 9: Vertical deformations during compensation grouting process

From Figure 9 it can be concluded that a maximum lift of approximately 6.5mm was needed to achieve a net lift of about 4mm. The compensation grouting operations were ended in the morning of September 23.

At the time the grouting stopped, the desired amount of lift was reached at all but one sensor and the sensor that did not reach the desired lift was only 0.1mm short. During the rest period of two weeks, the vertical displacement was monitored and it was concluded that the building was stable. At the first couple of days of the rest period a noticeable relaxation / consolidation was measured which can be explained by the bleeding effect and the natural behavior of the *Rotonde*.

6. CONCLUSION

During all stages of the work, the monitoring data was analyzed directly on the site and compared with the required limit values. This way, if necessary, the compensation grouting scheme could be adjusted immediately, which was vital due to the particular vulnerable construction and unpredictable behavior of the Rotonde building.

During TAM installation a maximum settlement of 2.5 mm was measured in the vicinity of the secant pile wall which meant a small but acceptable exceedance of the limit value of ± 2 mm. Because of the very strict and on the fly monitoring of the deformations and the excellent communication between all the involved parties this was allowed and the the installation process could be to continued.

After installation of the TAMs, the initial injections showed an very good reaction of the ground. At the same time the pores were filled and the vertical and horizontal stress were leveled. This meant that the first to stages of the grouting process were effectively executed simultaneously.

Subsequently, the actual charge grouting was performed. The foundation of the *Rotonde* was lifted for a maximum of approximately 7mm with a 4mm net heave. The grouting works have were completed successfully September 23rd 2010.

After this first grouting stage, grouting has been repeated successfully in July 2011 during the construction process. Finally the building pit has been excavated until the final depth (see Figure 9b en 10) without any further problems for the Panorma Mesdag building.

7. ACKNOLEGEMENT

The authors wish to thank Panorma Mesdag and contractors BAM Civiel Zuidwest and Smet-Keller for their cooperation in this publication.



Figure 9b: Frontal view of excavation level -1 with struts, piles wall and bottom part of the Rotonde

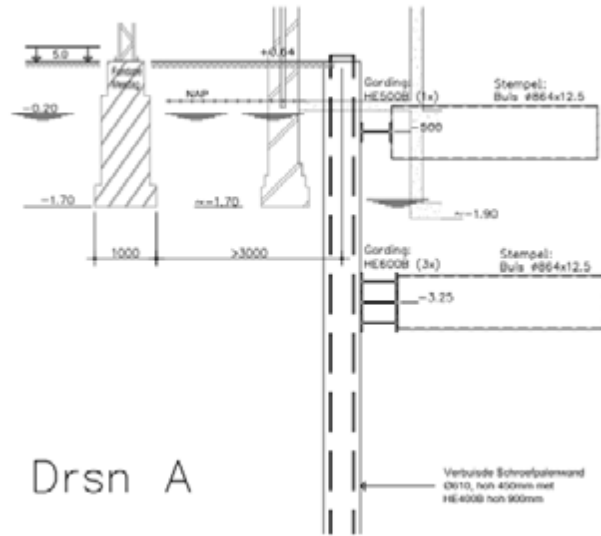
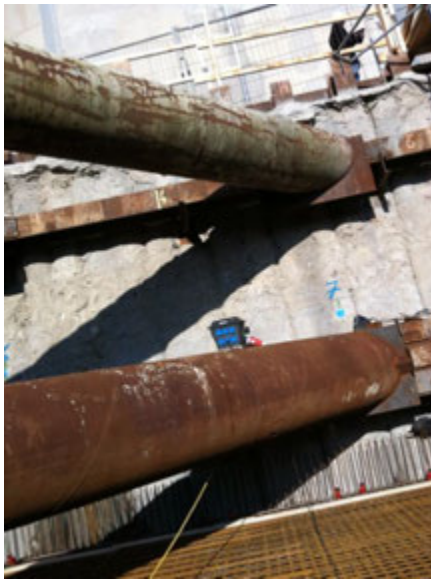


Figure 10: View and cross section of/at excavation level -2 with floor, struts, piles wall and bottom part of the Rotonde

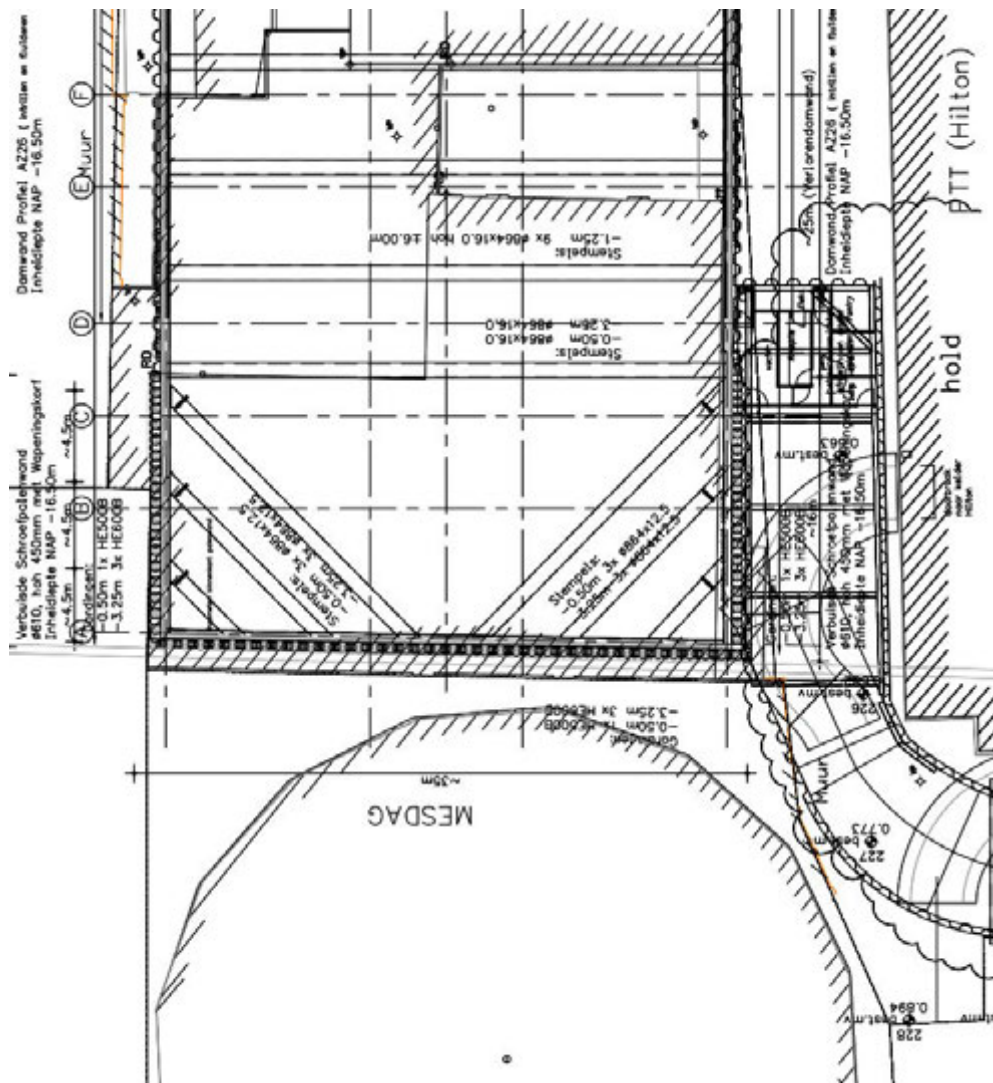


Figure 11: Plan view of the building pit and part of the Rotonde

Groutability of clean sand using sodium pyrophosphate modified bentonite suspensions

Jisuk Yoon, Department of Civil, Architectural and Environmental Engineering
The University of Texas at Austin, Austin, TX 78712-0280, USA, koyapple@mail.utexas.edu

Chadi El Mohtar, Department of Civil, Architectural and Environmental Engineering
The University of Texas at Austin, Austin, TX 78712-0280, USA, ElMohtar@mail.utexas.edu

ABSTRACT

Groutability of clean sands using sodium pyrophosphate (SPP) modified bentonite suspensions was studied to investigate its applicability for permeation grouting. The relative grain size of the soil and the grout has been widely used to evaluate groutability of particulate suspensions; however, such criteria does not account for either the specifics of the suspension particles (such as Cation Exchange Capacity,...) or the effects of chemical modifications of the suspensions on the groutability. The modification of grouts may improve the depth of its penetration, and thus changing the groutability of the granular media. In these cases, the rheological properties of grouts become crucial to evaluate groutability of soils. In this study, rheological parameters, such as yield stress and apparent viscosity, of bentonite suspensions were controlled by an ionic additive, sodium pyrophosphate (SPP). The rheological properties of the modified bentonite suspensions were measured at various bentonite fractions (7.5, 10 and 12% by total mass of suspension) modified with 1, 3 and 4% SPP (by dry mass of bentonite). The modified bentonite suspensions were injected into three different saturated sand columns (Ottawa ASTM C778, Monterey #0/30 and aggregate sand) under constant pressure. The results showed that the SPP effectively improved the mobility of the concentrated bentonite suspensions and the injected pore volume significantly increased depending on the changes in the rheological parameters, especially the apparent viscosity. A new groutability criterion for clean sand is proposed based on the rheological properties of the suspensions, relative density of the sand, and the relative grain size of the sand and bentonite. The new proposed groutability criterion provides a more accurate prediction of groutability of clean sands when using modified bentonite suspensions.

1. INTRODUCTION

Bentonite has been a common material used in hydraulic barrier systems such as landfill liners and slurry walls due to its high swelling capacity. Recently, the application of bentonite suspensions to improve soil performance under static and dynamic loading has been studied (Haldavnekar et al. 2003; El Mohtar et al. 2008; Rugg et al. 2011). However, the application of bentonite suspensions in permeation grouting has been limited due to its low mobility and penetration depth, especially when concentrated suspensions (exceeding 5%) are utilized. In order to improve the penetrability of the suspensions through soils, various additives can be introduced into bentonite suspensions. In these cases, the modification changes the rheological properties such as yield stress and viscosity which, in turn, affect the groutability of sand.

While groutability of sand using cement-based grout has been widely studied, the application of such groutability criteria to bentonite suspensions may cause inaccurate predictions because of the differences in particle sizes and shapes as well as rheological properties. The groutability of sand with cement-based grout has been studied based on the groutability number, N , using grain size of both, soil and cement (Burwell 1958; Bell 1993; Incecik and Ceren 1995). More advanced groutability criterion using soil and grout parameters (grain size, relative density, fines content, w/c ratio, and injection pressure) was proposed by Akbulut and Saglamer (2002). However, the existing criteria do not reflect any changes in rheological parameters when different types of materials are utilized. In addition, Santagata and Santagata (2003) showed that the penetration distance of micro-fine cement grout varied with the water-cement (w/c) ratio of grout, the effective grain size (or hydraulic conductivity) of the sand, the injection pressure, and the amount of super-plasticizer. They observed that micro-fine cement grouts having the same w/c ratios but varying viscosities resulted in different penetration distances. This implies that the rheological parameters of the grouts should be incorporated in the groutability criterion rather than the weight ratio. This study presents an attempt to link rheological properties of bentonite suspensions to groutability of the saturated clean sands using the SPP modified bentonite suspensions. The rheological and soil parameters were investigated and correlated to the injected pore volume of suspensions. Based

on these observations, a groutability criterion of clean sand using the modified bentonite suspensions is proposed.

2. EXPERIMENT

2.1. Material properties

Three different sands with different effective grain size (d_{10}) were used in this study. All sands were classified as a SP based on a USCS classification. Table 1 summarizes the index properties of the tested sands based on ASTM standards. Commercial sodium-bentonite was used to prepare the suspensions. The bentonite particles are platy-like and are usually less than 1 or 2 μm in size (Mitchell and Soga 1976). The raw bentonite was screened through a No.200 sieve to minimize the impurities such as plagioclase feldspar, orthoclase, and muscovite minerals (Abend and Lagaly 2000). No further purification and/or gradation were applied to simulate the expected process for mass production and field application. The physical properties of bentonite are summarized in Table 2. Figure 1 shows grain size distribution curves for the tested sands and sieved bentonite. The d_{85} and d_{95} of the sieved bentonite were 7 and 25 μm , respectively. The main component of the bentonite includes SiO_2 of 61%, AlO_3 of 18%, CaO of 1%, Na_2O of 2%, Fe_2O_3 of 4%, and 12% of organic materials. The Na/Ca ratio which strongly affects rheological properties of bentonite suspensions was measured and found to be equal to 2. An average pH of the suspensions measured using JENCO 60 pH meter was 9.3. De-ionized water with a constant ionic concentration of 2×10^{-5} mM was used throughout this research.

In order to control the rheological properties of the bentonite suspensions, commercially available sodium pyrophosphate decahydrated ($\text{Na}_4\text{P}_2\text{O}_7 \cdot 10\text{H}_2\text{O}$) was utilized since the ionic additive has a pronounced dispersing capability as well as retaining the time dependent buildup in rheological parameters, both of which are desirable properties as a grout (Tchillingarian 1952; Abend and Lagaly 2000; Rugg et al. 2011). Specific gravity and molecular weight of the chemical were 1.8 and 446.06, respectively. Since the amount of SPP needed for each batch was very small, a 5% SPP solution was prepared in advance and the appropriate amount of solution was added to the water and bentonite to increase the accuracy of the measurements. The average pH of the 5% SPP solution was 9.5.

Table 1: Properties of the tested sands

Sand type	Gs	e_{max}	e_{min}	D_{10} (mm)	D_{30} (mm)	D_{60} (mm)	Cu	Cc	USCS
Ottawa C778	2.65	0.76	0.50	0.20	0.32	0.40	1.94	1.28	SP
Monterey #0/30	2.64	0.85	0.57	0.31	0.46	0.59	1.92	1.13	SP
Aggregate	2.68	0.64	0.43	0.28	0.48	0.94	3.36	0.88	SP

Table 2: Physical properties of bentonite

Plastic Limit	38%	Cation Exchange Capacity	91 meq/100g
Liquid Limit	440%	Specific area	712 m^2/g
Specific Gravity (Gs)	2.7	pH	9.3
Initial water content	8.3%	Swelling capacity	16 ml/2 g

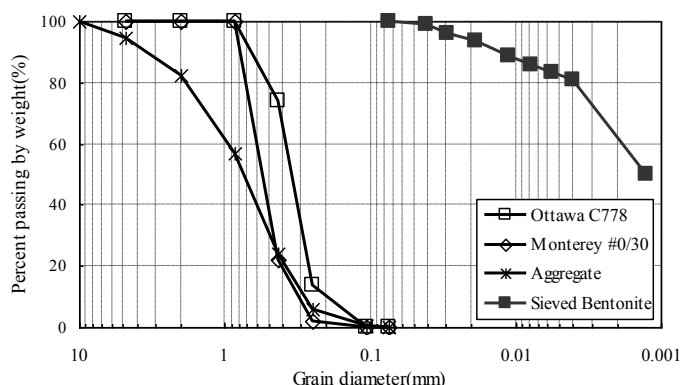


Figure 1: Grain size distribution curves for the tested sands and sieved bentonite

2.2. Sample preparation

The screened bentonite powder was mixed with de-ionized water; the weight fraction of bentonite suspensions was calculated as the weight ratio of bentonite to the total weight of suspensions. The concentration of SPP was calculated as the weight ratio of SPP to the dry weight of bentonite. In the calculation of bentonite fraction, the initial water content of bentonite was considered. The mixing process of bentonite suspensions included three steps; each step consisted of 5 minutes of high shear mixing of the grout followed by manual scraping of the sides and base of the mixing cup to remove any attached bentonite flocs. The mixing procedure greatly affects the rheological properties of the bentonite suspensions, particularly, the sequence of adding the SPP. In this study, 5% SPP solution was mixed with bentonite and water without any resting periods for immediate application of bentonite suspensions in the field. The sand was air pluviated with a funnel into a permeation cell, producing relative densities of 30 and 80%. A filter layer, consisting of a 25 mm thick layer of coarse sand ($1.2 \text{ mm} < D < 1.75 \text{ mm}$) on top of another 25 mm thick layer of pea gravel ($D > 4.75 \text{ mm}$), was placed at the top and bottom of the sand column to help produce a uniform supply of bentonite suspensions throughout the cross-section of the sand column.

2.3. Test equipment and procedures

2.3.1. Rheological test

A Physica MCR 301 rheometer, equipped with vane geometry, was utilized in this study. The vane used is a six-bladed vane, each having a thickness of 1 mm and a length of 16 mm and was inserted in a 80 mm in length and 29 mm in internal diameter cup. The radius of the vane was 11 mm, resulting in a 3.46 mm gap between the cup and the vane. Sample volume was maintained at 37 ml, which allows the vane to penetrate approximately twice its depth. The end effect of vane was small enough so that it was ignored for practical purposes (Barnes and Carnali 1990). All tests were performed at the room temperature of $22^\circ (\pm 0.03^\circ)$; the temperature was controlled using the built in Peltier temperature control system in the rheometer.

Stress ramp technique was utilized in this study. The shear stress was applied as a stepwise at a constant level of shear stress (3 Pa/step), resulting in a flow curve. The tests were programmed such that samples rested for 2 min after inserting the vane to provide a consistent initial condition. Each stress level was maintained for 12 sec and the data was recorded at the end of each interval. As shown in Fig.2 (a), yield stress in this technique is typically determined by fitting constitutive models such as Bingham, Herschel-Bulkley, and Casson to the experimental data. In this study, Herschel-Bulkley model (Eq.1) was utilized to estimate yield stress since it has been successfully adopted for bentonite suspensions in previous research (Kelessidis et al. 2007). The model produced an R^2 of at least 0.99 through all the experimental data.

$$\tau = \tau_y + K \left(\dot{\gamma} \right)^n \quad (1)$$

Where τ is the shear stress, τ_y is the yield stress, K is the flow consistency, n is the flow behavior index, and $\dot{\gamma}$ is the shear rate. However, it is difficult to capture the effect of SPP on the overall flow behavior of bentonite suspensions using the Herschel-Bulkley model which has 3 variables (Kelessidis et al. 2007) and therefore, the apparent viscosity, which is the ratio between the applied shear stress and shear rate, was monitored.

As shown in Fig. 2(b), the apparent viscosity of bentonite suspensions is highly dependent on the applied shear rate; for each bentonite suspension, the high shear rates (beyond 250 s^{-1}) produced essentially a steady-state (or equilibrium state) apparent viscosity. These equilibrium apparent viscosities were chosen for the analysis of permeation grouting since the injection process in permeation grouting is typically performed at high flow velocities (Markou and Atmatzidis 2002).

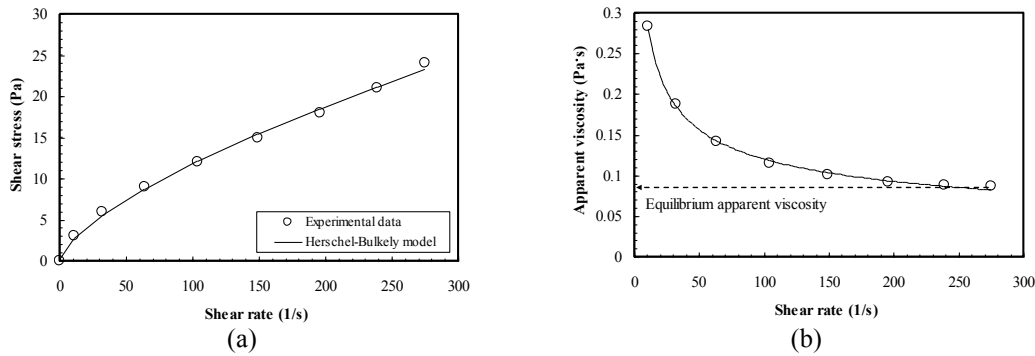


Figure 2: Determination of (a) yield stress and (b) apparent viscosity for 10% suspensions modified with 3% SPP

2.3.2. Injection test

Figure 3 depicts a schematic of the injection test setup. The rigid permeation cell was transparent and had a 3.8 cm in diameter and a 21 cm in height. The sand columns were saturated from bottom to top with a (head) pressure of 35 kPa to remove air bubbles in the specimen (ASTM D4320/D4320M-09). Bentonite suspensions were placed into a pressure cell within 2 min after mixing for consistency with the rheological tests. The bentonite suspensions were then injected into the sand column using a pressure panel at relatively low, but constant, pressures of 35 and 140 kPa. A balance was used to measure the weight of effluents during testing. The volume of effluent water was considered the same as the volume of the injected suspensions. Since the volume of effluents includes the amount of injected suspensions through the filter layer, the volume of injected suspensions was corrected for the pore volumes of the filter layer. The corrected volume of effluents was also normalized with the pore volumes of each sand column for consistent comparisons between different experimental parameters without having any effects from different porosities which were not controlled through this study. The grouting was considered successful if at least 1 pore volume could be injected at the pressure of 140 kPa for 10 min. This criterion has been used by Ozgurel and Vipulanandan (2005) for chemical grouting and was selected for this study based on the similarity of injection technique (constant pressure) and use of low injection pressures.

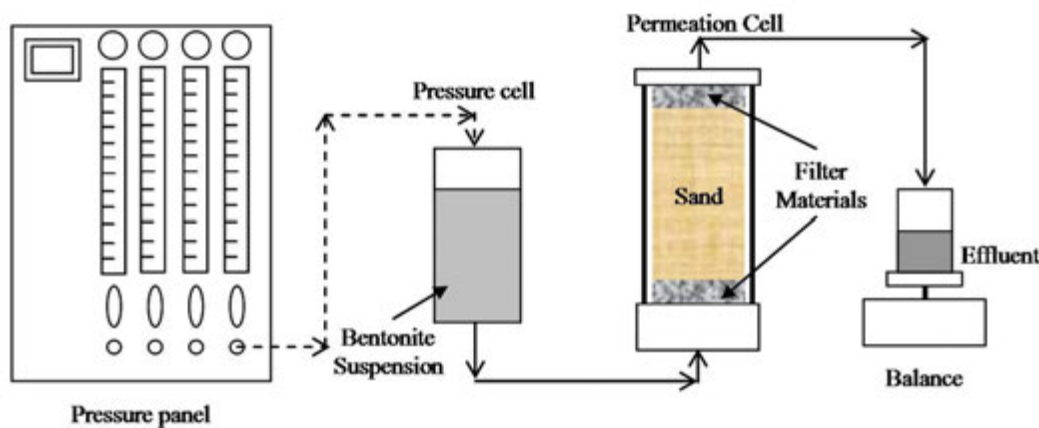


Figure 3: Schematic of constant pressure injection test setup (The dashed and solid lines represent a flow of air-pressure and liquid respectively)

3. RESULTS

Figure 4(a) and (b) display the yield stress and apparent viscosity at various bentonite fractions and SPP concentrations. Both rheological parameters were significantly reduced with the addition of small amount of SPP (1, 3, and 4% by dry weight of bentonite). The yield stress decreased significantly from 25, 137 and 467 Pa to 0.3, 0.3 and 0.9 Pa for 7.5%, 10% and 12% bentonite suspensions, when mixed with 1, 3 and 4% of SPP, respectively. In addition, the apparent viscosity at equilibrium was reduced by 30 to 50%. The results indicate that the SPP modification of bentonite suspensions can improve the mobility of concentrated bentonite suspensions. Since the yield stress of the modified suspensions reached very small values (approximately zero) with 1, 3, and 4% SPP concentrations, these mixes were selected for injection into the sand columns.

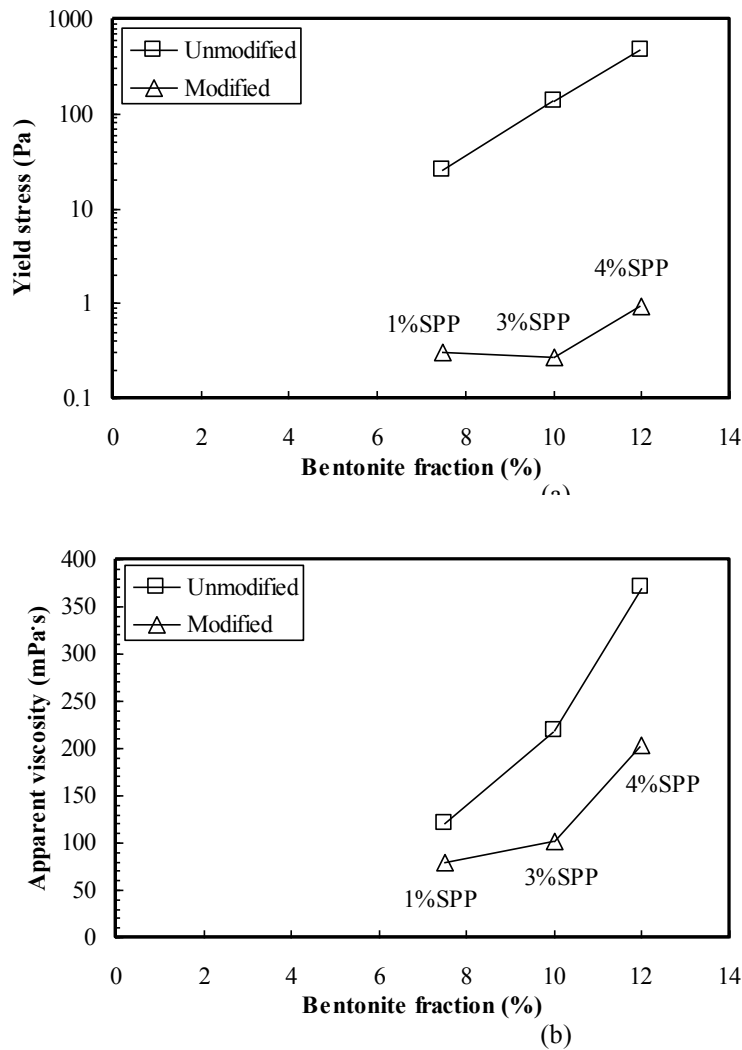


Figure 4: Rheological parameters of unmodified and modified bentonite suspensions (a) yield stress, and (b) apparent viscosity

Figure 5 shows the injected pore volume based on the yield stress of the bentonite suspensions injected at 35 kPa. As the yield stress increased, the injected pore volume of both the unmodified and modified bentonite suspensions decreased. However, there is no unique relationship between the pore volume of the injected suspensions and the yield stress. The injected pore volume (pV) of 7.5% bentonite suspensions increased from approximately 0.5 pV to 0.9 pV as the yield stress decreased from 25.1 Pa to 0.3 Pa, and the injected pore volume of 12% suspensions increased from approximately 0.1 pV to 0.3 pV with the decrease in the yield stress from 467.8 Pa to 0.9 Pa. The different injected pore volumes at a similar level of yield stress may be attributed to the fact that the flow of bentonite suspensions through sands was affected by both yield stress and particle fractions. Figure 6 displays injected pore volume based on the apparent viscosity at equilibrium which includes the effects of both, yield stress and particle fractions on suspension flow (De Paoli et al. 1992a). The injected pore volume consistently decreased with the increase in apparent viscosity regardless of bentonite fractions.

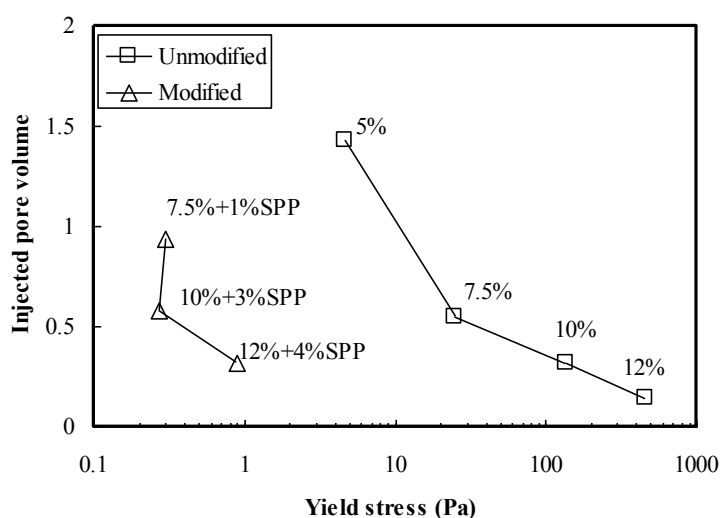


Figure 5: Injected pore volume based on yield stresses of various bentonite grouts at $d_{10}=0.20$ mm, $D_r=30\%$ and $P=35$ kPa

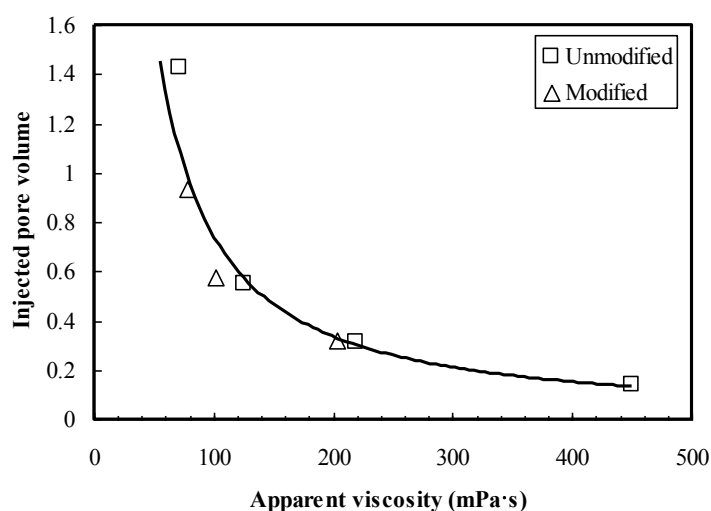


Figure 6: Injected pore volume based on equilibrium apparent viscosities of various bentonite grouts at $d_{10}=0.20$ mm, $D_r=30\%$ and $P=35$ kPa

Similar to cement-based grouts, the groutability of granular soils is related to the particle sizes of the soils, relative density and injection pressure. Although the degree of saturation can also affect the groutability, it was not considered in this study and all the tests were performed at nearly saturated conditions. Figure 7 shows injected pore volumes of 12% bentonite grouts with 4% SPP based on effective grain size of sands (d_{10}). The injected pore volume of grouts increased with the increase in effective grain size of sands, indicating an increase in the possibility of injection with an increase in effective grain size of sands. Akbulut and Saglamer (2002) and Santagata and Santagata (2003) observed similar trends. While the suspensions could not be injected up to 1 pore volume through Ottawa sand ($d_{10} = 0.20$ mm), they could be injected over 1 pore volume through aggregate and Monterey #30 sand ($d_{10} = 0.28$ and 0.31 mm, respectively). Figure 8 shows the comparison of the injected pore volumes at 35 kPa and 140 kPa. As the injection pressure increased, the injected pore volume increased for a given apparent viscosity and relative density. Figure 9 displays a comparison of the injected pore volumes at relative densities of 30 and 80%. The injected pore volume of suspensions slightly increased with an increase in the relative density of the sand. This is possibly due to the reduction in the total pore volume of sand with the increase of relative density implying that the same penetration distance would result in a higher grouted pore volume due to the lower void ratio. However, the overall effect of relative density on the injected pore volume was relatively small compared to other parameters such as effective grain size of sand and injection pressure.

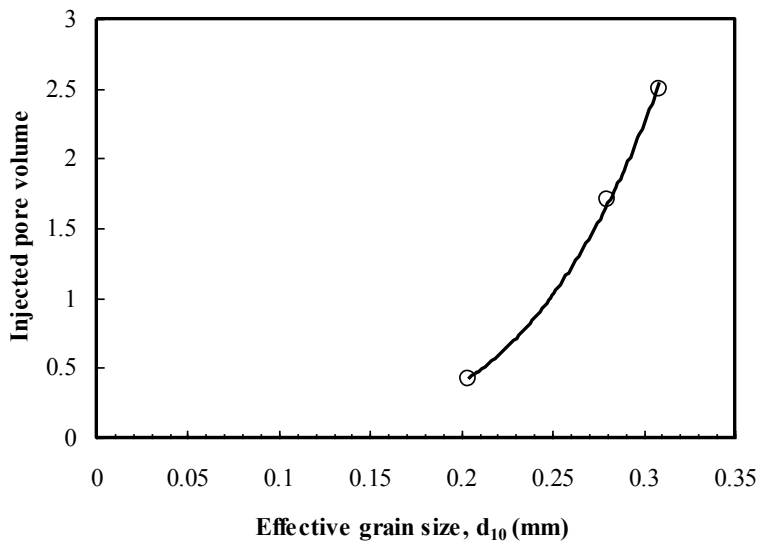


Figure 7: Injected pore volume based on effective grain size of sand at $\mu=203$ mPa·s, Yield stress=0.9Pa, $D_r=30\%$ and $P=140$ kPa

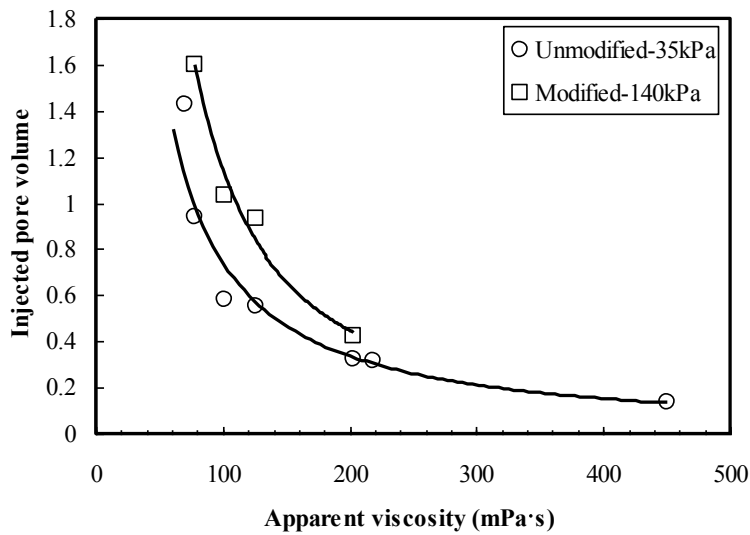


Figure 8: Injected pore volume based on injection pressure of 35 kPa and 140 kPa, $d_{10}=0.20$ mm and $D_r=30\%$

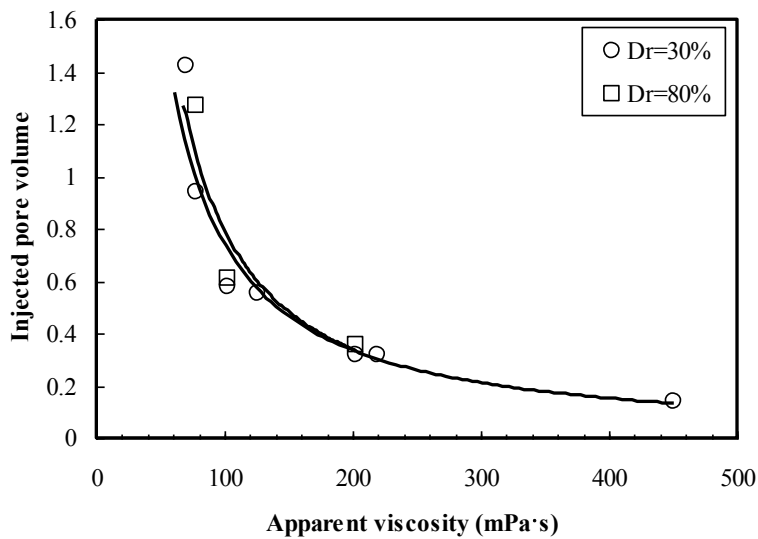


Figure 9: Injected pore volume based on relative density of sand, $d_{10}=0.20$ mm and $P=35$ kPa

4. DISCUSSION

Akbulut and Saglamer (2002) proposed a groutability criterion for granular soils considering factors that the Burwell's (1958) groutability ($N=d_{15,soil}/d_{85,grout}$) did not include such as injection pressure, relative density, fine contents, and water cement ratio. However, both criteria did not provide the quantity of the injected grout pore volumes; therefore, the definition of a successful grouting was vague or should be determined based on performance criteria after trial grouting.

In this study, a groutability criterion for bentonite suspensions was developed using the relationships observed for each parameter. The proposed groutability is similar to what Akbulut and Saglamer (2002) suggested in that similar parameters are utilized to evaluate groutability. However, the new criterion includes the rheological parameter rather than weight ratios of the grout. In addition, an attempt was made to correlate groutability to injected pore volume to quantify successful grouting (at least 1 pore volume at the pressure of 140 kPa for 10 min). For the global model to correlate the injected pore volume and a new groutability, a power function was selected since apparent viscosity showed a dominant effect on the injected pore volume with a power function. This function allows us to express the effects of all parameters with the following relationship:

$$N^* = \frac{d_{10,sand}}{d_{95,grout}} + \phi_1 \frac{(P/1 \text{ atm})^{\phi_2}}{(\mu_r)^{\phi_3}} + \phi_4 \left(\frac{Dr}{100} \right)^{\phi_5} \quad (2)$$

Where N^* is the groutability of bentonite grout, $\phi_1, \phi_2, \phi_3, \phi_4$ and ϕ_5 are the empirical constants, P is the injection pressure (kPa), μ_r is the relative viscosity ($\mu_{grout} \text{ (mPa}\cdot\text{s)}/\mu_{water} \text{ (mPa}\cdot\text{s)}$), Dr is the relative density. Initially, new groutability was calculated within the target range of groutability ($11 < N^* < 15$) with a trial and error basis, and then the empirical constants were determined by correlating the calculated groutability to the proposed equation using a root mean square error method. Based on this procedure, the empirical parameters of $\phi_1, \phi_2, \phi_3, \phi_4$ and ϕ_5 were determined as 295, 0.2, 0.9, 1.2 and 8.2 respectively.

Figure 9 shows the proposed correlation between groutability and the injected pore volumes. Since the proposed groutability is correlated to the injected pore volumes, a quantitative evaluation of successful grouting is possible based on the injected pore volumes. Based on this criterion, it was found that a soil is "Groutable" if N^* was greater than 12.5, and "UngROUTable" if N^* is less than 12.5. Most of the experimental data existed in $\pm 1\sigma$ of groutability with R^2 of 0.97, indicating that an approximated prediction of the injected pore volumes would be possible even in case of ungroutable soils or unsuccessful grouting prior to experiments.

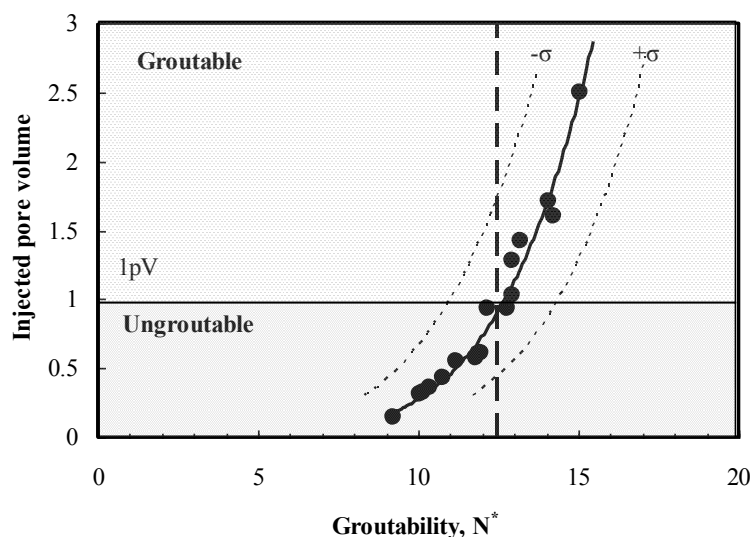


Figure 10: Proposed groutability criterion for clean sand using the modified bentonite suspensions

5. CONCLUSIONS

Rheological properties of the SPP modified bentonite grouts were investigated to be incorporated in determining the groutability of clean sands. It was observed that the introduction of small amounts of sodium pyrophosphate (1-4% by dry weight of bentonite) significantly reduced the yield stress and apparent viscosity of bentonite suspensions, and therefore, increasing the injected pore volumes. While the yield stress did not produce a unique relationship with the injected pore volume (possibly due to different particle fractions in each bentonite suspension), the apparent viscosity showed a consistent relationship with the injected pore volumes. The injected pore volume was also influenced by other parameters such as the effective grain size, injection pressure and relative density. As apparent viscosity and relative density decreased, the injected volumes increased. On the other hand, the injected pore volume increased with an increase in injection pressure. Based on the observed relationships between the injected pore volumes and experimental parameters (the properties of soil and bentonite grout and injection pressure), a new groutability criterion for clean sands using the SPP modified bentonite suspensions was proposed. The proposed groutability criterion suggests that clean sands are groutable when $N^* > 12.5$. This criterion also may be used for prediction of the injected pore volumes since most of experimental data was placed in the range of $\pm 1\sigma$.

REFERENCES

- Abend, S., and Lagaly, G. (2000). "Sol-gel transitions of sodium montmorillonite dispersions." *Applied Clay Science* 16(3-4), 201-227.
- Akbulut, S., and Saglamer, A. (2002). "Estimating the groutability of granular soils: a new approach." *Tunneling and Underground Space Technology* 17(4), 371-380.
- Barnes, H., and Carnali, J. (1990). "The vane-in-cup as a novel rheometer geometry for shear thinning and thixotropic materials." *Journal of Rheology* 34, 841-866.
- Bell, F. G. (1993). *Engineering Treatment of Soils*. E&FN Spon, London.
- Burwell, E. B. (1958). "Cement, clay grouting of foundations: Practice of the corps of engineering." *Journal of the Soil Mechanics and Foundations Division (ASCE)* 84, 1-22.
- De Paoli, B., Bosco, B., Granta, R., Bruce, D. A. (1992a). "Fundamental observations on cement based grouts: traditional materials." *Proceedings of Grouting, Soil improvement and Geosynthetics, GSP No. 40, ASCE, New Orleans, 474-495.*
- El Mohtar, C.S., Clarke J., Bobet A., Santagata M., Drnevich V. and Johnston C. (2008). "Cyclic response of a sand with thixotropic pore fluid." *Geotechnical and Earthquake engineering and Soil dynamics IV, Sacramento, CA. pp.1-10.*
- Haldavnekar, V., Bobet A., Santagata M., Drnevich V. (2003). "Soil treatment with a thixotropic fluid: an autoadaptive design for liquefaction prevention." *Proceedings of the 11th International Conference on Soil Dynamics & Earthquake engineering and 3rd Conference on Earthquake Geotechnical Engineering, Vol. II, pp. 553-560.*
- Incecik, M., and Ceran, I. (1995). "Cement grouting model tests." *Bulteni-Istanbul Teknik Universitesi*, 48, 305-318.
- Kelessidis, V. C., Tsamantaki, C., and Dalamarinis, P. (2007). "Effect of pH and electrolyte on the rheology of aqueous Wyoming bentonite dispersions." *Applied Clay Science*, 38, 86-96.
- Mitchell, J. and Soga, K. (1976). *Fundamentals of soil behavior*. Wiley, New York.
- Markou, I.N., and Atmatzidis, D.K. (2002). "Properties and performance of a pulverized fly ash grout." *Journal of Geotechnical and Geoenvironmental Engineering*, 128, 682-691.

Ozgurel, H., and Vipulanandan, C. (2005). "Effect of grain size and distribution on permeability and mechanical behavior of acrylamide grouted sand." *Journal of Geotechnical and Geoenvironmental Engineering*, 131, 1457-1465.

Rugg, D.A., Yoon, J., Hwang, H., El Mohtar, C.S., (2011). "Undrained shearing properties of sand permeated with a bentonite suspension for static liquefaction mitigation." *Proceedings of the Geofrontiers*, Dallas, TX, pp. 677-686.

Santagata, M., and Santagata, E. (2003). "Experimental investigation of factors affecting the injectability of microcement grouts." *Proceedings of the 3rd International Specialty Conference on Grouting and Ground Treatment*, ASCE, pp. 1221-1234.

Tchillingarian, G. (1952). "Study of the dispersing agents." *Journal of Sedimentary Petrology*, 22(4), 229-233.

SESSION OTHER

Ground freezing of diaphragm wall joints in Amsterdam

J.K. Haasnoot and D.G. Goeman, CRUX Engineering, the Netherlands, info@cruxbv.nl

ABSTRACT

This paper deals with the thermal design, sensitivity analyses and monitoring of the ground freezing in the Amsterdam North/South Line metro project. On two occasions in 2008 water and soil washed through a joint of the diaphragm wall at the "Vijzelgracht" metro station right in the historic city centre. This led to severe damage of houses adjacent to the station. The quality of all the joints in both Vijzelgracht and Rokin station was questioned, leading even to a questioning of the feasibility of the total project. As a measure to seal these joints, ground freezing is applied at every joint for the remaining excavation levels at the two station boxes. At each joint two freezing pipes are placed at the inside of the station. In total over 400 freezing pipes are used in the project. The paper describes the thermal design of the freezing pipe layout and the sensitivity analyses to minimise the risks during construction. In the design and also during monitoring, a combination of thermal and groundwater flow FEM calculations is used to control the freezing process. The excavation of both Vijzelgracht and Rokin station is now successfully finished. The ground freezing measure has proved to be successful in ensuring a watertight joint in complex circumstances.

1. INTRODUCTION

In recent years large scale ground freezing has been or will be applied in inner city projects in the Netherlands. To date ground freezing has only occasionally been used in the Netherlands. The technique was applied, using tailor made solutions, as part of the reconstruction of one of the busiest metro stations in Rotterdam (Haasnoot 2010). Ground freezing is applied to enhance soil strength and reduce permeability. The technique is considered to be expensive but also reliable, especially when water tightness is an important issue. The need for reliable techniques is high when constructing in busy and complex inner cities, where even a minor failure may lead to a severe effect on the surroundings and the project.

After an introduction of ground freezing and the application of this technique in the Netherlands, the paper focuses on the thermal design and sensitivity analyses that were performed both in the design stage and in the construction stage of the Amsterdam project.



Photo 1: Damaged historic houses adjacent to Vijzelgracht Station

2. GROUND FREEZING

2.1. Technique

Ground freezing is actually ground water freezing. The water in the ground is frozen, making the ground stronger and watertight. Consequently, the most important condition for the application of the technique is that the ground should contain water. The application of ground freezing is not dependent on the grain size or distribution of the soil, as is the case with many ground improvement techniques. Ground freezing is generally not limited by obstacles or objects in the substrata (Harris 1995).

The ice bonds the soil particles, enhancing ground strength and stiffness properties. Ice is impermeable, making a continuous ice body the perfect watertight sealant. Three phases can be distinguished in a freezing project; the freezing phase, the maintenance phase and the thawing phase. In the freezing phase the continuous frozen soil body is created according to the specifications. This phase requires the highest energy consumption. In the maintenance phase the actual construction works are executed. During this phase the frozen soil body should be kept according to specifications, which generally requires less energy consumption. The thawing phase starts when the freezing installation is stopped.

2.2. Closed and open system

The ground is frozen by extracting heat from the subsurface using a series of pipes in the ground through which a cold medium circulates. Distinction can be made between two systems to freeze the ground, a closed and open system. The closed system uses a cold fluid, generally a brine, that is circulated through the pipes and is cooled in the freezing plant. The operating temperature of brine freezing is generally around -35°C . The open system operates with a cold fluid that evaporates in the borehole. The latent heat that is required for the phase transition is extracted from the ground. The produced gas is flared. Usually liquid nitrogen is used in this process. The boiling temperature of liquid nitrogen is -196°C .

Freezing with the open system is relatively fast, because of the low temperature of liquid nitrogen. Its use is, however, relatively expensive and therefore it is employed in projects where the maintenance period is short. The closed system takes, with a relative high temperature of -35°C , more time to freeze the soil mass. The costs for this system are however relatively low and is generally applied in projects where the frozen ground needs to be maintained for a relative long period.

2.3. Thermal and mechanical design

The design of a ground freezing project consists of two parts; the thermal design and the mechanical design. The mechanical design is based on strength and stiffness parameters of frozen soil that are determined in laboratory tests. The strength and stiffness of frozen soil is temperature dependent. This means that the mechanical design sets the dimensions of the frozen soil body in combination with the allowable (average) maximum temperature. The objective of the thermal design is to provide a freeze pipe configuration that can fulfill these thermal conditions throughout the different construction stages of the project.

Monitoring is an integral part of the thermal design. The monitoring scheme should contain sufficient temperature measurements with which the status of the frozen soil body can be verified. The combination of monitoring information and thermal design calculations should lead to the conclusion that the frozen soil body fulfils the temperature criteria set in the mechanical design.

3. DUTCH FREEZING PROJECTS

One of the first large scale application of ground freezing in civil engineering in the Netherlands was in the seventies when ground freezing was used to connect caissons for the Amsterdam metro. Occasional examples are quoted where the technique was used inside existing structures. Where the basement floor, on which groundwater pressure is acting, temporarily needed to be removed (Rotterdam and Haren). In The Hague, the ground was frozen to allow connection of the underground parking garage to a governmental building. The reconstruction of the metro station Rotterdam Central Station is the Netherlands largest application of ground freezing to date and is an integral part of the construction process (Haasnoot 2010).

Cross connections in the bored tunnels that have been constructed in the past 15 years (tunnels in Betuweroute, Randstadrail, Western Scheldt tunnel, Hubertustunnel) in the Netherlands have all been

build using ground freezing. The construction of two cross connections in the Western Scheldt tunnels employing ground freezing closely monitored and analyzed within the Dutch centre of underground construction (COB). For a bored tunnel in the Rotterdam area the technique was used as a temporary measure to overcome construction problems in the start shaft. Also near the start shaft of the Amsterdam North/South metroline ground freezing has been applied. Near the start shaft, the bored tunnel was expected to go through existing wooden piles. The risk is that the pile tips are not cut off but will be displaced and possible get stuck in the tunnel boring machine (TBM). To fix these piles, a horizontal layer of frozen ground is to be created just above the TBM. The other application in this project has been to ensure water tightness for the joints in the diaphragm walls in two station boxes, as will be discussed in this paper.

4. GROUND FREEZING DEEP STATIONS NORTH/SOUTH LINE

4.1. Introduction

On two occasions in 2008 water and soil washed through a joint of the diaphragm wall at the “Vijzelgracht” metro station right in the historic city centre. This led to severe damage of houses adjacent to the station. The quality of all the joints in both Vijzelgracht and Rokin station was questioned, leading even to a political questioning of the feasibility of the total project. As a corrective measure ground freezing is considered, and after a first analyses it is concluded that brine freezing from the inside of the station box is feasible.

Besides each diaphragm wall joint, two freezing pipes are placed within the station box. After the frozen soil has reached the required dimensions, the soil is excavated. Once the joint is exposed, with a column of frozen soil besides it, steel plates are mounted over the joint. These steel plates will ensure a closed joint until the final concrete inner wall of the station is in place. The freeze pipes have a length of 15 m and with about 110 joints per station box, in total a 220 freezing pipes are installed at each station.

At the moment the freezing measures had to be taken the stations are half way excavation. The twelve meter thick Holocene top layer in Amsterdam, consisting of soft clay and peat layers, has already been removed. The remaining excavation levels are in sand and clayey sand conditions. The maximum excavation levels is 25 to 30 m, with an equivalent ground water head outside the station box. The final excavation level, and the tip of the freeze pipes, is in the stiff Eemclay layer.

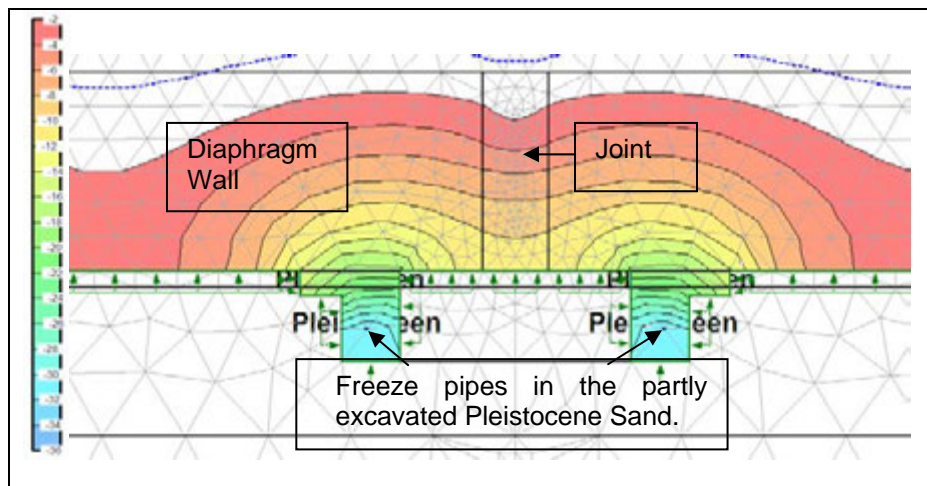


Figure 1: Detail of the isotherms at the diaphragm wall joint and partly excavation

4.2. Thermal Design

The main objectives of thermal design calculations are:

- Determination of the optimal lay-out of the freeze pipes in relation to the joint, both from drilling and thermal point of view;
- Determination of the energy capacity of the freezing installation;
- Determination of the required freezing up time.

The boundary conditions for the thermal design, in order to ensure the strength and stiffness requirements that followed from the mechanical design, are:

- Average temperature of the frozen soil in the joint should be lower than -5°C ;
- Thickness and location of the frozen soil mass is dependent of the depth and deviation of the diaphragm wall.

Furthermore it is required to take a ground water flow through the joint into account.

The thermal calculations are made with the finite element program TEMP/W. Both horizontal and vertical sections are analyzed. An example of the temperature field in a horizontal section is given in Figure 1.

4.3. Sensitivity analyses

Sensitivity analyses have been performed to further analyze the following important aspects;

- Influence of joint infill material;
- Influence of distance of freeze pipes to the wall;
- Influence of ground water flow through the joint;
- Influence of the vertical section.

The type of infill material in the joint is unsure, it could consist of the following material:

- Steel (when it was not possible to retrieve the stop-end);
- Sand;
- A sand – bentonite mixture.

From the sensitivity analysis it was concluded that a sand-bentonite mixture has the largest influence on the freezing up time. Besides this type of material also the width of the joint, e.g. the thickness of the infill material, has been varied in the calculations.

The influence of the possible deviations of the freezing pipes is analyzed by varying both the distance parallel and perpendicular to the diaphragm wall. The distance perpendicular has the most influence on the freezing up time. This part of the sensitivity analysis is implemented in the design by using a factor on the freezing up time.

The influence of ground water flow is determined with a combined calculation of TEMP/W and SEEP/W. An important input for the validity of this calculation is the total volume of water that is pumped out of the station in stationary situation. This volume was relatively low. From the calculations followed that the ground flow has an influence on the freezing up time, but, given the known total flow out of the station, this factor is not critical (see Figure 2).

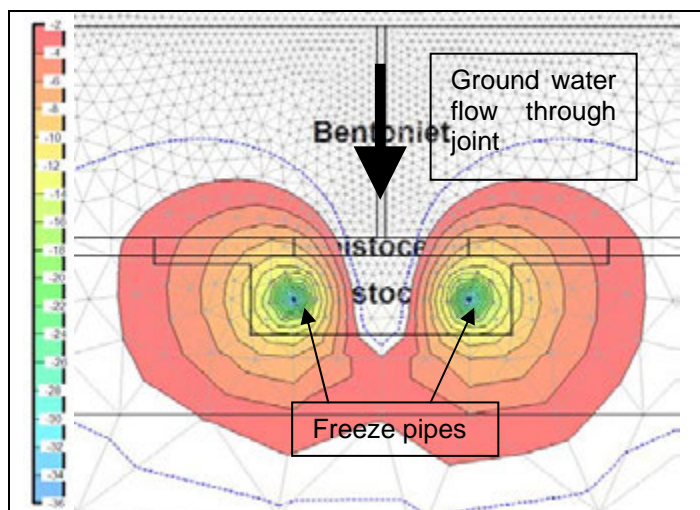


Figure 2: Detail of the isotherms with ground water flow through the joint during freezing up phase

Since the freezing pipes are placed from an excavation level in the station, the three dimensional heat flow will be a factor of influence. The excavation level will introduce additional heat in the ground which causes the isotherms to bend towards the inside of the station in the first meters below excavation level (see Figure 3). To reduce the freezing up time and to fulfill the temperature requirements within a reasonable time, isolation is applied. The influence of the excavation level on the isotherms will occur at

each excavation step. An additional measure that has been taken is to excavate deeper in the previous excavation step and to place the steel plates over the joints deeper than the excavation level. In this way the measure overlaps excavation steps, and the risk of not fulfilling the temperature criteria is minimized.

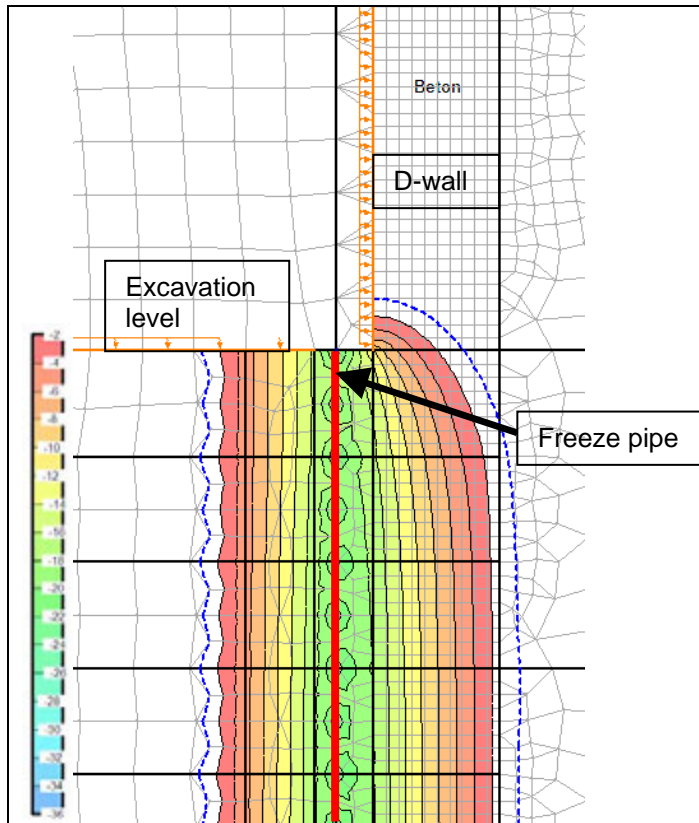


Figure 3: Example of the development of the isotherms in a vertical section

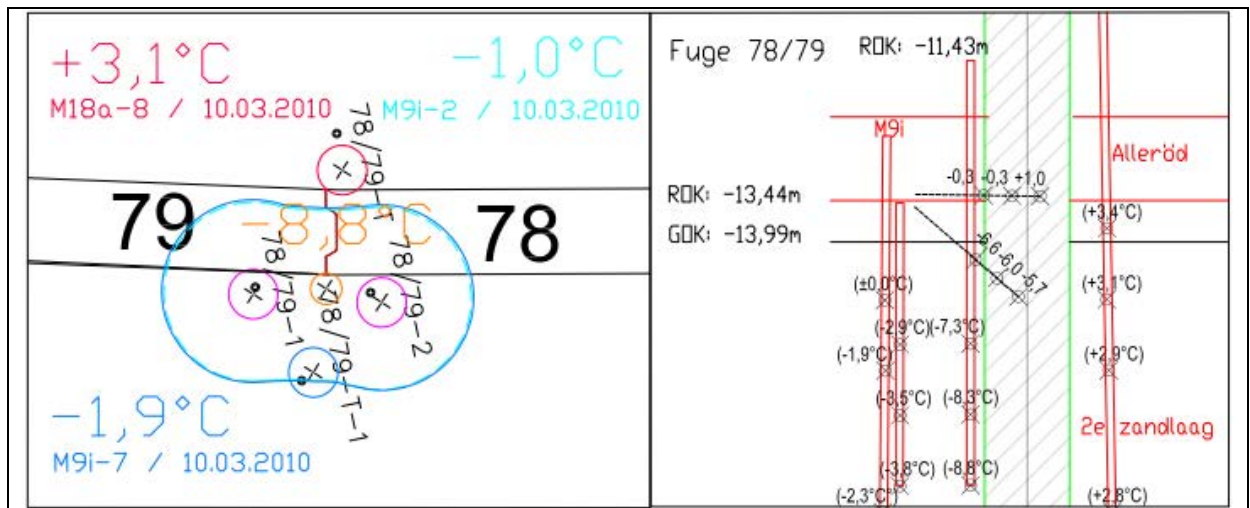


Figure 4: Example of monitoring top view (left) and section (right)

4.4. Monitoring

Monitoring is performed with two objectives:

- Determine the water tightness of the joint;
- Determine whether the joint fulfills the temperature criteria that are set by the mechanical design.

Especially the first criteria is, given the large consequences when failure would occur, very important to check by means of temperature monitoring. The sensitivity analysis has shown that the temperature development is slowed down within the station when a groundwater flow is present (Figure 2). To control

this risk it is necessary to perform a temperature measurement at each joint before the start of excavation. These temperature measurements are made just in front of the joint over the height of the next excavation level. To check the temperature criteria at a joint, the temperature profile over the joint has to be determined, which is relatively difficult measure. This detailed measurement is therefore only performed at a limited number of joints. At these joints also a temperature measurement is made in front of the joint as is done at every joint. With the temperature measurements, in combination with the thermal calculations, a conclusion can be made if the required criteria are fulfilled at all the joints. During the works monitoring has indeed proved its value as at several locations the temperature development stayed behind. At these locations different measures have been taken to reduce the additional heat flow and after some additional freezing time also at these locations the criteria have been fulfilled.

In Figure 4 an example of the monitoring set up of a detailed measurement is given. In the top view the freeze pipes are represented by purple circles. The other circles are boreholes with temperature measurements. An impression of the frozen soil mass is given by the large blue overlapping circles. In the section the temperature measurements point in depth are given, as well as the inclined drillings that are made in the diaphragm wall to get a temperature measurement at the joint itself.

5. CONCLUSIONS

Ground freezing is still hardly applied in the Netherlands, although large scale use of ground freezing in Dutch projects has shown that this technique contributes to a successful project design and execution of the work. The use of finite element calculations during design and execution of the works delivers an important contribution to the success of this technique. The use of ground freezing at Rokin and Vijzelgracht station of the Amsterdam North/South Line has shown that this technique is robust and provides a safe situation to continue excavation. From this recent experience can be concluded that ground freezing is a reliable ground improvement technique for complex inner city projects and that this technique will be more often applied in the Netherlands, given the fact that construction projects generally become more and more complex and challenging.

6. RECOMMENDATIONS

The application of ground freezing in large inner city projects leads to the following recommendations for the design and execution of the works:

- Sensitivity analyses contribute significantly in identifying and quantifying risks and defining effective measures.
- (Temperature) monitoring in combination with finite element calculation models play a key role in a successful ground freezing project
- The freezing up phase is generally the most critical part of the freezing process. Excavation can start as soon as the frozen soil mass fulfills the criteria. The program after “start excavation” should however be flexible and incorporate additional freezing-up time if, based on the temperature monitoring, a extension of the expected freezing up time is necessary. This additional time might also be necessary, as experience shows, because all the parties involved have to be convinced that the temperature requirements are fulfilled.
- Constructive cooperation and open communication between the parties involved, client and contractor, is of major importance for the progress of the project. The interpretation of temperature monitoring results can lead to discussions. Valuable construction time can be saved when the parties involved discuss and verify this data in an open discussion and together draw a final conclusion.

7. ACKNOWLEDGEMENTS

The authors want to kindly thank Max Bögl contractors and the city of Amsterdam for the cooperation in this challenging project.

REFERENCES

Haasnoot, J.K., 2010, *Large Scale application of Ground freezing in the Netherlands, Proceedings of the International Conference Geotechnical Challenges in Urban Regeneration, London 2010.*

HARRIS, J.S., *Ground freezing in Practice, 1995.*

SHRP 2 R02: Geotechnical Solutions for Transportation Infrastructure: A Web-Based Toolkit

Vernon R. Schaefer, Iowa State University, USA, vern@iastate.edu
Ryan R. Berg, Ryan R. Berg & Associates, USA, ryanberg@att.net
S. Caleb Douglas, Iowa State University, USA, calebd@iastate.edu

ABSTRACT

The second Strategic Highway Research Program (SHRP 2) was created by the U.S. Congress to address challenges of moving people and goods efficiently and safely on the nation's highways. Geotechnical transportation issues are addressed under the SHRP 2 Renewal Focus Area, in which the goal is to develop a consistent, systematic approach to the conduct of highway renewal that is (1) rapid, (2) causes minimal disruption, and (3) produces long-lived facilities. The R02 project is aimed at identifying geotechnical solutions for three elements: (1) construction of new embankments and roadways over unstable soils; (2) widening and expansion of existing roadways and embankments; and (3) stabilization of working platforms. The project includes evaluation of the effectiveness of mitigation measures; a catalog of materials and systems for rapid renewal projects; guidance for design and QC/QA procedures; methods for estimating costs; and sample specifications for the identified geotechnical materials, systems and technologies. This has all been integrated into a web-based, interactive information and guidance system to provide the data necessary for determining the applicability of 46 specific ground improvement and geoconstruction technologies to specific projects. This paper describes the information and guidance system and how it can aid users in accessing information about and engineering with these solutions.

1. INTRODUCTION

Although in existence for several decades, many geoconstruction technologies face both technical and non-technical obstacles preventing broader utilization in transportation infrastructure projects. The Strategic Highway Research Program 2, Project Number R02 (SHRP 2 R02) *Geotechnical Solutions for Soil Improvement, Rapid Embankment Construction, and Stabilization of the Pavement Working Platform* is investigating the state of practices of transportation project engineering, geotechnical engineering, and earthwork construction to identify and assess methods to advance the use of geoconstruction technologies. Such technologies are often underutilized in current U.S. practice, and they offer significant potential to achieve one or more of the SHRP 2 Renewal objectives, which are rapid renewal of transportation facilities, minimal disruption of traffic, and production of long-lived facilities. Project R02 encompasses a broad spectrum of materials, processes, and technologies within geotechnical engineering and geoconstruction that are applicable to one or more of the following "elements" of construction (as defined in the project scope): (1) new embankment and roadway construction over unstable soils; (2) roadway and embankment widening; and (3) stabilization of pavement working platforms.

The overall vision established for the project is "to make geotechnical solutions more accessible to public agencies in the United States for rapid renewal and improvement of the transportation infrastructure." Phase 1 of the R02 project consisted of six tasks focused on identifying those geotechnical materials, systems, and technologies that best achieve the SHRP 2 Renewal strategic objectives for the three elements. Explicit in the tasks was the identification and evaluation of technical issues, project development/delivery methods, performance criteria and quality control and quality assurance (QC/QA) procedures, and non-technical issues that constrain full utilization of geotechnical materials, systems and technologies. Through identification of obstacles, both technical and nontechnical, that constrain usage of geoconstruction methods, and mitigation strategies to overcome the obstacles, the research team developed an approach to identify existing and innovative technologies to enhance geotechnical solutions for transportation infrastructure. The Phase 1 work was discussed in detail in the SHRP 2 R02 Phase 1 report (Schaefer and Filz 2008) and Schaefer et al. (2009).

Phase 2 focused on 46 geotechnical materials, systems, and technologies that best achieve the SHRP 2 Renewal Strategic Objectives. These identified technologies are listed in Table 1. Phase 2 included development of a catalog of materials, processes, and systems for rapid renewal geoconstruction projects; and the evaluation and listing of design guidance and QC/QA procedures; methods for estimating costs;

and sample specifications. A catalog was developed which details the requirements for guidance on design, QC/QA, costs, and specifications into an integrated catalog and selection support system.

An information and guidance system was developed to provide a framework for applying the technologies. The system will promote more widespread use of ground improvement and geoconstruction technologies to achieve SHRP2 Renewal objectives. This system provides the data necessary for determining the applicability of specific technologies to specific projects, and then guides the user to information needed to apply and engineer with the selected technology. The information, guidance and selection system will guide the user to one or more potential technologies. From these potential technologies, the user can access the catalog which includes information necessary for screening (i.e., depth limits, applicability to different soil types, acceptable groundwater conditions, applicability to different project types, ability to deal with project-specific constraints, general advantages/disadvantages, etc.), as well as guidance on design methodologies, QC/QA, costs, and specifications. This paper describes the information and guidance system. Experienced engineers will benefit from the design, construction, and cost information provided in the catalog. Less experienced engineers, planners, etc. will also benefit from the technology selection assistance portion of the system to assess the feasibility of technologies to address project requirements/constraints.

Table 1: Technologies Included in the System

Aggregate Columns	Geotextile Encased Columns
Beneficial Reuse of Waste Materials	High-Energy Impact Rollers
Bio-Treatment for Subgrade Stabilization	Hydraulic Fill + Vacuum Consolidation + Geocomposite Drains
Blasting Densification	Injected Lightweight Foam Fill
Bulk-Infill Grouting	Intelligent Compaction
Chemical Grouting/Injection Systems	Jet Grouting
Chemical Stabilization of Subgrades and Bases	Lightweight Fill, EPS Geofoam, Low-Density Cementitious Fill
Column-Supported Embankments	Mechanical Stabilization of Subgrades and Bases
Combined Soil Stabilization with Vertical Columns (CSV)	Micro-Piles
Compaction Grouting	Mechanically Stabilized Earth Wall Systems (MSEW)
Continuous Flight Auger Piles	Onsite Use of Recycled Pavement Materials
Deep Dynamic Compaction	Partial Encapsulation
Deep Mixing Methods	Prefabricated Vertical Drains and Fill Preloading
Drilled/Grouted and Hollow Bar Soil Nailing	Rapid Impact Compaction
Electro-Osmosis	Reinforced Soil Slopes
Excavation and Replacement	Sand Compaction Piles
Fiber Reinforcement in Pavement Systems	Shoot-in Soil Nailing
Geocell Confinement in Pavement Systems	Screw-in Soil Nailing
Geosynthetic Reinforced Construction Platforms	Shored Mechanically Stabilized Earth Wall System
Geosynthetic Reinforced Embankments	Stone Columns
Geosynthetics Reinforcement in Pavement Systems	Vacuum Preloading with and without PVDs
Geosynthetics Separation in Pavement Systems	Vibrocompaction
Geosynthetics in Pavement Drainage	Vibro-Concrete Columns

2. DEVELOPMENT OF THE INFORMATION AND GUIDANCE SYSTEM

The scope of this information, guidance and selection system is limited to technologies applicable to one or more of the three “elements” of the project: (1) new embankment and roadway construction over unstable soils, (2) roadway and embankment widening, and (3) stabilization of pavement working platforms. The system was initially developed along the lines of these three elements. The system was developed with input from the research team members, the project Advisory Board (i.e., Stakeholders), an Expert Contact Group, Federal Highway Administration (FHWA), and SHRP 2. Comments from Stakeholder meetings assisted in developing the objectives and strategies of the final system. Stakeholder meetings were conducted throughout the project to bring together state agency transportation personnel, practitioners, contractors, and academics who work with the relevant geotechnical materials, systems, and technology areas. These meetings provided valuable brainstorming sessions to identify technical and non-technical obstacles limiting widespread, effective use of these technologies; to identify the available best opportunities for advancing the state of practice of existing and emerging technologies; and future directions of these technologies in transportation works. The goal of the system is to provide a comprehensive tool to provide guidance for applying these geoconstruction solutions to transportation infrastructure.

The objectives of the system were established as:

1. Identify potential technologies for design and construction of the following transportation applications:
 - Below grade applications (construction over unstable soils)
 - Above grade applications (construction over stable or stabilized soils)
 - Geotechnical pavement components (base, subbase, and subgrade) and
 - Working platforms
2. Provide guidance to develop a ‘short-list’ of applicable technologies based on a few key project and site characteristics.
3. Provide guidance for detailed project-specific screening of technologies with consideration of SHRP 2 Renewal Objectives: rapid renewal of transportation facilities, minimal disruption of traffic, and production of long-lived facilities.
4. Provide an interactive, programmed system to guide the user through the procedure.

Furthermore, the project Advisory Board stressed the following key points for the development of the system:

- The selection procedure should be simple.
- The process utilized for decision making should be transparent.
- Knowledge for potentially applicable technologies should emanate from the Phase 2 efforts.
- The user should be guided to a short-list (e.g., 3 to 5) of potential, unranked applicable technologies.
- Project research team and advisory board members should provide review as the system develops.

3. THE WEB-BASED INFORMATION AND GUIDANCE SYSTEM

An information, guidance and selection procedure has been developed for each “application.” In developing the system, the importance of properly identifying the potential applications was recognized. The first decision in the process is the potential application. The four applications (element (3) listed above was subdivided into two applications) for the R02 system are illustrated in Figure 1.

3.1. The Web-Based Information System

The homepage for the web-based information system is shown in Figure 2. The title of the web page is shown in the upper left. Along the left hand side of the page are buttons to the home page, project background, geotechnical design process, the catalog of technologies, the technology selection system, glossary, abbreviations, frequently asked questions, submit a comment, links, and an about this website; that are always available to the user. The part outlined in the bold box will change as other pages are selected. In subsequent screen shots only the material within the bold box will be shown. As shown within the bold box in Figure 2, there are four main parts to the system: Geotechnical Design Process, Catalog of Technologies, Technology Selection, and Glossary.

The Geotechnical Design Process page is included to alert the user to the basic background information needed to conduct geotechnical design such as project loading conditions and constraints, soil site conditions, and evaluation of alternatives. The page contains links to FHWA documents on review of

geotechnical reports, evaluation of soil and rock properties, subsurface investigation and instrumentation. During the development of the system it was realized that a large number of technical terms and abbreviations were used and that in some cases different technologies used terms in different ways. Thus, a Glossary is included with the system so that system users are able to find definitions of terms used in the various documents.

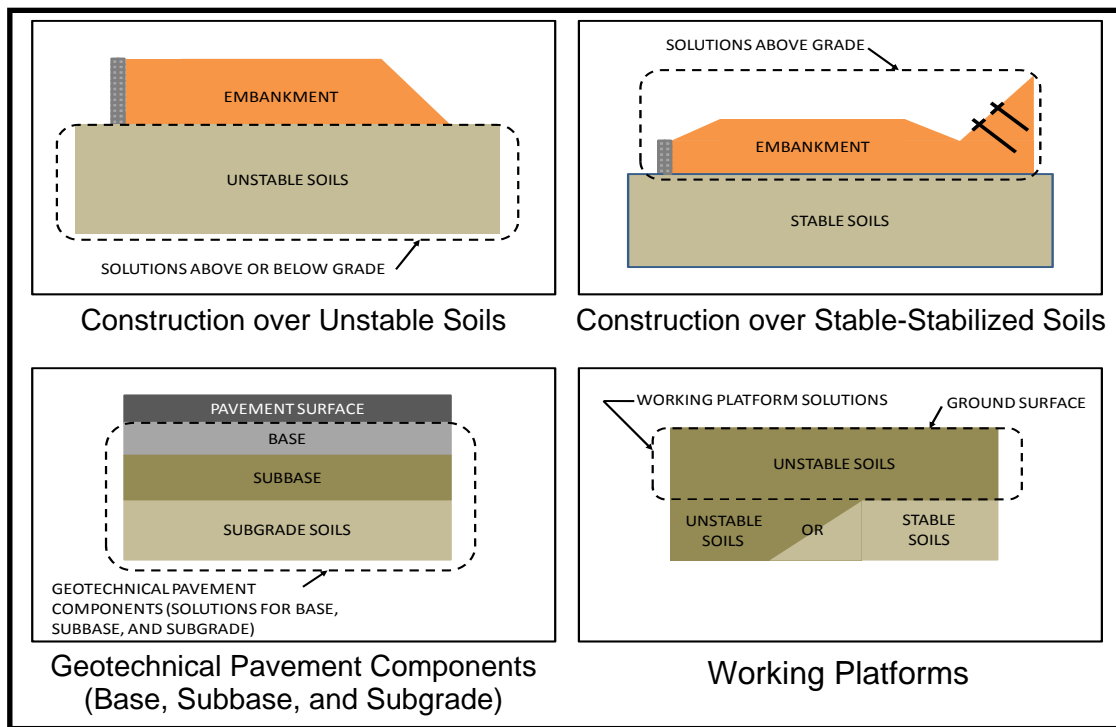


Figure 1: Illustration of the Four Application Areas for Technologies

The technologies can be accessed in several ways. The Catalog of Technologies page provides a listing of the 46 ground improvement and geoconstruction technologies in the system that addresses the four application areas. An exception is that two traditional technologies—excavation and replacement, and traditional compaction—are included as they are often-used “base” technologies, to which ground improvement and geoconstruction methods are compared. The list of technologies in the catalog is shown in Table 1. The name of each technology is a hot-link button on the website that takes the user to a web page for that technology, which will be discussed in more detail subsequently. The Technology Selection page provides two further means of accessing technologies: through a classification system and through an interactive selection guidance system. In the classification system, the technologies are grouped in the categories shown in Table 2. Thus an experienced engineer can access solutions according to particular categories of problems. The interactive selection system provides the user the opportunity to assess technologies based on several applications. A selection guidance procedure has been developed for each “application” area shown in Figure 1 and as defined in the R02 project work scope. In developing the system, the importance of properly identifying the potential applications was recognized. The Interactive Selection System is entered through the screenshot shown in Figure 3, wherein the first decision in the process is to select the potential application. In the selection system the list of applicable technologies is shown on the right-hand side of the page (see Figure 3), all of which are hot-linked to the respective technology pages. At the start of the selection all technologies will be shown on the right hand side, and as decisions are made, non-applicable technologies will be grayed out.

Table 2: Classification of Geotechnical Solutions by Application Categories

Earthwork Construction	Soft Ground Drainage & Consolidation
Densification of Cohesionless Soils	Construction of Vertical Support Elements
Embankments Over Soft Soils	Lateral Earth Support
Cutoff Walls	Liquefaction Mitigation
Increased Pavement Performance	Void Filling
Sustainability	

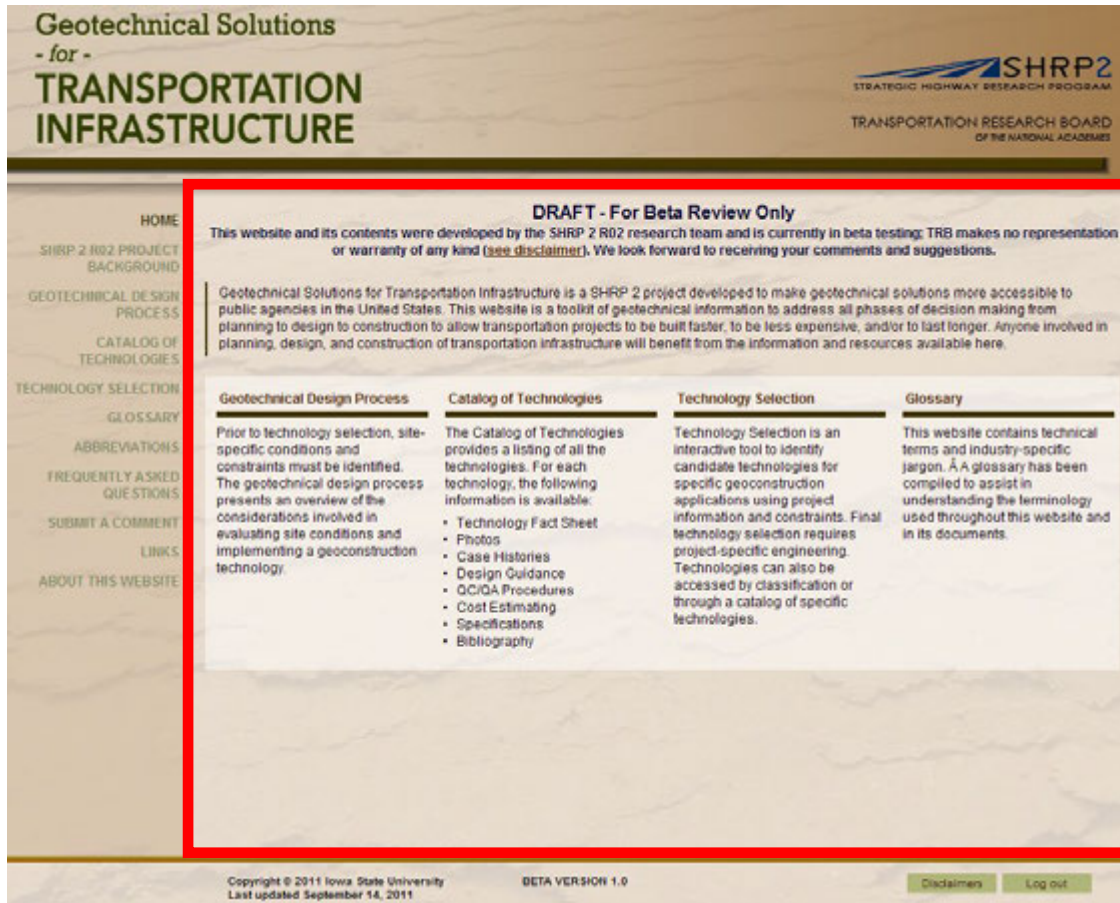


Figure 2: Homepage for the SHRP 2 R02 project information and guidance system.

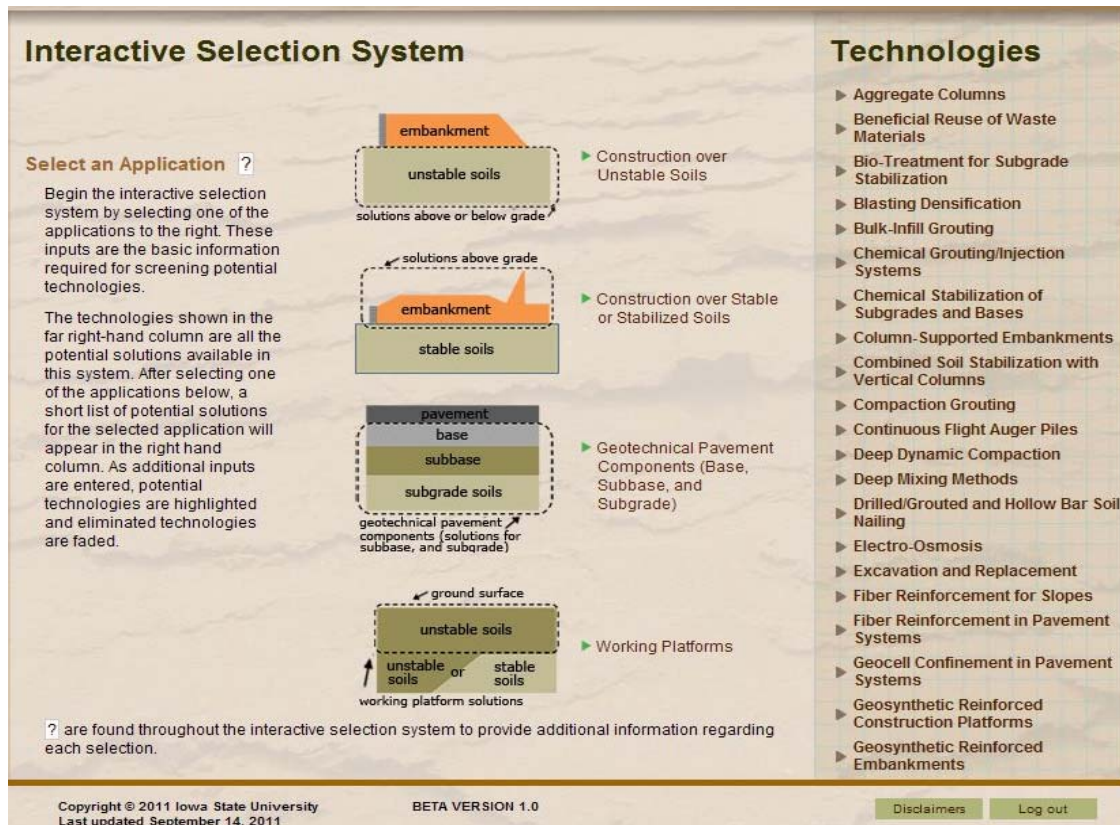


Figure 3: Screenshot for the interactive selection system page.

After clicking on one of the four application areas shown in Figure 3, the user will encounter a page requesting additional information to narrow the list of candidate technologies for the particular application. The number of possible queries for additional information is quite large and is dependent upon the application selected. The requested input and order of queries to the user were selected after considering the effect of the requested information on the determination of the potential technologies list. The potential queries (in no particular order) generated during development of the system are:

- What type of project is being constructed?
- What is the size of the project being constructed?
- Are there any project constraints to be considered in selecting a possible technology?
- What is the soil type that needs to be improved?
- To what depth do the unstable soils extend?
- At what depth do the unstable soils start?
- Is there a “crust” or “rubble fill” at the ground surface?
- What is the depth to the water table?
- How does the water table fluctuate?
- What constraints exist? (i.e., utilities, material sources, existing adjacent structures, etc.)
- What is the desired outcome of the improvement? (i.e., decrease settlement, decrease construction time, increase bearing capacity, etc.)
- What technologies does the user already have experience with?

The questions used to narrow the technologies are dependent upon the application selected. Generally, three or four questions are used to develop a short-list; which can then be further defined with answering additional questions. The user can select which questions to answer. To illustrate the use of the system, screenshots for Construction Over Unstable Soils are presented in below.

3.2. Construction Over Unstable Soils

Selecting the Construction Over Unstable Soils application leads to a decision process for foundation soil improvement or reduced loading. This application is focused on ground improvement to support embankments of any height or transportation structures such as walls or box culverts over unstable soils. This system is focused on identifying geoconstruction solutions to these problems; however, users must also consider that structural solutions to such problems may lead to the preferred alternatives.

From the list of potential queries, the two questions “What is the soil condition that needs to be improved?” and “To what depth do the unstable soils extend?” were selected as the initial questions to reduce the number of potential technologies for this application. These two queries were found to be most beneficial in providing a preliminary short list of applicable technologies. A screenshot of the first page for the Construction Over Unstable Soils application is shown in Figure 4. The list of technologies shown on the right of this page has narrowed from the complete list (46 technologies) shown on the previous Interactive Selection System page (Figure 3) to 26 technologies applicable to construction over unstable soils. The unstable soil conditions considered in the system are:

- Unsaturated and saturated, fine-grained soils
- Unsaturated, loose, granular soils
- Saturated, loose, granular soils
- Voids – sinkholes, abandoned mines, etc.
- Problem soils and sites – expansive, collapsing, dispersive, organic, existing fill, and landfills

The screenshot after answering the soil type is shown in Figure 5. On the right-hand side of the screenshot it can be seen that several technologies are grayed out, indicating that they generally are not appropriate for the soil type selected (unsaturated and saturated, fine-grained soil).

The next question to be answered is the depth range for improvement. The depth ranges selected for inclusion in the system are

- 0 – 5 feet (ft) (0 – 1.5 meters (m))
- 5 – 10 ft (1.5 – 3 m)
- 10 – 20 ft (3 – 6 m)
- 20 – 50 ft (6 – 15 m)
- Greater than 50 ft (15 m)

After answering the unstable soil depth question additional technologies may be grayed out on the right-hand side. At this point the user can stop and assess the candidate list of technology solutions or enter additional project-specific information as shown in Figure 6. Since many of these technologies may be used in combination with other ground improvement methods, guidance on combining technologies is contained in the linked *Integrated Technologies for Embankments on Unstable Ground* white paper (see Figure 4 or 5).

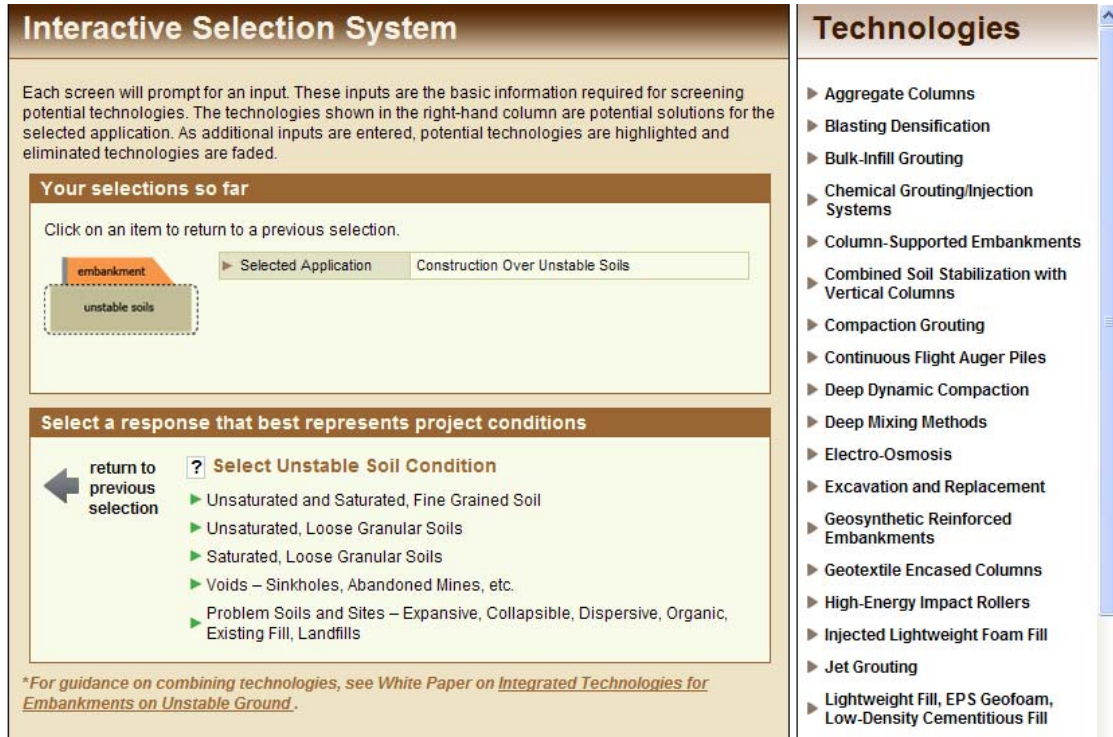


Figure 4: Screenshot for the first Construction Over Unstable Soils page.

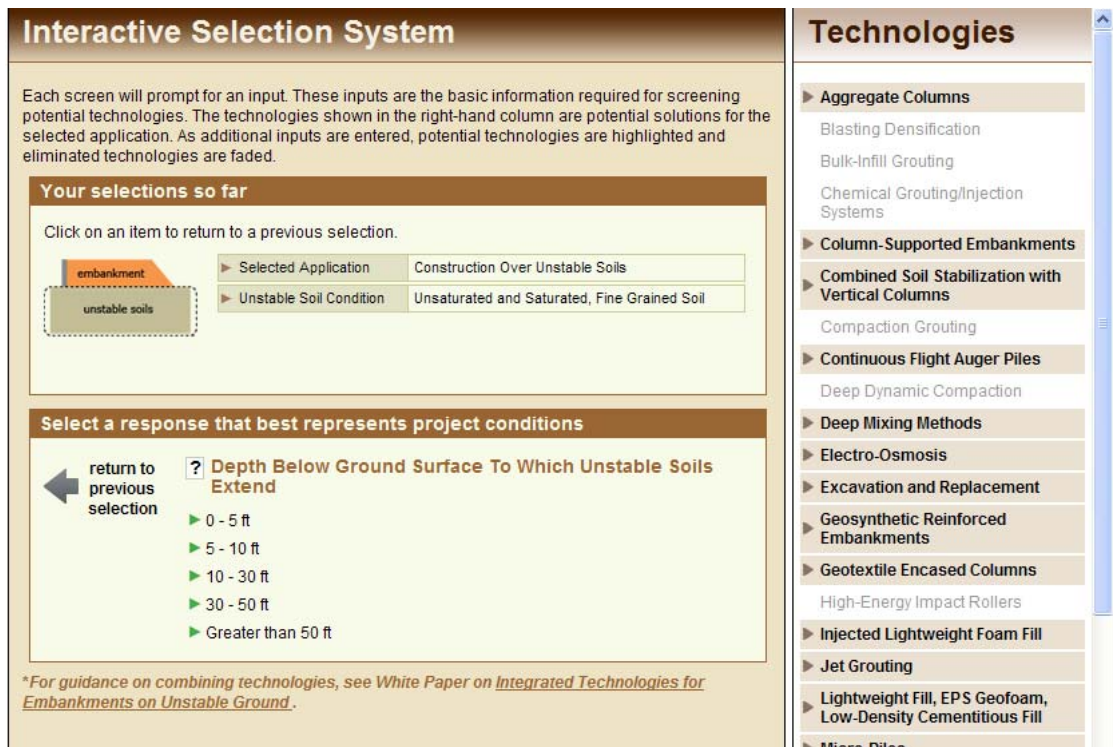


Figure 5: Screenshot for the second Construction Over Unstable Soils page.

Project-Specific Technology Selection

This will display selections made and the next set of questions.

Selections Made

The following selections have been made so far. Click on an item to return to a previous selection.

Selected Application: **Construction over unstable soils**

Unstable Soil Condition: **Unsaturated/Saturated, Fine Grained Soils**

Depth Below Ground Surface: **10 - 30 ft**

Select Project-Specific Characteristics

Select unstable soil condition that best describes site:

Are sufficiently thick peat layers present that will affect construction and settlement?

Are water bearing sands present in the soil to be improved?

Would any subsurface obstruction cause drilling difficulty, such as cobbles or boulders?

Purpose of Improvement:

Select Project Type:

Site Characteristics:

Size of Area to be Improved:

Project Constraints:

Technologies

- Aggregate Columns
- Blasting Densification
- Chemical Grouting/Injection Systems
- Column-Supported Embankments
- Combined Soil Stabilization with Vertical Columns
- Compaction Grouting
- Continuous Flight Auger Piles
- Deep Dynamic Compaction
- Deep Mixing Methods
- Electro-Osmosis
- Excavation and Replacement
- Geosynthetic Reinforced Embankments
- Geotextile Encased Columns
- High-Energy Impact Rollers
- Injected Lightweight Foam Fill
- Jet Grouting
- Lightweight Fills
- Micro-Piles
- Prefabricated Vertical Drains and Fill Preloading
- Rapid Impact Compaction
- Sand Compaction Piles
- Vacuum Preloading with and without Prefabricated Vertical Drains
- Vibrocompaction
- Vibro-Concrete Columns

Figure 6: Screenshot for the Project-Specific Technology Selection for Construction Over Unstable Soils.

A final technology selection screenshot in Figure 7 lists the resulting candidate technologies on the right-hand side of the page, when the questions have been answered as shown. It can be seen that the list of technologies applicable to the selected conditions has been narrowed. At this point one can click on any of the highlighted technologies to obtain technology specific information. For example, clicking on Prefabricated Vertical Drains and Fill Preloading will bring up the screenshot shown in Figure 8. The documents listed can be accessed through hot-links on the website. Ratings are provided for each technology on the degree of technology establishment and a technology’s potential application to SHRP 2 objectives.

As shown in Figure 8 a number of information documents about a given technology are accessible from the system. The list of documents available is shown in Table 3, which also indicates the format for the document. These documents are hot-linked and can be opened from this page or the box shown can be clicked and the selected documents can be printed or saved to a file for further use.

Table 3: Documents Available Through the Information and Guidance System

Available for Review or Download	File Format
Technology Fact Sheets	Adobe pdf
Photos	Adobe pdf
Case Histories	Adobe pdf
Design Procedures	Adobe pdf
QC/QA Procedures	Adobe pdf
Cost Estimation (General, Spreadsheet)	Adobe pdf and Microsoft Excel
Example and/or Guide Specifications	Adobe pdf and/or Microsoft Word
Bibliography	Adobe pdf

The information documents are generally provided in Adobe pdf format. The Technology Fact Sheets are two-page, summary information sheets that provide basic information on the technology including basic function, general description, geologic applicability, construction methods, SHRP 2 applications, complementary technologies, alternate technologies, potential disadvantages, example successful applications, and key references. The Photos show pictorially the equipment or methods used in the technology and can be valuable to obtain a perspective on the technology. The Case Histories provide

summaries of projects (which were preferably conducted in the U.S. by a state department of transportation (DOT)) and contain project location, owner, a project summary, performance, and contact information. The Design and QC/QA Procedures documents provide a summary of recommended procedures for the technology. The recommended design and QC/QA procedures come from an assessment of the current state of the practice of each technology. In cases where a well-established procedure (e.g., a FHWA manual) exists, that procedure is recommended. In cases of technologies with multiple design procedures, the assessment led to a recommendation of a procedure(s) to use. For a few technologies, design and/or QC/QA procedures were established based on additional research conducted during the project. For most technologies, there are two Cost Estimation documents available. The first provides an explanation of the cost item specific to the technology, generally emanating from the pay methods contained in specifications. Available regional cost numbers, generally from DOT bid tabs or national data bases, are compiled for each technology. The second document for Cost Estimation consists of an Excel spreadsheet developed to aid in estimating costs for use of the technology. The second document could not be prepared for some technologies (e.g., emerging technologies) due to insufficient information. The spreadsheet can be modified by the user to estimate specific project cost based on either a preliminary or final design. Guide specifications are provided for each technology in Adobe pdf and Microsoft Word (if available). The final document available for each technology is a bibliography compiled during the research project.

Figure 7: Screenshot for the Project-Specific Technology Selection with questions answered.

4. SUMMARY

The selection of a suitable method of ground improvement/geoconstruction method and optimization of its design and construction to meet specific project needs requires extensive background knowledge of available ground treatment technologies and careful evaluation of several factors. These factors include understanding the functions of the method, utilization of several selection criteria, the use of appropriate design procedures, implementation of the appropriate methods for QC/QA, and consideration of relevant cost components and environmental factors.

This paper describes a web-based toolkit developed for the SHRP 2 R02 project *Geotechnical Solutions for Soil Improvement, Rapid Embankment Construction, and Stabilization of the Pavement Working Platform*. A knowledge base has been compiled for 46 ground improvement and geoconstruction technologies, and a web-based information, guidance and selection system has been developed to facilitate and organize this knowledge so that informed decisions can be made. The value of the system is

that it collects, synthesizes, integrates, and organizes a vast amount of critically important information about ground improvement and geoconstruction solutions in a system that makes the information readily accessible to the user.

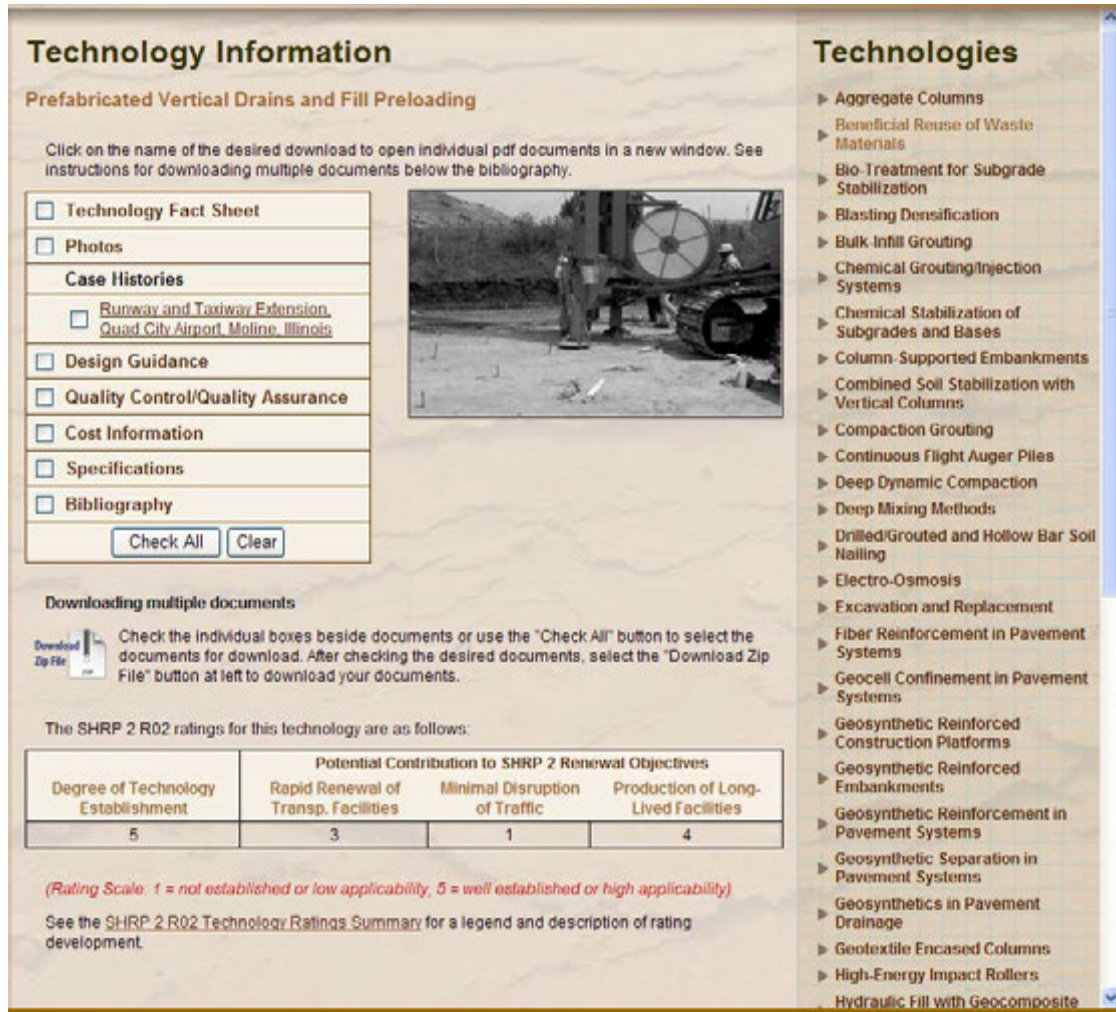


Figure 8: Screenshot for the Prefabricated Vertical Drains and Fill Preloading Technology showing list of available documents.

5. ACKNOWLEDGMENTS

The authors gratefully acknowledge the efforts of their colleagues on the research team: Donald Bruce, Barry Christopher, Jim Collin, Gary Fick, George Filz, Jie Han, Jim Mitchell, Dennis Turner, Linbing Wang, and David White. The contributions to the project of numerous graduate students from Iowa State University, Virginia Tech and the University of Kansas are greatly appreciated. This study was funded by the Strategic Highway Research Program 2, with James Bryant as program manager.

REFERENCES

Schaefer, V.R. and Filz, G.M. (2008). "SHRP2 R02 – Geotechnical Solutions for Soil Improvement, Rapid Embankment Construction, and Stabilization of the Pavement Working Platform, Phase 1 Report." Report to the Transportation Research Board of the National Academies.

Schaefer, V.R., Filz, G.M., and Vanzler, L.S. (2009). "SHRP2 R02 Phase 1 – Geotechnical Solutions for Soil Improvement, Rapid Embankment Construction, and Stabilization of the Pavement Working Platform." *Advances in Ground Improvement, Proceedings of the U.S.—China Workshop on Ground Improvement Technologies, GSP 188, Geo-Institute, American Society of Civil Engineers, Reston, VA, pp. 1-11.*

PLATINUM SPONSORS



GOLD SPONSORS



SILVER SPONSORS



ORGANIZING SECRETARIAT



Belgian Building Research Institute

With the support of TIS-SFT

